ENVIRONMENTAL EFFECTS ON BUILDINGS, STRUCTURES, MATERIALS AND PEOPLE

Edited by: Andrzej Flaga and Tomasz Lipecki

Lublin University of Technology, 2007

PREFACE

The Fifth Symposium "*Environmental Effects on Buildings and People – Actions, Influences, Interactions, Discomfort*" has been organized by Department of Structural Mechanics (Lublin University of Technology) and Wind Engineering Laboratory (Cracow University of Technology) under the auspices of Polish Group of International Association for Wind Engineering, The Science Committee of the Polish Association of the Civil Engineers and Technicians and Polish Society of Bridge Engineers.

The first Symposium within this subject was in Lublin (December 16–17, 1994), the second one in Kazimierz Dolny (October 26–28, 1997), the third one in Zwierzyniec (May 14–16, 2001); the fourth one in Susiec, (June 16–18, 2004). The fifth Symposium took place in Kazimierz Dolny (October 24–27, 2007) and was the second one of the international character.

The Symposium dealt, primarily, with the following topics:

- Environmental effects on buildings (wind action, snow load, ice covering load, thermal action of climatic and technological origin, effects resulting from thermal-humidity fields, etc);
- Interactions: building-wind, building-soil;
- Combinations of environmental actions and other types of actions on structures;
- Static and dynamic analysis of structures (high rise buildings, cooling towers, chimneys, masts, bridges, footbridges) subjected to environmental actions;
- Wind power engineering;
- Influences of wind on people in buildings and in built up areas;
- Thermal and fire influences on buildings and structures;
- Means and solutions of reduction of environmental effects on people and buildings (mainly aerodynamic);
- Changes of mechanical and physical properties of building materials and structures caused by weather influences;
- Problems of standardization of environmental effects on buildings and people;
- New measuring techniques of environmental effects on buildings and people.

Extended abstracts of 2-4 pages, containing objectives of the work, methods used, main results and conclusions, were invited. Nearby 50 contributions were received from 6 countries. Each abstract was reviewed by experts selected from the members of the Scientific Committee. As a results of the selection process, 40 papers of 71 authors were accepted for presentation and put together in the book of proceedings of this Symposium. Basing upon opinions of the Panel of Reviewers, the best papers presented during the Symposium were selected. These papers have been collected in this special monograph of the Symposium.

The papers published in this book have been elaborated by persons working professionally in many different scientific and scientific-research institutions. The papers have been divided into the following nine thematic groups:

- Building aerodynamics (3);
- Wind tunnel model tests (6);
- Snow loads and snow transport (4);
- Computational wind engineering (4);
- Damping and dampers (4);
- Wind energy and wind power plants (3);
- Thermal and fire influences on buildings, structures and materials (4);

- Steel and concrete corrosion (3);
- Miscellaneous (7).

Symposium topics are important from scientific and practical point of view. The published papers are of various character. These are original scientific and scientific-research works, studies of a review character, works referring to standards, codes and normalization documents as well as diagnostic elaborations.

During the Symposium, several special events took place, namely: bonfire, sightseeing of the historical town Kazimierz Dolny at the Vistula River and ship cruise on the Vistula River with beautiful landscapes on the both banks of the river.

We hope that discussions during this Symposium will be continued in the future during the next periodic meetings within this subject.

Both proceedings book of the extended abstracts and special volume of the selected papers can be ordered at the address of the Organizing Committee.

Chairman of the Organizing Committee   *Chairman of the Scientific Committee*
Prof. Andrzej Flaga   *Prof. Janusz Kawecki*

ACKNOWLEDGEMENT

Chairman of the Organizing Committee
Prof. Andrzej Flaga

4

TABLE OF CONTENTS

BUILDING AERODYNAMICS

THE USE OF SENSITIVITY ANALYSIS IN IDENTIFICATION OF VORTEX EXCITATION PARAMETERS

Tomasz Lipecki[*]

[*] Department of Structural Mechanics, Faculty of Civil and Sanitary Engineering,
Lublin University of Technology, Nadbystrzycka 40, 20-618 Lublin, Poland.

1. Introduction

In this paper the influence of several experimental parameters, which describe vortex excitation phenomenon of slender structures of circular cross-sections such as steel chimneys, concrete chimneys and concrete towers on lateral response of these structures has been considered.

Vortex excitation has been described by our own semi-empirical mathematical model. In general, equations of the model depend on experimental parameters, which can be defined on a basis of literature. Own computer program has been used to calculate both across-wind load caused by vortex shedding, as well as lateral response (displacements) of analyzed structures.

Time histories of lateral displacements have been calculated for characteristic (central) point of the vortex excitation domain along the structure. Several computations have been performed for various values of model parameters. Sensitivity analysis has been carried out on the obtained results of displacements. The following main aims of this analysis have been formulated:

1) To determine the significance of particular experimental parameters for lateral structure response under vortex excitation. In practice, it means that some parameters are less important for final results and some freedom in its determination can be left and from the other hand some parameters are crucial for result and should be determined carefully.
2) To indicate ranges of parameters values in which the influence on lateral response is strong or weak.
3) Finally, to indicate the most appropriate numerical procedures for those parameters.

2. Short description of the model

Detailed and precise description of the model can be found in several papers by Flaga [1,2,3], Flaga & Lipecki [4,5,6,7,8], Lipecki & Flaga [9], Flaga et al. [10].

This paper contains only short explanation of mathematical model bases and its numerical implementation, important from the point of view of sensitivity analysis. Semi-empirical model of vortex excitation has been described by five experimental parameters: α, $\sigma_{\hat{w}}$, k, B, L_w, of the following meaning:

11

α – experimental parameter which describes increase in effective cross-section diameter. This parameter is connected with the width of the vortex street of the lateral vibrating structure. On the basis of non-dimensional, theoretical analysis and experimental analysis from another hand its value should be taken from the range 0.7-1.54 (Flaga [1]; Flaga at al. [10]);

$\sigma_{\hat{w}}$ – standard deviation of vortex excitation. Value of this parameter depends on the amplitude level of the lateral vibrations. In the case when the amplitude level η exceeds (0.01-0.02)D or standard deviation of lateral displacements σ_{η} exceeds 0.006D, strong feedbacks of lateral vibrations and vortex shedding can appear. This can lead to considerable magnification of the coefficient $\sigma_{\hat{w}}$. In literature this value is often identified with the coefficient C_L which describes the whole across-wind load (not only vortex excitation). Values of $\sigma_{\hat{w}}$ can be obtained from Novak & Tanaka [11] as a function of cross vibration amplitude. It also can be taken from procedures given in ESDU in dependence on effective Reynolds number and surface roughness – ESDU 85038 [12];

k – factor of the value less then 1.0, that takes into account participation of atmospheric turbulence in the total across-wind load on a structure. The participation of the vortex excitation in the whole across-wind load can be given by relation: $\sigma_{wv}^2 = k \cdot \sigma_{wc}^2$, where σ_{wv}^2 – variance of the across-wind load caused by vortex excitation, $\cdot\sigma_{wc}^2$ – variance of the whole across-wind load. Usually, value of k is settled as equal to 1.0, which is not exactly correct, mainly in turbulent flow, when vortex excitation can appear in wider range of frequencies. Reduction of the value k below 1.0 has been proved in model investigations described by Howell & Novak [13], Novak & Tanaka [11];

B – non-dimensional bandwidth parameter. It depends evidently on turbulence intensity I_v. If I_v increases also the frequency bandwidth will increase. Exemplary values have been proposed by Novak & Tanaka [11], Vickery [14], Vickery & Basu [15].

In general, these parameters should be considered as functions of wind parameters such as: I_v – turbulence intensity, L_v – turbulence length scale, Re – Reynolds Number, α_w – mean angle of wind attack, and structure geometry parameters such as: K – cross-section shape, k_L – structure slenderness, k_B – cross-section slenderness, k_s – equivalent surface roughness. A lot of information about these values can be found in ESDU [12, 16,17].

The fifth parameter is L_w – non-dimensional correlation length scale. It depends on non-dimensional values of lateral amplitude of vibrations η or standard deviation of vibrations amplitude $\sigma_{\hat{\eta}}$, and can be derived from: ESDU [12] (as a function of standard deviation), Ruscheweyh [18, 19] or codes: DIN [20] and ENV [21] (as a function of amplitude).

Numerical simulation of vortex excitation is based on Weighted Amplitude Waves Superposition method (Shinozuka [22]). Load caused by vortex shedding is generated in point z_0 (the central point of the domain ΔL where vortex shedding is possible) in time interval T_0 and applied to the chimney in domain ΔL, where equivalent vortex load is fully correlated. Time history of displacements in point z_0 can be obtained using direct integration of motion equation of the analysed structure. Then standard deviation of displacements $\sigma_{\hat{\eta}}$ is calculated on the basis of short time interval of time history of displacements and next step(s) of load can be generated. The whole procedure is repeated M times and both time histories of load as well as of displacements are obtained in time

12

interval T, in which $\sigma_{\hat{\eta}} \neq 0$. All calculations are repeated N times and then estimator of maximum value, standard deviation and peak factor of displacements in time T, in point z_0 can be obtained according to the relationships:

- Standard deviation of displacements $\sigma\eta_j$ in time T in one process and estimator $\sigma\eta$ for N processes:

$$\sigma\eta_j = \sqrt{\frac{1}{T}\int_0^T \left(\eta_j(t) - \bar{\eta}_j\right)^2 dt} = \sqrt{\frac{1}{M}\sum_{i=1}^M \left(\eta_{ji} - \bar{\eta}_j\right)^2} \; , \qquad \sigma\eta = \frac{1}{N}\sum_{j=1}^N \sigma\eta_j \qquad (1)$$

- Maximum value of displacements $\eta_j^{\max}$ in time T in one process and estimator η^{max} for N processes:

$$\eta_j^{\max} = \max\left\{\eta_{j,i}\right\}, \qquad \eta^{\max} = \frac{1}{N}\sum_{j=1}^N \eta_j^{\max} \; . \qquad (2)$$

- Peak factor g:

$$\eta^{\max} = g \cdot \sigma\eta \; . \qquad (3)$$

In above equations: j – index of process, $j=1,2,...N$; i – index of predicted discrete values of time $t_i=i\Delta t$ in time T, $i=1,2,...,M$; $\eta_{ji}=\eta_j(t_i)$ – discrete values of displacements of the j-th process in time t_i.

3. Sensitivity analysis

There are two main versions of sensitivity analysis which can be used in practice:
1) First of them is based on the assumed aim function which is described by several parameters. In that case sensitivity is expressed by function derivatives against particular parameters. That variant has not been used in presented calculations because of too complicated procedures in which the coupled equation of motion should be solved at each step of computations. The right side of the equation of motion describing vortex excitation depends on standard deviation of lateral structure displacements $\sigma_{\hat{\eta}}$, and on experimental parameters which should be updated at each time step of calculations. Taking that into account another, simpler variant of analysis has been used in that paper.
2) In second variant lateral response of structure due to vortex excitation has been computed for various values of model parameters. The influence of one varying parameter, with other ones left constant at the average level has been investigated in calculations. The coefficient ω has been introduced to measure the sensitivity of lateral displacement to particular parameters. This coefficient has only theoretical meaning and can be estimated as follows:

$$\omega = \Delta w / \Delta p_i \,, \tag{1}$$

where: Δw – relative change in response of the structure, given by: η_{max} – maximum value of displacements, σ_η – standard deviation of displacements, g – peak factor; Δp_i – relative change in i-th model parameter. All considerations have been related to point z_0 of the domain ΔL.

4. Results

The most detailed results of sensitivity analysis concern steel chimney of the following basic data: height H=83.5m, outer diameter D=3.06m, steel width g=6-40mm. In the case of that chimney computations have been carried out in the wide range of experimental, input parameters. Sensitivity analysis for this chimney has indicated significance of particular parameters for final results. Obtained results have been confirmed by calculations conducted for other structures, but in the more narrow range of experimental input parameters. Sensitivity analysis has been used for lateral displacements of 7 steel chimneys, 6 concrete chimneys and 2 concrete towers.

All computations have been related to estimators of lateral displacements η_{max}, σ_η, g in central point z_0 of the domain ΔL where vortex excitation can appear.

Sensitivity analysis has been carried out for model parameters like: α, B, and k. Moreover, the influence of time interval length used in load simulation and the influence of equivalent surface roughness k_s have been also investigated.

The influence of the parameter σ_w has not been computed because it depends on determined value of Reynolds number Re and effective surface roughness k_s/D, as well. So, for the given structure changes of the value σ_w are small or similar to k_s. The influence of turbulence intensity I_v has been non-evidently checked according to the Vickery formula used in computations (B=2I_v+0.1). In general, values of experimental parameters have been estimated on the basis of procedures recommended by ESDU.

4.1. Domain ΔL, characteristic point z_0

The range of vortex excitation ΔL has a crucial influence on lateral displacements. Its range is limited only to a short part of the analysed structures. Moreover, there are only small changes of this range in time.

In the case of steel chimneys limitation of ΔL is caused mainly by small value of correlation length scale L_w (mainly for chimneys with small diameters) – fig. 1. In the case of concrete chimneys the limitation is caused by small value of the area under the curve of the mode shape which is computed in the procedure of assuming final domain ΔL – fig. 2. In the case of towers the limitation is also caused by small value of the area under the curve of the mode shape. Also the shape of structures themselves makes vortex shedding almost impossible to occur in large parts of the towers (many additional elements like antennas existing on the tower surface which disturb the wind flow around structure) – fig. 3.

14
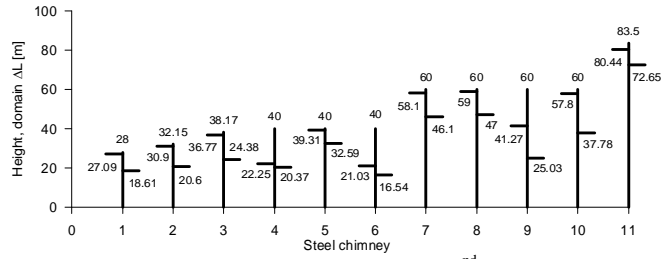
Fig. 1. Domain ΔL in the case of steel chimneys. (case 5,6,8,9 – 2nd mode shape of lateral vibrations).
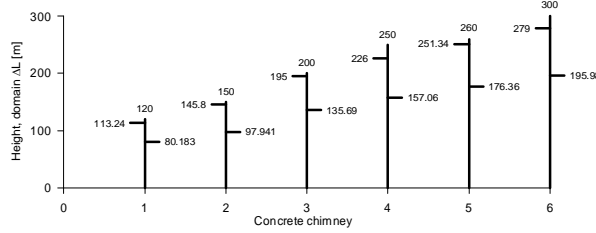
Fig. 2. Domain ΔL in the case of concrete chimneys.
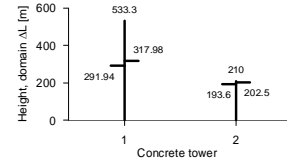
Fig. 3. Domain ΔL in the case of concrete towers.

Exemplary variation of values of domain ΔL and point z_0 location for steel chimney (H=83.5m) is presented in fig. 4. Upper limit of ΔL has been determined at the level of 80.44m. As it can be seen changes of these values in time are relatively small.
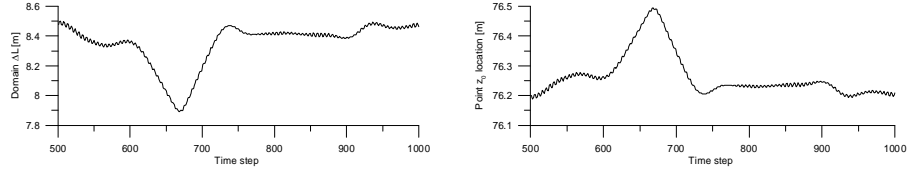
Fig. 4. Variation of ΔL domain (a), z_0 location (b).

4.2. Range of time steps

This is the basic value for load simulation. Both time of computations and computer power limitations caused that the algorithm of calculations should utilised short time interval of displacements to generate - in real time - next steps of load. So, several lateral responses of the structures have been computed taking into account different time intervals of the displacements used to provide load simulation. Considering results presented in fig. 5 two time steps Δt of load have been assumed in further simulations. Moreover, next steps of load have been generated on the basis of one period of natural vibrations of time steps of displacements. For short time intervals of displacements the increase of the value η_{max} is caused by feedback between lateral vibrations of the structure and vortex shedding.

15
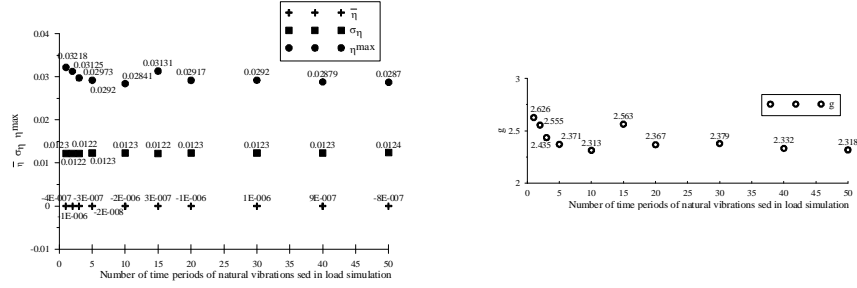
Fig. 5. Different time intervals of displacements used in simulation of two time steps of load.

4.3. Equivalent surface roughness k_s

This value is constant for given type of structures. Sensitivity analysis in that case can indicate type of structures that are more sensitive for any changes in surface (for example corrosion of the surface of steel chimney). Range of changes in value of k_s has been assumed as $5 \cdot 10^{-6} - 5 \cdot 10^{-4}$. Other input model parameters have been assumed at constant average level, respectively: $k=0.8$, $B=0.3$, $\alpha=1$. Lateral response of the exemplary structure has been more sensitive for small values of k_s (like for steel structures) – fig. 6. All discrete values have been approximated using logarithmic and power-law functions. Fitting coefficient is almost equal to 1.0 for both functions. The measure of sensitivity expressed by coefficient ω has been presented in fig. 7. Sensitivity coefficients reach relative high values for smooth surfaces (lower values of k_s) and decrease with increase in roughness.
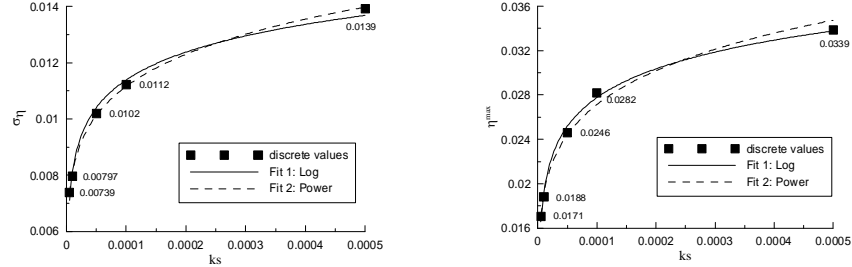
Fig. 6. Estimators σ_η and η_{max} against k_s.

Fig. 7. Sensitivity coefficients $\omega(\sigma_\eta)$ and $\omega(\eta_{max})$.

16
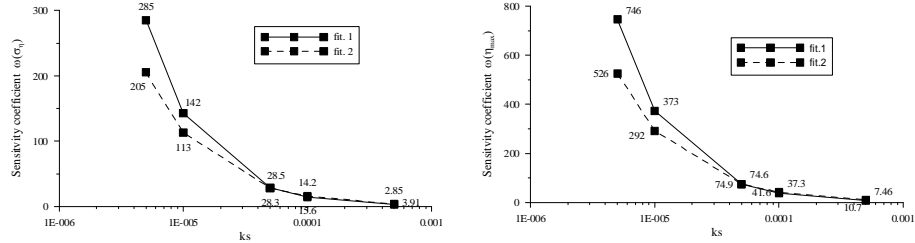
4.4. Parameter α

Parameter α used in calculation has been assumed in the range: 0.9-1.4 with the step 0.1. Other values have been constant and respectively equal to: k=0.8, B=0.3. It has been confirmed that for low values of lateral displacements the influence of α on results is small. Moreover, increase of α beyond 1.1 causes decrease in value of estimator η_{max}. This can be explained by self-limited character of vortex excitation. Parameter α has been established in further computations as α=1.0. There are values of σ_η and η_{max} collected together with approximation functions, and sensitivity coefficients computed as derivatives of those functions respectively in figs 8 and 9. As an approximation, polynomial and linear (in the case of σ_η) functions have been used. The presented results concern steel chimney (H=83.5m).
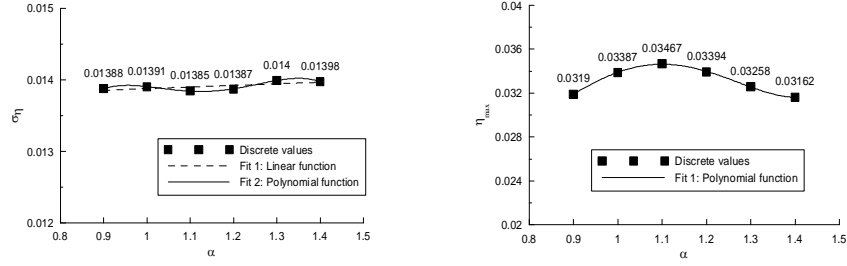
Fig. 8. Values of σ_η and η_{max} against α.
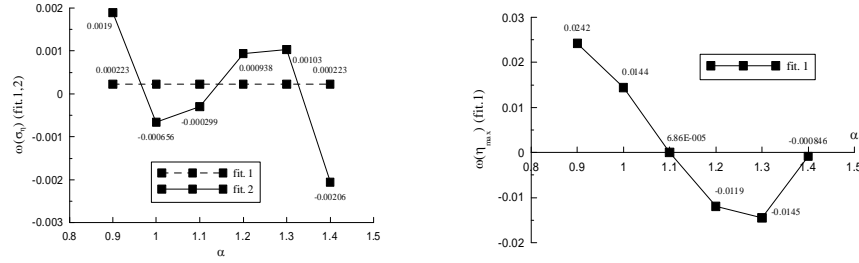
Fig. 9. Sensitivity coefficients $\omega(\sigma_\eta)$ and $\omega(\eta_{max})$.

4.5. Parameters B and k

Parameters B and k have been investigated in wide range. Values of other parameters have been settled at the constant level and then B has been assumed as equal to 0.05 (as for narrow-banded process) and k has been assumed as varying in the range 0.3-1.0. All calculations have been repeated for increasing values of B, up to 0.6 (as for extremely wide-banded process).

Power-law functions can be used as approximation functions in the case of varying B (fitting coefficient is in the range 0.97-1.0). Results given in σ_η and η_{max} are more sensitive for low values of B in each surface cross-section. Linear and power-law functions

17

have been assumed in perpendicular direction for varying k (coefficient of linear fitting is about 0.98, coefficient of power-law fitting is almost equal to 1.0). Both estimators σ_η and η_{max} are similarly sensitive in each surface cross-section.

The following diagrams present the obtained results, respectively: surface plots of σ_η and η_{max} collected together with approximation functions – fig. 10; approximation functions in surface cross-sections for $k=0.8$ – fig. 11 and for $B=0.8$ – fig. 12; surface plots of sensitivity coefficients computed as derivatives of exponential functions – fig. 13.
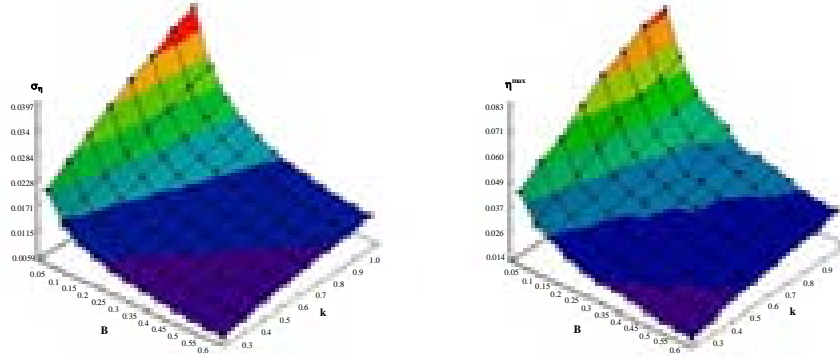
Fig. 10. Spatial distribution of σ_η and η_{max} for different B i k.
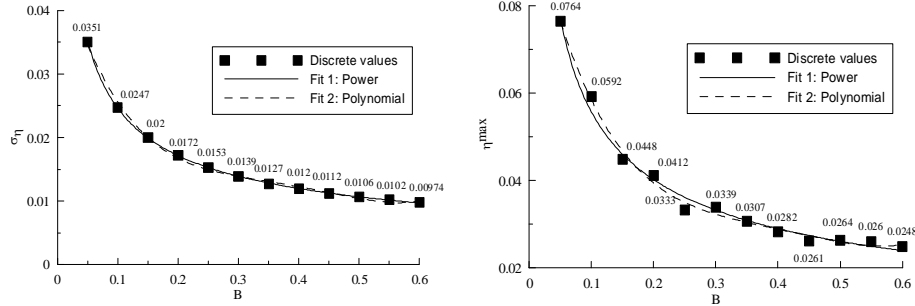
Fig. 11. Approximation functions in one of the surface cross-sections ($k=0.8$).
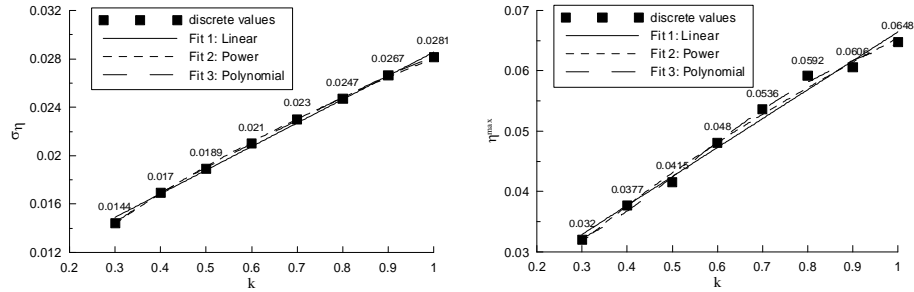
Fig. 12. Approximation functions in one of the surface cross-sections ($B=0.1$).

18
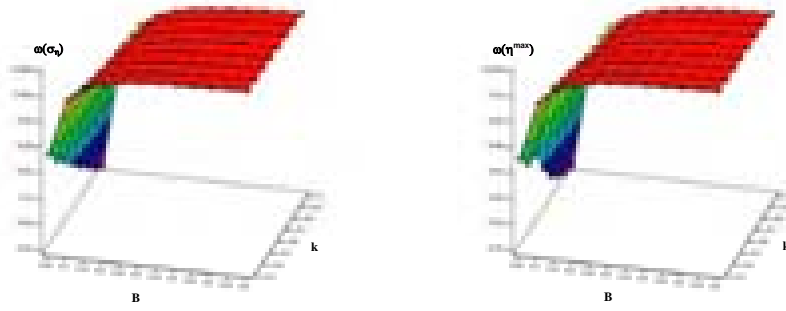
Fig. 13. Spatial distribution of sensitivity coefficients $\omega(\sigma_\eta)$ and $\omega(\eta_{max})$.

Precise sensitivity analysis for parameters B and k has been performed for steel chimney of the height 83.5m. Other structures have been computed in more narrow range of parameters variation, and sensitivity analysis has been used only to confirm the preliminary conclusions. There are some additional surface plots of estimators η_{max}; surface cross-sections for constant B and k respectively and surface distribution of sensitivity coefficients in the cases of other structures presented in figs 14-17.
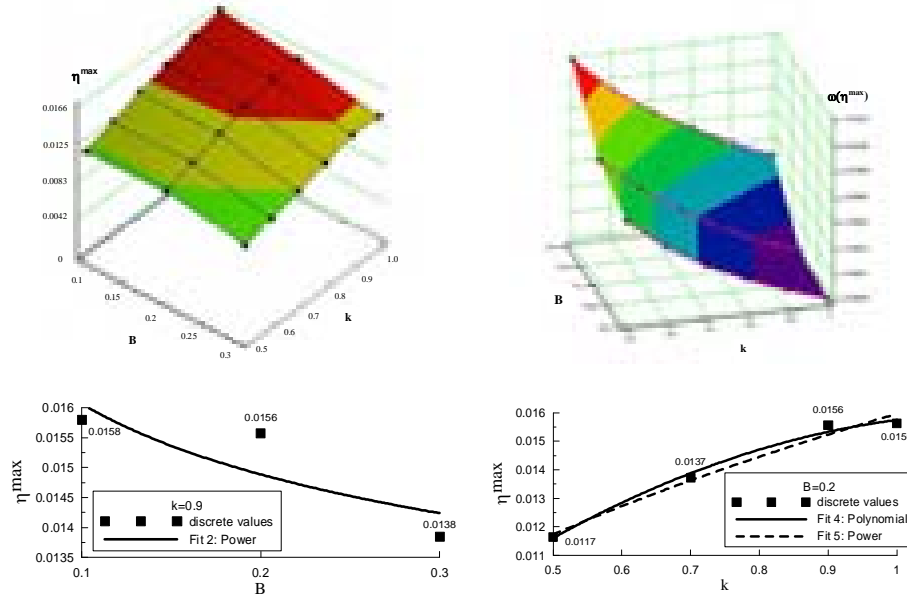
Fig. 14. Steel chimney: H=32.146m, D=1.25m.

19
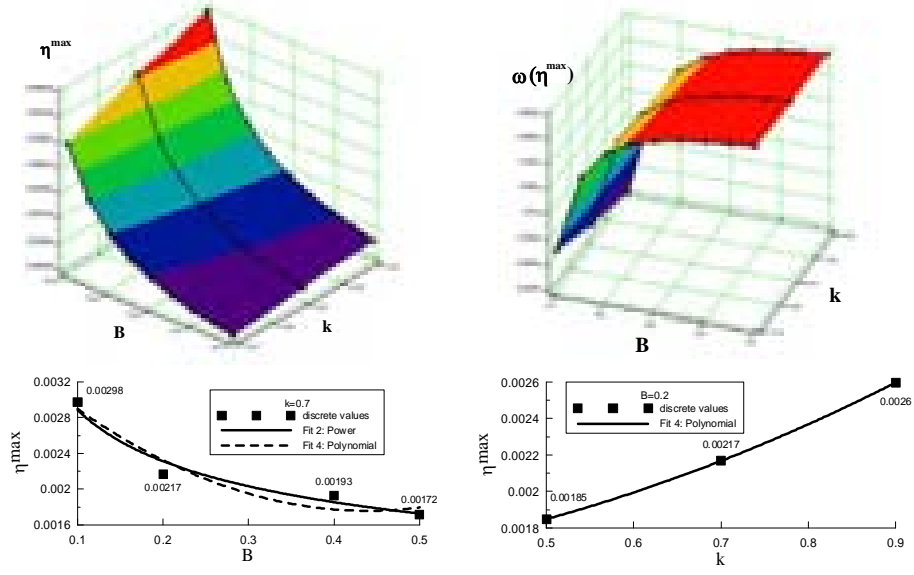
Fig. 15. Steel chimney: H=60m, D=4.0-1.0m.
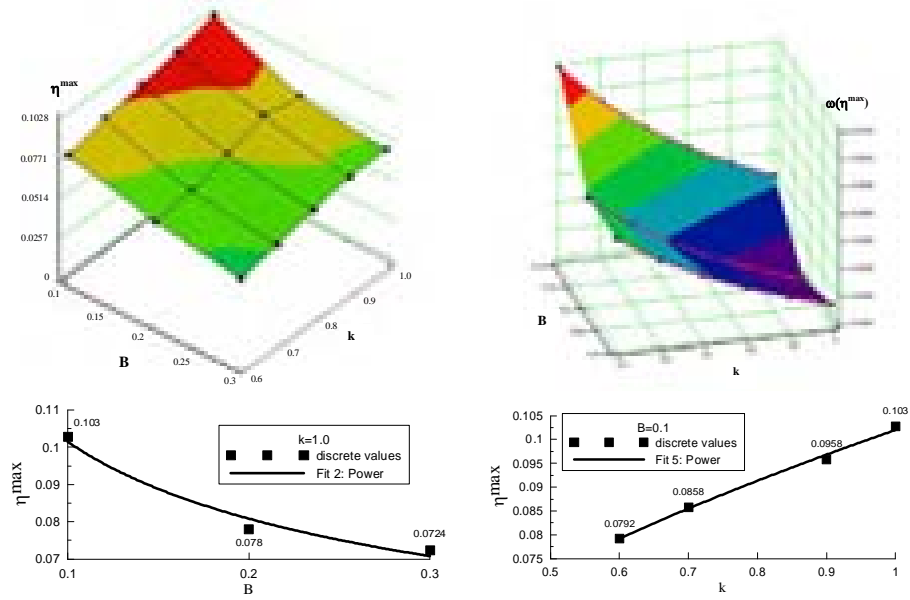
Fig. 16. Concrete chimney: H=260m, D_b=15.8m, D_t=7.7m.

20
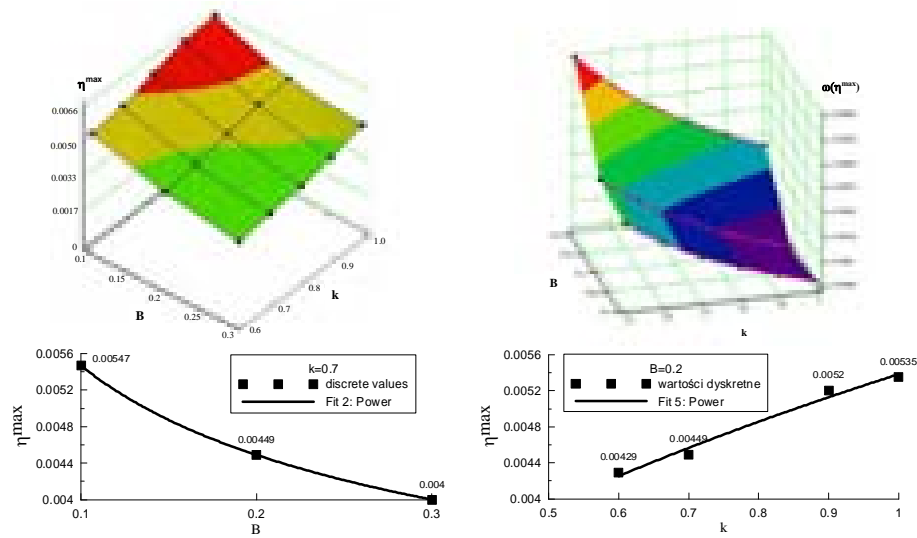
Fig. 17. Ostankino Tower: H=533m.

5. Conclusions

Considering results concerning the sensitivity analysis of lateral displacements of slender tower-like structures caused by vortex excitation, some final conclusions can be formulated:

1) Version of sensitivity analysis used in that paper can be a useful tool to determine the influence strength of particular mathematical model parameters on across-wind load and lateral response of the structure as well. Such analysis can indicate ranges of parameters in which lateral response is more sensitive, as well.

2) Lateral displacements of the chimney strongly depend on k and B. Computations of other steel chimneys and concrete chimneys and towers confirm that statement. The influence is the strongest in the case when the k value is high and the B value is low – it means that vortex excitation is deciding in across-wind load (k) and moreover, vortex shedding is almost of harmonic character (B).

3) Parameter α has the weak influence on lateral response, and its value can be accepted as equal to 1.0 in computations. For α>1.1 values of estimators σ_η and η_{max} decrease. It can be caused by self-limited character of vortex excitation.

4) There is a considerable influence of k_S on results, mainly for small values of k_S. Sensitivity coefficients ω are higher for smooth surfaces. It can be stated, that the lack of proper maintenance of steel chimney surface can magnify lateral response under vortex shedding.

References

[1] Flaga A., *Wind vortex-induced excitation and vibration of slender structures. Single structure of circular cross-section normal to flow*, Monograph 202, Cracow, Poland, 1996.

21

[2] Flaga A., *Nonlinear amplitude dependent self-limiting model of lock-in phenomenon at vortex excitation*, J. Wind Eng. Ind. Aerodyn., 69-71, 1997, p.: 331-340.

[3] Flaga A., *Universal formulae for power spectral density of vortex-induced excitation of elastically supported circular cylinder*, 4th BBAA., Bochum, Germany, 2000, p.: 625-629.

[4] Flaga A., Lipecki T., *Comparative study of vortex excitation for various tower-like structures*, Proc. 10th ICWE, Copenhagen, Dania, 1999, p.: 423-430.

[5] Flaga A., Lipecki T., *Simulation of across-wind action caused by vortex excitation*, Proc. 4th EACWE. Praha, Czech Republik, 2005, p.:112-113.

[6] Flaga A., Lipecki T., *Implementacja numeryczna własnego modelu wzbudzenia wirowego*, Inżynieria i Budownictwo 8, 2005, p.: 428-431 (in Polish).

[7] Flaga A., Lipecki T., *Wzbudzenie wirowe konstrukcji wieżowych o przekroju kołowym zmiennym wzdłuż wysokości*, Proc. 3rd Symp. EEBP, Zwierzyniec, Poland, 2001, p.: 45-54.

[8] Flaga A., Lipecki T., *Generation of vortex excitation of slender structures*, Proc. 4th Symp. EEBP, Susiec, Poland, 2004, p.: 15-18.

[9] Lipecki T., Flaga A., *Influence of corrosion of steel chimneys on its response under vortex excitation*, Proc. 12th ICWE, Cairns, Australia, 2007, p.: 983-990.

[10] Flaga A., Błazik-Borowa E., Podgórski J., *Aerodynamics of slender structures and bar-cable structures*, Monograph, Lublin Technical University, 2004 (in Polish).

[11] Novak M., Tanaka H., *Pressure correlations on a vibrating cylinder*, Proc. 4th Int. Conf. Wind Effects on Building and Structures, Heathrow 1975, Cambridge University Press, London, 1977, p.: 227-232.

[12] ESDU 85038, *Circular-cylindrical structures: dynamic response to vortex shedding, Part I: calculation procedures and derivation*, London, ESDU Int. Ltd, 1990.

[13] Howell J.F., Novak M., *Vortex shedding from circular cylinders in turbulent flow*, Proc. 5th ICWE, USA 1979, Pergamon, Oxford, 1980, p.: 619-629.

[14] Vickery B.J., *The response of chimneys and tower like structures to wind loading. A state of the art in wind engineering*, Wiley Eastern Limited, 1995, p.: 205-233.

[15] Vickery B.J., Basu R.J., *Simplified approaches to the evaluation of the across-wind response of chimneys*, Proc. 6th ICWE., Australia, J. Ind. Aerodyn., 14, 1983, p.: 153-166.

[16] ESDU 80025, *Mean forces, pressures and flow field velocities for circular cylindrical structures: single cylinder with two-dimensional flow*, London, ESDU Int. Ltd, 1986.

[17] ESDU 82026, *Strong winds in the atmospheric boundary layer, Part 1: mean - hourly wind speed*, London, ESDU Int. Ltd, 1982.

[18] Ruscheweyh H., *Codification of vortex excited vibrations, Recent advances in wind engineering,* Proc. 2nd APWE, Beijing, China, Int. Acad. Publ., Pergamon Press, 1, 1989, p.: 362-372.

[19] Ruscheweyh H., *Windlastannahmen für turmartige Bauwerke*, DIN-Mitt 71, 11, 1992 p.: 644-647. Berlin.

[20] DIN 1055, *Lastannahmen für Bauten, Windwirkungen auf Bauwerke*, 1989.

[21] ENV 1991-2-4, *Eurocode 1, Basis of design and actions on structures, Part 2.4: Wind actions*, 1994.

[22] Shinozuka M., *Stochastic Mechanics, v. 1*, Depart. of Civil Eng. & Eng. Mech. Columbia Univ., 1987, NY, USA.

22

NUMERICAL ANALYSIS OF WIND ACTION ON ARCH BRIDGE OVER VISTULA RIVER IN PUŁAWY

Jarosław Bęc[*], Ewa Błazik-Borowa[*], Andrzej Flaga[*,**],
Tomasz Lipecki[*], Jacek Szulej[*]

[*] Department of Structural Mechanics, Faculty of Civil and Sanitary Engineering,
Lublin University of Technology, Nadbystrzycka 40, 20-618 Lublin, Poland.
[**] Wind Engineering Laboratory, Faculty of Civil Engineering,
Cracow University of Technology, Jana Pawla II 37/3a, 31-864 Cracow, Poland.

1. Introduction

In this paper static and dynamic numerical analyses of the new designed and built arch bridge over Vistula River in Puławy are presented. This paper contains: (1) FEM modeling problems of the bridge, (2) analysis of the bridge response under dead weight and static wind action, (3) modal analysis of the bridge, (4) analysis of the bridge response under dynamic wind action. All numerical analyses have been conducted in cooperation with Wind Laboratory in Cracow, where tunnel tests had been performed. Computations have been carried on in FEM system – **Algor**. Moreover, our own computer software **AeroDynBud** and **WindSym** have been used in dynamic computations.

2. Bridge models

The bridge structure consists of the deck that is hanged to two steel arches. Main dimensions of the model of the arch bridge in Puławy are as follow (see fig. 1):

- Length: 544 m, main span: 212 m (span of the arch as well), five side spans of the length from 44 m to 80 m;
- Deck width: 21.76 m;
- Height of two symmetrical steel arches: 38.27 m;
- Main span deck is hanged to two arches with use of 112 steel rods of the diameters ϕ81 mm and lengths between 3.49 m and 23.97 m;
  All elements of the bridge have been modeled in FEM system **Algor** [1,2,3,4,5,6]

In general, plate, beam, truss or cable elements have been used in modeling. Two arches and the deck as well have been modeled with use of plate and beam elements. Taking into account the complex structure of the arches it has been decided to build their detailed FEM model. Deck has also been modeled in detail. On the other hand the simplified models have been created for the arches as well as for the deck. Consistency

between detailed and simplified models has been checked by comparisons of displacements (in four load cases: bending in vertical plane, torsion, bending in horizontal plane and tension) and by comparison of natural frequencies and mode shapes. Exemplary values are presented in table I for four modules of the deck (comp. fig.1). The same rules have been accepted in simplification procedure of arches. Steel hangers between arches and the deck have been modeled as truss elements in linear static calculations and as cables elements in dynamic analyses.

Finally, three following FEM models have been created:

1) The most detailed model consists of 67744 elements and 50726 nodes. This model has been used in computations of static response under dead weight and static wind action.

2) Simplified model no.1 consists of 42986 elements and 29001 nodes. It can be said, that this is also detailed model that has been simplified because of hardware power limitations in modal analysis.

3) Simplified model no.2 consists of 13268 elements and 10346 nodes. Detailed beam-plate models of arches and deck modules have been simplified to beam model according to the rules mentioned above. This model has been used in analysis of dynamic wind action.
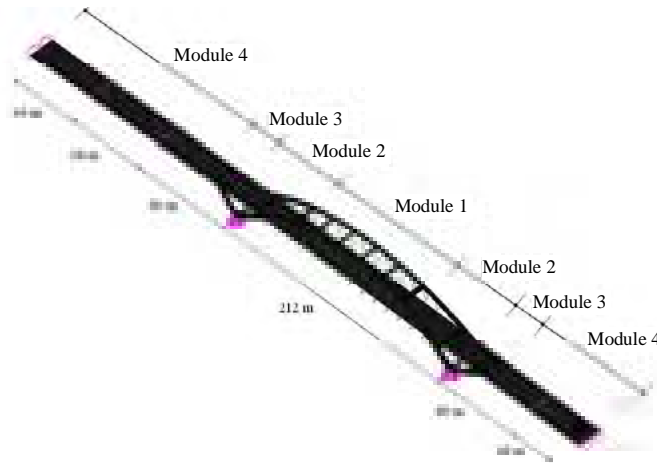
Fig. 1. Model of the arch bridge over Vistula River in Puławy.

Table I. Comparison of detailed and simplified models for one of the deck modules.

	General displacement			Frequency [Hz]	
Load case	Simplified	Detailed	Frq. number	Simplified	Detailed
1	0.345 m	0.346 m	1	0.57	0.54
2	0.075 rad	0.075 rad	2	1.02	0.95
3	0.0093 m	0.0095 m	3	3.44	3.34
4	$4.68\cdot10^{-5}$ m	$4.75\cdot10^{-5}$ m	4	3.57	3.39
			5	4.27	3.97

24

3. Modal analysis

Simplified model no. 2 has been used in modal analysis. Linear modal analysis of the bridge has been performed. It should be pointed that three first mode shapes are bending vibrations of the deck and arches (see fig. 2) and fourth one is bending-torsional vibration of the deck. Ten first mode shapes are described in table II.

Table II. Description of the modes (ω_i – angular frequency, f_i – frequency, T_i – period of vibrations).

	ω_i [rad/s]	f_i [Hz]	T_i [s]	Mode shape
1	4.247	0.676	1.479	Bending vibrations in vertical plane
2	4.759	0.757	1.320	Bending vibrations in horizontal plane
3	7.341	1.168	0.855	Bending vibrations in horizontal plane (opposite vibrations of the deck and arches)
4	8.000	1.274	0.784	Torsional vibrations of the deck and bending vibrations of arches in horizontal plane
5	8.405	1.337	0.747	Bending vibrations in vertical plane
6	8.654	1.377	0.725	Bending vibrations in vertical plane
7	9.768	1.554	0.643	Bending vibrations of the deck in vertical plane out of arches
8	10.122	1.611	0.620	Torsional vibrations of the deck in vertical plane out of arches
9	10.752	1.711	0.584	Torsional vibrations
10	12.025	1.913	0.522	Bending vibrations

a)

b)

25

c)
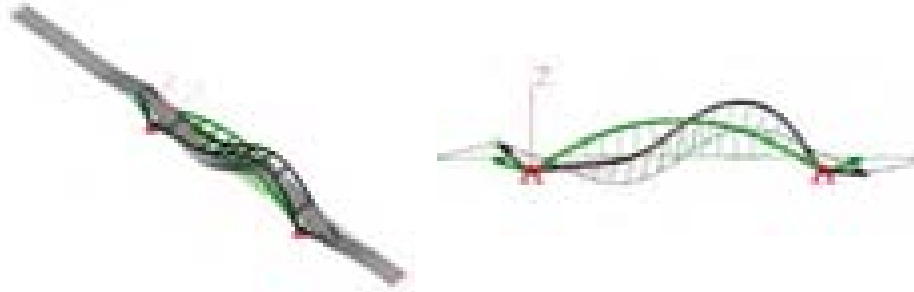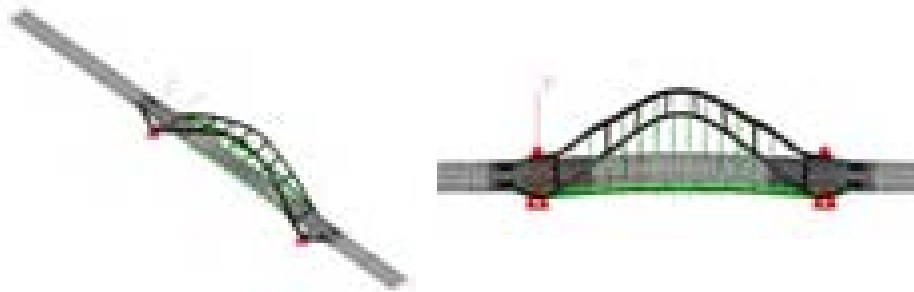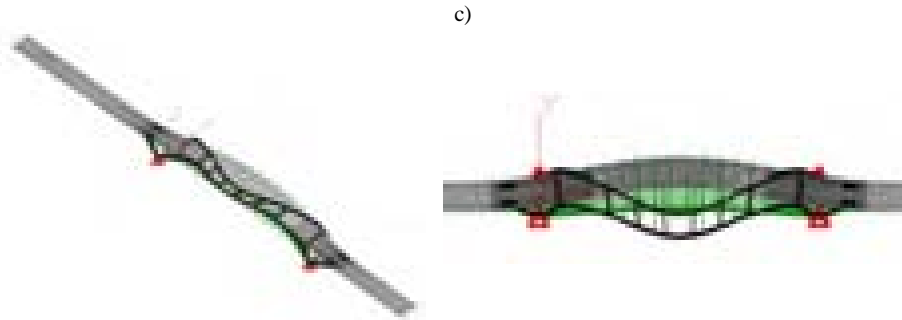
Fig. 2. Three first mode shapes: f_1=0.676Hz, f_2=0.757Hz, f_3=1.168 Hz.

It is worth notice that bending and torsional frequencies are close to each other. This can cause flatter instability. Moreover, dynamic analyses of some hangers have also been performed. The first frequency of natural vibrations of the longest rods f_{1r}=0.680Hz are close to the first frequency of the whole bridge f_1=0.676Hz, so amplification of the bridge vibrations might appear. Fortunately, directions of vibrations are different (bridge – vertical, rods – in arch plane), so, the occurrence of lock-in (frequency synchronization) is not really probable.

4. Self-excited vibrations of rods

Rods of circular cross-section placed in the vicinity of each other may be exposed to additional load that may occur in the case of the aerodynamic interference. Bridge deck has been hanged to two arches by 28 groups of 4 rods of the diameter ϕ81 (D=81mm). Main hangers dimensions and distances in cross-section are given in fig. 3. According to results which are presented in papers [7,8] it can be stated that for distances between two rods equal to 4.9D (wind direction no.1) or 27.7D (wind direction no.2) vibrations caused by aerodynamic interference would not have happened. Some longer rods are connected to each other by horizontal elements. Those rods are in special cover of the diameter ϕ139.7 in connection areas. According to increase of diameter the distance between rods decreases and is equal, respectively: 2.9D (wind direction no.1) and 16.0D (wind direction no.2). In general such values can cause self-excited vibrations of rods. However, the length of the rod cover is short and moreover horizontal elements appears in those areas, so in final, self-excited vibrations of rods cannot appear also in these regions.

Fig. 3. Group of rods.

5. Static analysis (dead weight and static wind action)

Detailed model no.1 has been used in linear static analysis. Moreover, nonlinear static analysis has been performed for bridge model no. 3. In the first part of computations dead weight only has been applied to the bridge. Exemplary displacements obtained in static analysis with consideration of dead weight only are presented in fig. 4a.

In the second part of computations static wind action has been applied to the bridge together with dead weight. Values of forces acting on particular elements of the bridge have been assumed according to the formula [9]:

$$p_y = q_k C_x C_e \beta \gamma \, , \tag{1}$$

- q_k – pressure of characteristic wind speed V_k. It has been assumed, that: V_k=20m/sec, so q_k=0.25 kPa,
- C_x – aerodynamic coefficient with exact values obtained on the basis of wind tunnel tests. Aerodynamic coefficients have been measured for the bridge deck, windward and leeward arches (rods have not been investigated). Appropriate values have been assumed as: 0.849 for windward arch, 0.609 for leeward arch, 0.285 for bridge deck, 1.2 – for all rods.
- C_e – exposure coefficient,
- β – dynamic coefficient, that has been assumed as equal to 1.8,
- γ – safety coefficient, that has been assumed as equal to 1.3.

Exemplary results of static analysis with consideration of dead weight together with static wind action are presented in fig. 4b.

It may be observed that the static wind action influence on overall bridge displacements is very small in comparison to the ones that are produced with dead weight only. Of course displacement component along y axis (wind action direction) is magnified, as it can be seen in fig. 5.

(a)   (b)

Fig. 4. Bridge displacements: (a) dead weight, (b) dead weight and static wind action.

27
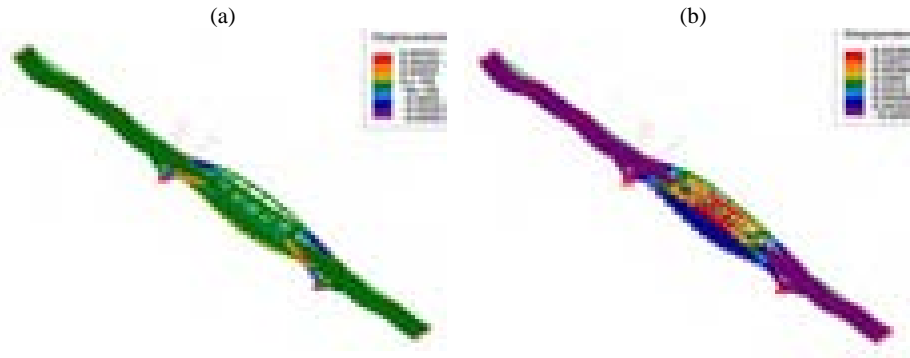
Fig. 5. Bridge displacements along y axis (wind action direction):
(a) dead weight, (b) dead weight and static wind action.

On the basis of values, which are presented in table III, it can be stated that along-wind load is small in comparison with dead weight load. There is wind action value together with estimated weight of the whole bridge and exemplary additional weight of cars at the bridge evaluated and presented in this table.

Table III. Comparison of wind action and dead weight load.

Arches weight	29037 kN
Weight of the deck between arches	93736 kN
Rods weight	728 kN
Overall weight	94464 kN
Overall, estimated wind load value	2900 kN
Overall, estimated wind load/ Overall weight*100%	3%
Exemplary weight of cars on the bridge	40·400 kN=16000 kN

The same conclusion can be drawn for the stresses as well. The nonlinear static analysis has confirmed the results obtained during the linear analysis. The obtained results are in accordance with the ones obtained during the linear analysis, so the nonlinearities in the structure are very small.

Some additional comparisons of bridge response under wind action and dead weight load can be found in tables IV and V.

Table IV. Comparison of displacements.

		Displacements [m]	
		Dead weight	Dead weight + wind load
Deck		0.1478	0.1484
Arches		0.1273	0.1337
Rods		0.1382	0.1416
Bridge	Maximum in x direction	0.0122	0.0128
	Maximum in y direction	0.0035	0.0338
	Maximum in z direction	0.1478	0.1483

28

Table V. Comparison of stresses.

	Stress [kPa]	
	Dead weight	Dead weight + wind load
Von Mises stresses	250041	257299
Stresses in beam elements of arches and in hangers P/A	130289	136826
Stresses in beam elements of arches and in hangers M_2/S_2	160926	167024
Stresses in beam elements of arches and in hangers M_3/S_3	227560	233961
$\sigma = P/A + M_2/S_2 + M_3/S_3$	254280	262266

6. Vortex excitation of rods

Across-wind load caused by vortex excitation has been investigated for several hangers. The following formula given by Polish Standard has been applied in computations:

$$p_y = \frac{\pi}{\Delta} C_y q_{cr} D,$$
(2)

where: Δ – logarithmic decrement of damping, C_y – aerodynamic coefficient, q_{cr} – pressure of critical wind speed $V_{cr} = f \cdot D/St$, f – frequency of natural vibrations, D – diameter, St – Strouhal number. Dynamic analysis has been performed for the longest single rod in each group of rods. Value of across-wind load caused by vortices [kN/m] has been compared to the value of along-wind load [kN/m] for analyzed hanger. Only two first mode shapes of natural vibrations have been taken into account, because of self-limited character of vibrations in higher modes. Results collected in table VI show that the level of across-wind load value is much lower then the level of along-wind action value.

Table VI. Comparison of along and across-wind action.

Hanger description	Frequency [Hz]		Length [mm]	Across-wind load caused by vortex excitation [kN/m]		Along-wind action [kN/m]
	f_1	f_2		f_1	f_2	
1-W1	1.076	2.152	23995	0.00037	0.00148	
2-W1	1.072	2.144	22977	0.00037	0.00147	
3-W1	1.111	2.222	21021	0.00039	0.00158	
4-W1	1.176	2.352	18127	0.00044	0.00177	0.04374
5-W1	1.672	3.343	14350	0.00089	0.00357	
6-W1	2.126	4.247	9687	0.00145	0.00577	
7-W1	4.367	8.680	3978	0.00610	0.02410	

7. Analysis of dynamic wind action

7.1. Calculation procedure

The bridge response to the dynamic wind action has been calculated on the basis of

quasi-steady theory with use of our own computer software **AeroDynBud** developed in Department of Structural Mechanics of LUT. This model is presented in detail in paper [10]. It has been accepted that the bridge displacements can be approximated as the linear combination of representative mode shapes. Schematic progression of calculations is presented in fig. 6. Rough model of the bridge consists of superelements that are connecting in supernodes. Such model has been used in wind load description because all values of aerodynamic coefficients have been related to particular structure sections.
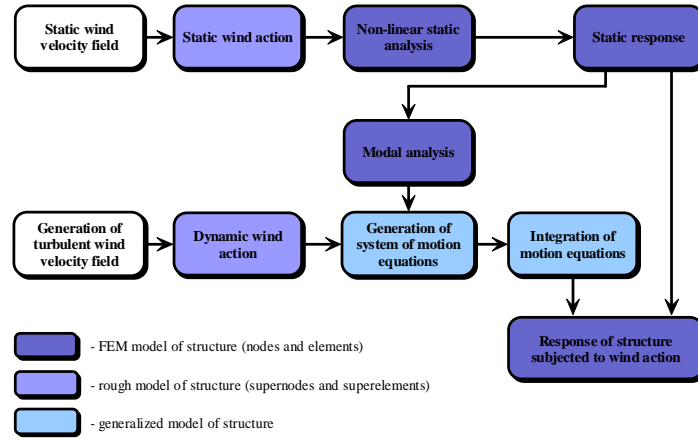
Fig. 6. Analytical procedure.

Static wind action components can be calculated according to the following relations:

$$W_n = \tfrac{1}{2}\rho\bar{v}_n^{\,2}C_n DL \quad \text{– normal wind action (aerodynamic drag),} \tag{3a}$$

$$W_n = \tfrac{1}{2}\rho\bar{v}_n^{\,2}C_b DL \quad \text{– binormal wind action (aerodynamic lift),} \tag{3b}$$

$$W_{ms} = \tfrac{1}{2}\rho\bar{v}_n^{\,2}C_m D^2 L \quad \text{– torsional wind action (aerodynamic moment),} \tag{3c}$$

where: ρ – air density, $\bar{v}_n$ – module of the normal component of the mean wind speed vector, C_n, C_b, C_m – respective aerodynamic coefficients, D – characteristic dimension of the superelement, L – superelement length.

Nonlinear response of the bridge under static wind action has been calculated in the first stage. Deflected shape of the bridge has been used in the following calculations (modal analysis and dynamic response under turbulent wind action). The shape of deflected structure as the result of static loads action obtained in static non-linear analysis is treated as the equilibrium position in linear modal analysis and in dynamic simulation.

It can be assumed that general nodal displacements are approximated by a linear combination of mode shapes:

$$\mathbf{q}(t) = \hat{\mathbf{\Phi}} \cdot \mathbf{\psi}(t), \tag{4}$$

Taking this into account system of the coupled equation of motion can be obtained. Relation for the i-th coordinate $\psi_i(t)$ is given by:

$$M_i \cdot \ddot{\psi}_i(t) + C_i \cdot \dot{\psi}_i(t) + K_i \cdot \psi_i(t) = W_i^{\Phi}, \tag{5}$$

where: M_i, C_i, K_i – respectively: general mass, general damping, general stiffness, W_i^{Φ} – general excitation force. In dynamic analysis of slender structures only three components of load have to be considered (two components of aerodynamic force and one component of aerodynamic moment). Those components can be obtained according to quasi-steady theory [11,12,13]:

$$W_{ne} = \tfrac{1}{2} \rho v_{ne}^2 D_e L_e \left(C_{ne} + C_{nbe} \phi_e \right), \tag{6a}$$

$$W_{be} = \tfrac{1}{2} \rho v_{ne}^2 D_e L_e \left(C_{be} + C_{bne} \phi_e \right), \tag{6b}$$

$$W_{mse} = \tfrac{1}{2} \rho v_{ne}^2 D_e^2 L_e \left(C_m + C_{mn} \phi_e \right), \tag{6c}$$

where ϕ_e is relative angle of wind attack on superelement, taking into account motion of superelement and mean angle of wind attack $\bar{\alpha}$.

The dynamic component of the wind action can be obtained from the relationship:

$$\mathbf{W}' = \mathbf{W} - \bar{\mathbf{W}}, \tag{7}$$

where $\bar{\mathbf{W}}$ is the static part of wind action.

Considering that the superelement displacement can be approximated by linear combination of representative mode shapes of the vibrating bridge, the equation of motion related to the i-th mode shape can be rewritten:

$$
\begin{aligned}
M_i \cdot \ddot{\psi}_i(t) + C_i \cdot \dot{\psi}_i(t) + K_i \cdot \psi_i(t) = \\
= F_i(t) + \sum_{j=1}^{Ni} A_{ij}(t) \cdot \psi_j(t) + \sum_{j=1}^{Ni} D_{ij}(t) \cdot \dot{\psi}_j(t) + \sum_{j=1}^{Ni} \sum_{l=1}^{Ni} G_{ijl}(t) \cdot \psi_j(t) \cdot \dot{\psi}_l(t)
\end{aligned} \tag{8}
$$

General coordinates $\psi_i(t)$ can be obtained at particular time steps t from the solution of the system of motion equations given by eq.8. On the basis of representative mode shapes $\hat{\mathbf{\Phi}}$ and general coordinates $\psi_i(t)$ time histories of general bridge displacements can be determined. Dynamic component of displacements can be expressed:

$$\mathbf{q}'(t) = \mathbf{q}^{dyn}(t) = \sum_{i=1}^{Ni} \mathbf{\Phi}_i \cdot \psi_i(t) = \sum_{i=1}^{Ni} \mathbf{q}_i(t), \tag{9}$$

31

Overall displacements is determined by relationship:

$$\mathbf{q}(t) = \mathbf{q}^{calk}(t) = \mathbf{q}^{st}(t) + \mathbf{q}^{dyn}(t) = \overline{\mathbf{q}}(t) + \mathbf{q}'(t), \qquad (10)$$

where: $\mathbf{q}^{st}(t)$ ($\overline{\mathbf{q}}(t)$) are displacements obtained in nonlinear static computations.

7.2. Results

In analyzed case, bridge vibrations around the neutral position are small and may be treated as linear ones.

Shape of deflected structure as the result of static loads action obtained in static non-linear analysis is treated as the equilibrium position in linear modal analysis and in dynamic simulation.

Turbulent wind velocity field has been generated with use of our software **WindSym**. Wind velocity field has been simulated in 140 points in the deck, arches and rods – fig. 7.

Fig. 7. Simulation points in the deck, arches and hangers.

Wind simulation has been performed using WAWS method (Weighted Amplitude Wave Superposition). The following wind field simulation parameters have been assumed:
- Mean wind velocity at $z_0=10$ m, $U_{10}=20$ m/s;
- Power-law wind profile;
- Time step: 0.01 s;
- Number of time steps: 8192.

Exemplary wind velocity variations for three wind directions are presented in fig. 8 for the highest point of the arch.

32
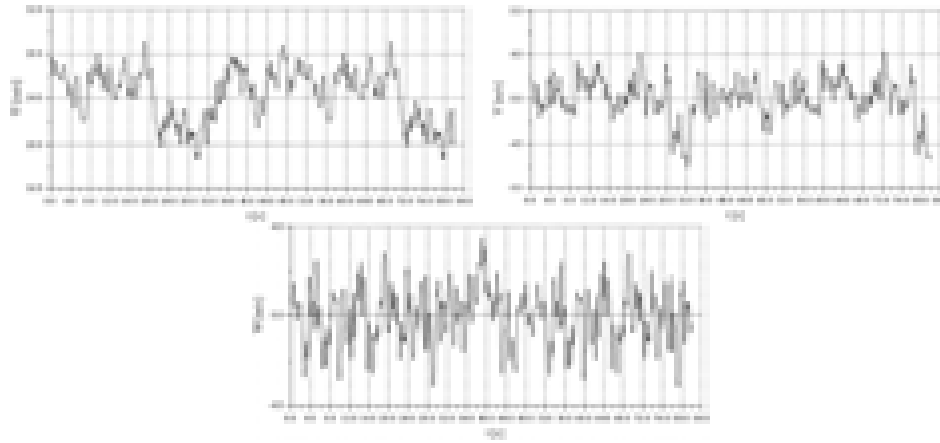
Fig. 8. Wind velocity time histories in the highest point of the arch.

Parameters in dynamic analysis have been assumed as follows:
- Number of representative mode shapes: 8;
- Time step: 0.01 s;
- Number of time steps: 8192;
- Damping: $\Delta = 0.04$.

Exemplary time histories of dynamic component of displacements around equilibrium position are presented in fig. 9. The calculated bridge response to dynamic wind action is small in comparison to the one obtained with static wind action. Since the static wind load had produced small displacements and stresses, the dynamic action influence on the total bridge response to all loads, especially dead weight, is even much smaller.
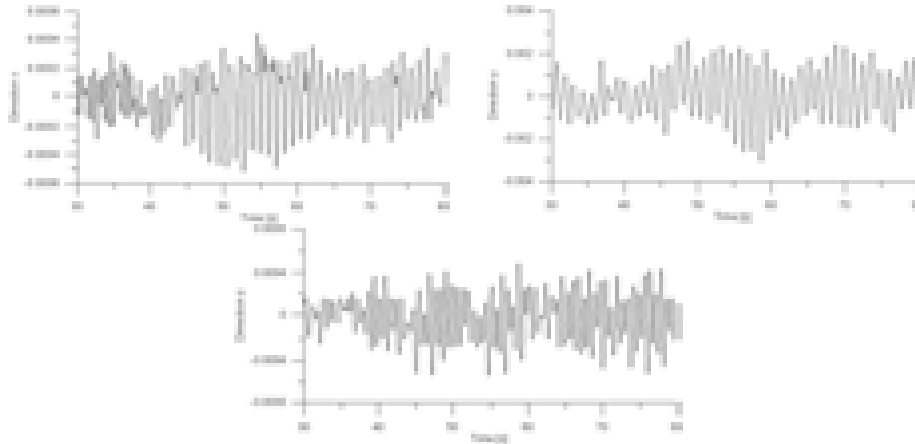
Fig. 9. Displacements time histories (dynamic component) in the highest point of the arch.

33

8. Conclusion

The following conclusions have been formulated on the basis of static and dynamic numerical analyses of the arch bridge in Puławy:

1) Maximum stresses produced with analyzed loads (dead weight and static wind action) are at the level of 260 MPa. The most stressed point of the structure is the arch and deck connection. The maximum bridge displacement produced with dead weight is about 1/1430 of span length.
2) Quasi-static wind action is small in comparison to dead weight. The small increase in stresses and displacements can be noticed in computations with quasi-static wind action together with dead weight load.
3) The structure response to turbulent wind action (buffeting) according to quasi-steady theory, taking into account aerodynamic coupling, is very small in comparison to values generated with static wind load and dead weight.
4) Natural frequencies of the bridge and the hangers are close, but the directions of vibrations are not in accordance, so the parametric resonant vibrations occurrence is not very probable.
5) Load caused by vortex excitation is small in comparison to quasi-static wind action.
6) Aerodynamic interference of rods is of secondary importance, as well.

References

[1] ALGOR. ViziCad Plus, *Algor classic modeling tools, Linear stress analysis release notes*, ALGOR, Inc. Pitsburgh, PA, USA. Copyright 1992 Algor Inc.
[2] ALGOR. ViziCad Plus, *Linear stress and vibration analysis release notes*, ALGOR, Inc. Pitsburgh, PA, USA. Copyright 1994 Algor Inc.
[3] ALGOR, *The accupak reference manual*, ALGOR, Inc. Pitsburgh, PA, USA. Copyright 1993 Algor Inc.
[4] Spyrakos C.C., *Finite Element Method in engineering practice*, West Virginia University Press, 1994.
[5] Zienkiewicz O.C., Taylor R.L., *The Finite Element Method, Vol.1 and 2*, McGraw Hill Book Company, 1994.
[6] Bathe K.J., *Finite Element procedures*, Prentice Hall Inc., 1996.
[7] Błazik-Borowa E, Flaga A., *Modeling of aerodynamic loads on a downstream cylinder caused by bistable flow between two circular cylinders*, J. of Wind Eng. and Ind. Aerodyn. 65, 1997, p.: 361-370.
[8] Błazik-Borowa E., *Interference loads of two cylinders in a side-by-side arrangement*, Wind & Structure, Vol.9, No. 1, 2006, p.:75-93.
[9] PN-93/B-03201, *Steel structures. Chimneys. Calculations and design*, 1993 (in Polish).
[10] Bęc J., *Aerodynamics of guyed masts*, Thesis, 2004, Lublin.
[11] Flaga A., *Quasisteady models of wind load on slender structures. Parts I & II*, Archives of Civil Engineering, XL, 1, 1994, p.: 3-41.
[12] Flaga A., *Quasisteady models of wind load on slender structures. Part III. Applications of quasisteady theory in aerodynamics of slender structures*, Archives of Civil Engineering, XLI, 3, 1995, p.: 343-376.
[13] Flaga A., *Quasisteady theory in aerodynamics of slender structures*, Sonderforschungsbereich Tragwerksdynamik, Ruhr Universitat Bochum, 1994.

HUMAN COMFORT CRITERIA FOR FOOTBRIDGES IN CASE OF WIND-INDUCED VIBRATIONS

Andrzej Flaga[*,**], Ewa Błazik-Borowa[*], Marek Pańtak[**]

[*] Department of Structural Mechanics, Faculty of Civil and Sanitary Engineering,
Lublin University of Technology, Nadbystrzycka 40, 20-618 Lublin, Poland.
[**] Wind Engineering Laboratory, Faculty of Civil Engineering,
Cracow University of Technology, Jana Pawla II 37/3a, 31-864 Cracow, Poland.

1. Specificity of vibrations influence on people in case of footbridges

Human comfort criteria presented in different recommendations and standard documents are mostly related to people in buildings. In case of footbridges, human comfort criteria should be relatively more restricted than for manufactories or for public means of transport and more less than for offices and dwelling houses. Comfort criteria for footbridges should take into account individual specificity of human perception of vibration on footbridges.

For footbridges (similarly as for other pedestrian structures) human perception of vibration is strongly dependent on human activity; usually its following types being distinguished: resting, walking or running. In general, vibrations are more annoying for standing than for walking people. Approximately, vibrations sensed as unpleasant by standing people are three times smaller than tolerated by walking people. Furthermore, people on footbridges can be subjected to additional psychological effects coming from: vibrating lamps, railings, cables or caused by acoustic effects, restricting all comfort requirements.

Vibrations caused by wind result from atmospheric turbulence and aeroelastic phenomena like: critical vortex excitation, galloping, flutter. The range of mean wind velocity 10 – 15 m/s is particularly important. Above wind velocity 15 – 20 m/s – in case of footbridges – pedestrian traffic on these structures is practically stopped. In such cases, human comfort criteria need not to be precisely formulated.

As a result of wind action, footbridges can experience significant vibrations which in particular cases can be horizontal ones. In such cases, special attention should be paid to: 1) much greater human sensitivity to horizontal than vertical vibrations; 2) frequencies below 1.0 Hz, neglected in existing standard documents, papers and recommendations for footbridges. The authors own comfort criteria presented in the paper are related to two frequency ranges, namely: 0.063 – 1.0 Hz and 1.0 – 25.0 Hz.

Contemporary footbridges are more and more slender and lighter than typical road and railway bridges. Because of small massiveness of footbridges, in comparison with bridges, curves of comfort criteria proposed for them, for vertical and horizontal vibrations, have to be lowered.

35

Additionally, in case of vibrating footbridges, so-called phenomenon of crowd psychology can take place (i.e. situation in which panic of sensitive people is imparting to other users). It is especially dangerous at big people density on footbridge. As a result of this phenomenon, human comfort criteria should be lowered once again.

Short staying time of people on footbridges (1 – 10 min.) has significant effect on the perception threshold for frequencies smaller than 1.0 Hz, where so-called motion sickness with nausea and dizziness can occur. The risk of feeling of this unpleasant phenomenon as a result of short time of vibration exposure is considerably reduced.

2. Authors' proposals of human comfort criteria for pedestrians on footbridges in case of wind induced vibrations

On the basis of different human comfort criteria encountered in several papers and standard documents – own proposals of comfort criteria for pedestrians on footbridges in case of wind-induced vibrations have been elaborated and presented in fig. 1 [1, 2].

a) vertical vibrations 1.0 – 25.0 Hz   b) horizontal vibrations 1.0 – 25.0 Hz

c) vertical vibrations 0.063 – 1.0 Hz   d) horizontal vibrations 0.063 – 1.0 Hz
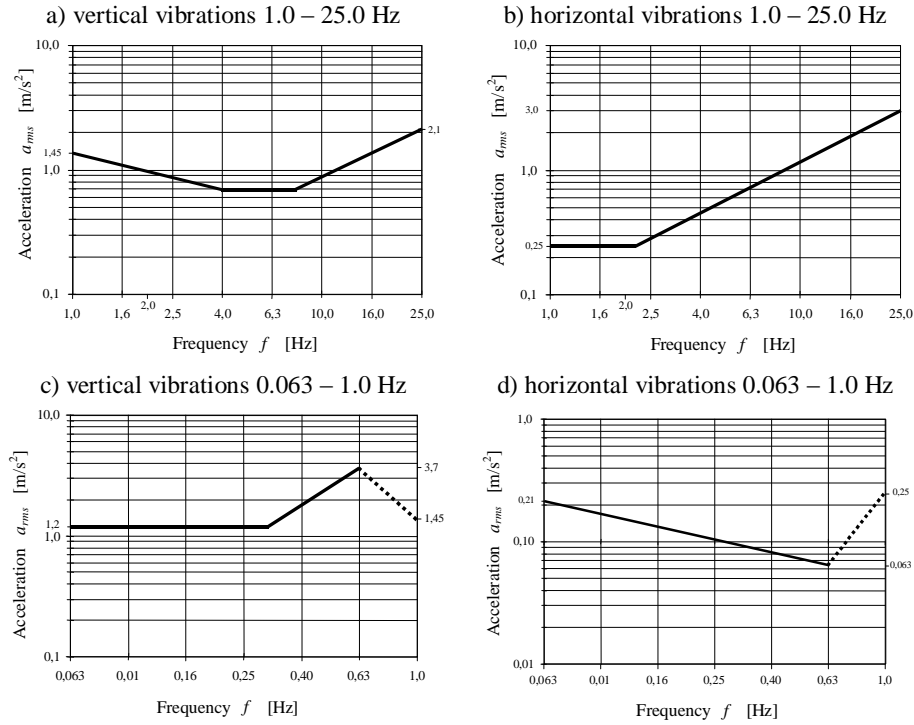
Fig. 1. Authors' proposals of human comfort criteria for footbridges in case of seldom occurring vibrations induced by wind (i.e. vibrations of stochastic character) [1, 2].

36

Proposed criteria take into account the courses of comfort criteria curves occurring in international standards ISO 2631 Part 2 and 3 [3, 4] and ISO 6897 [5] and have been formulated in terms of the effective acceleration (i.e. root-mean-square (*rms*) value of acceleration). In the frequency range 0.63 – 1.0 Hz, where diagram discontinuity occurs, due to lack of adequate investigation results, the proposals have been marked with a dashed line joining the border points of both ranges (below and above 1.0 Hz).

3. Characteristics of analyzed footbridges

New structural materials are characterized by its better and better mechanical and resistance parameters, what – against to older structures – leads to: grater spans and smaller cross sectional dimensions (i.e. more slender structures), smaller stiffnesses, smaller unit masses and lower damping in contemporary structures. All of such structures become more susceptible to dynamic actions.

Fundamental vibration frequencies of the lightweight and slender footbridges often appear in a frequency range of men and wind actions.

In fig. 2 several different suspension and cable-stayed footbridges analyzed in the paper are presented. Fundamental vertical and horizontal frequencies obtained from numerical calculations as well as in-situ measurements of them are given in fig. 3 [6, 7].

a) footbridge in Myslenice main span 75 m (ribbon footbridge)

b) footbridge in Piwniczna main span 102 m

c) footbridge in Rzeszow main span 64 m

d) footbridge in Tropie main span 110 m
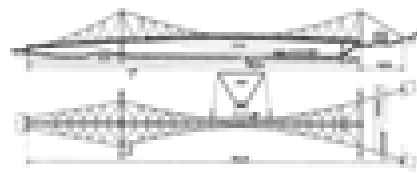
e) footbridge in Roznow main span 35 m

f) footbridge in Tylmanowa main span 84 m

g) footbridge in Tylmanowa main span 78 m
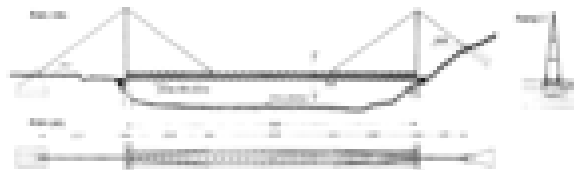
Fig. 2. Structures of the analysed footbridges in: Myslenice (a), Piwniczna (b), Rzeszow (c), Tropie (d), Roznow (e), Tylmanowa (f, g).
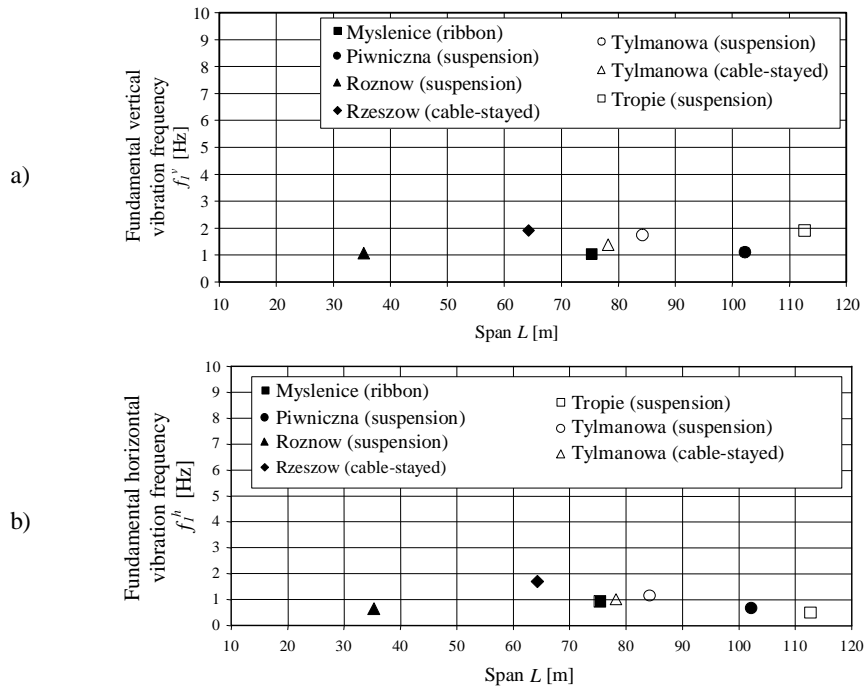
Fig. 3. Fundamental vertical (a) and horizontal (b) vibration frequencies (f_{1v}, f_{1h}) of some suspension and cable-stayed footbridges in Poland as a function of the span L [6, 7].

4. Results of aerodynamic calculations

Examples presented below (fig. 4) shows results of aerodynamic analyses of aforementioned footbridges. For all analysed footbridges, calculations have been performed at power win profile exponent $\alpha = 0.24$ and at mean wind velocity $\overline{\upsilon}_{max} = 28.4$ m/s.

There are four graphs for each footbridge: upper left – exemplary calculated time history response; upper right – power spectrum density of it; bottom left and right – maximal, filtered time history responses.

a) footbridge in Myslenice (ribbon footbridge)

$a_{max} = 3.21$ m/s^2
$a_{rms} = 1.15$ m/s^2

Calculated time history response

horizontal - 0.94 Hz,   vertical - 1.20 Hz,   tortional - 1.22 Hz

$a_{max} = 0.95$ m/s^2
$a_{rms} = 0.61$ m/s^2

Filtered time history response (band-pass 0.93-0.95 Hz)

$a_{max} = 3.36$ m/s^2
$a_{rms} = 2.12$ m/s^2

Filtered time history response (band-pass 1.19-1.21 Hz)

b) footbridge in Piwniczna

$a_{max} = 1.12$ m/s^2
$a_{rms} = 0.35$ m/s^2

Calculated time history response

horizontal-tortional - 0.70 Hz,   vertical - 1.16 Hz

$a_{max} = 1.45$ m/s^2
$a_{rms} = 0.92$ m/s^2

Filtered time history response (band-pass 0.68-0.71 Hz)

$a_{max} = 0.32$ m/s^2
$a_{rms} = 0.18$ m/s^2

Filtered time history response (band-pass 1.15-1.17 Hz)

c) footbridge in Rzeszow

$a_{max} = 0.32$ m/s^2
$a_{rms} = 0.09$ m/s^2

Calculated time history response

horizontal-tortional - 1.70 Hz, vertical - 1.98

40

a_max = 0.06 m/s²
a_rms = 0.04 m/s²

Filtered time history response (band-pass 1.69-1.71 Hz)

Acceleration [m/s²]
0.1, 0.05, 0, -0.05, -0.1

Time [s]: 30, 45, 60

a_max = 0.63 m/s²
a_rms = 0.41 m/s²

Filtered time history response (band-pass 1.97-1.99Hz)

Acceleration [m/s²]
0.8, 0.4, 0, -0.4, -0.8

Time [s]: 30, 45, 60

d) footbridge in Tropie

a_max = 0.40 m/s²
a_rms = 0.16 m/s²

Calculated time history response

Acceleration [m/s²]
0.4, 0.2, 0, -0.2, -0.4

Time [s]: 0, 15, 30, 45, 60, 75, 90, 105, 120, 135

horizontal-tortional - 0.50 Hz, horizontal-tortional - 0.86, horizontal-tortional - 1.20

Power Spectrum Density
0.04, 0.02, 0

0.50 **1.20** 0.86

Frequency [Hz]: 0.00, 0.10, 0.20, 0.29, 0.39, 0.49, 0.59, 0.68, 0.78, 0.88, 0.98, 1.07, 1.17, 1.27, 1.37

a_max = 0.15 m/s²
a_rms = 0.09 m/s²

Filtered time history response (band-pass 0.49-0.51 Hz)

Acceleration [m/s²]
0.2, 0.1, 0, -0.1, -0.2

Time [s]: 0, 15, 30, 45, 60

a_max = 0.11 m/s²
a_rms = 0.07 m/s²

Filtered time history response (band-pass 1.19-1.21 Hz)

Acceleration [m/s²]
0.14, 0.07, 0, -0.07, -0.14

Time [s]: 20, 35, 50, 65

e) footbridge in Roznow

a_max = 2.94 m/s²
a_rms = 1.12 m/s²

Calculated time history response

Acceleration [m/s²]
3, 1.5, 0, -1.5, -3

Time [s]: 0, 15, 30, 45, 60, 75, 90, 105, 120, 135

horizontal-tortional - 0.60 Hz,   horiyontal-tortionall - 0.68 Hz

Power Spectrum Density
0.4, 0.2, 0

0.68 0.60

Frequency [Hz]: 0.24, 0.30, 0.36, 0.42, 0.48, 0.54, 0.60, 0.66, 0.73, 0.79, 0.85, 0.91, 0.97, 1.03

a_max = 0.50 m/s²
a_rms = 0.32 m/s²

Filtered time history response (band-pass 0.59-0.61Hz)

Acceleration [m/s²]
0.6, 0.3, 0, -0.3, -0.6

Time [s]: 0, 15, 30, 45, 60, 75

a_max = 1.48 m/s²
a_rms = 0.98 m/s²

Filtered time history response (band-pass 0.67-0.69 Hz)

Acceleration [m/s²]
1.8, 0.9, 0, -0.9, -1.8

Time [s]: 0, 15, 30, 45, 60

41

f) footbridge in Tylmanowa span 84 m (suspension)

a_max = 0.74 m/s²
a_rms = 0.30 m/s²

Calculated time history response

horizontal - 1.21, vertical - 1,80

a_max = 0.03 m/s²
a_rms = 0.02 m/s²

Filtered time history response
(band-pass 1.19-1.21 Hz)

a_max = 0.96 m/s²
a_rms = 0.64 m/s²

Filtered time history response
(band-pass 1.77-1.79 Hz)

Fig. 4. Results of aerodynamic analysis of footbridges in: Myslenice (a), Piwniczna (b), Rzeszow (c), Tropie (d), Roznow (e), Tylmanowa (f).

In first approximation, it can be assumed that dynamical component of footbridge response depends linearly on mean wind velocity $\overline{\upsilon}$. Evaluation of fulfilment of comfort criteria for the analysed footbridges have been performed at assumption that $\overline{\upsilon} = 14.0$ m/s $\approx {}^{1}/_{2}\,\overline{\upsilon}_{max}$ i.e. when pedestrian movement on footbridges is still possible.

Fig. 5 presents results of all analyses with reference to human comfort criteria proposed by the authors.

a) vertical vibrations 1.0 – 25.0 Hz

b) horizontal vibrations 0.063 – 1.0 Hz
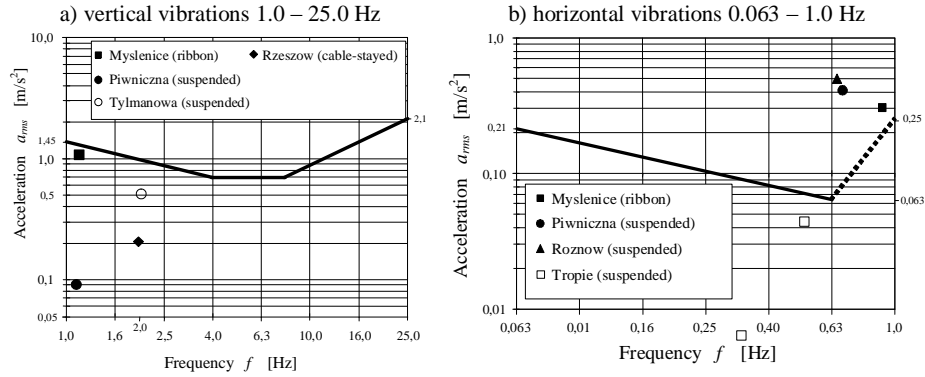
Fig. 5. Results of human comfort analysis for several suspension and cable-stayed footbridges in Poland in case of wind-induced vibrations.

42

5. Conclusions

Basing upon the obtained results, following general conclusions can be formulated:

1. Human comfort criteria are a serious problem in case of slender and lightweight footbridges. In case of wind-induced vibrations it relates to horizontal vibrations of low frequencies (below 1.0 Hz).
2. Dynamic analysis is necessary during design of modern footbridges. Static analysis is insufficient.
3. Footbridges without proper lateral bracing are prone to vibrations caused by dynamic wind action (as well as men-induced vibrations).
4. For some slender structures the static angle of torsion of a span is very big and does not fulfil the requirements.
5. In case of susceptible structures its upgrade is indispensable. The following preventive measures can be undertaken: application of flaps on a bridge girder, thickening of the slab, altering the length of the span(s), changing the mass of the structure or application of vibration absorbers (tuned mass dampers, tuned liquid dampers, viscous dampers).

Proposed comfort criteria have been partially verified on the basis of in situ observations of analysed footbridges behaviour. It seems that these criteria are quite reasonable.

References

[1] Flaga A., Pańtak M., *Vibration comfort curves with respect to footbridges according to ISO/CD 10137:2005 and own proposals*, Inżynieria i Budownictwo, No. 10/2006, Warsaw 2006, pp. 541-547 (in Polish).

[2] Flaga A., Pańtak M., *Comfort criteria for pedestrians on footbridges under wind action*, Proc. of the International Conference on Urban Wind Engineering and Building Aerodynamics, von Karman Institute, Rhode-Saint-Genese, Belgium, 2004, pp.E.5.1-E.5.9.

[3] *ISO 2631/2 Evaluation of human exposure to whole-body vibration. Continuous and shock-induced vibration in buildings (1 to 80 Hz), ISO 2631, Part 2*, International Standard Organization, 1989.

[4] *ISO 2631/3 Evaluation of human exposure to whole-body vibration. Part 3. Evaluation of exposure to whole-body z-axis vertical vibration in the frequency range 0.1 to 0.63 Hz,* International Standard Organization, 1985.

[5] *ISO 6897 Guidelines for the evaluation of the response of occupants of fixed structures, especially buildings and of-shore structures, to low-frequency horizontal motion (0.063 to 1 Hz)*, International Organization for Standardization, 1984.

[6] Michałowski T., *Aerodynamical analysis of the spatial stiffness of light steel footbridges*, Ph.D. Thesis, Cracow University of Technology, 2003 (in Polish).

[7] Flaga A., Bosak G., Michałowski T., *Study of aerodynamic behaviour and serviceability limit state of suspension footbridges under wind action*, Proc. of the 11th International Conference on Wind Science and Engineering, Research Center at Texas Tech University, Lubbock 2003, vol. II, pp. 1587-1594.

44

WIND TUNNEL MODEL TESTS

MODEL INVESTIGATIONS OF THE ARCH BRIDGE OVER VISTULA RIVER IN PUŁAWY

Andrzej Flaga[*,**], Grzegorz Bosak[*], Renata Rzegocka-Kłaput[*], Piotr Matys[*], Łukasz Flaga[***]

[*] Wind Engineering Laboratory, Faculty of Civil Engineering,
Cracow University of Technology, Jana Pawla II 37/3a, 31-864 Cracow, Poland.
[**] Department of Structural Mechanics, Faculty of Civil and Sanitary Engineering,
Lublin University of Technology, Nadbystrzycka 40, 20-618 Lublin, Poland.
[***] Department of Architecture, Urban Planning and the Landscape Studies, Faculty of Civil and Sanitary Engineering, Lublin University of Technology, Nadbystrzycka 40, 20-618 Lublin, Poland.

1. Object of investigations

The object of investigations is a new arch bridge over Vistula River in Puławy (fig. 1). The bridge crossing Vistula River is placed along national road No.12. The whole length of the bridge is equal to 544 m (the main span: 212 m, five side spans of the length from 44 m to 80 m). Deck, of the width 21.76 m, is hanged to two steel arches with use of 112 steel rods of the diameter equal to 81 mm and length between 3.49 m and 23.97 m. Height of the two symmetrical steel arches is equal to 38.27 m [comp. 7].

Fig. 1. Computer visualization of the arch bridge in Puławy [2].

47

2. Scope of tests in boundary layer wind tunnel of Cracow University of Technology

Scope of wind tunnel tests contained the following experiments:

1. Tests of the sectional model of the span (model scale 1:60) with respect to determination of aerodynamic coefficients as functions of angle of wind attack (fig. 2). The model consists of: bearing frame made of aluminum sections, deck and barriers made of plastic. Measurements of aerodynamic forces (F_x – aerodynamic drag; F_y – aerodynamic lift; M – aerodynamic moment) have been obtained by means of the three components of aerodynamic balance based on electric resistance wire strain gauges.
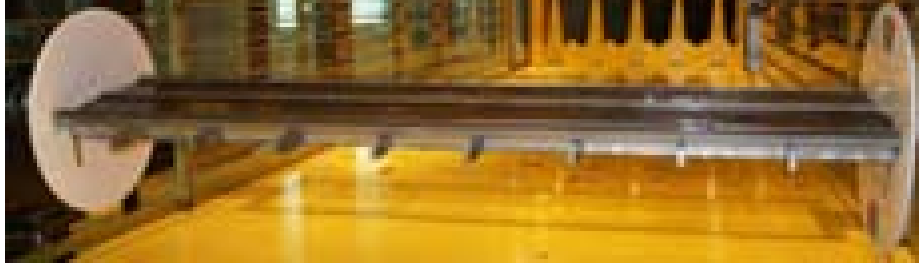
Fig. 2. Sectional model of the bridge span in the wind tunnel working section.

On the base of mean values of the measured forces aerodynamic coefficients (C_x – aerodynamic drag coefficient; C_y – aerodynamic lift coefficient; C_m – aerodynamic momentum coefficient) have been calculated as functions of angle of wind attack (fig. 3.).
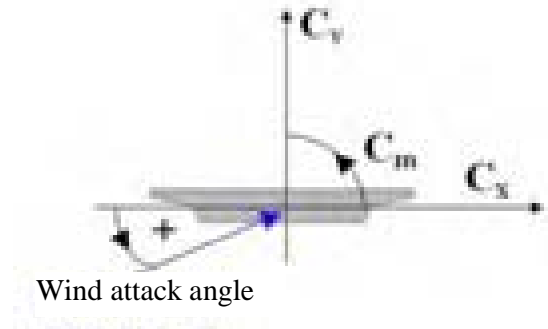
Fig. 3. Coordinate system of aerodynamic coefficients.

A way of changing the angle of wind attack on the model in the wind tunnel working section is presented in fig. 4.

Fig. 4. Change of angle of wind attack on the model in the wind tunnel working section.

2. Tests of the sectional models of two arches (model scale 1:10) with respect to determinate of aerodynamic coefficients as functions of angle of wind attack with and without influence of their mutual aerodynamic interference (fig. 5.)

Fig. 5. Sectional model of the two arches in the wind tunnel working section.

During the measurements, variable pressure distribution on the outer surface of the arch in the middle cross-section of the model has been obtained by means of 32 channel pressure scanner. A realization of a connection between measurement points on the outer surface of the arch girders and the sensors of the pressure scanner is presented in fig. 6.

Fig. 6. A realization of a connection between measurement points on the outer surface of the arch girders and the sensors of the pressure scanner.

Aerodynamic coefficients have been obtained by integration of wind mean pressure distribution on the outer surface of the arch girder.

3. Tests of sectional models of hangers (model scale 1:1.1) with respect to determinate of possibility of occurrence of bistable flows [1] between pipe elements constituting particular hangers (fig. 7).

49

Fig. 7. Sectional model of the hangers in the wind tunnel working section.

Variable pressure distributions on the outer surface of the hangers in the middle cross-section of the model have been obtained by means of 32 channel pressure scanner.

Measurement situation for two hangers is presented in fig. 8. Considered range of wind velocity has settled from 5 m/s to 17 m/s. Situations with angle β of values from 0^0 to 20^0 has been examined.
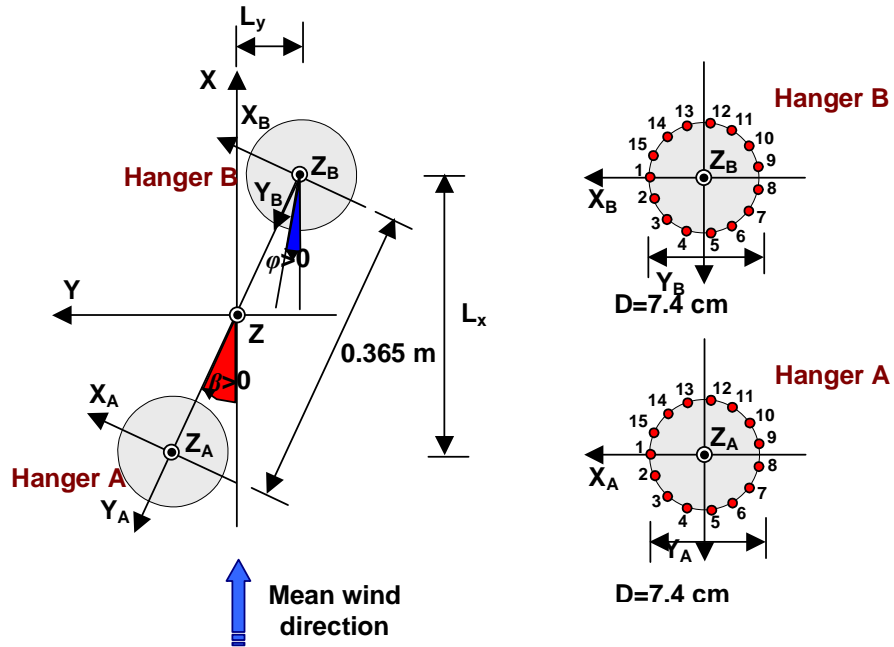
Fig. 8. Measurement situation of two hangers.

50

3. Exemplary experimental results

3.1. Span of the bridge

Functions of aerodynamic coefficients – drag coefficient C_x, lift coefficients C_y, moment coefficient C_m for the span of Puławy bridge are presented in fig. 9.

Wind attack angle
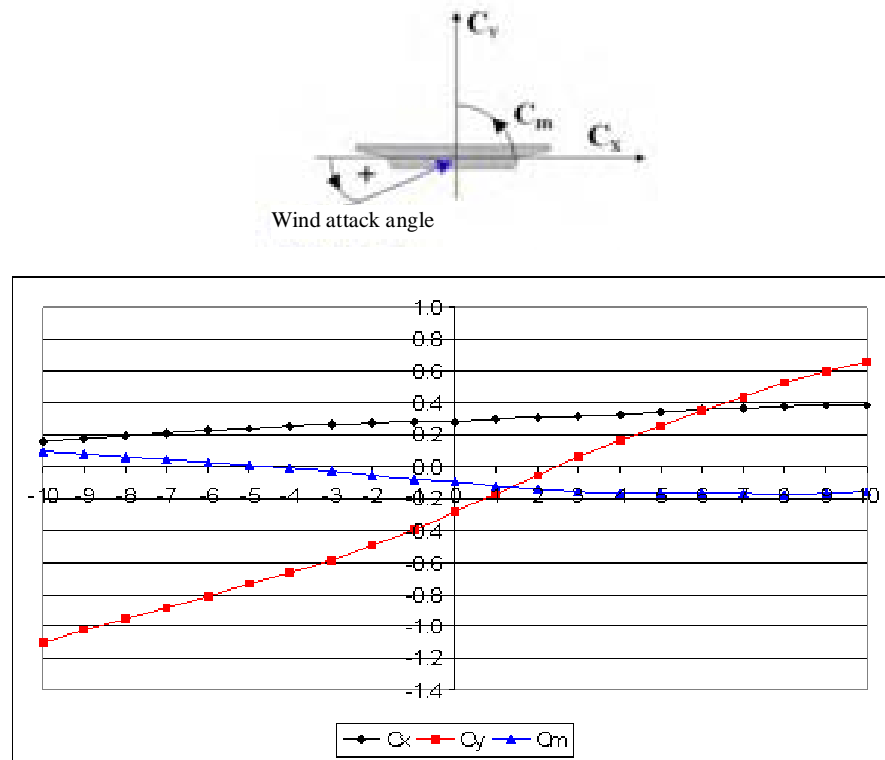
Fig. 9. Functions of aerodynamic coefficients – drag coefficient C_x, lift coefficients C_y, momentum coefficient C_m for the span of Puławy bridge obtained from wind tunnel tests.

Comparison of aerodynamic coefficients of span for two different bridges: the arch bridge in Puławy and the cable-stayed Siekierkowski Bridge in Warsaw [comp. 4-6] is shown in fig. 10.

51

a)

b)

c)
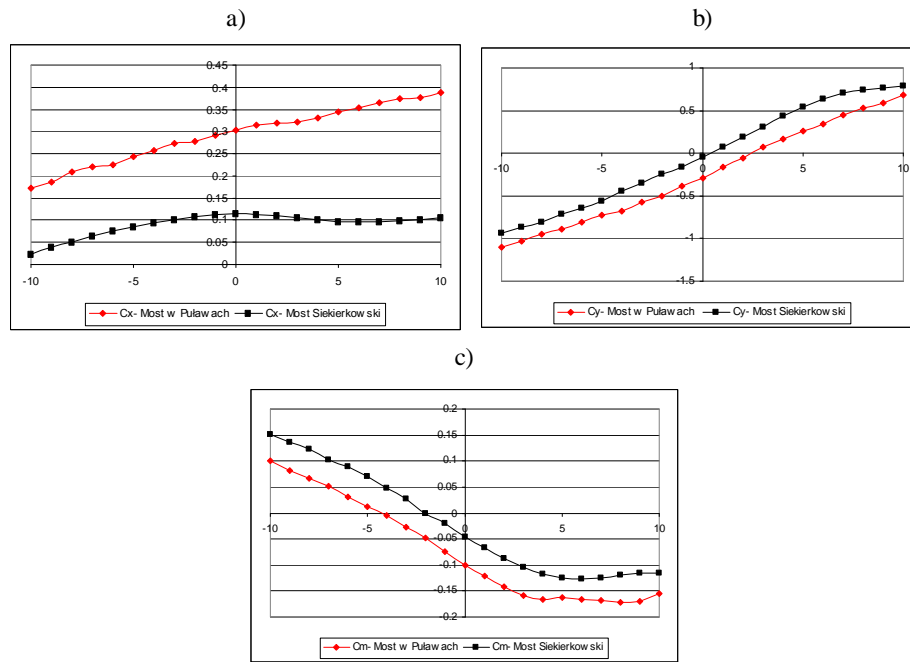
Fig. 10. Comparison of aerodynamic coefficients – drag coefficient C_x(a), lift coefficients C_y(b), moment coefficient C_m (c) - for the span of Puławy bridge and for the span of Siekierkowski bridge.

3.2. Arches of the bridge

Aerodynamic coefficients functions for windward and leeward arches obtained from wind tunnel tests are presented successively in fig. 11 and fig. 12.
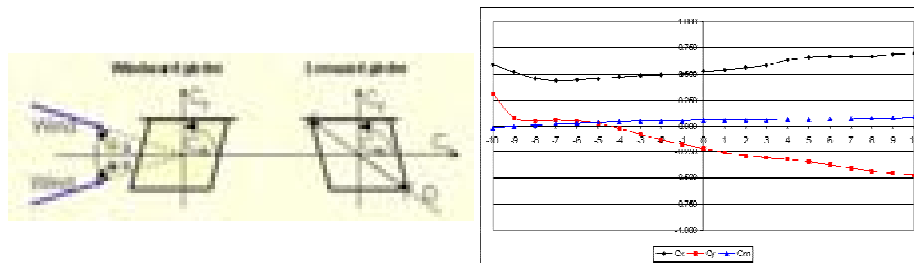
Fig. 11. Functions of aerodynamic coefficients – drag coefficient C_x, lift coefficients C_y, moment coefficient C_m for the windward arch of Puławy bridge obtained from wind tunnel tests.

52
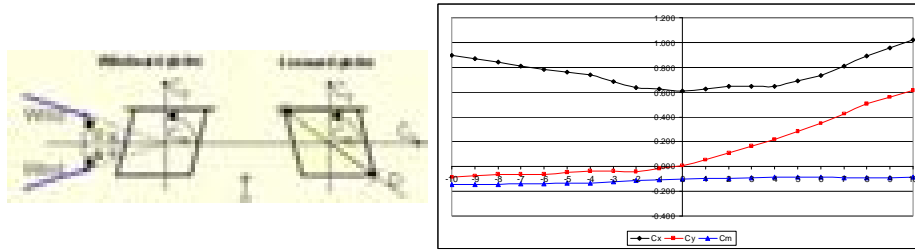
Fig. 12. Functions of aerodynamic coefficients – drag coefficient C_x, lift coefficients C_y, moment coefficient C_m for the leeward arch of Puławy bridge obtained from wind tunnel tests.

3.3. Hangers of the span

Pressure distributions on the outer surface of the leeward hanger B (comp. fig. 8.) for two chosen mean wind direction ($\beta=0^0$ and $\beta=16^0$) are presented respectively in fig. 13a and fig. 13b.
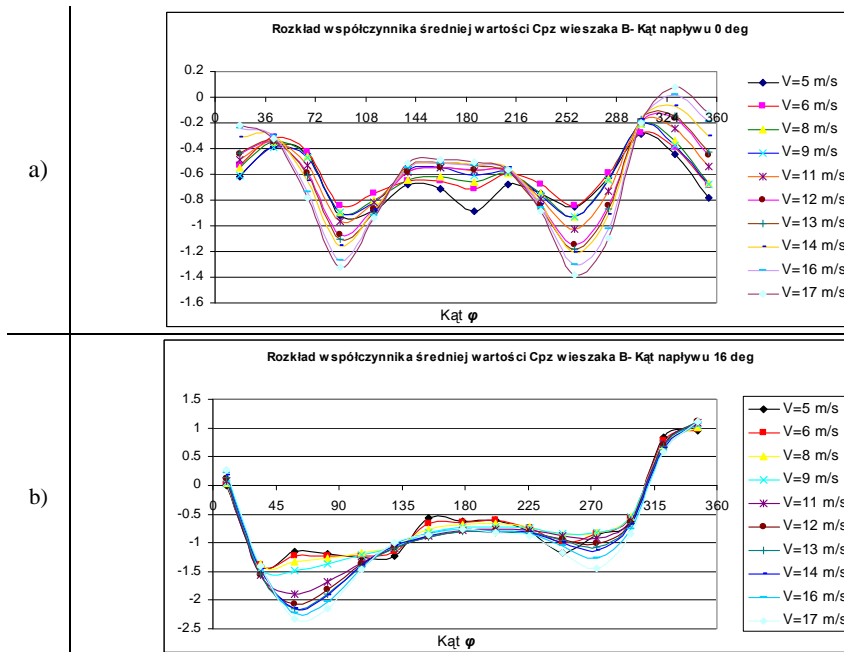
Fig. 13. Pressure distributions on the outer surface of the leeward hanger B
a) mean wind direction $\beta=0^0$; range of wind velocity <5m/s, 17m/s>
b) mean wind direction $\beta=16^0$; range of wind velocity <5m/s, 17m/s>.

53

4. Conclusions

On the base of experimental results of the wind tunnel tests following conclusions could be formulated:

1. Aerodynamic coefficients for span of two different bridges, i.e. the arch bridge in Puławy and the cable-stayed Siekierkowski Bridge in Warsaw are of similar character. In both cases derivatives $\frac{\partial C_y}{\partial \alpha}$ for $\alpha = 0$ is positive and $\frac{\partial C_m}{\partial \alpha}$ for $\alpha = 0$ is negative.

2. On the base of the coefficients functions, according to den Hartog conditions, galloping of the span of Puławy bridge is not supposed to occur.

3. 3.Taking into consideration a shape of the span cross-section, significant relative mass and stabilization role of arch girders it is supposed that flatter or vortex excitation rather will not occur for the span.

4. Windward arch decreases wind action on leeward girder by about 30%. The reduction of wind action on leeward girder applies to higher part of the arch, where the distance between two arch girders is smaller.

5. Tunnel tests have showed that bistable flows between hangers are not occur.

References

[1] Błazik-Borowa E., Flaga A., Kazakiewicz M. I., *Problem sof aeroynamical interferencje of two circular cylinders*, Studia z zakresu inżynierii nr 42 PAN-KILiW-IPPT Warszawa 1997. (in Polish).

[2] Bąk J., Oleksiak C., *Design of a new bridge over Vistula River in Puławy*, Materiały Międzynarodowej Konferencji „MOSTY", Kielce 2005, pp. 95-103, (in Polish).

[3] Flaga A., Flaga K., Michałowski T., *Problems of aerodynamics of cable-stayed and suspension bridges*, Inżynieria i Budownictwo 9/96, pp. 508-516, (in Polish).

[4] Flamand O., *Raport CSTB EN-AEC: The Sucharski Bridge in Gdansk: invastigations of aeroelastics model of the scale 1:100 in boundary layer wind tunnel*, Nantes 2000.

[5] Flamand O., *Aerodynamic stability of the Sucharski Bridge in Gdansk*, Centre Scientifique et Technique du Batiment-Service Aerodynamique et Environnement Climatique, Nantes 2000.

[6] Flamand O., *Aerodynamic stability of the deck of the Siekierkowski Bridge in Warsaw* Report CSTB, Nantes, 2001.

[7] Krysiak L., Pawelski S., *Road bridge construction of the arch bridge over Vistula River in Puławy*, Inżynieria i Budownictwo 11/2006, pp. 633-635, (in Polish).

WIND TUNNEL TESTS OF THE MUNICIPAL STADIUM ROOF IN TARNÓW

Andrzej Flaga[*,**], Grzegorz Bosak[*], Renata Rzegocka-Kłaput[*], Piotr Matys[*], Łukasz Flaga[***]

[*] Wind Engineering Laboratory, Faculty of Civil Engineering,
Cracow University of Technology, Jana Pawla II 37/3a, 31-864 Cracow, Poland.
[**] Department of Structural Mechanics, Faculty of Civil and Sanitary Engineering,
Lublin University of Technology, Nadbystrzycka 40, 20-618 Lublin, Poland.
[***] Department of Architecture, Urban Planning and the Landscape Studies, Faculty of Civil and
Sanitary Engineering, Lublin University of Technology, Nadbystrzycka 40, 20-618 Lublin, Poland.

1. Short description of main bearing structure of the municipal stadium in Tarnów

A main bearing structure of the municipal stadium in Tarnów consists of:
- Roof covering in a form of a prestrained membrane material such as fiberglass reinforced PTFE;
- Three dimensional steel frame-trusses supported on two rows of steel columns;
- Steel arches with stays linking trusses;
- Reinforced concrete tribune structures;
- Reinforced concrete spot footings on piles.

Computer visualizations of the stadium are presented in figs 1-3. Geometry of the main structures in turn is presented in fig. 4.

Fig. 1. Bird-eye view of the stadium roof.

55

The stadium has been designed in designing office "S.P.A.K. – Studium Projektowe Anny Kasprzyk" in Warsaw [1]. The main bearing structure of the stadium has been designed in the Wind Engineering Laboratory at the Cracow University of Technology by: A.Flaga, M.Pańtak and G.Kimbar [2].

a)

b)
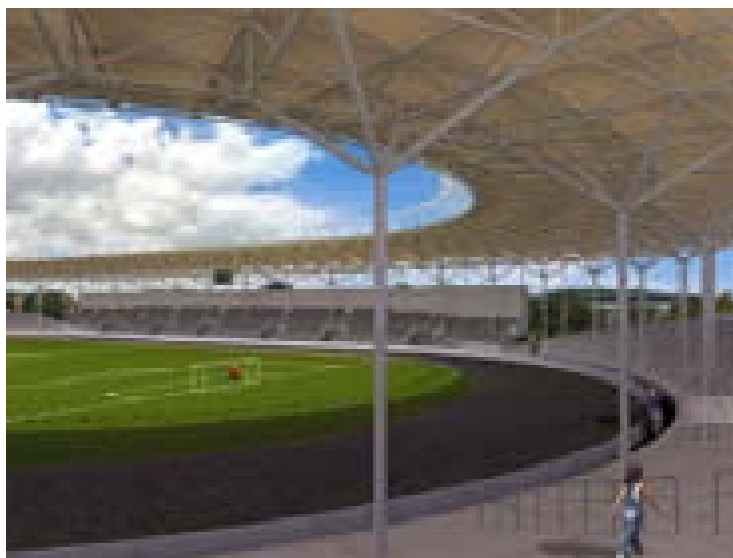
Fig. 2. Inside views of the stadium.

56

Fig. 3. Outside views of the stadium.

a)

b)
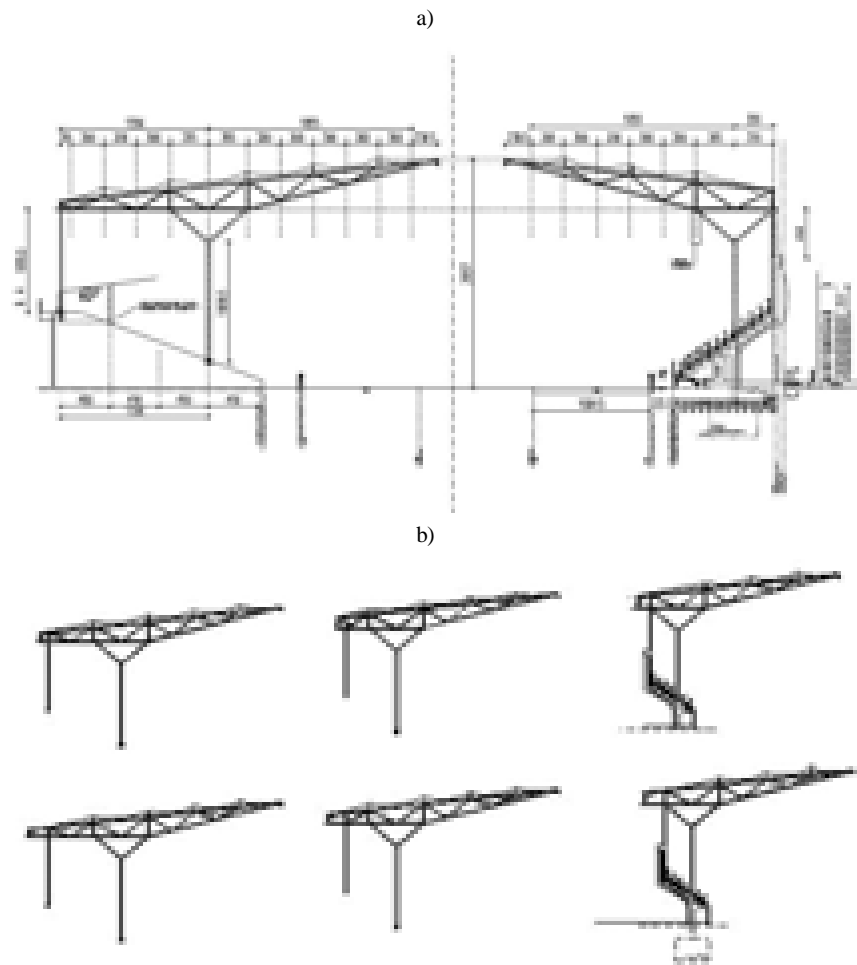
Fig. 4. Cross-section geometry of the bearing structure:
(a) – in main cross-sections; (b) – in different cross-sections.

2. Scope of the work

The basic aim of the aerodynamic tests of the municipal stadium roof in Tarnów is determination of the extreme unfavorable pressures distributions on the roof caused by wind action and – on the basis of experimental results – assuming simplified schemes of wind action distributions that will be used in static-strength calculations of the analyzed structure. A special attention should be placed on a wind action which causes roof unloading (suction).

58

In experiments, there are used following denotations and definitions:

$\Delta p(t)$ – differential wind pressure – the instantaneous difference of the wind pressure between upper and lower surface; $\Delta p(t) > 0$ – (pressure) – a differential wind pressure which causes a roof holding down to the carrying structure (fig 5); $\Delta p(t) < 0$ – (suction) – a differential wind pressure which causes a roof lifting (fig. 5);
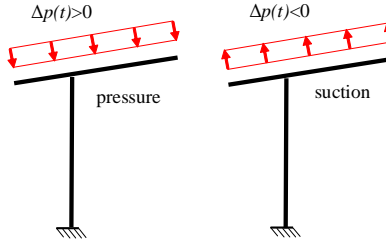
Fig. 5. Positive (pressure) and negative (suction) differential wind pressure.

q_{ref} – reference pressure i.e. the mean value of the dynamic wind pressure on the mean roof height measured in the undisturbed air flow in front of the model;

$\Delta \overline{p}$ – mean value of the differential wind pressure;

$\overline{C}_p$ – aerodynamic coefficient of the mean differential wind pressure:

$$\overline{C}_p = \frac{\Delta \overline{p}}{q_{ref}}, \tag{1}$$

$\sigma_{\Delta p}$ – standard deviation of the temporal run of the differential wind pressure;

C_p^{max} – aerodynamic coefficient of the maximum differential wind pressure:

$$C_p^{max} = \frac{\Delta \overline{p} + \sigma_{\Delta p}}{q_{ref}}, \tag{2}$$

C_p^{min} – aerodynamic coefficient of the minimum differential wind pressure:

$$C_p^{min} = \frac{\Delta \overline{p} - \sigma_{\Delta p}}{q_{ref}}. \tag{3}$$

The tests scope contains: determining of aerodynamic coefficients distributions on the roof: mean differential wind pressure coefficient, coefficient of the maximum differential wind pressure, coefficient of the minimum differential wind pressure. The distributions have been determined in the seven roof cross-sections on the one roof half (fig. 6).

59
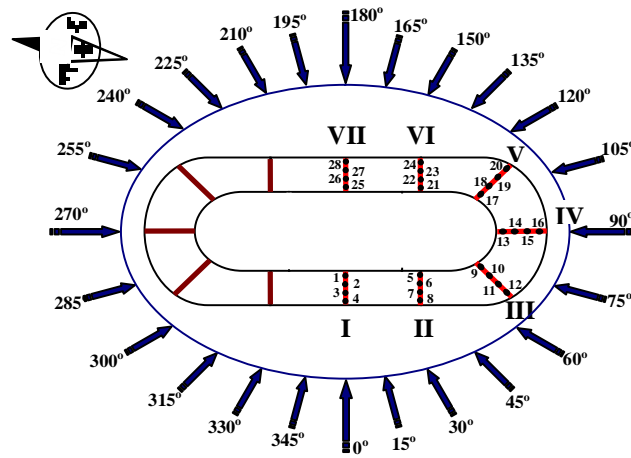
Fig. 6. Location of the measurement points in the seven cross-sections of the stadium roof with the considered wind flow directions.

3. Measurement scheme

The measurement point enables definition of the instantaneous difference of wind pressure on the both roof side (differential wind pressure $\Delta p(t)$). The scheme of the measurement is presented in fig. 7.
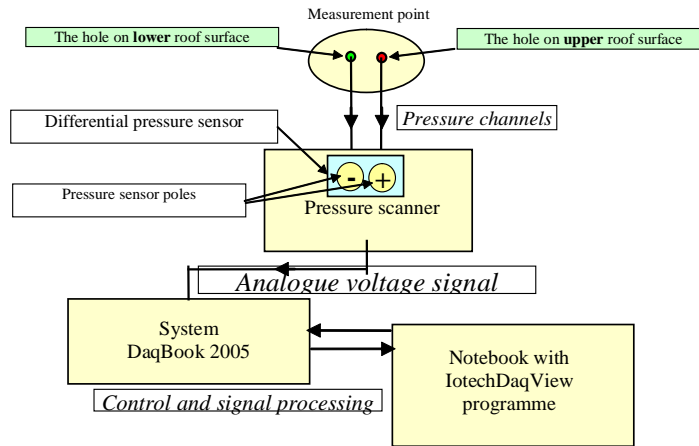
Fig. 7. The measurement scheme for the differential wind pressure.

4. Wind tunnel and model

Experiments have been carried out in the boundary layer wind tunnel of the Wind Engineering Laboratory at the Cracow University of Technology (fig. 8) [3].
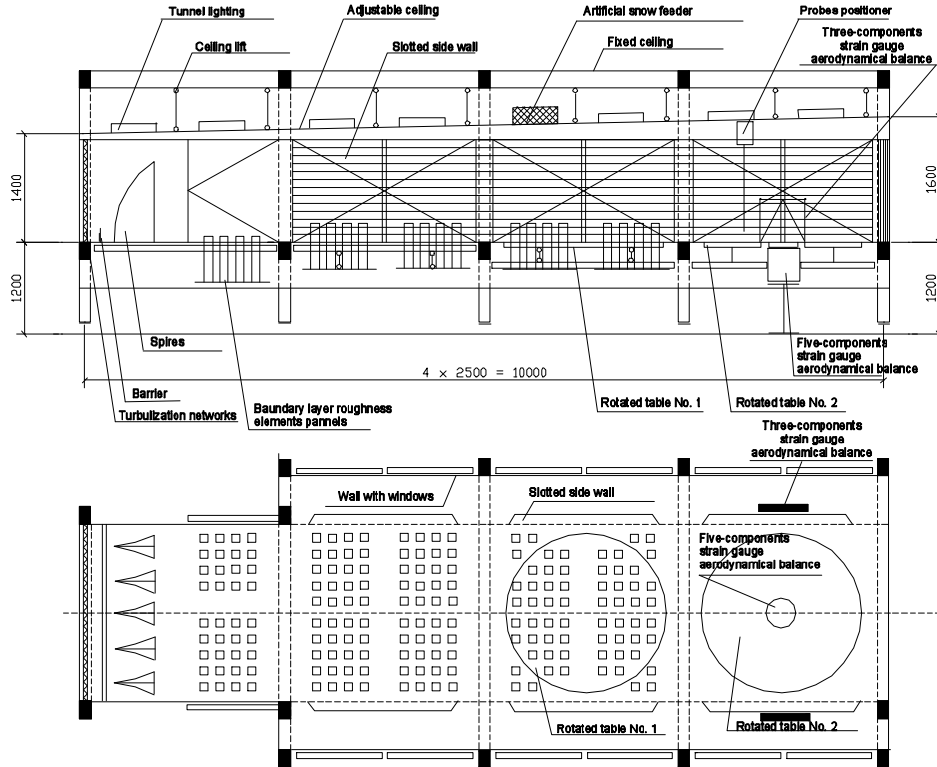
Fig. 8. Working section of the wind tunnel: vertical section (a), horizontal section (b).

An accurate model of the stadium roof of the scale of 1:200 has been manufactured from different plastic materials (figs 9 and 10).

Fig. 9. Model of the municipal stadium roof in the working section of the wind tunnel.
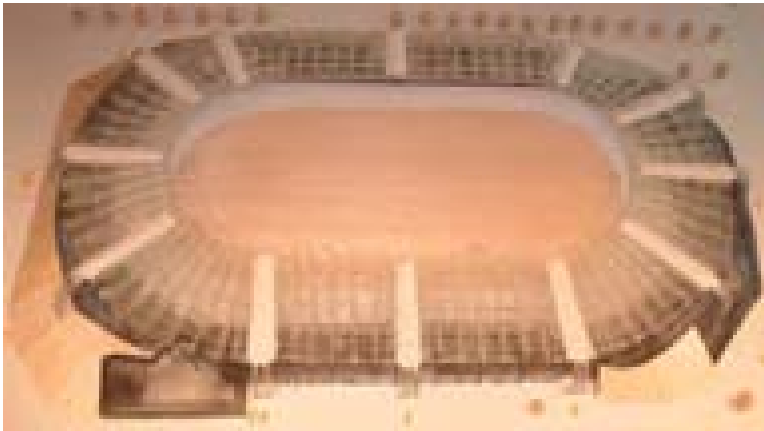
Fig. 10. Distribution of the measuring points on the roof.

5. Exemplary experimental results

5.1. Chosen distributions of the mean wind pressure coefficient $\overline{C}_p$ dependent on angle of wind attack

These distributions are presented in figs 11-17.
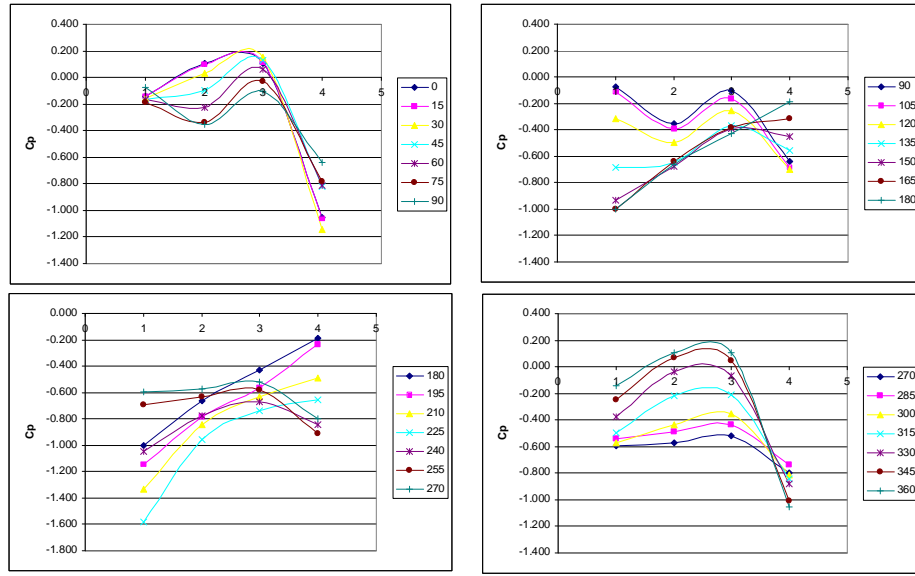
Fig. 11. Distributions of the coefficient $\overline{C}_p$ values in cross-section I for different angles of wind attack.
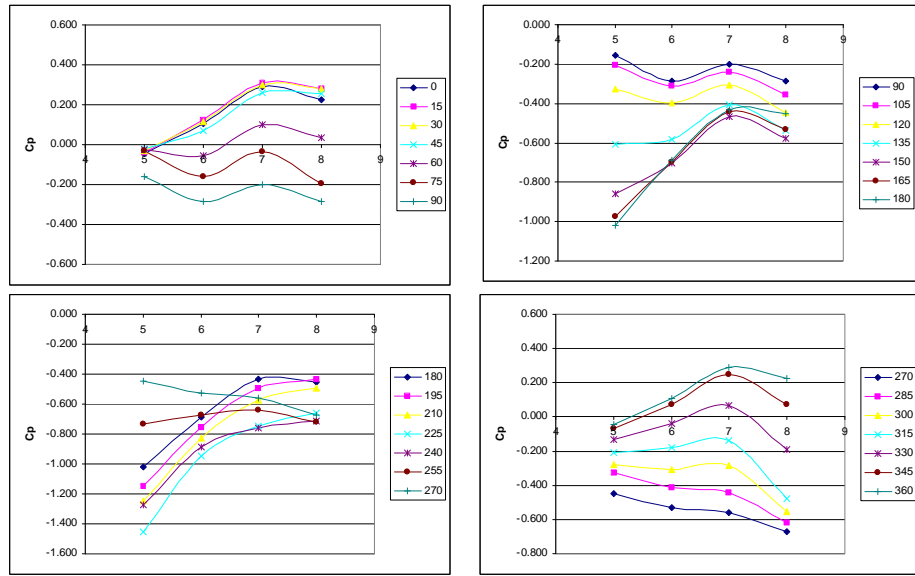
Fig. 12. Distributions of the coefficient $\overline{C}_p$ values in cross-section II for different angles of wind attack.

63
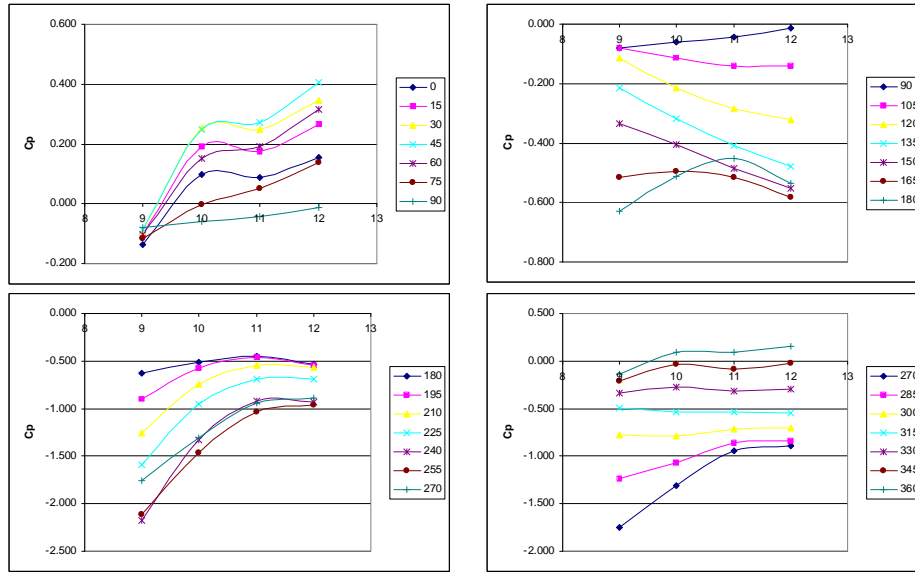
Fig. 13. Distributions of the coefficient $\overline{C}_p$ values in cross-section Ⅲ for different angles of wind attack.
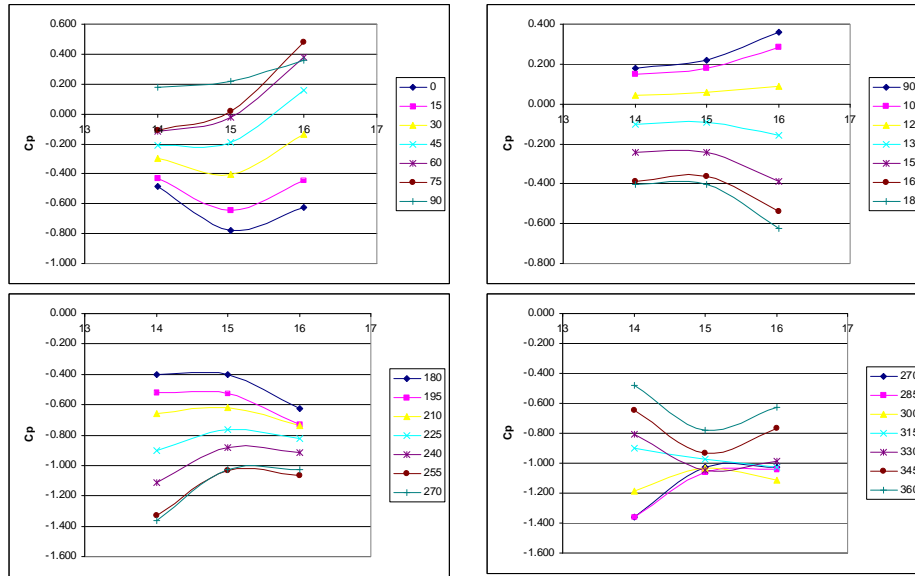
Fig. 14. Distributions of the coefficient $\overline{C}_p$ values in cross-section Ⅳ for different angles of wind attack.

64
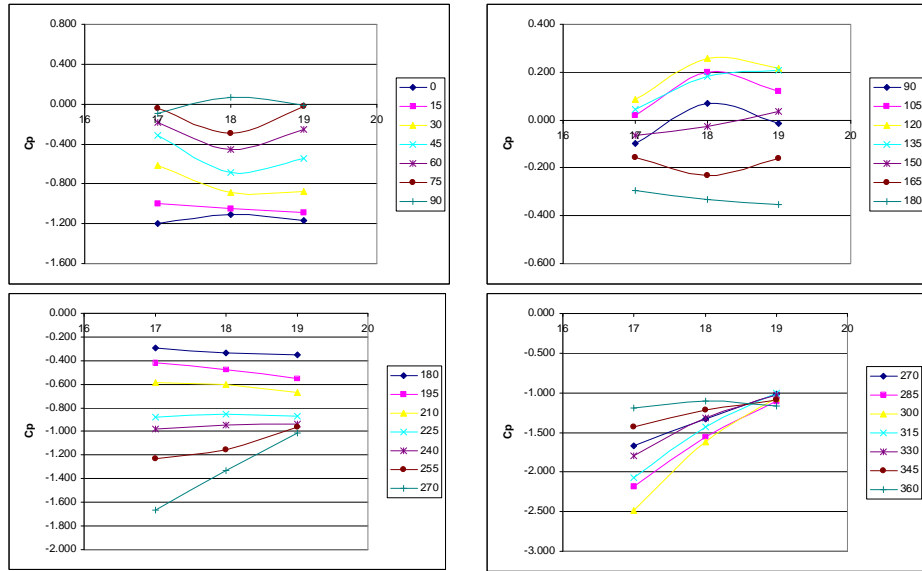
Fig. 15. Distributions of the coefficient $\overline{C}_p$ values in cross-section V for different angles of wind attack.
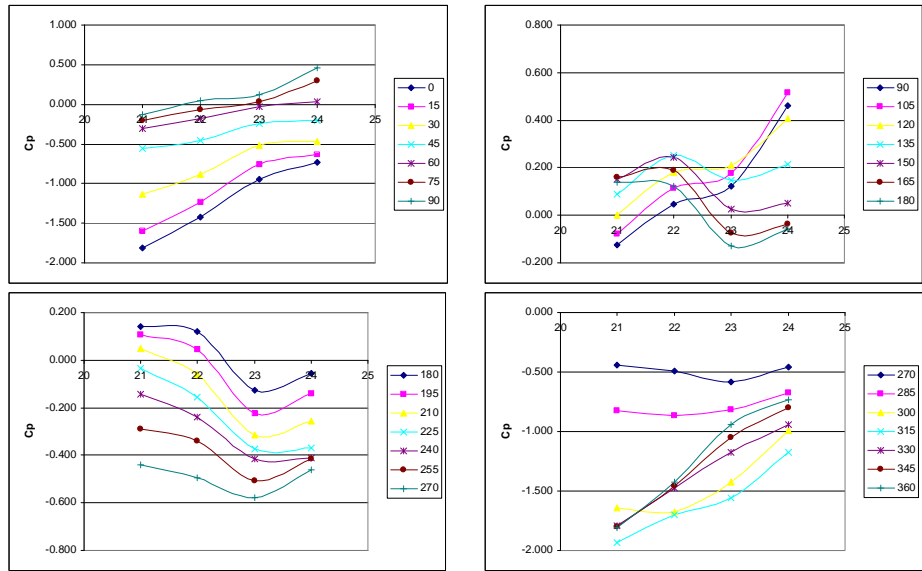
Fig. 16. Distributions of the coefficient $\overline{C}_p$ values in cross-section VI for different angles of wind attack.

65
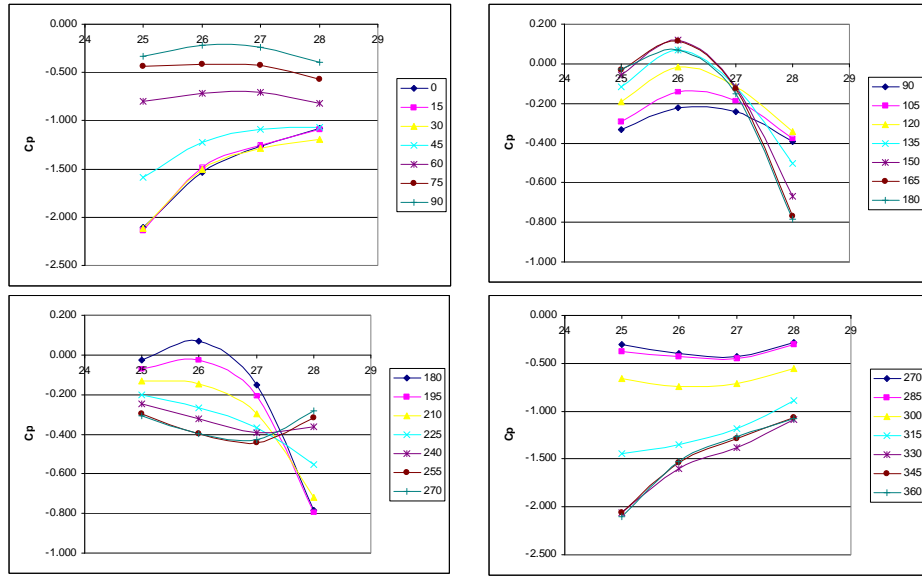
Fig. 17. Distributions of the coefficient $\overline{C}_p$ values in cross-section VII for different angles of wind attack.

5.2. Envelopes of distributions of the differential wind pressure coefficients C_p^{max} and C_p^{min} in particular measuring cross-sections

These envelopes are shown in the subsequent figures.

Cross-section I	1	2	3	4
C_p^{max}	0.245	0.279	0.385	0.030
C_p^{min}	-2.325	-1.394	-1.033	-1.932

Cross-section II	5	6	7	8
C_p^{max}	0.110	0.304	0.558	0.624
C_p^{min}	-2.252	-1.334	-1.028	-0.948

Cross-section III	9	10	11	12
$C_p^{\max}$	0.043	0.464	0.554	0.869
$C_p^{\min}$	-3.385	-1.955	-1.377	-1.224

Cross-section IV	13	14	15	16
$C_p^{\max}$	-	0.391	0.478	0.933
$C_p^{\min}$	-	-1.918	-1.466	-1.398

Cross-section V	17	18	19	20
$C_p^{\max}$	0.256	0.484	0.493	-
$C_p^{\min}$	-3.539	-2.196	-1.575	-

Cross-section VI	21	22	23	24
$C_p^{\max}$	0.239	0.368	0.372	0.876
$C_p^{\min}$	-2.276	-2.028	-1.851	-1.439

Cross-section VII	25	26	27	28
$C_p^{\max}$	0.058	0.247	0.043	-0.163
$C_p^{\min}$	-2.6	-1.869	-1.617	-1.255

Fig. 18. Envelopes of distributions of the coefficients $C_p^{\max}$ and $C_p^{\min}$ in particular cross-sections.

67

6. Proposed distributions of a coefficient of maximum suction on the stadium roof in static-strength calculations

In static-strength calculations of a membrane covering and particular frame-truss structures constituting the main bearing structures of the roof, the most unfavourable type of wind action is in general maximum wind suction. Basing upon analysis of obtained experimental results, distributions of a coefficient of maximum suction measured in several cross-section of the roof, proposed in static-strength calculations, have been determined. These distributions are given in fig. 19.
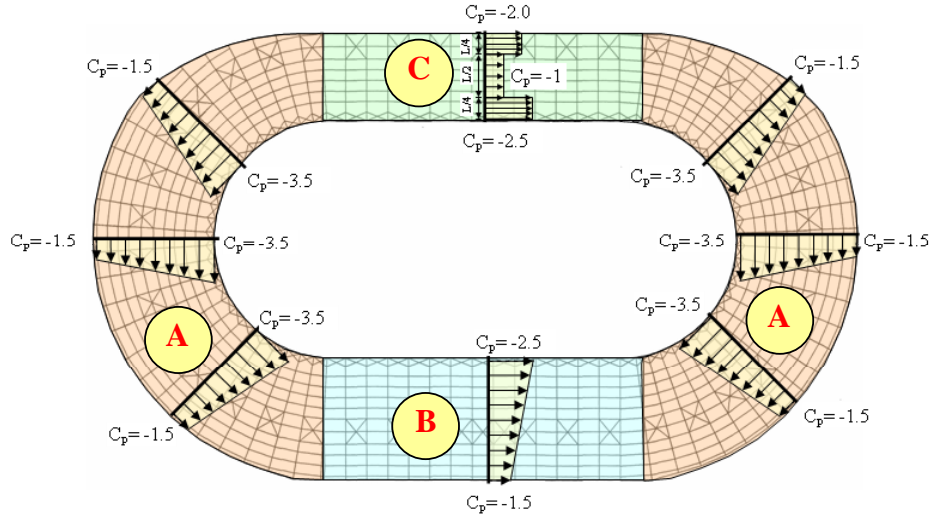
Fig. 19. Proposed distributions of a coefficient of maximum suction on the stadium roof in static-strength calculations.

7. Chosen schemes of wind actions on frame-truss structures assumed in statical calculations

Chosen schemes of wind actions on the two main bearing frame-truss structures of the roof, determined of the basis of distributions of a coefficient of maximum suction presented in fig. 20, are shown in fig. 21.

68

6,30 kN 18,20 kN 22,40 kN 22,40 kN 19,90 kN 13,60 kN 5,00 kN

Frame-truss in axis

6,30 kN 17,75 kN 10,07 kN 15,34 kN 12,00 kN

Frame-truss in axis
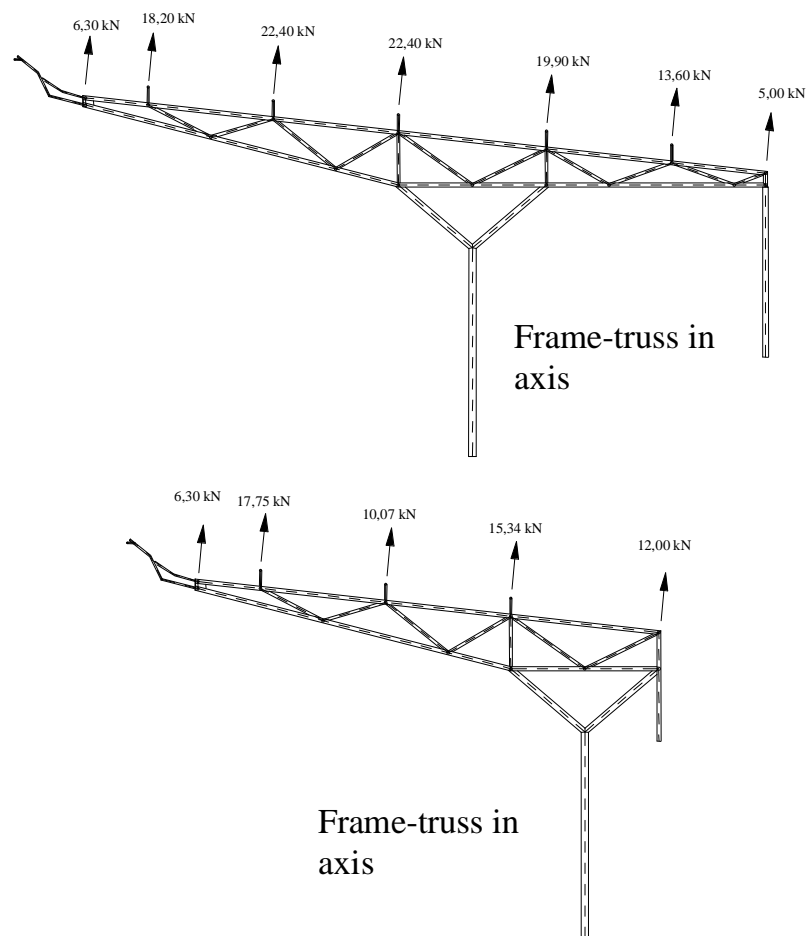
Fig. 20. Schemes of wind suction on the two chosen frame-truss structures.

Horizontal wind actions on the particular frame-truss structures have been evaluated on the basis of the standard PN-77/B-02011 according to the quasi-static model of wind action, assuming: q_k=350Pa (characteristic wind velocity pressure); C_e=0,8 (exposure factor); C_p=2,0 (wind pressure coefficient); G_p=2,2 (peak gust factor). W_k=$q_k C_e C_p G_p$=1232Pa (characteristic value of an equivalent horizontal wind pressure uniformly distributed on the vertical elements and walls); w_d=1,3w_k=1,7kN/m^2 (design value of this wind pressure). Obtained on the basis of this simple wind action model, horizontal forces acting on the two chosen frame-truss roof structures are presented in fig. 21.
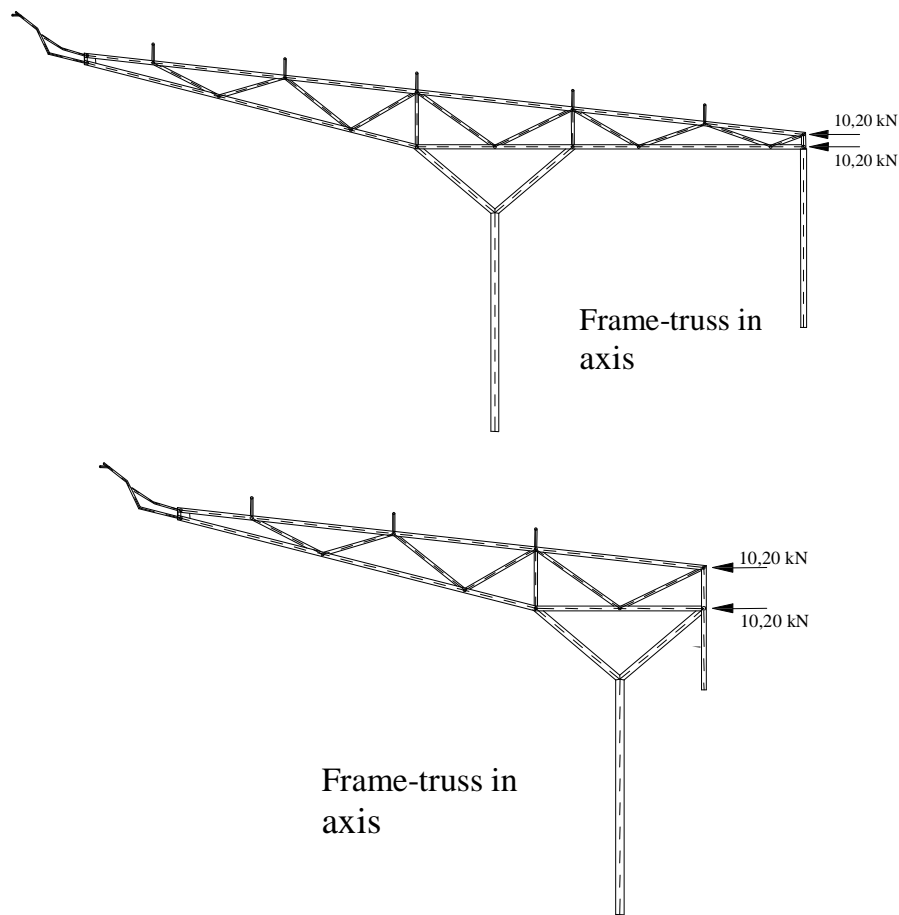
Fig. 21. Schemes of horizontal wind actions on the two chosen frame-truss roof structures.

8. Additional remarks concerning dynamical characteristics of the roof structure with respect to possible vibrations caused by wind

To determine basic dynamical characteristics of the roof structure, dynamical calculations of the whole roof structure free vibrations have been performed using FEM model of this structure. Chosen results of this calculations are given in figs 22 and 23.

As can be seen from these figures, the lowest free vibration modes and frequencies are dominated by horizontal displacements and not by vertical ones. In such case, a most probable form of whole roof structure vibrations caused by wind could be buffeting vibrations and rather not vibrations of the roof of flutter type.

70
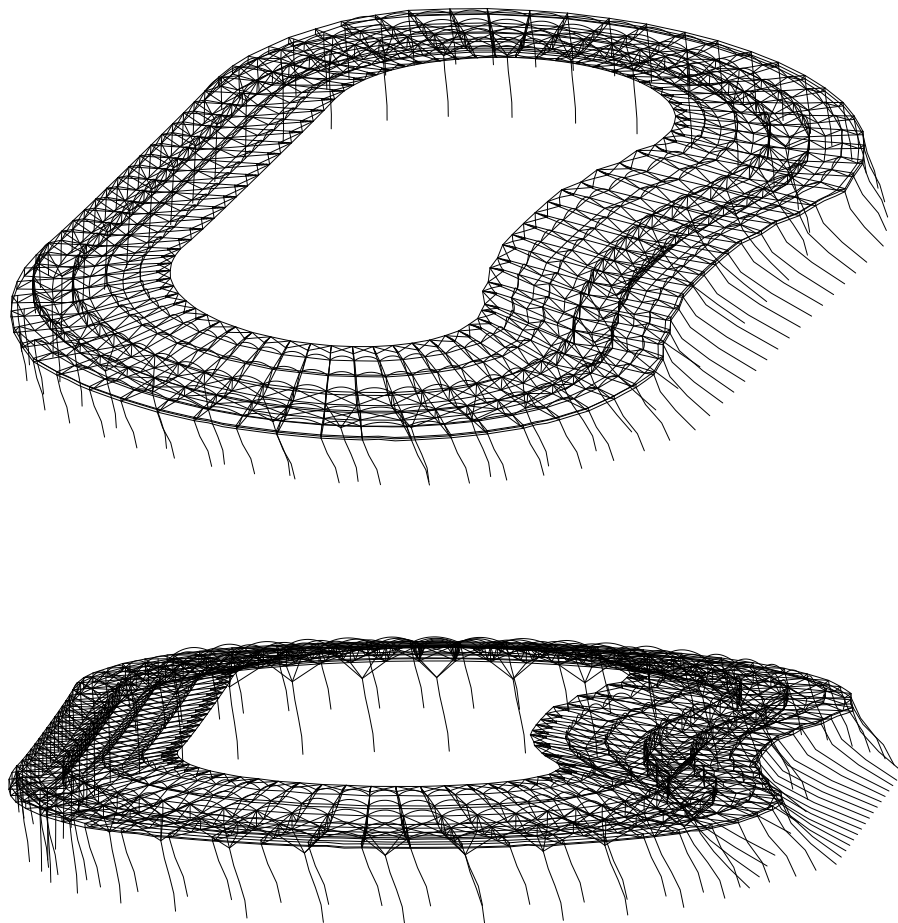
Fig. 22. Results of dynamical calculations – first free vibration mode, $f_1 = 0.55$ Hz.
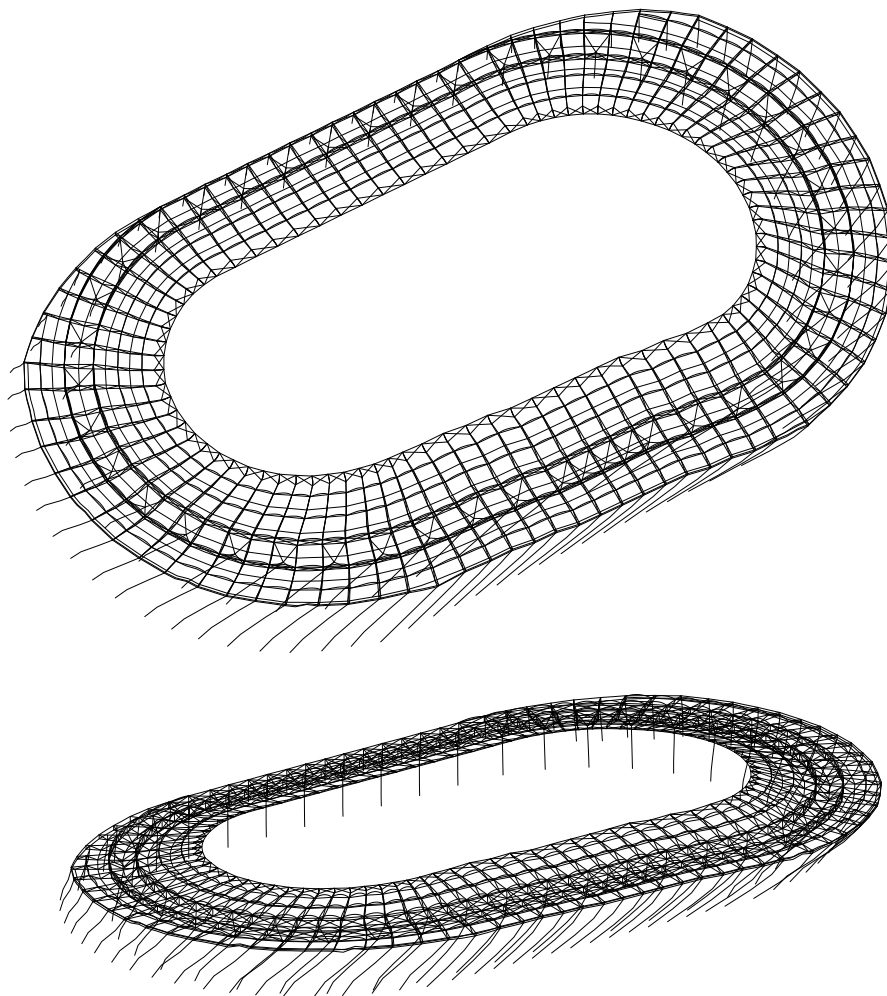
Fig. 23. Results of dynamical calculations – second free vibration mode, $f_2 = 0.61$ Hz.

References

[1] *Project of the municipal stadium roof in Tarnów*, Design Office "S.P.A.K. – Studio Projektowe Anny Kasprzyk", Miłobędzka street 23, Warsaw, 2007.
[2] Flaga A., Pańtak M., Kimbar G., *Building-structure project of the modernization of the municipal stadium in Tarnów*, Cracow University of Technology, Cracow, 2007.
[3] Flaga A., Bosak G., Rzegocka-Kłaput R., Matys P., Flaga Ł.: *Model tests of the municipal stadium roof in Tarnów in wind tunnel*. Cracow University of Technology, Cracow, 2007.

72

WIND TUNNEL TESTS
OF AERODYNAMIC INTERFERENCE
BETWEEN TWO STEEL DOUBLE-WALLS FUEL TANKS

Andrzej Flaga[*,**], Grzegorz Bosak[*], Mariusz Suwaj[*]

[*] Wind Engineering Laboratory, Faculty of Civil Engineering,
Cracow University of Technology, Jana Pawla II 37/3a, 31-864 Cracow, Poland.
[**] Department of Structural Mechanics, Faculty of Civil and Sanitary Engineering,
Lublin University of Technology, Nadbystrzycka 40, 20-618 Lublin, Poland.

1. Introduction

The influence on static and dynamic component of wind pressure have been examined for one and two steel double-walls fuel tanks in their different configurations. Pressure distributions on outer and inner walls of the tank and surface of the roof have been taken under consideration. Both tanks have had similar overall dimensions. Measurements have been carried out in a wind tunnel with boundary layer. It is known that influence of aerodynamic interference could be positive as well as negative [1-5]. The most interesting situations are these ones where the negative influence occur for tank configurations which could have place in petroleum refineries and fuel resources. It is worth mentioning that the observations of interference of cooling towers [5] and a behavior of two near situated circular cylinders [3] confirm statement that a character of an interference phenomenon of static to compare to dynamic components could be quite different in case of double-walls fuel tanks. In particular, the interference could have a significant influence on local wind pressure and investigation of such a case is important for design. The influence of aerodynamic interference has been evaluated on the base of analysis of: mean, extreme and standard deviation time history series of wind pressure by comparison of one tank situation to two-tank situations.

2. Brief description of the fuel tank models

Measurements have been carried out in a boundary layer wind tunnel of the Cracow University of Technology. Basic dimensions of the wind tunnel working section are: 2.20x1.40x10.00 m. Experiments have been performed at the following conditions: 1. Power law exponent of the wind profile α=0.20; 2. Intensity of turbulence I_v=20 %; 3. Reference velocity V_{ref}=20 m/s (it corresponds to Reynolds number Re=5.5x10^5). During the measurements, two models of fuel tanks have been used. The measurements have been accomplished using an active model i.e. equipped with radial distributed sensors on its

73

walls and the roof. The sensors have been connected to the pressure scanners making possible simultaneously collection of instantaneous wind pressure time series. The second one, called the passive model, has not any measurement systems. A geometric similarity scale of the model tanks is equal to 1:50. The diameter of the outer cylindrical wall equals 620 mm and the inner one 560 mm. Both of the tank models have fixed roofs. The active and passive models placed on a rotational table in the wind tunnel working section are presented in fig. 1.

Fig. 1. Active and passive models of double-walls fuel tanks in the wind tunnel working section.

On the top surface of the each roof, twenty five measurement points are cylindrically distributed. On the outer wall, seventy two measurement points enable taking measurements on the three high levels (comp. fig. 2.), for the inner as well as outer surfaces.

Inner wall   Outer wall
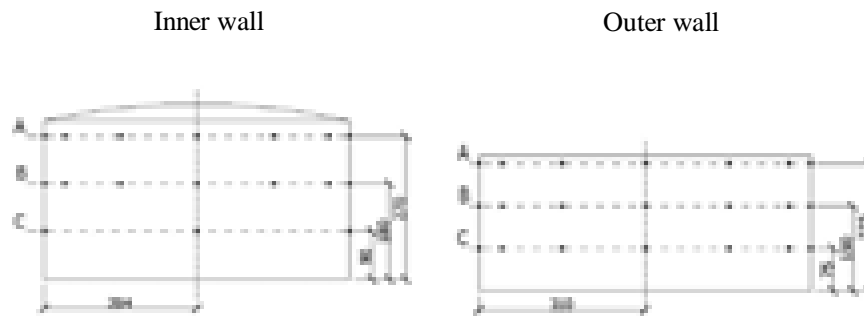
Fig. 2. Levels of measurement points on the inner and outer walls of the active model.

On each level, wind pressure can be obtained in twelve points every 30 degrees around the perimeter. The inner wall has fifty six measurement points on the three height levels. In contradistinction to the outer wall on the lowest level only 8 points have are installed every 90 degrees (four points in the inner surface and four in the outer one).

3. Wind tunnel tests – plan of measurements

Wind pressure distributions and adequate wind pressure coefficients on the walls (inner and outer) and on the roof surface has been the main aim of the wind tunnel tests. At the beginning, in the first stage, only active model has been examined. A plan of tests has contained experiments with tank model of fixed roof. In the second stage, configurations of the two tank models (active and passive one) have been taken under considerations. During the tests, two various distances between models (L) have been taken. In comparison to the outer wall diameter (D), the distances (L/D) have been equal to 1.47 and 1.63. The considered measurement configurations of the two tank models are schematically presented in fig. 3.
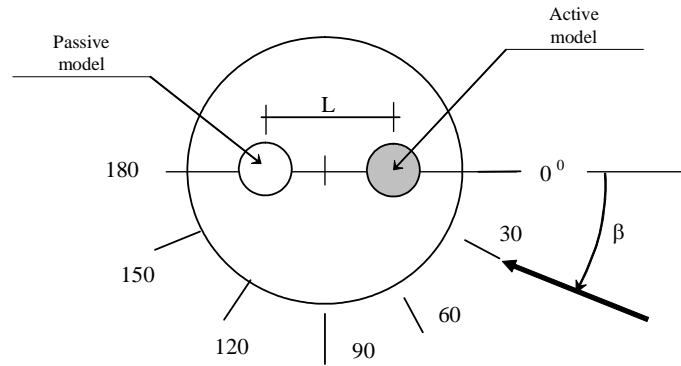
Fig. 3. Aerodynamic interference measurement situations of two tank models.

A comparison of mean and instantaneous wind pressure fields is the base of evaluation of an influence of aerodynamic interference in particular measurement situations.

4. Results of measurements

4.1. One tank measurement situation

Only exemplary experimental results connected with the analysis of mean wind pressure distributions on the tank wall surfaces are presented below. At the beginning, the coefficient of local mean wind pressure C_p has been introduced, which is defined as follows:

75

$$C_p\left(\theta, z, H\right) = \frac{\Delta \overline{p}(\theta, z)}{q\left(H\right)} \qquad (1)$$

where: $\Delta \overline{p}(\theta, z)$ -difference of mean wind pressure on inner and outer wall surfaces in cylindrical co-ordinate system $(r,\ \theta,\ z)$; $q(H) = \frac{1}{2}\rho V^2(H)$ - mean wind velocity pressure in the front of the model on the level H (H-height of the inner wall of the tank model), z – height above the terrain level.

For example, distribution of C_p coefficient on outer and inner walls for the A, B and C levels in one tank measurement situation for the model with fixed roof is shown in fig. 4. Below, in fig. 5 distribution of C_p coefficient on the roof of the model is presented.
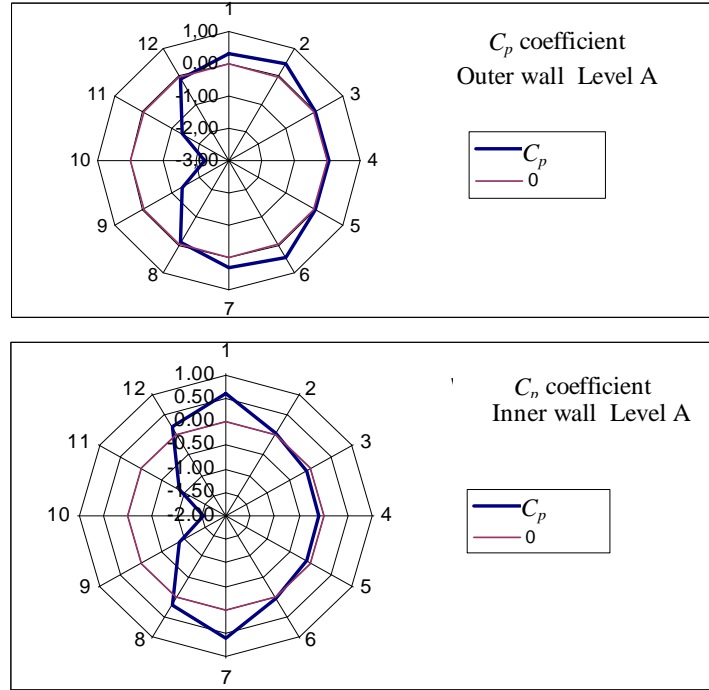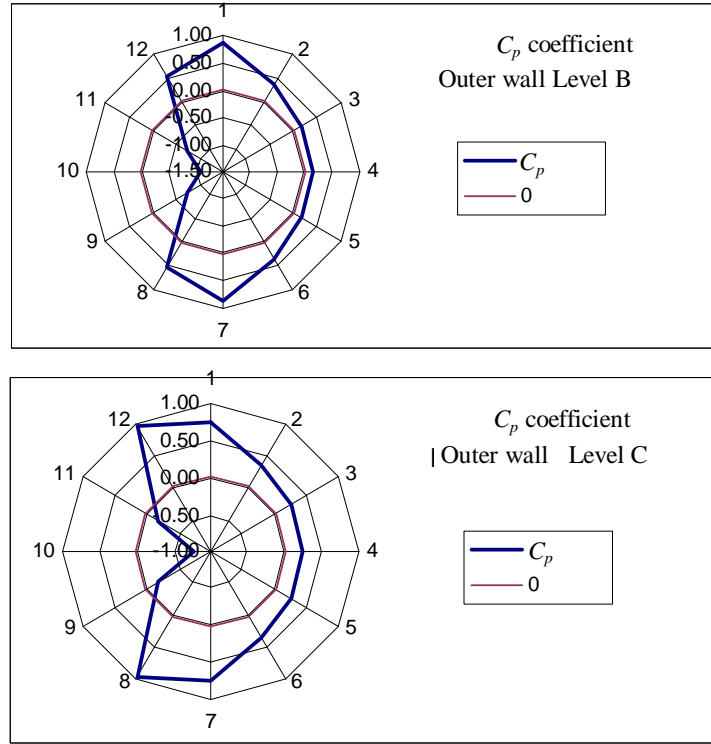
Fig. 4. Distribution of C_p coefficient on outer and inner walls in one tank measurement situation β=0.
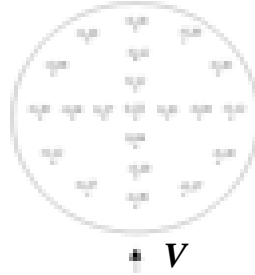
Fig. 5. Distribution of C_p coefficient on the roof in one tank measurement situation β=0.

4.2. Interference measurement situation

A coefficient of aerodynamic interference $\Phi_i(\theta,z)$ has been adopted in agreement with a formula:

$$\Phi_i(\theta, z) = \frac{C_p^G(\theta, z) - C_p^S(\theta, z)}{C_p^S(0, z)} \tag{2}$$

where: $C_p^G(\theta, z)$ – mean wind pressure coefficient in aerodynamic interference case; $C_p^S(\theta, z)$ – mean wind pressure coefficient in one tank measurement situation; $C_p^S(0, z)$ – mean wind pressure coefficient in one tank measurement situation for the wind inflow direction $\beta = 0°$. Values of the coefficient $\Phi_i(\theta, z)$ on outer and inner walls, obtained from measurements, are presented in tables I-III. Mean wind inflow direction $\beta = 0°$ referred to wall measurements points distributed around the perimeter is shown in fig. 6.
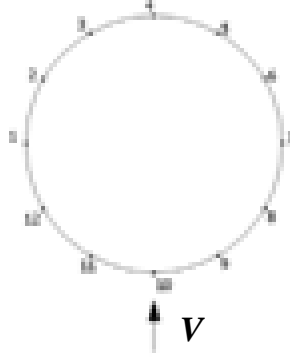
Fig. 6. Relations between mean wind inflow direction $\beta = 0°$ and wall measurements points distributed around the perimeter.

Table I. Distribution of the coefficient $\Phi_i(\theta, z)$ on outer wall, L/D=1.47, level A.

	I1	I7	I2	I8	I3	I9	I4	I10	I5	I11	I6	I12
1	-0.04	0.05	0.03	0.07	0.07	0.07	-0.11	0.14	-0.11	-0.04	-0.28	0.00
2	0.21	0.19	0.00	0.10	0.00	0.00	0.14	0.00	0.00	0.04	-0.56	0.04
3	0.05	-0.16	-0.19	0.02	0.05	-0.15	-0.12	-0.12	-0.05	-0.09	-0.64	-0.09
4	0.04	0.03	0.07	0.07	-0.10	-0.04	-0.07	-0.14	-0.04	-0.04	-0.07	-0.14
5	0.05	-0.09	-0.05	-0.15	-0.12	-0.05	-0.22	-0.02	-0.05	-0.12	-0.02	-0.71
6	0.04	-0.01	0.10	0.14	-0.07	0.10	-0.04	0.41	0.14	-0.04	0.00	-0.56
7	0.03	0.14	0.07	-0.04	0.07	0.17	0.14	-0.07	0.03	-0.11	0.03	-0.21
8	0.02	0.22	0.05	0.12	-0.12	0.15	0.15	0.29	0.19	0.02	0.29	0.08
9	-0.15	-0.50	0.02	0.02	-0.02	0.09	0.04	0.12	0.12	0.19	0.19	0.02
10	-0.24	-0.66	-0.21	-0.21	-0.21	-0.21	-0.14	-0.14	-0.07	-0.03	-0.03	0.00
11	-0.08	-0.47	-0.05	-0.08	0.02	-0.08	-0.02	-0.02	-0.02	0.09	-0.12	0.05
12	-0.02	0.06	0.05	0.05	0.12	0.08	0.08	0.08	-0.05	0.15	0.02	0.05

78

Table II. Distribution of the coefficient $\Phi_i(\theta,z)$ on outer wall, L/D=1.47, level C.

	I1	I7	I2	I8	I3	I9	I4	I10	I5	I11	I6	I12
1	1.36	0.25	-0.14	-0.24	-0.04	0.05	-0.74	0.05	-0.45	2.06	-0.95	-0.35
2	0.45	-0.28	-0.15	0.35	-0.26	-0.55	0.24	-0.36	0.14	-0.05	-0.86	0.65
3	1.26	0.43	-0.05	-0.05	0.85	0.04	0.24	0.24	0.04	0.35	-0.56	-0.05
4	0.00	-0.35	-0.09	0.00	0.10	-0.19	-0.09	-0.09	0.00	0.10	0.91	-0.09
5	0.78	-0.50	0.08	-0.22	0.08	-0.03	-0.03	0.08	0.38	-0.12	0.08	-0.32
6	0.05	0.21	0.24	-0.55	-0.36	-0.15	1.55	0.35	-0.26	-0.46	0.24	-0.86
7	0.76	0.32	-0.14	-0.14	1.96	-0.14	0.05	-0.74	0.05	-0.35	-0.04	-0.45
8	0.50	0.60	1.71	0.90	1.00	1.10	1.10	0.60	1.21	0.10	1.00	0.29
9	0.65	0.32	0.35	0.45	0.55	0.55	0.55	0.65	0.45	0.45	0.35	-0.65
10	0.81	-1.15	0.10	-1.91	0.51	0.00	0.00	0.21	0.10	0.31	-0.19	-0.19
11	1.26	-0.75	0.55	0.35	0.24	-0.46	0.55	0.45	0.24	0.45	-0.65	0.24
12	0.60	-0.04	0.81	0.81	0.90	0.81	2.01	0.81	-0.10	0.71	0.21	0.71

Table III. Distribution of the coefficient $\Phi_i(\theta,z)$ on inner wall, L/D=1.47, level A.

	I1	I7	I2	I8	I3	I9	I4	I10	I5	I11	I6	I12
1	0.05	-0.22	-0.05	-0.16	-0.15	-0.29	-0.28	-0.14	-0.31	-0.22	-0.59	-0.36
2	-0.10	-0.65	-0.15	-0.16	-0.15	-0.35	-0.13	-0.40	-0.15	-0.37	-0.84	-0.25
3	-0.16	-0.57	-0.16	-0.22	-0.21	-0.29	-0.18	-0.24	-0.21	-0.22	-0.75	-0.25
4	-0.10	-0.35	-0.10	-0.22	-0.16	-0.24	-0.18	-0.20	-0.21	-0.17	-0.24	-0.31
5	-0.10	-0.27	-0.16	-0.27	-0.21	-0.24	-0.24	-0.14	-0.25	-0.17	-0.28	-0.77
6	-0.15	-0.20	-0.15	-0.22	-0.31	-0.35	-0.33	-0.14	-0.46	-0.12	-0.44	-0.97
7	-0.05	-0.07	-0.10	-0.22	-0.05	-0.24	-0.23	-0.29	-0.25	-0.27	-0.28	-0.61
8	-0.18	0.22	-0.03	-0.08	-0.07	-0.06	-0.05	-0.01	-0.03	-0.19	-0.10	-0.28
9	-0.15	-0.30	-0.10	-0.22	-0.20	-0.09	-0.03	0.01	-0.10	-0.01	0.03	-0.25
10	-0.25	-0.55	-0.16	-0.17	-0.16	-0.24	-0.18	-0.14	-0.16	-0.12	-0.18	-0.16
11	-0.31	-0.48	-0.20	-0.22	-0.10	-0.24	-0.12	-0.19	-0.25	-0.16	-0.33	-0.15
12	-0.18	-0.13	-0.07	-0.24	-0.07	-0.16	-0.10	-0.06	-0.48	-0.08	-0.56	-0.23

5. Conclusions

- Influence of aerodynamic interference on mean wind pressure values is significant;
- Aerodynamic interference coefficients Φ_i have positive and negative values. An increase in overpressure and negative pressure could be occurred on outer or inner walls. The highest module value of the aerodynamic interference coefficient could reach level of 2.0.
- In most tests situations, values of the aerodynamic interference coefficient on the highest level (level A) of the inner wall are negative, which points on existence of low pressure areas around upper parts of the inner tank wall.

References

[1] Whithbread R.E., *Model simulation of wind effects on structures*, WEBS, Teddington 1963.

[2] Krishnaswamy T.N., Rao G.N., Durvasula S., Reddy K.R., *Model observations of interference effects on oscilatory response of two identical stacks*, Procedings of 4th International Conference on Wind Effects on Buildings and Structures, London, Heaththrow 1975.

[3] Zdravkovich M.M., *Review of interference – Induced oscillations in flow past two parallel circular cylinders in various arrangements*, 7th International Conference on Wind Engeneering, vol. 2, Aachen 1987.

[4] Niemann H.J. Köpper H.D., *Influence of adjacent buildings on wind effects on cooling towers,* Natural Draught Cooling Towers, Wittek & Kratzig, Rotterdam, 1996.

[5] Parameswaran L., *Interference studies on a group of natural draught cooling towers.* Wind Engeneering into the 21st Century, p. 517-523. Larsen, Larose & Livesey, Rotterdam, 1999.

80

AERODYNAMIC TESTS OF SECTIONAL MODELS OF BUILDING CRANE TOWER AND JIB

Marcin Augustyn[*], Andrzej Flaga[**], Bogdan Stolarski[*]

[*] Institute of Machine Design, Cracow University of Technology,
Jana Pawła II 37, 31-864 Cracow, Poland.
[**] Wind Engineering Laboratory, Faculty of Civil Engineering,
Cracow University of Technology, Jana Pawła II 37/3a, 31-864 Cracow, Poland.

1. Introduction

The paper presents selected results of experiments on sectional models of building crane tower and jib carried out in boundary layer wind tunnel of wind engineering laboratory at Cracow University of Technology. Influence of geometrical parameters of sectional models of building crane tower and jib in turbulent flow has been analyzed.

Measurements have been carried out for mean wind velocity of 20 m/s, turbulence intensity of 15% and for different angles of wind attack from 0° to 180° with step of 15°.

2. Formulae for determination of aerodynamic coefficients

Geometrical scale of the models is 1/7. Three different profiles of truss elements have been tested: i.e. cold-formed square, tube, angle iron (fig. 2 and 3).
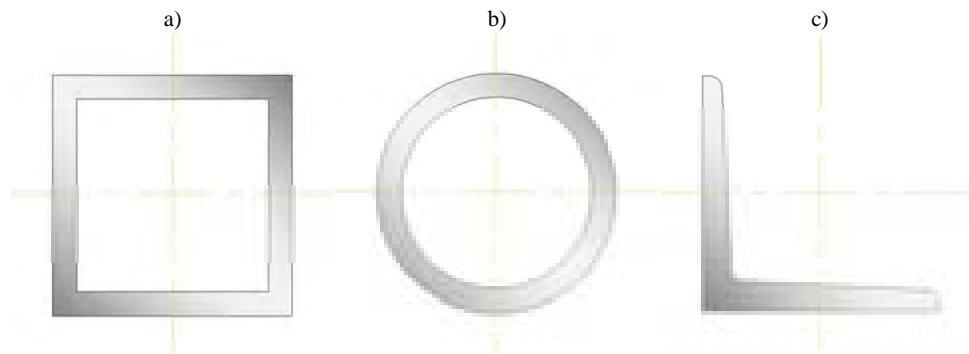
Fig. 1. Profiles of truss elements:
a) cold-formed square, b) tube, c) angle iron.

81

Formulae for determination of aerodynamic coefficients are as follows:

$$C_x = \frac{P_x}{q \cdot S_k} \quad - \text{coefficient of aerodynamic drag;} \tag{1}$$

$$C_y = \frac{P_y}{q \cdot S_k} \quad - \text{coefficient of lateral aerodynamic force;} \tag{2}$$

$$q = \frac{\rho V_{\acute{s}}^2}{2} \quad - \text{wind velocity pressure;} \tag{3}$$

$$\varphi = \frac{S_k}{S_o} \quad - \text{solidity ratio.} \tag{4}$$

Solidity ratio of building crane tower of square cross section:

$$\varphi = \frac{S_k}{S_o} = \frac{0.017304}{0.104244} \cong 0.17 \tag{4a}$$

Solidity ratio of building crane tower of equilateral triangle cross section:

$$\varphi = \frac{S_k}{S_o} = \frac{0.021438}{0.098532} \cong 0.22 \tag{4b}$$

In above equations: P_x, P_y – aerodynamic drag and lateral force respectively; V – mean wind velocity; ρ – mass air density; S_k – effective area of the one wall of the truss i.e. the area of the shadow normal projected by its members on a plane parallel to the wall; S_o – contour area of the one wall of the truss.
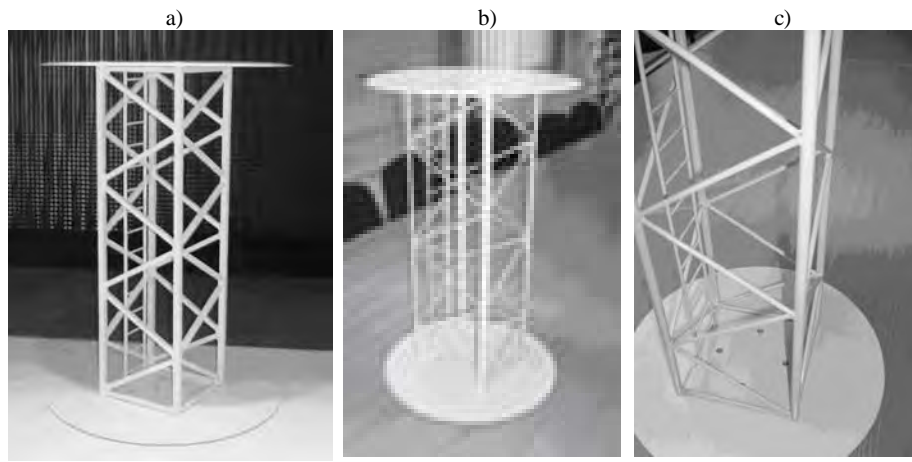
Fig. 2. Sectional models of building crane tower:
a) cold-formed square, b) angle iron, c) tube.
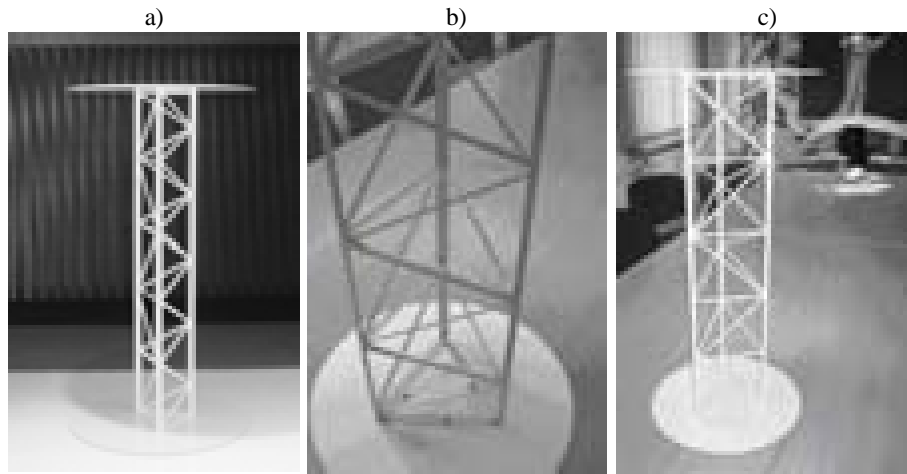
Fig. 3. Sectional models of building crane jib:
a) cold-formed square, b) angle iron, c) tube.

3. Experimental results

Obtained experimental results, i.e. aerodynamic coefficients of aerodynamic drag and lateral aerodynamic force for tower and jib respectively are presented in figs 4 – 9.

TOWER
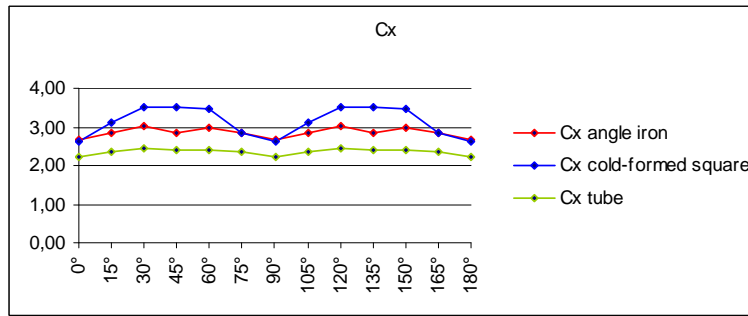
Fig. 4. Coefficient of aerodynamic drag of building crane tower of square cross-section
as functions of angle of wind attack.
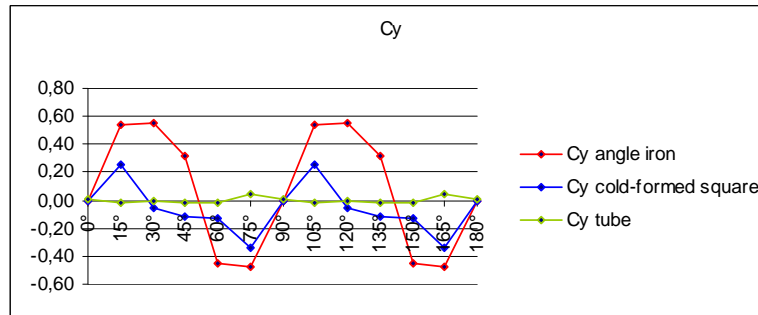
Fig. 5. Coefficient of lateral aerodynamic force for building crane tower of square cross-section
as functions of angle of wind attack.

JIB
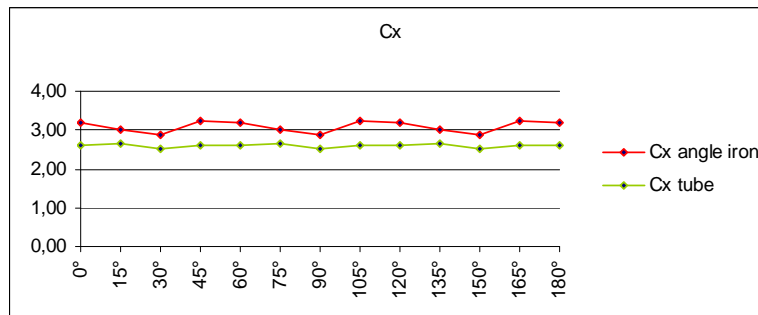
Fig. 6. Coefficient of aerodynamic drag of building crane jib of equilateral triangle cross-section
as functions of angle of wind attack.

84
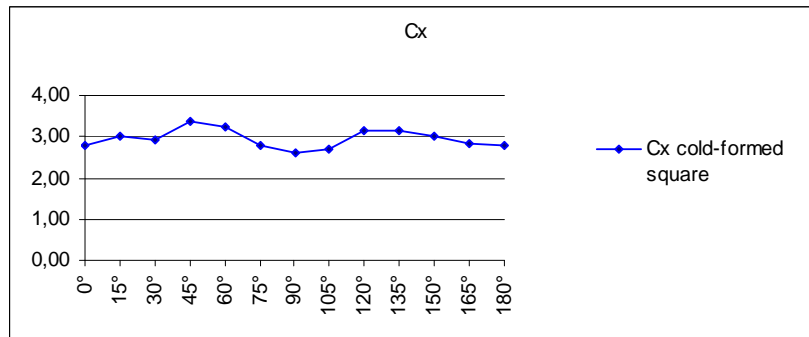
Fig. 7. Coefficient of aerodynamic drag of building crane jib of even-armed triangle cross-section as a function of angle of wind attack.
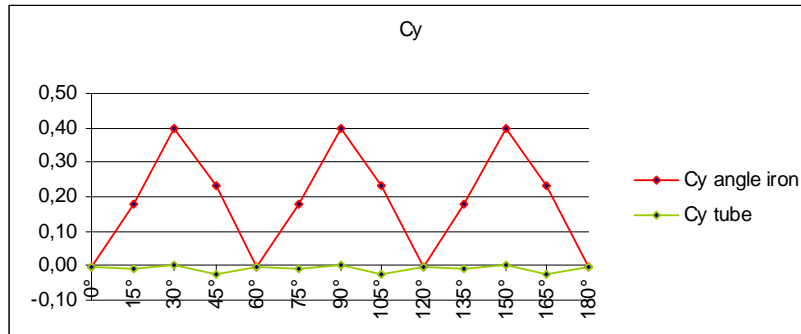
Fig. 8. Coefficient of lateral aerodynamic force for building crane jib of equilateral triangle cross-section as functions of angle of wind attack.
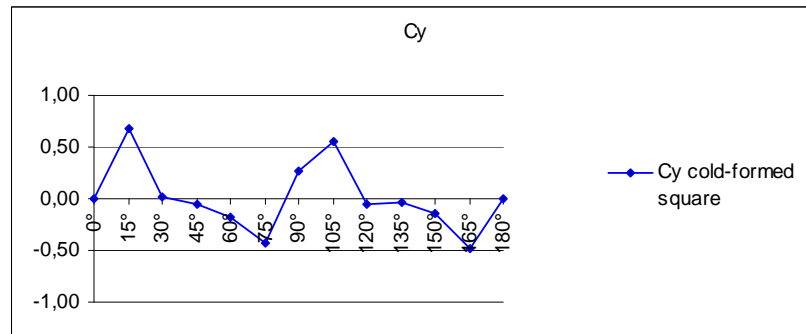
Fig. 9. Coefficient of lateral aerodynamic force for building crane jib of even-armed triangle cross section as a function of angle of wind attack.

85

4. Analysis of experimental results and conclusions

On the basis of experimental results the following conclusions can be formulated:

TOWER:

1. Influence of angle of wind attack on aerodynamic drag and lateral aerodynamic force is important.
2. The smallest values of aerodynamic drag and lateral aerodynamic force refer to tube elements.

JIB:

3. Influence of angle of wind attack on aerodynamic drag is rather small.
4. The smaller values of aerodynamic drag and lateral aerodynamic force are obtained for tube elements.
5. Influence of angle of wind attack on lateral aerodynamic force for angle iron elements and cold-formed square elements is important. This influence for tube elements can be neglected.

5. Comparison of obtained experimental results on aerodynamic drag and results presented in different papers

The comparison is presented in fig. 10 and fig. 11.

As it can be seen, differences between obtained experimental results in the case of aerodynamic drag and results presented in different papers are significant.

86
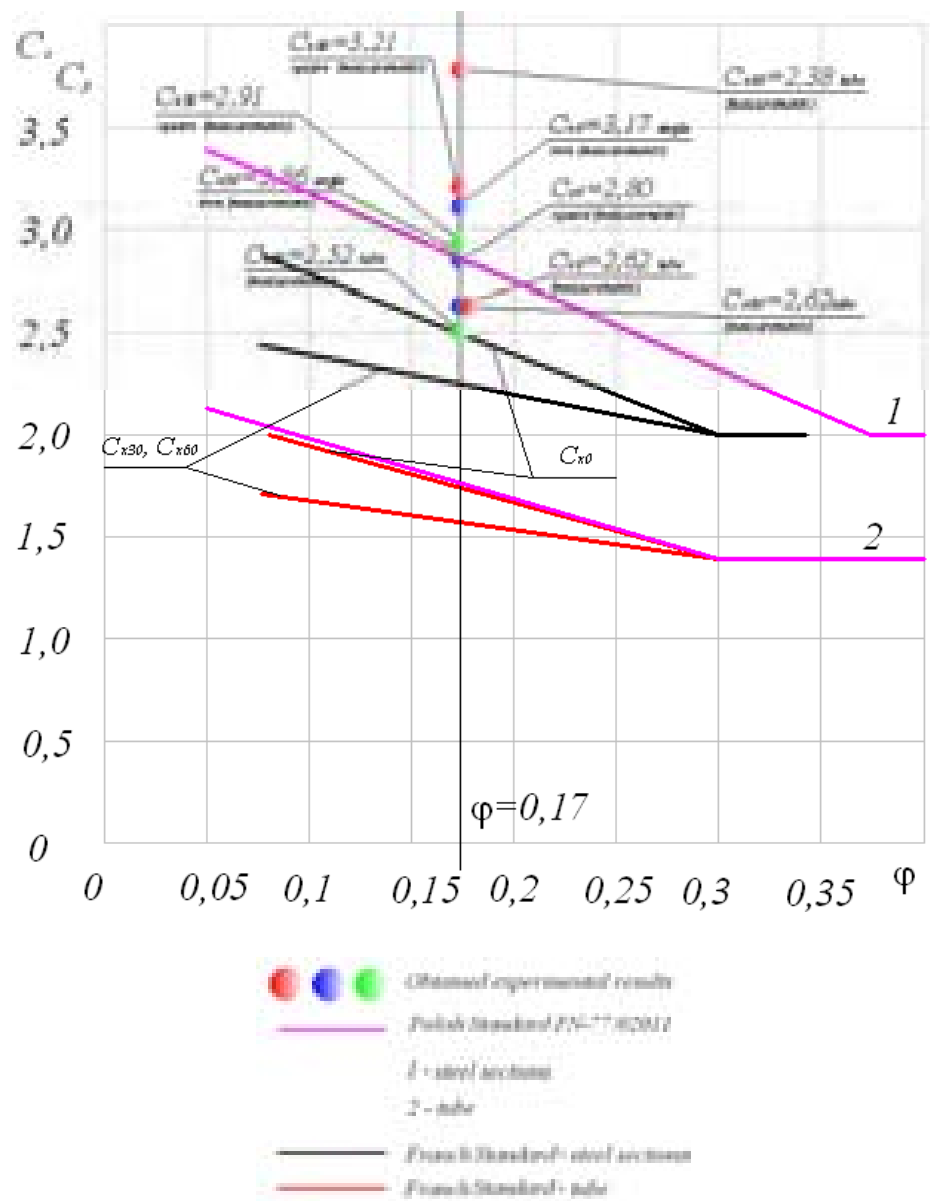
Fig. 10. Comparison of aerodynamic drag coefficient values for triangle cross – section.
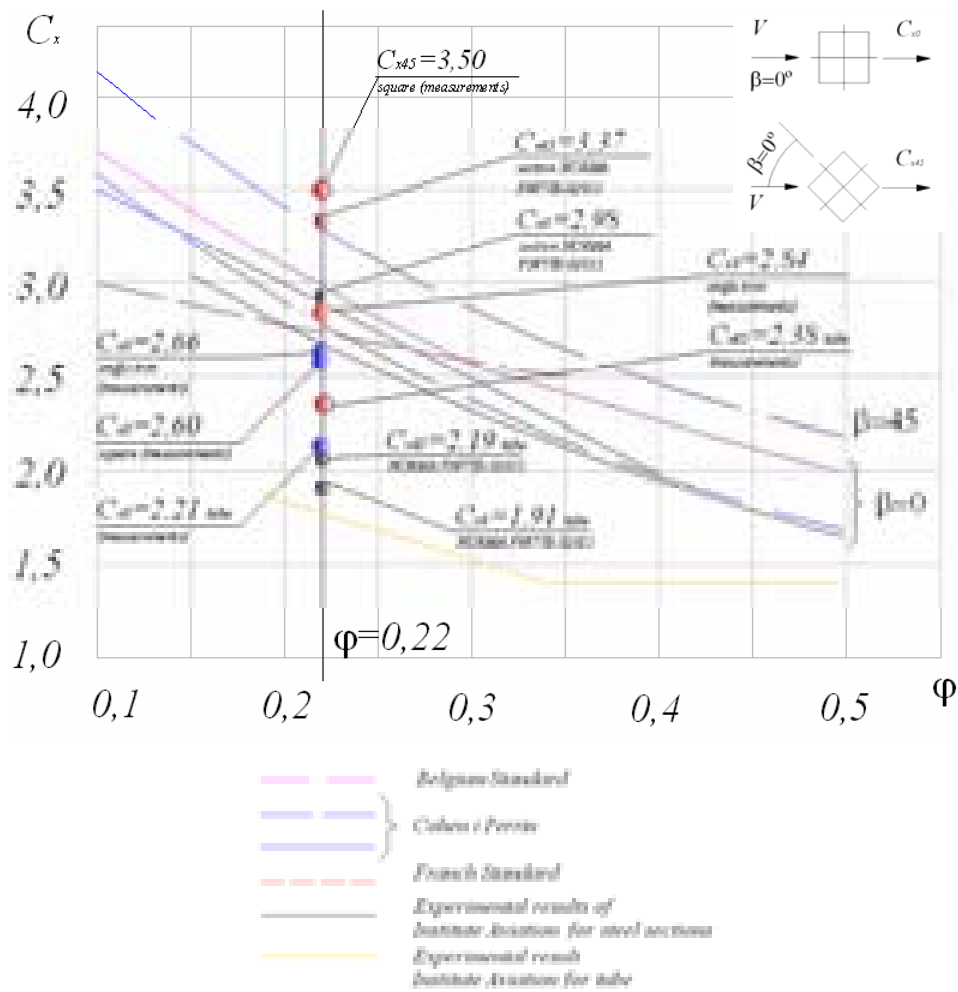
Fig. 11. Comparison of aerodynamic drag coefficients values for square cross – section.

References

[1] Kogan I.J.A., *Wieżowe żurawie budowlane*, Wydawnictwo Naukowo Techniczne, Warszawa 1974, (in polish).

[2] Zakopiański J., *Żurawie wieżowe: technologia robót i eksploatacja*, ARKADY, Warszawa 1975, (in polish).

[3] Żurański J.A., *Obciążenia wiatrem budowli i konstrukcji, Wydania drugie zmienione i rozszerzone*, ARKADY, Warszawa 1978, (in polish).

[4] *PN-77/B-02011, Obciążenie w obliczeniach statycznych, Obciążenie wiatrem,* (in polish).

88

THE INFLUENCE OF HEIGHT-TO-DIAMETER RATIO ON WIND LOAD OF DOUBLE-SHELL CYLINDRICAL, VERTICAL TANK

Aleksander Perliński[*]

[*] Department of Metal Structures and Management in Civil Engineering,
Faculty of Civil and Environmental Engineering, Gdańsk University of Technology,
Narutowicza 11/12, 80-952 Gdańsk, Poland.

1. Introduction

The double-shell cylindrical, vertical storage tanks with a floating roof are commonly used in petrochemical industry to store crude oil. They are equipped with two concentrically arranged shells and the double bottom. The internal shell is used to store product. In the case of an accidental leakage the additional external shell prevents oil from contaminating the environment, so the double-shell tanks are competitive to the single-shell tanks built in the earth embankments. The tanks are thin-walled structures which are designed for the circumferential tensile stress due to the hydrostatic internal pressure of product. The thin-walled steel shells are sensitive for compression stress which happens under wind load. The compression may cause the local buckling and damage of the shell. Additional ring wind girders located under the top edge and in some cases underneath stiffen the shells. The top wind girder is often used as an inspection walkway.

There are many papers referring to the effect of height-to-diameter ratio on wind load of cylindrical structures [1], [2], [3], [4]. The height-to-diameter ratio depends mainly on tank capacity and user requirements. In the code draft [5] there is no information about the influence of the height-to-diameter ratio on wind load of the double-shell tank. The model wind tunnel experiments were carried out to investigate this topic.

2. Models of a tank

The influence of the tank height-to-diameter ratio on wind load was analyzed on two types of rigid models (A and B) with a floating roof. The height-to-diameter ratio of model A is typical for medium size tanks of about 20000 m^3 in capacity, and the model B is for 100000 m^3 tanks. The shells and the roof of the models were made of plywood and timber. The top edges of shells were strengthened with a plywood ring wind girders. The pressure gauges were located on the floating roof and along one meridian on both sides of each shell, so that the pressure could be measured on the external and internal surface of the shells. The position of the floating roof was changed during the experiments. The models are shown in fig. 1 and their dimensions are presented in table I.
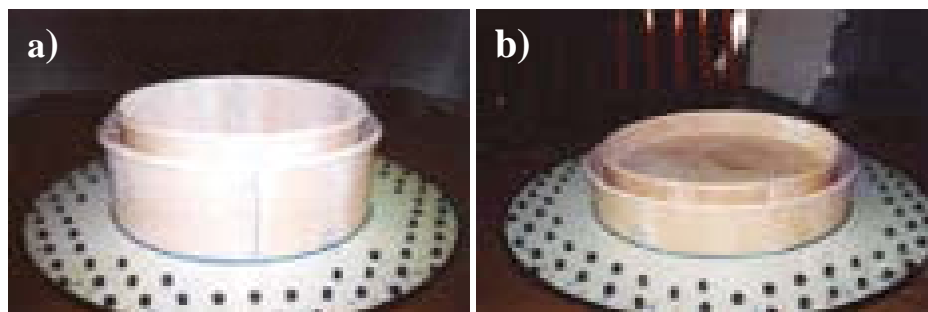
Fig. 1. Tank models during the tests: a) model A 2.4.1, b) model B 2.4.1.

Table I. Tank models dimensions.

Model	Height-to-diameter ratio h_i / d_i	External shell		Internal shell		Roof position
		Height h_e [mm]	Diameter d_e [mm]	Height h_i [mm]	Diameter d_i [mm]	
A 2.1.1	0.45	600	1800	720	1600	$0.95 \cdot h_i$
A 2.4.1	0.45	600	1800	720	1600	$0.25 \cdot h_i$
B 2.1.1	0.25	320	1800	400	1600	$0.95 \cdot h_i$
B 2.4.1	0.25	320	1800	400	1600	$0.25 \cdot h_i$

3. Wind tunnel experiments

The wind tunnel experiments were carried out in the Institute of Aviation in Warsaw. To obtain the air flow conditions similar to suburban area, the spires and group of cubes located before and around the model were used (fig. 2).
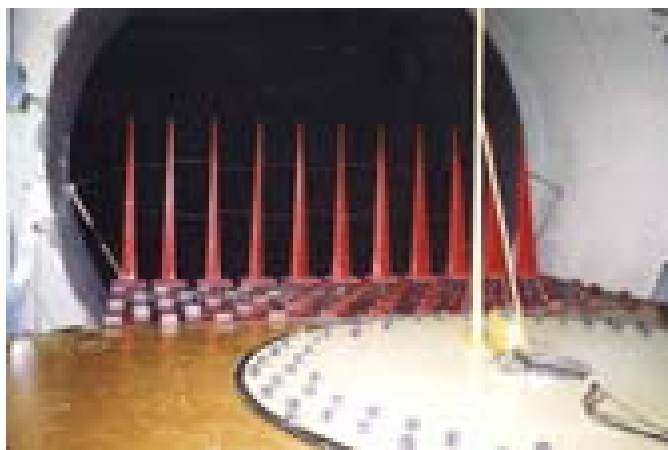
Fig. 2. Wind velocity profile measurements.

The wind velocity on the reference height $z_{ref}=h_i$ was $u_{ref}=30.44$ [m/s] for model A and $u_{ref}=27.23$ [m/s] for model B, hence the Reynolds's number for the models was $3.8 \cdot 10^6$ and $3.4 \cdot 10^6$ respectively. The velocity and turbulence intensity profiles of the air flow during the tests compared to the recommendations given in [5] are presented in fig. 3.
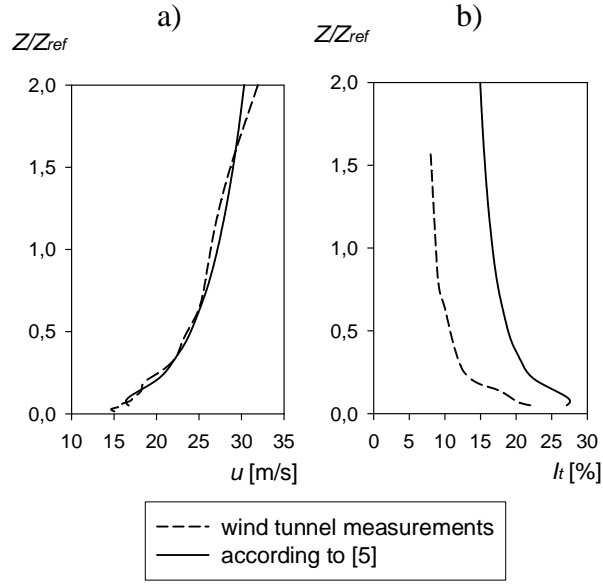
Fig. 3. Wind profile: a) velocity, b) turbulence intensity.

The measurements were done similarly to the experiments described in [4]. Due to the symmetry, the model was rotated around its vertical axis in range 0° to 180° and for every 10° the average values of pressure were measured with the pressure scanner Scanivalve 48DGM9. The measurements were recorded in a personal computer. After the test the pressure coefficients were calculated using the formula (1).

$$C_p = \frac{p_n - p_\infty}{q_\infty} \qquad (1)$$

where: p_n – pressure measured at gauge on model; p_∞ – static pressure in wind tunnel far in front of the model; q_∞ – dynamic pressure in wind tunnel far in front of the model

4. Wind tunnel experiments results

The results obtained in the wind tunnel experiments are presented in fig. 4 to fig. 11.
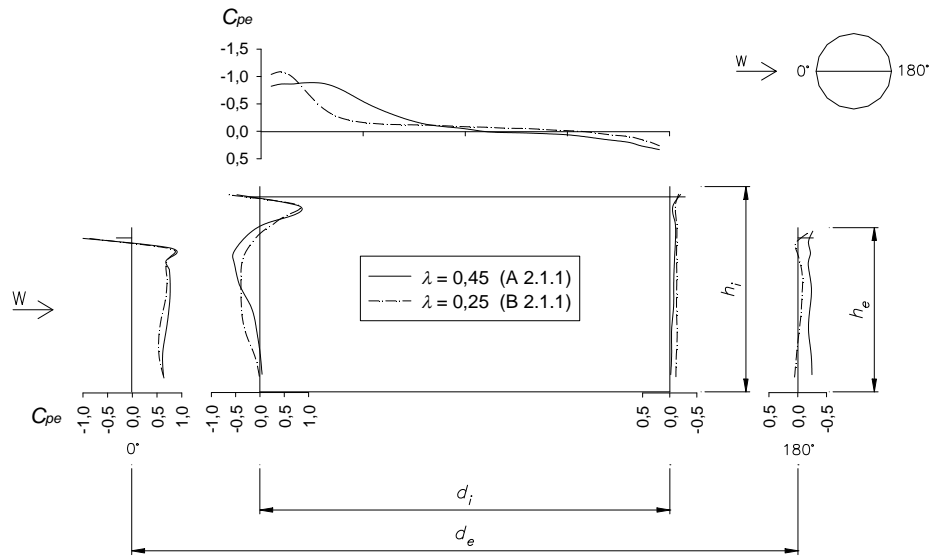
Fig. 4. The comparison of the external pressure coefficient (C_{pe}) on models with different height-to-diameter ratio; roof position $=0.95 \cdot h_i$; section 0°-180°.
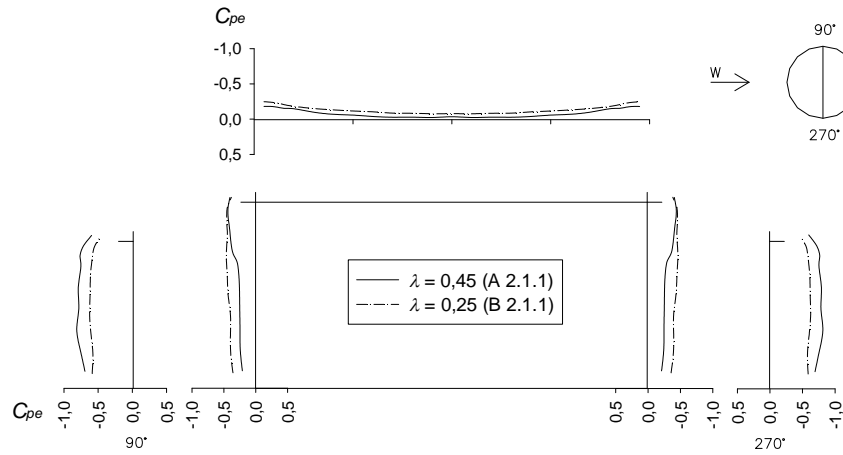
Fig. 5. The comparison of the external pressure coefficient (C_{pe}) on models with different height-to-diameter ratio; roof position $=0.95 \cdot h_i$; section 90°-270°.

92
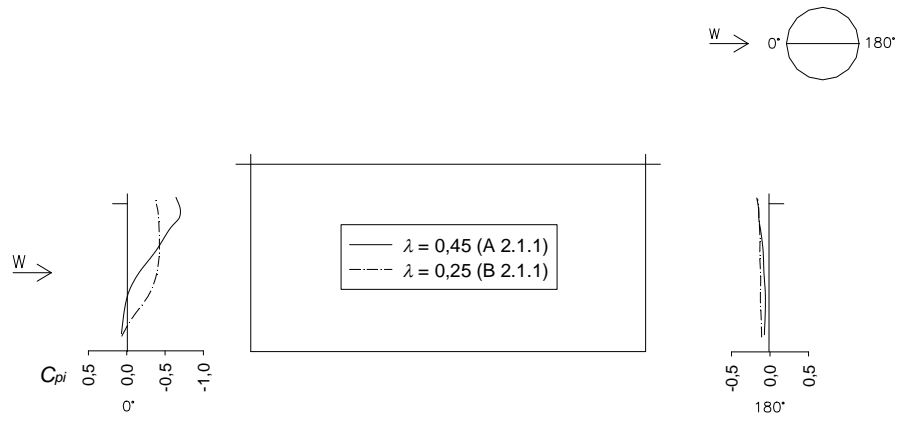
Fig. 6. The comparison of the internal pressure coefficient (C_{pi}) on models with different height-to-diameter ratio; roof position $=0.95 \cdot h_i$; section 0°-180°.
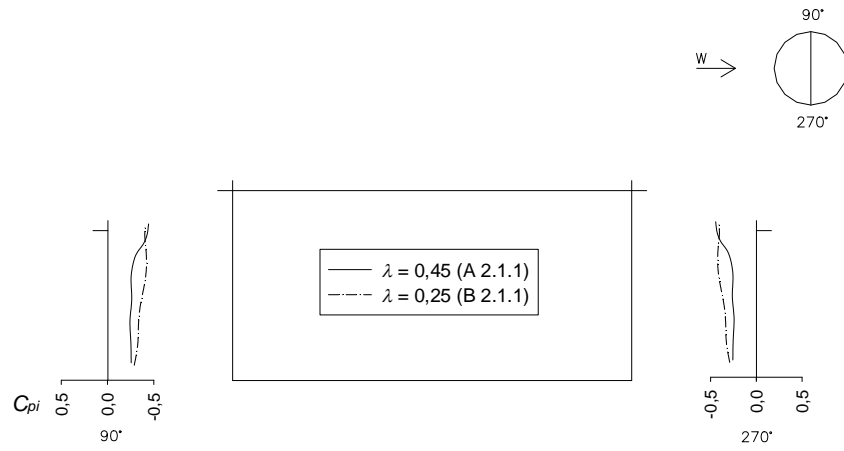
Fig. 7. The comparison of the internal pressure coefficient (C_{pi}) on models with different height-to-diameter ratio; roof position $=0.95 \cdot h_i$; section 90°-270°.

93
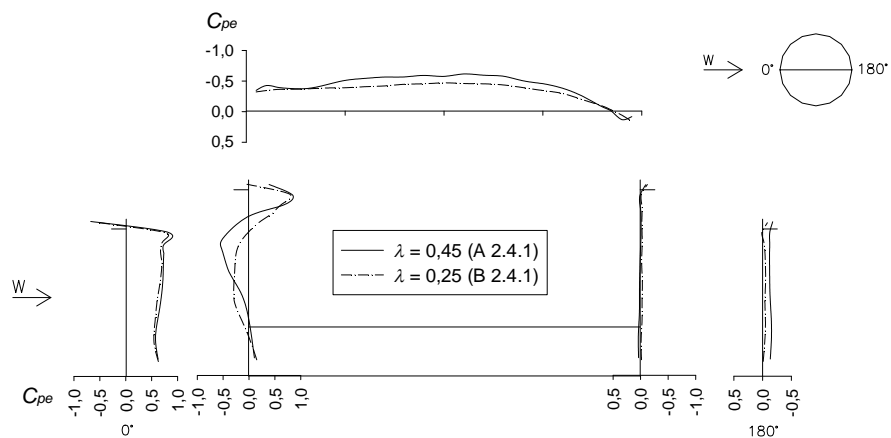
Fig. 8. The comparison of the external pressure coefficient (C_{pe}) on models
with different height-to-diameter ratio; roof position $=0.25 \cdot h_i$; section 0°-180°.
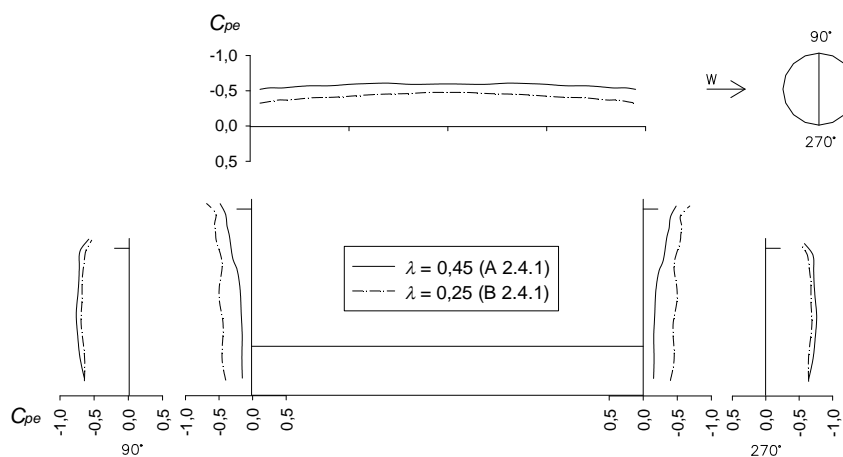
Fig. 9. The comparison of the external pressure coefficient (C_{pe}) on models
with different height-to-diameter ratio; roof position $=0.25 \cdot h_i$; section 90°-270°.

94
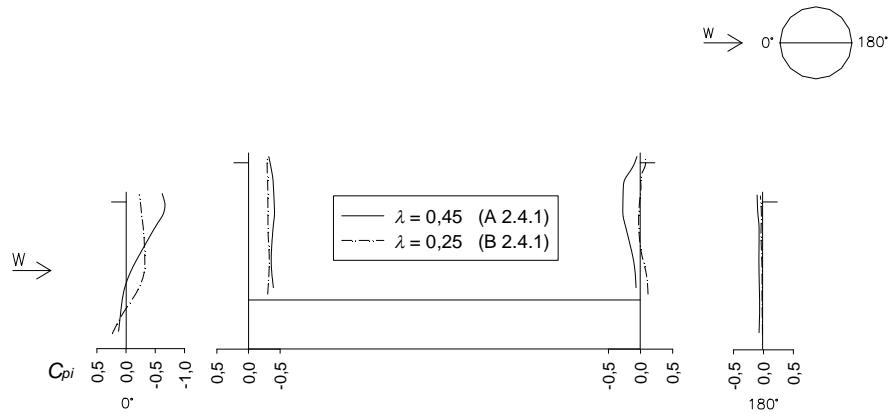
Fig. 10. The comparison of the internal pressure coefficient (C_{pi}) on models
with different heigth-to-diamater ratio; roof position $=0.25 \cdot h_i$; section 0°-180°.
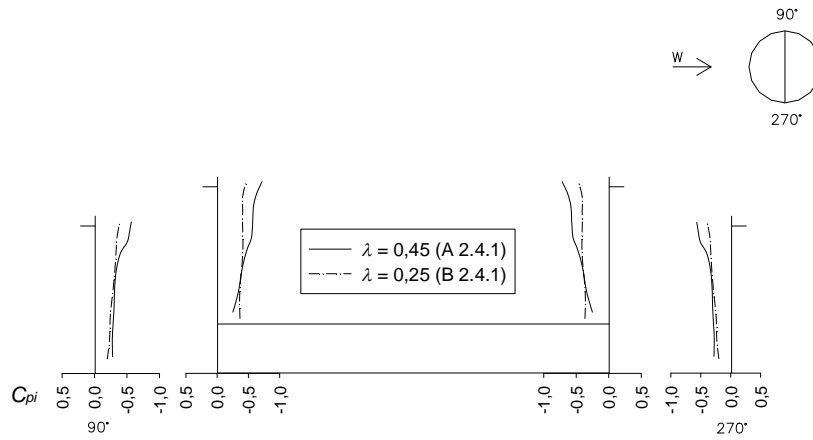
Fig. 11. The comparison of the internal pressure coefficient (C_{pi}) on models
with different height-to-diameter ratio; roof position $=0.25 \cdot h_i$; section 90°-270°.

5. Conclusions

The experiments carried out in the wind tunnel show the significant influence of the height-to-diameter ratio on the wind load of double-shell cylindrical, vertical tank. The following remarks can be pointed:

- The model A is subjected to higher negative pressure on the internal, windward side of the external shell (maximum C_{pi}=-0.8) than model B (maximum C_{pi}=-0.4). Not only the value but the distribution of the wind load along shell height is different as well.

- The external windward side of the internal shell is subjected to negative pressure in the area shaded by the external shell and positive pressure above. The highest negative pressure on model A was measured in 2/3 of the shell height from the bottom (C_{pe}=-0.6). The highest negative pressure on model B was measured in a mid-height of the shell (C_{pe}=-0.4). The wind load is the same on both models near the top edge, under the wind girder (C_{pe}=+1.0). In the perpendicular direction to the air flow (90°-270°) the negative pressure is higher for model B (maximal C_{pe}=-0.6) than on model A (maximal C_{pe}=-0.4).

- The internal side of the internal shell is subjected to negative pressure. The higher pressure values were obtained on model A – on the windward side C_{pi}=-0.4, in the perpendicular direction (90°-270°) C_{pi}=-0.6 and on the leeward side C_{pi}=-0.3.

- The floating roof in model A is subjected to higher negative pressure on the windward side (C_{pe}=-1.1) then the model B (C_{pe}=-0.8). The wind load is the same on both models in the mid-span and on the leeward side of the roof. When the floating roof is in the lowest position the value and distribution of load do not depend on height-to-diameter ratio of models.

References
[1] Eβlinger M., Ahmed S. R., Schroeder H. H., *Stationäre Windbelastung offener und geschlossener kreiszylindrischer Silos*, Der Stahlbau, 12/1971, pp. 361-368.
[2] Maher F. J., *Wind loads on dome cylinder and dome-cone shapes*, ASCE Journal of the Structural Division, ST 5, October 1966, pp. 79-96.
[3] Prudy D. M., Maher F. J., Frederick D., *Model studies of wind loads on flat-top cylinders*, ASCE Journal of the Structural Division, ST 2, April 1967, pp.379-395.
[4] Ziółko J., *Modelluntersuchungen der Windeinwirkung auf Stahlbehälter mit Schwimmdach*, Der Stahlbau, 11/1978, pp. 321-329.
[5] prEN 1991-4:2002, *Eurocode 1 - Action on structures. Part 4: Action on silos and tanks.*

RESEARCH ON THE INFLUENCE OF STADIUM'S ROOF SHAPE ON ITS AERODINAMIC LOAD

Roman Kinash[*], Oleksiy Kopylov[**], Jan Walaszczyk[*]

[*] Departament of Geomechanics, Civil Engineering and Geotechnics,
Faculty of Mining and Geoengineering, AGH University of Science and Technology,
Mickiewicza 30, 30-059 Cracow, Poland.
[**] Building Research Institute, Filtrowa 1, 00-611 Warsaw, Poland.

1. Introduction

Because of the great area of the roof, massive constructions with fairly small height (covered markets, covered sport centres) are very sensitive to atmospheric influence of snow or wind. Disregarding the importance of the load of this kind often results in the danger of a building catastrophe. According to the Polish Main Building Inspection Department, 94 out of 187 building catastrophes that happened in Poland in 2004 were caused by incidents (wind, rain, snow, fire, gas explosion, lightning or others). Mistakes in design combined with adverse atmospheric conditions were the causes of many catastrophes: Katowice 30.01.2006; Moscow 23.02.2006; Bad Reichenhall 02.01.2006; a series of catastrophes all over Europe in January 2007, caused by a hurricane. Often, these mistakes were caused by insufficient knowledge about the behaviour of the construction influenced by atmospheric conditions. That is the reason why there has been more and more research done all over the world, aiming at gathering more information about the behaviour of constructions under climatic factors, for example wind.

Despite the development of more efficient numerical methods, examination in the aerodynamic tunnel is still the best way of obtaining comprehensive knowledge of the influence of wind on building constructions, and it is considered by the best scientists to be the essential part of the project preparations [1, 2].

The main objective of this research paper was to increase the knowledge of the influence of architectural solutions used most frequently in designing stadiums (the roof form, the presence of walls around the coping) on the value of the static aerodynamic load of the roof construction. Similar research has been done by different teams of scientists in many countries, including: R. Jóźwiak, J. Kasprzyk, J.A. Żurański (Poland) [1], C. Borri (Italy) [2], I.M. Lebedich (Ukraine) [3].

2. Aim and scope of research

This paper is an introduction to a series of articles on the analysis of aerodynamic research of stadium models. The aim of the paper is to present the conditions in which the tests were held, the measuring site and the tested model. The main result of the research will be:

1. Determining the method and the measuring technique for the examination of a stadium model.
2. Finding optimal simplifications in stadium modelling for the purpose of construction aerodynamics.
3. Finding the best shape of roof stadiums considering the aerodynamic loads.
4. Estimating the influence of the stadium coping enclosure on the aerodynamic load.

3. The measuring site

The aerodynamic tests were held in the wind tunnel in the Department of Aerodynamics at Technical University in Warsaw in December 2006. The cross-section of the tunnel was a square with the side of 1m. This tunnel has been frequently described [4], so in this paper there are only its main characteristics.

The model was based on the stadium project prepared by the National Donetsk Academy of Building and Architecture for the FC *Shahtar-Donetsk*, in the scale of 1:500. Due to the fact that the model fulfilled only the geometrical similarity criterion, the dynamic tests like measuring the vibrations of the roof or the supporting constructions were not conducted.

The measuring site (fig. 1) was built only for testing the average pressure distribution on the roof surface – the influence of wind on the stands and the sports field was not tested.

Fig. 1. The measuring site.

98

Measuring tubes, the ends of which were connected to a multipunctual liquid manometer (pressure gauge), were placed all over the roof surface (figs 2 and 3).
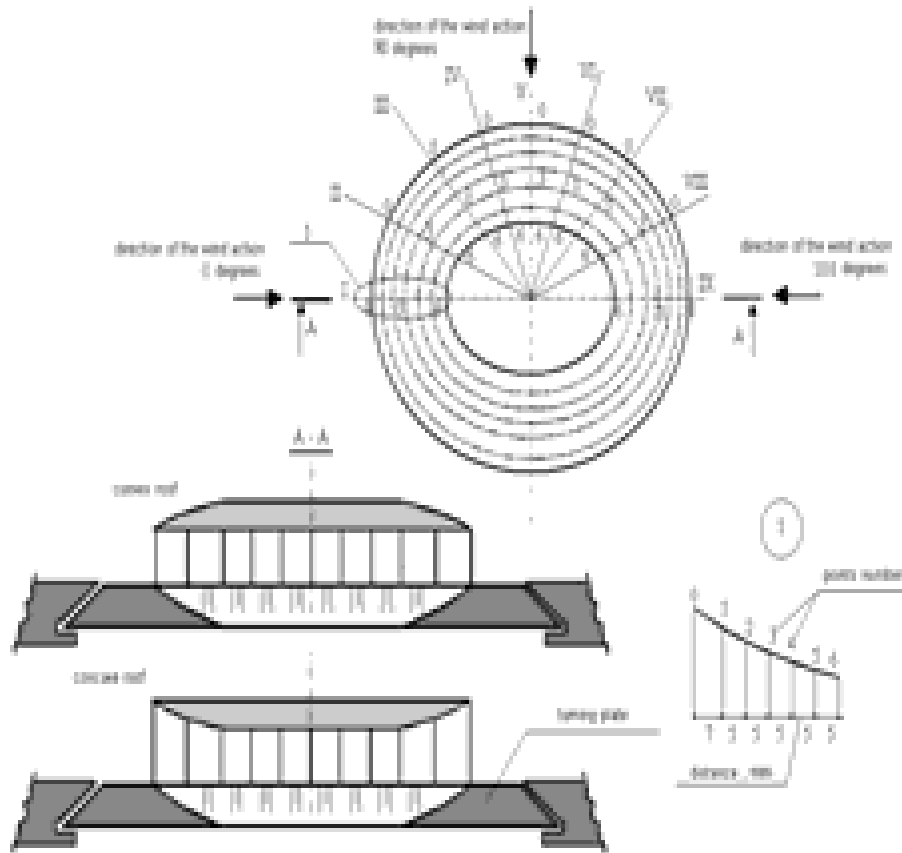
Fig. 2. The scheme of the distribution of measuring points on the roof surface.
Roman numerals mark the sections, in which the distributions of pressure were examined;
Arabic numerals – the numbers of measuring points.

The manometer allowed simultaneous measuring of static pressure in 48 points. The results were recorded by a moving beam with photoelements reacting to the level of liquid in each manometer tube and sending the transformed information to a computer. The tests were held with the velocity of wind inflow in the tunnel at around 25 m/s and the distribution of the turbulence level of 1.5%.

Fig. 3. Multipunctual liquid manometer.

The model was fixed to a plate on the tunnel floor level, revolving around the central vertical axis of the stadium, which allowed to conduct the tests for a wide range of air inflow angles: 0°, 45°, 90°, 135°, 180°, 225° and 270°. The average wind velocity, apart from the wall layer, was U=25 m/s.

A certain inaccuracy in modelling the surroundings was caused by the lack of information about the wind profiles and about the distribution of turbulences within the area.

4. Stadium model

The stadium has the view in the shape of an ellipsis with axes of 246m and 170m. The project assumes that the stadium is surrounded with stands. It was also assumed that the stands have a light steel construction above them, covered mainly with transparent material (such as polycarbonate plates). There were two variations of the roof prepared: a concave and a convex one (fig. 4a and 4b) with the coping open from all sides and surrounded with a sound-absorbing shield (fig. 4c).
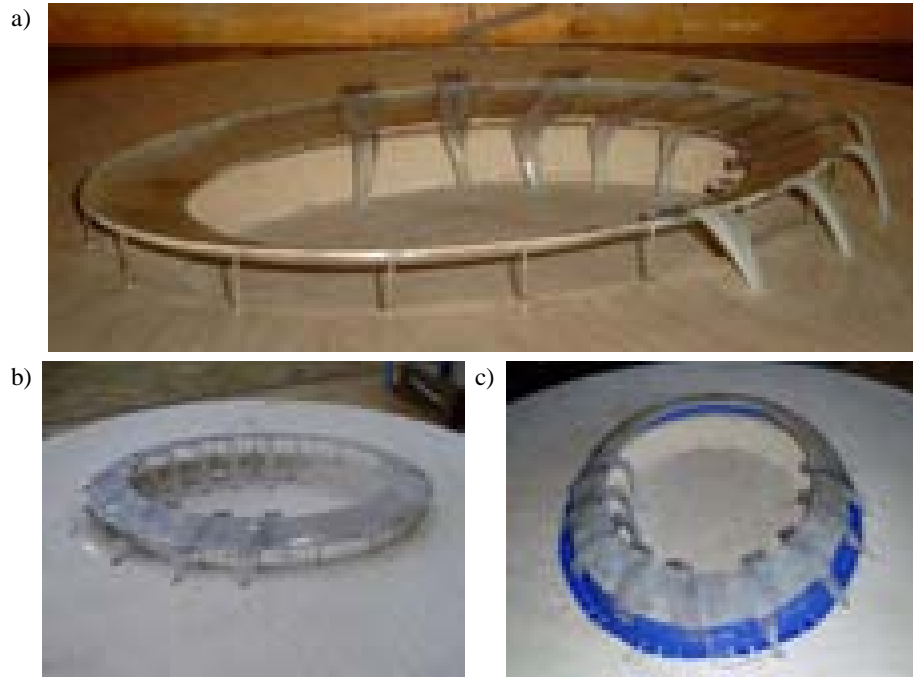
Fig. 4. The examined versions of stadium roofing: a – concave roof; b – convex roof;
c – convex roof with air-tight enclosure.

5. Scientific description of test results

The results of the tests will be presented in a series of articles as the coefficients of pressures C_p on the top and bottom surfaces of the roof, depending on the distance between the points of measurement.

The coefficient of pressure C_p was calculated according to the formula:

$$C_p = (p_{st} - p_\infty)/(\rho v^2_\infty/2), \tag{1}$$

where: p_{st} – measured pressure, p_∞ - static pressure of undisturbed inflow.

6. Analysis of test results

6.1. Analysis of test results for the inflow angles of 0°(180°)

6.1.1. Concave roof

The distributions of pressure measured on the top part of the stadium roof were

101

changing from –0.4 to +0.4. The minimum values were observed in the cross-sections perpendicular to the direction of the air inflow, the maximum ones – in the cross-sections parallel to the direction of inflow. The cross-sections placed perpendicularly to the wind direction were crucial in the respect of the direction of the aerodynamic load: there was the change of pressure from underpressure to overpressure. The values of pressures obtained in one cross-section differed from 5 to 7% (fig. 5a).

When measuring the distribution of pressures on the bottom surface of the roofing, minimum values were obtained in the cross-sections perpendicular to the inflow, maximum ones – in the cross-sections parallel to the inflow. Because of powerful whirls emerging under the roof, the values of pressure measured in one cross-section differed considerably. Minimal differences of pressure between the measuring points in one cross-section were observed in the cross-sections positioned at the angle of $90° \pm 15°$ to the direction of the inflow (fig. 5b).

6.1.2. Convex roof

After reversing the roof, a significant increase (15%) in the aerodynamic load value was noticed, compared to a concave roof (see figs 5 and 6). The shape of the pressure line is significantly changed.

Fig. 5. The change of pressure coefficient in cross-sections I-IX on the ellipses 0-6:
a – pressure measured in the top part; b – pressure measured in the bottom part.
Concave roof, inflow angle 0°(180°).

After surrounding the stadium coping with an air-tight enclosure, the C_p value decreased in the top part of the stadium roof in all cross-sections (compare fig. 7 with 5 and 6). The top part of the roof was in the underpressure area.

102

Fig. 6. The change of pressure coefficient in cross-sections I-IX on the ellipses 0-6:
a – pressure measured in the top part; b – pressure measured in the bottom part.
Convex roof, inflow angle 0°(180°).
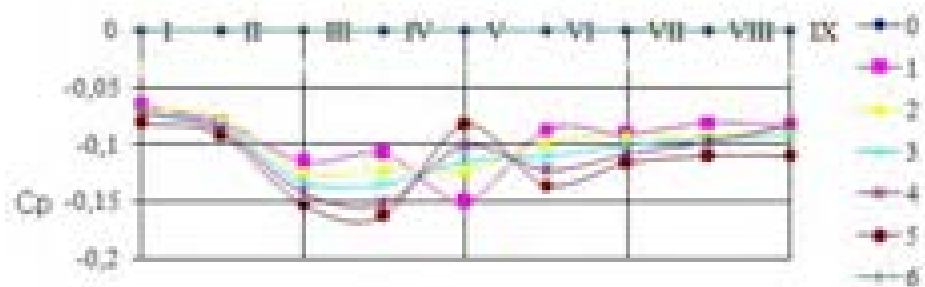
Fig. 7. The change of pressure coefficient in cross-sections I-IX on the ellipses 0-6:
Pressure measured in the top part. Convex roof. Enclosed coping. Inflow angle 0°(180°).

6.2. Analysis of aerodynamic resistance coefficients for the inflow angles of 45° and 135°

6.2.1. Concave roof

The largest load was detected in the cross-sections placed against the inflow (III and IV), as well as in the ones parallel to the inflow direction, on the opposite side of the pitch. Minimum loads appeared in the cross-sections perpendicular to the inflow direction (VI).

103

As it had been in previous cases, in the cross-sections situated at the angle of >90° to the inflow direction there was a change in the type of the load – from underpressure to overpressure. The pressures measured in the bottom part of the roof in cross-sections that were against the inflow (deflecting at ±15° from the main inflow direction) showed a significant dispersion of the pressure values (fig. 8).
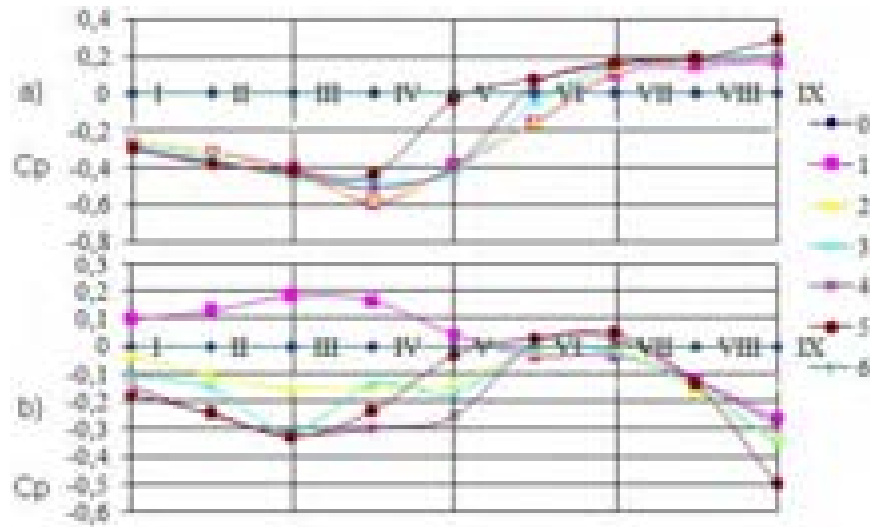
Fig. 8. The change of pressure coefficient in cross-sections I-IX on the ellipses 0-6:
a – pressure measured in the top part; b – pressure measured in the bottom part.
Concave roof, inflow angle 45°(135°).

6.2.2. Convex roof

The change of roof shape from concave to convex caused considerable changes of pressure distributions in different points of cross-sections. Cross-sections against the inflow were situated in areas of different pressure: underpressure and overpressure (fig. 9).

6.3. Analysis of pressure coefficients for the inflow angles of 90° and 270°

6.3.1. Concave roof

With this angle of inflow, as it was in the cases described above, the cross-sections parallel to the inflow were loaded the most. In cross-sections oblique to the inflow, C_p values decreased. The widest range of pressure measurement results was obtained in cross-sections situated against the inflow (fig. 10).

104
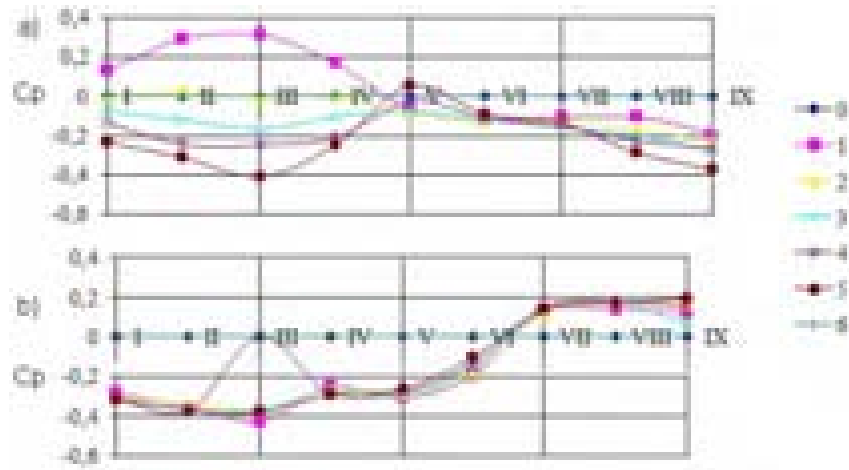
Fig. 9. The change of pressure coefficient in cross-sections I-IX on the ellipses 0-6:
a – pressure measured in the top part; b – pressure measured in the bottom part.
Convex roof, inflow angle 45°(135°).
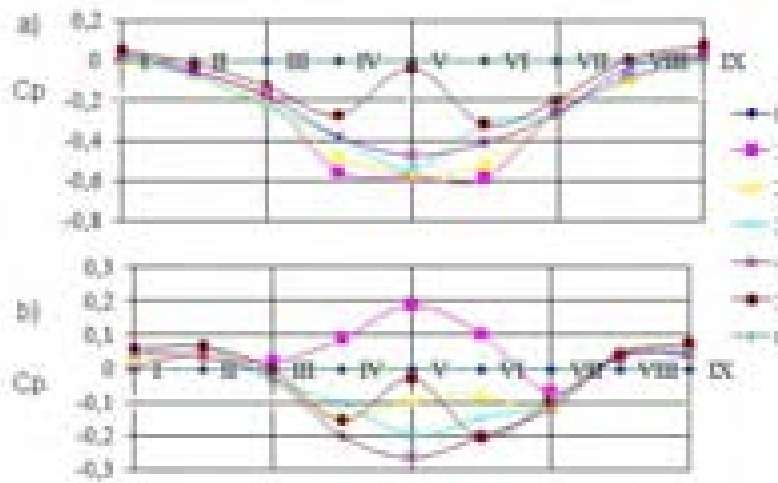
Fig. 10. The change of pressure coefficient in cross-sections I-IX on the ellipses 0-6:
a – pressure measured in the top part; b – pressure measured in the bottom part.
Concave roof, inflow angle 90°.

The aerodynamic load measured on the top surface of the roof in cross-sections parallel to the inflow direction situated on the opposite side of the pitch was almost 50% smaller than the values in cross-sections situated against the inflow. However, C_p values in the bottom part of the roof increased slightly (see figs 10 and 11).

105
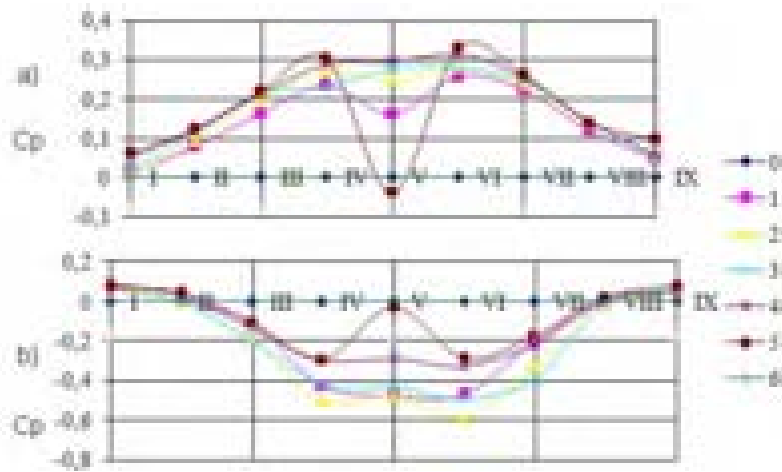
Fig. 11. The change of pressure coefficient in cross-sections I-IX on the ellipses 0-6:
a – pressure measured in the top part; b – pressure measured in the bottom part.
Concave roof, inflow angle 270°.

6.3.2. Convex roof

The change of roof shape from concave to convex caused the increase of pressure (about 20%) in the bottom part of the roof (fig. 12).
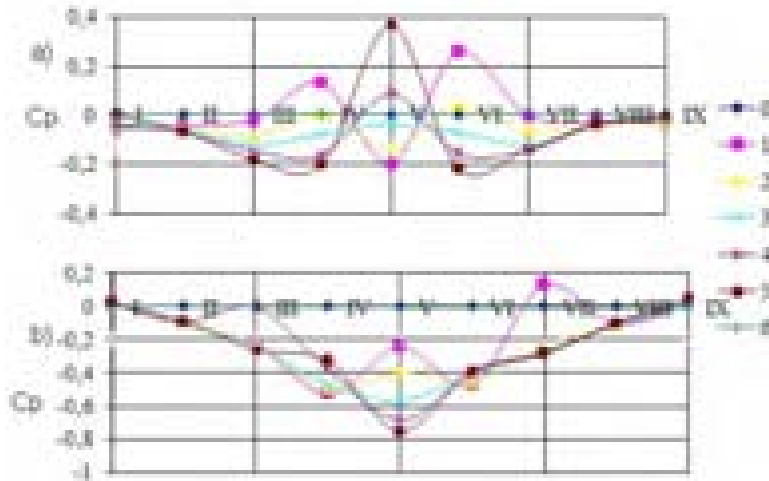
Fig. 12. The change of pressure coefficient in cross-sections I-IX on the ellipses 0-6:
a – pressure measured in the top part; b – pressure measured in the bottom part
Convex roof, inflow angle 90°.

106

Cross-sections on the opposite side of the pitch will be less loaded when compared to the cross-sections situated against the inflow. The range of Cp values in measuring points of particular cross-sections was also smaller (see figs 12 and 13).
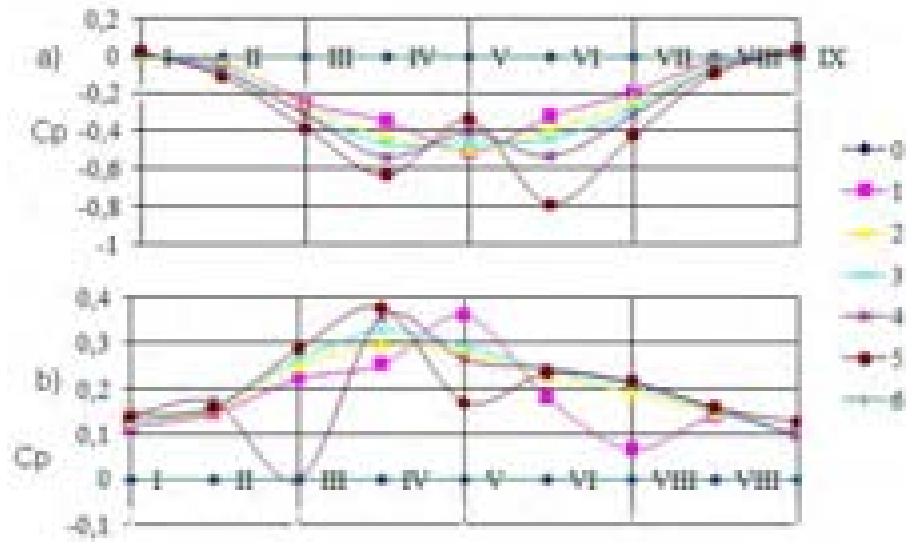
Fig. 13. The change of pressure coefficient in cross-sections I-IX on the ellipses 0-6:
a – pressure measured in the top part; b – pressure measured in the bottom part.
Convex roof, inflow angle 270°.

Surrounding the stadium coping with an air-tight enclosure caused the decrease in aerodynamic load of the top part of the roof (compare fig. 14 with 11 and 12), as well as reduced the range of pressure coefficients values in particular cross-sections.
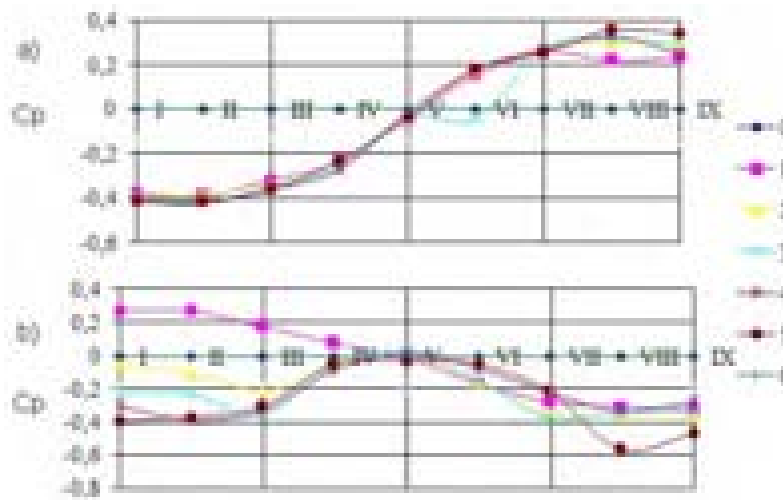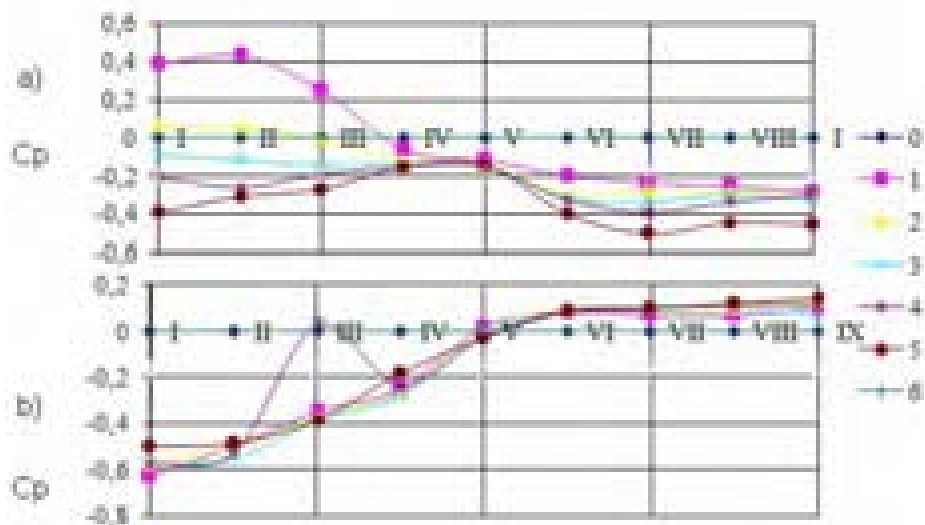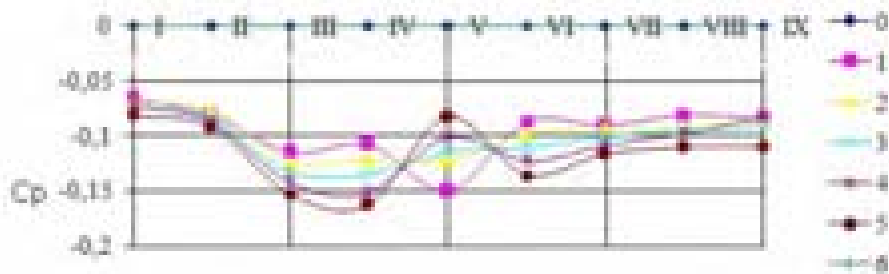

Fig.14. The change of pressure coefficient in cross-sections I-IX on the ellipses 0-6.
Pressure measured in the top part.
Convex roof. Enclosed coping. Inflow angle 90°.

107

7. Final conclusions

1) The conducted tests are the preliminary research that allow to assess the prospect and usefulness of possible further tests, model construction and measuring technique.
2) The obtained research results allow to choose the more effective type of stadium roof. Among the tested shapes, the most effective, in the aerodynamic load respect, was the concave form. The biggest loads, despite the roof shape, were observed in the cross-sections parallel to the direction of the air inflow.
3) When compared to a concave roof, a convex one was more loaded. Surrounding a convex roof with an air-tight enclosure allowed to reduce the range of pressure values obtained in measuring points of particular cross-sections. The influence of the extent of the coping enclosure on the aerodynamic load was not examined.
4) In future, the influence of the shapes of the roof and the enclosure on the aerodynamic conditions on the pitch should be examined.

References

[1] Jóźwiak R., Kasprzyk J., Żurański J.A., *Badania modelowe obciążenia wiatrem dachu stadionu śląskiego w Chorzowie*, Problemy naukowo-badawcze budownictwa. Krynica-Białystok, 2007.

[2] Borri C., Biagini P., *Wind response of large roofs of stadions and arena*, EACWE4 – the Fourth European & African Conference on Wind Engineering; ITAM AS CR, Prague, 11-15 July, 2005.

[3] Lebedich I.M., Pavlovsky R.M., Zhdanov O.I., *Analysis of aerodynamic features of the over-stand roof in Dnepropetrovsk FC "Dnipro" stadium*, 2007, pp. 43-52.

[4] Kopylov O., Wojciechowski J., *Aerodynamic interference of a set of circular cylinders*, EACWE4 – the Fourth European & African Conference on Wind Engineering; ITAM AS CR, Prague, 11-15 July, 2005.

SNOW LOADS
AND SNOW TRANSPORT

A NEW APPROACH TO SIMILARITY CRITERIA FOR PREDICTING A SNOW LOAD IN WIND TUNNEL EXPERIMENTS

Grzegorz Kimbar[*], Andrzej Flaga[*,**]

[*] Wind Engineering Laboratory, Faculty of Civil Engineering,
Cracow University of Technology, Jana Pawla II 37/3a, 31-864 Cracow, Poland.
[**] Department of Structural Mechanics, Faculty of Civil and Sanitary Engineering,
Lublin University of Technology, Nadbystrzycka 40, 20-618 Lublin, Poland.

1. Motivation

One of the most important issue arising during designing a new atypical roof structure is determining a snow load distribution. The snow cover is formed during snow precipitation and its subsequent redistribution. In both phenomena a wind action takes the very important part. The wind influence on distribution of a snow cover is described by the theory of dispersion [1]. However, in this case effects occurring at boundary conditions are very important.

Constitution of a full mathematical model of such influence is still to be determined, so usage of the CFD methods is very limited at present. Another approach is performing wind tunnel experiments. For those experiments, derivation of the similarity criteria – a set of rules allowing carrying them out – is needed.

In this paper a new approach to this problem is proposed. So far, only specific phenomena such as suspension or saltation were considered. Most of the derived similarity criteria where made with the assumption of the snow transport occurring on an infinite horizontal plane in an homogeneous wind field [2,3]. In the case of predicting a snow load over building roofs, these models may be inappropriate, because of occurrences of high positive and negative pressures at different roof parts.

2. Model physical fields

Snow transported in the air is treated as a dispersion, that is a bunch of small solid particles suspended in the fluid. A basic physical field describing the dispersion is its mass concentration:

$$k(\mathbf{x}) = \frac{1}{\delta\Omega} \sum_i m_{pi} \bigg|_{\delta\Omega} \tag{1}$$

where: $\delta\Omega$ – some finite but small volume containing the **x** point; $m_{pi} - i^{th}$ particle mass. The most important quantity describing an average rate and an average direction of the dispersion movement is a dispersion mass flux. The averaging is performed to dismiss irrelevant information about particles movement. The dispersion mass flux is a vector field determined on every point of the volume and is defined as (fig. 1):

$$\mathbf{Q}(\mathbf{x}) = \frac{1}{\delta\Omega} \sum_i \left(m_{pi} \mathbf{v}_{pi} \right)_{\delta\Omega},$$

(2)

where: $\mathbf{v}_{pi} - i^{th}$ particle velocity. Generally, a flux of some quantity is a product of velocity and density of this quantity. So, the mean (mass weighted) particle velocity ($\mathbf{v}_p$) may be introduced:

$$\mathbf{Q} = \mathbf{v}_p k.$$

(3)
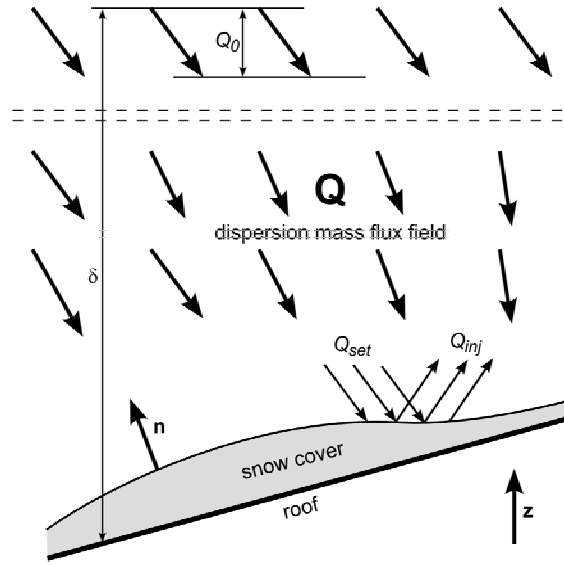
Fig. 1. Dispersion mass flux field and derivative quantities.

The assumption is taken that k and $\mathbf{v}_p$ are independent variables. This assumption is a conclusion of so-called one-way coupling assumption, which is true for low concentration dispersions. Thereafter, $\mathbf{v}_p$ can be separated into three components (fig. 2):

$$\mathbf{v}_p = -\mathbf{z}v_t + \mathbf{v}_{ine} + \mathbf{u},$$

(4)

112

where: $\mathbf{z}$ – upwards directed unit vector; v_t – dispersion terminal speed; v_{ine} – dispersion inertial movement velocity; $\mathbf{u}$ – fluid (wind) velocity. The dispersion terminal speed is a mean (mass weighted) particle speed in the state of free fall in perfectly calm conditions (i.e.: $\mathbf{u} = 0$). The ($-\mathbf{z}\, v_t + v_{ine}$) part is a mean relative dispersion velocity – v_{rel}, which may be modelled on the basis of single particle movement models if needed. The inertial component is a function:

$$\mathbf{v}_{ine} = \mathbf{v}_{ine}(t_r, \mathbf{u}, \nabla \mathbf{u}), \tag{5}$$

where: t_r – mean relaxation time – a dispersion property describing how fast particles are accelerated when exposed to fluid flow.
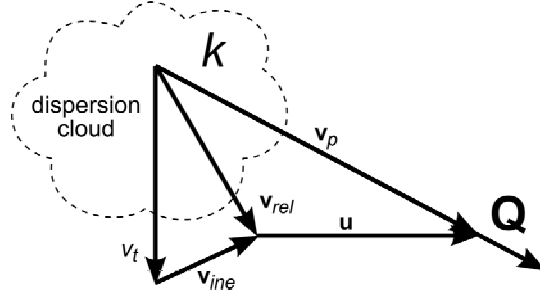
Fig. 2. Averaged velocities describing the dispersion behaviour.

Abovementioned quantities describe dispersion behaviour in the volume. There is a necessity to introduce some quantities describing boundary conditions on surfaces of this volume. First of all, there is a precipitation rate:

$$Q_0 = -\mathbf{Q}(z = \delta) \cdot \mathbf{z}, \tag{6}$$

where: $\mathbf{Q}(z=\delta)$ – dispersion mass flux at height δ, which is a high altitude (e.g. boundary layer height) at which conditions are homogenous; $\mathbf{z}$ – upward directed vector.

The precipitation rate is a snow mass amount falling trough unit area in unit time. The snow load is always defined as a ratio of the snow weight deposited on some surface to the horizontal projection area of this surface, so:

$$ds = Q_{acc}\, g\, dt; \qquad Q_{acc} = \frac{-\mathbf{Q} \cdot \mathbf{n}}{\mathbf{n} \cdot \mathbf{z}}, \tag{7}$$

where: s – snow load; Q_{acc} – accumulation rate determined on every point of the bottom boundary; g – acceleration due to gravity; t – time; $\mathbf{n}$ – outwards directed surface unit vector. Simulating of the Q_{acc} field in a wind tunnel will guarantee, that the particle bed

113

forming in an experiment corresponds with the snow load forming in the nature. The erosion occurs on areas where Q_{acc} is negative. The Q_{acc} is an averaged quantity but it can be separated into two nonnegative components (fig. 1) responsible for respectively: particles heading towards surface (i.e.: settling; $\mathbf{v}_{pi}\cdot\mathbf{n} < 0$) and particles injected from surface:

$$Q_{acc} = Q_{set} - Q_{inj}. \tag{8}$$

Particles do inject ("jump off") from surface only at certain conditions. The assumption is taken that Q_{inj} depends on snow cover density (ρ_c) and ψ – particle bed effort – dimensionless value (described further) which determines particles injections conditions from the particle bed to the open space. The Q_{set} depends on the $\mathbf{Q}$ in the surroundings. Injections (hence the ψ) should not be confused with erosion, which occurs only if injections predominate settling.

3. Model variables

In purpose to perform the similarity analysis there is a necessity to select some easy measurable variables (fig. 3) shaping model physical fields. Most of variables are grouped into sets for convenience:

$$(I) = \left\{ v_{ref}; z_{ref}; \alpha; I_u \right\}; \qquad (D) = \left\{ v_t; \frac{v_t}{g} \right\}; \qquad (B) = \left\{ (\rho_c - \rho_f) d_{cl} g; \chi \rho_c; \varphi \right\}; \qquad L; Q_0; \rho_c; \psi;$$

$$(G) = (G_o) \cup (G_c); \qquad (G_o) = \left\{ \frac{L_1}{L}; \dots; \frac{H_1}{L}; \dots; \beta_1; \dots \right\}; \qquad (G_c) = \left\{ \frac{h_1}{L}; \dots \right\}, \tag{9}$$

where: (I) – inflow parameters set (shaping the distant upstream $\mathbf{u}$ field); (G) – dimensionless geometrical properties (mostly ratios of characteristic dimensions and characteristic angles) set; with subsets: (G_c) – snow cover geometry parameters; (G_o) – examined object (building) geometry parameters; (D) – dispersion properties set; (B) – particle bed (snow cover) parameters set; v_{ref} – average reference horizontal flow speed (at z_{ref}); z_{ref} – reference height; α – velocity profile power law coefficient; I_u – intensity of turbulence; L – reference length; L_i, H_i, β_i – characteristic lengths, heights and angles; h_i – snow cover depths; v_t – dispersion terminal speed; g – acceleration due to gravity; ρ_c – snow cover density; ρ_f – fluid (air) density; d_{cl} – "cluster" diameter; χ – kinematical cohesion of the particle bed; φ – particle bed friction angle.

The Q_0, ρ_c and ψ were mentioned before. Those are so-called "boundary variables" and are introduced to simulate dispersion mass concentration (k) similarity. First one is used during precipitation simulation, the other two during subsequent redistribution simulation. Selective usage of them cause important differences in approach for simulating precipitation and subsequent redistribution. Hence, those two phenomena should be tested separately in wind tunnels.

The ratio v_t/g replaces the mean relaxation time t_r (see eq. 5) because those two are strongly dependent. Generally, the **u** field is also dependent on the Reynolds number. However, it is assumed that for purpose of the snow load prediction (high Re, sharp edges) the Re is irrelevant.
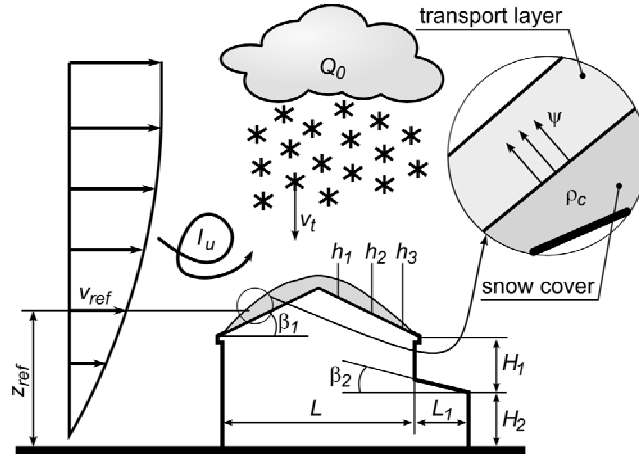
Fig. 3. Variables describing the snow transport model.

Selection of appropriate spatial scale is necessary to model injections. A "cluster" (a lump of few, possibly one, particles) is assumed to be exposed on the fluctuating resultant active force $\mathbf{F}_a = \mathbf{P} + \mathbf{G}$ (fluid stress driven force and gravity, see fig. 4) and the resultant passive force $\mathbf{F}_p$ (reaction from particle bed). When a cluster is at rest those two are counterbalanced. However, values that the $\mathbf{F}_p$ can take are limited by particle bed properties (the (B) set). So, injections occur when outwards directed $\mathbf{F}_a$ fulfils a condition:

$$\psi > 1; \quad \psi = \frac{\left|\mathbf{F}_a\right|}{\left|\mathbf{F}_p^{ult}\right|}, \tag{10}$$

where: $\mathbf{F}_p^{ult}$ – ultimate passive force (see fig. 4) opposing the $\mathbf{F}_a$. The d_{cl} is the mean "cluster" diameter, or for simplification just the particle diameter. Active forces originating from fluid are caused by nonuniform, unsteady pressure distribution over particle bed. Unsteadiness originate in inflow velocity fluctuations which are described by the I_u parameter. The nonuniform pressure distribution is caused by particle bed roughness – a result of how particles were deposited, which is described by the (B) set as well. Passive forces are caused by the cohesion and the inner friction of particle bed. Those are represented by two last elements of (B) in eq. 9. The kinematical snow cover cohesion χ is a property of particle bed which may be identified with a ratio of the material tensile strength to its density. This property may be measured in an experiment similar to bending test.

115
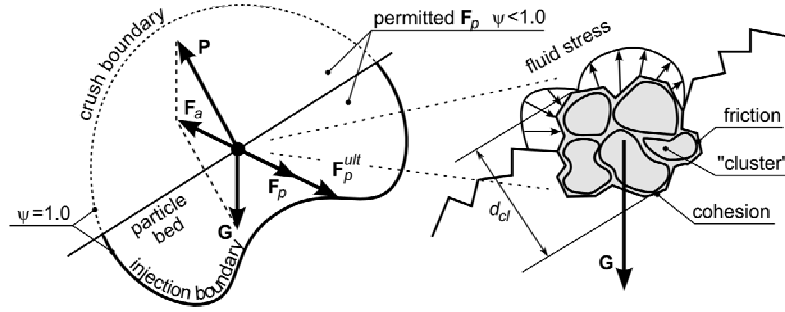
Fig. 4. A "cluster" in rest exposed to active and passive forces.

4. Dimensional analysis

As a conclusion of above considerations, it is assumed that analysed quantities are functions of following parameters:

$$Q_{acc} = Q_{acc}(\mathbf{Q},(G)); \qquad k = k(\psi, \rho_c, Q_0, L);$$
$$\mathbf{v}_{ine} = \mathbf{v}_{ine}((D), \mathbf{u}); \qquad \mathbf{u} = \mathbf{u}((I),(G)), \tag{11}$$

then from eq. 3, 4 and 11 one obtains for precipitation:

$$Q_{acc} = Q_{acc}((I),(D),Q_0,(G),L), \tag{12}$$

and for redistribution:

$$Q_{acc} = Q_{acc}((I),(D),\rho_c,\psi,(G),L); \quad \psi = \psi((I),(G),(B),\rho_f). \tag{13}$$

If an average (in the time interval Δt) value of the Q_{acc} is taken, it can be written from eq. 7 that the finite snow load change is:

$$\Delta s = Q_{acc}\, g\, \Delta t. \tag{14}$$

4.1. Precipitation

The L, Q_0, v_{ref} are chosen as dimension base set elements. Hence, the dimensionless accumulation rate during precipitation from eq. 12 is:

$$Q_{acc}/Q_0 = \Pi_p(\{z_{ref}/L; \alpha; I_u\}, \{\Pi_t; Stk\}, (G)), \tag{15}$$

where:

116

$$\Pi_t = \frac{v_{ref}}{v_t}; \qquad Stk = \frac{v_t/g}{L/v_{ref}} = \frac{v_t\, v_{ref}}{g\, L}. \tag{16}$$

Those two quantities are called "ballistic" because they describe airborne particles behaviour. The Π_t (named the "lash" number) is responsible for the particle movement in the free fall state. The Stk is so-called Stokes number and is responsible for the dispersion particles inertial movement. It is a ratio of the particle movement characteristic time to the fluid flow characteristic time (eq. 16). Parameters of Π_p are all dimensionless quantities forming adequate similarity criteria. Considering the snow load increase from eq. 14 and 15 one gets:

$$\Delta s = Q_0\, g\, \Delta t\, \Pi_p. \tag{17}$$

By definition, the snow load on the ground is a snow load averaged over large ground area. Then, averaging Π_p over large area (A) results in:

$$\int_A \Pi_p\, dA = \int_A \frac{Q_{acc}}{Q_0}\, dA = 1.0 \tag{18}$$

so, the snow load on the ground is $s_0 = Q_0\, g\, t$, where t – snow precipitation duration. Finally, the snow load on the roof (or any particular point on the bottom boundary) is:

$$s = s_0\, \Pi_p. \tag{19}$$

4.2. Redistribution

When considering redistribution, the L, ρ_c, v_{ref} are chosen as dimension base set elements. The dimensionless accumulation rate from eq. 13 is:

$$\frac{Q_{acc}}{\rho_c\, v_{ref}} = \Pi_r \left(\left\{ z_{ref}/L; \alpha; I_u \right\}, \psi, \left\{ \Pi_t; Stk \right\}, (G) \right), \tag{20}$$

so the only difference to precipitation in dimensionless quantity set is appearance of the particle bed effort (ψ), for which another analysis is performed further.

The snow load change from eq. 14 and 20 is:

$$\Delta s = \rho_c\, g\, v_{ref}\, \Delta t\, \Pi_r, \tag{21}$$

where Δt – redistribution duration.

117

4.3. Injection

As a supplement of redistribution consideration, the injection analysis is needed. The central problem of the redistribution simulation is to guarantee $\psi = idem$. In this case, dimension base set elements are: z_{ref}, ρ_f, v_{ref}. From eq. 13:

$$\psi = \psi\left(\left\{z_{ref}/L; \alpha; I_u\right\}, (G), \left\{\Pi_g; \Pi_\chi; \varphi\right\}\right), \tag{22}$$

where:

$$\Pi_g = \frac{(\rho_c - \rho_f)d_{cl}g}{v_{ref}^2 \rho_f}; \qquad \Pi_\chi = \frac{\chi\rho_c}{v_{ref}^2 \rho_f}, \tag{23}$$

which are similarity numbers named respectively: the particle bed gravitational number and the particle bed cohesive number.

5. Similarity criteria

All derived above similarity numbers form similarity criteria just by ensuring them to be equal in the prototype and experimental conditions. Some of them, however are believed to be of greater importance than another. Once again, for convenience, similarity criteria are grouped into sets. The most fundamental is the geometry criteria set:

$$\forall(a \in (G)) \; a = idem, \tag{24}$$

which provides the model shape similarity and possibly the initial snow cover shape.

Another very important one is the inflow criteria set, which contains:

$$z_{ref}/L = idem; \quad \alpha = idem; \qquad I_v = idem. \tag{25}$$

Those criteria do not involve the snow at all and are here to assure similarity of mean and turbulent inflow velocity profiles.

The so-called ballistic criteria set (mentioned before) is universal and concerns with precipitation and redistribution simulations:

$$\Pi_t = idem; \qquad Stk = idem. \tag{26}$$

Both of them influence the trajectory of dispersion particles. However, the higher the Π_t, the more important the Stk appears to be. Moreover, it is believed that for the precipitation simulation the Stk is of less importance, as well as the Π_t for the redistribution simulation.

118

The particle bed criteria set is relevant only during the redistribution simulation, and contains:

$$\Pi_g = idem; \qquad \Pi_\chi = idem; \qquad \varphi = idem; \qquad (27)$$

More detailed analysis of the Q_{set} and the Q_{inj} lets one assume that the Π_g is more important on erosion and the Π_χ on accumulation regions. The last criterion (i.e.: $\varphi = idem$) is difficult to use during planning of an experiment and is believed to be less important and is indirectly taken into account in other criteria. Hence, it may be neglected.

6. Experiment feasibility

In order to carry out an experiment a wind tunnel with some additional devices is needed (fig. 5). For precipitation simulation an "artificial snow" feeders shall be installed at the ceiling of the wind tunnel. At the end of the working section of the tunnel some artificial snow traps shall be installed. Also some measuring method shall be developed in the purpose of particle bed height measurements. Such laboratory setup has been made in the Wind Engineering Laboratory of the Cracow University of Technology.
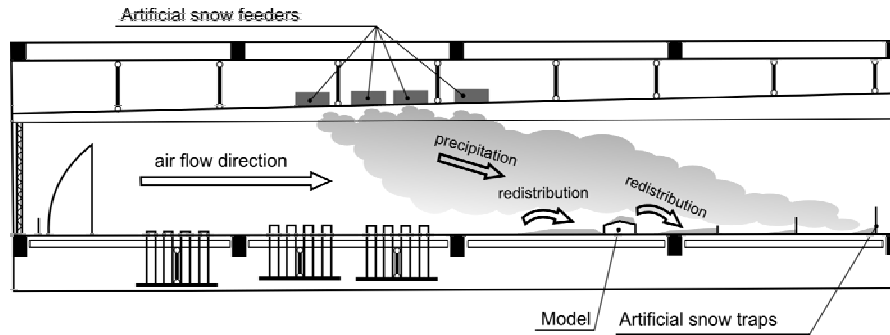
Fig. 5. Experimental setup in wind tunnel.

The artificial snow may be some loose material, such as sawdust, sand, glass spheres, grinded Styrofoam or sodium bicarbonate. As noted before, the snow cover is formed in two steps, and those both steps should be simulated in the wind tunnel. Unfortunately, similarity criteria are different at precipitation and wind induced redistribution phenomena (compare also [2-4]). Therefore, both experiment parts have to be simulated separately at different wind tunnel setups and even probably with different structure models and artificial snow substance.

The first experimental setup is then a precipitation simulation. This test allows one to determine the way the initial snow cover is formed. Applying appropriate similarity criteria to the precipitation simulation is relatively easy – it is easy to keep all similarity

119

numbers at any reduction scale. The most important thing is to find which part of the falling snow will be placed on top of the roof relatively to the total snow amount precipitating per unit ground area. This ratio will depend mainly on the falling snow properties particles and on the vertical wind speed profile. Assuming those parameters at different values from ranges occurring in the nature, one can calculate similarity criteria and perform a tests sequence. The answer should be the most probable worst case scenario, that is reasonable maximum ratio of accumulated snow on the roof to the snow precipitated. If any significant nonuniformities occur in the snow distribution, they should noted as well. This is very important for structures with multilevel roofs.

Similarity criteria for redistribution are more restrictive. They may be kept only for low reduction scales such as 1:10 to 1:25 because high ones may not allow to choose any appropriate "artificial snow" substance. Moreover, for the redistribution very important is detailed roof geometry reconstruction.

7. Example

As an example of the experiment planning procedure redistribution simulation parameters will be shown. Inflow similarity criteria (eq. 25) are met by appropriate setting up the wind tunnel devices shaping velocity and turbulence profiles. The first step is to assume snow dispersion and snow cover properties, which may vary considerably in nature. Here used ones were chosen on the basis of basic literature, additional hypothesis or thought experiments. They are surely in the same order of magnitude as real values. After assuming a reference length (L) all proposed similarity numbers can be determined. The model reduction scale (here 1:10) and the "artificial snow" properties should be picked up heuristically to meet those numbers. An example is shown in table 1.

Table.1 Example experiment parameters and similarity numbers.

		Prototype	Model
Substance		snow	sawdust
Substance density	ρ_p [kg m^{-3}]	~ 700	~ 400
Particle bed density	ρ_c [kg m^{-3}]	~ 250	~ 240
Particles diameter	$d = d_{cl}$ [μm]	500	190
Terminal speed	v_t [m s^{-1}]	~ 2.11	~ 0.37
Kinematical cohesion	χ [m^2 s^{-2}]	~ 1	~ 0.375
Reference length	L [m]	10	1
Fluid density	ρ_f [kg m^{-3}]	1.3	
Acceleration due to gravity	g [m s^{-2}]	9.81	
Reference velocity	v_{ref} [m s^{-1}]	10	6
Reference height	z_{ref} [m]	10	1
Similarity number	Π_t [–]	4.74	16.18
Stokes number	Stk [–]	0.215	0.227
Gravitational number	Π_g [–]	9.43×10^{-3}	9.56×10^{-3}
Cohesive number	Π_χ [–]	1.92	1.92

120

The kinematical cohesion of snow and sawdust should be measured. For "artificial snow" it may be adjusted by dripping it with some cohesive liquid, such as glycerine. Stokes and particle bed numbers were met almost exactly. The Π_t for model is in the same order of magnitude as for prototype, but as mentioned before, it is assumed that this one is less relevant in redistribution simulation. Main experiment output is the final particle bed shape, which may be easily converted (with known ρ_c) into the snow load.

The planning of precipitation experiment is even simpler because only two ballistic criteria should be fulfilled. Full snow distribution predicting simulation should consist of those both experiments. The v_{ref} chosen here (10 m/s) is only an example. Full simulation should take into account few wind speeds originating from few directions. Assembly of data obtained from those set-ups is another complex issue.

8. Conclusions

In the purpose of performing the wind tunnel test some more sophisticated model has been developed. This model served as a basis for similarity criteria derivation. The model needs to take into account the behaviour of dispersion in the volume as well as with the origin of the dispersion: a cloud or a particle bed. Only understanding of those two aspects of the phenomenon (with help of some additional assumptions) allows one to build up the similarity criteria. Moreover, model should be expressed in terms of averaged quantities because only such ones can be measured in real life experiment.

Criteria were divided into sets concerning a different aspect of the phenomenon, namely: the geometry set, the inflow set, the ballistic set and the particle bed set.

References
[1] Crowe C.T., Sommerfeld M., Tsuji Y., *Multiphase flows with droplets and particles*, CRC Press 1998, NY.
[2] Iversen J.D., *Drifting snow similitude*, J. of The Hydraulics Division, June 1979.
[3] Kind R.J., *A critical examination of the requirements for model simulation of wind-induced erosion/deposition phenomena such as snow drifting*, Atm. Env. 10 (1976).
[4] Petersen R.L., Hoppe E. W., *Simulating snow loads on fabric roofs, Advancements in Aerodynamics*, Fluid Mechanics, and Hydraulics, 1986.

SNOW LOAD PREDICTION FOR SPEEDWAY STADIUM IN TARNÓW

Grzegorz Kimbar[*], Andrzej Flaga[*,**], Marek Pańtak[*]

[*] Wind Engineering Laboratory, Faculty of Civil Engineering,
Cracow University of Technology, Jana Pawla II 37/3a, 31-864 Cracow, Poland.
[**] Department of Structural Mechanics, Faculty of Civil and Sanitary Engineering,
Lublin University of Technology, Nadbystrzycka 40, 20-618 Lublin, Poland.

1. Introduction

When designing a new structure the second step, after establishing a structure geometry, is computing all loads acting on this structure. There exist a number of different load types, but the most important are: self weight, wind and snow load, and live load.

The structure described here is a steal roof structure over speedway stadium in Tarnów (fig. 1.) structurally designed at Wind Engineering Laboratory of Cracow University of Technology. The roof covering is a light, initially strained membrane material such as fiberglass reinforced PTFE (fig. 2.). The supporting steel structure is a three dimensional truss which response on loads may be considered as linear. The truss girders of length of about 30m lined up in 6m spacing in form of closed oval over stands and the speedway track. The approximate maximum characteristic load per one girder is for self weight: 140kN, for wind: 120kN, and for snow: 200kN. As can be seen all those three loads are of similar magnitude, with snow load slightly higher.
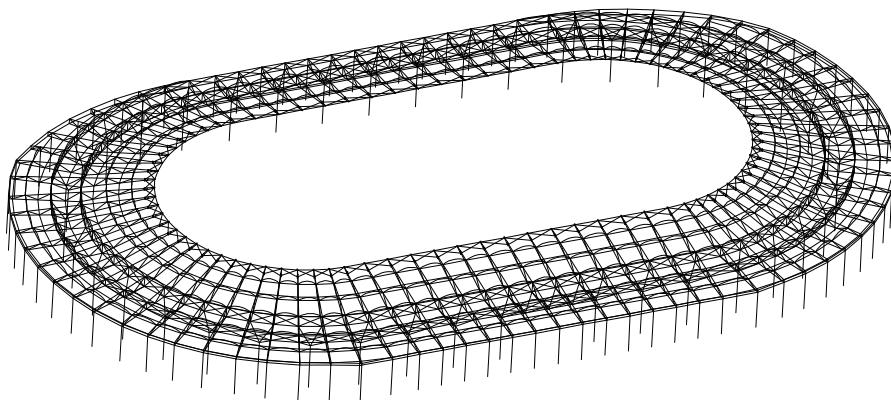
Fig. 1. The roof structure over speedway stadium in Tarnów.

123

On the other hand the membrane covering is highly nonlinear susceptible to stability lost. Therefore not only the wind pressure should be considered but the wind suction as well. More precisely: the initial membrane strain should be high enough to provide the wind suction will not effect in stability lost, and low enough to ensure the snow load will not effect in membrane breakdown. The membrane weight (about 1.5kN per girder) is negligible.

Fig. 2. Membrane cover.

2. Loads

The self weight is easily determinable from the structure project. The wind action on structure was determined by examining a building model in wind-tunnel [1]. It is a 1:100 reduction model equipped with pressure measuring points positioned on both sides of selected membrane spans. The results obtained from the test were distributions of pressure coefficient. Mean and peek values of this coefficient were determined.

The snow load distribution is easily predictable for few common roof shapes included in many available standards and codes. For more complex geometries, the interpolation of standard regulations and approaches may be performed. Although, this interpolation must be made with respect to the course of complicated snow cover shaping processes. Typically, snow cover forms by an initial snow accumulation occurring during the snow precipitation, and by subsequent snow cover redistribution induced mainly by wind and gravity. Having those in mind, the snow load distribution was approximated on the base of polish standard [2] (fig. 3.). The general shape of the roof is a one-slope roof geometry repeated around the stadium. Although, in closer look, the shape details (caused by the membrane covering) are visible. Those two shapes (one-slope and cylindrical) where interpolated. Moreover additional effects were considered as well. The first one is a small snowdrift directly behind roof top. It was imposed by wake in wind flow occurring in this place, which is believed, will influence the snow redistribution. The second additional effect is an occurrence of a ice layer, which may appear in process of continuous melting and frosting of accumulated snow.

3. Static analysis results

The girder is made of welded pipe elements. Cross-sections of truss elements for a typical girder were established as shown at fig. 4. The static analysis of the plane truss girder was performed with a FEM computer program. The maximum wind load pressure coefficient for this girder varies form −1.5 at the lowest part of the girder to −2.5 at the top of the girder. Stresses in truss elements caused by wind action are shown at fig. 5.

124
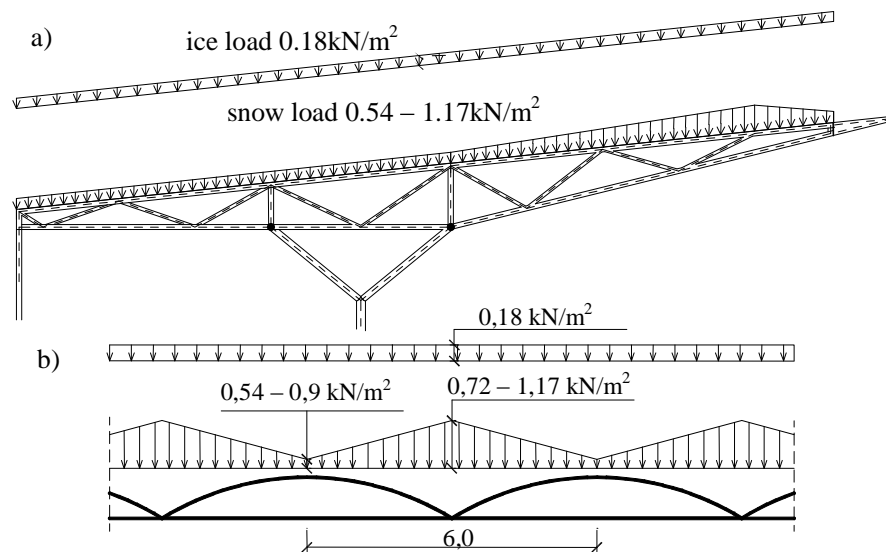
Fig. 3. Snow and ice load acting on a girder,
side view (a) and cross-section through the membrane covering (b).
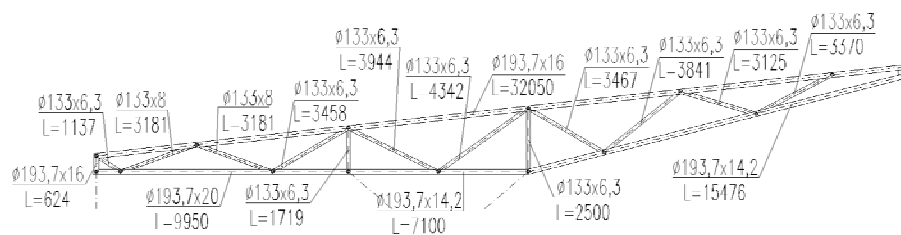
Fig. 4. Assumed truss elements cross-sections for typical girder.
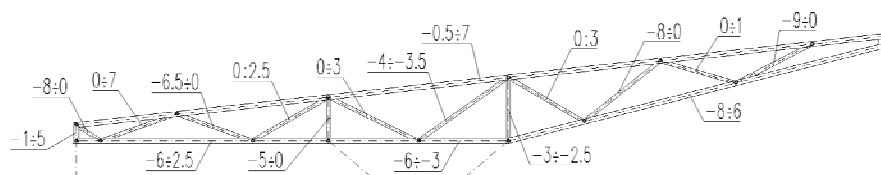
Fig. 5. The stresses envelope (MPa) in the girder elements caused by:
self weight + dead load + wind load (suction).

125

Stresses in truss elements caused by snow load are shown at fig. 6. The snow load was taken as shown at fig. 3.
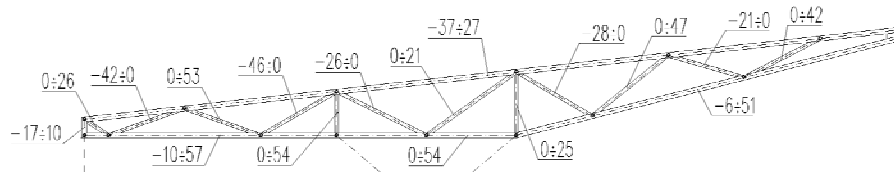
Fig. 6. The stresses envelope (MPa) in the girder elements caused by:
self weight + dead load + snow load.

4. General conclusions

As can be seen (by comparison of fig. 5. with fig. 6.) the snow load is predominant type of load for such structures. Especially important is fact that snow cover can be redistributed over the roof and form snowdrifts. Moreover, ice layer occurrence is also very important factor.

Approach presented above is not fully reliable. For such non-typical roof shapes the snow load distribution should be predicted in wind-tunnel experiments [3]. In that case, to the experimental area an additional agent (so called artificial snow) is introduced. As noted before, the snow cover is formed in two steps, and those both steps should be simulated in the wind-tunnel. Results of these tests should be supplemented with considerations about gravity and temperature influence on the snow cover. The gravity may cause the slide (phenomena similar to avalanche) of the snow cover, but this will reduce the snow load in this case, so it may be neglected in the design process. The temperature influence may result in appearance of ice layer in the snow cover as mentioned before.

References
[1] Flaga, A., Bosak G., Rzegocka-Kłaput R., Matys P., Flaga Ł., *Wind tunnel tests of Municipal Stadium in Tarnów*, printed in this book, 2007, Lublin.
[2] PN 80/B-02010: *Snow load* (in polish).
[3] Kimbar G., Flaga A., *A new approach to similarity criteria for predicting a snow load in wind-tunnel experiments*, printed in this book, 2007, Lublin.

SNOW PENETRATION IN TO VENTILATION OPENINGS IN BUILDINGS

Thomas K. Thiis[*], Philippe Delpech[**]

[*] Dept. of Mathematical Sciences and Technology,
Norwegian University of Life Sciences, 1432 Ås, Norway.
[**] Centre Scientifique et Technique du Bâtiment, 44323 Nantes, France.

1. Introduction

Ventilation of buildings situated in areas where snow particles are transported horizontally by the wind can cause problems for ventilation systems. The snow particles follow the air-flow and enter into the ventilation system, causing moisture damage and irregular service of the ventilation system (Hanssen [1]). Also openings in ventilated cladding and roofs suffer from snow penetration in these areas. This study addresses the design of ventilation openings in snow-drifting areas. Three different methods have been applied to analyze air-flow and snow penetration into a cavity similar to a ventilation opening. First, Computational Fluid Dynamics (CFD) was used to analyze basic airflow in the cavity and to determine the measure of the cavity. Then a wind tunnel study was performed in an environmental wind tunnel. The wind tunnel study was then confirmed with outdoor measurements of the same experimental set-up.

2. Methods

To investigate the penetration of snow particles into a ventilation opening, a 2.5 meter cube was chosen to represent the building in which the ventilation opening was situated. Figure 1 shows the cube, its openings and internal baffles. The cubical shape was chosen for several reasons. The particle tracks of the snow particles are influenced by the air flow pattern around the building implying that the building shape is important for the amount of snow entering a ventilation inlet. A cube is a well known shape with well known and documented aerodynamics. The building should also be of a manageable size in the field experiments. Even if the experimental site has a unidirectional wind direction, some adjustments of the direction of the opening was necessary just before the experiments started. For that reason, the building should be of a modest size and easily moveable.

2.1. CFD

To simulate the air flow around and inside the cube and to prepare the basic shape of the ventilation inlet and the arrangement of baffles inside the cube, the general-purpose finite volume CFD code Ansys CFX was applied. The CFD code solves the well known

incompressible, time averaged Navier-Stokes equations. The permeable walls is considered as porous media and the drag effect is included in the simulations as the a source term S_i

$$S_i = C_{R1}u_i - C_{R2}|u|u_i \qquad (1)$$

Here C_{R1} and C_{R2} are linear and quadratic resistance coefficients respectively. The resistance coefficients are found from separate simulations of the flow through the slotted wall with varying slot space, using the CFD solver. table I show the coefficients used in equation 1. The standard k - ε turbulence model is used to close the equations.
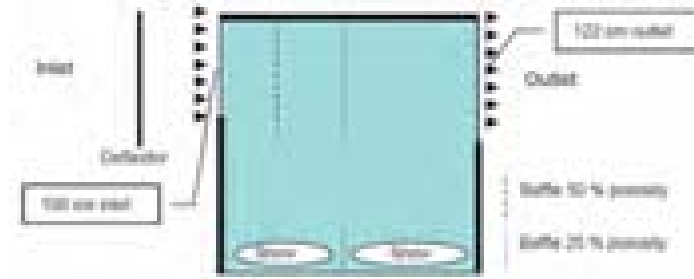
Figure 1. Sketch of the cube used in the experiments.

Table I. Linear and quadratic resistance coefficients used in equation 1.

25%		50%	
C_{R1}	C_{R2}	C_{R1}	C_{R2}
17.5	0.1	2.4	0.1

The inlet velocity was 15 m/s with no vertical variation in the velocity profile. This corresponds to the wind conditions in the wind tunnel. The turbulence intensity on the inlet boundary is set to 5 %. The outlet boundary is continuative, meaning that the normal derivatives of all quantities are set to zero. On the surface boundaries, a law-of-the wall velocity profile is assumed. The lateral and top boundaries have symmetry conditions.

2.2. Wind tunnel

The Jules Verne climatic wind tunnel, with artificial snow making capabilities, can reproduce various kinds of snowstorm events. Wind velocity, ambient air temperature and air/water ratio in the snow guns are fully controllable and mainly determine the snow properties (dry or wet snow). The large dimension of the test chamber, 25 m long, 10 m wide and 7 m high, enables simulation of mechanisms of snow/building interaction at moderately reduced scale. The appropriate thermodynamic conditions (air temperature and humidity) are controlled by two heat exchangers (cold and warm) across the section of the wind tunnel. Snow guns are fitted into the test section nozzle. They are used to generate a freezing water spray, which produces the snow cover. The air temperature, and air/water

128

ratio in the snow guns, was set to make sure the artificial snow was dry. This was assumed to occur at an air temperature of -10 to -15°C (i.e. air density: 1.37 kg/m^3, kinematic viscosity: $1.2 \cdot 10^{-5}$ m^2/s). During the blowing phase the wind velocity was set to 15 m/. The climatic wind tunnel used in the experiments is not a boundary layer wind tunnel and no attempt was made to reproduce the atmospheric boundary layer wind profile. The vertical wind profile at 2 meter height was uniform and the turbulence intensity close to 4~5%. The objective of the tests was to provide a comparative evaluation of snow penetration into different openings, hence the experimental set-up and large size of the model, aimed at providing realistic snowstorm conditions similar to full scale field experiments. Wind tunnel data was obtained from three different experiments of 20-minute periods. The differences were limited to the inlet and are summarized in table 2. During the experiments, the snow transport in the wind tunnel was measured continuously to assure the same experimental conditions for every test. Mechanical snow traps with the shape of a tube with one end closed by netting were used for measuring the snow flux in the wind tunnel, and also any eventual snow transport out of the cubes. Also, the air velocity in the inlet was measured at several positions to be able to find the volume of air entering the box. At the end of each 20-minute period, the snow inside the box was collected and weighted. The mean snow flux in the wind tunnel was approximately 62 g/m^{2}s at a height of 135 cm above the floor, upwind the cube, which is somewhat higher than in a real snow storm at the same wind velocity.

2.3. Full-scale outdoor testing

The full scale outdoor testing in the experiment was performed at Finse in the mountains of Norway the winter of 2006/07. The uniform wind direction combined with low temperature at this site makes Finse an excellent site for experimenting with blowing snow and buildings. Three 2.5 meter cubes of the same type as was used in the wind tunnel studies were installed on a frozen lake with enough space to avoid any influence on the flow pattern around the cubes. The openings of the cubes were equipped with different design of the inlets to be able to study the snow penetration into the boxes during equal conditions. The different inlets are summarized in table II.

3. Results

With the help of CFD simulations several different variations of the interior and exterior of the box was investigated. Position and porosity of the internal baffles were among the variations. Figure 2 shows the simulated air pattern and velocity distribution within the box that was used in the wind tunnel and field experiments. The velocity upwind the box is 10 m/s. To verify that the wind tunnel experiment represented field conditions, the same experiment was performed both places. Figure 3 shows a comparison between the ratio of snow flux into the cube and snow flux in the uniform surroundings with open inlet and insect netting for both field and wind tunnel experiments. The results compare reasonably well indicating that the wind tunnel simulations give valid results. Figure 4 shows the snow penetration ratio for all the different experiments. An interesting result is that the snow penetration is lower in the case of inlet with an insect screen than the slotted wall even if the mean air velocity is larger in the case of the insect screen.

Observations of the snow particle paths show that the slotted wall produces local jets in the slots that entrained snow particles. In the case of insect screen, there were no local jets and more particles were deflected away from the inlet.
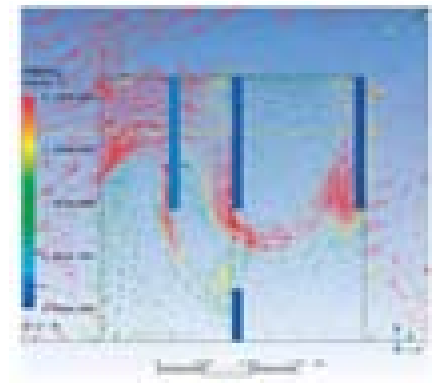
Fig. 2. CFD simulations of the interior and exterior flow pattern of the box.
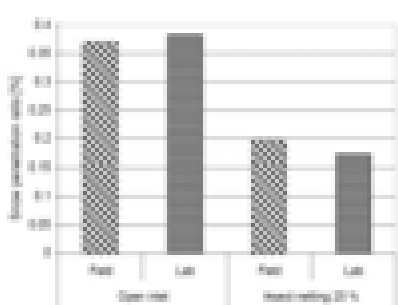
Fig. 3. Comparison between field and wind tunnel –experiments.
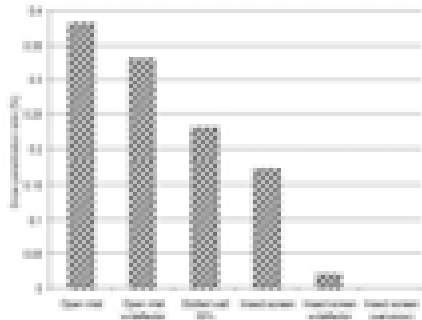
Fig. 4. Snow penetration ratio for all the experiments.

Table II. Summary of the different experiments in the wind tunnel and in the field.

Inlet type	Wind tunnel experiment	Field experiment
Open inlet	▪	▪
Open inlet w deflector		▪
Insect screen 25% porosity	▪	▪
Insect screen 25% porosity w deflector		▪
Slotted wall 30% porosity	▪	

References

[1] Hanssen, S.O., *HVAC - the importance of clean intake section and dry air filter in cold climate,* INDOOR AIR 14: 195-201 Suppl. 7, aug 2004.

130

GROUND SNOW LOADS IN BELARUSIAN CODE

Victor Tur[*], Vladimir Valuev[*], Stanislav Derechennik[*], Oleg Meshik[*]

[*] Department of Building Structures, Faculty of Civil Engineering,
Brest State Technical University, Moskowskaja 267, 224017 Brest Belarus.

1. Introduction

Many roof collapse or damages have been reported due to snow loads in various region of the world during winter season (for example: Russia, Transvaal Water Park in Moscow; Poland, Katowice Exhibition Hall; Belarus, Secondary School in Krasnopolje, etc.).

During last years many countries (Poland, Ukraine, Lithuania), that are situated around Belarus, Have changed National Snow load Maps and characteristic values of snow loads in accordance to Eurocode [1]. This new maps were revised by the Belarusian Technical Committee TC8 and were pointed significant differences in characteristic values of ground snow load. In Belarusian Code (BC) and EC [1] Snow Load Research Program was started in 2004.

The ground snow load is the force per unit area exerted on a horizontal surface at ground level by a snow cover.

According to the safety concept of the Eurocodes [1] the characteristic value of snow load is determined as 50 years MRI (mean recurrence interval or return period) value. This corresponds to the 0.98-fractile of distribution of the annual maxima of snow load. For each station the best fitting probability distribution function (PDF) should be selected among other (e.g. Type I extreme value distribution, Lognormal and Normal distributions, Weibull distribution). This could be done using different statistical procedures [2-4], with application of parametrical criteria of consent (more often Pirson, Kolmogorov, etc.). Then, proceeding from established recurrence interval T (years), characteristic value of snow load should be estimated with probability $p = 1 - 1/T$ – as p-fractile of theoretical probability distribution. The parameters of distribution should be determined by mean of Least Squares Method (or Moment's Method or Maximum Likelihood Method). The type of PDF can depend on the type of climate and geographical parameters.

2. Belarus Snow Climatology

Winter period with continuous snow cover (>2.5 cm) on territory of Belarus averages 75 days in south-west part and 125 days in north-east part of country. During the cold period the snow cover can repeatedly collapsed under the thaws (especially at the beginning and the end of the winter period). More than 50% of the days in thaw period have a positive average temperature, which often leads to full destruction of a snow cover. For example, in December to 10% of thaws are formed at average daily temperature more

131

than 40ºC. Continuous snow cover (which is lying more than one month) is formed in first decade of December (on north-east part) and in the third decade of December (on south-west part of country).

The important characteristic of the ground snow cover is its density. In Belarus the density of snow fresh-fallen is 0.08-0.12 g/cm^3 (on north-east) and 0.12-0.79 g/cm^3 (south-west part). Eventually there is a consolidation of snow. The average long-term density value of snow in the end of January makes 0.23-0.28 g/cm^3, in February – 0.25-0.30 g/cm^3. Density of the thawing snow, impregnated with water 0.80 g/cm^3 is marked.

Meteorological data on a ground snow cover during 1944/45 – 2005/06 and their intra-annual dynamics are presented in table I (meteorological station Minsk).

Table I. Intra-annual dynamics of snow cover characteristics of meteorological station Minsk (1944/45 – 2005/06).

Parameters		Oct	November			December			January			February			March			April	
		3	1	2	3	1	2	3	1	2	3	1	2	3	1	2	3	1	2
snow depth [cm]	mean	0	1	2	4	6	8	10	12	14	16	17	19	19	18	14	6	2	0
	max	9	15	18	23	25	28	33	34	36	38	37	45	49	53	47	47	23	6
density [g/cm^3]	mean	0.20	0.15	0.19	0.20	0.20	0.23	0.21	0.24	0.24	0.25	0.26	0.26	0.27	0.29	0.31	0.32	0.32	0.13
	max	0.20	0.24	0.26	0.28	0.30	0.43	0.31	0.42	0.38	0.38	0.39	0.37	0.45	0.44	0.45	0.38	0.42	0.13
Snow water equivalent (SWE) [mm]	mean	0	1	3	6	11	16	21	27	35	41	44	50	53	50	41	19	5	0
	max	13	22	34	51	55	64	81	86	95	105	123	147	135	140	141	137	88	8

Spatially-time variability of atmospheric precipitations (annual, monthly values) during 1944-2006 was characterized by the coefficient of variation (C_v). The differentiated estimation time (C_{vpb}) and spatial (C_{vi}) components of variability of an atmospheric precipitations has shown, that its resultant keeps within limits $0 \le C_v \le C_{vi} + C_{vpb}$.

The received average value (C_{vi}) for territory of Belarus is presented in table II.

132

month	1	2	3	4	5	6	7	8	9	10	11	12	year
C_{vi}	0.11	0.10	0.09	0.08	0.06	0.05	0.07	0.07	0.08	0.07	0.10	0.10	0.05

Experimental data on an atmospheric precipitation during the winter period (December-February) are united in spatially-time fields which posses properties of stochastic processes.

The description of existential fields is carried out by statistical methods when instead of separate consideration of individual properties of a stochastic field $\zeta(\rho)$, the statistical parameters characterizing its general statistical structure are used. The structure of a stochastic field represents a set of independent components:

$$\zeta(\rho) = \eta(\rho) + \kappa(\rho), \tag{1}$$

where $\eta(\rho)$ – a small-scale component; $\kappa(\rho)$ – a large-scale component; ρ – distance between meteoric-points.

Correlation function (r), possessing properties of additively to independent components of a field, is defined as:

$$r\zeta(\rho) = r\eta(\rho) + r\kappa(\rho). \tag{2}$$

Intra-annual parities between components are investigated on each month, a season and as a whole for a year. Spatially – correlation functions (SCF) an atmospheric precipitation during the winter period are presented in fig. 1.
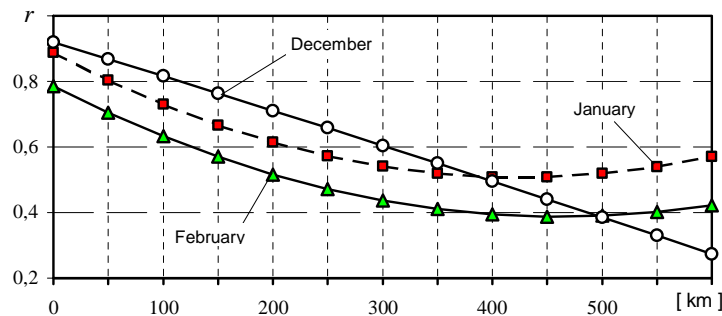
Fig. 1. Spatial correlation functions (r) an atmospheric precipitation in territory Belarus during the winter period.

133

In course of atmospheric circulation, heat and moisture redistribution takes place on a terrestrial surface of Belarus and are formed areas with most general sign (fig. 2).
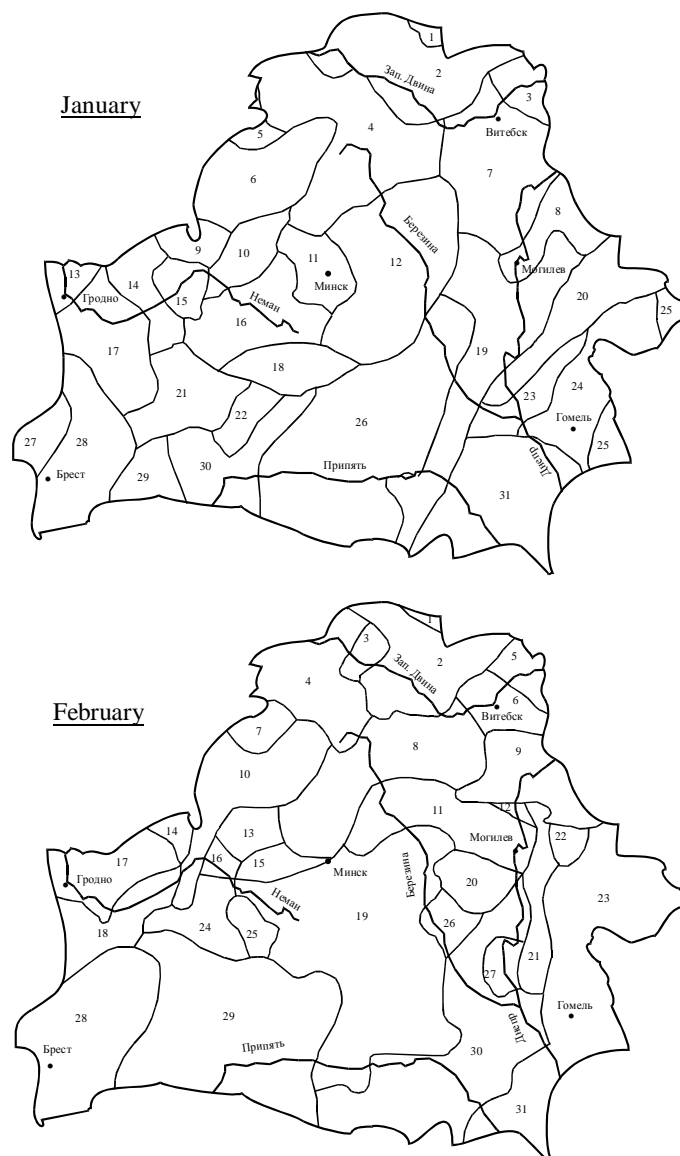
Fig. 2. Division into districts Belarusian territory (synchronism of atmospheric precipitation).

134

3. Statistical forecasting of snow loads

In view of small reference period (no more than 50, and sometimes less than 20 years) and small volume of sample (primary data) executing of adequate estimation and forecasting of snow loads by specific methods are practically impossible. The problem consists also in parametrical criteria.

First, the result of their application depends in the solving image on a way of grouping of data (in particular, on samples of small volume). Secondly, they are intended for a deviation of incorrect hypotheses, instead of for acknowledgement of the true. Thirdly, they are convenient for an estimation of the consent of distributions in area median values, in area of the greatest and least values, i.e. on "tails" of distributions - are practically disabled.

More effective for problems of forecasting of so-called large events is use the statistic of extreme values to whom many submit natural, including the climatic phenomena [3, 4]. Usually thus first limiting Gumbel distribution - only already in the field of "tails" of distributions of the predicted parameter where it has good linear approach in a scale «the double logarithm of probability - value of parameter» is a priori used besides. Difficult natural systems can be characterized, however, not only mentioned Gumbel statistics, but also sedate or indicative by laws of distribution of probabilities (with so-called heavy and easy "tails", accordingly). MAGATE Code for an estimation of platforms for nuclear stations recommends checking conformity of empirical meteorological data to one of types (families) of laws of distribution: to type I (Gumbel, or Fisher-Tippet), to type II (Freshet) or to type III (Weibull) [5].

Using the specified recommendations, we have executed statistical data snow water equivalent (SWE) on 18 meteorological stations of all regions of Belarus for 1947-2006. The basic stages of a technique: 1) construction and a preprocessing of empirical probability distribution function (PDF); 2) allocation of a "tail" part of distribution - more to the right median the value increased on standard deviation; 3) approximation of a "tail" part of empirical function by dependence of type I, II or III; 4) calculation characteristic values, proceeding from set values p or T.

Approximation of "tails" of empirical distributions was carried out in all cases linearly in the scales of a similar kind differing only by frequency rate logarithmic probabilities: unitary (type II), double (type I) or triple (type III). Definitively type of distribution was defined on the greatest reliability of the approximation reached at displacement of the beginning of "tail" to the right from a median so, that its length changed in limits 30÷10 empirical results. As a result empirical data on 8 stations have been carried to type I (to standard Gumbel distribution), and on 10 - to types II or III. The found then standard snow loadings for $T = 50$ ($p = 0.98$), as one would expect, insignificantly differed years from the greatest observed for 48-50 years of values. However the similar forecast of extreme snow loadings (as special influences with $p > 0.995$) has resulted, in most cases, in obviously overestimated results exceeding standard values in 1.5 and more times.

135

For this reason empirical data have been in addition investigated about primary presence at them of extreme (special) values which could deform results of forecasting.

So, at station Zhitkovichi in the winter 1969-70 SWE value of 160 mm was fixed, that considerably exceeds other greatest value of a sample. We have repeated approximation of an empirical number, having excluded this value, as is shown in fig. 3.
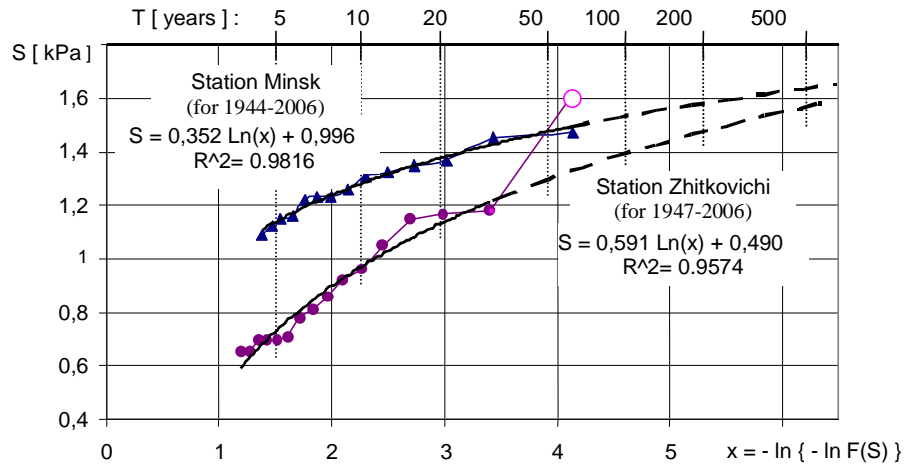
Fig. 3. Approximation of "tail" parts of distributions of annual maxima
of snow loading (based on the data of two meteorological stations).

The type of new approximating function has changed from type II to type III, moreover the settlement annual probability of occurrence of value does not exceed of $S_k = 1600$ Pa, is equal 0.015, i.e. such event can occur on the average one time in 695 (!) years and, certainly, should be accidental events. Standard characteristic value of the snow load found by means of approximation corrected by specified image, makes $S_k = 1300$ Pa, (against 1510 Pa in the previous analysis), and for $p > 0.996$ ($T = 250$ years) - $S_k = 1500$ Pa.

The analysis of applicability and accuracy of methods of construction of snow maps in isolines has allowed establishing, that the most exact at available spatial distribution of data is Kriging. Developed and presented above maps of territorial distribution of the basic characteristics of a snow cover in territory of Belarus (figs 4 and 5) are put in a basis of the representative meteorological data analyzed, investigated in a context of the revealed independent structures spatially – time fields (small-scale and large-scale components) and the constructed surfaces of their trends. Auxiliary function is thus taken away to the factor of synchronism of loss of an atmospheric precipitation in territory of Belarus during the cold period (fig. 2).

136
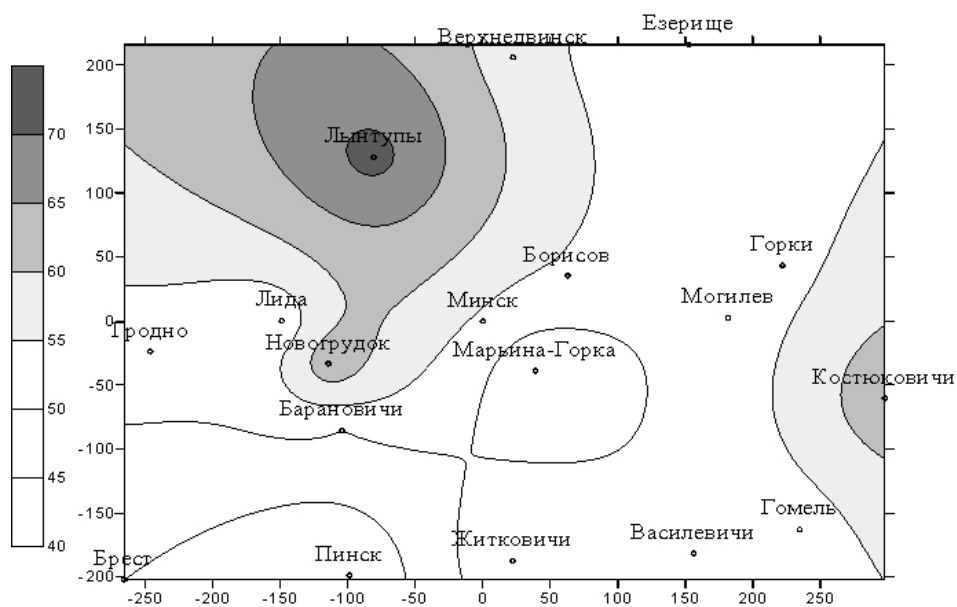
Fig. 4. Distribution of the maximum depth of a snow cover [cm].
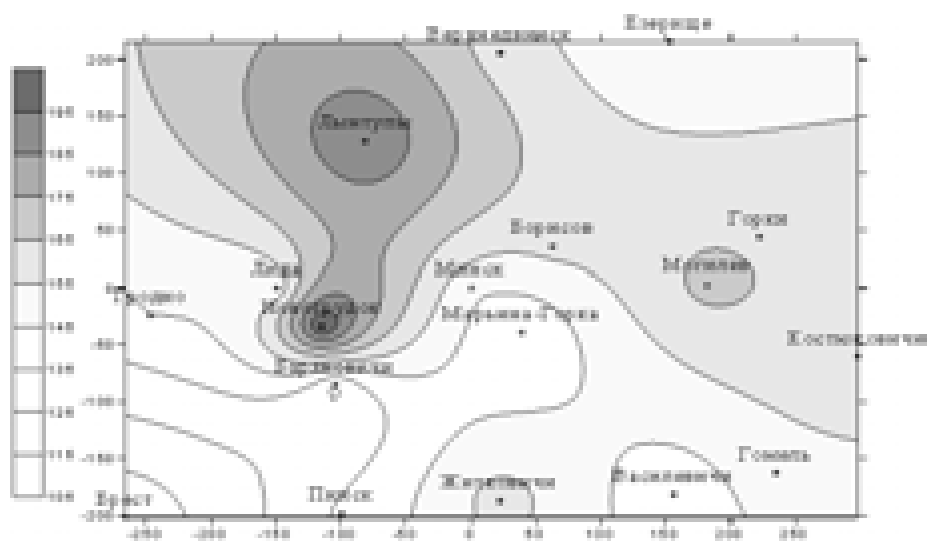
Fig. 5. Distribution of annual maximum of water equivalent of snow cover [mm].

137

References

[1] EN1991-1-3 Eurocode 1 − *Actions on structures – Part 1-3: General actions – Snow Loads*.

[2] Filipov V.V., Kopylov A.T., Kornilov T.A., etc. *Snegovye nagruzki na pokrytijah zdanij v uslovijah Severa*, Moskva: Nauka, 2000, 246 p.

[3] Bak P., *How nature works: the science of self-organized criticality*, N.Y.: Springer-Verlag, 1996, 205 p.

[4] Vladimirov V.A., Vorobjev J.L., Salov S.S, *Upravlenie riskom*, Moskva: Nauka, 2000, 431 p.

[5] *Account of the meteorological phenomena at an estimation of platforms for atomic power station* // A Series of MAGATE Codes NS-G-3.4, MAGATE, Vienna, 2005.

138

COMPUTATIONAL WIND ENGINEERING

NUMERICAL INVESTIGATION ON CIRCULAR CYLINDERS UNDER AERODYNAMIC INFLUENCES

Roman Kinash[*], Marian Branny[**], Oleksiy Kopylov[***], Jan Walaszczyk[*]

[*] Department of Geomechanics, Civil Engineering and Geotechnics,
Faculty of Mining and Geoengineering,
AGH University of Science and Technology, Mickiewicza 30, 30-059 Cracow, Poland.
[**] Department of Underground Mining, Faculty of Mining and Geoengineering,
AGH University of Science and Technology, Mickiewicza 30, 30-059 Cracow, Poland.
[***] Building Research Institute, Filtrowa 1, 00-611 Warsaw, Poland.

1. Introduction

Turbulence is the most widespread phenomenon in the prevailing majority processes which arise in the nature and interest us from the technical point of view. Movements of atmospheric air and waters of oceans, streams in channels, jets, and also in an aerodynamic trace become swollen phenomenon. Therefore turbulence is this phenomenon which interests astrophysicists and meteorologists, engineers of industrial and water construction, experts in branch of flowing machines, the chemical equipment, protection of environment, aviation, ground and a sailing charter, and also many other things branches are turbulent between star gas clouds and a solar wind. Not looking that turbulence has interdisciplinary character in the widest value of this word, however as the phenomenon which acts during movement of liquids and gases makes one of sections which develops most dynamically in last years.

2. Airflow area

Tests will concentrate on the flow over two identical slim cylinders with the diameters much smaller than their height. The aim will be to determine velocity and pressure fields around the objects exposed to air-flow and to estimate forces operating on such objects. Because of the fact that $D<<H$, this issue will be examined in 2D geometry. The area of air-flow around the cylinders (placed in several variants) is shown in fig. 1. The calculations were made using FLUENT 6.1 program.

141
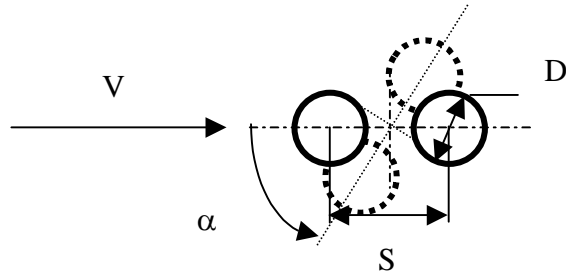
Fig. 1. Cylinder examination scheme: *D* – cylinder diameter, *S* – cylinder spacing,
α - change of airflow angle.

3. Mathematical model

It was assumed that the flow is steady and incompressible. The issue discussed here is described by a set of continuity equation (1) and by Navier-Stokes and a turbulence model k-ε equations which have a general form (2) FLUENT Inc., 2005 [5], Kazimierski, 2004 [1].

$$\frac{\partial(\rho v_j)}{\partial x_j} = 0 \, , \tag{1}$$

$$\frac{\partial}{\partial x_j}(\rho v_j \phi) - \frac{\partial}{\partial x_j}(\Gamma \frac{\partial \phi}{\partial x_j}) = S_\phi \, . \tag{2}$$

Table I presents the meaning of variable ϕ, coefficient Γ and quantity S_ϕ.

Table I. Meanings of symbols used in the equation (2).

Φ	Γ	S_Φ
v_i	μ_{ef}	$\frac{\partial}{\partial x_j}(\mu_{ef} \frac{\partial v_j}{\partial x_i}) - \frac{2}{3}\frac{\partial}{\partial x_i}(\mu \frac{\partial v_l}{\partial x_l}) - \frac{\partial}{\partial x_i}(p + \frac{2}{3}k\rho\delta_{ij}) + \rho g_i$
k	$\mu + \frac{\mu_T}{\sigma_k}$	$G_k - \rho\varepsilon$
ε	$\mu + \frac{\mu_T}{\sigma_\varepsilon}$	$C_1 \frac{\varepsilon}{k} G_k - C_2 \rho \frac{\varepsilon^2}{k}$

where: v_i – i-th coordinate of average velocity vector, m/s; ρ – local density, kg/m^3; $\mu_{ef} = \mu + \mu_T$ – molecular and turbulent coefficient of dynamic viscosity, kg/ms; g_i – i-th coordinate of gravitational acceleration vector, m/s^2; k – kinetic energy of turbulence, m^2/s^2; ε – dissipation rate of kinetic energy of turbulence, m^2/s^3; δ_{ij} – Kronecker symbol; C_1, C_2, C_3, σ_k, σ_ε – model's constants.

142

The element representing the generation of the kinetic energy of turbulence caused by the gradient of velocity field (average) G_k has the following form:

$$G_k = \mu_T \left(\frac{\partial v_i}{\partial x_j} + \frac{\partial v_j}{\partial x_i} \right) - \frac{2}{3} \left(\rho k + \mu_T \frac{\partial v_i}{\partial x_i} \right) \delta_{ij} . \tag{3}$$

4. Boundary conditions

- In the inlet opening there was assumed constant velocity of air-flow and a constant values of kinetic energy of turbulence and this of energy's dissipation rate, calculated with the assumption of 10% intensity of turbulence and the scale of turbulence $L=1$m. In FLUENT program this are the boundary conditions of *inlet velocity* type.
- It was assumed that pressure in the outlet cross-section is constant, and for other variables towards the flow direction $\frac{\partial \phi}{\partial x} = 0$ (so-called *pressure outlet* condition).

  The *outflow* condition was used interchangeably as well, but no significant influence of the above mentioned boundary conditions at the outlet on the distribution of velocities and pressures around the tested objects was noticed.
- When describing wall conditions, a classical model of wall function was used, assuming that the surface of walls is hydraulically smooth.

5. Discretisation of the area

The flow area was covered with a numerical mesh, with increase of its density near the boundary of the cylinders and being composed of about 250,000 elementary cells in cases of axially-symmetrical flow (cylinders were placed along horizontal and vertical axes). For the case where the angle between the line going through the middles of circles and the horizontal axis was 45° the number of cells was about twice as big – calculations were made for the whole flow area.

6. Test results

As the first, the flow around an infinitely high cylinder was considered. For this kind of flow there are experimental test results available in specialist literature, that is why it was treated as a reliability test for numerical calculations. The calculated coefficient of aerodynamic drag, at the flow velocity in a free stream of 20m/s ($Re=0.7$ x 10^5), equals 0.83 and is smaller than the estimates presented in: Daugherty, Franzini 1977 [2]; White, 1994 [3] $C_D=1.2$; Roberson, Crowe 1993 [4] $C_D=1.0$-1.1; Kinash at al., 2002, 2006 [6, 7] $C_D=1.0$. Qualitatively, the distribution of pressure on the cylinder surface is similar (fig. 2). The biggest difference between theoretically and experimentally obtained pressure coefficient is visible on the windward side with the angle measured between the direction

of the flow and the radius of a cylinder equals 0°. Numerically determined angle of stream detachment equals 127° and, as it can be concluded from literature, this value appears to be too big. Similar differences between theoretical and measured values were obtained at the stream velocity of 30m/s ($Re=10^5$). Because of inaccurate representation of the above elements, the error while determining the aerodynamic drag coefficient of a cylinder using a numerical method amounted to 20-30% of real value.

The following examples refers to the calculation of velocity fields and pressure distribution around two cylinders in three geometrical arrangements and their aerodynamic drags. Calculations were made for 2D geometry and the air-flow velocity in a free stream of 20m/s and 30 m/s. The cylinder diameters were D=60mm, and their mutual distances (measured from the middles) 1.8D.
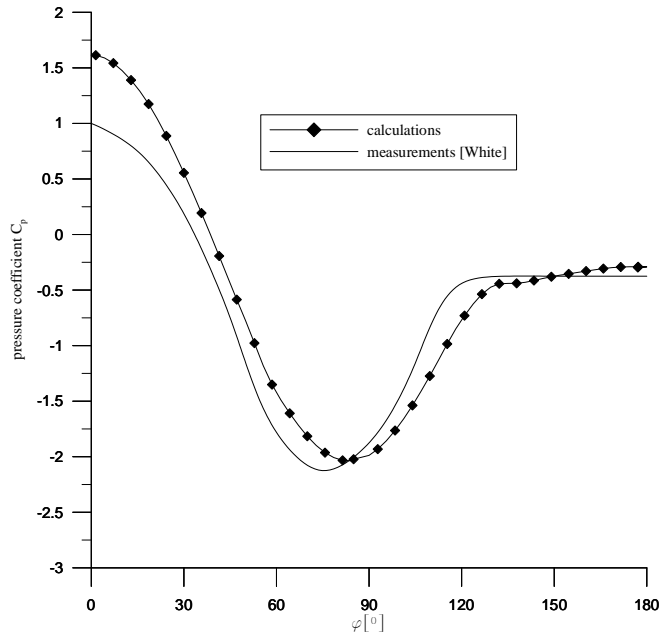
Fig. 2. Distribution of pressure coefficient on surface of one cylinder.

Representation of velocity field and distribution of static pressure in case of cylinders placed along the line perpendicular to the flow direction with the velocity of 20m/s is shown in fig.3. Fig.4. shows the schedule of static pressure upon surface of top cylinder, as function of an angle between a mainstream of air and radius of the cylinder.

For the top cylinder the maximum pressure on the windward side (φ=0°) equals 337 Pa, and on the leeward side for the angle $\varphi = 180°$ it equals -128 Pa (relative pressure). The minimum value of relative pressure on the surface of -856 Pa appears in the point described by the angle $\varphi = 270°$. An identical graph can be drawn for the bottom cylinder, but while

144

measuring the angles anticlockwise arrangement should be applied. Aerodynamic drag coefficient is 0.825 and this value is close to the one obtained while testing a single cylinder immersed in a uniform flow. The value of this coefficient acquired by examination in an aerodynamic tunnel [7] equals 0.73. For this case, the error assigned to the aerodynamic drag coefficient obtained by numerical method in relation to the measured value equals 13%.

a)

b)
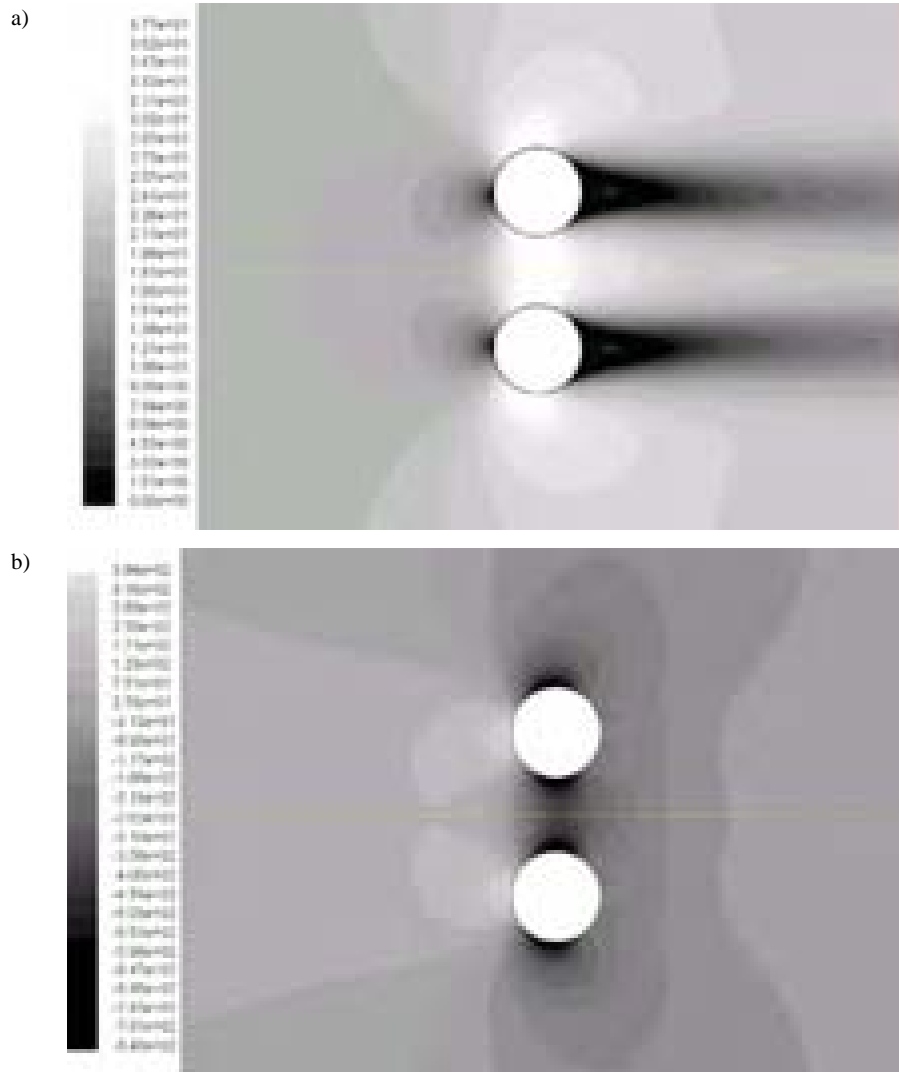
Fig. 3. Distribution of velocity (a) and static pressure (b) around cylinders.
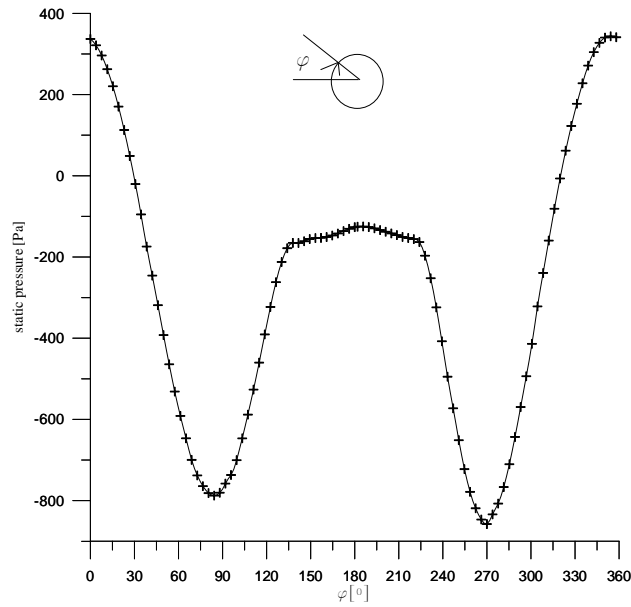
Fig. 4. Distribution of static pressure on surface of the top cylinder.

Characteristic values for three considered positions of spatial arrangements of cylinders are resulted in table II.

Table II. Results of calculations and their comparison with data of experimental researches.

Type	Velocity of free stream [m/s]	Relative pressure on the windward side for $\varphi=0^0$ [Pa]	Relative pressure on the leeward side for $\varphi=180^0$ [Pa]	Maximal value of relative pressure on surfaces of cylinders [Pa]	Calculated aerodynamic drag coefficient C_S	Measured aerodynamic drag coefficient acc. [6], [7] C_D	C_D/C_S *100 [%]
cylinders along perpendi-cular line	20	357	-106	-839	0.817	0.73 [7]	89
	30	799	-233	-1904	0.804	0.86 [7]	107
cylinders along horizontal line	20	cylinder 1 397 cylinder 2 -47	cylinder 1 -73 cylinder 2 -98	cylinder 1 -499 cylinder 2 -340	cylinder 1 0.828 cylinder 2 0.295	cylinder 1 0.8226 cylinder 2 0.36[7]	99 122
	30	cylinder 1 871 cylinder 2 -21	cylinder 1 -55 cylinder 2 -99	cylinder 1 -874 cylinder 2 -522	cylinder 1 0.795 cylinder 2 0.291	cylinder 1 0.8 cylinder 2 0.37[7]	100.6 127

cylinders along inclined line of a slope 45⁰	20	top cylinder 405 bottom cylinder 380	top cylinder -81 bottom cylinder -72	top cylinder -569 bottom cylinder -510	top cylinder 0.642 bottom cylinder 1.057 for system* 0.570	for 25m/s and S=2.0 D [6] top cylinder 0.8-0.9 bottom cylinder 1.0 for system* 0.45	
	30	bottom cylinder 910 top cylinder 856	bottom cylinder -172 top cylinder -161	bottom cylinder -1280 top cylinder -1149	bottom cylinder 0.655 top cylinder 1.059 for system* 0.575		

*The conventional surface for system of cylinders is calculated on dependence $S=D+(D+1.8D)\sin\alpha$ according to with [6].

Figs 5÷6 shows distributions of pressure on surfaces of cylinders for velocity of free stream 20 m/s. Comparison of figs 4-6 together with values in table II shows influence of cylinder's location on characteristic aerodynamic quantities.
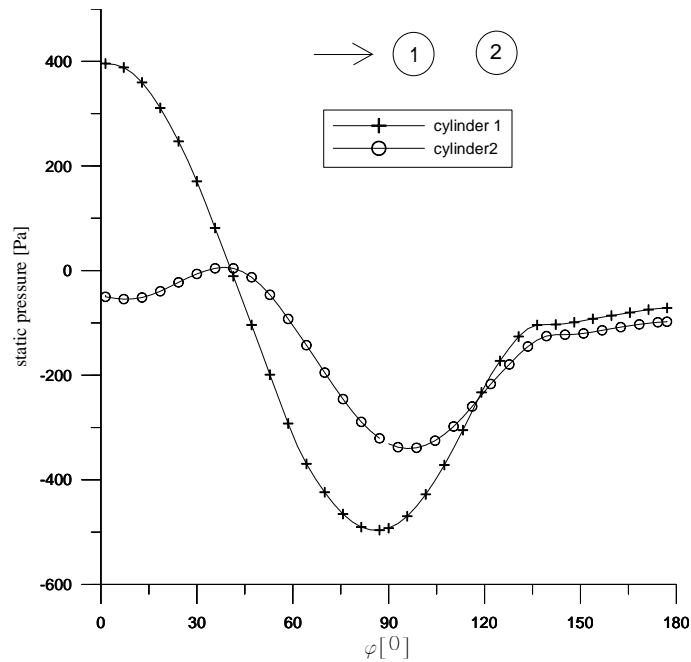
Fig. 5. Distribution of static pressure on surfaces of cylinders located under an angle 0^0 to a direction of free stream.
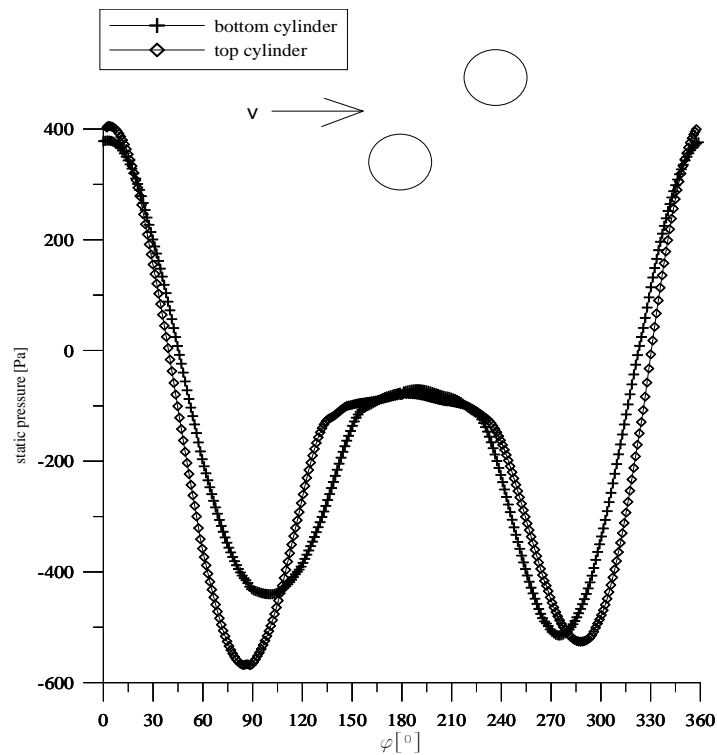
Fig. 6. Distribution of static pressure on surfaces of cylinders located along an inclined line of a slope 45^0 to the direction of free stream.

7. Conclusions

The executed numerical researches of two circular cylinders by means of program FLUENT 6.1 have shown, that deviations between calculations and results of researches of models in a wind tunnel are within -21 % to +32 %. These significant divergences are partly caused by imperfection of boundary layer's modeling and calculation of an arrangement of separation points for circular sections.

References
[1] Kazimierski Z., *Podstawy Mechaniki Płynów i Metod Komputerowej Symulacji Przepływów*, Politechnika Łódzka, 2004.
[2] Daugherty R.L, Franzini J.B., *Fluid Mechanics with Engineering Applications*, McGraw-Hill, Inc., 1977.
[3] White F.M., *Fluid Mechanics*, McGraw-Hill, Inc., 1994.

148

[4] Robertson J.A., Crowe C.T., *Engineering Fluid Mechanics*, John Wiley&Sons, Inc., 1993.

[5] FLUENT Inc. FLUENT 6.1 Documentation, 2005.

[6] Kinash R., Kopylov O., Kopylova I., *The laboratory investigation of aerodynamic interference of a set of circular cylinders*, Proceeding of 3rd international conference "Problems of the technical meteorology". Lviv, 2006, pp. 57–64.

[7] Кінаш Р.І., Копилов О.Є., *Аеродинамічні дослідження тандему з двох колових циліндрів*, Вісник НУ "ЛП" "Теорія і практика будівництва" N 441, Львів, НУ "ЛП", 2002. – с.85-94.

[8] Elsner J.W., *Turbulencja Przepływów*, Wydawnictwo PWN, Warszawa, 1987. – 380 s.

[9] Teranath B.S., *Wind and Earthquake Resistant Buildings Structural Analysis and Desing*, Marcee Dekker, Los Angeles, California, 2005. – 882 p.

[10] Simiu E., Miyata T., *Design of buildings and bridges for wind*, Wiley, 2006. – 308p.

Acknowledgments

THE INFLUENCE OF INPUT FLOW PROPERTIES ON THE QUALITY OF THE SOLUTION OBTAINED WITH USING THE k-ε TURBULENCE MODEL

Ewa Błazik-Borowa[*]

[*] Department of Structural Mechanics, Faculty of Civil and Sanitary Engineering, Lublin University of Technology, Nadbystrzycka 40, 20-618 Lublin.

1. Introduction

The k-ε model is often used to model turbulence of a flow in computational fluid dynamics problems. Numerous versions of this model have been developed since the 1970s, when the standard version model was popularised by Launder and Spalding [1] and others. The largest number of papers concerning the k-ε model were written in the 1990s. In spite of the fact that turbulence models based on LES method are currently being developed, k-ε turbulence models are still in common use within commercial programs. Since users of the k-ε turbulence model know its limitations, they are able to avoid them. It is anticipated, therefore, that the new flow modeling methods (such as LES or DVM) will be an alternative to the k-ε method for as long as research devoted to adjusting the old method to new issues remains useful.

The properties of the air flow around a building depend on the geometry of the building and properties of the flow in front of the building. The quality of the solution depends on the mesh of the model which describes the flow around the building, boundary conditions, turbulence model parameters and input properties of the flow.

This section deals with the influence of input values of a velocity, a turbulence intensity and Reynolds number on the correctness of the solutions which are obtained with using the k-ε turbulence model. The calculated flow properties depend on model parameters and input flow properties. Hence the analysis is based on the comparison of calculation results and tunnel measurements and the estimation of the influence of input properties on the sensitivity analysis of a flow to the k-ε turbulence model parameters.

2. The description of research methods

The discussed problem will be presented in the examples of the k-ε model in the standard version for steady incompressible flows. The described examples concern: the 2D air flow around a single square cylinder with the dimension D=0.04m (fig.1a) and the flow around a square cylinder at the ground with the height H=0.06m (fig.1b). These models can model horizontal and vertical cross-sections of length or high buildings.

151

a)

b)
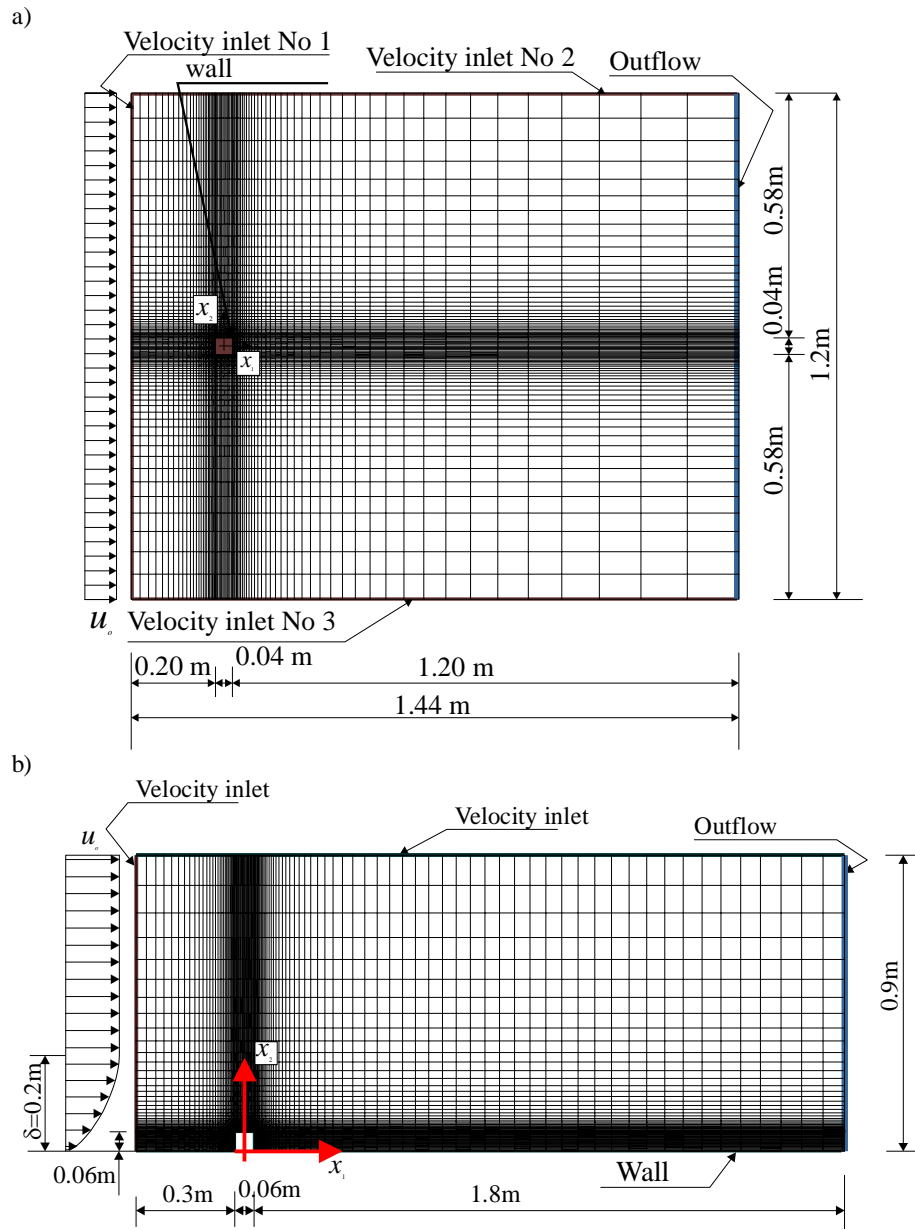
Fig. 1. The calculation domains of the analysed flow problems:
a) free square cylinder; b) square cylinder at the ground.

The flow is determined by the pressure p, the velocity vectors $\mathbf{u}=[u_1 \ u_2]^T$, the kinetic turbulence energy k, the dissipation rate of kinetic turbulence energy ε, the turbulence dynamic viscosity μ_t. For the civil engineering the most important flow properties are a pressure at walls of models, as the effect of wind action, and velocities in the wake used for comfort problems. They are calculated from the system of differential equations which contain the follow parameters of the k-ε model: $C_{\varepsilon 1}$, $C_{\varepsilon 2}$, C_μ, σ_k and σ_ε. In this section these parameters are equal to $C_{\varepsilon 1}=1.44$, $C_{\varepsilon 2}=1.92$, $C_\mu=0.09$, $\sigma_k=1.0$ and $\sigma_\varepsilon=1.3$.

In order to check the quality of numerical solutions for flow problems two methods are used:

- comparison of measurements results in wind tunnels and numerical results, obtained with using the k-ε turbulence model (comp. fig.2 and fig.3),
- sensitivity analysis of the flow properties to parameters of the k-ε method.

The calculation results for the single square cylinder are compared with measurements results presented in the follow papers: [2], [3], [4], [5], [6], [7] and [8], and for the flow around a square cylinder at the ground with results obtained by Noda et. al. [9] and Sitheeq et.al. [10].

Legend:
—— calculation results
The measurement results from the follow papers:
- ● Bearmana&Obasaju [2] at $Re=2 \cdot 10^4$
- × Otsuki et al. [3] at $Re=7 \cdot 10^4$
- ◆ Wong et al. [4] at $Re=5 \cdot 10^4$
- ■ Okajima et al. [5] at $Re=7 \cdot 10^4$
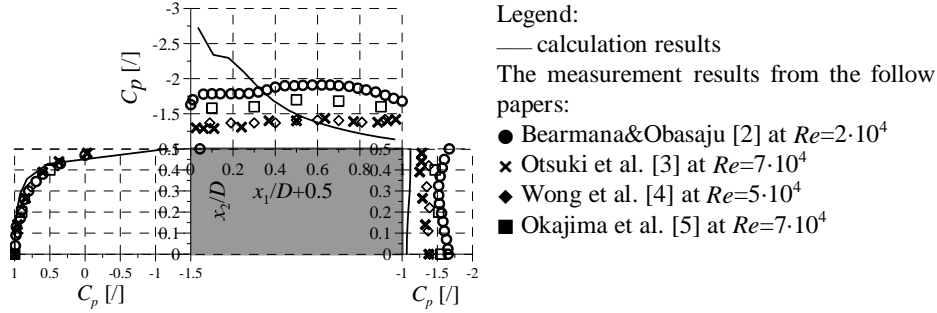
Fig. 2. The pressure distribution at walls of the free square.

The results obtained directly from FLUENT program:
◇ $dx_1=-0.3$m, $dx_2=-0.0$m; ○ $dx_1=-0.9$m, $dx_2=-0.06$m; □ $dx_1=-0.9$m, $dx_2=-0.3$m;
and
● research from [9];
+ calculation made with use of the Poisson2D program on the basis of velocity fields from the FLUENT program.
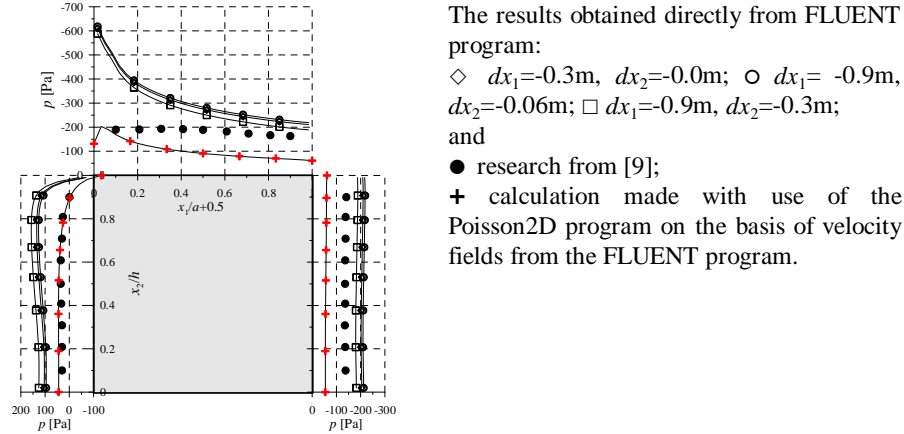
Fig. 3. The pressure distribution at walls of the square which is located at the ground.

153

The sensitivities of the properties to the parameters are described by fields of thirty derivatives for a 2D problem and thirty six for a 3D problem which may be set into the following matrix (in relation to one point of fields in a 2D problem):

$$
\mathbf{J} =
\begin{bmatrix}
\tilde{p}_{C_{\varepsilon 1}} & \tilde{p}_{C_{\varepsilon 2}} & \tilde{p}_{C_{\mu}} & \tilde{p}_{\sigma_k} & \tilde{p}_{\sigma_{\varepsilon}} \\
\tilde{u}_{1C_{\varepsilon 1}} & \tilde{u}_{1C_{\varepsilon 2}} & \tilde{u}_{1C_{\mu}} & \tilde{u}_{1\sigma_k} & \tilde{u}_{1\sigma_{\varepsilon}} \\
\tilde{u}_{2C_{\varepsilon 1}} & \tilde{u}_{2C_{\varepsilon 2}} & \tilde{u}_{2C_{\mu}} & \tilde{u}_{2\sigma_k} & \tilde{u}_{2\sigma_{\varepsilon}} \\
\tilde{k}_{C_{\varepsilon 1}} & \tilde{k}_{C_{\varepsilon 2}} & \tilde{k}_{C_{\mu}} & \tilde{k}_{\sigma_k} & \tilde{k}_{\sigma_{\varepsilon}} \\
\tilde{\varepsilon}_{C_{\varepsilon 1}} & \tilde{\varepsilon}_{C_{\varepsilon 2}} & \tilde{\varepsilon}_{C_{\mu}} & \tilde{\varepsilon}_{\sigma_k} & \tilde{\varepsilon}_{\sigma_{\varepsilon}} \\
\tilde{\mu}_{C_{\varepsilon 1}} & \tilde{\mu}_{C_{\varepsilon 2}} & \tilde{\mu}_{C_{\mu}} & \tilde{\mu}_{\sigma_k} & \tilde{\mu}_{\sigma_{\varepsilon}}
\end{bmatrix}
=
\begin{bmatrix}
\frac{\partial p}{\partial C_{\varepsilon 1}} & \frac{\partial p}{\partial C_{\varepsilon 2}} & \frac{\partial p}{\partial C_{\mu}} & \frac{\partial p}{\partial \sigma_k} & \frac{\partial p}{\partial \sigma_{\varepsilon}} \\
\frac{\partial u_1}{\partial C_{\varepsilon 1}} & \frac{\partial u_1}{\partial C_{\varepsilon 2}} & \frac{\partial u_1}{\partial C_{\mu}} & \frac{\partial u_1}{\partial \sigma_k} & \frac{\partial u_1}{\partial \sigma_{\varepsilon}} \\
\frac{\partial u_2}{\partial C_{\varepsilon 1}} & \frac{\partial u_2}{\partial C_{\varepsilon 2}} & \frac{\partial u_2}{\partial C_{\mu}} & \frac{\partial u_2}{\partial \sigma_k} & \frac{\partial u_2}{\partial \sigma_{\varepsilon}} \\
\frac{\partial k}{\partial C_{\varepsilon 1}} & \frac{\partial k}{\partial C_{\varepsilon 2}} & \frac{\partial k}{\partial C_{\mu}} & \frac{\partial k}{\partial \sigma_k} & \frac{\partial k}{\partial \sigma_{\varepsilon}} \\
\frac{\partial \varepsilon}{\partial C_{\varepsilon 1}} & \frac{\partial \varepsilon}{\partial C_{\varepsilon 2}} & \frac{\partial \varepsilon}{\partial C_{\mu}} & \frac{\partial \varepsilon}{\partial \sigma_k} & \frac{\partial \varepsilon}{\partial \sigma_{\varepsilon}} \\
\frac{\partial \mu_t}{\partial C_{\varepsilon 1}} & \frac{\partial \mu_t}{\partial C_{\varepsilon 2}} & \frac{\partial \mu_t}{\partial C_{\mu}} & \frac{\partial \mu_t}{\partial \sigma_k} & \frac{\partial \mu_t}{\partial \sigma_{\varepsilon}}
\end{bmatrix}
\tag{1}
$$

A particular set of coefficient fields corresponds to a particular set of parameters. The fields of the sensitivity coefficients may be determined using a finite difference approximation to the sensitivity which consists in calculating flows at the values next to the value of the parameter being analysed, and then determining the sensitivity coefficients with the following formula:

$$
\tilde{s}_m = \frac{\partial s}{\partial C_m} \approx \frac{w_2 - w_1}{\Delta C_m}
\tag{2}
$$

where: C_m – examined parameter, w_1, w_2 – results of calculations at $C_m - \Delta C_m / 2$ and $C_m + \Delta C_m / 2$, respectively. In the further analyses the ΔC_m increment equals to $\Delta C_{\varepsilon 1} = \Delta C_{\varepsilon 2} = \Delta \sigma_k = \Delta \sigma_{\varepsilon} = 0.04$, $\Delta C_{\mu} = 0.004$.

In order to estimate the sensitivities described by more complex graphs the average sensitivity coefficients for the cross-section of the calculation domain are used:

$$
\overline{\tilde{u}}_{1C_m} = \frac{1}{H} \sum_{i=1}^{n} \tilde{u}_{1C_m i} dx_{2i} ,
\tag{3}
$$

where: $\tilde{u}_{1C_m i}$ – sensitivity in the volume i; dx_{2i} – size of the volume i along the x_2 axis; n – number of volumes along the x_2 axis.

The description and examples of applications of the sensitivity analysis of flow properties to model parameters can be found in papers: [11], [12], [13] and [14]. Here, it should be noted that the dependence between the errors of the solution for flow problems and the sensitivity coefficients exists. It probably comes from the fact that the regions of

154

significant sensitivities correspond to places with high gradients of flow properties. The model parameters are multipliers of the terms of equations which usually contain derivatives of flow properties with regards coordinates. The high values of the terms cause that the parameters from these terms significantly influence on the results and the parameters from the small terms have smaller influence on them. Hence the high sensitivity can indicate significant errors of calculations which can be caused both by the wrong assumption of model parameters and numerical errors which always exist for high gradients of approximated properties. Therefore the results of sensitivity analysis can be applied by the user of the CFD program to find the places where significant errors can be expected.

3. The calculation results

3.1. The influence of input flow velocities

The influence of an input velocity on the pressure distribution on model walls and the values of velocities behind this model are known. The increase of the pressure on walls is directly proportional to the square of the input velocity and the values of flow velocities are directly proportional to the input velocity. The same dependencies are seen in calculations, but the sensitivity coefficients for the pressure and velocity are also directly proportional to the input velocity (comp. fig. 4). Therefore we can expect the increase of errors for the bigger input velocities.

Moreover in opinion of Launder and Spalding [1] the dependence between the Schmidt number σ_k exists, which is the σ_k parameter should be smaller for smaller values of flow velocities. It is confirmed by graphs shown in fig. 4. As it is seen in fig. 2 and fig. 3 the calculated negative pressure at the side wall and the roof, respectively, is too high. In order to make correction of the value of the pressure, the σ_k parameter should be decreased and this change should be bigger for higher velocities.

a)

b)
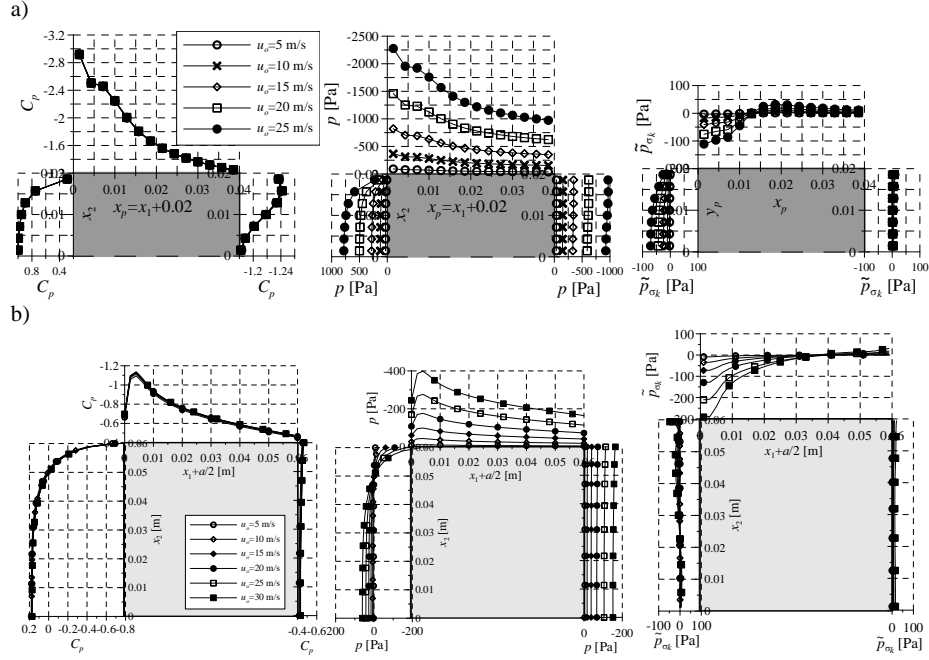
Fig. 4. The distributions of the pressure and its sensitivity to σ_k for the different input velocities:
a) for free square cylinder; b) for square cylinder at the ground.

3.2. The influence of input turbulence intensities

Noda et. al. [9] performed the research of the effect of the shape of a velocity profile on a pressure distribution at walls of the square at a ground. For example, the results presented in fig. 3 were obtained for the velocity described by formula:

$$u_1(x_2) = 19.7 \text{m/s} \left(\frac{x_2}{0.06 \text{m}} \right)^{0.2} \quad dla \quad x_2 < 0.2$$

$$u_1(x_2) = 25.0 \text{m/s} \quad dla \quad x_2 \geq 0.2.$$

(4)

It comes from the paper [9] that for the bigger input turbulence intensity of the flow and the power from eq. 4 the increase of a positive pressure on an upstream wall and the increase of a negative pressure on side and downstream walls are seen. It seems that this statement is not always true. The results which are presented in paper [10] show that the negative pressure at the roof of the model decrease for the higher turbulence intensity. For both cases, the different turbulence intensities correspond to different shapes of the velocity profiles and, therefore, it is difficult to find dependence between the pressure and the wind turbulence. It is easier for the flow around the free square cylinder where the

156

relationships between the turbulence intensity and other flow properties do not exist. The measurement results from paper [8] show that the increase of the input turbulence intensity causes the decrease of the negative pressure at the side walls. Whereas the results from paper [15] show that the increase of the turbulence intensity induces the decrease of the negative pressure at downstream walls. Unfortunately, for numerical calculations there is the increase of the negative pressure both at the side and downstream walls for higher the input turbulence intensity, which is not correct.
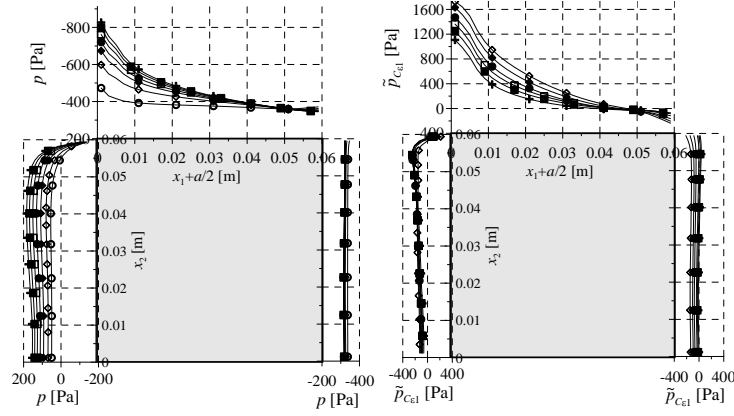
Fig. 5. The influence of a turbulence intensity on a pressure and a pressure sensitivity to $C_{\varepsilon 1}$ for the cylinder square at the ground: ○ I_u=0.0%; ◇ 2.0%; ◆ 4.0%; ● 6.0%; □ 8.0%; ■ 10.0%; + 12.0%.

The exemplary distributions of the pressure sensitivities are shown in fig. 5 and fig.6. The pressure sensitivities to the model parameters directly increase with the increase of the input turbulence, but it is particularly seen at the roof of the model for the square at the ground and at the downstream wall of the free square. The velocity sensitivity nearly does not depend on the input turbulence intensity, which is shown in fig. 7.
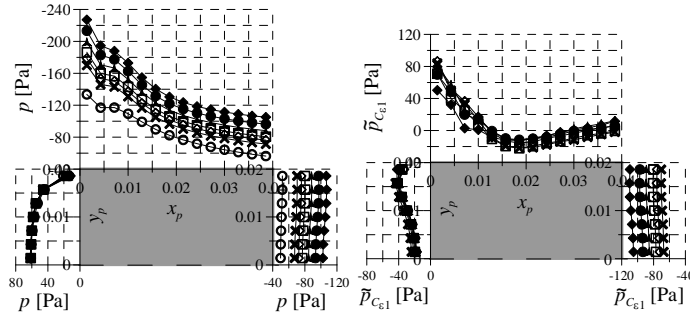
Fig. 6. The influence of a turbulence intensity on a pressure and a pressure sensitivity to $C_{\varepsilon 1}$ for the free square: ○ I_u=0.0%; × 1.0%; ◇ 2.0%; □ 3.0%; ⋏5.0%; ● 7.0%; ◆ 10.0%.

157
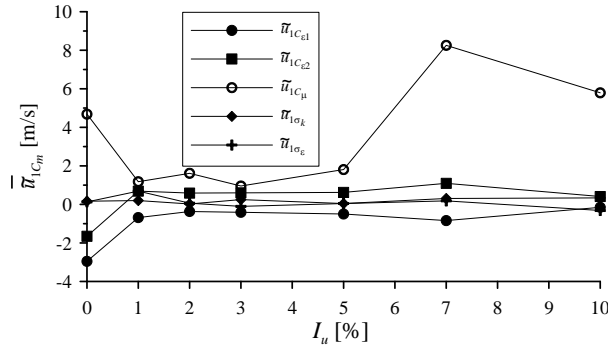
Fig. 7. The influence of the turbulence intensity on the velocity sensitivity in the aerodynamic wake of the cylinder square located on the ground.

3.3. The influence of Reynolds number

The fact that the increase of the Reynolds number has the negative influence on the quality of the solution for the flow around body without edges is known. For the bluff body the fields of pressure and velocity are similar for $Re>100$, while the sensitivity coefficients (comp. fig.8) are quite different. It is caused by the dependence between the Reynolds number and the sizes of cells at walls. The higher Reynolds number is the smaller sizes of cells should be used. The solution of the problem with the high Reynolds number is sometimes impossible because it is needed to solve too big numerical exercise. Simultaneously the k-ε model is the turbulence model for the high Reynolds numbers and at the low Reynolds number the mesh with the proper value y^* is too rare in order to correctly describe flow properties.
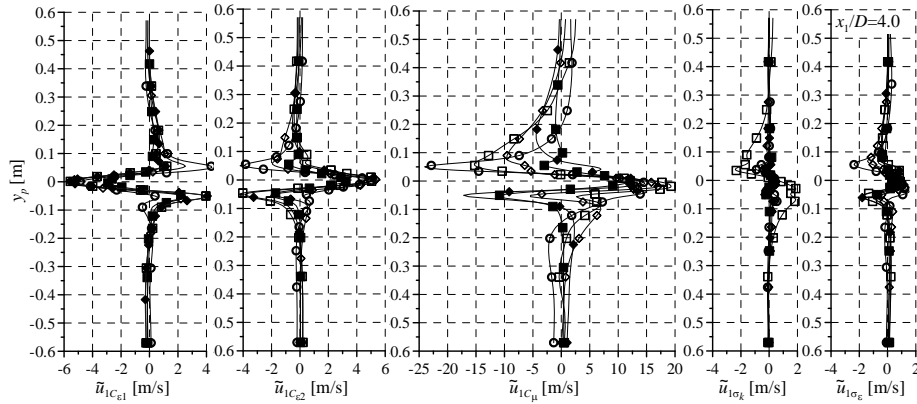
Fig. 8. The graphs of velocity sensitivity coefficients at $x_p/D=4.5$ for: ■ - $Re=2.7\cdot10^2$, ○ - $Re=2.7\cdot10^3$, □ - $Re=2.7\cdot10^4$, ◆ - $Re=2.7\cdot10^5$, ◇ - $Re=2.7\cdot10^6$.

158

The sensitivity analysis for different Reynolds numbers, but for the same mesh, shows that the sensitivity coefficients are the highest for this Reynolds number which is the most suitable one for the assumed mesh. For too rare meshes the sensitivity is smaller because bad meshes cause the artificial decrease of gradients of flow properties and too dense meshes with regard to the value y^* can cause that the boundary layer model is applied in too small distance from walls. It also causes the decrease of the gradients at walls.

4. Conclusions

The turbulence k-ε model is not a perfect model and it is obvious that the solutions are burdened with errors caused by simplification, which are used in this model. The presented example of the calculation of the flow around square cylinders shows that calculations results strongly depend on parameters of the k-ε model. Results of the sensitivity analysis can be applied to control numerical solutions by pointing to regions with high gradients of flow properties, where calculations results may be invalid.

Finally, it can be noted that:
- Calculation results are not correct at downstream walls and behind a square, it means: the negative pressure at walls and the velocity in aerodynamic wake are too small.
- At the increase of the input velocity the calculated velocity and pressure grow directly proportionally to the velocity and the square of velocity value, respectively. Unfortunately, the sensitivity coefficients to the model parameter also rise at the increase of the input velocity what means the increase of numerical errors.
- At the increase of the input turbulence intensity the calculated negative pressure on the side and downstream walls grows. It does not agree with measurements (comp. [10]).
- The increase of Reynolds number negatively influences numerical results.
- The sensitivity coefficients can be useful at the creation of the FVM mesh, because they are the highest for this mesh which is the most suitable for the analysed Reynolds number.

References
[1] Launder B.E., Spalding D.B., *The Numerical Computation of Turbulent Flows*, Computer Methods in Applied Mechanics and Engineering, 3, 1974, pp.269-289.
[2] Bearman P.W., Obasaju E.D., *An Experimental Study of Pressure Fluctuations on Fixed and Oscillating Square-Section Cylinders*, J. of Fluid Mechanics, 119, 1982, pp.297-321.
[3] Otsuki Y., Fuji K., Washizu K., Ohya A., *Wind Tunnel Experiments on Aerodynamic Forces and Pressure Distributions of Rectangular Cylinders in a Uniform Flow*, The Proc. of the Fifth Symp. on Wind Effects on Structures, 1978, pp.169-176.

[4] Wong P.T.Y., Ko N.W.M., Chiu A.Y.W., *Flow Characteristics around Two Parallel Adjacent Square Cylinders of Different Sizes*, J. of Wind Eng. and Ind. Aerodynamics, 54/55, 1995, pp.263-275.

[5] Okajima A., Sugitani K., Mizota T., *Fluid Characteristics of Two Rectangular Cylinders Arranged Side-by-Side*, Bull. Res. Inst. App. Mech. Kyushu University, 60, 1984, pp.59-87.

[6] Luo S.C., Li L.L., Shah D.A., *Aerodynamic Stability of the downstream of Two Tandem Square-Section Cylinders*, Journal of Wind Engineering and Industrial Aerodynamics, 79, 1999, pp.79-103.

[7] Nakagawa S., Nitta K., Senda M., *An Experimental Study on Unsteady Turbulent Near Wake of Rectangular Cylinder in Channel Flow*, Experiments in Fluids, 27, 1999, pp.284-294.

[8] Saarhoff P., Melbourne W.H., *Effects of freestream turbulence on streamwise pressure measured on a square-section cylinder*, J. of Wind Eng. and Ind. Aerodynamics, 79, 1999, pp.61-78.

[9] Noda M., Utsunomiya H., Nagao F., *Basic Study on Blockage Effects in Turbulent Boundary Layer Flows*, J. of Wind Eng. and Ind. Aerod., 54/55, 1995, pp.645-656.

[10] Sitheeq M.M., Iyengar A.K.S., Farell C., *Effect of turbulence and its scales on the pressure field on the surface of a free-dimensional square prism*, J. of Wind Eng. and Ind. Aerodynamics, 69-71, 1997, pp.461-471.

[11] Błazik-Borowa E., *Analiza wrażliwości rozwiązań CFD z użyciem modelu k-ε na "stałe" modelu turbulencji*, Systems, Journal of Transdisciplinary Systems Science, Vol.11. No 1 (Appendix), 2006, pp.145-152.

[12] Błazik-Borowa E., *The application of the sensitivity analysis of flow properties to parameters of the k-ε method*, Proc. of CMM-2007, Łódź-Spała, 2007, pp.91-92.

[13] Błazik-Borowa E., *The sensitivity analysis of the flow around a square cylinder to parameters of the k-ε method*, Proc. of 12th ICWE, Australia, 2007, pp.1919-1926.

[14] Colin E., Etienne S., Pelletier D. and Borggaard J., *Application of a sensitivity equation method to turbulent flows with heat transfer*, Int. Journal of Thermal Science, 44, 2005, pp.1024-1038.

[15] Tamura T., Miyagi T., *The effect of turbulence on aerodynamic forces on a square cylinder with various corner shapes*, J. of Wind Engineering and Industrial Aerodynamics, 83, 1999, pp.135-145.

Acknowledgments

CALCULATING AERODYNAMIC COEFFICIENTS FOR SHAFTS OF GUYED MASTS

Ewa Błazik-Borowa[*], Jarosław Bęc[*], Piotr Wielgos[*]

[*] Department of Structural Mechanics, Faculty of Civil and Sanitary Engineering,
Lublin University of Technology, Nadbystrzycka 40, 20-618 Lublin, Poland.

1. Introduction

The main load in case of guyed masts is wind action. Obtaining the values of forces caused by this action requires calculation of aerodynamic coefficients. There are some different approaches allowing us to achieve such results with use of:
- formulae from standards and codes;
- calculations based on numerical methods of fluid mechanics;
- wind tunnel simulations.

Here in this paper first two methods have been used. Different types of mast shafts have been taken into account. The results have been compared and good agreement has been achieved.

2. Wind action on slender structures

Wind action components for a slender structure or structural element may be calculated with the following formulae:
- Normal wind action (aerodynamic drag):

$$W_n = \frac{1}{2} \rho \overline{v}_n^2 C_n D L \; ; \tag{1}$$

- Binormal wind action (aerodynamic lift):

$$W_b = \frac{1}{2} \rho \overline{v}_n^2 C_b D L \; ; \tag{2}$$

- Torsional wind action (aerodynamic moment):

$$W_{ms} = \frac{1}{2} \rho \overline{v}_n^2 C_m D^2 L \; . \tag{3}$$
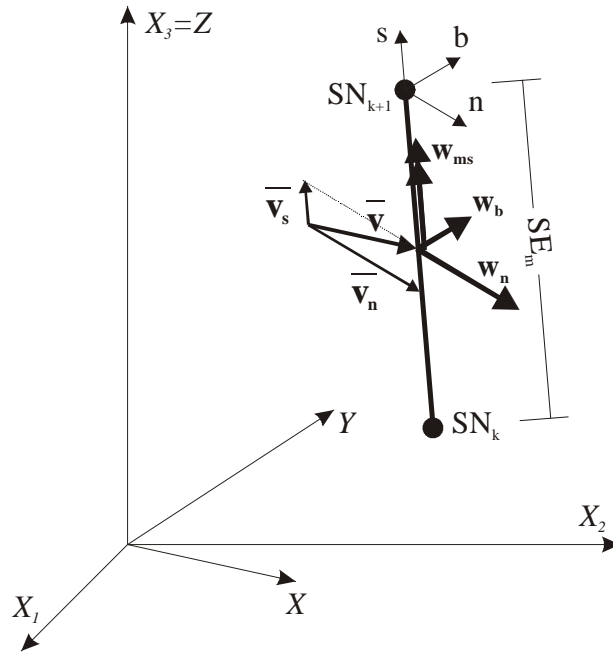
Fig. 1. Wind action components on structure segment or structural element.

3. Standards and codes

Two codes have been used to calculate aerodynamic coefficients for shafts of masts:
- British code ESDU considering lattice structures;
- European standard for antenna towers and guyed masts – Eurocode 3.

3.1. ESDU

According to ESDU forces acting on shaft segment may be calculated with the following formulae:

$$W_{Xi} = \frac{1}{2} \rho v_i^2 A_{si} C_{Xi},$$ (4)

$$W_{Yi} = \frac{1}{2} \rho v_i^2 A_{si} C_{Yi},$$ (5)

$$W_{mZi} = \frac{1}{2} \rho v_i^2 \left(A_s + A_{sa} \right) C_m B \cdot$$ (6)

162
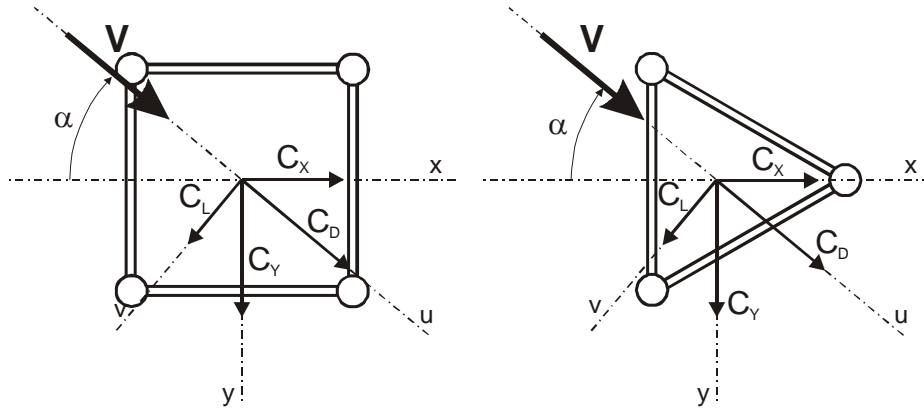
Fig. 2. Co-ordinates systems – local based on wind direction (uv) and global (xy).

Aerodynamic coefficients may be transformed to the global coordinate system from coefficients obtained in the coordinate system based on mean wind direction (drag and lift coefficients) with use of the following formulae:

$$C_X = C_D \cos\alpha - C_L \sin\alpha \,, \tag{7}$$

$$C_Y = C_D \sin\alpha + C_L \cos\alpha \cdot \tag{8}$$

Shafts composed of flat sided elements

Aerodynamic drag coefficient for mast shaft composed of flat sided elements may be calculated with the following formula:

$$C_D = C_{D_0} \cdot f_\alpha \,, \tag{9}$$

where C_{D_0} is the drag coefficient at the wind incidence angle $\alpha = 0^\circ$, and f_α is the wind incidence coefficient.

These coefficients may be described with formulae:

- For triangular cross-section shafts:

$$C_{D_0} = 3.3 - 4.8\phi + 5.05\phi^2 - 3.00\phi^3 + 1.3\phi^4 \,, \tag{10}$$

$$\begin{aligned} f_\alpha &= 0.4 + 0.6\cos^2\alpha \quad \text{for } 0 \le \alpha \le 30^\circ \\ f_\alpha &= 0.85 \qquad\qquad\quad \text{for } 60^\circ \le \alpha \le 90^\circ \end{aligned} \tag{11}$$

163

and the aerodynamic lift coefficient may be calculated with the expression:

$$C_L = \left(0.65 + 1.2e^{-2.6 \cdot 10^5 \phi^6}\right)\sin 3\alpha \ . \tag{12}$$

- For rectangular cross-section shafts:

$$C_{D_0} = 4.0 - 9.85\phi + 20.7\phi^2 - 24.7\phi^3 + 11.9\phi^4 \ , \tag{13}$$

$$f_\alpha = 1 + 0.32 k_\phi \sin^2 2\alpha$$
$$\text{where} \quad k_\phi = (3.66 - 4.44\phi) - (3.6 - 6\phi)\sin 2\alpha \tag{14}$$

and the aerodynamic lift coefficient may be calculated with the expression:

$$C_L = c\left(0.7\sin 4\alpha + 0.3\sin 3\alpha\right)$$
$$\text{where} \quad c = 0.1 + 1.2e^{-5.9 \cdot 10^4 \phi^6} \tag{15}$$

Shafts composed of circular cross-section elements
Aerodynamic drag coefficient for mast shaft may be calculated with the following formula:

$$C_D = C_{D_1} \cdot f_s \cdot f_\alpha \tag{16}$$

where C_{D_0} is the drag coefficient at the angle $\alpha = 0°$, and f_α is the wind incidence coefficient and f_s is shading coefficient.

These coefficients may be described with formulae:
- For triangular cross-section shafts:

$$C_{D_0} = 1.96 - 1.18\phi - 2.91\phi^2 + 7.09\phi^3 - 3.00\phi^4 \ , \tag{17}$$

$$f_\alpha = 0.85 + 0.15\left|\cos 3\alpha\right| \ . \tag{18}$$

- For rectangular cross-section shafts:

$$C_{D_0} = 2.40 - 2.75\phi - 0.89\phi^2 + 6.24\phi^3 - 3.04\phi^4 \ , \tag{19}$$

$$f_\alpha = 1 + 0.35 k_\phi \sin^2 2\alpha$$
$$\text{where} \quad k_\phi = (3.79 - 4.65\phi) - (3.6 - 6\phi)\sin 2\alpha \tag{20}$$

164

Shaft composed of both flat-sided and circular cross-section elements
The aerodynamic coefficients may be calculated as weighted average of coefficients obtained for shafts composed of elements of one type:

$$C_{D_0(mix)} = C_{D_0(flat)} \frac{A_{s(flat)}}{A_{s(total)}} + C_{D_0(circ)} \frac{A_{s(circ)}}{A_{s(total)}} ,$$ (21)

$$C_{L(mix)} = C_{L(flat)} \frac{A_{s(flat)}}{A_{s(total)}} .$$ (22)

3.2. Eurocode 3

Wind load in the mean wind direction may be calculated with use of the following formula coming from Eurocode 3:

$$W_n = \frac{\rho}{2} v^2(z) \sum R_W .$$ (23)

The total wind drag may be calculated with the formula:

$$\sum R_W = R_{WS} + R_{WA} ,$$ (24)

where R_{WS} is the wind drag of the bare structure section and R_{WS} is the wind drag of the ancillaries.

Aerodynamic drag for triangular or square shafts may be calculated with the following formula:

$$R_{WS} = K_\theta C_N A_S ,$$ (25)

where K_θ is wind incident factor, C_N is the overall normal drag coefficient and A_S is the total area projected normal to the face of structural components.

The coefficient K_θ may be calculated with the following formulae:
- In case of rectangular cross-sections:

$$K_\theta = 1.0 + K_1 K_2 \sin^2 2\theta ,$$ (26)

where:

$$K_1 = \frac{0,55 A_f}{A_F} + \frac{0,8 \left(A_c + A_{c,sup} \right)}{A_F} ,$$ (27)

165

$$K_2 = 0,2 \qquad \text{gdy} \quad 0 \le \phi \le 0,2 \quad \text{lub} \quad 0,8 \le \phi \le 1,0$$
$$= \phi \qquad \text{gdy} \quad 0,2 < \phi < 0,5 \qquad\qquad . \tag{28}$$
$$= 1 - \phi \qquad \text{gdy} \quad 0,5 < \phi < 0,8$$

- In case of triangular cross-sections:

$$K_\theta = \frac{A_c + A_{c,\text{sup}}}{A_F} + \frac{A_f}{A_F}\left(1 - 0,1\sin^2 1,5\theta\right). \tag{29}$$

The overall normal drag coefficient may be calculated with the following formula:

$$C_N = C_{Nf}\frac{A_f}{A_F} + C_{Nc}\frac{A_c}{A_F} + C_{Nc,\text{sup}}\frac{A_{c,\text{sup}}}{A_F}, \tag{30}$$

where the weights may be calculated with following formule:
- for flat sided elements:

$$C_{Nf} = 1,76C_1\left(1 - C_2\phi + \phi^2\right), \tag{31}$$

- or circular cross-section elements in critical range:

$$C_{Nc} = C_1\left(1 - C_2\phi\right) + \left(C_1 + 0,875\right)\phi^2, \tag{32}$$

- circular cross-section elements in supercritical range:

$$C_{Nc,\text{sup}} = 1,9 - \sqrt{\left(1 - \phi\right)\left(2.8 - 1.14C_1 + \phi\right)}. \tag{33}$$

The coefficients C_1 and C_2 may be taken with values:
- For rectangular cross-sections: $C_1 = 2.25$ and $C_2 = 2.25$,

- For triangular cross-sections: $C_1 = 1.9$ and $C_2 = 1.4$.

4. Numerical calculations

Calculations based on k-ε method in the laminar range have been provided with use of the FLUENT fluid dynamics computer system. The following properties of flow have been used in calculations:
- Input wind velocity v = 5 m/s;
- Air density ρ= 1.23 kg/m3.

166

Calculations have been made for three guyed masts. The following mast sections have been subjected to 3D analysis:

- Test mast of 100m height and triangular shaft cross-section;
- Mast of 342m height in Piaski:
  - o Triangular shaft cross-section in lower segments;
  - o Rectangular shaft cross-section in upper segments;
- Mast of 130m height in Giedlarowa:
  - o Rectangular shaft cross-section in lower segments;
  - o Top antenna segments.

Six shaft segments have been modeled for each mast section. Wind forces acting on two sections in the middle have been used in the analysis. Top antenna segments of Giedlarowa mast have been assumed as closed ones and planar model has been used.

The exemplary meshes have been presented in figures.
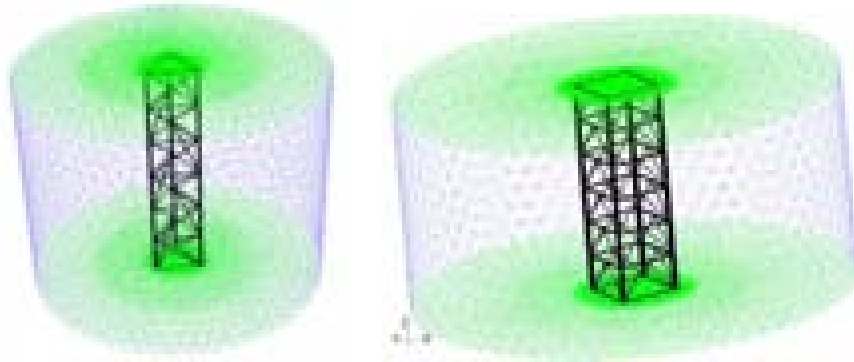
Fig. 3. Exemplary 3-D meshes.
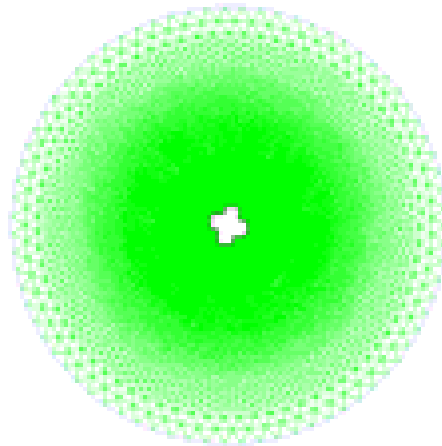
Fig. 4. Mesh used in planar analysis of top antenna segments of Giedlarowa mast.

167

Each model has been analyzed with various values of wind incidence angle in order to find the aerodynamic coefficient functions versus the angle. This made possible later calculation of derivatives of aerodynamic coefficients, which may be used in aerodynamic analysis of guyed masts based on quasi-steady theory.

In each case of calculations the aerodynamic coefficients have been calculated with use of the following formulae:

$$C_{X_1} = \frac{W_{X_1}}{\frac{1}{2}\rho v^2 DL}, \tag{34}$$

$$C_{X_2} = \frac{W_{X_2}}{\frac{1}{2}\rho v^2 DL}, \tag{35}$$

$$C_{mX_3} = \frac{W_{mX_3}}{\frac{1}{2}\rho v^2 D^2 L}. \tag{36}$$
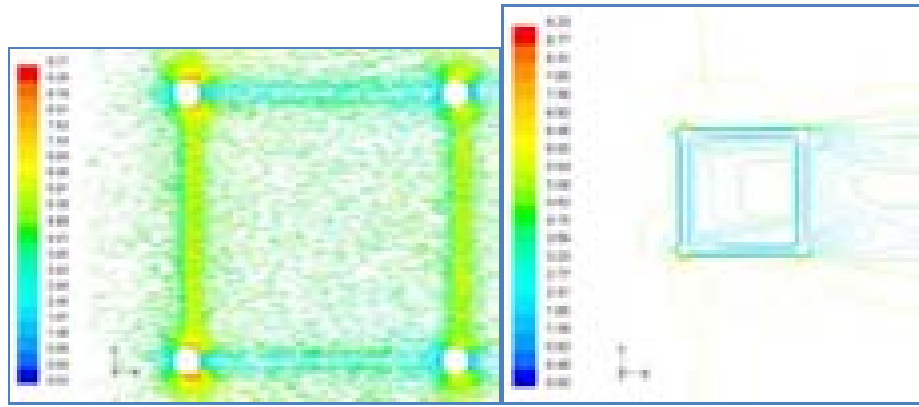
Fig. 5. Exemplary wind velocity field – rectangular cross-section.
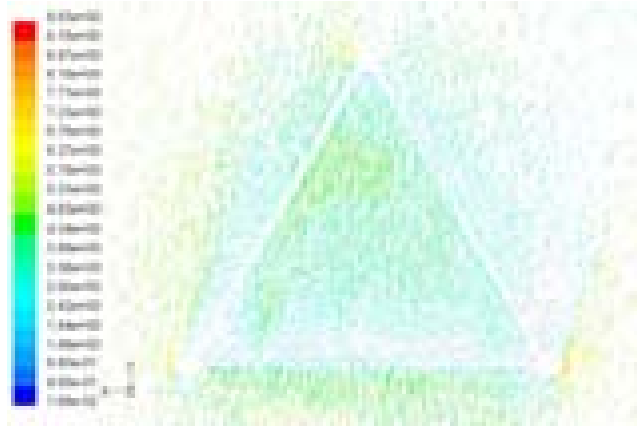
Fig. 6. Exemplary wind velocity field – triangular shaft cross-section.
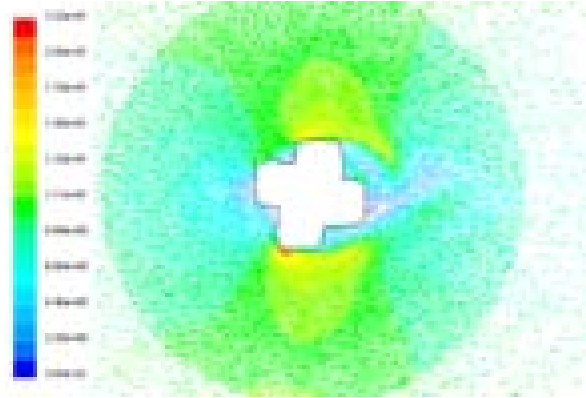
Fig. 7. Exemplary wind velocity field – top antenna segments of Giedlarowa mast.

The obtained coefficient values have been transformed to the coordinate system based on mean wind direction as coefficients of aerodynamic drag, lift and moment with use of the following formulae:

$$C_n(\alpha) = C_{X_1}(\alpha).\cos(\alpha) + C_{X_2}(\alpha)\cdot\sin(\alpha), \tag{37}$$

$$C_b(\alpha) = -C_{X_1}(\alpha)\cdot\sin(\alpha) + C_{X_2}(\alpha).\cos(\alpha), \tag{38}$$

$$C_{ms} = C_{mX_3}. \tag{39}$$

169

5. Comparison of the results and conclusions

The results obtained with use of both standards and numerical calculations have been compared on the graphs. The exemplary results for the Piaski triangular and rectangular cross-sections with respect to global and wind-based coordinate systems have been presented in figures.
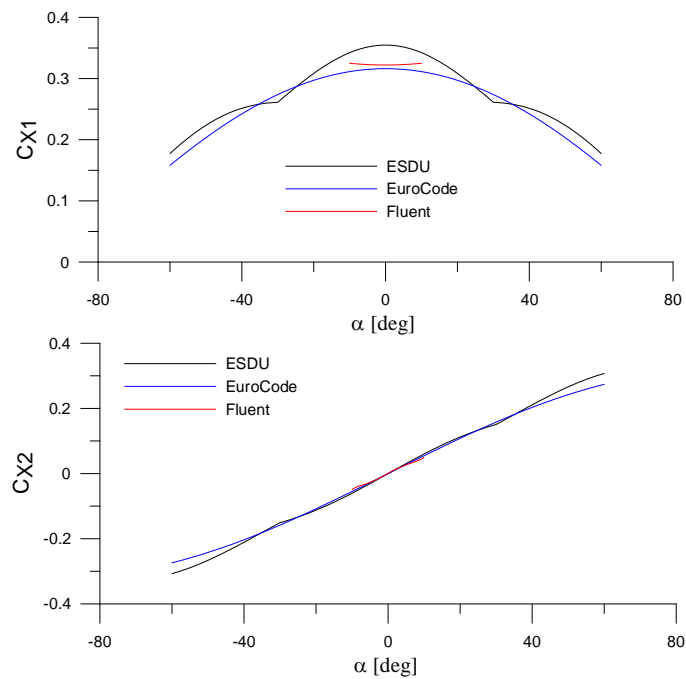
Fig. 8. Exemplary coefficients comparison for triangular cross-section segments of Piaski mast with respect to global coordinate system.

170
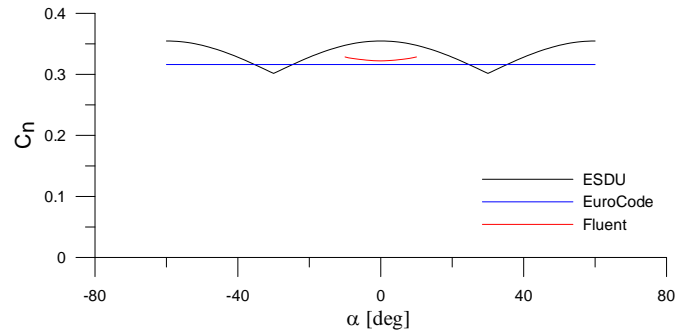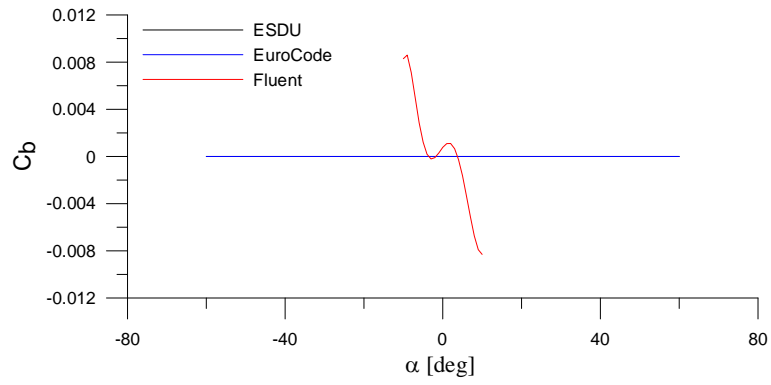
Fig. 9. Exemplary coefficients comparison for triangular cross-section segments of Piaski mast with respect to wind-based coordinate system.
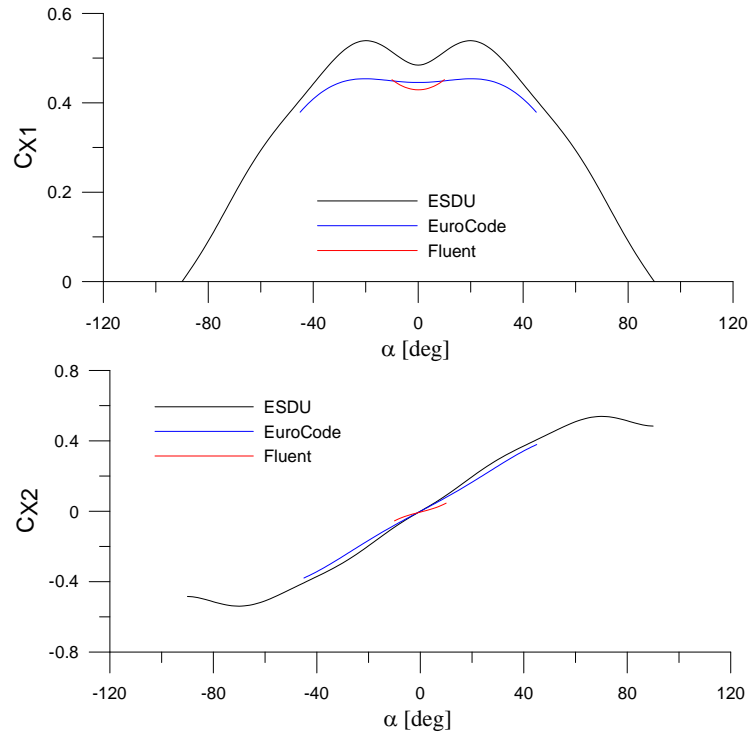
Fig. 10. Exemplary coefficients comparison for rectangular cross-section segments of Piaski mast with respect to global coordinate system.

171
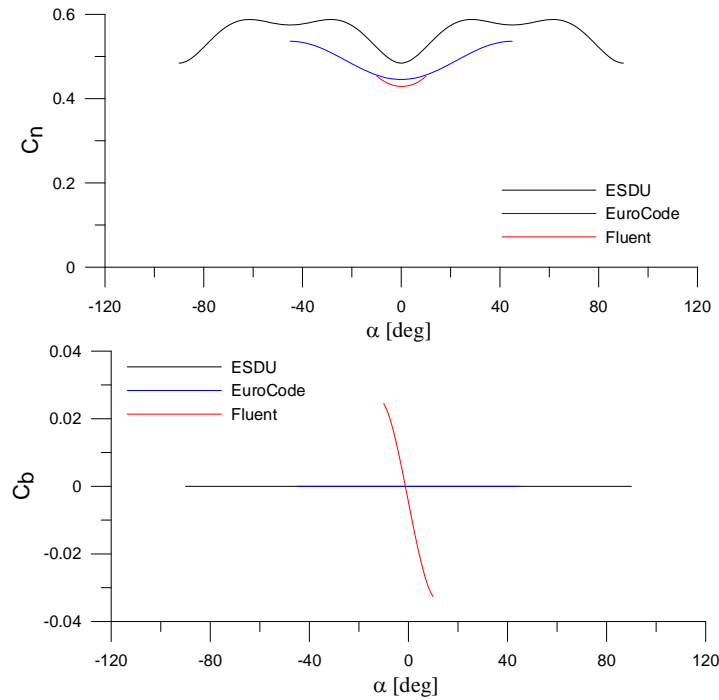
Fig. 11. Exemplary coefficients comparison for rectangular cross-section segments of Piaski mast with respect to wind-based coordinate system.

Values of aerodynamic coefficients calculated with use of standard formulae for typical truss shafts are in good agreement with the ones obtained with numerical simulation in FLUENT. For non-typical shafts numerical simulation is a great tool for obtaining aerodynamic coefficient values. Further tests in wind tunnel are planned to be conducted.

References

[1] EIA/TIA-222F, *Structural Standards for Steel Antenna Towers and Antenna Supporting Structures*, Electronic Industries Association, 2001.
[2] ENV 1991-2-7, *Eurocode 1: Basis of design and actions on structures – Part 2-4: Actions on structures – Wind actions.*
[3] ENV 1993-3-1, *Eurocode 3. Design of steel structures. Towers and masts, CEN 1997*
[4] *ESDU 80025 Mean forces, pressures and flow field velocities for circular cylindrical structures: single cylinder with two-dimensional flow*, ESDU International LTD 1986.
[5] ESDU 81028, *Lattice structures. Part 2: Mean fluid forces on tower-like space frames*, November 1981.
[6] ESDU 85020, *Characteristics of atmospheric turbulence near the ground. Part II: single point data for strong winds (neutral atmosphere)*, October 1985.

172

APPLICATION OF LOW-COST COMPUTER CLUSTERS TO OVERCOME THE N-BODY PROBLEM IN DISCRETE VORTEX METHOD

Tomasz Nowicki[*], Jerzy Podgórski[*], Stanisław Grzegórski[**]

[*] Department of Structural Mechanics, Faculty of Civil and Sanitary Engineering,
Lublin University of Technology, Nadbystrzycka 40, 20-618 Lublin, Poland.
[**]Institute of Computer Science, Faculty of Electrical Engineering and Computer Science,
Lublin University of Technology, Nadbystrzycka 38a, 20-618 Lublin, Poland.

1. Introduction

Discrete Vortex Method (DVM) is an alternative to mesh based methods used for solving Navier-Stokes equation. If Finite Differentiate Method, Finite Element Method and Finite Volume Method are based on an arbitrary chosen mesh, the DVM does not make use of a mesh. The lack of a mesh makes the method very attractive for computer simulation of turbulent flows because the vortex elements are free to propagate in a computational domain. The freedom of propagation enables the vortexes to shape the phenomenon of turbulence during direct simulation process.

The attractiveness of the method is balanced with its computational cost. For n vortex elements mutual interactions between them entails the need to perform n^2 calculation of velocities for one simulation step. For a typical engineering problem there is a need to use about 50 000 elements and perform a few dozen thousands simulation steps, so the total calculation time would be to long to be accepted. Presented paper focuses on methods of reducing the time with making use of a low-cost computer cluster and presents obtained results.

2. Applications of Discrete Vortex Methods

DVM has proved to be a powerful tool in wind engineering. It has been successfully used in civil engineering for about 20 years. Results obtained from computer simulations tallies with experimental ones. Its applications ranges form simulation of flows over whole buildings (fig.1a) to simulation of aeroelastic phenomenon of bridge decks (fig.1b).

173
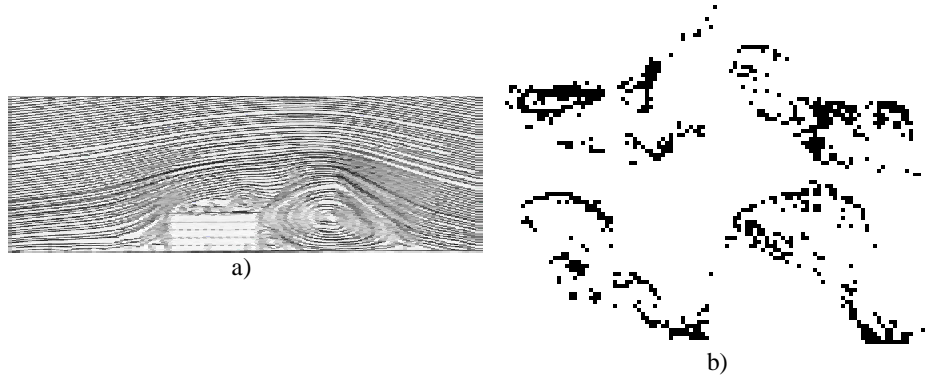
Fig. 1. a) Streamlines of the flow over the Texas Tech building [2]; b) Simulated flow around Tacoma Narrows Bridge [3] (4 snapshots of the deck).

3. Basic equations

DVM is based on discrete vortex elements. For the 2D case the vortex element is described with its position and strength. The strength Γ equals the circulation of the vorticity field (eq.1) around a closed curve L, surrounding a surface S with unit normal n (eq. 2, fig. 2a).

$$\omega = \nabla \times \mathbf{V} , \tag{1}$$

$$\Gamma = \int_L \mathbf{V} \cdot \mathbf{dr} = \int_S \omega \cdot \mathbf{n} dS , \tag{2}$$

where V-velocity field, ω-vorticity field; dr – an element of the curve L.

If we take the Navier-Stokes equation for incompressible fluids (3) into consideration:

$$\frac{\partial \mathbf{V}}{\partial t} + (\mathbf{V} \cdot \nabla)\mathbf{V} = -\nabla p + \frac{1}{\mathrm{Re}} \nabla^2 \mathbf{V} . \tag{3}$$

Then after decomposition and calculation of rotation of the vector V we obtain the vorticity transport equation:

$$\frac{\partial \omega}{\partial t} + (\mathbf{V} \cdot \nabla)\omega = \frac{1}{\mathrm{Re}} \nabla^2 \omega , \tag{4}$$

where: Re – Reynolds number.

The solution of the equation (4) consist of two parts: advection (5) and diffusion (6). The advection part:

174

$$\frac{\partial \omega}{\partial t} + \left(\frac{\partial \omega}{\partial x} V_x + \frac{\partial \omega}{\partial y} V_y \right) = \frac{D\omega}{Dt} = 0 \tag{5}$$

and the diffusion part:

$$\frac{\partial \omega}{\partial t} = \frac{1}{\text{Re}} \left(\frac{\partial^2 \omega}{\partial x^2} + \frac{\partial^2 \omega}{\partial y^2} \right). \tag{6}$$

The equation (5) means dwindling of the material derivative of the vorticity field and is usually solved using the incremental method (the Euler method) in Lagrangian coordinates for single vortices. Using a first-order forward difference scheme we obtain a position of a middle the i-th vortex:

$$\begin{aligned} x_{adv}^{k+1} &= x_i^k + V_x(x_i^k, y_i^k) \cdot \Delta t \\ y_{adv}^{k+1} &= y_i^k + V_y(x_i^k, y_i^k) \cdot \Delta t \end{aligned}, \tag{7}$$

where: Δt is a time step increment and upper indexes: k; $k+1$ mean the number of a time step.

In polar coordinates for the case when the middle of the i-th vortex is in the origin of the coordinates system the solution of the diffusion equation (6) can be presented in the following form [1]:

$$\omega(t) = \sum_{i=1}^{n} \omega_{0i}(r_{0i}, t)$$

$$\omega_i(r_0, t) = \frac{\Gamma_1}{4\pi / \text{Re}} \exp(\frac{-r_{0i}^2}{4t / \text{Re}}) \tag{8}$$

The vorticity field consisting of n discrete vortices (8) after the time step Δt can be approximated by a random vortices field with Gaussian distribution with its mean value equal zero and its variance equal $2\Delta t/Re$ (Lewis[1], Turkiyyah [2]). The polar coordinates of i-vortex (r_{0i}, θ_{0i}) can be taken as:

$$r_{0i} = \sqrt{\frac{4t}{\text{Re}} \ln \left| \frac{1}{P_i} \right|} , \quad \vartheta_{0i} = 2\pi Q_i , \tag{9}$$

where: P_i and Q_i are random numbers from the interval of [0;1].

4. Kinematics of vortexes and the n-body problem

After the discretization a set the elements describes the flow field in every point of a domain of interest. A vortex element induces velocity at a arbitrary point according to the Biot-Savart law (eq. 10, fig. 2b).

$$V(\mathbf{x}) = \sum_{i=1}^{n} \Gamma_i \cdot \mathbf{K}(\mathbf{x} - \mathbf{x}_i) ,$$ (10)

$$\mathbf{x} = (x, y)$$

where: n-number of vortex elements, $\mathbf{K}$- Biot-Savart's kernel.

The simplest Biot-Savart's kernel is a kernel of order 2:

$$K_\varepsilon = \begin{bmatrix} \dfrac{(-y,x)}{2\pi\varepsilon} & r \le \varepsilon \\ \dfrac{(-y,x)}{2\pi r^2} & r > \varepsilon \end{bmatrix} .$$ (11)

Therefore a velocity can be calculated for every vortex element. Knowing the velocities let as for chosen step time Δt find next positions of the vortexes. Simulation of a flow consist in repeating of the process.

The simulation process is simple but requires recalculation of velocities at every simulation step. For n vortex element there is need for performing n^2 calculation at every step. This is so called "n-body problem". It leads to prohibitively long computational times for the direct algorithm. For a typical engineering problem there is a need to use about 50 000 elements and perform a few dozen thousands simulation steps. This would take months or even years to run such a simulation on one PC computer. So there is need to develop faster algorithms to overcome this problem.

a)   b)
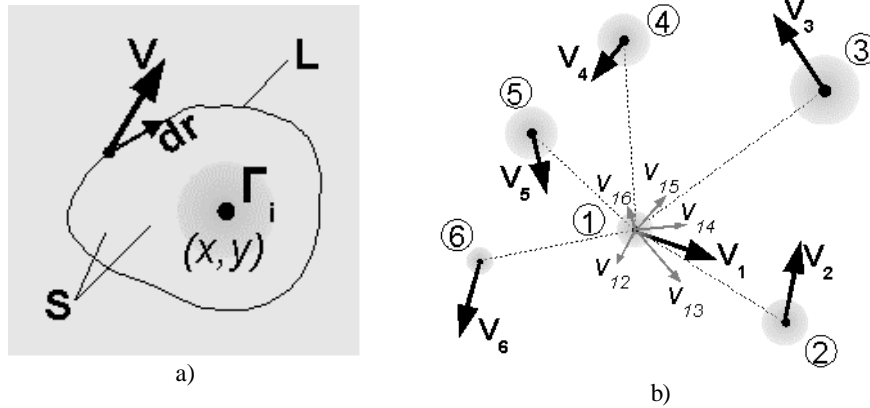
Fig. 2. a) Discretization of a velocity flow field (description in the text);
b) Interactions between vortexes; V_i – velocity induced at point i by other elements; v_{jj} –velocity induced at point i by a vortex at point j.

176

5. Quick algorithm and quick-parallel algorithm

N-body problem occurs in many scientific fields including astronomy, plasma physics, high energy particle physics, etc. In this paragraph we describe a "quick" algorithm. Using this algorithm we are able to reduce the run-time of the simulation form months to hours.

The algorithm is based on decomposition of simulation domain into cells (fig. 3). Interactions within one cell are calculated in the direct way but the longer distance interactions are calculated form group to group rather then from vortex to vortex. Each cell is characterized by the position of its center, the sum of its vortexes' strengths and vortex moments around its center. This parameters let us to calculate velocity at arbitrary point outside the cell. The avoidance of direct interaction works in reduction of calculation complexity form $O(n^2)$ to $O(n \cdot ln(n))$.

The long distance interaction are given in complex plane in [1]. The sum of vorticity strength in a cell:

$$\Gamma_0 = \sum_{i=1}^{m} \Gamma_i , \qquad (12)$$

where: *m*-number of vortex elements in the cell.
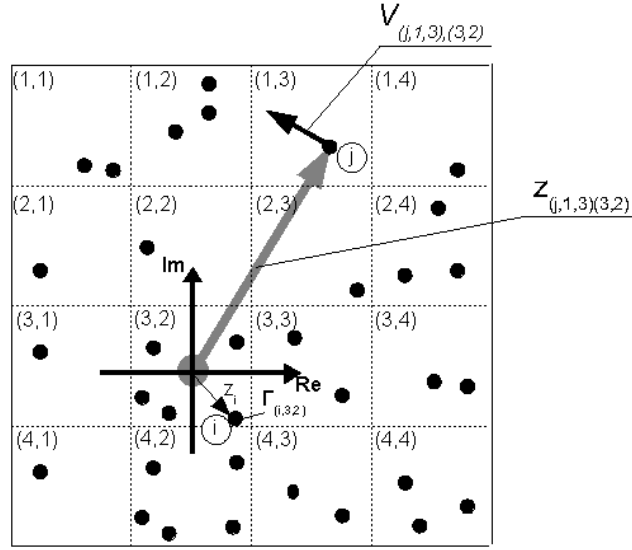
Fig. 3. The division of simulation domain into cells; $V_{(i1,3),(3,2)}$ stands for velocity induced at point *j* in a cell (1,3) by all vortex elements in cell (3,1), $\Gamma_{(i,3,2)}$ is strength of o vortex element in cell (3,2) at point *i*, $z_{(j,1,3)(3,2)}$ is a distance from a cell center (3,2) to a point *j* in a cell (1,3), z_i – distance from a cell center to point *i* in the same cell.

The complex vortex moment for a cell of order k is calculated as:

$$Z_k = \frac{\sum_{i=1}^{m} \Gamma_i z_i^{\,k}}{\Gamma_0}, \qquad (13)$$

where: z_i − distance from a cell center to point i in the same cell

The velocity induced by all vortexes in a cell outside the cell and distant for its center of z_j is expressed by a formula:

$$V = \frac{i\Gamma_0}{2\pi z_j}\left[1 + \frac{Z_1}{z_j} + \frac{Z_2}{z_j^{\,2}} + \frac{Z_3}{z_j^{\,3}} + ...\right], \qquad (14)$$

where i is the imaginary unit.

Further improvements consist in distribution the cells onto separate computers (Fig.4). It is so called domain decomposition. Such a computer cluster executing a quick-parallel algorithm enables to perform simulation with even higher number of vortex elements with shorter times.
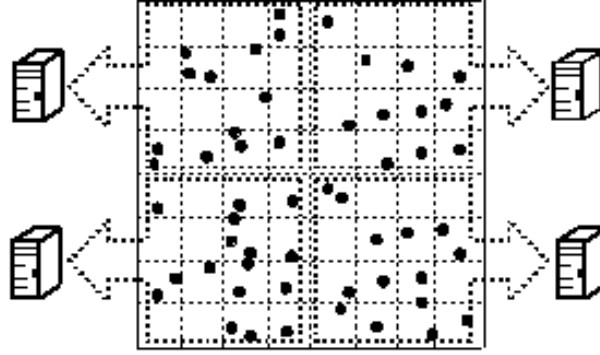
Fig. 4. A calculation domain with discrete vortex elements distributed onto calculation nodes.

6. Computer cluster

The computer cluster was built in a computer laboratory of the Department of Civil and Sanitary Enginering (fig. 5). The laboratory is equiped with 12 standard PC computers connected with Fast Ethernet network. The TCP/IP version 4 is used as a communication protocol. All the computers are one processor machines with AMD Atlon 1600+ 1.4GHz and 256 MB RAM.

The cluster system was created only on the basis of open source software available on the GNU licence. The computers run *Ubuntu Linux 6.10* operating system. For communication purposes *Mpich 2* library (an implementation of MPI-II library) and Open Ssh are used. Network File System (NFS) is applied for data exchange between the nodes.

The cluster is symmetrical one with one distinguished node that provides a share folder for other nodes. It is possible to reconfigure easily any other node to provide a share folder in the event of failure of the distinguished one.

Fig. 5. Computer laboratory at the Faculty of Civil and Sanitary Engineering, Lublin University of Technology.

7. Software implementation

Three computer programs have been written: *vorsym_slow*, *vorsym_quick*, *vorsym_parallel*. They implements the three version of the algorithm: direct (slow), quick and quick-parallel respectively.

In order to find out the potential ability of the computer cluster serious simulations were carried out. Simulation concerns a specially prepared problem. A square simulation domain were randomly filled with vortex elements (fig. 6a). The number of vortexes varied from 10 up to 1 000 000. In order to keep the same amount of vortex elements during simulation 'curl-up' boundary conditions were applied (fig. 6b).
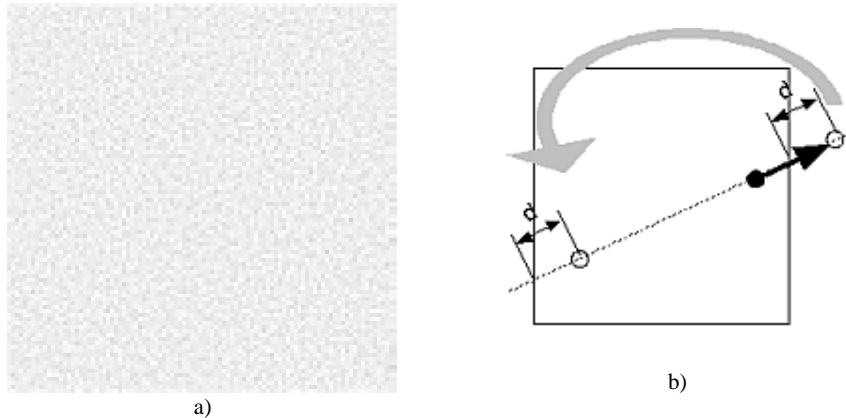
Fig. 6. a) Calculation domain filled with 10 000 vortex elements;
b) 'Curl-up' boundary condition.

179

8. Results

Results compare computational times (in seconds) needed by one computer running *vorsym_slow* or *vorsym_quick* and computer cluster running *vorsym_parallel* on 4 or 9 nodes (fig. 7 and fig. 8).
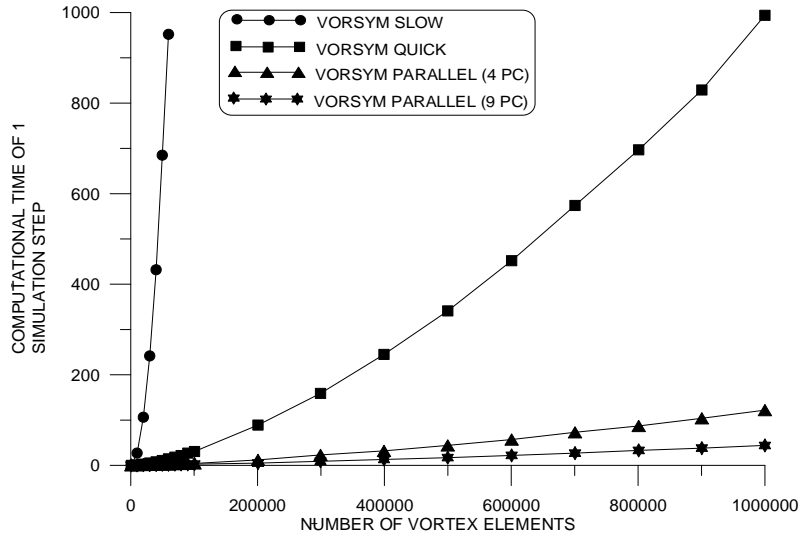
Fig. 7. Computational times of 1 simulation step in dependence of number of vortex elements in the calculation domain.
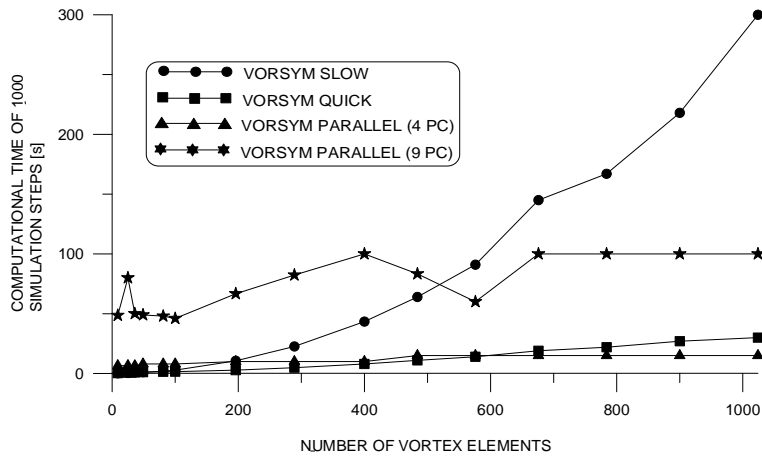
Fig. 8. Computational times of 1000 simulation steps in dependence of number of vortex elements.

180

Acceleration times are calculated as a ratio between times needed by different programs to finish the same task fig. 9.
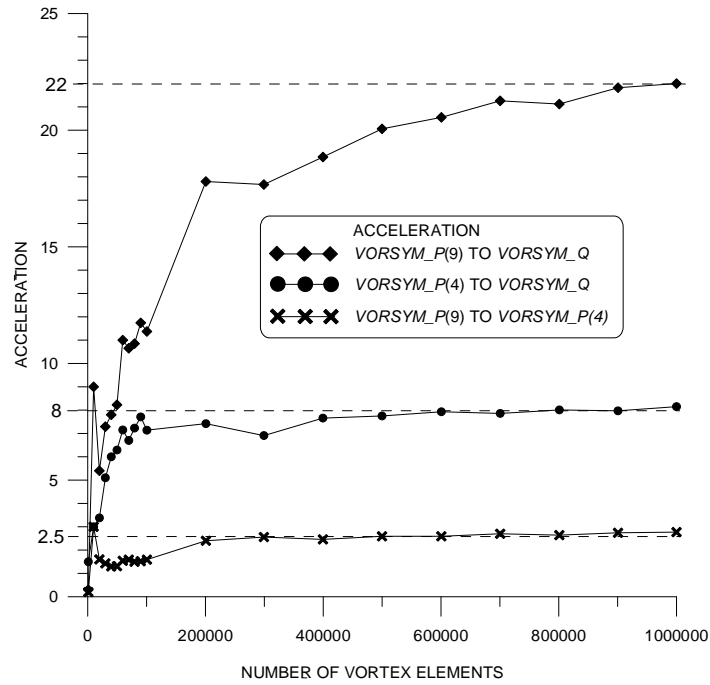
Fig. 9. Acceleration of calculations.

Efficiencies of 1 processor in the cluster were obtained by comparison tasks that gives the same amount of vortex elements for one processor (fig. 10).
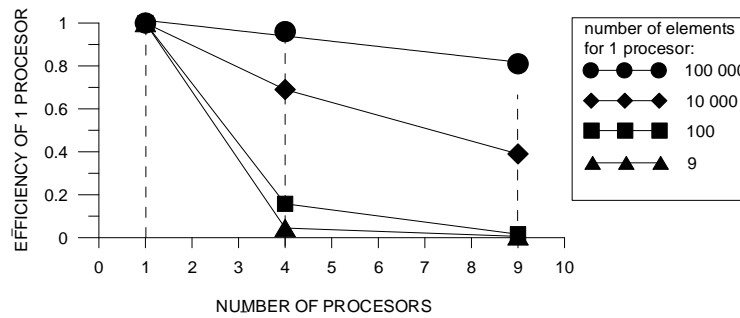
Fig.10. Efficiency of 1 processor in the cluster for different sizes of simulations.

181

Table I presents estimated times of 100 000 simulation steps for jobs of different sizes.

Table I. Estimated simulation times for simulations of different sizes

problem's size →	20 000	50 000	100 000
program	Estimated times of 100 000 simulation steps		
vorsym_s	4 months	2 years	9 years
vorsym_q	3 days	12 days	36 days
vorsym_p(4)	22 hours	47 hours	5 days
vorsym_p(9)	14 hours	36 hours	75 hours

9. Conclusions

The Discrete Vortex Method is a modern and promising numerical tool of wind engineering.

Algorithms of DVM are time consuming and more complicated simulation must be conduct on a computer cluster.

The high acceleration observed on a cluster is a result of domain decomposition and nonlinear increase of parallel part of the calculation.

The efficiency of 1 processor in a cluster drops according to Amdahl's law.

Computer clusters build in existing computer laboratories are powerful computational tools.

References

[1] Lewis R. I., *Vortex Element Methods for fluid dynamic analysis of engineering systems*, Cambridge University Press, 1991.

[2] Turkiyyah G., Reed D., Yang J., *Fast vortex methods for predicting wind-induced pressures on buildings*, Journ. of Wind Engineering and Industrial Aerodynamics, Vol. 58, 1995, pp 51-79.

[3] Larsen A., J.H.Walther J. H., *Aeroelastic analysis of bridge girder sections based on discrete vortex simulation*, Journ. of Wind Engineering and Industrial Aerodynamics, Vol. 68 & 68, 1997, pp 253-265.

[4] Podgórski J. Błazik-Borowa E. Nowicki T., *Application of Discrete Vortex Method to determining parameters of fluid flow around bluff body*, EACWE4, 2005, Paper #185.

[5] Podgórski J. Nowicki T., *Zastosowanie metody wirów dyskretnych w wyznaczaniu parametrów przepływu wokół ciał o ostrych krawędziach*, IV Symp. Wpływy Środowiskowe na Budowle i Ludzi – obciążenia, oddziaływania, interakcje, dyskomfort, 2004.

DAMPING AND DAMPERS

IDENTIFICATION OF DAMPING IN SOIL

Bogumił Wrana[*], Bartłomiej Czado[*]

[*] Institute of Structural Mechanics, Faculty of Civil Engineering,
Cracow University of Technology, Warszawska 24, 31-155 Cracow, Poland.

1. Introduction

Most of the common methods for experimental determination of the damping parameters use the proportional damping assumption. The equations of motion for free vibration of a viscously damped linear discrete system with N degrees of freedom can be written as

$$\mathbf{M}\ddot{\mathbf{y}}(t) + \mathbf{C}\dot{\mathbf{y}}(t) + \mathbf{K}\mathbf{y}(t) = 0 , \tag{1}$$

where $\mathbf{M}$, $\mathbf{C}$ and $\mathbf{K}$ are NxN mass, damping and stiffness matrices, respectively, and $\mathbf{y}(t)$ is the Nx1 vector of the generalized co-ordinates.

A typical procedure can be described in determination of damping with used modal method [1]:

1. Measure a set of transfer functions $H_{ij}(\omega)$ at a set of grid points on the structure.

2. Obtain the natural frequencies ω_k by a pole-"fitting method.

3. Evaluate the modal half-power bandwidth $\Delta\omega_k$ from the frequency response functions, then the Q-factor $Q_k = \omega_k / \Delta\omega_k$ and the modal damping factor $\xi_k = 1/2Q_k$.

4. Determine the modal amplitude factors a_k to obtain the mode shapes, $\mathbf{z}_k$.

5. Finally, reconstruct some transfer functions to verify the accuracy of the evaluated parameters.

Such procedure does not provide reliable information about the nature or spatial distribution of the damping, though the reconstructed transfer functions may match the measured ones well.

The next stage, followed by many researchers, is to attempt to obtain the full viscous damping matrix from the experimental measurements. Methods can be divided into two basic categories: (a) damping identification from modal testing and analysis [2,3] and (b) direct damping identification from the forced response measurements [4,5]. All these methods are based on the assumption that the damping mechanism of the structure is viscous, and their efficiency when the damping mechanism is not viscous is largely unexplored.

185

In a soil damping depends on a strain values, and is proportional for a small strain and non-proportional for a large strain (see fig. 1).
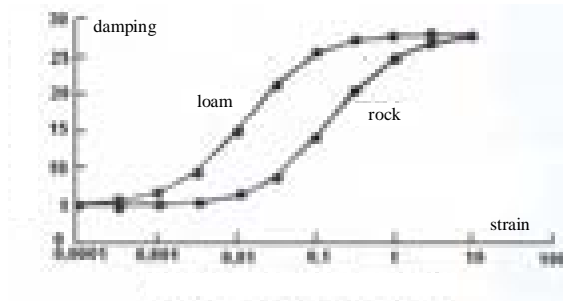
Fig. 1. Damping in a soil.

2. Damping calculation by wavelet transformation

For the narrowband processes common to civil engineering, small spectral bandwidths place restrictions on the frequency resolution of the transformed data, as the spectral resolution must be fine enough to resolve the sharp spectral peak.

As a consequence of the windowing applied by the Gaussian function in the Morlet wavelet, the bandwidth of the resulting wavelet instantaneous spectra are larger than their Fourier equivalent. This gives the appearance of a larger value of effective damping in the signal, the extent of which depends on the scale analyzed. Consider the Morlet wavelet expression the half-power bandwidth can be used to provide a simple measure of the bandwidth of wavelet spectra [6,7]. Assuming symmetry of the spectral peak, the HPBW is then defined as the difference between these two frequencies: $B_r = f_2 - f_1$, with the frequency corresponding to the spectral peak taken as the natural frequency of the system, shown as f_1 and f_2 in fig. 2.
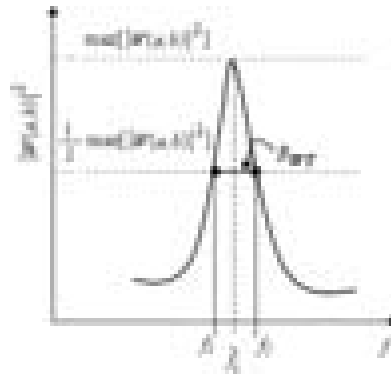
Fig. 2. Half-power bandwidth method – HPBW.

186

The two frequencies corresponding to the half-power level of the Morlet spectra are given by:

$$f = f_o \pm \frac{\sqrt{\ln(2)}}{2\pi}, \tag{2}$$

yielding a half-power bandwidth of:

$$B_{morl} = \frac{\sqrt{\ln(2)}}{\pi}. \tag{3}$$

Note that in the definition of the half-power bandwidth, the spectra are assumed symmetrical. Due to the multi-resolution nature of wavelets, wavelet spectra broaden toward the higher frequencies, but for a narrow-banded spectrum, the assumption of symmetry can be retained. Therefore, the scale at which this half-power bandwidth is evaluated should be the scale defining the ridge of the transform, at which the signal energy is focused. Understandably, this scale corresponds to the instantaneous frequency of the system, or in this case, the frequency of a simple sine wave, f_n. Thus the half-power bandwidth of a wavelet-transformed sine wave is given by:

$$B_{WT} = \frac{\sqrt{\ln(2)}}{\pi} \frac{\bar{f}}{f_o}. \tag{4}$$

Damping coefficient is define in HPBW method as:

$$\xi = \frac{B_r}{2\bar{f}}. \tag{5}$$

3. Example of damping calculation by wavelet transformation

We consider a problem of damping calculation based on the measurement date of the Szombierki mine crump. Fig. 3 shows the measurement data in time and wavelet analysis in the horizontal direction. Fig. 4 shows the measurement data in time and wavelet analysis in the vertical direction.

a)

b)

c)

d)
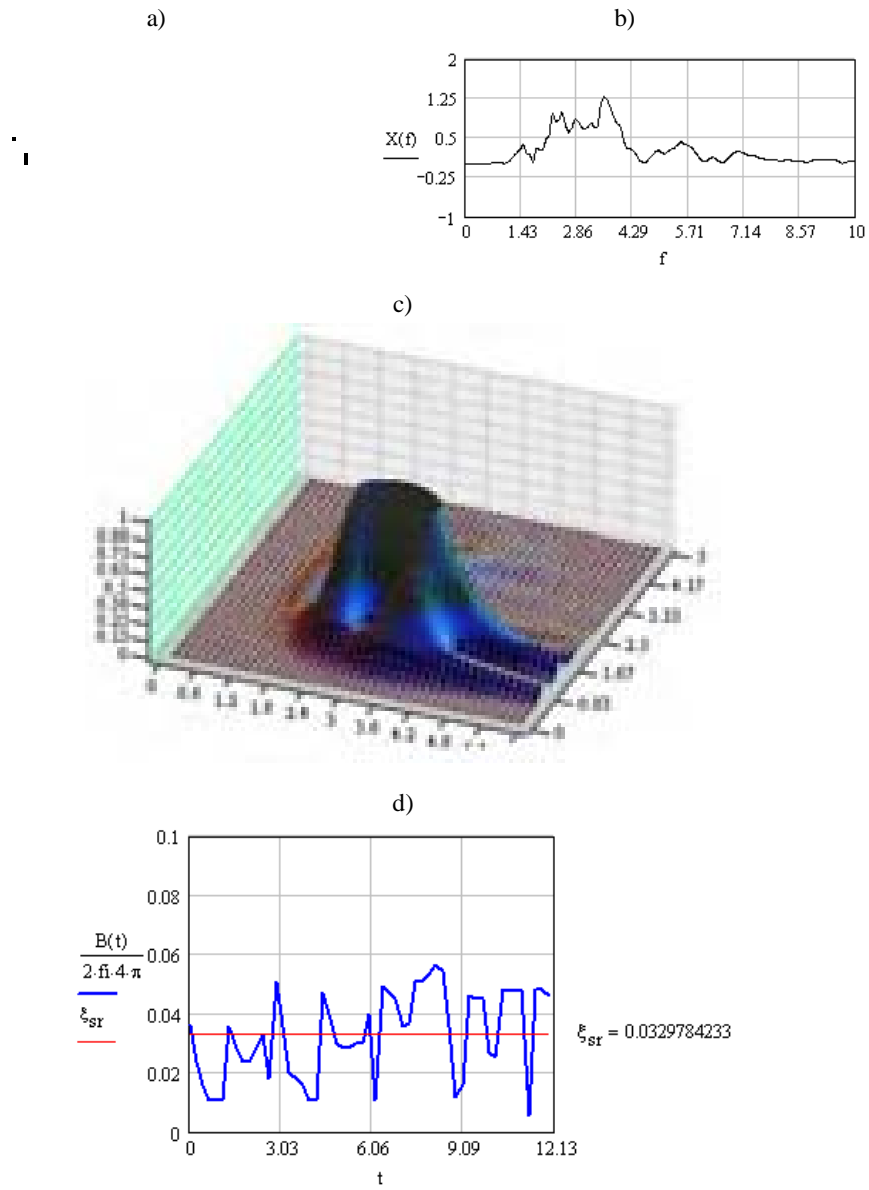
Fig. 3. Damping calculation by HPBW method: a) acceleration in time in horizontal direction,
b) Fourier transformation, c), wavelet map with Morlet wavelets function,
d) damping according to eq. (5).

b)

c)

d)
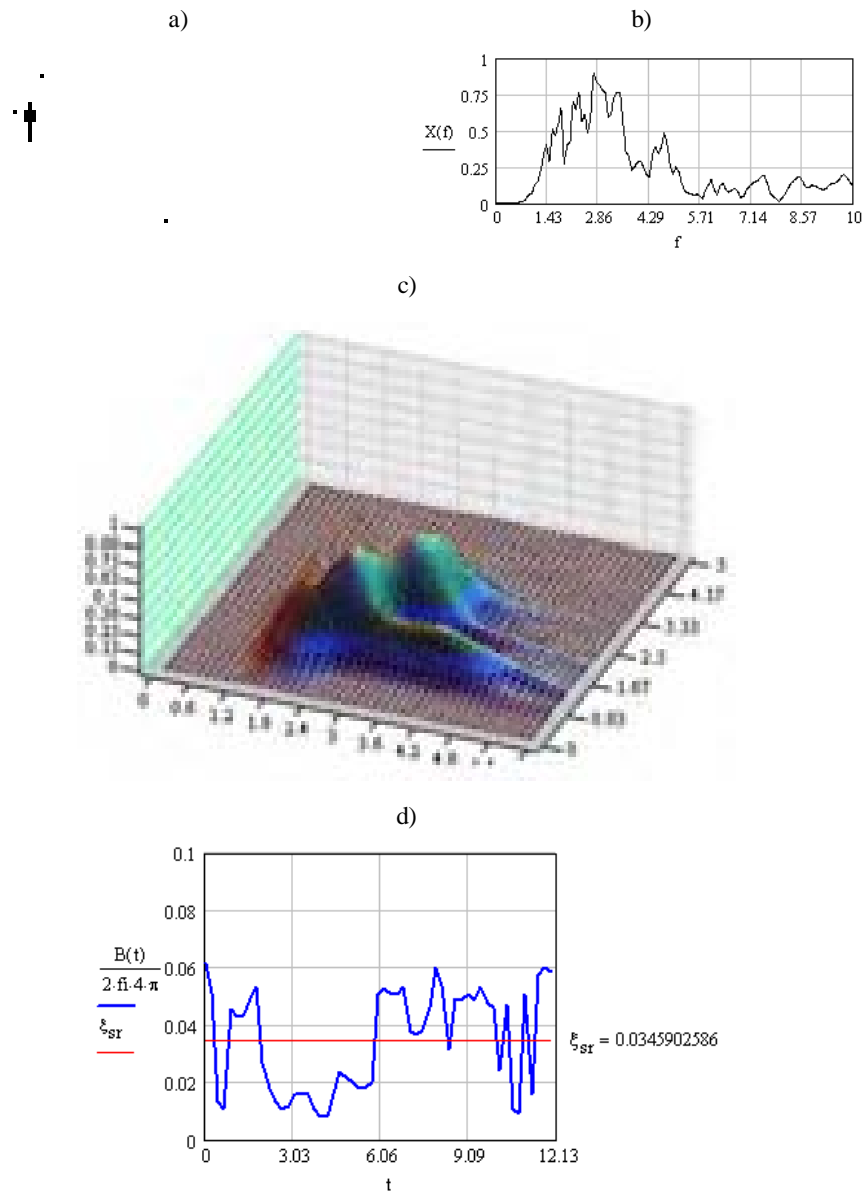
Fig. 4. Damping calculation by HPBW method: a) acceleration in time in vertical direction,
b) Fourier transformation, c), wavelet map with Morlet wavelets function,
d) damping according to eq. (5).

4. Conclusion

In this paper, a method has been proposed to identify a viscous damping. The method is simple, direct, and compatible with conventional modal testing procedures. Numerical experiments have been carried out. The main features of the results have been illustrated on the measurement data of the Szombierki mine crump.

References
[1] Adhikari S., Woodhouse J., *Identification of damping: Part 1,Viscous damping*, Journal of Sound and Vibration, 2001, 243(1), 43-61.
[2] Hasselsman T.K., *A method of constructing a full modal damping matrix from experimental measurements*, American Institute of Aeronautics and Astronautics Journal, 1972, 10, 526-527.
[3] Alvin K. F., Peterson L. D., Park K. C, *Extraction of normal modes and full modal damping from complex modal parameters*, American Institute of Aeronautics and Astronautics Journal, 1997, 35, 1187-1194.
[4] Mottershead J. E., *Theory for the estimation of structural vibration parameters from incomplete data*, American Institute of Aeronautics and Astronautics Journal, 1990, 28, 559-561.
[5] Baruch M., *Identification of the damping matrix*, Technical Report 1AE No. 803 1echnion, Israel Faculty of Aerospace Engineering, Israel Institute of Technology, Haifa, 1997.
[6] Wrana B., Ruchała P., *Identification of damping by means of wavelets in intelligent structures*, 3rd International Congress on Intelligent Building Systems InBus 2004, Cracow University of Technology, 249-254.
[7] Wrana B., Ruchała P., *Application of wavelets to identification of damping of structures*, Proceeding of CMM-2005 Computer Methods, 2005.

RESPONSE OF REINFORCED SOIL RETAINING WALL TO DYNAMIC EXCITATION

Bogumił Wrana[*], Michał Kowalski[*]

* Institute of Structural Mechanics, Faculty of Civil Engineering,
Cracow University of Technology, Warszawska 24, 31-155, Cracow, Poland.

1. Introduction

The article deals with the methods of calculation of a reinforced soil by geosynthetics the retaining wall to earthquake excitation. The proposed method was compared to the method based on the sliding block concept Ling [5] and Newmark [6]. A brief review of recent applications of sliding block is given by Ling [4]. The equations to determine seismic factor of safety, yield acceleration, and permanent displacement are presented. The set of equations for seismic design degenerates to those of static conditions when seismic coefficients are assumed as zero.

In the sliding soil block, earthquake inertia force is considered to be pseudo-static through a seismic coefficient, which is a fraction of the weight of potential sliding soil mass. For combined horizontal and vertical seismic accelerations, Ling [4] used the functions, k and ϕ (see fig. 1)

$$k = \sqrt{k_h^2 + (1 \pm k_v)^2} \,, \qquad \tan \phi = \frac{k_h}{1 \pm k_v} \,, \tag{1}$$

where k_h and k_v are horizontal and vertical coefficients of acceleration.
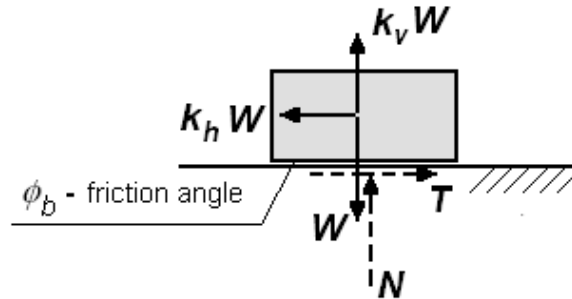
Fig. 1. Rigid block reactions to earthquake loading.

191

The vertical acceleration may act upward or downward considering the most critical conditions for design. A typical value of horizontal seismic coefficient may be obtained from the seismic map e.g., AASHTO, 1983. In using the sliding block concept for permanent displacement analysis, a yield or critical acceleration is defined for the soil mass at sliding where the factor of safety is equal to unity. During seismic excitation, sliding accumulates whenever this yield value is exceeded. The sliding block concept has been used for practical design of earth dams Haynes and Franklin [1]. The idea of permanent displacement limit has also been used for the seismic design of retaining walls Whitman [8].

In the article authors consider computer method of calculation of a reinforced soil by geosynthetics the retaining wall to earthquake excitation. The computer program FLAC is used to find the solution of the equation of motion.

2. Yield acceleration

The force equilibrium equations are obtained for the traction T and normal force N (fig.1):

$$T = k_h W , N = (1 - k_v)W .$$ (2)

The interface friction is governed by Coulomb's law:

$$T = \tan \phi_b N .$$ (3)

When sliding occurs, the coefficient of horizontal acceleration equals the yield value, compare (2) and (3):

$$k_{hy} = (1 - k_v) \tan \phi_b ,$$ (4)

where k_{hy} is the yield value of the coefficient of horizontal acceleration. If k_v acts downward, the yield coefficient of horizontal acceleration is expressed as:

$$k_{hy} = (1 + k_v) \tan \phi_b .$$ (5)

If the earthquake acceleration exceeds the yield acceleration, sliding occurs. The equation of motion is double integrated to give displacement:

$$d = \iint (k_h - k_{hy}) g \cdot dt ,$$ (6)

where d is horizontal displacement and g is earth gravity.

192

3. Reinforced soil retaining wall

The design of reinforced soil retaining walls encompasses several different components, such as the internal stability that gives the length and strength of geosynthetic layers against rupture and pullout, and the external stability against direct sliding and overturning Leshchinsky et al, [2]. The procedure of internal stability analysis can be conducted using Rankine/Coloumb analysis or a rigorous log-spiral analysis (fig. 2a). The direct sliding is determined by a two-part wedge analysis (fig. 2b). Note that the most critical acceleration for tieback and direct sliding acts in the downward and upward directions, respectively.

The required strength and lengths of geosynthetic for a design are conveniently expressed using normalized coefficients:

$$K = \frac{\sum t_j}{0.5\gamma H^2} \approx \frac{t_j}{\gamma h_j D_j} \,, \tag{7}$$

$$L_c = \frac{l_c}{H} \,, \qquad L_{ds} = \frac{l_{ds}}{H} \,, \tag{8}$$

where: γ and H are the unit weight of soil and the wall height, respectively; h_j is the depth of the j-th geosynthetic layer measured from the wall crest; t_j and D_j are the required geosynthetic tieback strength and tributary area of the j-th layer; l_c and l_{ds} are the required length to resist tieback/compound failure and direct sliding, respectively; t_j is the required strength of the j-th layer to ensure local stability; K is analogous to conventional earth pressure coefficient.

a)   b)
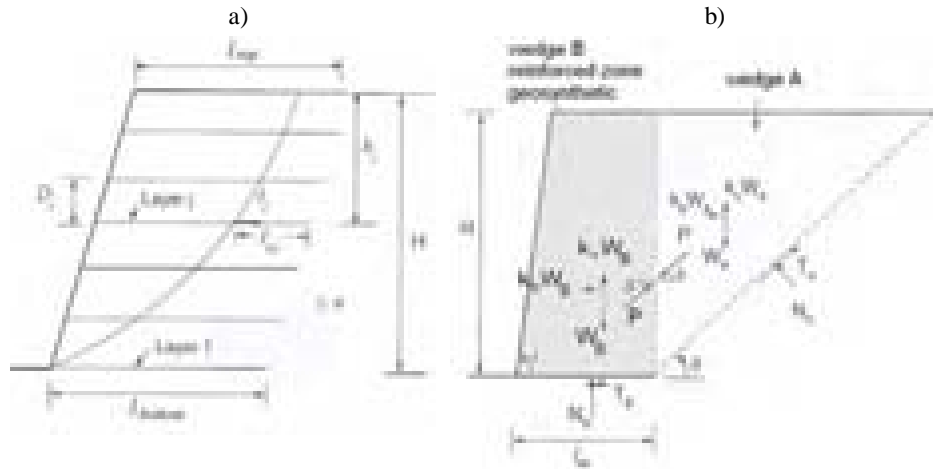
Fig. 2. a) Tieback analysis, b) Direct sliding analysis.

In a design, it is practical to select the required length at the top layer based on L_c and at the bottom based on the greater length of L_c and L_{ds}, whereas length of other layers is obtained by interpolation. The construction may use a constant length, based on the greater value of L_c and L_{ds}, for all geosynthetic layers.

Typically, at the j-th layer, the specified geosynthetic has an allowable strength, $t_{j-allowable}$, larger than the required strength, t_j. It is, thus, practically required that only the bottom m layers are designed against compound failure. That is,

$$\sum_{j=1}^{n} t_{j-allowable} \geq \sum_{j=1}^{n} t_j \ . \tag{9}$$

The required anchorage length of each layer, l_{ej} is determined using t_j or $t_{j-allowable}$, whichever the greater, to prevent pullout failure:

$$l_{ej} = \frac{t_j \ \text{or} \ t_{j-allowable}}{2(1 - k_v) \cdot \sigma_{vj} C_i \tan \phi} \ , \tag{10}$$

where ϕ, C_i, σ_{vj} are the internal friction angle, soil-geosynthetic interaction coefficient, and average overburden pressure acting on the j-th layer, respectively. C_i is expressed as the ratio of the soil-geosynthetic pull out strength to the soil strength, i.e., $\tan \phi$.

The difference between the length of static and seismic designs is much larger for direct sliding along the base of the wall. In fact, small soil friction angle and large acceleration may require an excessively long geosynthetic or may render design impossible because equilibrium is not attainable. Consequently, a performance-based design should be employed to avoid excessive length of the geosynthetic layer needed to resist direct sliding.

For direct sliding mechanism, the coefficient of yield acceleration of reinforced soil block is determined by Ling and Leshchinsky [3]:

$$k_{hy} = (1 - k_v) \frac{W_B C_{ds} \tan \phi + W_A \tan(\phi - \alpha) \Lambda}{W_B + W_A \Lambda} \ , \tag{11}$$

where

$$\Lambda = \frac{1 - C_{ds} \tan \delta \tan \phi}{1 - \tan \delta \tan(\phi - \alpha)} \ , \tag{12}$$

$$C_{ds} = \frac{\tan \phi_s}{\tan \phi} \ , \tag{13}$$

194

where: ϕ_s – friction angle between soil-geosythetic, ϕ – friction angle of soil, W_A and W_B are the weights of reinforced soil and potential sliding backfill soil; δ is the interwedge friction angle (equal to relevant values such as ϕ or $\phi/2$); α is the angle of inclination of the most critical failure plane, which may be determined numerically or using the expression of Richards and Elms [7].

For the design where only horizontal acceleration is used, the permanent displacement limit is straightforward.

4. Permanent displacement under vertical acceleration

The vertical acceleration may be required for the design of earth structures. Under a combined vertical and horizontal acceleration, the equations to determine permanent displacement require k_{hy} and therefore k_v, which varies with time. The procedure implies that a separate set of vertical acceleration records is needed in addition to that of horizontal acceleration. However, the vertical acceleration may be considered in a simplified manner using a ratio of peak vertical seismic coefficient to peak horizontal seismic coefficient. That is, $\lambda = k_{vo}/k_{ho}$. The vertical acceleration is thus assumed to be in phase with the horizontal acceleration.

For the horizontal block and reinforced soil block, the yield seismic coefficient and displacement are rewritten as follows for the simplified analysis:

- Block sliding along horizontal plane:

$$k_{hy} = \frac{\tan \phi}{1 + \lambda \tan \phi}, \tag{14}$$

$$d = (1 + \lambda \tan \phi) \iint (k_h - k_{hy}) g \cdot dt . \tag{15}$$

- Reinforced soil:

$$k_{hy} = \frac{W_B C_{ds} \tan \phi + W_A \tan(\phi - \alpha) \Lambda}{W_B (1 + \lambda C_{ds} \tan \phi) + W_A [1 + \lambda \tan(\phi - \alpha)] \Lambda} , \tag{16}$$

$$d = (1 + \lambda C_{ds} \tan \phi) \iint (k_h - k_{hy}) g \cdot dt . \tag{17}$$

Note that Eqs. (15) and (17) are the same since $C_{ds} \tan \phi$ represents the angle of friction of the soil-geosynthetic interface. The simplified approach to include vertical acceleration has been discussed in [3].

195

5. Reinforced soil retaining wall analysis by program FLAC

We consider dynamic analysis of the reinforced soil with geosynthetic in the retaining wall. Computer program FLAC is used to find the solution of the equation of motion:

$$\mathbf{M}\ddot{\mathbf{d}}(t) + \mathbf{C}\dot{\mathbf{d}}(t) + \mathbf{K}\mathbf{d}(t) = -\ddot{a}(t)\mathbf{M} , \qquad (18)$$

where $\ddot{a}(t)$ is ground acceleration.

The quiet boundary was used to ration of the wave energy in vertical boundary.

Fig. 3 shows a retaining wall (3a) and the soil reinforced with geosynthetic (3b).
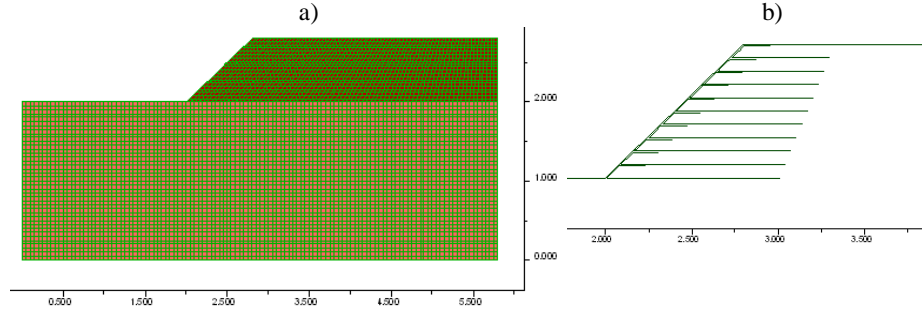
Fig. 3. The retaining wall: a) geometry, b) soil reinforced with geosynthetic.

Fig. 4 shows dynamic excitation applied to the bottom of the numerical model.
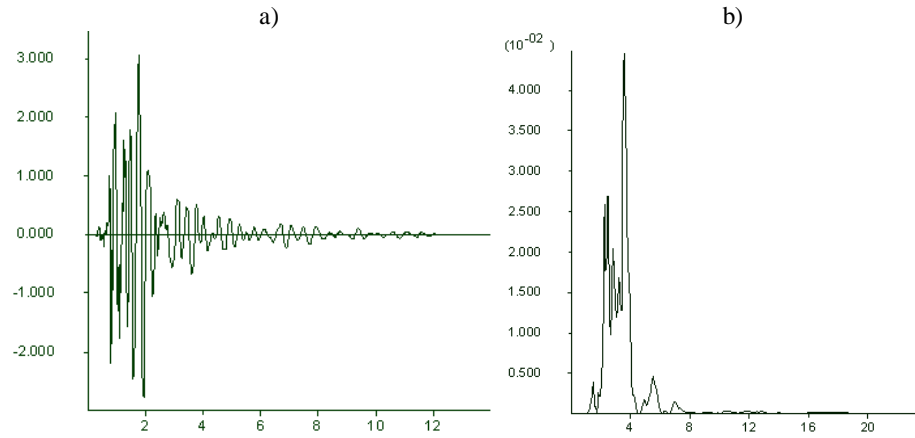
Fig. 4. The dynamic excitation: a) in time, b) Fourier transformation.

196

Fig. 5 shows the displacement of the top of the retaining wall.
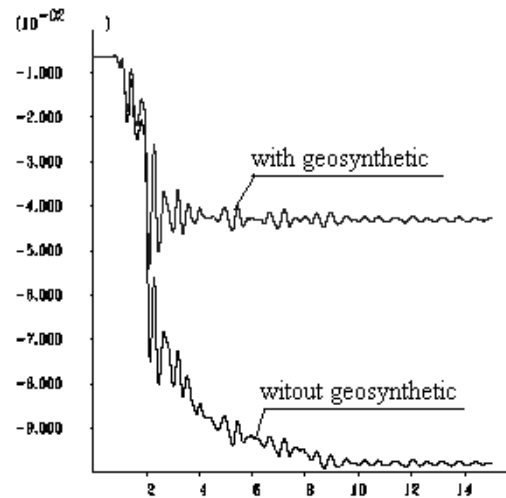
Fig. 5. The displacement of the top of the retaining wall

6. Conclusion

Equations for the yield seismic coefficients and permanent displacement were presented for reinforced soil retaining walls. A simplified procedure to include vertical acceleration was presented for yield acceleration and permanent displacement. The permanent displacement would be a more rational criterion for performance-based design under low seismic load.

References
[1] Haynes M.E., Franklin A.G., *Rationalizing the Seismic Coefficient Method*, Miscellaneous paper GL-84-13. Waterways Experiment Station, Corps of Engineers, Vicksburg, MS, 1984.
[2] Leshchinsky D., Ling H.L, Hanks G., *Unified design approach to geosynthetic reinforced slopes and segmental walls*, Geosynth. lnt. 2(5): 845-881, 1995.
[3] Ling H.I, Leshchinsky D., *Effects of vertical acceleration on seismic design of geosynthetic-reinforced soil structure*, Geotechnique 48(3):347-373, 1998.
[4] Ling H.I., *Recent application of sliding block theory to geotechnical design*, Soil Dyn. Earthquake Eng. 21(3): 189-197, 2001.
[5] Ling H.I., *Application of sliding bloch concept to geosynthetic-constructed facilities*, in: Ling H.I, Leshchinsky D., Tatsuoka F., *Reinforced Soil Engineering. Advances in Research and Practice*, Marcel.Dekker, Inc., 95-111, 2003.

[6] Newmark N.M., *Effects of earthquakes on dams and embankments*, Geotechnique 15(2): 139-159, 1965.

[7] Richards R., Elms D.G., *Seismic passive resistance of tied-back walls*, J. Geotech. Eng. ASCE 118(7):996-1011,1992.

[8] Whitman R.V., *Seismic design and behavior of gravity retaining wall*, Proc. Conf. Design Performance Earth Retaining Struct. ASCE: 817-842. 1990.

198

RESULTS OF THE OBSERVATIONS OF MECHNICAL VIBRATION DAMPERS MATING WITH TOWER-TYPE STRUCTURES – OWN EXPERIENCES

Janusz Kawecki[*], Ryszard Masłowski[*]

[*] Chair of Statics and Dynamics of Structures, Faculty of Civil Engineering, Cracow University of Technology, Warszawska 24, 31-155 Cracow, Poland.

1. Introduction

Steel tower-type structures are particularly susceptible for dynamic actions. This susceptibility comes mostly from the low values of the parameters characterising the damping of the structures. Action of the wind is one of basic dynamic actions on the tower-type structures and the susceptibility of this structures to the vortex shedding, substantially effects their dimensioning (e.g. fatigue effect). Improved models of the phenomena of vortex shedding, better and better describing the situations observed on the objects in natural scale, are being introduced into the design codes [2, 12]. There are also special conditions, fulfilment of which ensures, that the vortex shedding effect is not accompanied with substantial load of the analysed structure.

The reduction of the excessive vibrations of tower-type structures, one can reach by the means of applying the mechanical vibration dampers (MVD) to mate with these structures (comp. [4, 11]). Mechanical vibration dampers (MVD) are being installed on the tower-type structures in Poland, since the early 80'es. The authors of the work have been participating in the solving of theoretical and design problems, concerning the MVD mating with the tower type structures. First, in [8], the method of determination of the optimum parameters of a MVD, has been worked out. Experimental investigations of the elastic-damping elements, which are a part of the MVD, have been carried out next [9, 6]. Finally – in cooperation with designers – the concrete technical solution of such MVD has been proposed (comp. e.g. [7, 10]).

2. Procedure of MVD design

In the model of a MVD mating with a structure, there are three parameters (comp. fig. 1): mass (M_t), stiffness (K_t) and damping (C_t).
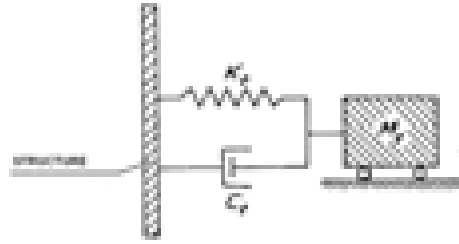
Fig. 1. Model of a MVD mating with a structure.

Optimum parameters of a damper are determined in the process of minimization of the maximum a chosen amplitude - frequency characteristics of a damper - structure system, in a chosen frequency interval (comp. fig. 2). The methodology of determination of the optimum parameters of a MVD has been described in the work [8].

Fig. 2. The result of the task of calculating optimum parameters of a MVD
(line „a"- without MVD, line „b"- with optimum MVD and the mass M_{t1},
line „c"- with optimum MVD and the mass $M_{t2}>M_{t1}$).

MVD-s are most often placed close to the top of a structure. In general considerations, however, the position of a damper can be treated as an additional parameter to be determined in the optimization procedure. When the parameters M_t, K_t, C_t calculated, it is possible to select an appropriate design solution for the MVD mating with a structure. The ideal scheme of a MVD is given in the fig. 3. The mass M_t is hanged by a steel rope to an upper element which is a part of the main structure. The intermediate level of fixing the rope, makes it possible to change the length of hanging "l" in the process of the fine tuning of a MVD, to the frequency of a structure. The length of the hanging influences directly the frequency of the MVD vibration.

200
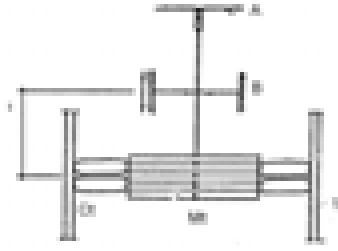
Fig. 3. Ideal scheme of MVD.

The mass of a MVD is connected to the structure by means of elastic-damping elements made of rope loops. The number of the applied loops and their dimensions influence the actual value of the parameter C_t. The rope loops increase also the stiffness K_t of the MVD. The application of a MVD with the elastic-damping elements enforces the change of the length of the mass hanging (it is necessary to increase the length). The procedure of tuning of a designed MVD, to the analytically determined optimum parameters, can be carried out only when one knows the characteristics K_s and C_s of the elastic-damping elements. The best way to obtain these characteristics is to carry out properly planed experiments. An exemplary results of such experiments and the way of their utilisation in the design process of MVD has been described in [6, 9].
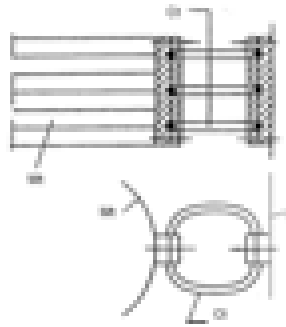
Fig. 4. Connection of a damper mass M_t with a structure by means of exchangeable rope loops.

3. Application of MVD - general information

Multiple MVD-s mating with tower-type structures have been already realized. The MVD-s mating with transmitting antennas installed on the tops of guyed masts and les frequently on the tops of steel towers, constitute a substantial group of them. In the set of the realized MVD-s there are also dampers mating with steel chimneys. Exemplary information concerning the structures with MVD-s and the design parameters of the MVD have been given in the table I.

Table I. Information concerning exemplary structures with MVD-s.

Type of structure	Height [m]	Point of MVD installation	M_t [kg]	K_t [kN/m]	C_t [kg/s]	Calculated vibration reduction rate
Guyed mast, 4 levels of guys	243.7	Antenna, height 19.6 m at the top	300	24788	660	8.3
Guyed mast, 5 levels of guys	293.9	Antenna, height 19.6 m at the top	300	12288	656	6.4
Guyed mast, 5 levels of guys	317.3	Antenna, height 19.6 m at the top	300	15038	624	10.0
Guyed mast, 4 levels of guys	290.75	Antenna, height 21.7 m at the top	450	19224	1459	10.0
Tower	41.75	Antenna, height 15.62 m at the top	365.5	635	485	9.8
Chimney	120.0	At the top	2000	14875	1700	8.9
Chimney	76.8	At the top	2000	14311	1519	7.0
Tower	116.2	Antenna, height 20 m, at the top	500	3445	512	14.0
Tower	77.0	Antenna, height. 13 m, at the top	300	26508	1015	7.4
Chimney with intermediate support	100.0	At the top	2000	23943	2989	13.8
Chimney	75.0	At the top	2000	46658	2473	14.6

4. Evaluation of MVD-s exploitation

The basic evaluation of MVD-s efficiency was carried out after fixing MVD-s to the structures and making them operational. The program of such dynamic examinations assumes the application of controlled dynamic excitation and the registration of dynamic response of a structure, to this dynamic action. Coordinated action of a group of people (3-4 persons), positioned on a platform close to the top of a structure, is the most frequently used type of excitation of the structure vibration. After the initial excitation of the structure vibration, the action is stopped and the structure performs free damped vibration. Utilizing the recording of this vibration, it is possible to determine the value of the parameter describing the damping of a structure mating with a MVD and to compare it with the previously measured value of this parameter for the structure without a MVD.

During the experimental examination of the actual rate of vibration reduction, it would sometimes happened, that it was impossible to reach oscillatory vibration, using the

procedure described above [comp. 7]. It meant that the optimum effect of the vibration reduction, after activating the realized MVD, had been achieved.

The opinions of the users of the objects with MVD-s have been an additional factor in the evaluation of MVD-s efficiency. These opinions have been collected in the form of answers of the users of the objects, to the questions contained in a specially prepared questionnaire (comp. [10]).

The opinions from the inquiry constituted an important factor in the process of evaluation the efficiency of a MVD mating with the evaluated structure. In this process of evaluation, it is vital to collect the data concerning the behavior of the structure-MVD system, in the time when the phenomena of vortex shedding takes place (at the critical wind speed). It is the user of the object, who has in his disposal, all the information concerning the behavior of the object during the entire time of the object exploitation. If any excessive structural vibration happened during this time, it could be observed by the technical service of the object's owner. If it does not happen in a long enough period of time, it can be treated the evidence of the MVD's efficiency. More complete conclusions concerning this problem could be drown only, if one checked whether and how often, in the considered period of time, the wind speed equal to the critical value had occurred.

Taking into consideration the described above sets of information, it can be stated that, the MVD-s attached to the tower-type structures, have proven to be an efficient technical means of the structures' vibration reduction.

Basing on the hitherto experiences, concerning the application of the MVD-s as the elements mating with chimneys, the design solution of a MVD presented in the fig. 5, has been proposed.
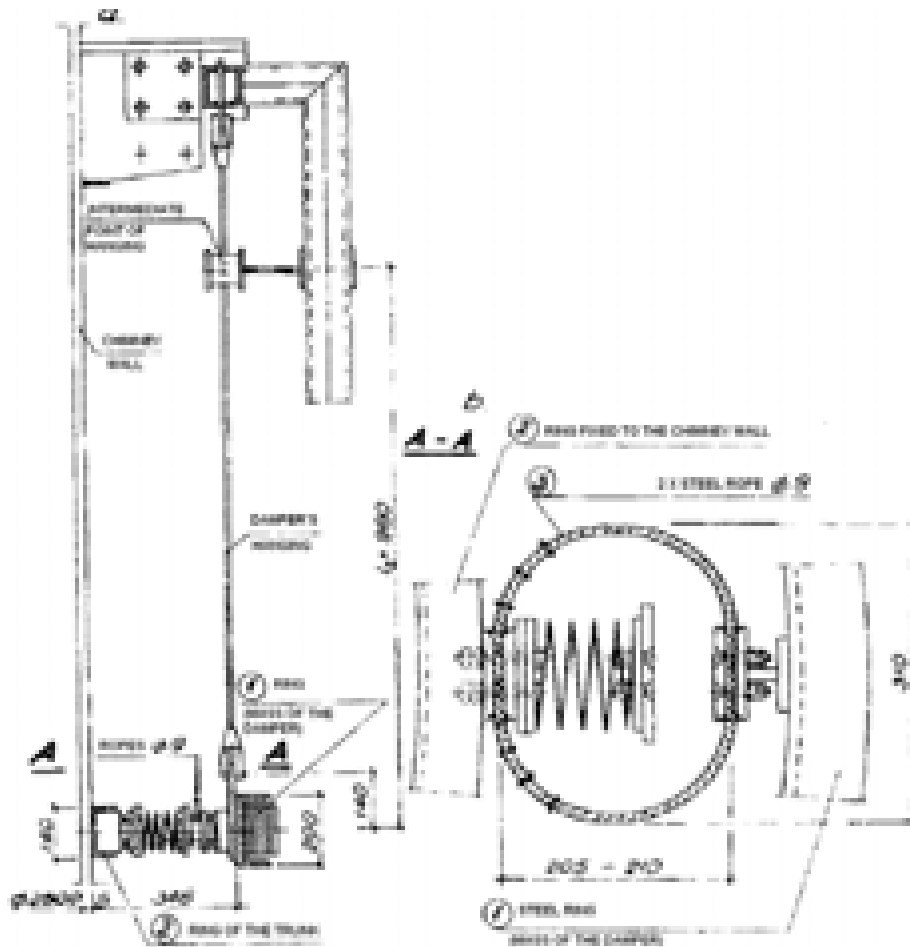
Fig. 5 The scheme of a design solution of MVD (a- side view, b- top view of the connection of the ring with the chimney wall).

The mass M_t made in the form of the ring, is hanged outside of the chimney, by means of the four cables, fixed to the bearing structure of the chimney at its top. The length of the hanging (l_s) can be changed by moving vertically the intermediate point of the hanging fixing. The elastic-damping elements are positioned between the ring an the chimney trunk. The number and dimensions of the elements are determined basing on the results of model calculations. In the MVD constructed in this way, it is possible to realize different values of K_t and C_t, during the measurements. Thanks to this, it is possible to tune the parameters of the MVD, to the structure it is supposed to mate with. It is also possible to

tune the parameters of the MVD to new conditions of its mating with a structure, if the characteristics of the structure changes during its exploitation (e.g. the thickness of the wall diminishes due to corrosion).

5. Conclusions

Participating in the technical activities that are supposed to lead to the reduction of excessive vibrations of tower-type structures, we have made also efforts to examine the efficiency of these activities, during a structure exploitation. That is why we decided to participate in the experimental examination of structure-MVD systems. We also consider, that the survey of the opinions concerning the behavior of these structures during their exploitation, carried out among the users of structures, provides an important supplementary part of the relevant information.

On the grounds of the information collected from the users of objects with MVD-s, it is possible to state, that the dampers described in the present paper, have proven to be an efficient technical means, leading to the reduction of tower-type structures' vibrations.

The verified technical solution of a MVD mating with a chimney, has been also presented in the paper. Such a MVD must be situated outside a chimney.

References:
[1] Abratański A., Kawecki J., *Badania dynamiczne układu budowla wieżowa- mechaniczny tłumik drgań,* Czasopismo Techniczne, z. 5-M, 2004.
[2] CICIND: *Model Code for Steel Chimneys,* revision 1-1999, amendment A- March 2002.
[3] EN 1991-1-4 Eurocode 1: *Action on structures,* Part 1-4 General actions - Wind actions, April 2005 (CEN).
[4] Hirsch G., *Kritischer Vergleich von aktiven und passiven Dämpfungssystemen zur Unterdrückung winderregter Schwingungen Schlanker Structuren,* Beiträge zur Anvendung der Aeroelastik im Bauwesen, München, 1980.
[5] ISO 4354: 1997, *Wind actions on structures,*
[6] Kawecki J., *Rola elementów sprężysto- tłumiących w mechanicznych tłumikach drgań,* Mat. III Ogólnopolskiego Sympozjum „Wpływy Środowiskowe na Budowle i Ludzi", Zwierzyniec 2001.
[7] Kawecki J., *Doświadczalna weryfikacja skuteczności mechanicznego tłumika drgań budowli wieżowej,* Rozprawy z mechaniki konstrukcji i materiałów, Monografia nr 302, Seria Inżynieria lądowa. Politechnika Krakowska, Kraków 2004.
[8] Kawecki J., Masłowski R., *Wyznaczanie optymalnych parametrów mechanicznego tłumika drgań budowli wieżowej,* Archiwum Inżynierii Lądowej, t. 34, nr 4, 1988.
[9] Kawecki J., Masłowski R., Pieronek M., *Doświadczalne wyznaczanie parametrów mechanicznego tłumika drgań stalowej budowli wieżowej,* Mat. XXXV Konferencji Naukowej KILiW PAN oraz KN PZITB, Wrocław- Krynica, t. 1, 1989.

205

[10] Kawecki J., Masłowski R., Świątek R., *Eksploatacja mechanicznych tłumików drgań konstrukcji wieżowych,* Księga IX Międzynarodowej Konferencji: Konstrukcje Metalowe, Kraków 1995, t. 3.

[11] Masłowski R., *Zastosowanie tłumików mechanicznych do zmniejszania drgań budowli wieżowych,* Inżynieria i Budownictwo, nr 1, 1983.

[12] PN-93/B-03201: *Konstrukcje stalowe. Kominy. Obliczenia i projektowanie.*

RANDOM RESPONSE OF TALL BUILDING WITH TUNED MASS DAMPER

S. Hračov[*], S. Pospíšil[*], J. Náprstek[*]

[*] Institute of Theoretical and Applied Mechanics v.v.i., Academy of Sciences of Czech Republic, Prosecka 76, 190 00 Prague, Czech Republic.

1. Introduction

Influence of the wind load on dynamic behavior of tall buildings is significant. One of the most important wind property is its pressure random character which is generated by fluctuation part of the wind velocity. It changes not only along the vertical coordinate but also in time. The response due to this excitation is random and it is highly affected by the type of a damping. In the past the assumption of proportional damping has been used, which is far from the reality especially in the case of building with installed tuned mass damper (TMD). Many papers, see e.g. Náprstek [1], determined the absorber as a weighty origin of the non-proportional damping. Taking it into the consideration leads to the problem of an interaction of eigen-functions on the level of the system itself. Also the level of the stochastic interaction of the response with respect to the generalized coordinates should not be omitted.

In this study the authors focus on an analysis of the particular tall building. Factor of various non-proportionality ratio is assessed in a relation with damping efficiency of individual eigen-forms from the point of view of their interaction and their influence on the final results. The analysis deals with along wind random vibrations of a tall building and only the effect of wind pressure on windward area is assumed.

2. Mathematical model

Tall building discrete mathematical model, see e.g. fig.1, and its response could be described by very well known differential equation of the second order :

$$\mathbf{M} \cdot \ddot{\mathbf{u}}(t) + \mathbf{C} \cdot \dot{\mathbf{u}}(t) + \mathbf{K} \cdot \mathbf{u}(t) = \mathbf{p}_p(t). \tag{1}$$

Orthonormal eigen-functions $\mathbf{u}_o$ of the undamped system can be used as a Galerkin set for a solution of eqn. (1):

$$\mathbf{u}(t) = \sum_{j=1}^{n} \mathbf{u}_{oj} \cdot f_j(t). \tag{2}$$

Only the eigen-vectors corresponding to the wind direction are taking into consideration. The equation (1) can be then expressed in generalized coordinates the time behavior of which is determined by the vector $\mathbf{f}(t)$. The vector $\mathbf{f}(t)$ has to satisfy the following system:

$$\boldsymbol{\Theta}^2 \cdot \mathbf{f}(t) + \mathbf{B} \cdot \dot{\mathbf{f}}(t) + \mathbf{I} \cdot \ddot{\mathbf{f}}(t) = \mathbf{p}(t), \tag{3}$$

$$\boldsymbol{\Theta}^2 = diag[\Theta_1^2, ..., \Theta_n^2], \qquad \mathbf{B} = \mathbf{u}_0^T \cdot \mathbf{C} \cdot \mathbf{u}_0, \qquad \mathbf{p}(t) = \mathbf{p}_p(t) \cdot \mathbf{u}_0^T. \tag{4}$$

$\boldsymbol{\Theta}^2$ is diagonal matrix contains second power of eigen-values of the undamped system. In general $\mathbf{B}$ is full matrix. Case apart is proportional damping matrix $\mathbf{C}$, for which eigen-vectors $\mathbf{u}_o$ diagonalize matrix $\mathbf{B}$. The origin problem solution (1) then splits into solution of uncoupled equations describing vibrations in eigen-modes of damped system. It can be proved, that they are identical to origin undamped eigen-vectors. Proportional damping assumption is in many cases from accuracy point of view sufficient, but not for all. Illustrative example of the second event and necessary using of non-proportional damping is the structure with TMD. The installing of TMD significantly changes the structure damping characteristic and thus the proportional hypothesis is inappropriate.

For eigensolution of system (3), which provides the complex eigen-vectors $\mathbf{q}$ and eigenvalues ξ of a non-proportionally damped system, the equation is rewritten in normal form of dimension *2n*:

$$\dot{\mathbf{F}}(t) = \mathbf{Q} \cdot \mathbf{F}(t) + \mathbf{P}(t), \tag{5}$$

$$\mathbf{F}(t) = \begin{bmatrix} \mathbf{f}(t) \\ \dot{\mathbf{f}}(t) \end{bmatrix}, \qquad \mathbf{Q} = \begin{bmatrix} \mathbf{0} & \mathbf{I} \\ -\boldsymbol{\Theta}^2 & -\mathbf{B} \end{bmatrix}, \qquad \mathbf{P}(t) = \begin{bmatrix} \mathbf{0} \\ \mathbf{I} \end{bmatrix} \cdot \mathbf{p}(t) = \mathbf{H} \cdot \mathbf{p}(t). \tag{6}$$

3. Analysis of random response

Incoming and outcoming quantities can be written in a form based on the spectral differentials of incoming processes:

$$\mathbf{p}(t) = \int_{-\infty}^{\infty} e^{i\omega t} d\boldsymbol{\Phi}(\omega), \qquad \mathbf{F}(t) = \int_{-\infty}^{\infty} \mathbf{F}^*(\omega, t) d\boldsymbol{\Phi}(\omega), \tag{7}$$

$d\boldsymbol{\Phi}(\omega)$ is a vector of spectral differentials of process $\mathbf{p}(t)$ being of white noise type. Their correlations is given by Wiener-Kchincin relation:

$$E\left\{d\mathbf{\Phi}(\omega)\cdot\overline{d\mathbf{\Phi}^T(\omega')}\right\} = dir(\omega'-\omega)\mathbf{S}_p(\omega)d\omega\cdot d\omega'. \tag{8}$$

$E\{.\}$ is mathematical mean operator with respect to the Gaussian probability density function, $\mathbf{F}^*(\omega,t)$ is matrix of unknown deterministic functions, that describe transformation from random excitation in generalized coordinations to random response in time. $\mathbf{S}_p(\omega)$ is spectral density matrix of process $\mathbf{p}(t)$. Inserting eqns. (7) to system (5) and applying mathematical mean operator one obtains :

$$\int\limits_{-\infty}^{\infty}\left(\dot{\mathbf{F}}^*(\omega,t)+\mathbf{Q}\cdot\mathbf{F}^*(\omega,t)\right)\cdot\mathbf{S}_p(\omega)\cdot d\omega = \int\limits_{-\infty}^{\infty}\mathbf{H}\cdot\mathbf{S}_p(\omega)\cdot e^{i\omega t}d\omega. \tag{9}$$

Change order of mean operator and integration is allowed due to independence and arbitrariness of spectral differentials $d\mathbf{\Phi}(\omega)$. Formula (9) have to be fulfilled for every point in time t :

$$\dot{\mathbf{F}}^*(\omega,t)+\mathbf{Q}\cdot\mathbf{F}^*(\omega,t)=\mathbf{H}\cdot e^{i\omega t}, \qquad \mathbf{F}^*(\omega,t)|_{t=0}=0. \tag{10}$$

If eigen-values of $\mathbf{Q}$ are unique, the solution of (10) can be, using Laplace transform, $(t\rightarrow\xi)$ given in the form:

$$\mathbf{F}_L^*(\omega,\xi)=(\mathbf{Q}+\mathbf{I}\cdot\xi)^{-1}\frac{\mathbf{H}}{\xi-i\omega}=\sum_{k=1}^{2n}\frac{\mathbf{Z}_k\mathbf{H}}{i\omega-\xi_k}\left(\frac{1}{\xi-i\omega}-\frac{1}{\xi-\xi_k}\right). \tag{11}$$

Matrix $\mathbf{Z}_k$ ($2n\times2n$) is expressed in a form of diadic product:

$$\mathbf{Z}_k=\mathbf{q}_k\cdot\overline{\mathbf{q}_k^T}. \tag{12}$$

$\mathbf{q}_k$ is the k-th normalized eigen-vector of matrix $\mathbf{Q}$. ξ_k is the k-th eigen-value of matrix $\mathbf{Q}$. For subcritical damped eigen-vectors the eigen-values form complex conjugate pairs with negative real parts. Inverse transform of results in:

$$\mathbf{F}_L^*(\omega,t)=\sum_{k=1}^{2n}\frac{2\mathbf{Z}_k\mathbf{H}}{i\omega-\xi_k}\left(e^{i\omega t}-e^{\xi_k t}\right). \tag{13}$$

First exponent in (13) characterizes stationary response part, the second one influence of homogenous initial conditions. Due to negative real part of ξ_k, the second exponent diminishes in time and could be neglected.

209

Correlation matrix of the response is derived from following definition:

$$\mathbf{K}_F\left(t_1,t_2\right) = \mathbf{E}\left\{F\left(t_1\right)\overline{F^T\left(t_2\right)}\right\} = \mathbf{E}\left\{\int_{-\infty}^{\infty}\mathbf{F}^*\left(\omega_1,t_1\right)d\mathbf{\Phi}\left(\omega_1\right)\int_{-\infty}^{\infty}\overline{\mathbf{F}^{T*}\left(\omega_2,t_2\right)d\mathbf{\Phi}^T\left(\omega_2\right)}\right\} =$$

$$= \int_{-\infty}^{\infty}\mathbf{F}^*\left(\omega,t_1\right)\cdot\mathbf{S}_p(\omega)\cdot\overline{\mathbf{F}^{*T}\left(\omega,t_2\right)}\cdot d\omega. \tag{14}$$

For stationary state eqn. (14) can be expressed in the form:

$$\mathbf{K}_F\left(t\right) = \int_{-\infty}^{\infty}\sum_{k,l=1}^{2n}e^{\mathrm{i}\omega t}\cdot\frac{\mathbf{q}_k\cdot\mathbf{q}_k^T\cdot\mathbf{H}\cdot\mathbf{S}_p\left(\omega\right)\cdot\mathbf{H}^T\cdot\mathbf{q}_k\cdot\mathbf{q}_k^T}{\left(\mathrm{i}\omega-\xi_k\right)\left(\mathrm{i}\omega-\overline{\xi_l}\right)}\cdot d\omega. \tag{15}$$

For dispersion matrix quantification the time t is set to zero. Square root of diagonal items of dispersive matrix are seen as a decisive value characterizing response to the random excitation. Stochastic part of response is determined by correlation function:

$$\mathbf{K}_u\left(P,R,t_1,t_2\right) = \mathbf{E}\left\{u\left(P,t_1\right)\overline{u\left(R,t_2\right)}\right\} = \sum_{ij=1}^{n}u_{io}(P)\overline{u_{jo}(R)}\cdot\mathbf{E}\left\{f_i\left(\theta_i t_1\right)\overline{f_j\left(\theta_j,t_2\right)}\right\} =$$

$$= \mathbf{u}_o^T(P)\cdot\mathbf{K}_{f11}(t_1,t_2)\cdot\overline{\mathbf{u}_o(R)}. \tag{16}$$

P and R stand for two arbitrary points of the structure. Matrix $\mathbf{K}_{f11}(t_1,t_2)$ denotes correlations between vectors $\mathbf{f}_i(t)$ corresponding to eigen-vector $\mathbf{u}_{0i}$. For stationary case equation can be rewritten as:

$$\mathbf{K}_u\left(P,R,t\right) = \mathbf{u}_o^T(P)\cdot\mathbf{K}_{f11}(t)\cdot\overline{\mathbf{u}_o(R)}. \tag{17}$$

4. Excitation due to wind turbulence

The random component of wind load is described by the spectral density $\mathbf{S}_p(\omega)$. The correlation matrix of external load $\mathbf{K}_p(t)$ is formulated by equation:

$$\mathbf{K}_p\left(t\right) = \mathbf{E}\left\{\mathbf{p}(\tau)\overline{\mathbf{p}^T\left(t+\tau\right)}\right\} = \mathbf{E}\left\{\int_A\mathbf{u}_0\left(P\right)\mathbf{p}\left(P,\tau\right)\cdot dA_P\int_A\overline{\mathbf{u}_0^T\left(R\right)\mathbf{p}\left(R,t+\tau\right)}\cdot dA_R\right\}. \tag{18}$$

Due to linear character of integrative operator and mathematical mean operator one obtains for (18) :

210

$$\mathbf{K}_p(t) = \int_A \int_A \mathbf{u}_0(P) \overline{\mathbf{u}_0^T(R)} \cdot \mathbf{E}\{\mathbf{p}(P,\tau) \cdot \mathbf{p}(R, t+\tau)\} \cdot dA_P dA_R =$$

$$= \int_A \int_A \mathbf{u}_0(P) \overline{\mathbf{u}_0^T(R)} \mathbf{K}_{pu}(P, R, t) \cdot dA_P dA_R \cdot \tag{19}$$

After Fourier transformation of eqn. (19) it results in:

$$\mathbf{S}_p(\omega) = \int_A \int_A \mathbf{u}_o(P) \overline{\mathbf{u}_o^T(R)} \cdot \mathbf{S}_{pu}(P, R, \omega) dA_P dA_R =$$

$$= \int_0^H \int_0^H \int_0^B \int_0^B \mathbf{u}_o(z_P) \overline{\mathbf{u}_o^T(z_R)} \cdot \mathbf{S}_{pu}(z_P, z_R, x_P, x_R, \omega) dz_P dz_R dx_P dx_R \cdot \tag{20}$$

Spectral density $\mathbf{S}_{pu}(P, R, \omega)$ describes correlation of wind pressures between points P and R of the structure. Only the along wind pressure component is considered. Spectral density $\mathbf{S}_{pu}(P, R, \omega)$ is defined by:

$$\mathbf{S}_{pu}(P, R, \omega) = c_D^2 \rho^2 v_P v_R A_P A_R \cdot \mathbf{G}_{vv}(\omega) \cdot \chi_z \chi_x \cdot \tag{21}$$

$\mathbf{G}_{vv}(\omega)$ is Davenport's spectral density of wind speed's fluctuation, χ_x resp. χ_z are aerodynamic admittances, that describe space correlation of the pressure on acting windward area. After substitutions equation (20) becomes:

$$\mathbf{S}_{pu}(P, R, \omega) = c_D^2 \rho^2 v_P v_R A_P A_R \cdot 4K \frac{v_{10}^2 \cdot x^2}{\omega(1+x^2)^{4/3}} \cdot e^{-\frac{C_x \omega}{v_{10} 2\pi}|x_P - x_R|} \cdot e^{-\frac{C_z \omega}{v_{10} 2\pi}|z_P - z_R|}, \tag{22}$$

where $x = 1200\omega/(2\pi v_{10})$, K is roughness coefficient, C_x a C_z are exponential decay coefficients, c_D is aerodynamic coefficient, ρ is air density, v_P is mean value of the wind speed in point P, v_{10} is mean value of the wind speed at 10m height, A_p is area corresponding to point P.

5. Numerical analysis

The theoretical procedure has been used to calculation of the response of the real 100 m tall building, see fig. 1. On the tops of both towers of the building the TMDs for suppressing undesirable vibration are installed.
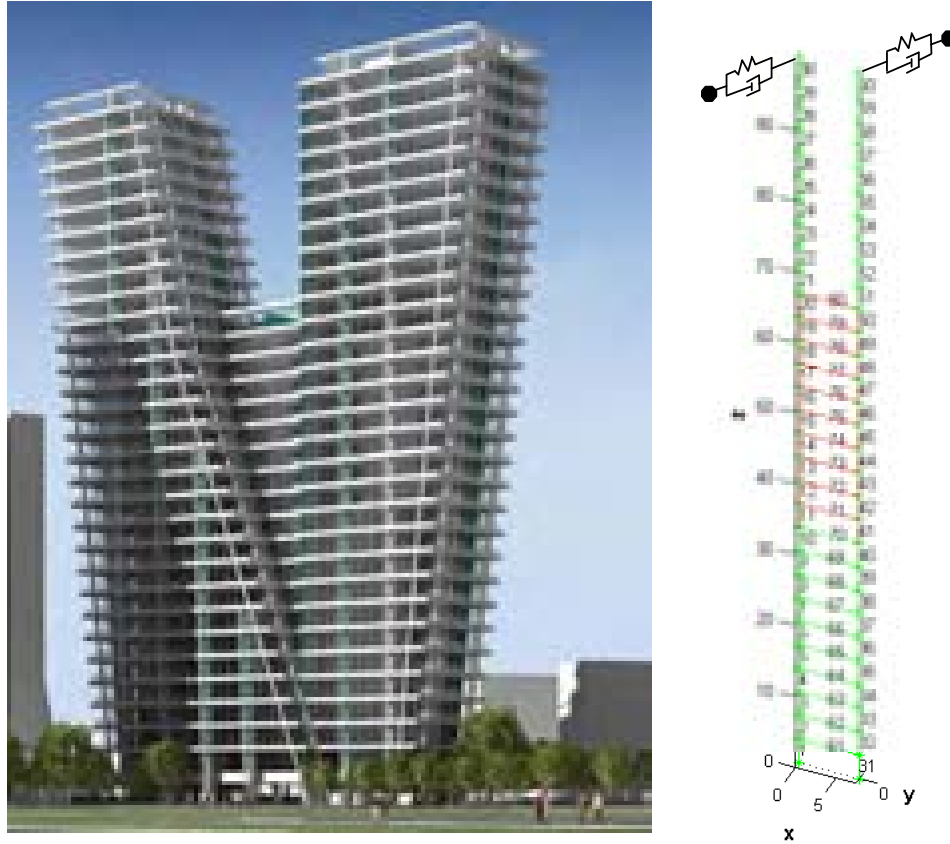
Fig. 1. Prototype of a tall building and its FEM model.

Discrete mathematical model of structure is created in CALFEM, which is Matlab toolbox for computing by the finite elements method. It has 62 nodes (including 2 representing absorbers), each with 1 degree of freedom. Damping matrix **C** of basic system is proportional to the mass matrix. The damping ratio is set to $\zeta = 0.04$. TMDs are tuned the first eigen-frequency of the basic system. The weight of each absorber is 200 tones. The damping ratio of TMD was set for different cases in range $\zeta_{TMD} = (0.04; 4.5)$. Random wind load is defined by the Davenport's spectral density for wind velocity. The reference mean value of wind speed at 10 m height is $v_{10} = 14$ m/s. Modal analysis provides the eigen-vectors and eigen-values of the whole undamped system (building + TMDs), see fig. 2. The first five eigen-vectors were used as the Galerkin base for reducing of the system and computing of the response.

212

$\omega_1 = 2{,}63$ rad/s $\qquad$ $\omega_2 = 2{,}79$ rad/s

$\omega_3 = 3{,}14$ rad/s $\qquad$ $\omega_4 = 3{,}67$ rad/s
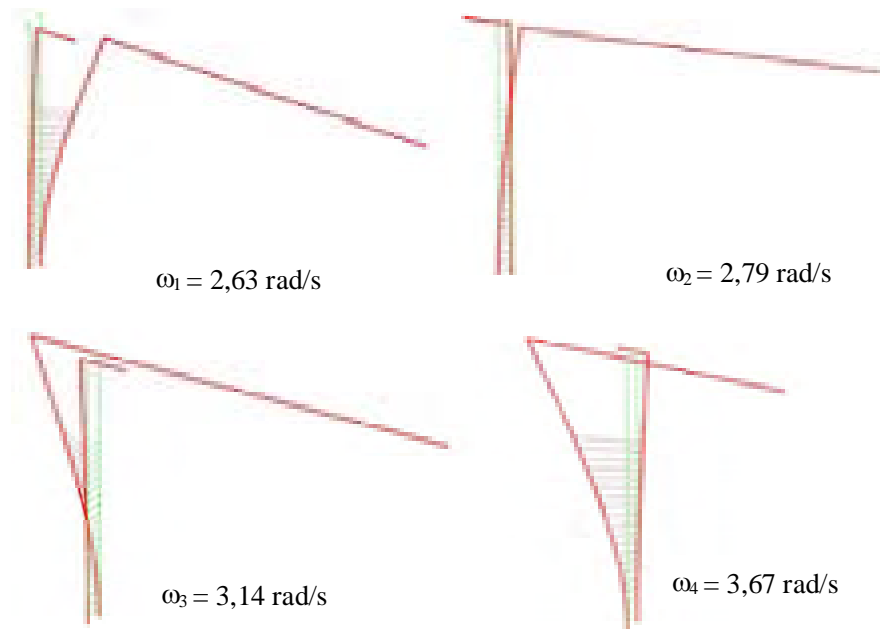
Fig. 2. First four eigen-vectors of the building with TMDs.

The procedures from chapters 2.-4. have been applied on the non-proportional system for many cases, which differ in values of the damping ratios ζ_{TMD}. For every change of the damping the correlation matrix of response and root-mean-square (RMS) displacements at the various heights have been calculated. On fig.3 there are depicted first four eigen-values of non-proportionally damped system in Gaussian plane. The character of the curves is given by interaction of the eigen-vectors. See also table I for concrete values.

Table I. First four pairs of complex eigen-values as function of ζ_{TMD}.

ζ_{tmd}	$\xi_{1,2}$	$\xi_{3,4}$	$\xi_{5,6}$	$\xi_{6,7}$
0.0	$-0.026 \pm 2.626i$	$-0.005 \pm 2.788i$	$-0.031 \pm 3.140i$	$-0.053 \pm 3.674i$
0.3	$-0.355 \pm 2.602i$	$-0.706 \pm 2.697i$	$-0.590 \pm 3.084i$	$-0.242 \pm 3.667i$
0.7	$-0.793 \pm 2.504i$	$-1.642 \pm 2.253i$	$-1.336 \pm 2.842i$	$-0.495 \pm 3.641i$
1.0	$-1.122 \pm 2.375i$	$-2.344 \pm 1.509i$	$-1.895 \pm 2.504i$	$-0.685 \pm 3.610i$
1.2	$-1.341 \pm 2.258i$	-2.446 ± 3.178	$-2.268 \pm 2.172i$	$-0.811 \pm 3.584i$

213
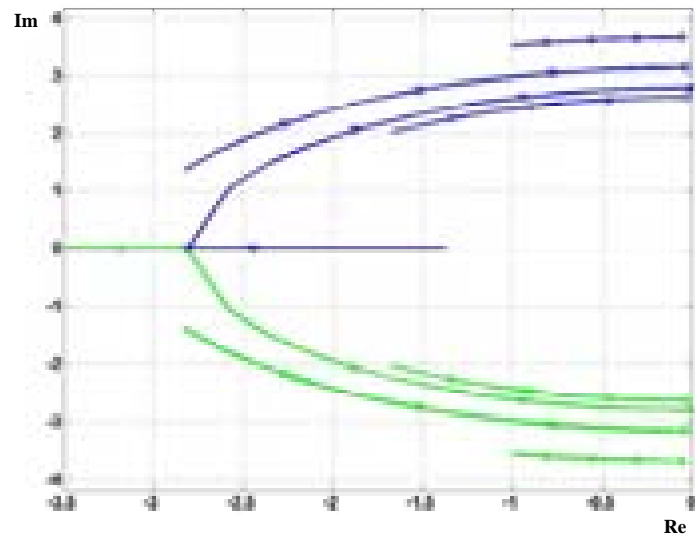
Fig. 3. First four pairs of complex eigen-values as function of ζ_{TMD} in Gaussian plane.
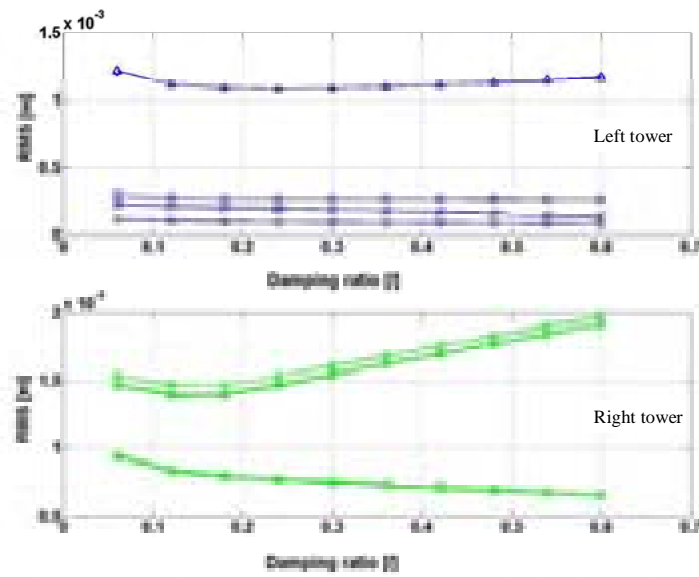
Fig. 4. The RMS displacement of the tops of both towers as function of ζ_{TMD} for various number of eigen-modes (first eigen-vector : O, first two e. : ×, first three e.: □, first four e.: Δ, first five e.: ∗).

214

The RMS displacement results are affected by number of used eigen-modes of undamped system. It holds especially in case of random vibration, where the role of stochastic interaction of the eigen-vectors is significant. Also the mechanical interaction of eigen-modes of non-proportionally damped systems cannot be neglected. The example of RMS values for displacements of the points (floors of the towers) is depicted on fig. 5. Each picture stands for concrete value of damping ratio of the TMD ($\zeta_{TMD} = 0.24$) and first eigen-mode. The fig. 4 shows convergence of the RMS value of the tower's tops due to number of used eigen-modes. It confirms, that the assumed number of the eigen-modes has been satisfactory.
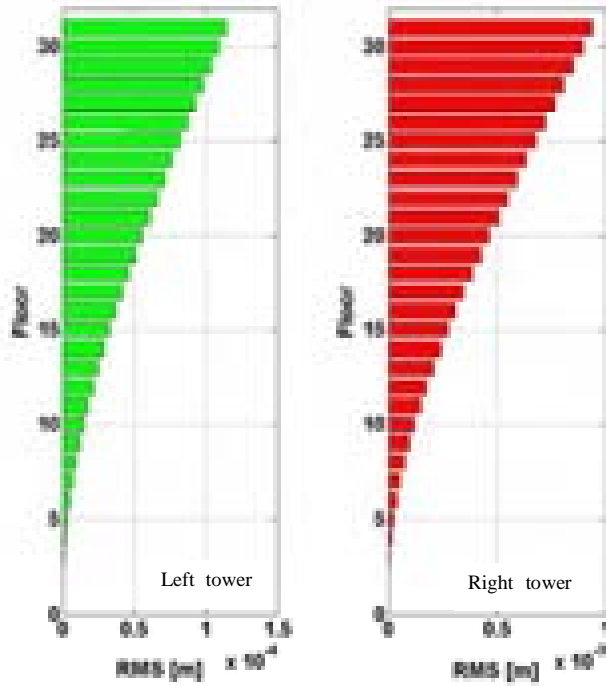
Fig. 5. The RMS displacement of the both towers along its height
($\zeta_{TMD} = 0.24$, only first eigen-vector is considered).

6. Conclusions

From the point of view of a designer, the influence of individual eigen-forms should be considered more carefully in the case of non-proportionally damped structure with stochastic loading then in cases of tall buildings with less significant modes interaction and load correlation.

215

The article presents a method for assessment of structure such as tall building exposed to random wind load. The used analysis takes a place in genaralized coordinates, which are close to eigen-forms of an investigated structure. Energetic volume of individual eigen-functions decreases quickly with increase of their order. It implies a possibility to limit quite easily a number of eigen-functions needed. It also leads to significant reduction of time consumption when stochastic analysis should be done.

The article results in the following conclusions:

- In case of presence passive or active damping equipment in structure influence of non-proportional damping must be respected.
- Stochastic interactions of eigen-forms are significant and their influence decay exponentially with difference of eigen-form numbers.

References

[1] Náprstek J., Pospíšil S., *Along wind random vibrations of a structure with non-proportional damping*, In: Proc. 12th Int. Conf. Wind Engineering (J.Cheung edt.). Monash University, Cairns (Australia), 2007, in print.

[2] Bolotin V.V., *Random vibrations of elastic systems*, (Russian). Nauka, 1979, Moscow.

[3] Davenport A.G., *The dependence of wind Loads on Meteorological parameters*, Proc. International Research Seminar, Wind Effects on Buildings and Structures, 1967, Toronto Press, Toronto, Canada, pp. 19-83.

[4] Davenport A.G., *Gust loading factor*, in: Jour. Struct. Div. ASCE, 1967, 93, pp.11-34.

[5] Dyrbye C., Hansen S.O., *Wind loads on structures*, Wiley and Sons, Chichester, 1996.

[6] Fischer O., Pirner M., *Dynamika kotvenych stozaru*, Academia, Praha, 1987.

[7] Koloušek V., Pirner M., Fischer O., Náprstek J., *Wind Effects on Civil Engineering Structures*. Academia - Elsevier, Praha, 1983.

[8] Materazzi A.L., Venanzi I., *Wind response of cable stayed masts*, In: Proc. The Fourth European & African Conference on Wind Engineering, (J. Náprstek, C. Fischer eds), 2005, ITAM ASCR, Prague, 10 pgs, CD ROM.

[9] Náprstek J., *On non-linear transfer between random variable velocity of fluid motion and frontal pressure on the bypassed cylindrical body*, Acta Technica ČSAV, 1975, 4, pp. 479-494.

[10] Náprstek J., Pospíšil S., *Along wind random vibrations of a slender structure - modelling by continuous elements*, In: Proc. Engineering Mechanics 2006 (J. Náprstek, C. Fischer eds). ITAM ASCR, Prague, 2006, 8 pgs, CD ROM.

[11] Simiu E., Scanlan R.H., *Wind Effects on Structures. Fundamentals and Applications to Design*. J. Wiley, New York, 1996.

216

WIND ENERGY
AND WIND POWER PLANTS

COMPUTER SIMULATION OF SELECTED PROBLEMS OF CHIRALIC TURBINES AERODYNAMICS

Andrzej Flaga[*,**], Piotr Matys[*]

[*] Wind Engineering Laboratory, Faculty of Civil Engineering,
Cracow University of Technology,Warszawska 24, Cracow, Poland.
[**] Department of Structural Mechanics, Faculty of Civil and Sanitary Engineering,
Lublin University of Technology, Nadbystrzycka 40, Lublin, Poland.

1. Introduction

Chiralic turbines are a development of constructional idea initiated in 1920. These are horizontal axis wind turbines which have quickly spinning rotors instead of blades (fig. 1).

Fig. 1. Modern chiralic wind tubine constructed in Poland by company Eneco [6].

The principle of operation of such turbine is based on Magnus effect, i.e. generating lift force on spinning rotor under the influence of wind. Rotation of blades is forced by electrical engines. Experiments with such turbines aimed at finding the best shape of the blade were conducted in Italy in 1997. Designed blade looks as in the fig. 2

219
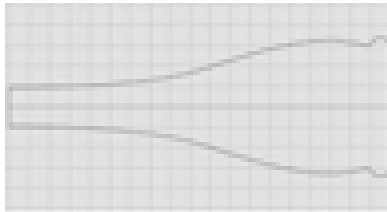
Fig. 2. The result of aerodynamic study on blade shape in Institute of Power Industry in Italy [3].

Italian scientists compared models of chiralic and typical propeller wind turbines (all of them of a diameter of 1.2 m) in wind tunnel. As research shows, the biggest advantage of chiralic turbines is much better exploitation of weak winds, i.e. those which are the most common throughout the year. Furthermore, such turbines revolve much slower than propeller ones what results in much less noise. Furthermore, such turbines revolve much slower than propeller ones what results in much less noise. Wake generated by classic wind turbine significantly differs from the wake generated by chiralic wind turbine.

The foregoing facts were an inspiration for writing computer simulation enabling initial examination of the turbine before its construction.

2. Description of established computational model

2.1. Blade geometry

The blade must be a rotating solid, it is put together by means of segments and curves available in the program. The drawn outline of the blade may be saved in a file. That allows us to create the database of blades which may be subsequently tested and compared one to another.

Then, the program computes the aspect ratio (slenderness) λ of the blade designed by the user. Designer also selects the number and size of discs located along the blade and at the ends of the blade.

Then, blade is divided into computational elements, out of which every element is in the distance r from the axis of a rotation as shown in fig. 3.
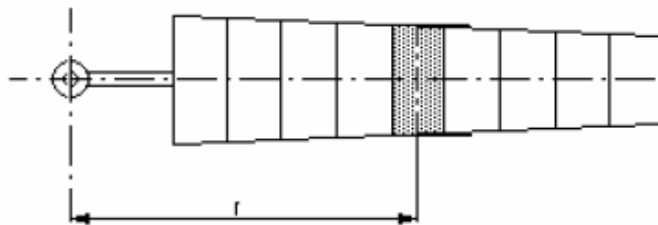
Fig. 3. The division of the blade in to computational elements [1].

220

2.2. Aerodynamic coefficients

The most important parameters in terms of wind energy that describe revolving cylinder are α – ratio of cylinder surface velocity to wind velocity, C_L and C_D – non-dimensional coefficients describing lift properties and drag force, Re – Reynolds number, λ – elongation, k – parameter describing discs properties limiting disturbances on cylinder ends. Rotating cylinders were examined in wind tunnels all over the world which bears fruit in abundant family of empirical curves describing physics of the phenomenon much better than theoretical formulas. Exemplary curves are depicted on the fig. 4.
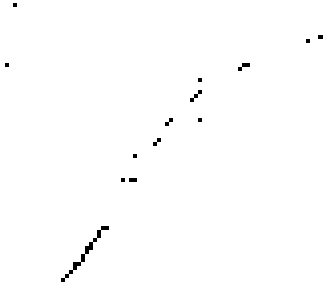
Fig. 4. C_L values in function α for different experiment parameters [4] where: a – theoretical curve, $b - k$ – empirical curves.

Therefore, taking empirical curves and basic aerodynamic equations describing lift and drag force on a rotating cylinder, wing or sail:

$$F_L = \frac{1}{2}\rho w^2 A C_L, \qquad F_D = \frac{1}{2}\rho w^2 A C_D, \tag{1}$$

where: A – body surface; w – velocity of inflowing stream; ρ – air density.

We may determine lift and drag force on almost every freely designed blade.

2.3. Determination of sectional aerodynamic forces, wind turbine power and torque

Wind velocity v is perpendicular to the plane of the rotor. Taking peripheral velocity u of the blade resulting from rotation of the wind wheel into consideration:

221

$$u_k = \frac{2 \cdot \pi \cdot r_k \cdot N}{60} = \frac{\pi \cdot r_k \cdot N}{30} \tag{2}$$

where: N – rotational frequency $\left[\dfrac{rev}{min}\right]$, r_k – distance from the axis of the wind turbine, u_k – peripheral velocity of the k – th element, one obtains relative velocity w_k of the air stream (fig. 5).

$$w_k = \sqrt{v^2 + u_k^2} \tag{3}$$

The program assumes minimal rotational frequency N of the rotor and minimal rotational frequency N_b of the single blade. N_b value allows for finding velocity U_k tangent to a given computational element:

$$U_k = 2\pi R_k N_b \tag{4}$$

where: R_k – radius of a given computational element,

which in turn leads to α_k:

$$\alpha_k = \frac{U_k}{w_k} \tag{5}$$

The program contains the database of the experimental curves $C_L(\alpha)$ and $C_D(\alpha)$. They are saved in the form of combined polynomials of the degree greater than 2. Using the equations of those polynomials one may find values $C_L(\alpha)$ and $C_D(\alpha)$ for $\alpha = \alpha_k$.

Another window of the simulation serves to select wind velocity v, the number of the blades of the tested wind turbine, pressure p and temperature T. Air density ρ is also computed from the formula [1]:

$$\rho = 1.2928 \cdot \frac{p}{101325} \cdot \frac{273.15}{(273.15 + T)} \tag{6}$$

For a given part of the blade, when having the surface A_k, lift F_{Lk} and drag F_{Dk} force components are computed from formulas (1). Forces affecting particular computational elements in relation to the whole wind turbine may be depicted in the following way (comp. fig. 5.):

222
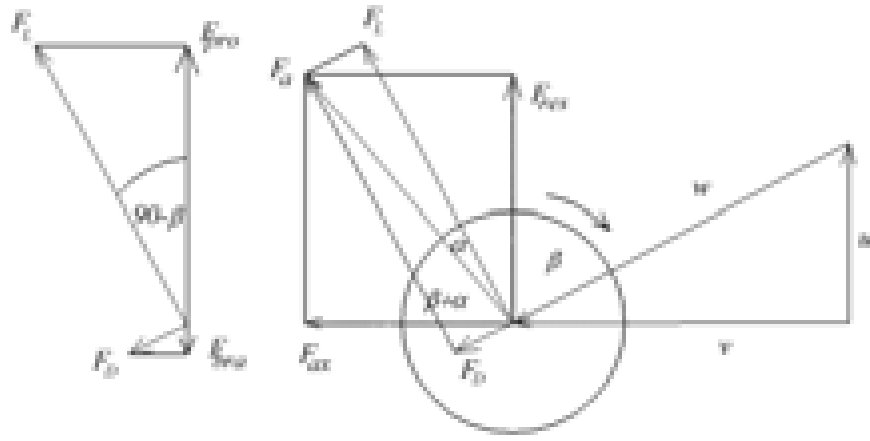
Fig. 5. Distribution of forces affecting revolving rotors under the influence of relative wind velocity w, where: v – wind velocity; u – rotor peripheral velocity for given r (distance from rotor axis); w – relative velocity of stream inflow into a rotor; F_L – lift force, F_D – drag force, F_a – resultant of these forces; F_{pro} – force propelling rotor; F_{bra} – force braking rotor; F_{res} – resultant of F_{pro} and F_{bra} i.e. force revolving wind turbine; F_{ax} – axis force.

Using fig. 5 and basic trigonometric dependencies one may derive formulas for forces affecting rotor from particular computational elements of the blade:

$$F_{bra(k)} = \cos \beta \cdot F_{D(k)}, \tag{7}$$

$$F_{pro(k)} = \sin \beta \cdot F_{L(k)}, \tag{8}$$

$$F_{bra(k)} = \frac{u}{w} \cdot F_D, \tag{9}$$

$$F_{pro(k)} = \frac{v}{w_k} \cdot F_{L(k)}. \tag{10}$$

The difference between F_{pro} and F_{bra} is nothing else but peripheral force causing the revolution of the wind wheel:

$$F_{res(k)} = F_{pro(k)} - F_{bra(k)} = \frac{1}{w_k}\left(v \cdot F_{L(k)} - u \cdot F_{D(k)}\right) \tag{11}$$

Torque and power of the designed wind turbine one can get by summing up the forces from particular computational elements of the blade:

223

$$N_u = \eta_a \cdot \eta_m \cdot i \cdot \sum_{k=1}^{n} F_{res(k)} \cdot u_k \; , \qquad\qquad (12)$$

$$M_u = \eta_a \cdot \eta_m \cdot i \sum_{k=1}^{n} F_{res(k)} \cdot r_k \; , \qquad\qquad (13)$$

where: N_u – power of wind turbine for a given wind welocity; M_u – torque of the designed wind turbine; n – number of computational elements that the blade was divided into; k – number of successive element; $F_{res(k)}$ – peripheral force for k element; u_k – peripheral velocity for k element; η_a – aerodynamic efficiency of wind turbine; η_m – mechanical efficiency of wind turbine.

Using one of the selected algorithms (maximalization of wind turbine power or maximalization of blade lift/drag ratio), program matches suitable blade rotations N_b for a given wind velocity v and rotational frequency N, computes forces affecting rotor and wind turbine mast, calculates force and torque of wind turbine. Subsequently, the program increases N value and repeats the calculations. The whole operation is repeated untill the further increase N value stops bringing any satisfying results.

2.4. Corrections of the computational model

The program tests showed that it made the error of approximately 200% for large N values. Below a corrective function used in the program is presented.

Coefficients C_D and C_L used in the program were obtained experimentally for different cylinders. Their dependency on Re is known only for very small α and some λ values. Consequently, we have not been able to use experimental dependencies $C_D(Re)$ and $C_L(Re)$, as in the case of wind turbines we use large α and a wide span of λ.

Experiments on rotating cylinders performed in wind tunnels included only cylinders rotating around their own axis. In our model, they revolve also around the axis of the wind turbine, so dependencies $C_D(N)$ and $C_L(N)$ are not known either. On the basis of dimensional analysis and experimental results obtained by Di Maria at al. [3] we have thus built the corrective function which takes the form:

$$\eta_a = a((G), Re, I_v, \alpha^{max})Z^2 + b((G), Re, I_v, \alpha^{max})Z + c((G), Re, I_v, \alpha^{max}) \qquad (14)$$

where: $a()$, $b()$, $c()$ – coefficients which need to be selected in such a way so that N_u and M_u are as much similar to experimental results as possible, with the same parameters of the environment and geometrical dimensions of the blade; (G) – geometry of the blade; Re – Reynolds number; I_v – intensity of wind turbulence; α_{max} – matched dimensionless parameter of blade rotation around its own axis; Z – dimensionless parameter responsible for the rotation of main rotor:

$$Z = \frac{\pi \cdot D \cdot N}{60 \cdot v} \qquad (15)$$

where D – wind turbine diameter.

Assuming: *(G), Iv, α_{max}* and *Re* as in Di Maria et al. [3] experiments.

The coefficients *a, b, c* were established minimizing the difference between experimental values and the results of the program.

3. Exemplary calculation results

Program enables comparison of simulation results with empirical curves obtained in wind tunnel and turbines previously designed by the user. The charts depicted below are exemplary results of the simulation.
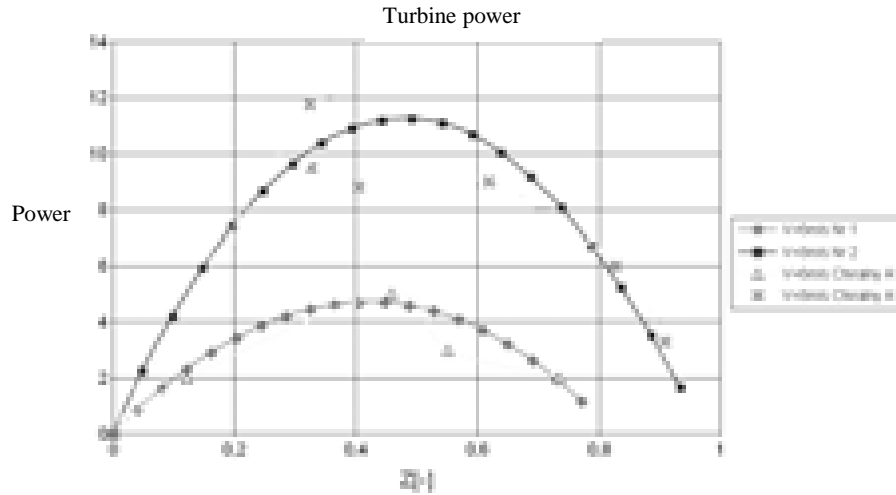
Fig. 6. Wind turbine power – comparison of program results and experimental data, where:
Z – dimensionless parameter responsible for the rotation of main rotor; *No 1* and *No 2* – program results (one-blade turbine); chiralic A1 – experimental results (one-blade turbine).
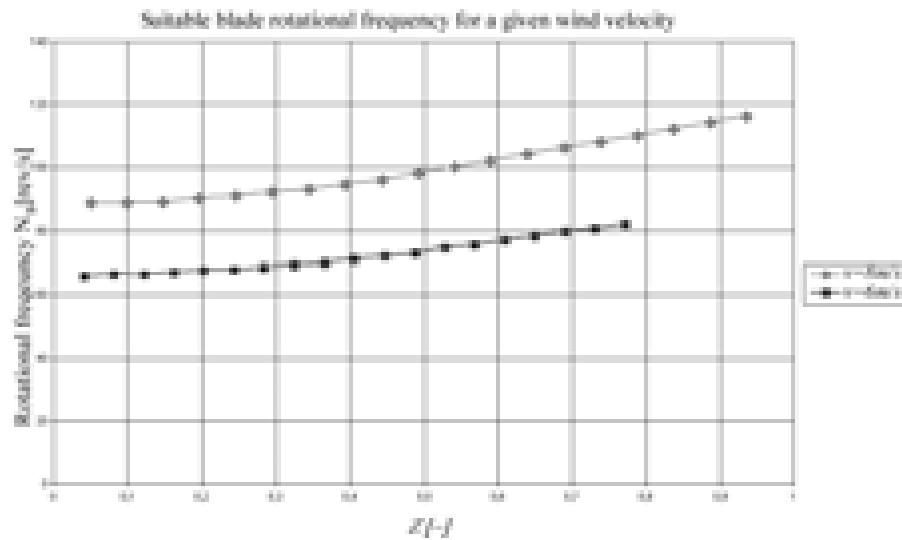
Fig. 7. Matched with respect to maximum at wind turbine power suitable rotational frequency N_b as a function of Z for two different wind velocity.

4. The construction of the model and studies in the wind tunnel

Using devices available in Wind Engineerig Laboratory the 1m – diameter model of the wind turbine was built. It is a single bladed wind turbine which allows for experiments with different shapes of the blades.

Fig. 8. The wind turbine in the wind tunnel – front view.

226

One of the problems which was overcome having very limited budget was the supply of power to the rotating engine. Problem was solved by mounting rolling bearings (fig. 6) which proved to be much more efficient than typical brushes used in DC motors.

Fig. 9. The shaft of the wind turbine model and the system supplying voltage to the rotating engine.

Another problem that we managed to solve was the measurement of power. Due to time and financial limitations we decided to use a friction brake. It allows for a relatively accurate measurement by a comparative method.

We experimented with numerous shapes of the blades made of aluminium and glass fiber. The film we enclosed shows only two examples of them.

The foregoing studies allowed to achieve several goals:

- We partially checked the correctness of the computer simulation written before.
- Using comparative method we proved experimentally that the modifications of the blade shape may bring promising results (fig 10).
- We expanded the simulation by the results of the measurements, which allow to apply for more funds for further research.

The following chart is the experimental comparison of the two turbines:

Classic – one-bladed Magnus wind turbine, 1.1 meter in diameter, two end fences,
Revised – one-bladed Magnus wind turbine aerodynamically improved, 1.1 m in diameter.

For technical reasons we compared those two turbines only at the weak wind speed (around 2-3 m/s). The power absorbed by the engine was established at a constant level. The curve shows that the wind turbine with the revised blade has a bigger torque because it can revolve about two times faster under the same load.

227
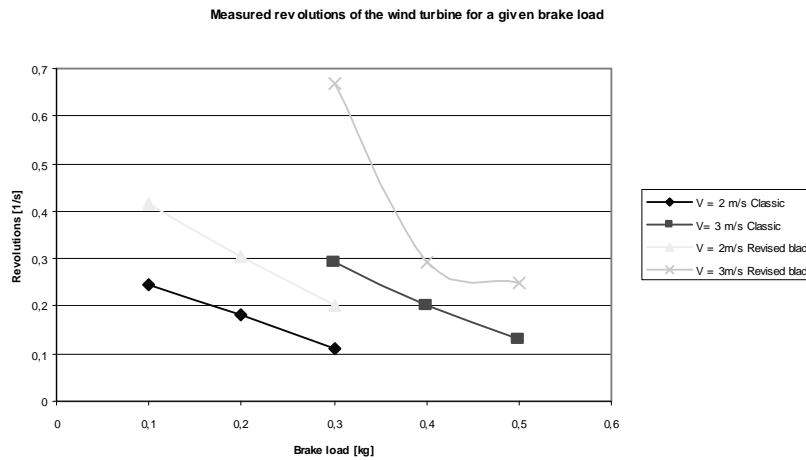
Fig. 10. Example results of the experimental comparison in the wind tunnel.

5. Conclusions

- As it can be observed in fig. 7, the program simulates the performance of the assumed wind turbine in a very good way.
- Using the research results, a series of simulation calculations for blades with densely arranged discs was performed [2,5]. The calculations concerned blades rotating around their own axis. The promising simulation results for blades in that configuration encourage to further comprehensive theoretical and experimental research.
- In further considerations concerning chiralic wind turbines it is necessary to perform series of experimental tests in wind tunnels aiming at validation of the presented computational model.

References
[1] Jagodziński W., *Silniki Wiatrowe*, PWT, Warszawa, 1959.
[2] Norwood J., *Rotors*, 21st Century Multihulls, Nr 2, 1996.
[3] Di Maria F., Mariani F. and Scarpa P., *Chiralic bladed wind rotor perfomance*, 2nd European and & African conference on wind engineering, Palazzo Ducale, Genova, Italy 22-26, 1997.
[4] Swanson W.M., *The Magnus Effect: A summary of investigations to date*, Journal of basic engineering, Nr. 83, 1961, 471-470.
[5] Thom A., *Effects of discs on the air forces on a rotating cylinder*, ARC R and M 1623, 1934.
[6] www.elektrownie-wiatrowe.org.pl/t_magnus.htm

OPTIMIZATION OF WIND LOADS AND OPERATING CHARACTERISTICS OF A VERTICAL AXIS WIND TURBINES WITH THE CONTROL MECHANISM OF BLADES

Vladymyr P. Kayan[*], Victor A. Kochin[*]

[*] Department of Information Systems in Hydro-aeromechanics and Ecology, Institute of Hydromechanics of National Academy of Sciences of Ukraine, Zelyabova 8/4, Kyiv, Ukraine.

1. Introduction

The wind is an inexhaustible source of energy on the Earth. Researches carried out in many countries have shown that modern wind-power electric plants can be effectively used in regions with the mid-annual wind speed exceeding $5 - 6$ m/sec. Today wind-power plants with horizontal axis windmills are the most widespread. Now maximum length of the blade of such a windmill (by estimations of experts) cannot exceed 60m, therefore the power of such windmills cannot exceed $5 \div 7$ MW [1]. It limits the ability of decreasing the costs of energy produced by a wind-power plant to be competitive. The most powerful wind-power plant of such type was built in Germany in 2005. Its power is equal to 5 MW, the length of blade is 61m, height of the tower 120m; the tower is installed in Northern sea at depth 40m. Wind power plants with vertical-axis wind turbines (VAWT - Darrieu rotor type) are free of such restrictions and their power can measure up to $10 \div 20$ MW, by estimations of experts.

Advantages of such wind turbines are the independence of their functioning from the wind direction, a two-basic fastening of the wind turbine axis instead of console fastening, a possibility to mount an energy consumer (an electricity-generator, a pump) in the basis of the wind-power plant (requirements for strength and rigidity of a support can be weaken), simplification of the design of blades and their fastenings, etc. A disadvantage of VAWT with blades fixed rigidly concerning crosspieces is the high velocity of self-starting of the turbine and lower rate of use of stream energy in comparison with a horizontal-axis windmill. As a result, designers have to supply such wind turbines with additional devices (an electric motor, Savonius rotor, etc.) to spinup the turbine and put it in operation.

The high speed of self- starting of VAWT arises because its vertical blades are fixed on horizontal cross-pieces rigidly and cannot create necessary magnitude and direction of aerodynamic forces on blades and, hence, sufficient torque on the shaft. Application in design of VAWT the control mechanism a position of blades allows to turn blades concerning crosspieces so that the magnitude and direction of aerodynamic forces on blades allow self- starting of VAWT even at the flow speed of $4 \div 5$ m/sec. Besides controlling the position of blades allows to improve considerably the operating characteristics of VAWT [2], to reduce the magnitude of aerodynamic drag of VAWT by some times.

229

2. Experimental installation and wind turbine models

In the late 1990th, a mechanism for controlling the position of VAWT blades during their movement on a circular trajectory [3] has been offered in Institute of Hydromechanics NASU (Kiev, Ukraine), on which the patents of Ukraine [4,5] have been issued.

With the purpose to study the features of work of VAWT with such mechanism to compare the obtained data with characteristics of classical VAWT (Darrieu rotor type) with blades fixed rigidly concerning crosspieces, the experimental installation (fig. 1) and several VAWT models were created. Researches were performed in the hydrotray of Institute, at flow velocities of $V_{av} = 0.3 \div 0.7$ m/sec.

The VAWT model with vertical shaft **1** was placed in the rectangular frame **2** which was hinging fastened to vertical racks **3** of rigid frames **4** in the hydrotray **5**. The flow working cross-section in the hydrotray near the location of VAWT model was $S=0.36$м² The rectangular frame **2** was connected with strain-gauge dynamometer **8** by means of the upright lever **6** and horizontal carrier **7**. Strain-gauge dynamometer **8** was rigidly fixed on the frame **4**. The VAWT model consisted of two disk crosspieces **9** parallel to each other, the connecting shaft **1** and blades **10.** Longitudinal axes of blades were parallel to the shaft **1** axis. The top of the vertical shaft **1** was connected to the flexible shaft **11**. Free end of the flexible shaft **11** with a calibrated spool was horizontally fastened to the side wall of the hydrotray **5**. On the upper cross timber of the frame **2,** the device **12** was mounted to measure the angular velocity of VAWT model. Velocity of the flow in the working cross-section was permanently measured with the speed-gage **13**.
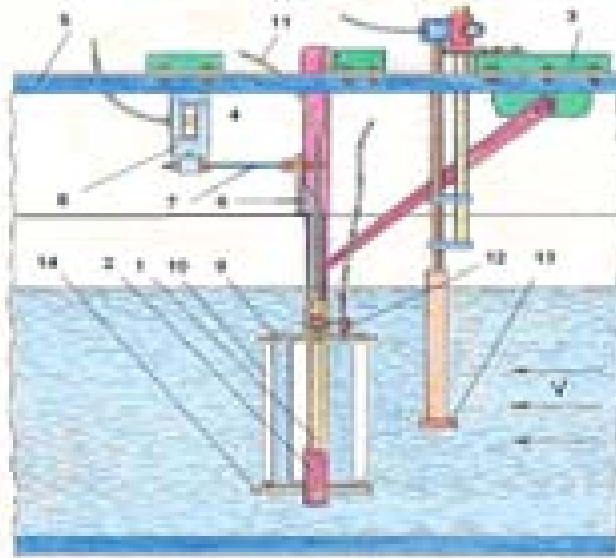
Fig. 1. The schematic drawing of experimental installation for research of VAWT models in hydrotray.

230

Three VAWT models with rectangular blades in the cross-section have been created. The blade profile was axisymmetric of the type NACA-0015 [6]. The VAWT models №1, 2 and 3 differed in the length of blades l_{bl} and radius R of installation of blades on crosspieces of VAWT model. The incidence of the blade profile chord to the tangent of the rotation circle was equal to $+4^o$ [6]. The VAWT models with 2, 3 and 4 blades were tested.

Key parameters of models are shown in table I.

The control mechanism for the blade incidence (fig. 1) included a disk **14** with a circular groove placed under the bottom disk crosspiece **9.** The disk **14** can move streamwise concerning the bottom cross timber of the frame **2**. Therefore there was some eccentricity "*e*" between the axis of shaft **1** of VAWT model and the center of circles on disk **14**. The blades **10** had two axes at the bottom face (the blade chord length is $b = 5 \times 10^2$ m, distance between axes is 0.36*b*). The forward axis was installed hinged on the bottom crosspieces of blades. The back axis passed freely through a crack in the bottom cross-piece of blades. The back axis had a ball-bearing at the end which was placed in the groove on the bottom disk **14**. Thus, at each certain magnitude of an eccentricity "*e*" the mechanism provided strictly defined position of the blade in time. The frequency of angular oscillations of blades concerning the forward axis was equal to the rotational speed of VAWT model.

Table 1.

Models blades	Length of the blade l_{bl}, m	Elongation of blades	Radius of installation of blades R, m
1	0.30	6	0.175
2	0.30	6	0.0875
3	0.15	3	0.0875

3. The equipment and technique of researches

Two-level automated measuring system for collecting and processing the experimental data was used in the analysis of parameters of VAWT models. The measuring system consisted of three measuring channels: 1) the channel of measurement of water flow velocity in the working part of hydrotray, 2) the channel of measurement of instantaneous magnitude of the hydrodynamic resistance force of VAWT model, 3) the channel of measurement of the rotational speed of VAWT model.

In the channel of the average flow speed, specially designed tube of hydrodynamic pressure connected to the differential pressure gauge " Motorola " MPXV5004DP was used as a primary converter. In the channel of measurement of instantaneous magnitude of the hydrodynamic resistance force, a strain-gauge dynamometer was used as a primary converter. In the channel of rotational speed, a magnetoelectric sensor was used as a primary converter.

The magnitude of torque on the shaft was determined by the weights lifted vertically at reeling-in a thread on the spool connected to the shaft **1** of VAWT model by the flexible shaft **11** (fig. 1).

First level of the measuring system was a digital storage oscilloscope on the basis of 12-digit 32-channel analog-digital converter L-264 of the manufacturer "L-Card". The analog-digital converter was an expansion card to an IBM compatible computer. Basic purposes of the first level are to collect and digitize data, to storage the data in non-volatile memory, to write protocols of measurements, rapid processing of the measured information.

Second level of the measuring system was an IBM PC compatible computer on the basis of Pentium-IV-2000 MHz. Basic aims of the second level of system were full post-processing of the collected data by the specified algorithm, graphical representation of the data, documenting and storing the measured information.

4. Technique of the experimental researches and post-processing of the measured data

The average flow velocity, V_{av}, ahead of VAWT model was set by regulating the fluid flow in the forward part of the hydrotray. Magnitude of the torque M on the shaft was determined by weights lifted vertically at reeling-in a thread on the spool connected to the shaft of VAWT model by the flexible shaft **11**. The rotational speed of VAWT model, n, and magnitudes of total drag, Rx, of VAWT model were measures at the specified values of flow velocity, torque M and eccentricity "e".

It is necessary to note, that at increase in the loading torque M on the turbine shaft (V_{av}=const), for all VAWT models the rotational speed of turbine, n, decreased and the value of this decrease depended on the magnitude of eccentricity and the design of models. Dependence of n on M was precisely linear in most cases.

Then calculation tables were composed, which allowed to calculate basic characteristics of VAWT models for each identified operating mode.

The coefficient of specific speed of turbine, Z, was determined as

$$Z = 2\pi n\, R\, /\, V, \tag{1}$$

where: n is rotational speed of the turbine, R = const is radius of blades installation on crosspieces of VAWT model, V is flow velocity.

It is necessary to note, that for a wind-power plant with an orthogonal rotor (i.e. the rotation axis is perpendicular to the wind direction) the coefficient of specific speed Z is equal to the ratio of the blade peripheral velocity, $V_{per} = 2\pi n\, R$, to the flow velocity V.

The use factor of flow energy C_p was determined as

$$C_p = 2\, P\, /\, \rho V^3 S, \tag{2}$$

where: $P = 2\pi n\, M$ is the useful power of a turbine, ρ is density of water, $S = 2\, R\, l_{bl}$ is area the of hydrodynamic (working) cross-section of a VAWT model.

232

The coefficient of turbine torque C_m was determined as:

$$C_m = C_p / Z. \tag{3}$$

The average and maximum coefficients of hydrodynamic drag of VAWT model, Cx_{av} and Cx_{max}, were determined according to formulas

$$Cx_{av} = 2\, Rx_{av} / \rho V^2 S, \tag{4}$$

$$Cx_{max} = 2\, Rx_{max\ av} / \rho V^2 S. \tag{5}$$

The coefficient of pulsations of loading on the shaft of VAWT model was determined as:

$$Kd = (Cx_{max} - Cx_{av}) / Cx_{av}. \tag{6}$$

Fig. 2 shows an example of hydrodynamic drag, Rx (in millivolts), recorded for the VAWT model №2 with 2 blades at flow velocity $V=0.6$ m/sec, at constant magnitude of torque on the shaft of the VAWT model.
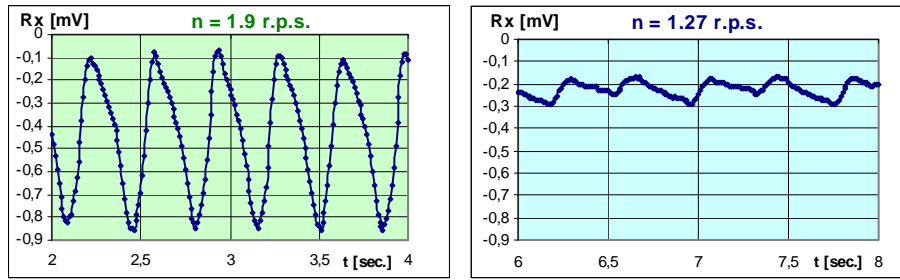
Fig. 2. Pulsation of magnitude of hydrodynamic resistance Rx of VAWT model №2 with 2 blades (V=0.6 m/sec and a loading torque on the model shaft M=0,065 Nm): a – rigidly fixed blades; b – controlled blades ($\varepsilon = 0.08$).

It is clearly seen that average hydrodynamic drag, Rx_{av}, and oscillations of hydrodynamic drag, Rx, are considerably smaller on the model with controlled blades (fig. 2b) in comparison with the same model with rigidly fixed blades (fig. 2a).

5. Results of experimental researches in a hydrotray

During 1st stage (in 2003, 2004) researches with a constant relative eccentricity of $\varepsilon = e/R = 0.08$ were performed.

233

Comparison of the use factors of flow energy C_p for models №1 and №2, which have only different radius of rotation ($R_{№1} = 2\ R_{№2}$), shows that model №2 is more preferable. Research of characteristics of all three VAWT models (at ε = const) in more detail and comparison with same geometrically similar with VAWT models with the blades fixed rigidly concerning cross-pieces are resulted [6,7].

During 2nd stage (in 2005, 2006) only model №2 was investigated in the hydrotray, with use of a device allowing to vary smoothly the relative eccentricity ε from 0 up to 0.14. It was noted, that at small flow velocity in the hydrotray ($V_{av} = 0.3 \div 0.4$ m/sec) and zero eccentricity ($e = 0$, blades are motionless relative the crosspieces) the VAWT model was not self-started. When the controlling disk was shifted by some "e", the VAWT model began to rotate and the greater was "e" the smaller was the speed of self-starting.

The researches have shown that for any magnitude of the specific speed coefficient, Z, there exist a maximum (fig. 3) in the functions $C_p(\varepsilon)$ and $C_m(\varepsilon)$ which describe the overall performance of VAWT model. It was revealed that the less the specific speed coefficient Z of VAWT model (i.e. the less rotation speed of VAWT model) the greater is ε_{opt} at which a maximum coefficients C_p and C_m are reached.

As soon as the dependence of the rotation speed n of VAWT model on ε at a constant power P on the shaft of the VAWT model is precisely of the kind shown in fig. 3, then it is possible to control the rotation speed n of VAWT model by changing the eccentricity "e".
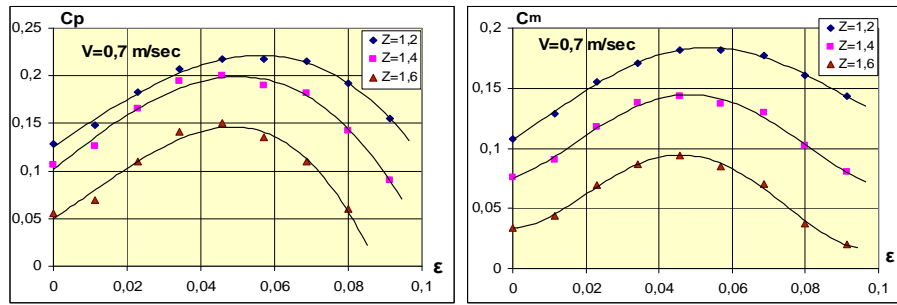
Fig. 3. Dependences of magnitudes of the use factor of flow energy C_p and the coefficient of torque C_m of VAWT model №2 from magnitude of relative eccentricity ε (flow velocity in hydrotray V=const) at varied values of the specific speed coefficient Z.

Measurements of the hydrodynamic resistance Rx of the VAWT model №2 have shown that control of blades of the VAWT model can essentially decrease the loading on the shaft of the VAWT model (fig. 2). Fig. 4a presents the experimental dependences of the coefficient of average hydrodynamic drag, Cx_{av}, depending on the relative eccentricity ε and the specific speed coefficient, Z, obtained at a constant flow velocity V in the hydrotray.

234
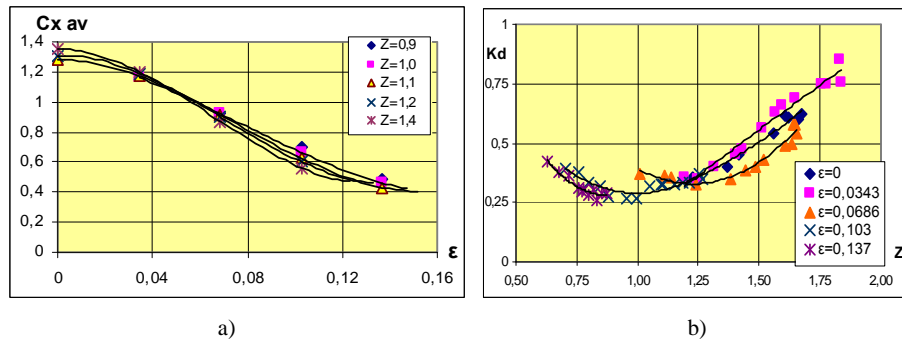
Fig. 4. The action of magnitude of relative eccentricity ε of control mechanism of blades on magnitude of coefficient of average hydrodynamic drag Cx_{av} on VAWT model shaft (*a*) and on its coefficient of pulsations of loading on the model shaft (*b*).

It appeared that all experimental data are well approximated by a 3rd order curve of the kind:

$$Cx_{av} = 513\,\varepsilon^3 - 110.15\,\varepsilon^2 - 0.765\,\varepsilon + 1.315 . \tag{7}$$

There are evident maximum (at $\varepsilon = 0$) and minimum in drag (at $\varepsilon = 0,15 \div 0,16$), thus Cx_{cp} decreases more than three times. Besides, the operating conditions of the VAWT model shaft essentially improve because with increasing eccentricity "*e*" at constant flow velocity the rotation speed n of turbine model decreases (i.e. the specific speed coefficient of turbine model, *Z*, decreases). It leads to a reduction of dynamic loads on the shaft by several times (fig. 4b). At that there is clear minimum of the coefficient of pulsations of loading, Kd, at $Z = 0.9 \div 1.0$.

6. Results of experimental researches in a wind tunnel

To confirm the results obtained with small models in a hydrotray, in 2006-2007 the team of the Institute of Hydromechanics together with "Prodmash" company (Melitopol, Zaporozhye region, Ukraine) designed a pattern of three-bladed VAWT with rated capacity of the shaft 1 kWt. In 2007 the VAWT with the blade control mechanism offered in Institute of Hydromechanics was tested in the wind tunnel of Kiev National Aviation University.

The wind turbine (fig. 5) has the following sizes - length of the blade $l_{bl} = 1.955$m, length of a blade profile chord $b = 0.41$m, the blade profile is NACA-0015, elongation of the blade $\lambda = 4.77$, radius of blades installation on cross-pieces of VAWT $R = 0.8$m, diameter of the control circle $D = 1.45$m, area of the working cross-section of VAWT

235

$S = 3.13 \text{m}^2$, the fill factor $\sigma = 3b/2R = 0.77$, maximum magnitude of the relative eccentricity $\varepsilon = 0.12$ (12 %). The velocity range during first stage of experimental researches made from 5 to 13 m/sec.

Fig. 5. The pattern of VAWT in wind tunnel.

For creation of the loading (braking) torque on the VAWT shaft, four brake clutches manufactured by "INTORQ" (Italy) with the brake torque on the shaft of 7.5; 15; 30 and 60 Nm accordingly were used. Clutches were installed on the top of the additional basic shaft outside the working part of the wind tunnel (not shown in fig. 5). There was also placed a two-component strain-gauge dynamometer for measurement of mutually perpendicular horizontal forces on the top shaft bearing of VAWT. The rotation speed of VAWT was determined by means of a tachometer manufactured by "Promsat" company (Ukraine) and an inductive contactless sensor manufactured by "Sensor" (Russia). Linear displacements of the control circle along the direction air stream were carried out by means of a electric motor with a worm reductor and controlled by a sensor of motion manufactured by "Honeywell" (USA).

During measurements there were set the air flow speed, V, in the working part of the wind tunnel, the brake torque M on the shaft of VAWT and eccentricity "e" of the center of the control circle relative the axis of rotation.

236

Fig. 6 represents dependences of the rotation speed of VAWT, n [1/sec], from the loading torque M and relative eccentricity e/R at constant velocity of air stream V. The character of the presented curves $n(e/R)$ convincingly shows that for any possible magnitude of the loading torque on the shaft there is certain magnitude of the relative eccentricity e/R, at which the rotation speed n of VAWT is maximum (digits 1 through 11 in fig. 6 and 7 corresponds to the loading torque $M = 2.5$; 10; 17.5; 25; 32.5; 40; 47.5; 55; 62.6; 70.2 and 77.8 Nm, correspondingly). These maximum values of n at various M=const lay on a straight line (fig. 6).
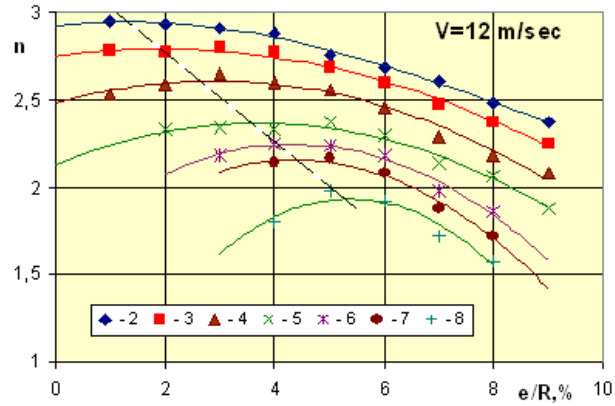
Fig. 6. Dependences of a rate of rotation speed n [1/sec] of VAWT from magnitude of relative eccentricity e/R at flow velocity V=12 m/sec at any magnitudes of loading torque M (curves 2 – 8).
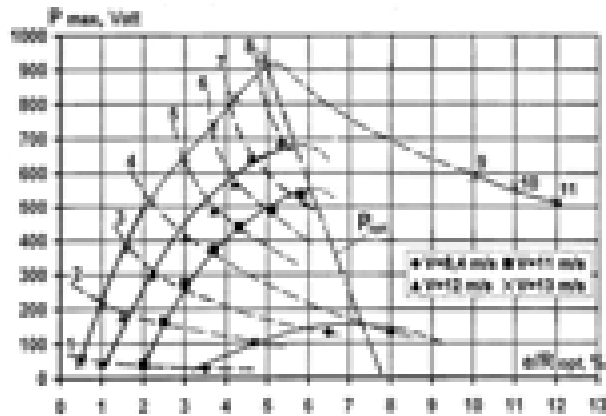
Fig. 7. Dependences of magnitudes of the maximum power P_{max} on VAWT shaft from magnitude of relative eccentricity e/R at any flow velocity V and loading torque M (curves 1 – 11).

237

Maximum values of n at a specified loading torque M match correspond to maximum power supplied by the shaft of VAWT. Dependences of the maximum power, P_{max}, on the shaft of VAWT from the relative eccentricity $\varepsilon = e/R$ at various flow velocity, V, in the wind tunnel are presented in fig. 7. The dashed lines 1 - 8 connect points of equal values of the loading torque M. Maxima on the curves corresponding to the velocities specified in the figure lay on a line P_{opt}, which shows the necessary magnitude of relative eccentricity ε for obtaining a maximum power at given velocity of the wind stream.

The characteristics our triple-bladed VAWT with the control mechanism of blades can be compared with the characteristics of VAWT with two blades fixed rigidly concerning crosspieces with the following sizes: $l_{bl} = 2.55$m, $b_{bl} = 0.4$m, and the working area of the turbine $= 7.65$ m ^{2}. Tests of thas VAWT were performed in the end of 80s both in the wind tunnel in TsAGI (Moskow) and in natural conditions [9]. In the latter case the distance from the bottom edge of the blade to the land surface was 2.8m. At the air stream velocity of V=11 m/sec, that VAWT produced 65 Watt per 1m^2 of the working cross-section in the wind tunnel, and 85 Watt in natural conditions. The corresponding parameter for our VAWT in the wind tunnel was 170 Watt, i.e. 2.5 times higher. Thus we can expect that it full-scale tests at the specified wind velocity it is possible to obtain more than 200 Watt per 1m^2 of the VAWT working cross-section.

Fig. 8 shows the measurements of the wind load on the VAWT shaft. It should be noted that the amplitude of oscillation of both the longitudinal and transverse forces registered by two-component tensometer, and accordingly the coefficient of pulsations of horizontal loading on the VAWT shaft, Kd_x, were much higher than those obtained for small VAWT models in water stream (see fig. 4b). It can be explained by technological features of manufacturing of blades because of which the weight of each blade was 20 kg and the inertial forces became dominating in comparison with aerodynamic ones. For experiments in the hydrotray the model blades were made of acrylic plastic and have minimum weight in water. The rotation speeds of VAWT models were twice less than that in the wind tunnel; therefore pulsations of the longitudinal load due to hydrodynamic forces dominated the inertia. The force Rx measured with a tensometer was recalculated to a point on the VAWT axis corresponding to the location of the fastening of the shaft of the top crosspiece. Fig. 8a presents the calculation results for the coefficient of average wind load, Cx_{av}, at various magnitudes of the loading torque $M = 2.5 \div 40$ Nm (points 1 - 6), in dependence on the relative eccentricity e/R of the control circle. It appeared that irrespective of the loading torque M, most of values Cx_{av} lay on the same (bottom) curve. Values of Cx_{av} corresponding to the loading torque of $M = 10$ and 40 Nm lay on the top curve. It can be explained by that, as it appeared, engaging of one of the brake electromagnetic clutches affected the tensometer (additional longitudinal force appeared).

Of big interest were plots of the coefficient of resistance Cx_{av} in dependence on the power output, P, of the VAWT. Fig. 8 shows the VAWT resistance at M=const (curves 2-6),

238

at varying relative eccentricity e/R. It appeared that it is possible, when maintaining the power level on the VAWT shaft close to its maximum for a given magnitude M, to reduce the VAWT resistance Rx. For example, at M=10 Nm and constant power of P=160 Watt (P_{max} = 170 Watt) on the VAWT shaft, it is possible to lower Cx_{av} by 3-3.5 times due to variation of the eccentricity 'e', and by 2 times at M=40 Nm and P=430 Watt.

a) b)
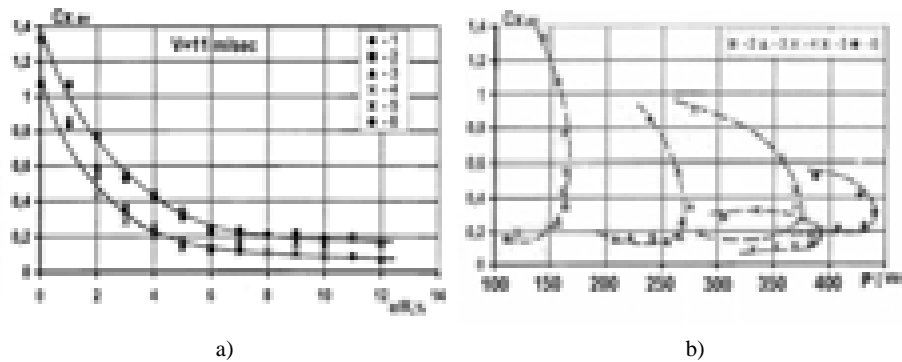
Fig. 8. Dependences of magnitude of coefficient of average longitudinal wind load Cx_{av} at any magnitudes of loading torque M (points 1-6) from magnitude of relative eccentricity e/R (*a*) and from magnitude of power P which obtain on VAWT shaft (*b*).

Thus, using the control mechanism of VAWT blades, which is very simple constructively and technologically, one can essentially lower the wind speed of self-triggering, decrease both the wind load on the VAWT shaft and amplitude of its oscillations, considerably improve operating characteristics of VAWT (the working torque on the VAWT shaft especially increases), in comparison with VAWTs of same sizes with blades fixed rigidly concerning crosspieces. It gives a hope that wind-power plants with turbines of the above-described design will be rather effective as pump plants for taking and swapping oil or water.

References

[1] Denisenko O.G., Kozlovski G.A., Fedosenko L.P., Osadchy A.I., *Trasformation and utilization of wind energy*, "Technique", Kiev, 1992, 176p. (in Russian).

[2] Avallone E. A., Baumeister T., *Standard Handbook for Mechanical Engineers*, 9-th Ed., McGraw Hill., 1978, 645p.

[3] Parhisenko V.M., Tsyganiuk A.I., Tshehovcov O.V., *The experimental researches of kinematic and dynamic characteristics of rotary wind energy converters with active controls of blades*, The bulletin of the Donbass State Academy of Construction and Architecture: The engineers problems of wind action on constructions and buildings, 1999, №6 (99), pp. 149-153. (in Ukrainian).

239

[4] Bojko P.M., Glushko V.M., Dovgy S.O., Kayan V.P., Parhisenko V.M., Tsyganiuk A.I., *Rotor of wind power plant*, Patent of Ukraine №58189A, F03D 7/06, 2003. Publ. 15.07.03. Bull. №7. (in Ukrainian).

[5] Kayan V.P., Dovgy S.O., Bojko P.M., Lebid O.G., *Wind power plant*, Patent of Ukraine №16097 on usefull model, F03D 3/00, F03D 7/06. – 2006. - Publ. 17.07.06. Bull. №7. (in Ukrainian).

[6] Guly S.V., Eremejev I.D., Krashanica Ju.A., Usik Ju.F., Tchmovsz V.V., A*erodynamic optimization of vertical axis wind turbine model*, The bulletin of the Donbass State Academy of Construction and Architecture: Wind action on constructions and buildings, 2001, №4 (29), pp. 149-153. (in Russian).

[7] Dovgy S.O., Kayan V.P., *Researches of hydroaerodynamic of wind rotor models with vertical axis of rotation*, Applied hydromechanics. – Kiev, 2004, v.6, №3, pp. 76-80. (in Russian).

[8] Dovgy S., Kayan V., Kochin V., *Experimental Researches of Characteristics of Windrotor Models with Vertical Axis of Rotation*, In: Wind Energy – Proceedings of the Euromech Colloquium, Berlin, Springer, 2007, pp.183-186.

[9] Zubkovsky S.L., Ljather V.M., Fjodorov M.M., Tsvang L.R., *Interaction of wind stream with wind power*, Physics of atmosphere and ocean (Bulletin of AS of USSR), 1990, v.26, №9, pp.899-905. (in Russian).

240

PRODUCTIVITY OF WIND TURBINES
IN THE CENTRAL POLAND REGION

Tomasz Walczak[*], Elżbieta Kossecka[*]

[*] Institute of Fundamental Technological Research, Polish Academy of Science,
Świętokrzyska 21, 00-049 Warsaw, Poland.

1. Introduction

For detailed analysis of the wind turbine productivity at a given site, many years' wind speed data is of prime importance. With such a data, it's possible to make a thorough study of time variations of the produced energy and also examine fluctuations of the seasonal and annual outputs. If only monthly or annual averages of wind speed are known, statistical techniques may be applied, and wind turbine energy production may be predicted assuming standard (Rayleigh or Weibull) probability distribution function [1, 2, 3, 4, 5].

The power output of a wind turbine varies with wind speed and every wind turbine has a characteristic power performance curve. The power curve gives the electrical power output as a function of the hub height wind speed. Power curves for existing machines can normally be obtained from the manufacturer.

In this paper, results of the efficiency analysis for selected models of wind turbines, in the climate conditions of Central Poland, are presented. As the representative meteorological data set results of measurements of wind speed in Warsaw were used.

2. Wind energy resource in the Central Poland region

The wind power per unit area, P_w, or wind power density, is a function of the air density ρ and wind speed v, and is given by:

$$P_w = \frac{1}{2} \rho \, v^3 \, .$$

(1)

Energy production of wind turbines is normally predicted for standard conditions of atmospheric pressure and temperature (sea-level, 15ºC, air density 1.225 kg/m^3). The wind speed at hub height is usually significantly higher than measured at anemometer height, due to wind shear. The power law represents a simple model for the vertical wind speed profile; its basic form is [1, 2, 3, 4]:

$$v_2 = v_1 \left(\frac{z_2}{z_1} \right)^{\alpha}.$$ (2)

v_1 is the wind speed at height z_1, v_2 is the reference wind speed at height z_2, and α is the wind shear exponent.

The power law exponent α depends on various parameters, in particular on the surface roughness, wind speed and air temperature. It is a common practice in estimating wind resources, to assume a constant value of α, depending on surface roughness and time of averaging of the wind speed measurements.
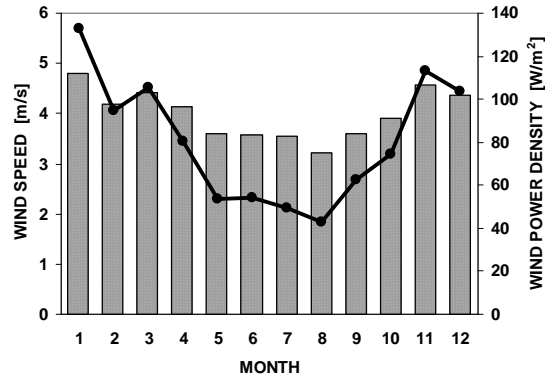
Fig. 1. Monthly averages of the wind speed and wind power density;
Warsaw – Okęcie, data period 1976 – 1985.
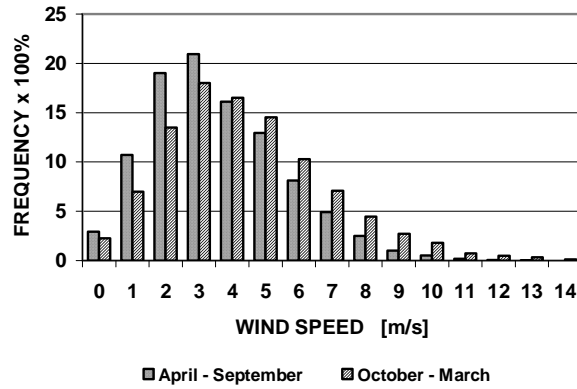
Fig. 2. Frequency distribution of the wind speed at Warsaw – Okęcie station in the Summer and
Winter season (data period 1976 – 1985).

The map of wind resources in the area of Poland, presented in the book by H. Lorenc [1], shows that wind conditions around Warsaw are rather typical for the large region of Central Poland.

Meteorological data used in the present work for analysis of wind turbines, come from the National Institute of Meteorology and Water Management, and were collected over period of 1976-1985 at the weather station Warsaw – Okęcie Airport. Wind speed is measured at 12 m, measurement values are 10 min averages. Surface roughness for the terrain around this station is of class 1, and the corresponding value of α is 0.14 [1].

Table I. Estimated mean values of the wind speed at different height [m/s]
(Warsaw – Okęcie, data period 1976 – 1985; $\alpha = 0.14$).

Season	10 m	30 m	50 m	70 m	100 m
Summer	3.52	4.10	4.41	4.62	4.86
Winter	4.27	4.98	5.35	5.60	5.89
Year	**3.89**	**4.54**	**4.88**	**5.11**	**5.37**

Table II. Estimated mean values of the wind power density at different height; [W/m^2]
(Warsaw – Okęcie stadion, data period 1976 – 1985; $\alpha = 0.14$).

Season	10 m	30 m	50 m	70 m	100 m
Summer	53	84	105	120	140
Winter	97	154	191	220	255
Year	**75**	**119**	**148**	**170**	**197**

Annual average wind speed at Warsaw – Okęcie station is 4 m/s, annual average wind power density is 81 W/m^2, and average wind energy density per year is 710 kWh/m^2. Values given by H. Lorenc in [1], calculated for the period 1966 – 1990, are slightly higher. In principle, locations with good wind conditions are those with average wind speed at least of 5 m/s. In Poland, such situation is only at the Balic Sea coast and in the northern part of the Suwałki region. Southern and western regions of Poland have, in general, poor wind resources; for many locations yearly average wind speed is below 3 m/s.

Monthly averages of the wind speed and wind power density at the station Warsaw – Okęcie are represented in figs 1 and 2. Tables I and II show estimated seasonal values of the wind speed and wind power density at different height.

3. Wind turbine energy production analysis

Common models of wind turbines, easily available at European market and designed for inland sites, with medium wind speeds, were selected for the energy production

analysis. Their basic parameters are collected in table III. Two small turbines, with rated power below 100 kW, and four large ones, with rated power around 800 kW and 2000 kW, were considered. Energy production has been estimated using the power curves given by the manufacturers [6, 7, 8].

Table III. Models of wind turbines considered and their basic parameters.

Wind turbine model	Rated Power [kW]	Hub height [m]	Diameter [m]
VERGNET GEV 6/5	5.2	18	6
VERGNET GEV 15/60	65	40	15
ENERCON E53	800	73	52,9
GAMESA G58	850	71	52
ENERCON E82	2000	108	82
GAMESA G90	2000	100	90
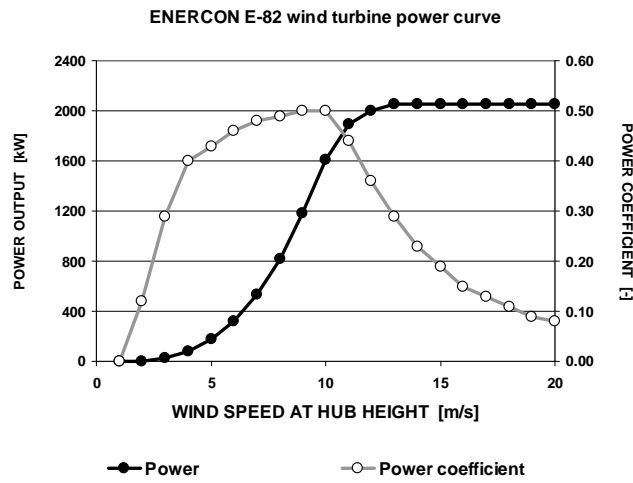
Fig. 3. Power curve of the wind turbine ENERCON E-82.

Fig. 3 presents an example power curve for the wind turbine model ENERCON E-82. Power coefficient is the ratio of the electrical power output to the product of wind power density and rotor swept area. Fig. 4 presents predicted monthly average power for this turbine, with tower version 108 m, in the site under consideration. Predicted annual energy production and mean power output for all six turbines are collected in table IV.

244

ENERCON E-82 wind turbine; hub height 108 m
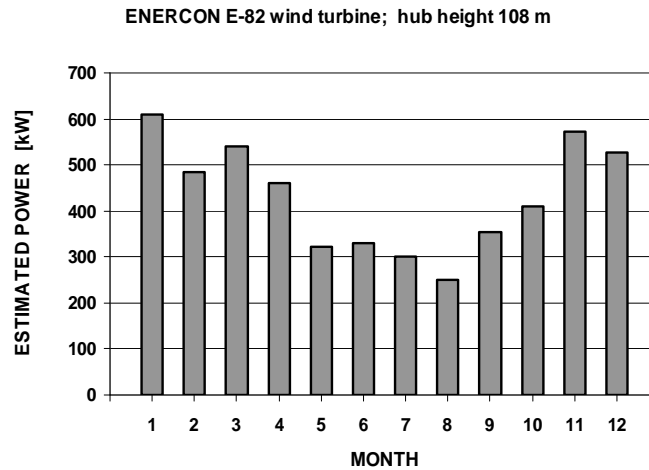
Fig. 4. Predicted monthly average power for the wind turbine ENERCON E-82
(Warsaw – Okęcie; wind speed data period 1976-1985).

Table IV. Predicted annual energy production and mean power output for six models of wind turbines in Warsaw – Okęcie; (wind speed data period 1976-1985.

Wind turbine model	Rated Power [kW]	Mean power [kW]	Annual energy [MWh/yr]
VERGNET GEV 6/5	5.2	0.6	5.3
VERGNET GEV 15/60	65	5.9	51.6
ENERCON E53	800	156	1 369
GAMESA G58	850	163	1 430
ENERCON E82	2000	429	3 761
GAMESA G90	2000	441	3 863

4. Conclusions

Results of the analysis indicate that power production performance of wind turbines with given rated power, from different manufacturers, is approximately the same.

In climate conditions of the Central Poland region, predicted mean power of small turbines, with comparatively low towers, is about 10% of the rated power, whereas predicted mean power of big turbines, with towers of 100 m or above that height, is about 20% of the rated power.

245

Predicted average output of the wind turbines is approximately twice as high in the Autumn – Winter season (October – March), as compared with the Spring – Summer season (April - September).

References

[1] Lorenc H., *Wind structure and wind energy resources in Poland.* [in Polish], Serie: Meteorology No. 25, Institute of Meteorology and Water Management, Warsaw 1996.

[2] Manwell J.F., McGowan J.G., Rogers A.L., *Wind Energy Explained*. Theory, Design and Application, Chichester, 2006.

[3] Burton T., Sharpe D., Jenkins N., Bossanyi E., *Wind Energy Handbook*, John Wiley & Sons, Ltd., Chichester, 2001.

[4] *Clean Energy Project Analysis: Wind Energy Project Analysis Chapter*, RETScreen® Engineering and Cases Textbook, www.retscreen.net.

[5] *Surface meteorology and Solar Energy Data Set*, NASA's Earth Science Enterprise Program; http://eosweb.larc.nasa.gov

[6] Manufacturer's Website: www.enercon.de

[7] Manufacturer's Website: www.gamesa.es

[8] Manufacturer's Website: www.vergnet.fr

THERMAL AND FIRE
INFLUENCES
ON BUILDINGS, STRUCTURES
AND MATERIALS

247

ACTION ON STRUCTURES AND USERS DURING FIRE

Mirosław Kosiorek[*]

[*] Department of Fire Research, Building Research Institute,
Ksawerów 21, 02-656 Warsaw, Poland.

1. Introduction

Fire is defined as thermal decomposition of flammable materials uncontrolled in time and space. The basic physical and chemical reaction taking place during a fire is the very fast oxidation process accompanied by the releasing of significant amounts of heat. The action of fire on a building has unique effects.

Unlike other phenomena causing unique effects [1] fire has the following two characteristic features:

- In majority of cases (excluding atmospheric discharges or secondary effects of earthquakes, for example) it is caused by human activity,
- Its action does not have the character of direct mechanical influence, but changes the environment of a building and its surroundings, and the mechanical action on the structure is secondary.

Fire changes:

- Thermal conditions,
- Pressure,
- Chemical composition of the atmosphere (reduced oxygen contents and toxic combustion products),
- Visibility (smoke).

The factors influence the building structure and users (fig. 1), and also the building surroundings. In some cases, like oil refinery fire or large chemical plant fire, the fire can be the cause of extensive environmental pollution.

The environment condition changes over time and is different in individual rooms and parts of a building. This condition depends on numerous factors and the structure's ability to carry loads under strong thermal influences, properties of building partitions, spatial solutions, the quantities of stored flammable materials, time and placement of flammable materials, fire suppression systems (sprinkler systems, extinguisher systems) and smoke and heat exhaust systems installed in the building designed for extinguishing fire and limiting the propagation of smoke.

The fire safety level is determined by numerous different technical, organizational, cultural, sociological and psychomotorical factors. It depends not only on the building spatial and structural solutions, but also on the used construction methods and materials, quality of electrical and heating systems, ability to handle materials and equipment, technical culture and cautiousness of the users, reaction of users and groups to threats, organization, skills and equipment of the rescue teams, accessibility of the building on fire.
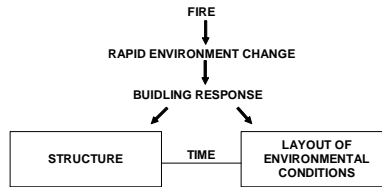
Fig. 1. Action of fire

Fire safety status at the given time $t = t_p$ is defined by:
- Structure status,
- Environment status.

When analyzing the action of fire one should distinguish:
- Action on users: Thermal (through heat radiation and convection), physiological – due to change of atmosphere contents and visibility,
- Action on structure: thermal (through heat radiation, convection and, in to a smaller extent, conduction), mechanical (caused by increasing pressure) and chemical (corrosive products of combustion and following reactions).

2. Thermal action of fire

The EU documents[1], [2] specify the following thermal action levels (fig. 2):
- Small source of fire (e.g. burning cigarette or match),
- Individual items on fire (e.g. bin, couch),
- Developed fire.

Thermal actions Fire start Developed fire
 Small source of fire Single burning items Temperature increase Cooling
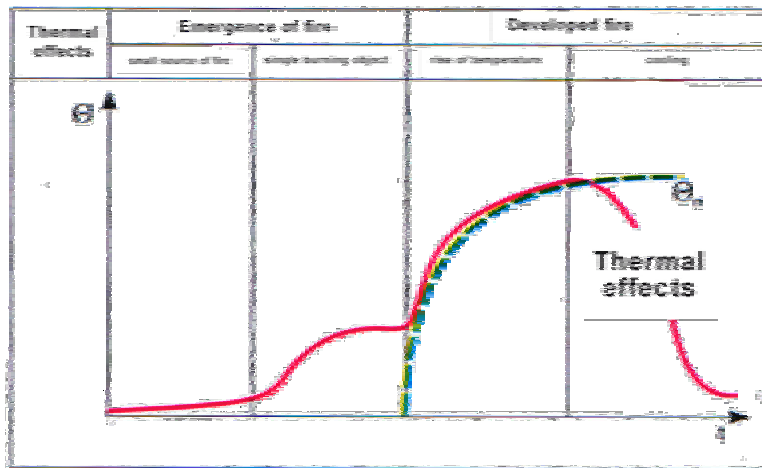
Fig. 2. Thermal action levels. Θ – temperature, t – time, Θ_{gn} – temperature according to standard dependence, Θ_g – temperature in the room.

250

Four [2], [3], so-called nominal, time-temperature dependencies have been assumed (t – time in minutes, Θ_g – temperature of gases in °C) when describing the developed fire (fig. 3); they are used to determine the classes of construction products:

1) standard curve (N):

$$\Theta = 345 log \ (8t + 1) + 20, \tag{1}$$

2) external fire curve (E)

$$\Theta = 660[1 - 0.687 \exp \ (-0.32t)0.313 \exp \ (-3.8t)] + 20, \tag{2}$$

3) hydrocarbon curve (H)

$$\Theta = 1080[1 - 0.325 \exp(-0.167t) - 0.675\cdot \exp \ (-2.5t)] + 20, \tag{3}$$

4) dependencies of smoldering fire

$$\Theta_g = 159t^{0,25} + 20 \quad \text{for } 0 < t \le 21, \tag{4}$$
$$\Theta_g = 345 \log[8(t - 20) + 1] + 20 \quad \text{for } t > 21.$$
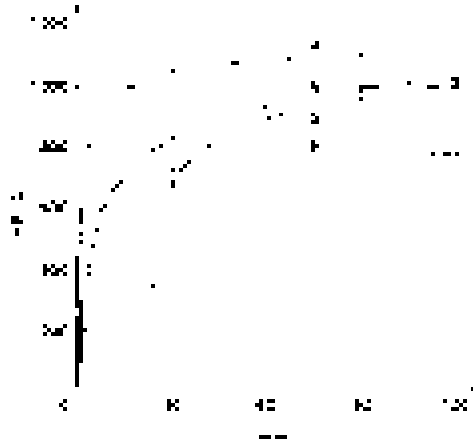
Fig. 3. Conventional fire scenario H – hydrocarbon dependence, N – standard dependence, S – smoldering fie dependence, E – external fire.

Standard dependence (N) defines the changes of temperature in a room during the burning of lignocellulose materials (furniture, clothing, paper).

External fire curve (E) defines the temperature acting on external wall by fire rising out of a window.

Hydrocarbon dependence (H) defines the course of drilling rig or fuel and grease storage fires.

Smoldering fire dependence (S) defines the action of fire on products that can loose

251

their properties with the initial slow temperature increase (swelling gaskets and paints containing organic constituents that can burn out during the initial stage).

In case of rooms the area of up to 500 m² and up to 4 m high, without any openings in the ceiling, assuming complete combustion of materials presenting the fire load, one can adopt parametrical temperature-time dependence (fig. 4), in the growth stage, based on a model developed in Sweden, according to the following formula:

$$\Theta_g = 20 + 1325(1 - 0.324e^{-0.2t^*} - 0.204e^{-1.7t^*} - 0.472e^{-19t^*}), \tag{5}$$

where: t^* – parameter depending on time, thermal properties of partitions, coefficient of the geometry of openings in walls, fire load, Θ_g – temperature inside the room.
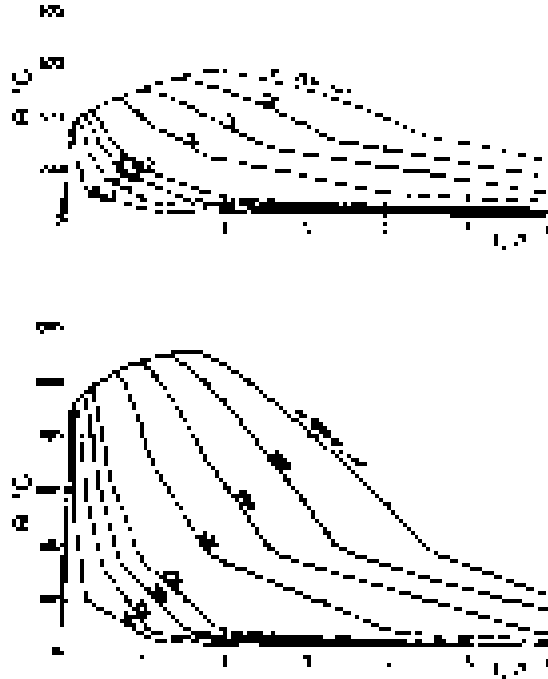
Fig. 4. Examples of parametric temperature-time dependencies q – fire load density

One can also assume a scenario of localized fire or models based of fluid mechanics formula [3].

Changes of temperature during a fire in a road tunnel is described in fig. 5. The power of a fire in case of a burning automobile is approximately 15 MW, whereas in case of a tank truck with fuel it can reach 300 MW.

252

Fig.5. Curves showing temperature changes during a fire in road tunnel:
RWS – Dutch curve– road tunnel [3]; RABT/ZTVI – German curve –road tunnel [3]
RABT/ZTVII – German curve – railway tunnel [4].

The effect of thermal action on the structure is, generally speaking, the loss of strength and modulus of elasticity, degradation of construction material resulting in a change of cross-section (carbonization of wood, concrete cracking and dropping off), indirect mechanical action, i.e. internal forces and torques caused by linear expandability and temperature gradient and the inhomogeneity of mechanical properties. The temperature of $300 \div 400°C$ does not usually cause the loss of structure's load bearing capacity. In case of people, the temperature of 120°C causes 1st degree burns after approximately 8 minutes, and after $2 \div 3$ minutes in case of 200°C. Temperatures exceeding 200°C result in burns to the respiratory tract. The critical value is 60°C. Human body can withstand the thermal radiation of $2\ kW/m^2$ for longer time, but at $3.5\ kW/m^2$ this time is reduced to just 60 seconds (fig. 6).

Exposure time (S) / Heat flux (kW/m2)
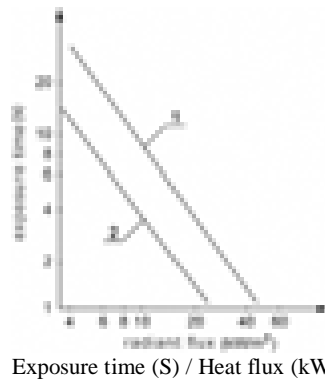
Fig. 6. Heat radiation action on human body [5]: 1 – boils, 2 – pain.

3. Smoke and toxicity of combustion products

Smoke is an aerosol consisting of a mixture of air and combustion products, particulates and liquid dispersed in gaseous phase. Smoke changes person's motoric abilities by limiting visibility, having irritating and toxic effect, and contributing to oxygen deficiency. It also acts through increased temperature and radiation.

253

During a fire all these factors can have a combined effect on the building users, however, the research work conducted so far does not allow to determine their interactions or synergism of chemical compounds.

Toxicometric indicators (W_{LC50SM}), calculated in such a way that the toxic effect is the sum of effects of individual smoke components, are used for assessing the toxic hazard. The basic toxic components of smoke are: carbon monoxide (CO), carbon dioxide (C_2), hydrogen cyanide (HCN), nitrogen dioxide (NO_2) and hydrogen chloride (HCl). The lethal concentrations of these compounds for 30 minutes exposure time are as follows:

- CO – 3.75 g/m^3,
- HCN – 16 g/m^3,
- CO_2 – 196.4 g/m^3,
- NO_2 – 0.205 g/m^3,
- HCl – 1.0 mg/m^3.

At the following concentrations the loss of functional takes place after 5 minutes: CO – $6000 \div 8000$ ppm, HCN – $120 \div 200$ ppm, CO_2 – $7 \div 8\%$ and oxygen content reduced to $10 \div 13\%$.

With flameless thermal decomposition caused by the lack of oxygen, combustion is not complete and CO_2/CO ratio is close to 1. Such conditions, with poor ventilation, lead to so called asphyxiation. Carbon monoxide bonds the hemoglobin, forming carboxyhemoglobin and causing lack of oxygen in the organism. Similar is the mechanism of HCN influence. The difference is that deadly effects of the HCN influence will occur with much lower doses than in the case of CO_2.

Influence of CO_2 consist in hyperventilation effect i.e. increase in the breath rate, which causes the quick accumulation of CO_2 within the organism. In case of low oxygen concentration, the presence of CO_2 may have a positive effect by oxygen supply.

In the initial stage of a fire, with high air supply the HCN, CO and other toxic compounds burn producing atmosphere with low toxicity. In case of oxygen deficiency the thermal decomposition products are highly toxic.

On the developed fire stage, after flashover, there is usually oxygen deficiency and overpressure in the room. Decomposition products, usually containing CO and HCN, spread through the building causing hazards over large areas.

Examples of toxicity indicators values for combustion products of some materials and smoke generating ability of these materials, according to the tests conducted at ITB, are shown in table I.

There is no correlation between the smoke growth rate and combustion product toxicity, i.e. these value are independent.

Critical value of environment in a specified area is the level of action that the subject being acted upon can withstand. The following basic objects for the actions can be distinguished:

- structure (including building partitions),
- user,
- equipment (e.g. information carriers),
- installations.

254

The structure and installations can be adapted to expected level of actions. Also equipment which needs particular protection can be protected by specially designed means. These possibilities do not concern the users, who are affected by:

- temperature of fire atmosphere,
- heat radiation,
- toxic and irritating products of combustion,
- decrease of oxygen content,

and visibility is limited by smoke absorbing and dispersing of light.

The critical time, which is the time needed to leave the small compartment of the dimensions: 5 x 4 m, and 2,5 m high, with assumed visibility range of not less than 3 m at the level of 1.5 m - is about 2 minutes.

The temperature of 120°C causes the burns of 1st degree after about 8 minutes, and the temperature of 200°C causes the burns of respiratory system. The temperature of 60° C may be considered as critical. The human being can tolerate the heat radiation of 2 kW/m^2 for a fairly long period of time, but radiation of 3.5 kW/m^2 - for only about 60 s (fig. 3).

Table I. Toxicity and smoke growth rate indicators (examples [5], [6]).

Toxicity		Smoke growth rate	
WLC50SM ≤ 15	– high toxicity	Y M ≤ 7 m^2/(kg·s)	– small
15 < WLC50SM ≤ 40	– medium toxicity	7 < Y M ≤ 20 m^2/(kg·s)	– medium
WLC50SM > 40	– low toxicity	Y M > 20 m^2/(kg·s)	– intensive

Material	Toxicity	Smoke growth rate
Flexible PU foam	21.9; 12.5	11.0; 30.5
Rigid PU foam	12.6; 10.9	7.06; 12.1
Styrofoam	56.4	15.0
Silicone rubber	65.8	3.0
Natural rubber	7.0	3.7
Hard fiberboard	41.7	9.0
Soft fiberboard	36.2	6.5
Oak, acacia	~53.0	~2.0
Poplar	42.6	21.7
Pine, spruce	~41.0	~3.5

4. Fire safety critical conditions

The idea of fire safety is closely connected with the model of regulations and two extreme cases of their formulation can be distinguished:

1) in form of orders and bans relating to the certain conventional characteristics,

2) in form of performance requirements.

In the first case the regulations, to a large extent, have a formal and legal character. The measure of fire safety in this case is the conformity of the constructed building with the regulations. This measure, as a conjunction of requirements having different significance can receive two values only:

255

0 – if any of the regulation requirements is not fulfilled, i.e. the building does not provide the fire safety,

1 – if all of requirements are fulfilled, i.e. the building is safe.

In second case, the measure of fire safety is the time necessary to reach the critical value of:

1) structure of the building,

2) environment in particular parts of the building.

Critical value of the structure is the state, in which a loss of load bearing capacity that takes place due to effects determined by emergency combination. If the level of thermal effect is known, we have the tools to determine the temperature fields in the structure and its mechanical condition in optional interval of time. The rules for the design are codified in Eurocodes. They allow for verification of construction load-bearing capacity in case of fire with different levels of mechanical analysis and with various models of thermal effects. Some of the provisions established in Eurocodes could be discussed, but basically we have the rules for determination of design values of mechanical actions and design values of physical parameters. It may be assumed that design thermal actions are determined by nominal or parametric curves and in this range we can speak about ultimate states of the structure under fire conditions, in relation to load-bearing capacity, displacement and deflection.

For other scenarios of fire development design thermal actions are not determined.

Design values of fire environment action on construction works other than structure are not yet defined.

However, the fire environment has an action on the structure and the users, different properties of this environment or different action levels are considered in both cases. Critical structure condition and critical condition of the environment due to its action on the users are also separated in time and space. Because of this the methodology of analyzing both the critical conditions is also different; the structure is designed taking into consideration the expected actions, whereas when taking users into consideration, the building has to be designed so that in a specific time in some locations the critical environment condition will not be exceeded. The structure can be designed taking into consideration the expected thermal actions of a fire environment, and from he viewpoint of the users, the environment must be adapted in such a way that it will be possible to leave the threatened area within specific time (fig. 7).
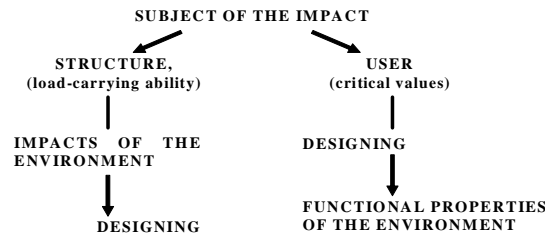
Fig. 7. Relation from the viewpoint of the subject of the impact.

Essential condition in achieving required level of fire safety is to assure load bearing capacity of the structure for the specific period of time, which is $t \geq t_{kr}$.

The t_{kr} value may be determined in various ways, depending on the type of building's intended use. For example, it can be the time needed to evacuate the occupants or the time needed to start the firefighting and rescue operation. In certain buildings, like high-rise buildings or hospitals, the complete evacuation of which is impossible, this time can extend over the entire duration of the fire.

The requirement for assuring building structure load bearing capacity over specific time $t \leq t_{kr}$ can be defined according to the following formula:

$$E_{fi,d} \leq R_{fi,d,t} \tag{6}$$

where: $E_{fi,d}$ – effects of actions in case of fire (generalized internal forces), $R_{fi,d,t}$ – load bearing capacity of the structure defined according to time, e.g. by limit values of generalized internal forces.

Due to the action of fire environment on users and evacuation possibilities in individual parts of buildings determined by generalized coordinates κ the critical value of environment condition should not be exceeded during the specified period of time $t \leq t_{\kappa,kr}$. Usually κ indicates the discrete areas in the building, like the room where fire has originated, corridor, staircase that can be designated as k_i.

The time $t_{kr,i}$ is different for individual areas κ_i, because users usually leave the room where the fire started and the room directly threatened first, then reach the stairwell through a corridor. So if we assign the times needed to leave the compartment, corridor and staircase as t_{e1}, t_{e2} and t_{e3} respectively, the following inequalities should be fulfilled for particular areas k_i :

$$\begin{aligned} t_{\kappa1,kr} &\geq t_{e1} \\ t_{\kappa2,kr} &\geq t_{e1} + t_{e2} \\ t_{\kappa3,kr} &\geq t_{e1} + t_{e2} + t_{e3t} \end{aligned} \tag{7}$$

This means that the time required to reach the critical environment condition in a given area should be greater than time required for evacuation from this area.

Do to the action on users and optical characteristics of smoke, at which evacuation is possible, the following environment parameters are significant: temperature, heat flux, toxic and irritating products concentration, decreased oxygen content, reduced visibility. If we define the set of safe values of environment condition parameters as $\Phi_{i,j}^{b}(t)$ and the set of values defining the environment condition as $\Phi_{i,j}(t)$, then the value $\Phi_{i,j}(t)$ should belong to the set $\Phi_{i,j}^{b}(t)$:

$$\Phi_{i,j}(t) \subset \Phi_{i,j} \tag{8}$$

for $t \leq t_{\kappa i,kr}$ for every area i and size j, at the same time the condition (6) should be fulfilled for $t \geq \max t_{\kappa i,kr}$.

Table II shows critical values according to parameters.

Table II. Critical value.

Parameter	Critical value
Environment temperature	$\theta \approx 60°C$
Thermal radiation	$W_{kr} \approx (2 \div 2.5)\ kW/m^2$
Oxygen content	$O_2 \approx (10 \div 15)\%$
Smoke concentration (visibility, toxicity)	Np. 1:1000

Due to the evacuation and safety of rescue teams the essence of the problem consists in not allowing the fire to reach the developed stage in certain areas (fig. 2) or to extend the duration of first two stages and at the same time not exceed the environment limit condition at specific level (fig. 8).
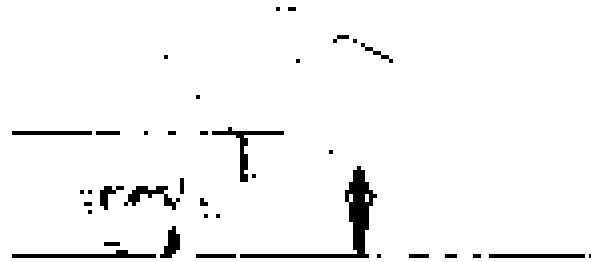
Fig. 8. Principle of assuring evacuation routes from large retail spaces
1 – smoke curtain.

References
[1] Kosiorek M., *Oddziaływanie pożaru na budynek*. XIX Konferencja Naukowo-Techniczna „Awarie budowlane". Maj 1999. Tom 1: Referaty problemowe.
[2] *Interpretative document to Directive 89/106/EEC on construction products. Basic requirement No. 2 Fire safety*. ITB, Warszawa 1995.
[3] *PN-EN 1991-1-2:2006 Eurocode 1: Actions on structures - Part 1-2: General actions - Actions on structures exposed to fire*.
[4] Lönnemark A., Ingason H., *Gas temperatures in heavy good vehicle fires in tunnels*. Fire safety Journal, Volume 40, September 2005 (p. 506-527).
[5] Klote J.W., James M.A., *Principles of Smoke management*. ASHRAE, SFPE.
[6] Kolbrecki A., *Badanie pożarowego zagrożenia toksycznego*. Prace ITB nr 2-3 (58, 59), Warszawa 1986.
[7] Kolbrecki A., *Zagrożenie dymem w pożarach budynków*. Prace ITB nr 3 (67), Warszawa 1998.

258

MODELING OF HEAT TREATMENT AND WELDING PROCESSES OF STEEL ELEMENTS

Marcin Gajewski[*], Stanisław Jemioło[*]

[*] Institute of Structural Mechanics, Faculty of Civil Engineering,
Warsaw University of Technology, Armii Ludowej 16, 00-637 Warsaw, Poland.

1. Introduction

Taking into consideration the phase change phenomena in metals during unbalanced heat transfer is an essential issue in description of forming metal elements through casting, processes such as heat treatment, especially setting, stress relaxing and tempering, etc. and in the description of welding process [1-4, 8]. Thermo-mechanical properties of each metal phase in steel elements are in many situations very different and can determine the utilitarian role of the product, see [4, 5, 7]. First attempts of theoretical description of phase change processes in metals started in the forties of the previous century, compare source articles quoted in [2, 3]. From the mid-twentieth century in areas such us material science and metallurgy the standard procedure for estimation of metal alloys properties are analysis of so-called phase balance graphs and graphs of cooling/heating made for different temperature velocity, [4]. These data, rational setting of chemical composition, proper heat and mechanical treatment technology allow to design metal alloys with needed properties. First theoretical works considering coupled problems of nonlinear thermo-metallurgy were published in the eighties of previous century, but effective numerical applications were made in last ten years, e.g. [7, 8]. The main goal of this work is formulation of an initial-boundary problem of unbalanced heat transfer including phase transformations and coupled with mechanical fields as well as application of finite element method for tasks of cooling/heating and welding of steel structural elements.

In the paper theory of elasto-plastic materials combined with thermo-metallurgical phenomena is used, [2, 3]. This approach can be treated as formulation with weak coupling of thermo-metallurgical effects with mechanical fields. The main consequence of such formulation is that the mechanical field has no impact on phase transformation process in considered material. It is worth emphasizing, that tasks analyzed in this work are "strongly" nonlinear and finding their analytical solution is impossible. The FEM system SYSTUS-SYSWELD is now one of few commercial software, which can be used for simulation of considered tasks.

2. Theoretical formulation of coupled thermo-mechano-metallurgical problem

The equation of unbalanced heat transfer with enthalpy function and latent heat in following form

$$\rho c \dot{\theta} - \operatorname{div}\big(\lambda(\theta)\operatorname{grad}\theta\big) + \sum_{j \neq i} L_{ij} A_{ij} = 0 , \tag{1}$$

is used in theoretical formulation. In eq. (1) $\theta = \theta(\mathbf{x}, t)$ is an unknown temperature field, ρ is material density, c is specific heat, λ is thermal conduction coefficient, L_{ij} is a latent heat during phase transformation $i \to j$, A_{ij} define amount of i-th phase, which was transformed into j-th phase.

We establish that material density $\rho = \widetilde{\rho}(\mathbf{x})$ is not varying with respect to time, $\dot{\rho} \equiv 0$. In order to describe the fact that material consist of various phases which can transfer into each other we are using mixture theory. In general we have N material phases with phase proportion p_k (in volume sense), where $\sum_{k=1}^{N} p_k = 1$. That means that we have:

$$\rho(p_k, \theta) = \sum_{k=1}^{N} p_k \rho_k(\theta), \quad c(p_k, \theta) = \sum_{k=1}^{N} p_k c_k(\theta) = \sum_{k=1}^{N} p_k \frac{dH_k(\theta)}{d\theta}, \quad \lambda(p_k, \theta) = \sum_{k=1}^{N} p_k \lambda_k(\theta) \tag{2}$$

and $\rho_k(\theta) > 0$, $\lambda_k(\theta) > 0$, $p_k \in [0,1]$. Phase transformations can depend among other things on temperature, temperature velocity and parameters describing steel microstructure. For each unknown p_k field the kinetic equations are formulated in the following form:

$$\dot{p}_i = -\sum_{j \neq i} A_{ij}\big(\theta, \dot{\theta}, p_i, p_j\big), \qquad i, j = 1, \ldots, N \quad , \qquad \sum_{k=1}^{N} \dot{p}_k = 0 . \tag{3}$$

The latent heat is evaluated on the basis of enthalpy function for i-th and j-th phase

$$L_{ij}(\theta) = H_j(\theta) - H_i(\theta). \tag{4}$$

For proper formulation of unbalanced heat transfer problem we need Dirichlet and Naumman (for temperature and heat flux) boundary conditions with compatibility conditions, for details cf. [2, 3].

The deformation of steel element depends on the history of thermal loading and phase transformations. Of course such deformed element has to fulfill local balance

260

equations, Cauchy geometrical relationships between displacement vector field and strain tensor field and assumed constitutive relationships which define each individual part of strain velocity field:

$$\dot{\boldsymbol{\varepsilon}} = \dot{\boldsymbol{\varepsilon}}_E + \dot{\boldsymbol{\varepsilon}}_P + \dot{\boldsymbol{\varepsilon}}_\theta , \quad \dot{\boldsymbol{\varepsilon}}_P = \dot{\boldsymbol{\varepsilon}}_{PC} + \dot{\boldsymbol{\varepsilon}}_{P\gamma} . \tag{5}$$

The strain velocity tensor $\dot{\boldsymbol{\varepsilon}}$ we divide additively into three parts: elastic $\dot{\boldsymbol{\varepsilon}}_E$, thermal $\dot{\boldsymbol{\varepsilon}}_\theta$ and plastic one $\dot{\boldsymbol{\varepsilon}}_P$ with incompressibility assumption $\mathrm{tr}\dot{\boldsymbol{\varepsilon}}_P = 0$. Elastic part is evaluated from isotropic Hook's relationship where:

$$E = \sum_{k=1}^{N} p_k E_k(\theta), \quad \nu = \sum_{k=1}^{N} p_k \nu_k(\theta) . \tag{6}$$

Velocities of thermal strain tensor we obtain from relationship,

$$\dot{\boldsymbol{\varepsilon}}_\theta = \sum_{k=1}^{N} p_k l_k(\theta) \dot{\theta} \, \mathbf{I} , \tag{7}$$

where l_k are thermal expansion coefficients. The thermal expansion coefficient functions (similarly like other thermo-mechanical data) are approximated via piece-wise linear function distinguishing two group of phases i.e.: α phases (bainite, perlite, ferrite and martensite) and γ phase (austenite), cf. [4]. Plastic strain velocity consists of two parts: $\dot{\boldsymbol{\varepsilon}}_{PC}$ which results from associated flow rule

$$\dot{\boldsymbol{\varepsilon}}_{PC} = \lambda \frac{\partial f}{\partial \boldsymbol{\sigma}} , \quad \lambda \geq 0 \tag{8}$$

and $\dot{\boldsymbol{\varepsilon}}_{P\gamma}$ caused by austenite phase transformation. In (8) we assume Huber-Mises yield condition,

$$f(\boldsymbol{\sigma}) = \sqrt{\frac{3}{2} \mathrm{tr}(\mathbf{s} - \mathbf{r})^2} - \sigma_P = \sigma_z - \sigma_P = 0 , \quad \text{where } \mathbf{s} = \boldsymbol{\sigma} - \frac{1}{3}(\mathrm{tr}\boldsymbol{\sigma})\mathbf{I} . \tag{9}$$

In eq. $(9)_1$ the yield stress $\sigma_P(e_p, \theta)$ is a function of temperature and plastic strain intensity. Deviator $\mathbf{r}$ describes standard kinematic strain material hardening. Yield stress for steel as a function of temperature can be expressed as

$$\sigma_P(\theta) = [1 - f(p_\alpha)] \sigma_\gamma(\theta) + f(p_\alpha) \sigma_\alpha(\theta) , \tag{10}$$

261

where $f(p_\alpha)$ is a corrective function (with values from 0 to 1) and

$$\sigma_\alpha(\theta) = \sum_{k=1,k\neq\gamma}^{N} p_k \sigma_{Pk}(\theta). \tag{11}$$

In this paper we employ following relationship expressing strain velocity $\dot{\varepsilon}_{P\gamma}$, as a consequence of Leblond model assumption, cf. [4, 5]:

$$\dot{\boldsymbol{\varepsilon}}_{P\gamma} = -\frac{3}{2} Kh\left(\frac{\sigma_z}{\sigma_P}\right)\ln(p_\gamma)\dot{p}_\gamma \mathbf{s}, \tag{12}$$

where K is a coefficient of plasticity caused by martensitic transformation, and h is a corrective function, see also SYSWELD manual [9].

3. Preparation of thermo-mechano-metallurgical data for 16MnCr5 steel

Detailed information about preparation of thermo-mechano-metallurgical data for chosen steels can be found in our papers [2, 3] and in SYSWELD manual [9]. It is worth noting here that it is necessary to know: specific heat, density, thermal conduction coefficients, thermal expansion coefficients, elasticity constants and yield stresses for each phase as a function of temperature, cf. figs 1-4. Additionally, parameters and material functions in kinematic equations can be established from metallurgical data i.e. standard steel heating and cooling diagrams. In typical low-carbon or low-alloyed steels four characteristic phases can be distinguished: phase 1 (mixture of ferrite and perlite), phase 2 (bainite), phase 3 (martensite) and phase 4 (austenite).
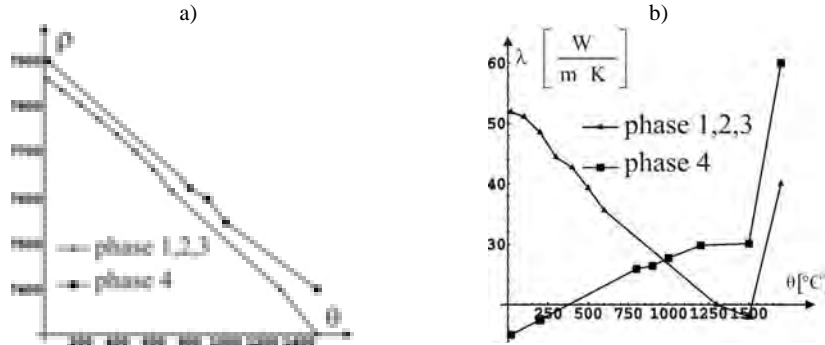
Fig. 1. Density (a) and thermal conduction coefficient (b) for each particular phase of 16MnCr5 steel as a function of temperature (phases 1,2,3 are described with the same function).

262
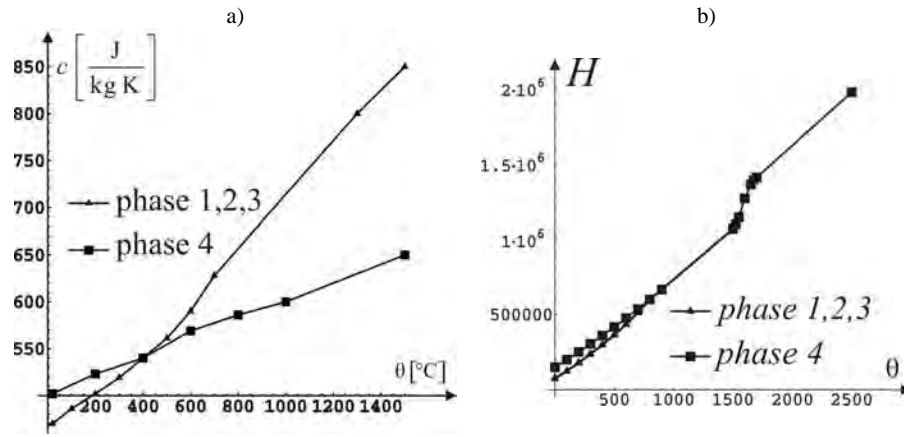
Fig. 2. Specific heat (a) and enthalpy (b) for each particular phase of 16MnCr5 steel as a function of temperature.

During heating (so called astenitizing) following phase transformations are possible: mixture of ferrite and perlite can change into austenite (1→4), bainite into austenite (2→4) and martensite into austenite (3→4). However during cooling possible transformations are as follows: austenite into ferrite and perlite (4→1), austenite into bainite (4→2) and austenite into martensite (4→3). Preparing data on a basis of IT (Isothermal Transformation diagrams) and CCT (Constant Cooling Transformation diagrams) is very laborious and require application of nonlinear optimization methods. Basic verification of metallurgic data can be carried out through reproducing IT and CCT diagrams using numerical solutions of kinetic phase transformation equations and comparing with experimental data. As an example at fig. 3 the theoretical CCT diagram for typical low-alloyed 16MnCr5 steel was shown.

In numerical calculations assumption was made, that elasticity constants: Young moduli and Poisson ratios for all steel phases are identical functions of temperature, what is a rational simplifying assumption. As an example at fig.4a Young modulus as a function of temperature is presented. Functions of yield stresses σ_{Pk} for each particular phase as a function of temperature are shown at fig. 4b (martensite has the highest yield stress in room temperature).

263
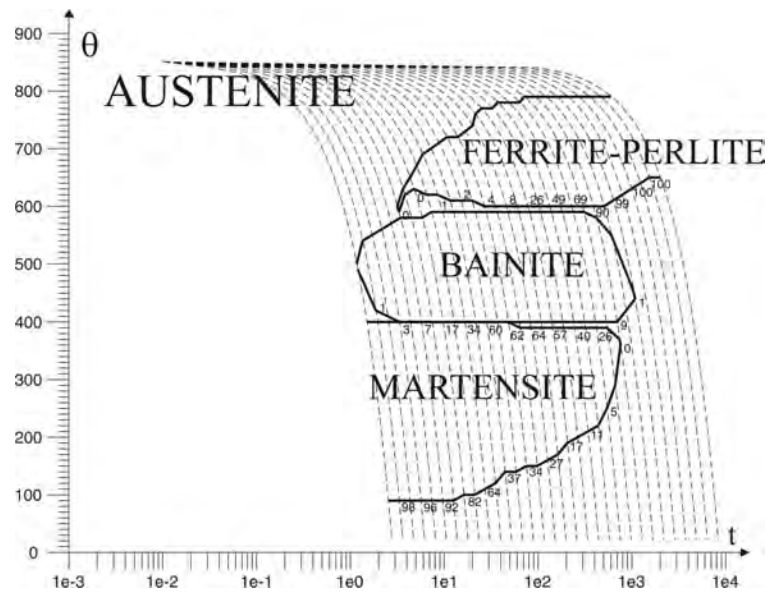
Fig. 3. CCT diagram (obtained from theoretical model).

a)   b)
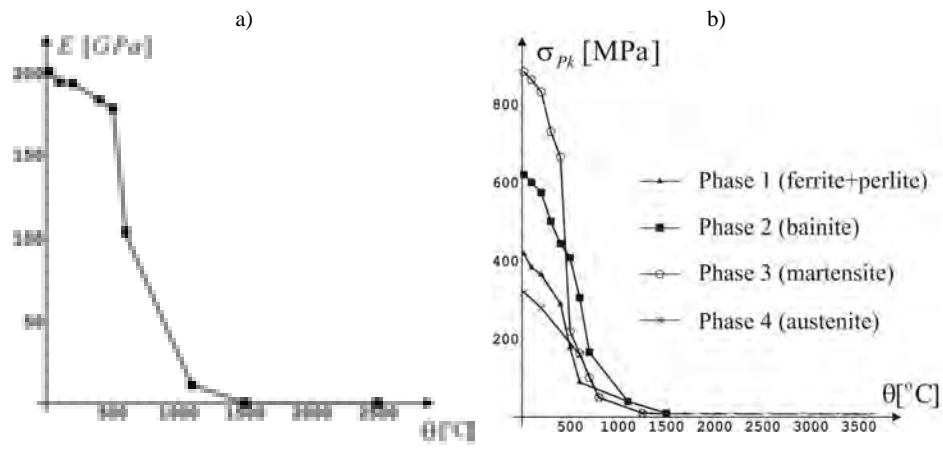
Fig. 4. a) Young modulus and b) yield stress for each particular steel (16MnCr5 grade) phase, as a function of temperature.

264

4. Modeling of heat source for welding simulations

Suitable selection of moving heat source model is a key problem in FEM modeling of welding. Additionally, an important numerical problem (because of high temperature gradients and suddenly happening phase changes around fusion zone) is achieving a proper temperature distribution and determination of so called heat affected zone.

In literature, for example [7,8], a lot of place is devoted to heat source modeling taking into account: way of heat inducing (arc, laser, MIG, TIG, gas welding, etc.), geometry, efficiency of heat source in front of and after electrode, electrode path and welding speed.

For arc welding simulations Goldak [7,8] proposed heat source model as a function (13):

$$Q(x,y,z,t) = \eta \frac{6\sqrt{3}f_\alpha W}{abc_\alpha \pi \sqrt{\pi}} e^{-\frac{3x^2}{a^2}} e^{-\frac{3y^2}{b^2}} e^{-\frac{3((vt)-z)^2}{c^2}}, \tag{13}$$

where W is a heat source power [W], Q intensity of heat source [W mm^{-3}], a, b, c_α dimensions in [mm] characterizing region of fusion zone in material, $f_\alpha, \alpha = 1,2$ are a division coefficients for heat intensity before and after electrode, v welding speed [mm s^{-1}], t time (steering parameter) [s], η heat source efficiency.

In FEM simulations the heat source intensity in all integration points belonged to whole region described by geometrical data marked at fig. 6 is set according to (13). Establishing these parameters, heat source power and move velocity for (13) allows for verification of model and data. Model (13) with obtained parameters should give a temperature distribution at the surface of the plate analogues to this showed at fig. 5.
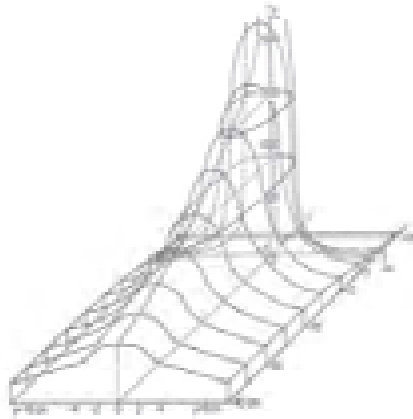
Fig. 5. Approximate temperature distribution at the plate surface for submerged arc welding (*I*=1170 A, *U*=33V, *v*=0.5 cm/s).
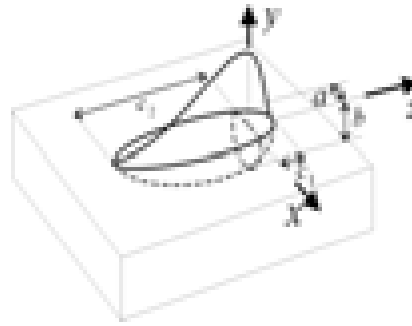
Fig. 6. Geometrical parameters for heat source model proposed by Goldak.

265

5. Numerical simulations

5.1. Heat treatment of steel elements – gear quenching in water

Cooling of steel gear with 28 teeth was modeled as three dimensional FEM task. Gear heated up to 900°C was cooled in water to achieve the temperature of 20°C (constant in the whole element). It was established that the body was treated in temperature 900°C for so long that, the phase structure is pure austenitic. Then the process of gear cooling in water starts and volume phase proportions are monitored in subsequent time moments. Thermo-mechanical data for these analysis were taken from [2, 3] for steel grade 16MnCr5. Because of the symmetry only a part of gear was modeled. FEM mesh consists of 29500 elements with linear displacement approximation.

After 900s of cooling the final temperature was obtained with accuracy of four digits. Some example results for volume phase proportions at the end of cooling process are shown in fig. 7. There are no graphs for ferrite, perlite and austenite because the volume proportion for these phases is very low.

a)   b)
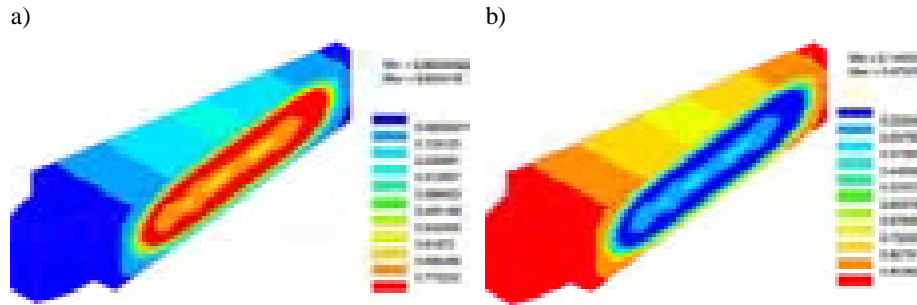
Fig. 7. Contour graphs of volume phase proportion of:
a) bainite, b) martensite after complete cooling process of gear.

Presented process of heat treatment can be called surface tempering process. Martensite is a steel phase of the highest hardness, thus tempering process gave expected results.

5.2. Plate thermally loaded with moving heat source- modeling of butt joint welding

Steel plate (16MnCr5 grade with data shown in point 3) with dimensions $l = 200$ mm and $h = 15$ mm, see fig. 8 is analyzed. Plate was loaded with a moving along AB line heat source modeling thermal influence from arc welding. In such situation realistic temperature distribution around electrode was shown at fig. 5. Parameters for Goldak model heat source (cf. fig. 6 and equation (13)) are as follows: W=2800W, a=4.45mm, b=6.5mm, c_1=3mm, c_2=20mm, v=4mm s^{-1}, η=0.6, f_1=0.8, f_2=1.2.
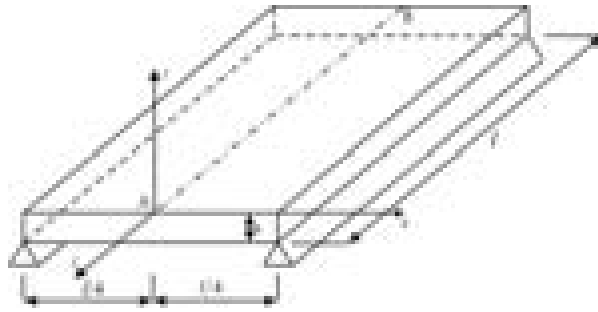
Fig. 8. Plate geometry, displacement boundary conditions and heat source path (AB).
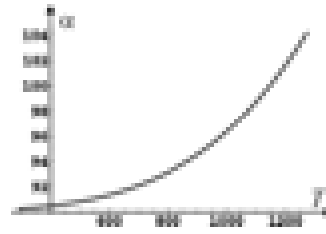
Fig. 9. Heat transfer coefficient in convection boundary condition on the plate surfaces as a function of absolute temperature (α $\left[\text{W/(m}^2\text{K)}\right]$).

During determination of initial conditions it was assumed that at the beginning plate temperature is $20\,^\circ$C and its structure is austenitic (so austenite phase proportion for t=0s is 1.0). Plate is loaded with heat source which cause heating some plate regions above melting temperature of considered steel. Plate is cooled because all the time the convective and radiation boundary conditions are active, according to the relation $q = \alpha\left(\theta_0 - \theta\right)$ with parameter α presented at fig. 9.

Steel with austenitic structure at the beginning in some regions is changing its structure because of phase change phenomena depending on temperature and temperature velocity. Heat source is moving through distance l during 50s. Then 3200s is needed to achieve thermal balance in considered plate. Some chosen results are shown at fig. 10 and fig. 11. Contour graphs of bainite and martensite proportion after achieving thermal balance are shown at fig. 10. At fig. 10 quite large phase proportion fields heterogeneity is visible so plate material is heterogeneous as well.

At fig. 11a a contour graph of displacement norm is shown. Maximum value of displacement norm is close to 0.16mm. At fig. 11b contour graph of Huber-Mises stresses is presented. Maximum value of Huber-Mises stresses is close to 450Mpa (what is half of the yield stress for martensite in room temperature). Both graphs were made after achieving thermal balance.
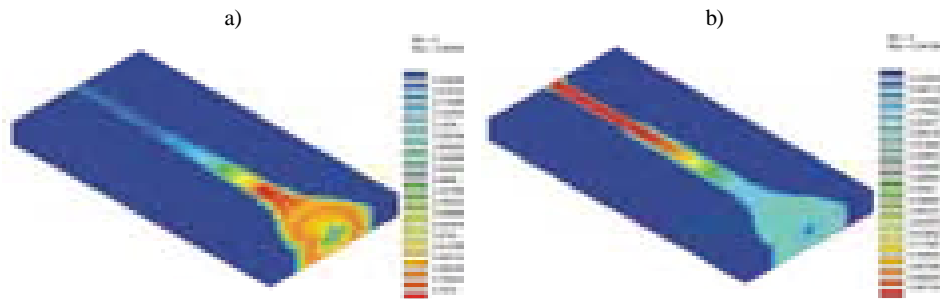
Fig. 10. Contour graphs of bainite and martensite proportion after achieving thermal balance.
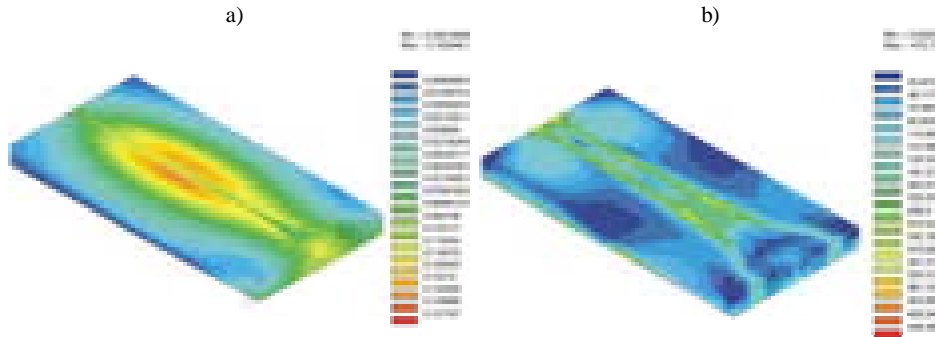
Fig. 11. Contour graphs of a) displacement norm, b) Huber-Mises stresses after achieving thermal balance.

5.3. Welding – model of T-joint

The model of T-joint made of steel 16MnCr5 (two plates with dimensions 55x20x4mm and 30x20x4mm) was analyzed. Geometry was modeled with three dimensional elements with finer mesh in a plate connection area. The T-joint was exposed to moving heat source, which is simulation of thermal impact from welding. The moving heat source was described with Goldak model (compare [5, 6]), with parameters showed in [3].

Thermal initial boundary conditions in this case are as follows – the temperature of whole body is set to 20°C. The boundary conditions on each surface bounding the body describe free exchange of heat with surrounding air and have convective nature. Zero displacement boundary conditions were set in selected nodes on plate edges. Fig. 12 shows contour graphs of phase proportions for selected steel phases in full thermal balance situation. Because at the beginning of the process it was established that phase structure of steel plates is ferritic-perlitic, then at the end of the process in heat affected zone the main phase composition is bainitic with small amount of martensite. In welded joint volume proportion of martensite should be very small because of its fragility and hardness.

268
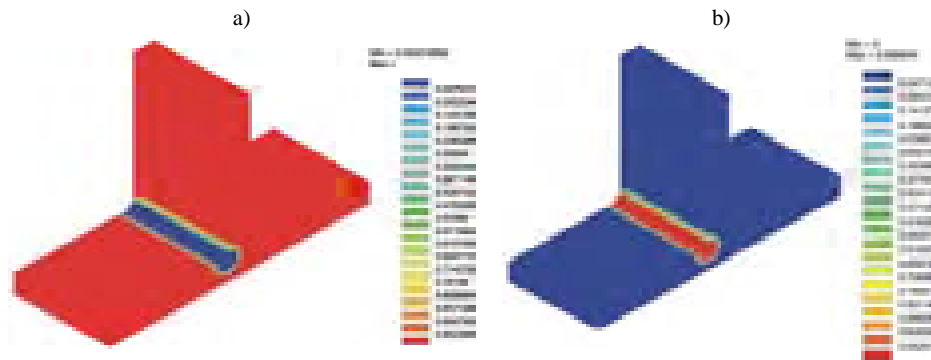
Fig. 12. Contour graphs of volume phase proportions for t=500s, after achieving thermal balance: a) ferrite-perlite, b) bainite.

Fig. 13 shows contour graphs of Huber-Mises effective stresses after time period t=500s. The main stress concentrations during and after welding are located mainly in heat affected zone.
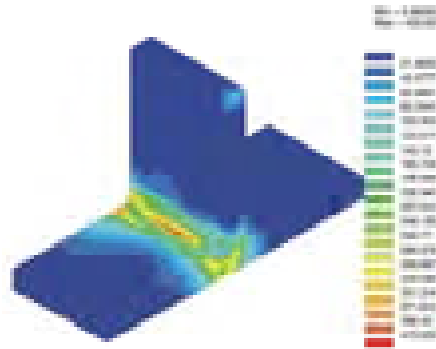
Fig. 13. Contour graphs of Huber-Mises effective stresses ($\left[\text{MPa}\right]$).

6. Conclusions

Thanks to intensive development of numerical methods in last ten years referred to thermodynamics coupled issues, there is possibility to analyze the high temperature impact on thermo-mechano-metallurgical properties of steel and structural steel elements. For instance there exist possibility to estimate volume proportion and localization of martensite, which is the key issue in tempering and welding process designing. At present, such procedure is used in motor and shipbuilding industry.

From technological (technology of heat treatment and welding for metals) point of view still the most important problem to solve is proper identification of parameter and material functions for steel grades used in civil engineering.

269

References

[1] Giżejowski M.A., Jemioło S., *Modelowanie numeryczne zachowania się spawanych węzłów podatnych z blachami czołowymi*, Inżynieria i Budownictwo nr 11, 2004, str. 623-629.

[2] Jemioło S., Gajewski M., *Symulacja MES obróbki cieplnej wyrobów stalowych z uwzględnieniem zjawisk termo-metalurgicznych, Część1. Nieustalony przepływ ciepła i przejścia fazowe, Część 2. Przykłady numeryczne z zastosowaniem programu SYSWELD*, Prace naukowe Politechniki Warszawskiej, z.143, Budownictwo, 2005, str. 5-63.

[3] Jemioło S., Gajewski M., *Zastosowanie programu SYSWELD w modelowaniu resztkowych naprężeń pospawalniczych*, Prace naukowe Politechniki Warszawskiej, z.143, Budownictwo, 2005, str. 65-93.

[4] Lancaster J.F., *Metallurgy of welding*, Third edition, George ALLEN & UNWIN, London, 1980.

[5] Leblond J.B., Devaux J., *A new kinetic model for anisothermal metallurgical transformations in steels including effect of austenite grain size*, Acta Metall., Vol. 32, No. 1, 1984, pp. 137-146.

[6] Leblond J.B., Mottet G., Devaux J., *A theoretical and numerical approach to the plastic behavior of steels during phase transformations. I: Derivation of general relations, II: Study of classical plasticity for ideal plastic phases*, J. Mech. Phys. Solids, Vol. 34, No. 4, 1986, pp. 395-432.

[7] Lindgren L. E., *Finite element modelling and simulation of welding*, Part 1-3, Journal of Thermal Stresses, Vol. 24, 2001, pp. 141-334.

[8] Rońda J., Oliver G.J., *Consistent thermo-mechano-metallurgical model of welded steel with unified approach to derivation of phase evolution laws and transformation-induced plasticity*, Comput. Methods Appl. Mech. Engrg., Vol. 189, 2000, pp. 361-417.

[9] SYSWELD^{TM} 2003, Reference Manual. ESI Group, The Virtual Try-Out Space Company.

270

DISTRIBUTION OF TEMPERATURE IN THE VENTILATED SPACE OF THE MULTI-FLUE INDUSTRIAL CHIMNEY

Lesław Tarczyński[*]

[*] Faculty of Civil Engineering, Opole University of Technology,
Katowicka 48, 45-061 Opole, Poland.

1. Introduction

Modern industrial chimneys consist of several (usual three to six) flues packed together in a reinforced concrete shell. The air volume left between the outer surface of the flues and the internal surface of the outer shell of the chimney is usually referenced as ventilated space. The word "ventilated" means that the air in the chimney compartment can flow freely subjected to laws of convection in order to keep the temperature of the chimney's stack in the acceptable limits. The other purpose is to gain a free access of personnel to the interior of the chimney structure. The conditions for additional utilisation of the chimney interior depends on the structure itself (system of flue support) and the temperature and rate of flow of the internal air. The data concerning the temperature load of chimneys is available generally for single-flue chimneys without ventilating space (Ciesielski [1]). Papers concerning multi-flue chimneys are less available (Aschieri [2]). Results of author's investigations of influence of operating and environmental conditions on the values of temperature in two separate levels of the reinforced concrete six-flue chimney is presented in the paper Tarczyński [3]. Of main interest of the submitted paper is spatial distribution of the air temperature in the ventilated space of the chimney with relation to operational and environmental factors. The presented results have been obtained on the full-scale 250 m chimney during the last year of extreme climatic conditions.

2. Description of the investigated chimney

A six-flue 250 m high chimney was investigated (Cieślik, Mateja [4]). The chimney structure is composed of two RC coaxial stacks (main, 24 m in diameter, auxiliary, 7 m in diameter), carrying steel girders which in turn support six thermally insulated brick flues (6 m in diameter) (fig. 1).

Additional steel tubes (4.5 m in diameter) are placed inside the brick flues as flue ducts, creating extra non-ventilated space filled with very hot air with temperature very close to the exhaust gases temperature (80-90 deg C).

271
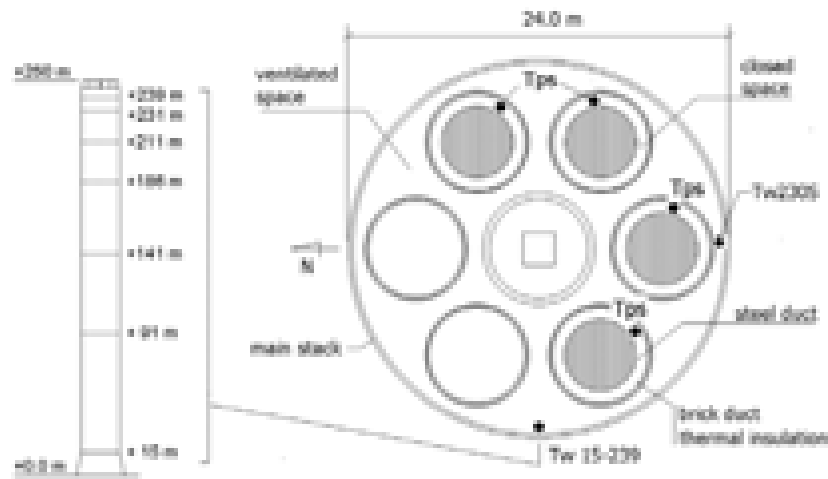
Fig. 1. Location of the fixed temperature sensors.
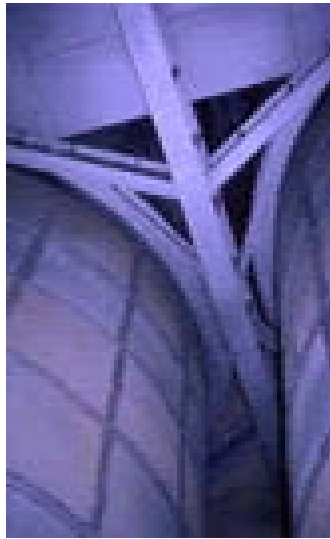
Fig. 2. Steel girders supporting flues.

A volume between the external brick ducts and the main RC stack is filled with steel decks spaced each 10 m in the vertical direction (fig. 2).

272

3. Program of research and the measurement equipment

The following parameters influencing the temperature at the ventilated space have been assumed:
- ambient air temperature (Ta),
- wind velocity (Wv),
- number of operating flues.

The values of ambient air temperature and wind velocity were recorded at the distance of 8 km from the investigated chimney. The operating status of flues (hot or cool) was determined using temperature gauges placed between the ceramic shell and the steel flue duct (fig. 1). The air temperature at the ventilated space was recorded at selected levels of the chimney (fig. 1). The accuracy of the sensors was in the range ± 0.2 deg C. The data was recorded in 30 minutes intervals using automatic digital recorders.

4. Data organisation and processing

The measurement data had been successively transferred to a desktop computer and organised in form of a relational database [5]. The following three relations were defined:

$R_1 = METEO$ *(date, amb. air temp. Ta, wind velocity Wv)*

$R_2 = T\_FLUES$ *(date, flue temp. $Tps_{k=1:4}$)*

$R_3 = T\_VENT\_SPACE$ *(date, internal air temp. $Ti_{l=1:n}$).*

where:

$METEO$ represents selected meteorological parameters,

T_FLUES represents measured values of the air temperature in the closed space between ceramic and steel flues,

T_VENT_SPACE t represents measured values of the air temperature in the ventilated space.

In order to find required parameters and dependencies, the data was processed using classical database procedures like projection, selection, join and sorting [5].

5. Results of measurements

Air temperature in the ventilated space is changing in diurnal and year cycles due to varying external ambient air temperature and other meteorological parameters (mainly wind velocity and solar radiation) (fig. 3).

At first a selection procedure was applied to the R3 relation in order to extract extreme temperature values in the ventilated space. The highest recorded temperature reached 66 deg C, at the 230 m level on the south side (fig. 4).

273
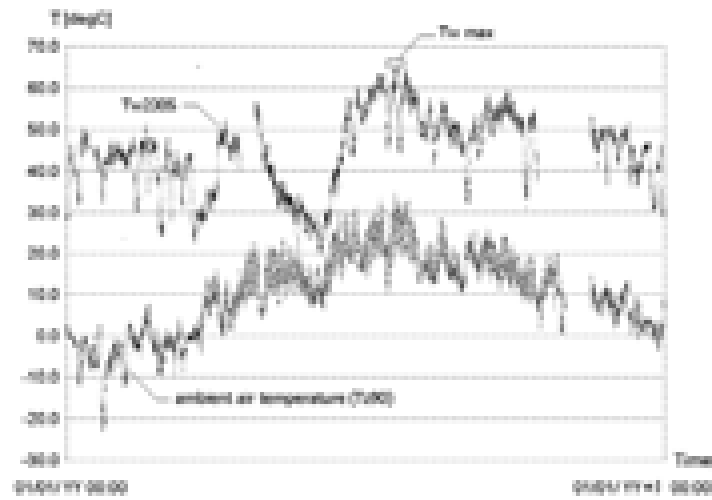
Fig. 3. A one-year cycle of ambient air temperature (Tz90) and ventilated space air temperature at the 230 m level (Tw230S).
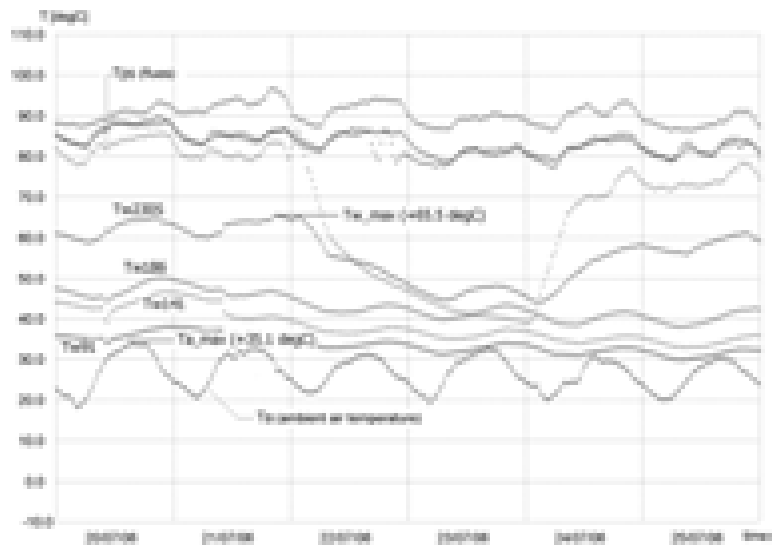
Fig. 4. Air temperature at the ventilated space at selected locations during extreme summer conditions (summer 2006, 6 days period).

Internal air temperature recorded during the low winter temperatures is presented in fig. 5.

274
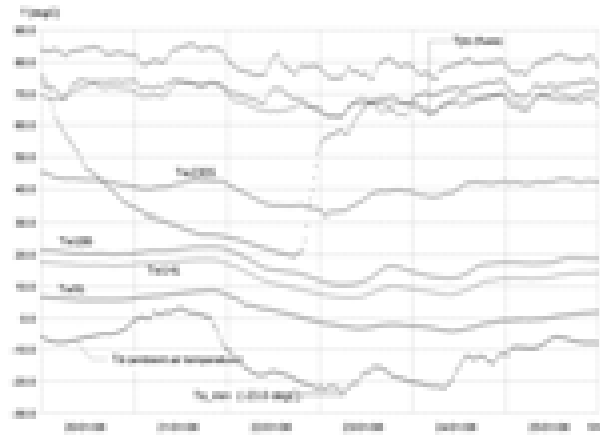
Fig. 5. Air temperature at the ventilated space at selected locations during extreme winter conditions (winter 2005/2006, 6 days period).

The obtained temperature profiles along the vertical and circumference directions are generally non-uniform (figs 6 and 7).
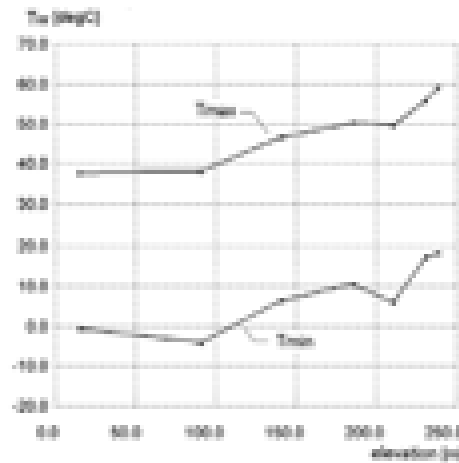
Fig. 6. Measured extreme temperatures at the ventilated space along the height of the chimney (7 levels, 1 year data).

A difference between bottom and top levels reach 20 deg C. The circumference direction (measurements carried out with hand-held sensor) exhibits variation of temperature reaching 10 deg C, depending on the level. The greatest differences were recorded at the upper levels of the chimney (fig. 7).

275
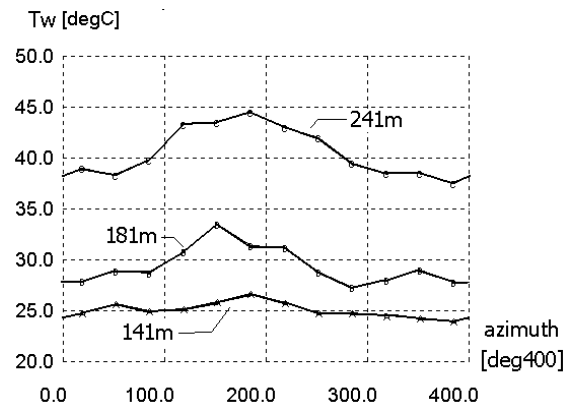
Fig. 7. Circumference distribution of the ventilated space air temperature measured at the vicinity of the inner surface of the main stack (levels: 141, 181, 241 m).

A number of actually operating flues plays a major role on values and distribution of the inside air temperature. The thermal load of flues is subjected to occasional variations in response to changing demand for electric energy. An example of such phenomena is presented in fig. 8, where the process of cooling and subsequent heating of one of the flues is indicated by relevant temperature variations at the closed space between the ceramic cylinder and the bare steel surface of the flue.
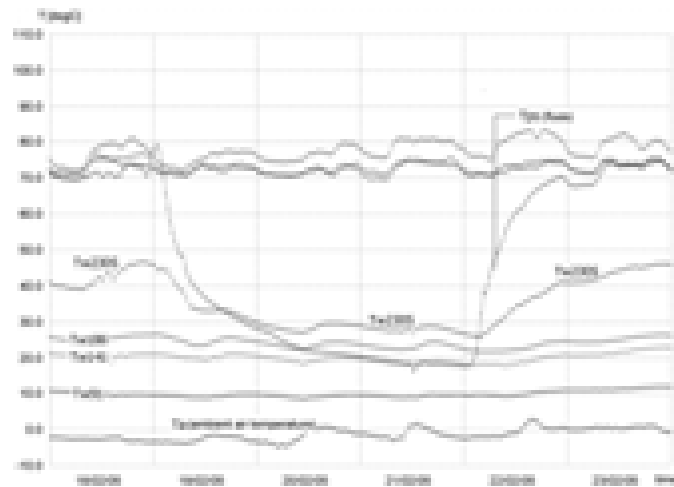
Fig. 8. An example of cooling and subsequent heating of one of the flues indicated by relevant temperature variations at the closed space between the ceramic cylinder and the bare steel surface of the flue.

276

The obtained database was also analysed in order to find empirical relations between the values of the assumed factors (Ta, Wv, number of operating flues) and the resulting air temperature in the selected locations of the ventilated space.

An empirical dependence between the ambient air temperature and air temperature in the ventilated space at the level 230 m of the chimney for two levels of thermal load (3 and 4 operating flues) is presented in fig. 9. In the reported case the increase of the number of hot flues from 3 to 4 is indicated by 8 degC increase of inside air temperature.
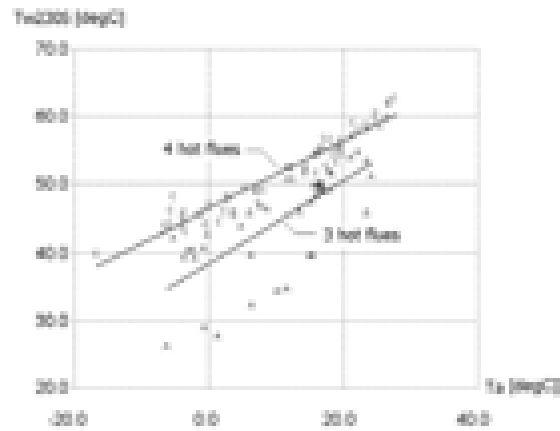
Fig. 9. Empirical relation between the ambient air temperature (Ta) and air temperature at the ventilated space near the top of the chimney (Tw230S), for three and four operating (hot) flues.
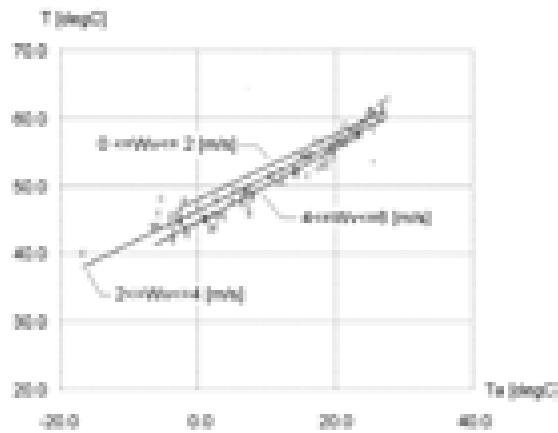
Fig. 10. Empirical relation between the ambient air temperature (Ta) and air temperature at the ventilated space at the 230 m level of the chimney (gauge $Tw230S$), for 3 distinct boundaries of the wind velocity (number of operating flues = 4, data base: 1 year of continuous monitoring).

277

An empirical dependence between the ambient air temperature and air temperature in the ventilated space at the level 230 m of the chimney for three boundaries of wind velocity is presented in fig. 10. The influence of the wind velocity on the air temperature in the ventilated space is clearly visible.

6. Concluding remarks

Prediction of the air temperature at the ventilated space of the high reinforced concrete industrial chimney can be achieved by full-scale measurements at several fixed points spaced along its height during all four seasons. It is necessary to include at least the influence of ambient air temperature and the number of operating (hot) flues. Additional data can be obtained by hand-held sensor complementary measurements in order to determine the non-uniform temperature profiles along the circumference and radial directions, especially in locations where access of personnel is considered. The investigated example of chimney can be classified as relatively "hot" case, where upper segments of the ventilated space may be in practice non-accessible for unequipped people for long periods of time, especially during hot summer seasons with inner temperatures reaching 60-70 deg C.

References
[1] Ciesielski R., *Kominy przemysłowe*, Budownictwo betonowe, t.XIII, Arkady, Warszawa, 1966.
[2] Aschieri F., *Monitoring of Chimney Performance*, 2nd Chimney Design Symposium and Exhibition, Edinburgh, 1976, Vol.1, pp. 253-262.
[3] Tarczyński L., *Wpływ parametrów eksploatacyjnych i środowiskowych na temperaturę w przestrzeni wentylowanej wieloprzewodowego komina przemysłowego*, Inżynieria i Budownictwo, 02/2007, pp. 88-91.
[4] Cieślik J., Mateja O., *Sześcioprzewodowy komin przemysłowy o wysokości 250 m*, Inżynieria i Budownictwo, 7-8/1976, pp. 305-309.
[5] Cellary W., Królikowski Z., *Wprowadzenie do projektowania baz danych*, WNT, Warszawa 1988.

THE INFLUENCE OF HIGH TEMPERATURE ON MECHANICAL PROPERTIES OF REINFORCING COLD WORKED STEEL PRODUCTS

Marta Słowik[*]

[*] Department of Building Structures, Faculty of Civil and Sanitary Engineering, Lublin University of Technology, Nadbystrzycka 40, 20-618 Lublin, Poland.

1. Introduction

In building structures made by concrete reinforcing steel or prestressing steel is used. The mechanical and physical properties of concrete steel depend on chemical contents and technology of production.

Steel is an alloy consisting mainly of iron, with a carbon which is the most effective alloying material for iron, but various other alloying elements are also used. The properties of steel vary widely, based on what alloying elements are in it, and, for steel with carbon as its only alloying element, how much carbon is present.

Carbon and other elements act as a hardening agent, preventing dislocations in the iron atom crystal lattice from sliding past one another. Varying the amount of alloying elements and form of their presence in steel controls qualities such as the hardness, ductility and tensile strength of the resulting steel. Steel with increased carbon content can be made harder and stronger than iron, but also more brittle.

In prestressed concrete structures the high strength steel is needed, so the high-carbon steel (characterized by the tensile strength more than 1500 MPa) or low-alloy steel (with the tensile strength of $1000 \div 1200$ MPa) is used to provide additional strength. In high-carbon steel used in prestressed concrete members the carbon content is between 0.7% and 1.0%. In low-alloy prestressing steel the addition of other elements, usually less than 2% by weight, are used, mainly manganese ($0.5 \div 1\%$).

The low-carbon steel is used in reinforced concrete structures where such high tensile strength as in prestressed concrete ones is not necessary. Carbon content in low-carbon steel is less than 0.22% by weight depending on steel grade.

But the mechanical characteristics of concrete steel depend not only on the chemical contents but also on the method of steel production. The steel is heat-treated to produce a desirable crystal structure, and than it is sometimes "cold worked" to produce the final shape.

There are two types of production technology of reinforcement used in concrete structures: hot rolled steelmaking and cold worked steelmaking.

In reinforced concrete structures mostly steel bars of a diameter 6 mm and bigger are

279

used. Such bars are produced as hot rolled steel. But also steel products of a diameter less than 6 mm are used in reinforced concrete members. They are called not bars but wires. In order to get such small diameters a strain hardening manufacturing is necessary. Such wires are produced from low-carbon steel by cold worked process.

In the present study, the steel wires used in reinforced concrete structures are considered.

2. Properties of reinforcing steel

The main mechanical parameters of reinforcing steel, specified in the codes PN-ISO 6935-1 [1] and PN-ISO 6935-2 [2], are the yield stress R_{eH} and the tensile strength R_m. In the code for designing reinforced concrete structures PN-B-03264:2002 [3] these parameters are defined as the characteristic yield stress f_{yk} and the characteristic tensile strength f_{tk}. In fig. 1 two typical stress-strain diagrams of reinforcing steel are shown. The hot rolled steel (fig. 1a) has better ductility and well marked the yield stress. For the cold worked steel (fig. 1b) the yield stress is not clear and it is defined as the 0.2% proof stress.

a)   b)
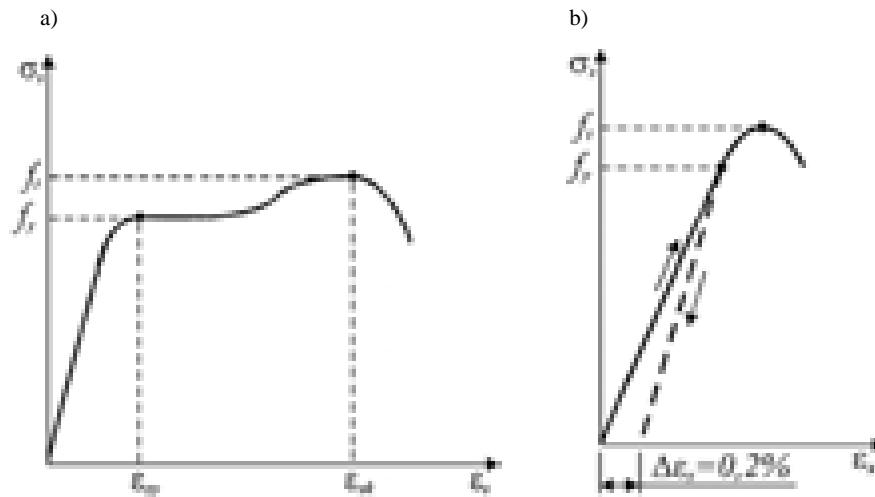
Fig. 1. Stress-strain diagrams of typical reinforcing steel:
a) hot rolled steel, b) cold worked steel.

Recapitulating the information given in the technical literature [4-8] it may be said that mechanical properties of reinforcing steel in its final product are the function of:
- steel chemistry,
- reheat temperature,
- rate of deformation,
- heat of deformation recovery time,

280

- recrystallisation time, and
- subsequent rate of cooling after deformation.

The above conditions make, that the stress-strain relationship in cold worked steel wires is different than in hot rolled steel bars.

3. The influence of high temperature on reinforcing steel

The mechanical properties of reinforcing steel change after it is exposed to high temperature. Although building structures made by concrete are generally thought to have a good fire resistance, they lose their original capacity when subjected to such temperatures as during the fire [9]. As far as reinforcement is concerned, concrete cover may provide some protection against high temperature (see reference [10]) but the experimental results show, that at the temperature over 400°C the mechanical properties of steel bars start to change significantly.

Prestressing steel has been studied at high temperature, for example [11].

With reference to reinforcing steel, mostly the hot rolled steel bars have been tested at high temperatures (for example [12-14]). Hot rolling permits large deformations of the steel to be achieved. When the temperature increases, the elastic properties of hot rolled low-carbon steel decrease, for example the limit elastic stress and the Young's modulus. At first, as the steel is heated, the tensile strength increases. At the temperature of $250 \div 300$°C the tensile strength reaches the maximum value, approximately 20% greater then in normal temperature. When the temperature increases over 300°C, the rapture decrease of tensile strength is seen. With increasing temperature decrease of the yield stress is observed, and at the temperature above 400°C the yield stress disappears completely. The changes of hot rolled steel parameters in accordance to growing temperature are shown in fig. 2.

The lattice structure in cold worked steel wires at normal temperature is different than in hot rolling bars. Because of differences in microstructure and the fact that steel is an allotropic element, it may be suspected that material properties will change in the other way in cold worked steel than in hot rolled steel during heating. Test results concerning worked-hardened steel bars (8 mm in diameter) exposed to high temperature has been reported
in [15]. There is an absence of experimental data concerning small diameter steel wires treatment at heating in technical literature. So the author's own research program has been made to analyze the influence of high temperature on the reinforcing wires made by low-carbon cold worked steel.
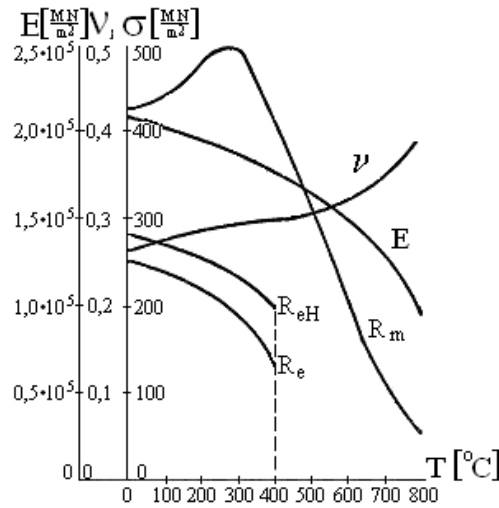
Fig. 2. The influence of temperature on the mechanical properties of hot rolled steel bars.

4. The author's own test program and the obtained results

Steel wires of 4 mm in diameter were used in the experiment. Five series of specimens (three specimens at every series) were prepared. The specimens from the first series called A were not heated at all. The specimens from the next series (series B, C, D and E) were exposed to the temperature ranging from 400 °C to 750 °C and then cooled in air to room temperature. The specimens were heated to the required temperature in a muffle furnace of the type RTs-61. The maximum temperature, T_{max}, and the time of heating at maximum temperature, t, were different for every series:

- series B – T_{max} = 400°C, t = 1 hour and half;
- series C – T_{max} = 500°C, t = 6 hours;
- series D – T_{max} = 620°C, t = 1 hour and half;
- series E – T_{max} = 750°C, t = 1 hour and half.

The yield stress and the ultimate tensile strength were measured for the as-received material (specimens of the series A) and for the specimens after a complete cycle of heating and cooling (specimens of the series B, C, D and E) during the typical tension test. Tensile tests were carried out on specimens according to the code PN-EN-10002-1 [16]. As the first, the wire specimens which were not exposed to high temperature (series A) were tested. Then the specimens of series B, C, D and E were tested at the same way as in the case A. The tensile machine used in the experiment was a ZD100 model of 100 tons capacity.

The typical force – elongation (P-Δl) relationships obtained during the experiment are shown in fig. 3.

282

Fig. 3. Relationships P-Δl obtained during the experiment.

Based on experimental data the investigated parameters were calculated: the yield stress and the tensile strength. The obtained results (the mean value, standard deviation and coefficient of variation) for every series of tested specimens are listed in table I.

Table I. Test results.

Property	Specimens not exposed to high temperature Series A	Specimens exposed to high temperature			
		Series B	Series C	Series D	Series E
		Maximum temperature [^{o}C]			
		400 ^{o}C	500 ^{o}C	620 ^{o}C	750 ^{o}C
f_{ym}[MPa] s [MPa] v [%]	Not measured	Not measured	334.4 11.4 3.4	246.2 6.6 2.7	218.9 12.0 5.5
f_{tm}[MPa] s [MPa] v [%]	731.2 6.1 0.8	644.9 5.9 0.9	411.4 6.6 1.6	352.6 4.5 1.3	310.5 10.6 3.4
The loss of f_{tm}	-	11.8%	43.7%	51.8%	57.5%

For better understanding and explaining what happens in low-carbon steel wires at high temperature, the description of phase change and accompany processes which may follow in heated steel has been made.

5. The description of heat processes in cold-worked steel

The method used to produce cold-worked steel make that steel absorbs a great deal of energy, and it is used after cold working to produce a specific grain structure. The type of steelmaking has a major impact on the size, number, and shape of crystal produced. When the steel is mechanically deformed by strain hardening operation, the grain becomes elongated. As heat is applied to steel, a number of things begin to happen (see fig. 4). When the temperature is increased the following processes take place: a recovery process, a recrystallization process and than a secondary recrystallization process.
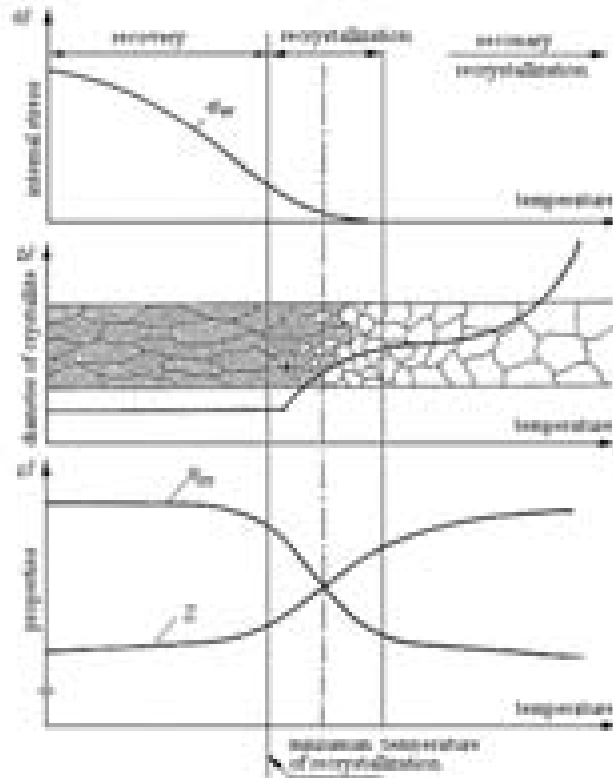
Fig. 4. Effect of heating on: a) internal stress σ_w, b) microstructure, c) mechanical properties-
R_m – the tensile strength of steel, Z – degree of deformation, (based on [17]).

284

The recovery process may start at relatively low temperature, and when the temperature increases it goes more intensively. No phase change of steel microstructure occurs, only the reduction of residual stresses takes place.

The recrystallization is the process which results in forming a completely new crystallized microstructure of steel. It is carried out after the temperature reaches the "minimum recrystallization temperature" T_R. New crystal nucleuses start to appear. With temperature growing, the residual stresses are reduced to zero and the process goes up to the moment when all grains are recrystallized.

At relatively high temperature the secondary recrystallization process may take place. When steel is heated to temperatures above some critical value, the single grains of steel grow very strongly. The secondary recrystallization probably starts at so called "critical temperature", when the pearlite changes to austenite. The term "critical temperature", when used in regard to steel, means the temperature that the carbon in steel is transformed into an austenitic crystal structure. The austenite grain size increases with increasing temperature.

Based on the fig. 4, where the effect of high temperature on main parameters of cold-worked steel exposed to high temperature is shown, it can be concluded that the increase in finishing temperature causes a decrease in residual stresses and in the tensile strength of steel but results in an increase of the degree of deformation. Also the change in the grain size is dependent on finishing temperature, due to the atomic structural change.

6. The analysis of test results

The presented investigation has been taken up to evaluate the effect of high temperature on the mechanical properties of hot rolled low-carbon steel wires. The wide range of microstructure and mechanical properties is discussed based on processes which may take place during heating.

Research work, performed for reinforcing steel wires of small diameter 4 mm, has confirmed that the low-carbon cold worked steel wires are characterized by the relatively high tensile strength. The average value of f_{tm} was 731.2 MPa. The obtained results of the specimens series A, which were not exposed to high temperature, has showed that the type of manufacturing by strain hardening causes in decay of plastic properties in steel and the absence of the clear yield stress. Such steel characteristics are effected by dislocation configurations and distributions of strains induced during the manufacturing process.

With regard to test results of specimens from series B, which were heated at the temperature 400ºC, it has been noticed that their mechanical characteristics varied in a small degree when compared with specimens of series A. The average loss of tensile strength was 11.8%. The small decrease of hardness and not significant increase of measured elongation indicates that recovery process occurred in tested steel wires of series B. Heating in temperature 400ºC had also a small effect on the shape of the relationship between P and Δl, as it is presented on fig. 3. The obtained results and the fact of an absence of the clear yield stress led to the conclusion that, in test specimens of series B, no

micro structural changes occurred and only residual stress were reduced due to recovery phenomena.

The significant decrease of the tensile strength was obtained for specimens of series C, which were exposed to temperature 500°C (43.7% compared to specimens of series A), and the well marked yield stress appeared. The average value of f_{ym} was 334.4 MPa. The big drop of the measured tensile strength and the appearance of the yield stress in steel specimens of series C should be attributed to the recrystallization phenomena, described previously in Section 5. From the tensile test measurements, it comes out that the minimal temperature above which heating causes the yield stress to bring back is between 400°C and 500 °C. The minimum recrystallization temperature given in technical literature [17] for low-carbon steel is 460°C, and the obtained test results have confirmed this value.

The resulting shape of relationship P-Δl was quite different in case of series C than in specimens of series A and B. The wide change in the character of the diagram P-Δl is the evidence that at the temperature 500°C the recrystallization process started to go. It made that internal stresses and hardening started to disappear and plastic properties came back.

In specimens of series D (heated in the temperature 620°C) and series E (heated in the temperature 750°C) the mean value of the measured yield stress and tensile strength was: f_{tm}=352.6 MPa; f_{ym}=246.2 MPa in specimens of series D, and f_{tm}=310.5 MPa; f_{ym}=218.9 MPa in specimens of series E. The decrease of tensile strength, compared to as-received specimens of series A, was 51.8% (series D) and 57.5% (series E). The mechanical properties of steel heating at 620°C or 750°C did not differ very much. At these temperatures the increase in finishing temperature causes a small decrease in the yield stress and tensile strength, but results in a significant increase of the elongation. Cold worked reinforcing steel wires exposed to high temperature as in case D and E present a pronounced increase of strains after heating which results to a big growth of its initial values. The evaluation of the elongation after heating for all examined steel wires is shown in the fig. 3.

Furthermore, it has been found that the coefficient of variation of the measured properties f_{tm} and f_{ym} was bigger for series E than for other series of steel specimens. This may be attributed to replacement of pearlite structure with austenite and also an increase in temperature over the "critical" value. The "critical temperature" of phase change from peaerlite to austenite given in literature [18] is 723°C. Steel wires of series E were heated up to higher temperature than the critical one, so the secondary recrystallization process started to go. As the reason of it more heterogeneous structure of steel appeared due to austenic grains growing during heating over the critical temperature. It is unfavorable for steel product when microstructure tends to evolve into more homogeneous one.

7. Conclusions

The cold worked steel manufacturing used to produce small diameter low-carbon steel wires causes in high tensile strength but low ductility. The main properties of steel wires change after exposure to high temperature.

286

Based on the present investigation, the following conclusions may be drawn of the influence of high temperature on the resulting mechanical properties of reinforcing steel wires:

- heating to temperature $460^{\circ}C$ leads, as a result of the recovery process, only to a slight decrease of tensile strength;
- in the range of heated temperature from $460^{\circ}C$ to $723^{\circ}C$, the recrystallization process goes and the most intensive changes of mechanical properties take place: the plastic properties are brought back and the significant drop of the tensile strength is seen; with growing temperature the tensile ductility (measured by the elongation) has been found to increase;
- at temperature higher than $723^{\circ}C$ the secondary recrystallization process is initiated, what results in more heterogous microstructure of steel.

References

[1] PN-ISO 6935-1 *Stal do zbrojenia betonu. Pręty gładkie*.

[2] PN-ISO 6935-2 *Stal do zbrojenia betonu. Pręty żebrowane*.

[3] PN-B-03264:2002 *Konstrukcje betonowe, żelbetowe i sprężone. Obliczenia statyczne i projektowanie*.

[4] Teoh L.L., *Thermo-mechanical processing and microstructure of microalloyed steel bar and wire rod products*, Journal of Materials Processing Technology, Vol. 48, 1995, pp. 475-481.

[5] Wu H.B., Jiang H.T., Yang S.W., Tang D. and He X.L., *Thermal Stability of Non-Equilibrius Microstructure in Microalloyed Steel during Reheating*, Acta Metallurgica Sinica, Vol. 20, 2007, pp. 313-326.

[6] Zhang X., Wang C.X., Liu X.M. and Shi Q.N., *Microstructure evolution and mechanical hardening of hypereutectoid pearlitic steel during cold rolling*, Acta Metallurgica Sinica, 20, 2007, pp. 287-292.

[7] Pye D., *Steel Heat Treating*, Gardner Publications, Inc., 2007.

[8] Garbarz B., *Stal zbrojeniowa*, XVII Ogólnopolska Konferencja: Warsztat pracy projektanta konstrukcji, Ustroń, 20-23 lutego 2002 r., materiały konferencyjne.

[9] Kosiorek M., Pogorzelski J.A., Laskowska Z., Pilich K., *Odporność ogniowa konstrukcji budowlanych*, Arkady, 1988.

[10] Unluoglu E., Topeu I., Yalaman B., *Concrete cover effect on reinforced concrete bars exposed to high temperatures*, Journal of Materials Processing Technology, Vol. 187-188, 2007, pp. 555-558.

[11] Bednarek Z., *Zmniejszenie siły sprężającej w splotach w warunkach pożaru*, Inżynieria i Budownictwo, nr 6/96.

[12] Bednarek Z., *Studium wpływu nieustalonych warunków termicznych na stosowane przy ocenie bezpieczeństwa pożarowego konstrukcji parametry wytrzymałościowe stali budowlanych*, Zeszyty Naukowe SGSP, Nr 1(10/1992, Warszawa 1992.

[13] Kruszka L., *Dynamiczne badania wytrzymałościowe budowlanych stali konstrukcyjnych w podwyższonych temperaturach*, XLIX Konferencja Naukowa KILiW PAN i KN PZITB, Krynica 2003 tom III, pp. 179-186.

[14] Miłowanow A., Sałmanow G., *Wlijanie wysokich tiempieratur na machaniczeskije swojstwa armaturnych stalej i wieliczinu scieplienia armatury s bietonom*, Zbornik CNIPS Issledowanija po żaroopornym bietonu i żelezobietonu, Gosstrojizdat, Moskwa, 1954.

[15] Nikolau J., Papadimirtou G.D., *Microstructures and mechanical properties after heating of reinforcing 500 MPa class weldable steels produced by Various processes (Tempcore, microalloyed with vanadium and work-hardened)*, Construction and Building Materials, 18, 2004, pp. 243-254.

[16] PN-EN-10002-1 *Metale. Próba rozciągania. Metoda badania w temperaturze otoczenia.*

[17] Prowans S., *Metaloznawstwo*, Wydawnictwo PWN, Warszawa, 1988.

[18] *Poradnik Warsztatowca Mechanika*, Wydanie V, Wydawnictwo Naukowo-Techniczne, Warszawa 1969.

STEEL AND CONCRETE CORROSION

SPECIAL ASPECTS OF SLENDER STRUCTURES VORTEX EXCITATION

Andrzej Flaga[*,**], Tomasz Lipecki[*]

[*] Department of Structural Mechanics, Faculty of Civil and Sanitary Engineering,
Lublin University of Technology, Nadbystrzycka 40, 20-618 Lublin, Poland.
[**] Wind Engineering Laboratory, Faculty of Civil Engineering,
Cracow University of Technology, Jana Pawła II 37/3a, 31-864 Cracow, Poland.

1. Introduction

This paper presents two particular aspects of vortex excitation of slender structures of circular cross-sections as well as its response, respectively: (1) corrosion of inner side of steel chimneys pipe, (2) feedbacks between vortex shedding and lateral vibrations of slender structures. All calculations have been performed according to our own mathematical model of vortex excitation, using computer programme that has been created to implement this model. Considerations concern slender, tower-like structures of circular cross-sections like steel and concrete chimneys and also concrete towers.

1.1. Corrosion of inner side of steel chimneys' pipe

Inner corrosion of steel chimneys is one of more important aspects that should be considered in calculations of its response due to vortex excitation. Our results of computations concerning steel chimneys under vortex excitation have been compared with results from full-scale measurements and no information about corrosion degree in full-scale data have been found. It seems that it is the main reason that can explain the result scattering in publications. This fact leads to difficulties and misunderstandings in comparisons of results obtained from computer calculations and full-scale measurements.

Polish Standard [1] gives exemplary recommendations of assuming the degree of corrosion danger – S in steel pipe. This value is estimated on the basis of aggressive environmental circumstances inside steel pipe and on the basis of the surface maintenance methods. Final degree of corrosion danger – $\sum S$ is a sum of appropriate values taken from Table 1. Value S equal to 1 corresponds to decrease in steel pipe thickness at the level of Δg=0.1 mm/year. Finally $\sum S$ will be in the range (0-10), so in extremely unfavourable environment when $\sum S$=10 – maximum value of decrease in steel pipe thickness Δg can achieve the level of 1mm/year. Such high value is of course only theoretical and is not possible in the real situation. Taking into account the time period of chimney exploitation the influence of corrosion can be of great importance.

291

This paper is trying to give the answer to a question: how corrosion can influence the lateral response of steel chimneys under vortex excitation. All computations of across-wind load caused by vortex shedding as well as chimneys' responses have been carried out using our own computer programme "Vortex Load". The obtained maximum displacements have been compared with full-scale data from literature. Computations have been performed for 6 steel chimneys.

Table I. Degree of corrosion danger – S.

Conditions	S
No particular aggressive factors	0
Strong aggressive external environment	1 to 2
Exhaust gases of carbon or petroleum	2 to 4
Acid vapours	3 to 6
Possibility of electrolyte condensation due to general low temperature of chimney	2 to 4
Possibility of local electrolyte condensation	1 to 4
Steel resistant against corrosion	-1 to –8
Special cover on chimney	-3 to –6

1.2. Feedbacks between vortex shedding and lateral vibrations of slender structures

When the frequency of lateral vibrations of slender structures of circular cross-sections is close to the frequency of vortex shedding it can cause the significant increase in structure response. This phenomenon is called lock-in (frequency synchronization) and can cause resonance. On the basis of full-scale and model investigations it can be stated that lock-in appears when $\eta > (0.01\text{-}0.02)D$ or $\sigma_\eta > 0.006D$, where η – amplitude of lateral displacements, σ_η – standard deviation of lateral displacements, D – diameter of the cross-section (Kwok & Melbourne [2], Vickery & Basu [3]). In this paper we would like to check, whether this phenomenon has large influence on final results for analysed tower-like structures. Our mathematical model of vortex excitation takes into account feedbacks between vortex shedding and lateral vibrations (comp. eq. 1). Estimation of feedbacks importance is based on computations according to our model which have been carried out for the same model parameters with and without feedbacks. It has been assumed that standard deviation of structure displacements is equal to zero at each step of computations in the case of lack of feedbacks, whereas, standard deviation of displacements is updated at each step of computations in the case of real situation (with feedbacks). Computations have been performed for 6 steel chimneys, 6 concrete chimneys and 2 concrete towers.

2. Method of computation

All computations have been carried according to our own mathematical model of across-wind load induced by vortex excitation which parts have been described in detail in several papers by Flaga [4], Flaga & Lipecki [5,6], Lipecki & Flaga [7], Lipecki [8], Flaga et al. [9]. This model takes into account real situation, it means: unsteady wind flow in the front of slender structure and lateral - to the wind direction - vibrations of the structure. It consists of two parts: (1) mathematical description of vortex excitation and (2)

deterministic description of vortex shedding zones along the structure. Own computer programme "Vortex Load" has been created to implement mathematical model as well as to calculate structure lateral response. This model can be applied in the cases of tower-like structures of circular cross-sections.

2.1. Mathematical description

There are three equations which describe the phenomenon of vortex excitation in the model, respectively:

- equivalent critical vortex excitation in the case of unsteady wind flow and lateral vibrations of slender structure:

$$w_y(t) = \left[q_c \cdot D \cdot (1 + \alpha \cdot \sigma_{\hat{\eta}})^3 \cdot \hat{w}_y(t) \right]\Big|_{z=z_0} \cdot Y(z), \tag{1}$$

- non-dimensional vortex excitation:

$$\hat{w}_y(t) = \left[\left[\frac{V_m(t)}{V_c} \right]^2 C_y(t) \cdot \sin\left(2\pi f_i t + \varphi\right) \right]\Big|_{z=z_0}, \tag{2}$$

- power spectral density function of non-dimensional vortex excitation which is in general narrow-banded process of harmonic or Gausian character:

$$\frac{f \cdot G_{\hat{w}_y}(f)}{\sigma_{\hat{w}}^2} = \frac{k}{\sqrt{\pi} B} \frac{f}{f_i} \exp\left[-\left(\frac{1 - f/f_i}{B} \right)^2 \right]. \tag{3}$$

Above equations depend explicitly on 4 experimental parameters:
α – parameter of increase in effective cross-section diameter; $\sigma_{\hat{w}}$ – standard deviation of vortex excitation; k – factor which takes into account participation of atmospheric turbulence in the total across-wind load on a structure; B – non-dimensional bandwidth parameter. These parameters depend on several wind parameters: I_v – turbulence intensity, L_v – turbulence length scale, Re – Reynolds Number, α_w – mean angle of wind attack and on structure geometry parameters: K – cross-section shape, k_L – structure slenderness, k_B – cross-section slenderness, k_s – surface roughness.

Standard deviation of chimney response under vortex excitation (given in non-dimensional displacement) $\sigma_{\hat{\eta}}$ appears in eq. 1. Next steps of load caused by vortex excitation are accepted on the basis of this value

Moreover in above equations: z, t – co-ordinate and time respectively; $q_c = 0.5\rho V_c^2$ – pressure of critical wind speed V_c, D – cross-section diameter; $\left(1 + \alpha \cdot \sigma_{\hat{\eta}}\right)^3$ – factor which takes into account the increase in effective cross-section diameter D of the vibrating

293

structure; $Y(z)$ – deterministic function which describes zone (or zones) ΔL of the structure where vortex excitation can appear; z_0 – central point of the domain ΔL; $V_m(t)$ – mean wind speed, spatially averaged in the front of the structure in the area $\Delta A = \chi D$, where χ is the number of the order 3, and χD is the width of the disturbances in wind field in front of the structure; $C_y(t)$ – aerodynamic coefficient which depends on parameters of wind flow and structure geometry; f_i – i-th eigenfrequency; φ – shift phase angle; f – frequency.

2.2. Deterministic description

The deterministic, zero-one function $Y(z)$ depends on 4 zero-one functions: $\Theta_1(z)$, $\Theta_2(z)$, $\Theta_3(z)$, $\Gamma(z)$, each of them takes into account various physical aspects of the flow around circular cylinder, in particular:

- $\Theta_1(z)$ – function of disturbances caused by boundary zones (base and top of the structure) and significant changes in the cross-section;
- $\Theta_2(z)$ – function of influences of wind profile and of critical wind speed profile. It has been assumed that lock-in can happen in the range $0.9V_c(z) < V_m(z) < 1.3V_c(z)$;
- $\Theta_3(z)$ – function of the mode shape – in fig. 1 for the first mode shape $\Phi_1(z)$;
- $\Gamma(z)$ – function connected with normalised space correlation function of equivalent vortex excitation process which is fully correlated in domain ΔL. It can be assumed that this function is equal to $2L_w$, where L_w – non-dimensional correlation length scale (depending on $\hat{\eta}$ or $\sigma_{\hat{\eta}}$) can be taken from: ESDU 85038 [10]; Ruscheweyh [11]. Two cases of function $\Gamma(z)$ are presented in fig. 1. Length scale L_w is the fifth experimental parameter that describes the model.
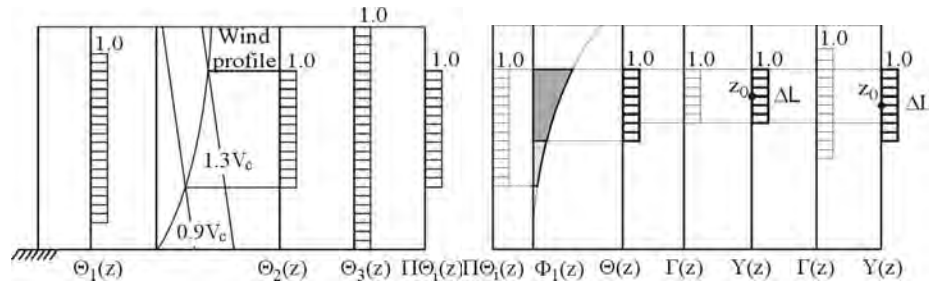
Fig. 1. Zero-one function $Y(z)$, domain ΔL with central point z_0 for a cantilever structure.

The way of assuming function $Y(z)$, area ΔL and point z_0 for cantilever structure of circular cross-section is presented in fig. 1. Particular steps of the whole procedure can be described as follow:

- Determination of functions $\Theta_i(z)$;
- $\prod \Theta_i(z)$ – product of the functions $\Theta_i(z)$;
- Assumption of the function $\Theta(z)$ – which takes into account the influence of

294

vibration amplitude values variation along the structure and can be determined according to the following rules: (1) the area of function $\Theta(z)$ is equal to the area under the curve of the mode shape $\Phi_1(z)$ in the domain given by function $\prod \Theta_i(z)$, (2) new domain of function $\Theta(z)$ is referred to the maximum value of $\Phi_1(z)$ in this region;

- Determination of correlation of vortex excitation – function $\Gamma(z)$;
- Final function $Y(z)$ – product of $\Theta(z)$ and $\Gamma(z)$. This function defines the final domain ΔL and its central (characteristic) point z_0.

2.3. Numerical implementation

Vortex excitation as a stochastic process has been simulated with the Weighted Amplitude Waves Superposition (WAWS) method (Shinozuka [12], Flaga et al. [9]). WAWS variant presented in this paper has been used to generate the load caused by vortex shedding in one point – z_0 (because the process is fully correlated in ΔL). WAWS simulation is based on the knowledge of the power spectral density function of analysed process (PSD), which in our model is given by eq. 3. Simplified equation of WAWS method can be given by:

$$p(t) = \sum_{k=1}^{N} \sqrt{2G_i\left(f_k\right)\Delta f_k} \, \cos\left(2\pi f_k t + \Phi_k\right), \qquad (4)$$

where: $G_i(f_k)$ – power spectral density function (PSD), f_k $(k=1,2....N)$ – central frequency of frequency interval Δf, N – number of spectrum intervals, Φ_k – N random values of phase shift angles taken from the range $0, 2\pi$.

Schematic idea and progression of calculations are presented in fig. 2.
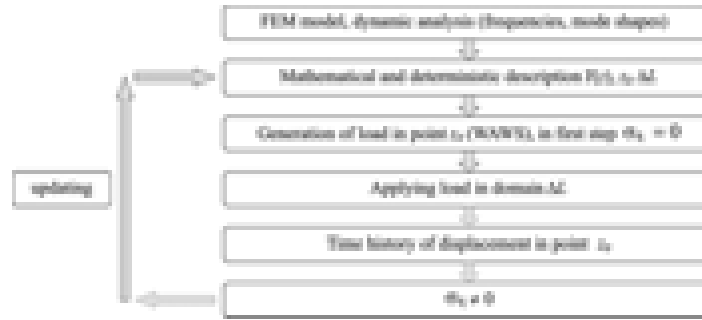
Fig. 2. Computation algorithm.

Equivalent critical vortex excitation is generated (using WAWS, on the basis of PSD function) in central point z_0 of the domain ΔL where vortex shedding can appear. First generation is performed in time domain T_0 for $\sigma_{\hat{\eta}}=0$. Fully correlated equivalent load is applied to the structure in the domain ΔL (fig. 3).

295
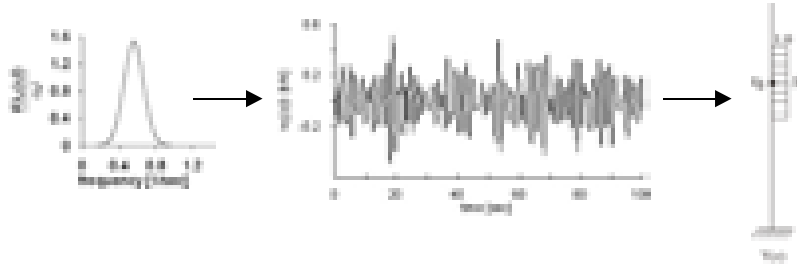
Fig. 3. Load simulation with the WAWS method, on the basis of PSD function. Domain ΔL.

The time history of displacements in point z_0 and in time T_0, is calculated using direct integration method (ALGOR). New value of standard deviation of displacement $\sigma_{\hat{\eta}}$ is calculated on the basis of a short time interval of time history of displacement $\chi_1 T_1$, where T_1 – first period of natural vibrations of analysed structure; χ_1 – parameter >1. Values $Y(z)$, ΔL, z_0 and also eq.1 are actualised and on the basis of the new $\sigma_{\hat{\eta}}$ next step(s) of load in time domain (T_0, $T_0+\Delta\tau$) are generated (fig. 4). The whole procedure is repeated M times and both time histories of load as well as of displacements are obtained in time T ($\sigma_{\hat{\eta}} \neq 0$). So, it can be stated that simulation is performed in real time (fig. 5).
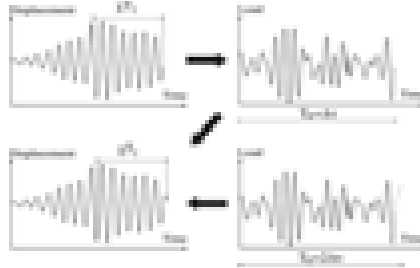
Fig. 4. Load simulation on the basis of time history of displacements in time interval $\chi_1 T_1$.

Fig. 5. Time histories of load and displacements in time T.

To obtain statistical characteristics of the analysed stochastic processes it is necessary to repeat all calculations several times (N times). Respective estimators (maximum displacement, standard deviation of displacements, mean value of displacements) in time T in point z_0 can be obtained. Maximum top displacement of analysed structures are calculated simultaneously with displacement in point z_0 according to the following rule:

$$\eta_{top}^{\max} = \frac{1}{N}\sum_{j=1}^{n}\eta_{j,top}^{\max} , \tag{5}$$

where j – index of the process, $j=1,2,...,N$.

296

This value gives an opportunity to compare the results obtained according to our model with the results from the full-scale measurements.

To implement numerically described procedures, our own computer programme "Vortex Load" has been created.

3. Structures

Influence of corrosion has been considered for six steel chimneys of the following basic dimensions given in Table II, where: H – height; D – outer diameter; g – steel pipe thickness; f_1, f_2, – natural frequencies of vibrations; Δ – logarithmic decrement of dumping; λ – slenderness ratio; Sc – Scruton Number.

Table II. Basic parameters of analysed steel chimneys.

	H [m]	D [m]	g [mm]	f_1 [Hz]	f_2 [Hz]	Δ	λ	Sc
Steel chimney 1	32.146	1.25	5-7	1.2767	7.4324	0.02	25.717	3.684
Steel chimney 2	38.174	1.4	5-7	0.8445	5.4065	0.02	27.267	4.37
Steel chimney 3	40	0.56-2	6-7	0.6495	2.4726	0.02	51.282	4.538
Steel chimney 4	60	1-4	10-16	0.5804	2.5983	0.02	32.952	5.699
Steel chimney 5	60	2.2	8-12	0.6412	3.5806	0.02	27.273	3.762
Steel chimney 6	83.5	3.06	6-40	0.4952	2.2204	0.026	27.288	2.947

Feedbacks have been estimated for above mentioned steel chimneys and for six concrete chimneys of basic data collected in Table III.

Table III. Basic parameters of analysed concrete chimneys.

	H [m]	D_b [m]	D_t [m]	g [m]	f_1 [Hz]	f_2 [Hz]	Δ	λ	Sc
Concrete chimney 1	120	11.56	6.76	0.2-0.4	0.54	2.49	0.15	13.10	52.36
Concrete chimney 2	150	7.2	4.2	0.3-0.44	0.20	0.92	0.15	26.32	127.56
Concrete chimney 3	200	15	5	0.2-0.38	0.29	1.09	0.15	20.00	41.81
Concrete chimney 4	250	24	24	0.3-0.7	0.22	1.09	0.15	10.42	49.19
Concrete chimney 5	260	15.8	7.7	0.15-0.7	0.21	0.69	0.15	22.13	46.38
Concrete chimney 6	300	27.8	21	0.25-0.9	0.30	3.88	0.15	12.30	24.72

Moreover two concrete towers: Ostankino Tower (Russia) of the height 533.3m, and Hornisgrinde Tower (Germany) of the height 210m have been analysed with and without feedbacks.

As it can be seen, considerations have been performed for cantilever, tower-like structures of circular cross-sections with constant diameter (steel and concrete chimneys), stepped-diameter (some steel chimneys), tapered diameter (concrete chimneys) and structures of the strongly varying cross-sections along the height (towers).

297

4. Results

4.1. Corrosion of inner side of steel chimneys' pipe

Calculations have been performed assuming chimneys' design parameters without corrosion, and then corrosion of inner side of steel pipe has been taken into account. Maximum top displacements occurred for almost harmonic process of across-wind load caused by vortex excitation. It means that model parameters have been respectively: $k \approx 1.0$, $I_v \approx 0$, $B = 0.1 + 2I_v \approx 0.1$. Chimneys with corrosion have been analysed only in the worst cases of load. Significant increase in chimneys response (maximum top displacements) can be observed due to decrease of steel pipe thickness as it can be seen in fig. 6a, where values of maximum top displacements η_{max} in the function of corrosion degree Δg [mm] are given. Local decreases in maximum top displacements level can be noticed in some diagrams. It is caused by the fact that vortex excitation is a stochastic process (all computations have been repeated only 10 times). The percentage changes in maximum top displacements have been estimated according to the eq. 6 and are presented in fig 6b.

$$percentage\ change = \frac{\eta_{max,i} - \eta_{max,0}}{\eta_{max,0}} \cdot 100\% \ . \tag{6}$$

There are: $\eta_{max,i}$ – maximum top displacement calculated in the case of the appropriate corrosion degree, $\eta_{max,0}$ – maximum top displacement calculated without corrosion in eq. 6.

Steel chimney no. 1.

a)
b)

Steel chimney no. 2.

a)
b)

298
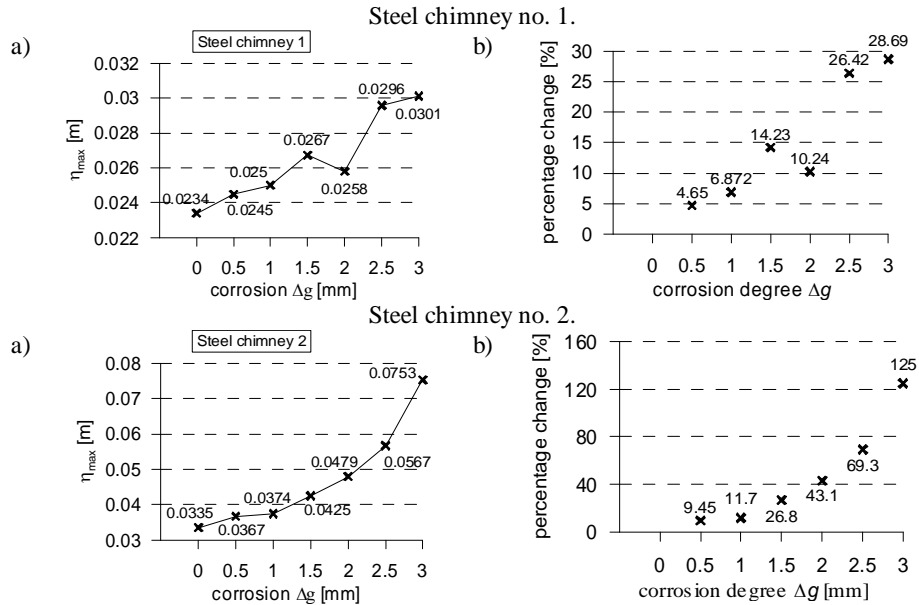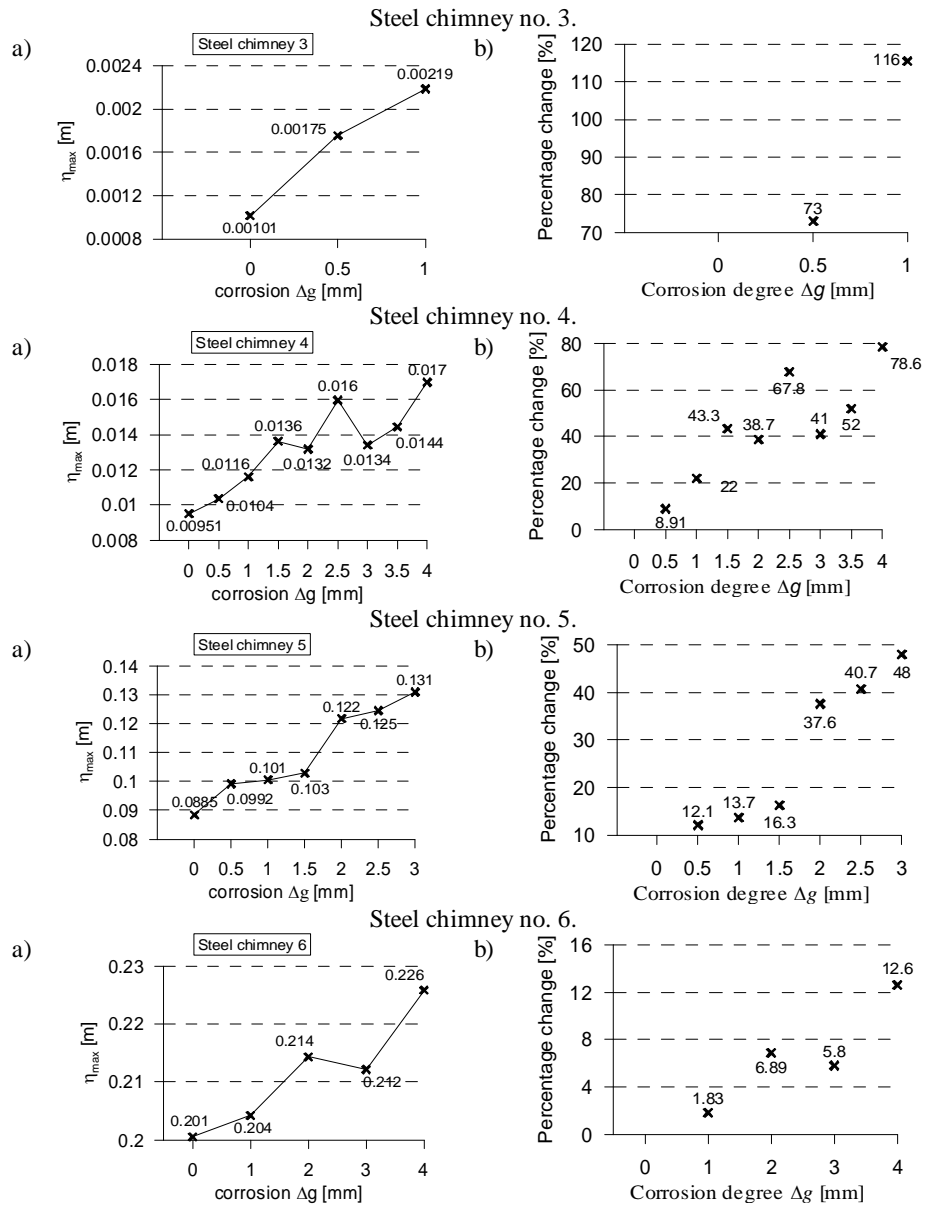
Fig. 6. Changes in steel chimneys top response under vortex excitation due to increase in corrosion degree of inner side of steel pipe: a) Maximum top displacement η_{max} [m] in relation to corrosion degree Δg [mm], b) Percentage changes in top displacements.

4.2. Feedbacks of vortex shedding and lateral vibrations for slender structures

Computations have been carried out for the same model parameters with and without feedbacks. In the first case standard deviation of structure displacements $\sigma_{\hat{\eta}}$ used in load simulation has been updated at each step of computations. In the second case standard deviation of structure displacements used in load simulation has been applied as equal to zero at each step of computations. Fig. 7a illustrates differences in structure response given in maximum top displacements η_{max} in both cases of computations. Percentage changes of computations results given in fig. 7b can be evaluated according to the following relationship:

$$percentage\ change = \frac{comp.\ with\ feedbacks - comp.\ without\ feedbacks}{comp\ with\ feedbacks} \cdot 100\% . \quad (7)$$

Steel chimneys

Concrete chimneys

Towers
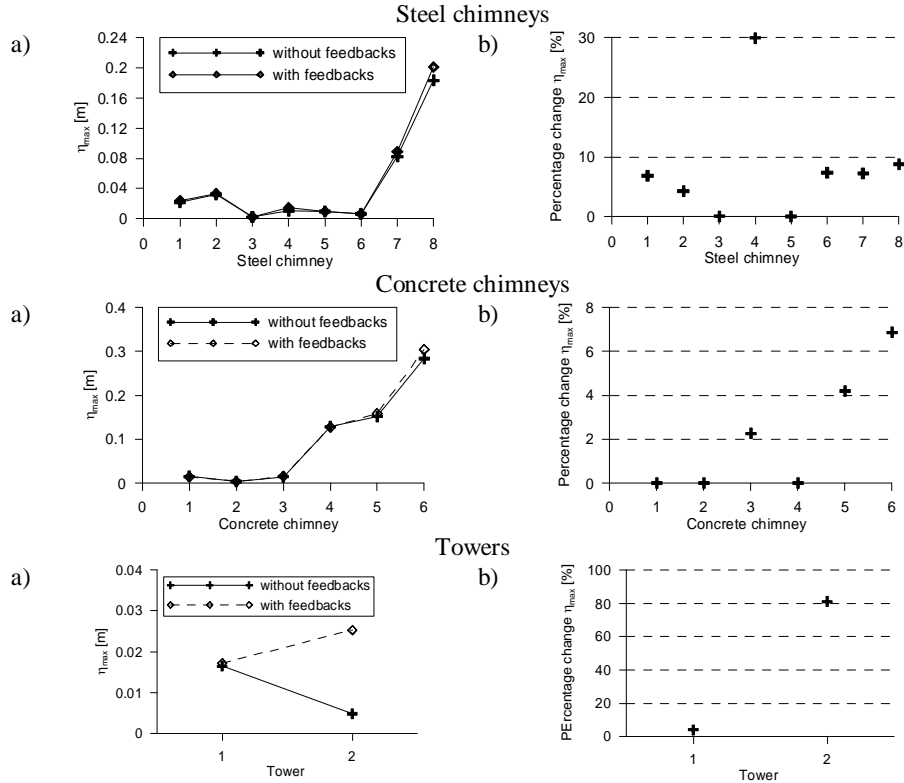
Fig. 7. Differences in lateral response of analysed structures computed with and without feedbacks. Some steel chimneys have been also computed in the second mode shape, in particular: case 1 – ch1, 2 – ch2, 3 – ch3, 4 – ch3, second mode, 5 – ch4, 6 – ch4, second mode, 7 – ch5, 8 – ch6. Moreover, tower 1 – Ostankino, tower 2 – Hornisgrinde.

5. Comparison with full-scale results

To validate the model and moreover to point possible scattering of the results due to corrosion, our results obtained in calculations have been compared with full scale measurements presented by Ruscheweyh & Galemann [13] for steel chimneys. This comparison is presented in fig. 8 as the value of normalized top displacement η_{max}/D in the function of non-dimensional Scruton Number (Sc). Our results are in a relatively good agreement with full scale.
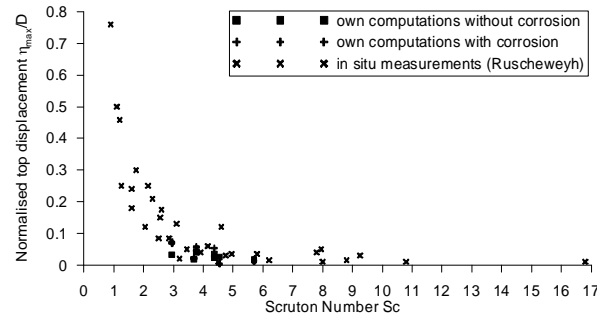
Fig. 8. Comparison of calculations with full-scale measurements.

Computation results for concrete chimneys have also been compared with full-scale data collected by: ESDU [10], Sanada [14], Waldeck [15]. Accessible data are limited, so our comparisons are also partial. We compared maximum top displacements against height and slenderness in fig. 9a and r.m.s. value of η_{max} against normalised wind speed at the top of the chimney – fig. 9b.
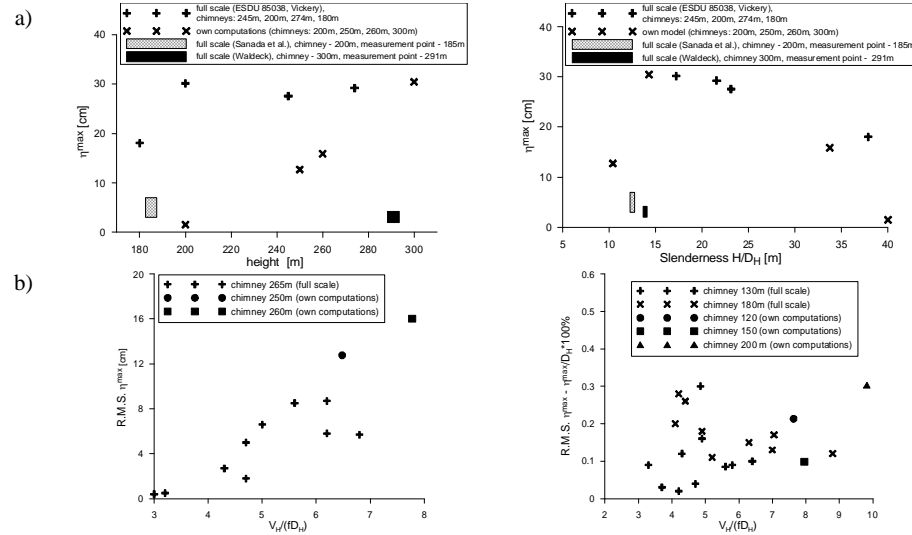
Fig. 9. Comparison of computation results with full-scale data.

301

6. Conclusions

Some final conclusion have been formulated:

- Lateral response of steel chimneys caused by vortex excitation can be significantly influenced by corrosion. There is no sufficient information about degree of corrosion both in full-scale reports and in codes and standards, as well.
- Results obtained according to the model of the critical vortex excitation presented in this paper are in agreement with full-scale data.
- It seems that feedbacks between vibrating structure and vortex shedding in the cases of analysed structures have secondary importance. The possible reason is that the values of lateral displacements have been at low levels.
- This new approach of estimation of across-wind load caused by vortices as well as structure response (expressed in displacements) can be a useful tool in designing processes of cantilever structures of circular or compact cross-sections.

References

[1] PN-93/B-03201, *Steel structures. Chimneys. Calculations and design*, 1993 (in Polish).

[2] Kwok K.C.S., Melbourne W.H., *Cross-wind response of structures due to displacement dependent lock-in excitation*, Proc. 5th ICWE, Colorado, USA, 1979, Pergamon, Oxford, 1980, p.: 699-708.

[3] Vickery B.J., Basu R.I., *Across-wind vibrations of structure of circular cross-section*, Part. 1, J. Ind. Aerodyn., 12 (1), p.: 49-74, Part. II, J. Ind. Aerodyn., 12 (1), p.: 75-98, 1983.

[4] Flaga A., *Wind vortex-induced excitation and vibration of slender structures. Single structure of circular cross-section normal to flow*, Monograph 202, Cracow, Poland, 1996.

[5] Flaga A. Lipecki T., *Comparative study of vortex excitation for various tower-like structures*, Proc. 10th Int. Conf. Wind Eng. Copenhagen, Dania, 1999, p.: 423-430.

[6] Flaga A., Lipecki T., *Simulation of across-wind action caused by vortex excitation*, Proc. 4th European-African Conf on Wind Eng. Praga, Czechy, 2005, p.:112-113.

[7] Lipecki T, Flaga A., *Influence of corrosion of steel chimneys on its response under vortex excitation*, Proc. 12th Int. Conf. Wind Eng. Cairns, Australia, 2007, p.: 983-990.

[8] Lipecki T., *Vortex excitation of tower-like structures of circular cross-sections*, Thesis, Lublin, Poland, 2006 (in Polish).

[9] Flaga A., Błazik-Borowa E., Podgórski J., *Aerodynamics of slender structures and bar-cable structures*, Monograph, Lublin Technical University, 2004 (in Polish).

[10] ESDU 85038, *Circular-cylindrical structures: dynamic response to vortex shedding, Part I: calculation procedures and derivation*, London, ESDU Int. Ltd, 1990.

[11] Ruscheweyh H., *Codification of vortex excited vibrations, Recent advances in wind engineering*, Proc. 2nd Asia-Pacific Symp. on Wind Eng., Beijing, China, Int. Acad. Publ., Pergamon Press, 1, 1989, p.: 362-372.

[12] Shinozuka M., *Stochastic Mechanics, v. 1*, Depart. of Civil Eng. & Eng. Mech. Columbia Univ., 1987, NY, USA.

[13] Ruscheweyh H., Galemann T., *Full-scale measurements of wind-induced oscillations of chimneys*, J. Ind. Aerodyn., 65, 1990, p.: 55-62.

[14] Sanada S., Suzuki M., Matsumoto H., *Full scale measurements of wind force acting on a 200m concrete chimney and the chimney response*, J. Ind. Aerodyn., 43, 1992, p.: 2165-2176.

[15] Waldeck J.L., *The measured and predicted response of a 300m concrete chimney*, J. Wind Eng. Ind. Aerodyn., 41, 1992, p.: 229-240.

CONCRETE ELEMENTS DURABILITY IN AGGRESSIVE ENVIRONMENTS: CELLULAR AUTOMATA SIMULATION

Adam Zaborski[*]

[*] Institute of Structural Mechanics, Faculty of Civil Engineering,
Cracow University of Technology, Warszawa 24, 31-155 Cracow, Poland.

1. Introduction

The corrosion of concrete elements in aggressive environments is the reason for which result the important economical losses. The structural complexity and great diversity of structural material compositions are accompanied by a wide range of possible interactions encountered with aggressive environments. This poses difficult problem for mathematical description of concrete behavior.

Three main forms of corrosive deterioration have been specified, Moskvin [1]:

- dissolution and leaching of cement hydration product, namely lime leaching,
- exchange reactions between acid and salts of the environment and the concrete components,
- crystallization of salts in voids and capillaries and subsequent spalling of concrete due to internal pressure.
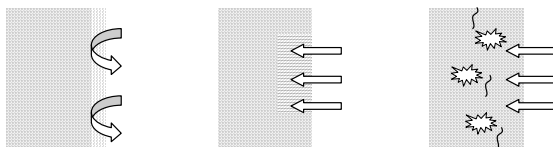
Fig. 1. Three forms of concrete corrosion.

In most cases the concrete corrosion may be described as transport phenomenon of corrosive agents through the porous matrix with diverse chemical reactions that occur simultaneously. The most important exceptions of the above description are: surface abrasion during the first form of corrosion, causing distinct front of deterioration, as well as the concrete spalling, due to wedging action of crystallizing products. Such cases should be treated in a distinct way.

The transport processes in concrete structures are caused by thermodynamical forces, mainly by concentration, pressure and electrical field gradients. In large part of the processes the concentration gradient plays crucial role and the description can be limited to this one exertion, Neville [2].

303

Results of the acting factors can be significantly different depending on circumstances: mechanical loading, saturation state or cross effects between flows. It is obvious that load level exerts a synergetic effect along with the aggressive environment: the resultant corrosion rate resulting from action of both factors is clearly greater than simple sum of deterioration the factors acting separately. The capillaries filled up by liquid form the paths for faster diffusion. Furthermore, the moisture movement turns out to be important mean of transport for aggressive constituents.

The reinforcement corrosion, if occurs, is very important factor that influences load capacity and deformability of cross-section but it is not considered here because it is the final stage, usually not accepted in practice.

2. Model of stress-assisted corrosion of concrete

The material can be described in scope of continuum theory of mixture, Bowen [3]. The overlapping continua consist of concrete as a porous solid, an aggressive liquid entering the concrete and various products of reactions (liquid and/or solid). Macroscopic phenomenological description is based on the averaged field variables.

In order to describe possibly wide class of processes some arbitrary assumptions have been adopted. The flows through porous matrix are described by transport equations. It is assumed that the process is diffusion driven i.e. the diffusion is viewed as predominant. The state of stress of solid material is not directly affected by flowing media. The state of stress affects the diffusion through influence on effective diffusion coefficient.

Deterioration of material may be described within continual damage mechanics. The considerations have been limited to the concrete deterioration of second type and the initial stage of corrosion of third type.

For the sake of simplicity, the material is assumed to be without electric charge. It is worth to underline however, that the case can also be simulated in similar way.

The constitutive equations for concrete as for viscoelastic material with fading memory may be expressed in creep form, where the strain depends on the stress history and the integral kernel is the compliance function in form of a Dirichlet series.

The constitutive equations for the diffusion fluxes, in the linear form based on Onsager theorem, owing to mass balance, equation can be expressed in the local form as:

$$\rho \frac{\partial c_i}{\partial t} = -\rho \mathbf{w} \cdot \mathbf{grad}\, c_i + \mathrm{div} \sum_{k=1}^{s-1} D_{ik}\, \mathbf{grad}\, c_k + r_i \,, \tag{1}$$

where c_i stands for the component's concentration, $i \neq k$ is the case of cross-effects between the i-th and the j-th component flow. The last term describes the sources.

The diffusion coefficient depends on concentration as well as on the applied loading. Following the Aifantis' original idea of tensorial representation, [4]-[7], we assume that the diffusion coefficient depends on mean stress tensor in a linear form:

304

$$D = D_{ef}(c) + \eta \overline{\sigma}, \tag{2}$$

where the coefficient η may differ depending on sign of mean stress tensor. The Aifantis' proposition of stress gradient use is not confirmed during experiments carried out by Schneider and Chen [8], [9]. For the sake of simplicity we assume that the diffusion coefficient is independent of material deterioration. The model including cross effects between material deterioration and diffusion coefficient requires much complicated modeling, cf. [10]. It is true for moderate load level, Chen and Han [11], expected for concrete structures in aggressive environments.

The concrete deterioration due to chemical processes is usually described by a scalar parameter, ψ, calculated from an evolution equation:

$$\psi = 1 - \zeta K \quad \text{with} \quad \frac{dK}{dt} = \chi \langle c_a - c_{a0} \rangle_+. \tag{3}$$

where K is a reaction extent, ς and χ some empirical parameters and the Macaulay brackets stand for positive difference of concentration.

3. Cellular automaton rule

The alternating direction implicit scheme (ADI method) is standard procedure for transport equations solution, [12] and [13]. The procedure is somewhat cumbersome in programming although fast when applied with Crank-Nicholson rule. The main idea consist on dividing each time step into two steps each with implicit scheme along one direction and explicit in another. As result the transport constitutive equations are divided in four parts.

The much simpler procedure of cellular automata has been recalled in [14]. The procedure follows von Neumann's original idea of cellular automaton. The cellular automata are characterized by parallelism, locality and homogeneity. A simulation is run by conducting a series of updates, consisting of set of application rules. The rules are the same for all cells and typically consist of looking at cells' neighbors to determine what will be in the cell at the next step. The rules are applied to all cells in exactly the same manner and at exactly the same time.
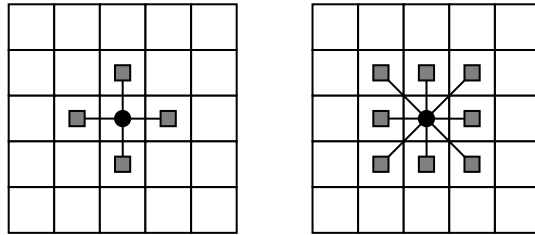

Fig. 2. Typical neighborhood: von Neumann (left) and Moore.

The cellular automata seem to be particularly useful for effective applications to diffusion processes simulation. The first reason is their simple formulation and adaptability to more detailed and complex analysis. The second advantage is modeling real discrete system directly by discrete numerical system instead of two-stage approximation: real discrete system – continuous boundary value problem – numerical discretization of the problem.

In [14] the cellular automata have been adopted with the following assumptions:
- space is divided into regular, uniform cells,
- each cell possesses a property called "cell's state",
- local rule is applied at each time step,
- the rule uses the von Neumann neighborhood,
- the constant value of diffusion coefficient has been assumed throughout.

The authors obtained fast and effective numerical solution in the case with mechanical damage added and proposed a way to take into consideration the effects of damage anisotropy.

The constant value of diffusion coefficient seems to be the most limited case. However, the method can be easily generalized on the case of locally changeable diffusion coefficient as well as on the case of cross effects. The idea consists on suitable scaling of the calculation time.

By adopting a von Neumann neighborhood with radius 1 and the rule of evolution accounting for the neighborhood in the form of FDM explicit scheme:

$$\frac{c_{m,n}^1 - c_{m,n}}{8D\Delta t}\Delta x^2 = \tfrac{1}{8}\left(c_{m+1,n} + c_{m,n+1} + c_{m-1,n} + c_{m,n-1}\right) - \tfrac{1}{2}c_{m,n} \tag{4}$$

and substituting:

$$\frac{4D\Delta t}{\Delta x^2} \equiv \alpha , \tag{5}$$

we obtain the rule of the von Neumann automaton in the form:

$$c_{m,n}^1 = c_{m,n}\left(1 - \alpha\right) + \alpha\,\tfrac{1}{4}\left(c_{m+1,n} + c_{m,n+1} + c_{m-1,n} + c_{m,n-1}\right) \tag{6}$$

with the stability condition:

$$\alpha \leq \tfrac{1}{2} . \tag{7}$$

In the case of multiple and coupled fluxes, further development of cellular automaton rule may also be acquired. Denoting:

$$\frac{4D_{ik}\Delta t}{\Delta x^2} \equiv \overline{\alpha} , \tag{8}$$

306

the final form of cellular automaton rule is then easily obtained:

$$c_{m,n}^1 = c_{m,n}(1-\alpha) + \alpha\tfrac{1}{4}\left(c_{m+1,n} + c_{m,n+1} + c_{m-1,n} + c_{m,n-1}\right) - $$
$$- \overline{\alpha}\,\overline{c}_{m,n} + \overline{\alpha}\,\tfrac{1}{4}\left(\overline{c}_{m+1,n} + \overline{c}_{m,n+1} + \overline{c}_{m-1,n} + \overline{c}_{m,n-1}\right) \quad, \tag{9}$$

were the bar over concentration stands for conjugated values.

4. Numerical examples

The effectiveness of the proposed cellular automata rules is demonstrated through several numerical examples for different cross-section shape and environmental influence.
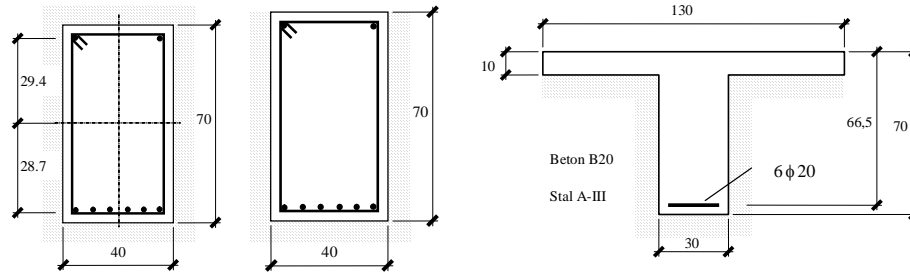
Fig. 3. Cross sections and aggressive environment.

The above formulae were successfully applied to computation of diffusion processes, cf. fig. 4. The solution for doubly condensed cells is visibly the same as for ADI.

The fig. 5 presents comparison of coupled and non-coupled solutions for the concentration profiles. It is clearly seen from the profiles lines that one dominant flow serves as a carrier of another one and can significantly influence it. In the calculations performed, the result of the cross-effect on concentration profile of influenced component increases with time. The same effect can be observed on continuity parameter profiles.

The next figures 6-9 show typical concentration and damage parameter contours. The influence of the stress state manifests in the lack of solution symmetry. The asymmetry is visible together with corrosion-rounded cross-section corners.

The concrete is not an isonomic material. On the contrary, its behavior strongly depends on the sign of mean stress. The last example shows numerical results for different load parameter, η in eq. 2, according to the sign of stress. It was assumed that coefficient is 4 times greater for tension then for compression. Despite the difference of corrosion damage is significant on the tensioned side, fig. 10, the bearing capacity of the cross-section differs less then 1%.

307
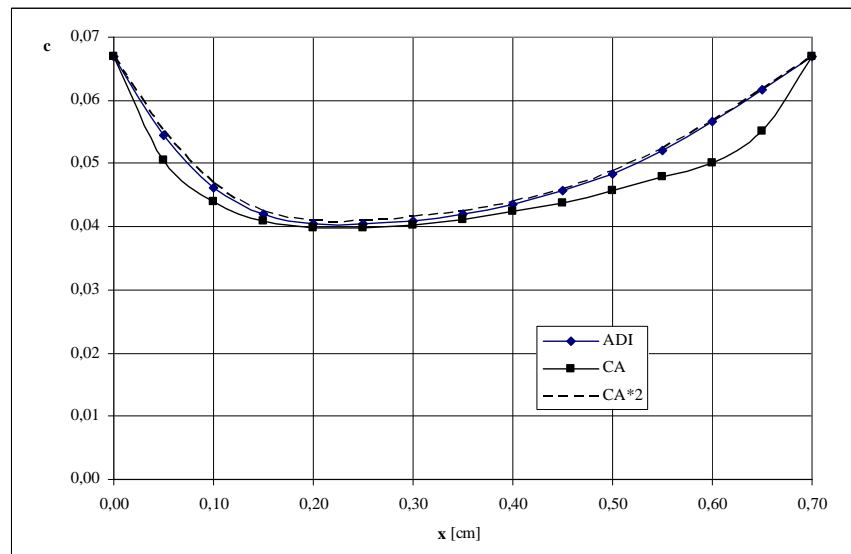
Fig. 4. Concentration profile: comparison of ADI and CA solutions.
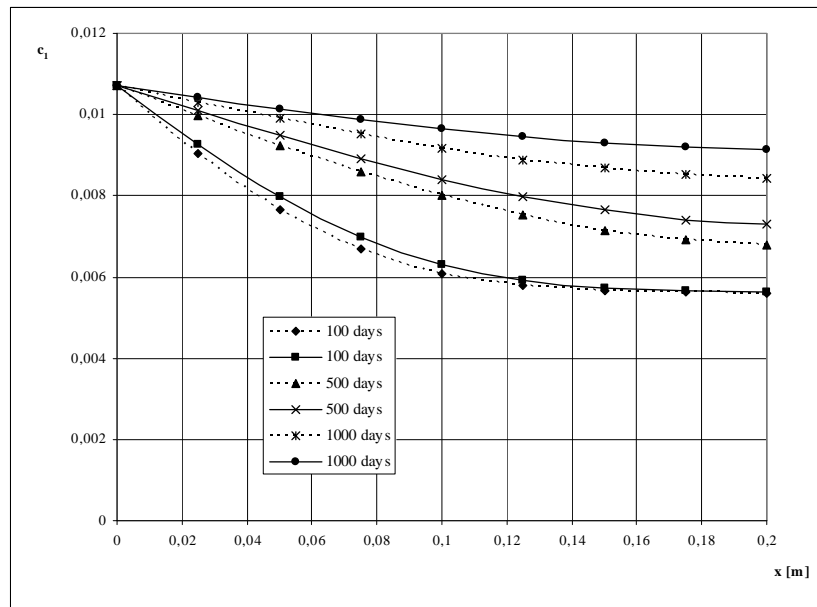
Fig. 5. Concentration profiles with cross-effects (solid lines) and without (dashed lines).

308
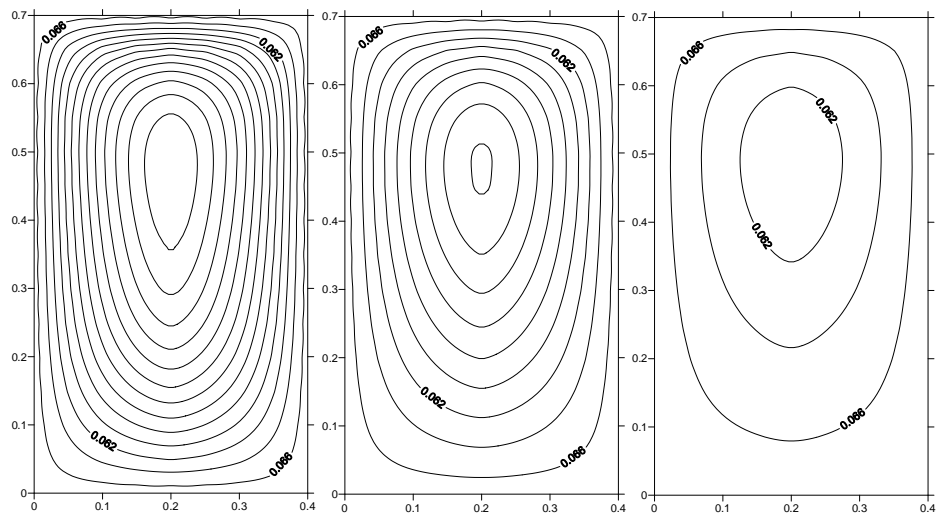
Fig. 6. Concentration contours during loading, 500, 1000 and 2000 days.
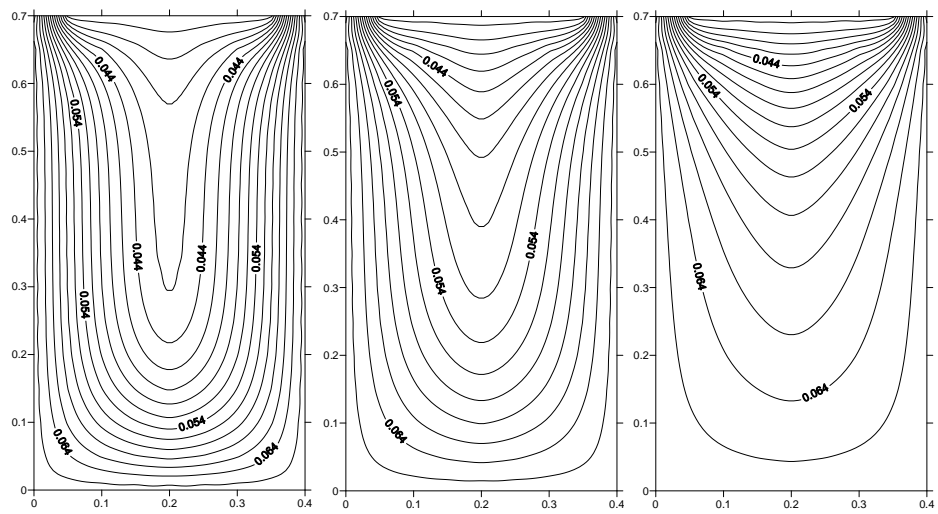
Fig. 7. Concentration contours: 500, 1000 and 2000 days.

309
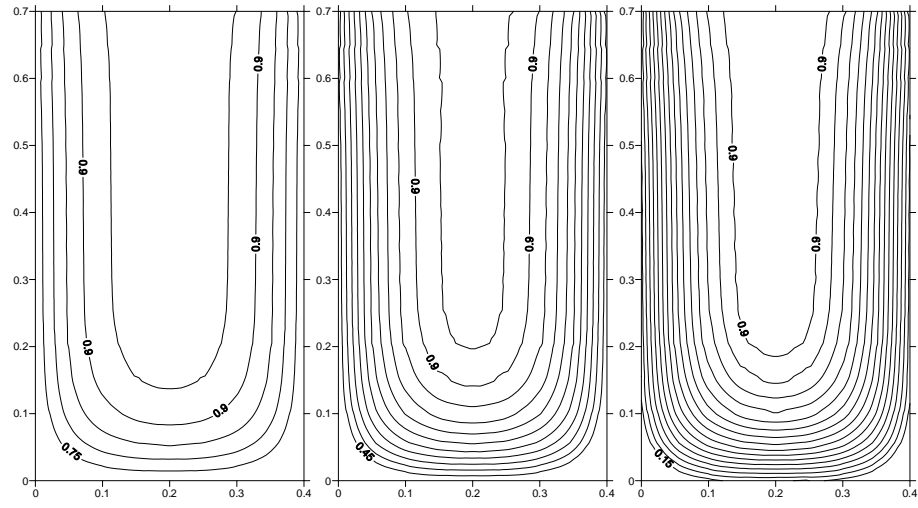
Fig. 8. Damage parameter contours, 500, 1000 and 2000 days.
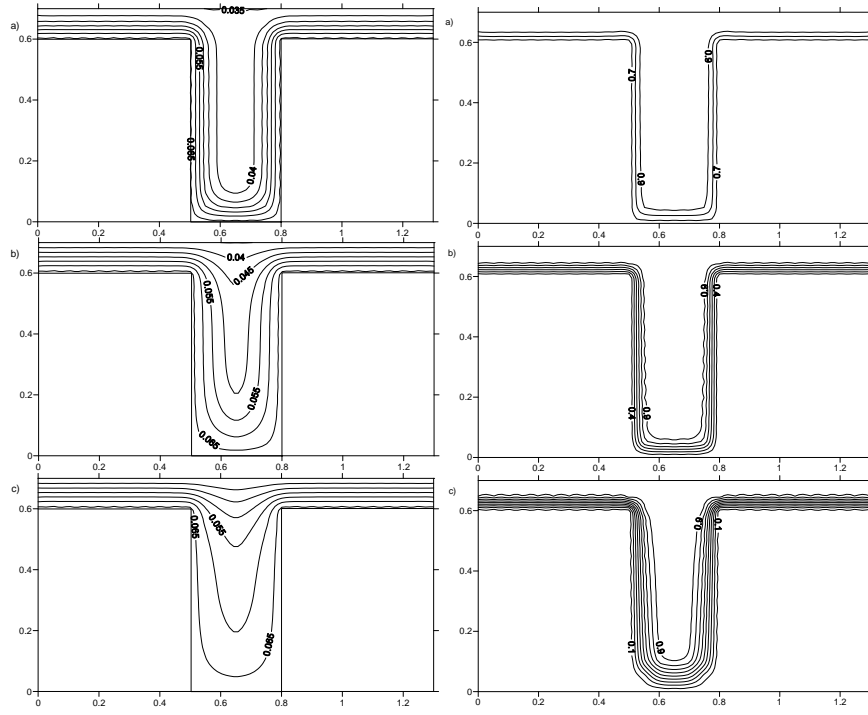
Fig. 9. Concentration and damage parameter contours: 100, 500 and 1000 days.

310
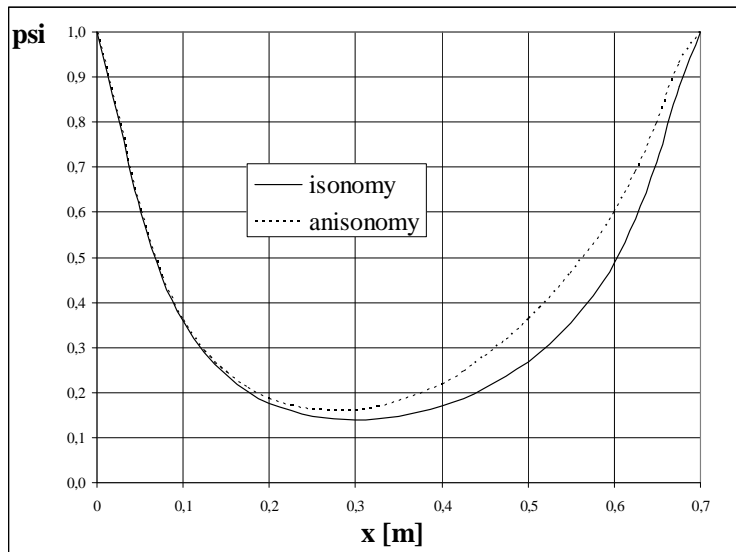
Fig. 10. Damage profiles for anisonomic- and isonomic cases.

5. Conclusions

The cellular automata are simple but powerful method of solution to the problems where the locality plays an important role. A simulation is run by conducting a series of updates, consisting of running a set of rules that all cells follow.

The calculations prove that the method can simulate various specific situations of mutual influence between flows that depend on process parameters, for example when the predominant flow stabilizes and its influence on the minor flow obviously decreases with time.

The results of presented applications prove empirically well known fact that corrosion of concrete from the tensioned side is unimportant unless the reinforcement corrosion is considered, [15]. On the contrary, the corrosion of compressed area is fundamental for cross-section capacity.

References
[1] Moskvin V., (ed.), *Concrete and Reinforced Concrete Deterioration and Protection*, Mir Publishers, Moscow, 1983, 399 pp.
[2] Neville A.M., *Properties of Concrete*, Wiley ed. 1996, 844 pp.
[3] Bowen R.M., *The Thermochemistry of a Reacting Mixture of Elastic Materials with Diffusion*, Arch.Rational Mech. Anal., vol.34, nr 2, 1969, pp. 97-127.
[4] Aifantis E.C., *On the Problem of Diffusion in Solids*, Acta Mech., No. 37, 1980, pp. 265-296.

[5] Taylor P.A., Aifantis E.C., *On the Theory of Diffusion in Linear Viscoelastic Media*, Acta Mech., No. 44, 1982, pp. 259-298.

[6] Wilson R.K., Aifantis E.C., *On the Theory of Stress-Assisted Diffusion, I*, Acta Mech., No. 45, 1982, pp. 273-296.

[7] Unger D.J., Aifantis E.C., *On the Theory of Stress-Assisted Diffusion, II*, Acta Mech., No. 47, 1983, pp. 117-151.

[8] Schneider U., Chen S.-W., *The Chemomechanical Effect and the Mechanochemical effect on high-performance concrete subjected to stress corrosion*, Cem.Concr.Res., Vol.28, No 4, 1998, pp.509-522.

[9] Schneider U., Chen S.-W., *Deterioration of high-performance concrete subjected to attack by the combination of ammonium nitrate solution and flexure stress*, Cem. Concr. Res., Vol. 35, 2003, pp. 1705-1713.

[10] Kuhl D., Bangert F, Meschke G., *Coupled chemo-mechanical deterioration of cementitious materials*, Part 1: Modeling. Int. J. of Solids & Struct., vol. 41, 1984, pp. 15-40.

[11] Chen W.F., Han D.J., *Plasticity for Structural Engineers*, Springer Verlag, 1988, 605.

[12] Zaborski A., *Corrosion of reinforced concrete due to stress-assisted diffusion*, Arch.Civ.Engng., XLI, 1995, pp.447-460.

[13] Ababneh A., Benboudjema F., Xi J., *Chloride penetration in nonsaturated concrete*, J.Mat.Civ.Engng., Vol. 15, 2, 2003, pp. 183-191.

[14] Biondini F., Bontempi F., Frangopol D.M., Malerba P.G., *Cellular Automata Approach to Durability Analysis of Concrete Structures in Aggressive Environments*, J. Struct. Engn., Vol. 130, 11, 2004, pp. 1724-1737.

[15] Wang K., Weiss W.J., Yoon S., Shah S.P., *Combined Effect of Corrosion and Stresses in Reinforced Concrete Beams*, ASCE ME, 2000, 7pp.

312

THE INFLUENCE OF THE AGGRESSIVE ENVIRONMENT ON REINFORCED-CONCRETE BUILDING CONSTRUCTIONS

Zinovij Blikharskyy[*], Roman Khmil[*]

[*] Institute of Civil and Environmental Engineering, Lviv Polytechnic National University, 12 Bandera St., 79013, Lviv, Ukraine.

1. Introduction

Often the reinforced concretes constructions of buildings are exploited under the action of aggressive environment. Carbon dioxide (CO_2) is present in the ordinary environment. The action of acid gases results in chemical transformations in a concrete (the carbonation). This phenomenon neutralizes the protective functions of concrete in relation to an armature which causes its corrosion. In the industrial environment, especially near chemical enterprises, the pollutant emission creates an aggressive environment. An analysis shows that pollutant emission of the chlorine and sulphurs creates an acid aggressive environment. The action of the acid environment results in corrosive destructions of concrete and armature of structural elements of buildings reduces their load-carrying capacity and service ability. It confirms the research topicality of the acid environment influence on the reinforced concrete constructions.

It is known, that for today one of the most widespread building materials is reinforced concrete. This material has found its application in production, and in a constructional engineering. It successfully carries out carrying functions in structural designs at a wide range of power load and other factors which are determined by an application conditions in different environments. It is known, that all existing constructions in this or that way are influenced by the corrosion processes. In nonferrous metallurgy, chemical, wood-pulp and paper industry, energy-generating factories from 20 up to 70 % of total of constructions come under effect of various corrosive environments. At acting of aggressive environment of small concentration this process can stretch for a long years, at the same time, at acting of high concentration corrosive environment construction can collapse very quickly.

Durability and load-carrying capacity generally depends not only on power load, but also on the effect of the environment [1-3]. Every year losses from corrosion in our country, as well as abroad, are estimated by different specialists in boundary lines of 4-6 % of gross national product [1]. Constructions of buildings of galvanic workshops, chemical enterprises and other elements of buildings which directly contact with reactive material come under effect of corrosive processes most of all [4-5]. Out comings of this process can

313

be the decrease of a cross section of elements, decrease of crack resistance and strength, build-up of deformations. All these processes are factors which warn of danger of a construction serviceability.

For this reason, operating of constructions at active effect of corrosive environment should be accompanied by the account of this effect in design which is not less important for a look-over of these constructions by specialists. An estimation of the load-carrying capacity of reinforced concrete constructions which have corrosion - mechanical injuries of concrete can be given on the basis of results of theoretical and experimental research of such designs that is necessary at definition of their durability and that is put as the basic purpose at conducting the given research.

2.   Experimental research

For the experimental research there were projected three series of reinforced concrete beams by the sizes of 2100×200×100 mm with reinforcement in the stretched working area 2∅12, 14, 16 A-III accordingly, and in upper compressed area 2∅5 Bp-1, and the transverse reinforcement ∅5 Bp-1 with step of 75...100 mm. The concrete mix of series is accepted with the following relationship of constituent parts Cement:Sand:Stone= =1:1.13:2.59 at water-cement ratio V/C=0.42. Brand of cement is M500 of the Mykolayiv cement plant. The sand was of the quartz unblended type taken from Yaseneckij borrow pit of the Lviv area with the Abram's fineness modulus Mc=1.36. A crushed stone granite was fractions 10...20 mm. The prism strength made 44 MPa. In general 12 beams - four specimens in each series have been tested.

At first for definition of characteristics of strength of experimental beams without effect of the corrosive environment of them were tested for a bending by a short term load till its failure. Applying of a short term load occurred by two concentrated forces in thirds of its length loading applied in increments. The loads were applied in steps. Thus deflection, presence and evolution of cracks, deformations of concrete and the reinforcement were fixed. Failure of beams has passed owing to the yield line of the reinforcement in the acting area of the greatest bending moment with the following crushing of the compressed zone of concrete.

For research of effect on strength of simultaneous acting of the corrosive environment and loading on two beams of each series were loaded simultaneously by the corrosive environment and the power load and on one beam of each series only - the corrosive environment no-load. The research time of the corresponding beams - twins in the corrosive environment under loading and without load was accepted as equal. After staying of beams in the corrosive environment they were tested by a short term load till failure. Schemes of special stands on which the experimental research was carried out are presented on fig. 1.

Beams at simultaneous acting of the corrosive environment and load were loaded to a level 0.7 from magnitude of the breaking load that was given from the yield line of the reinforcement M_u^{exp}. Magnitude of loading was controlled by special ring-balance

314

dynamometers. The external force was put with use of special spring devices which provided a constant of loading. In the area of a corrosive environment a 10 % solution of sulphuric acid H_2SO_4 was used. Such environments occur in separate chemical productions, electroplating shops, smoke pipes etc. High concentration of solution also has resolved for rather small period simulation effect of simultaneous acting of the corrosion and external loading.

The solution of acid was put in to special baths, processed by corrosion-resistant coatings, timbered on the beams. The constant supervisory control of concentration of the corrosive environment was carried out. At decrease of concentration of acid more, than on 1 %, according to size standards [6], the solution was renewed. During research the reinforcement ratio of all beams has been changed. It occurred on the account of corrosion cross section of the concrete. The reinforcement at given loadings level did not corrod. At achievement by experimental samples of limiting condition the steel ratio made for a series 3 (2∅12) – 1.93...1.99%, for a series 1 (2∅14) – 2.6...2.8 %, for a series 4 (2∅16) – 3.43...3.54%. According to design of reinforced concrete beams of a series 4 value ξ has exceeded the limiting relative magnitude of compressed zone of concrete ξ_R.

a)

315

b)

c)

Fig. 1. Stands experimental research of beams:
a) on short-term act of loading; b) on collateral long-term acting of loading and corrosive environments; c) on separate acting of a corrosive environment and loading.

Achievement of the yield line of the reinforcement in beams of all series was comprised practically equally – for 46...50 day. Final cross section of the concrete of beams - twins at physical failure at simultaneous acting of the corrosive environment and loading and without acting of loading were approximately equal (table 1). It does not enable to compare strength of beams at achievement of limiting condition by them on the

316

yield line, nevertheless the comparison of strength at physical failure is possible. For beams which were only in the corrosive environment, the BD-1.4к of a series 1, magnitude of the bending moment at physical failure was greater ($M_f^{exp} = =1773.3$ kN·cm> 1759.4 kN·cm) or approximately equal with a beam of the BD-4.4к of a series 4 ($M_f^{exp} =2122.0$ kN·cm $\approx$2141.9 kN·cm), than for beams - twins of the corresponding series that were under effect of simultaneous acting of a the corrosive environment and loading. Physical failure of a beam of the BD-3.4к of a series 3 has passed on sloping section and earlier from exhaustion of a load-carrying capacity normal section by the yield line of the reinforcement. It happened at M=1318 kN·cm with strength normal section according to standards [7] M_f^{exp} =1467.8 kH·cm. The reason of failure was corrosion of cross bar of a beam which has not enabled to compare between itself load-carrying capacity of normal cross-sections of beams of a series 3.

Table I. Strength of experimental beams affected by corrosion.

Series	Beams	End cross section (yield line) (physical failure) concrete b×h, [mm]	bar, [mm]	Bending moments, kN·m Experiment (yield line) (failure) $\dfrac{M_u^{exp}}{M_f^{exp}}$	Theoretical (yield line) (failure) By SNiP [7] M_u^{norm}	$\dfrac{M_u^{norm}}{M_u^{exp}}$	Time, [days] yield line t_u	Physical failure t_f	kind
1	ВД(БД) 1.2-0.7к	$\dfrac{74.4\times174.3}{65.0\times166.0}$		$\dfrac{1759.4}{1759.4}$	$\dfrac{1956.9}{-}$	1.112	46	56	normal section
	ВД(БД) 1.3-0.7к	$\dfrac{70.2\times169.6}{61.0\times166.0}$	∅ 14 ∅ 14		$\dfrac{1921.2}{-}$	1.092	49	60	sloping section
	ВД(БД) -1.4к	60.0×167.0		$\dfrac{1773.3}{1959.5}$	$\dfrac{1785.6}{-}$	1.007	short-time act of loading		normal section
3	ВД(БД) 3.2-0.7к	$\dfrac{70.4\times177.2}{60.0\times176.0}$		$\dfrac{1352.2}{1352.2}$	$\dfrac{1558.1}{-}$	1.152	46	54	sloping section
	ВД(БД) 3.3-0.7к	$\dfrac{68.2\times176.9}{58.0\times174.0}$	∅ 12 ∅ 12		$\dfrac{1550.6}{-}$	1.147	47	56	normal section
	ВД(БД) -3.4к	60.0×169.0		$\dfrac{-}{1318.0}$	$\dfrac{1467.8}{-}$	–	short-time act of loading		sloping section
4	ВД(БД) 4.2-0.7к	$\dfrac{71.3\times171.0}{66.5\times172}$		$\dfrac{2141.9}{2141.9}$	$\dfrac{2176.9}{-}$	1.016	50	54	normal section
	ВД(БД) 4.3-0.7к	$\dfrac{72.9\times175.0}{65.0\times173.0}$	∅ 16 ∅ 16		$\dfrac{2246.3}{-}$	1.049	48	57	normal section
	ВД(БД) -4.4к	60.0×171.0		$\dfrac{1933.3}{2122.0}$	$\dfrac{1910.5}{-}$	0.989	short-time act of loading		normal section

Experimental and design quantities according to SNiP 2.03.01-84* [7] values of the bending moments which answer the loss of a load-carrying capacity on the yield line of the

reinforcement and physical failure, and also their comparison are presented in table 1.

It is necessary to note, that the technique of standards [7] allows to determine strength of the beams affected by corrosion at absence of simultaneous effect of the corrosive environment and loading with adequate accuracy. The deviation between theoretical and actual values made 1.1 % for a beam of the BD-4.4к of a series of 4 and –0.7 % for a beam of the BD-1.4к of a series 1 towards excess of experimental magnitudes above theoretical.

The scheme of typical failure of beams samples of series 1, 3, 4 is presented on fig. 2.

The analysis of results shows, that simultaneous acting of the corrosive environment and loading for research of strength of beams is a worse possible position of external effects, than research of beams by a simple seasoning in the corrosive environment with the subsequent short-term test till its failure. It is explained by the fact that the cracks revealed by the microscope in concrete at long act of loading, being passed round come together at a macro crack. It increases deformability concrete, influences its strength and results in its premature failure. At short-term acting of loading this effect has no time to reveal itself.
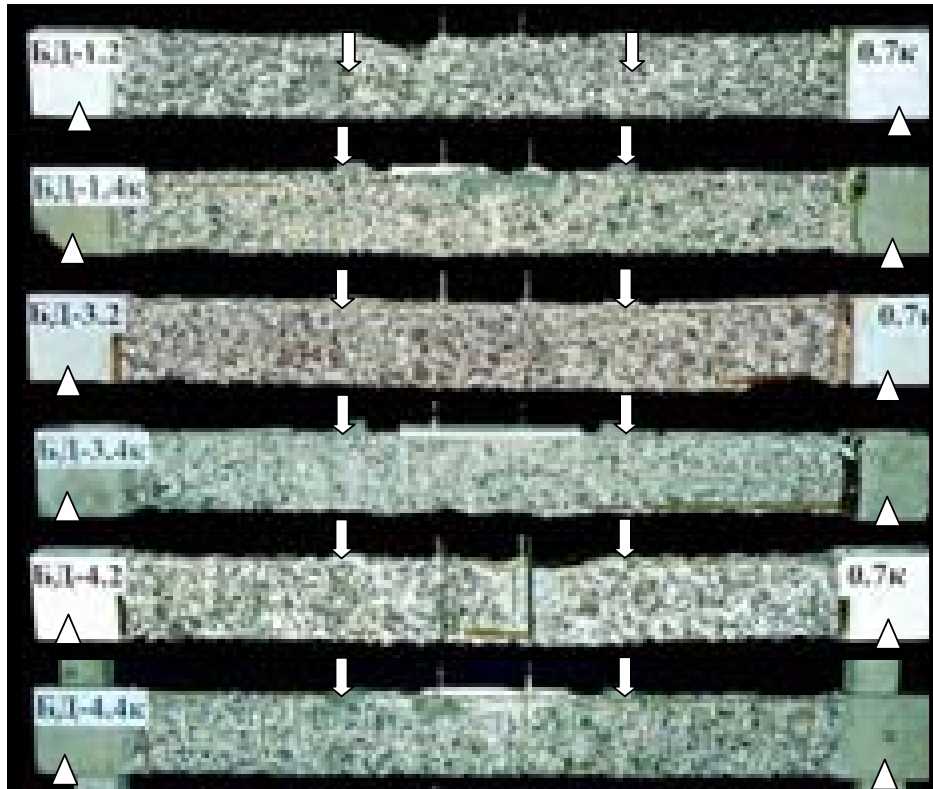

Fig. 2. The scheme of typical failure of experimental beams.

318

This research shows that failure of reinforced concrete beams in environment of sulphuric acid has passed owing to corrosion of concrete, sometimes in union with corrosion of the reinforcement. Corrosion of concrete was caused by chemical reactions of acid with constituent parts of cement stone which contains calcium. Thus corrosion proceeded gradually from external sides of concrete in depth of experimental samples with formation of a contact layer on a surface of concrete. It is necessary to notice, that corrosion of concrete of beams passed all time from the moment of putting beams into aggressive environment. Gypsum testifies to it, as it was constantly gained on the surface of beams. The quartz sand and granite crushed stone practically did not give in to corrosion and fell out from the surface of a beam during the corrosion of a cement stone.

The corrosion processes have resulted in decrease of the sizes of beam cross sections in time on linear dependences. The reduction of area of the compressed zone of concrete, as well as effective height of section has caused the increase of stresses in concrete and in the reinforcement. Failure of beams has passed at achievement of stress in the reinforcement of yield line with the further crushing of the compressed zone of concrete. On occasion physical failure passed on sloping section owing to gradual corrosion practically of all cross bar.

The analysis has also shown, that the technique of standards [7] in all cases at account of bending reinforced-concrete elements with the corrosion damage taking at long simultaneous acting of a corrosive environment and loading does not allow to determine a load-carrying capacity of such elements with the real accuracy. The deviation between theoretical and actual values made up to 15.2% towards excess of theoretical values above experimental. It is explained by effect of the corrosion micro cracks, as stress concentrators in the compressed concrete and as consequence the decrease of strength of concrete at presence of the corrosion processes and long act of loading. It is offered to be taken into account by coefficient of the concrete service conditions γ_{bc} of the compressed concrete and taking into account the presence of a contact concrete layer with the lowest physical-mechanical characteristics and strength. In beams (affected and not affected specimens by the corrosive environment) tested without long acting of load, the technique of standards [7] give sufficient convergence of results. So, the given research shows that it is possible to draw a conclusion that presence of simultaneous act of corrosive environment and loading essentially influences strength of beams affected by corrosion

3. Summary

It is shown, that simultaneous acting of the corrosive environment considerably reduces strength of reinforced concrete beams which are under loading. The deviation between theoretical and real values made up to 15.2% towards overestimate of theoretical values by SNiP 2.03.01-84* above experimental. At the same time for beams without simultaneous acting of the corrosive environment and loading the deviation made – 0.7...1.1%. That is effect of simultaneous acting of the corrosive environment and loading for research of strength of beams is a worse possible position of external effects, than testing of beams by a simple seasoning in the corrosive environment with following short-term test of it till failure

References

[1] Moskvin V.M., *Corrossion concrete and reinforced concrete constructions*, - M., Stroyizdat, 1980 – 536 p. (in Russian).

[2] Alekseev S.N., Ivanov F.M., Modry S., Shysel P., *Durability of reinforced concrete in corrosive environment*, - M., 1990 – 316 p. (in Russian).

[3] Savitskyy M.V., Punagin V.M., Pryhod'ko A.P., *Working of concrete and reinforced concrete products and conctructions,* - Kiev: UKMPO (УМКВО) - 1988.-112 p. (in Ukrainian).

[4] Bliharskyy Z.J., *Corrosion of construction of building with the galvanic production*, Interdepartmental scientific and technical symposium. Building construction. Kiev, SRIBC (НДІБК) - 1999 pp. 195-198. (in Ukrainian).

[5] Bliharskyy Z.J., Khmil R. E., *Influences of the corrosion environment on a condition of reinforced-concrete smoke pipes*, The bulletin of the Donbass State Academy of Construction and Architecture: Building construction, buildings and structures. - Volume 2001-5 (30) - Makeyevka: Publishing house DonDABA. - 2001. - pp. 97-100. (in Ukrainian).

[6] *The GOST 9.905-82. The methods of corrosion tests. General demands*, Publishing house of standards, 1983. - 5 p. (in Russian).

[7] *SNiP 2.03.01-84*. Concrete and reinforced concrete constructions*, СТІР (ЦИТП) Gosstroy of the USSR, 1989. - 80 p. (in Russian).

320

MISCELLANEOUS

MEASURMENTS OF ELASTIC DISPLACMENTS OF CHIMNEYS CAUSED BY EFFECTS OF THE SUN

Peter Breuer[*], Tadeusz Chmielewski[**], Piotr Górski[**], Eduard Konopka[*], Lesław Tarczyński[**]

[*] University of Applied Sciences, Schellingstrasse 24, 70174 Stuttgart.
[**] Faculty of Civil Engineering, Opole University of Technology, Katowicka 48, 45-061 Opole.

1. Introduction

This paper deals with GPS measurement to quantify the displacements of tops of two industrial chimneys caused by variable daily temperature and solar radiation. The objects of the investigations were two chimneys located in a power station in Bełchatów.

Fig. 1. The Power station in Bełchatów with two 300 m high chimneys. Chimney No. 1 – left, chimney No. 2 – right.

323

2.   The objects

The power station in Bełchatów is the biggest in Europe. It has the performance of about 4400 Megawatt. It has 6 cooling towers and two tall reinforced concrete chimneys. They are shown in fig. 1. The chimneys have a height of 300 m and a horizontal distance between them is 330 m. They were the objects of the measurements.

3.   The Global Positioning System (GPS)

Monitoring the displacement of the top of the tower using optical surveying methods, can only be carried out during daylight with sufficient visibility. Vibration cannot be monitored by traditional surveying techniques because the frequency of the oscillation is too high. Using a Global Positioning System (GPS) data can be collected regardless of the visibility or the weather. Using sophisticated GPS equipment in two Dual Frequency-Receivers (Reference and Rover Station) the satellites signals can be tracked with a high precision and with a data rate down to 0.1 second. A small data rate is applied, if the monitoring of wind induced vibration is demanded.

To monitor the daily course (path) of a chimney top in relation to the ground-plan the so-called Static GPS Method was applied. In spite of the motion rate of the chimney's top (maximum 4 cm/h) the Static Method is favorable if the observation time is limited to a small time interval, i.e. 10 minutes.   To trace the course of a chimney's top it is recommended to take such a sample every 30 or 60 minutes.

The data interval over 10 minutes aiming to Static Processing can be used for a Kinematic Post Processing, if some control parameters are changed. For a Kinematic GPS solution, the so-called KOF (Kinematic On the Fly) method, a long observation chain of some hundred data sets is necessary. Taking into account a data rate of 0.5 second, during every 10-minute-interval about 1000 antenna positions can be monitored. The number of data and their quality are straightforward and are adequate for the purpose to analyze vibrations with high precision.

Automatic registration permits the collection of the data samples over a long period up to several days. In summer 2006 (26-30 June) the chimneys in Bełchatów were monitored by GPS for 96 hours. Every 30 minutes the GPS units were switched on automatically and simultaneously for 10 minutes, to record the satellite's signals in a data rate of 0.5 second.

The Reference Station was mounted on a tripod close to the entrance of the power station. Two Rover Stations were installed, one on each chimney on the breastwork at the most southerly point of the top of the chimney. The lengths of the inclined baselines were 555 m (Chimney 1, East), and 915 m (Chimney 2, West).

4.   Daily drift of the tops of chimneys due to effects of the sun

Fig. 2 presents the daily drift of the chimney 1 and 2 during 4 days in the summer of 2006. The monitored GPS positions are drawn in one-hour-intervals and marked with the belonging day and time. The consecutive positions are connected by a line indicating the

direction of motion by an arrow. Fig. 3 shows the corresponding meteorogical data recorded at the meteorological station in Wieluń, 60 km westerly of Bełchatów.
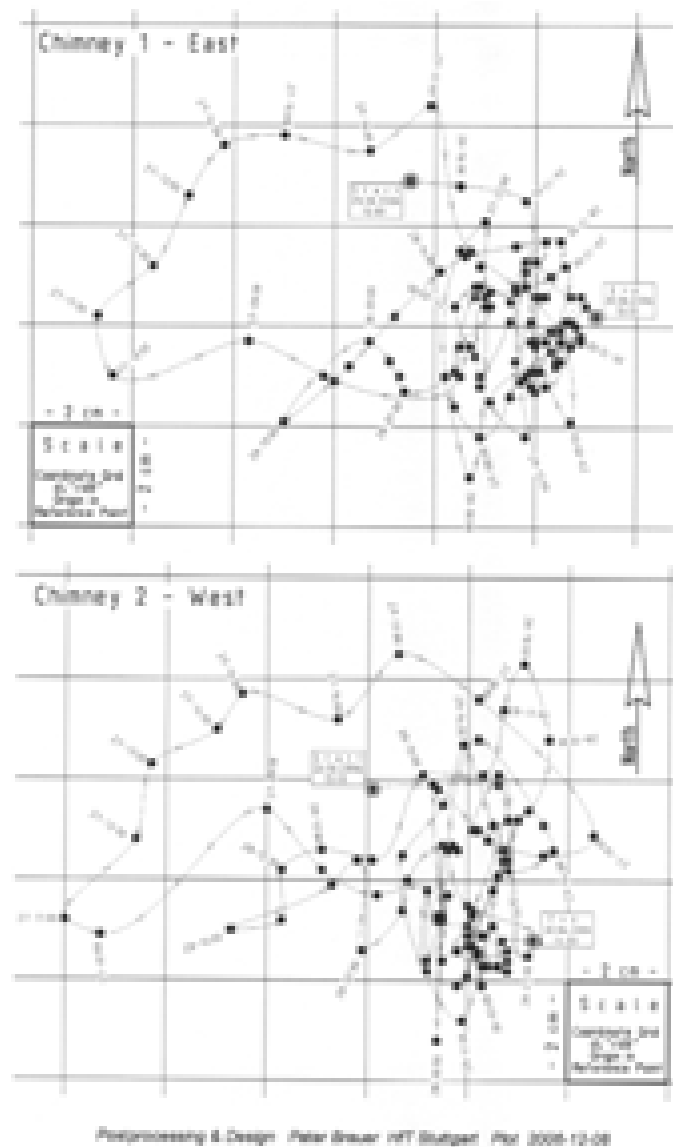

Fig. 2. The GPS-monitoring of chimneys 1 & 2, daily horizontal drift of the tops of the chimneys, during 4 days measurements 26-30 June 2006.

In fig. 2 the trace of both courses is nearly identical. On 27 July 2006 the displacements in the West-East direction are evident for both chimneys. It is the only day when a very significant the West-East motion was observed. The maximum motion is up to 3cm/h. On June 27, 2007 the temperature rose to 29-30 °C at noon, accompanied by high radiation rate. During the following two days the temperature did not exceed 23-25 °C and the appearance of sunshine was minimal. Therefore the moving rate of the tops of the chimneys was strongly reduced.

Fig. 3. Meteorogical data recorded at the Meteorogical Station in Wieluń.

5. Conclusions

a) The results clearly show that it is possible to monitor long-period structures due to effects of the sun. The applications can also be extended to monitoring wind or earthquakes deformations of such structures.

b) The structure (stiffness) of both chimneys is similar, so the displacements due to the effects of the sun are approximately equal.

References
[1] Celebi M., *GPS in dynamic monitoring of long-period structures*, Soil Dynamics and Earthquake Engineering, Vol. 20, 2000, pp. 477-483.
[2] Breuer P., Chmielewski T., Górski P., Konopka E., *Application of GPS technology to measurements of displacements of high-rise structures due to weak winds*, Journ. of Wind Engineering and Industrial Aerodynamics, Vol. 90, 2002, pp. 223-230.

DYNAMIC RESPONSE OF A BUILDING IN STRONG WINDS

Jaromír Král[*]

[*] Department of Mechanics, Klokner Institute, Czech Technical University in Prague, Šolínova 7, 166 08, Praha 6, Czech Republic.

1. Introduction

The repeated cold front transitions of January 2007 in the Czech Republic were accompanied by occurrences of strong winds. Prior to these strong winds, an accelerometer and a recorder had been placed high up at the Shiran Tower (formerly VUMS) in the west-end of Prague. A dynamic part of the building's response to these gusts of wind in this period was recorded. This paper includes the dynamic features of the building, the standard effects of wind, measuring results and corresponding meteorological data from the station Praha, Ruzyně.

In the introduction of the text there is information about the new wind map for the Czech Republic and a comparison of initial estimates of wind speeds with speeds measured in January 2007.

2. The wind map for the Czech Republic

The analysis of meteorological data from hourly series of measurements from 16 CHMI (Czech Hydrological and Meteorological Institute) professional stations in the period 1981 – 2000 showed the necessity of modernizing the wind maps for the Czech Republic and the possibility of including the altitude influence [1]. In CHMI, on the basis of the recommendations stated in this work, the relation between the estimates of ten-minute speeds from hourly and climatologic series of measurements in all professional stations has been verified and confirmed. This step has enabled to use the verified and digitalized files of data from a bigger number of stations and from the period 1961 – 2000. The stations with incomplete series of data or variable conditions in the period of measuring have been excluded. Out of the total number of approximately two hundred stations files of annual maxima from 43 stations in the territory of the Czech Republic were selected. Short record sequences from neighbour German stations (Grosser Arber, Fichtelberg and Zinnwald) have been included as well.

A 10-minute, mean wind-speed regional map has been drafted in accordance with Eurocode requirements and in collaboration with CHMI and the Klokner Institute of the Czech Technical University in Prague (KI CTU). Dr. Hostýnek (CHMI) has performed the final processing of the wind map [2]. Upon selection of annual maximum 10-minute speeds, a suitable statistical model was chosen by means of the QCExpert 2.5 statistical software. The module seeks a best-fitting statistical model (distribution) for description of

327

data by using the MLE (Maximum Likelihood Estimate) method. The module calculates parameters of these distributions for given data and selects the best-fitting distribution according to two criteria: the likelihood function and the correlation coefficient of the P-P plot. The highest average value of P-P coefficients was found in the lognormal distribution. However, it was not possible to use this model to fit all speed series. The Gumbel distribution showed second highest average value of P-P coefficients and it was possible to obtain speed estimates in all wind speed series. The area distribution of the speed estimates was processed with Geographical Information System environment (GIS) using orographic interpolation, a digital elevation model (DEM) and the mathematical IDW method. The calculation was aimed at grid representation with a 200-metre pitch. Square smoothing was performed with a low pass filter and a five-fold cycle.

The construction of the map was based on corrected estimates of speeds localized at station locations. Due to irregular distribution of stations across the Czech Republic, virtual stations (nodes) were included to increase the calculation node density in areas containing extremely distant real stations. The formerly calculated the relation between the wind speed estimates at selected return period and the sea level altitude were extrapolated to these nodes.

The influence of the terrain in the place of the station was excluded by means of a standard transformation of speed estimates to the terrain type II. Apart from that the wind maps corrected in the region of South Bohemia with respect to the estimates of maximum gusts. The correction was implemented with the rising of the speed by 2.5 m/s, that means moving to an area with a higher wind speed.

The map is used as a part of the national annex of the ČSN EN 1991-1-4 standard [3]. The constructed map of estimates mean 10-minute wind speeds with an annual probability of deviation of $p = 0.02$ is shown in fig. 1.

3.   The wind speeds in January 2007

On 18 January in the afternoon and at night from 18/19 January 2007 there was an extraordinary meteorological situation during the passage of the cold front over Western and Central Europe. The passage of the cold front was accompanied by strong storms. In the means of communication the strongest storm was named firstly as cyclone "Kyrill", later as the "Hurricane Kyrill". (Note: The official terminology does not acknowledge this name). It attacked the whole of the Czech Republic; however, the strength of the wind was very diverse. Many places measured record wind gusts, but these were mainly mountain meteorological stations.

It was the first occasion to verify the reliability of the wind-speed map. The measured wind speeds of the 46 reference stations used to make the wind speed map were compared with those of statistical estimates ($p = 0.02$) and local, historical maximum wind speeds. The statistical estimations of medium ten-minute speeds were exceeded in five meteorological stations – see table I and fig. 2. The numbers show the proportion between the biggest measured medium ten-minute speed (F) and its statistical estimation in the related station for p = 0.02 (F_{50}).
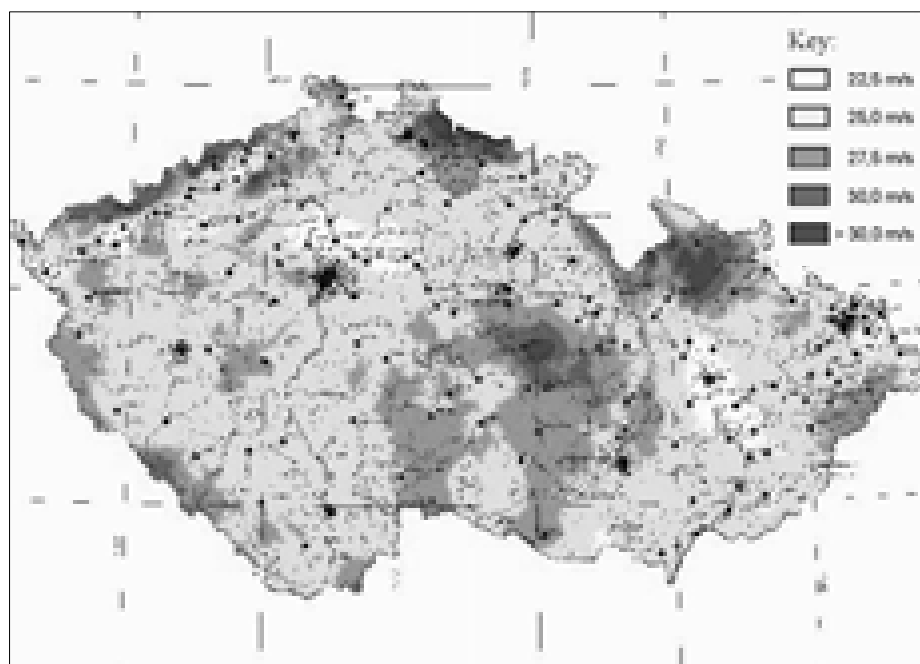
Fig. 1. Ten-minute wind speed regions in the Czech Republic.

Table I. The proportion between the biggest measured ten-minute speed (*F*) and its statistical estimation (*F*$_{50}$).

Station	*F*/*F*$_{50}$	Station	*F*/*F*$_{50}$
Praha, Karlov	1.47	Temelín	0.95
Kocelovice	1.21	Milešovka	0.93
České Budějovice	1.10	Praha, Ruzyně	0.93
Fichtelberg (FRG)	1.09	Praha, Kbely	0.93
Plzeň	1.05	Přimda	0.92
Pardubice	1.02	Dukovany	0.92
Kuchařovice	0.97	Liberec	0.90

The biggest proportion of the measured and estimated speeds was found out in the station Praha, Karlov. There is a high probability that the rise was caused by the orography of the ground and non-standard placement of the anemograph at the height of 19 m. The

329

meteorological station is situated in a built up area on the right bank of a river in the extension of the axis of the valley on the left riverbank. In the given meteorological situation the wind direction was parallel with the axis of the valley and the station was situated on the windward side at the end of it.

A small rise in the measured speeds in Plzeň and Pardubice is covered by the gradation of speeds in the separate areas. In case of the meteorological stations Kocelovice and České Budějovice the stated speed excesses confirmed the justifiability of the correction, done on the basis of the estimations of maximum gusts already during processing the map.
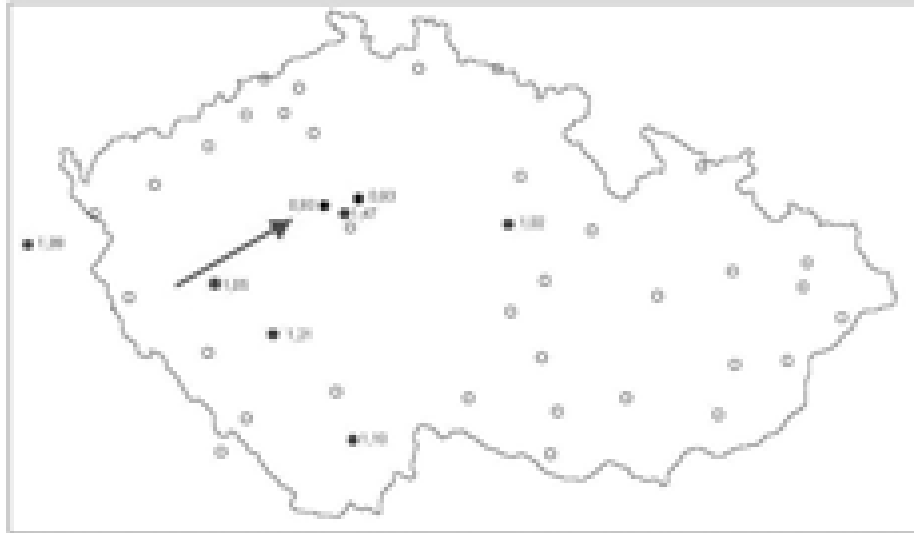
Fig. 2. 10-minute mean wind speeds ratios: (a measured mean speed on January 18, 2007) / (an estimate for $p = 0,02$).

At the end it is necessary to mention that during this meteorological situation the dominating wind direction was approximately from 230° to 250°. That might be the reason why the damages to building constructions were relatively small. In the territory of Bohemia the dominating wind directions in maximum gusts were from 270° to 280° in the past, in the territory of Moravia from 300° to 310°. The wind map passed this first exam.

4. Response of building in strong wind

4.1. The building

The prefabricated supporting structure of the building on the north-western part of Prague is 63.8 m high after the reconstruction of the cladding. It has a rectangular cross-

330

section with dimensions of 31 m x 14 m. The supporting system consists of two supporting external walls on the shorter sides of the cross-section and of one longitudinal wall in the axis of the building oriented in the direction of the longer dimension of the cross-section. The diagram of the building is in fig. 3. In 1972 there was a dynamic test implemented on this building and during this the force of rocket engines [4] were used to initiate vibrations. The target of the test was to find out the natural frequencies and modes of vibration. Based on the response of the building to the power impulse the value of the logarithmic decrement of damping was determined $\delta = 0.074$ for the vibration in the fundamental mode.

On the basis of available concepts, the building was modeled in a program called NEXIS 32. The resulting model was of an informative character and it was aimed at comparing responses of the building to wind load.

The equivalent static load was determined pursuant to ČSN 73 0035 and ČSN EN 1991-1-4. For calculating of the response, the above-stated calculation model of the building was used. The equivalent static deviation on the top of the building was calculated for the load according to stated standards and for the load corresponding with the maximum measured medium wind speed on 18 January 2007. Also the actual frequencies of the flexural and torsional vibrations of the building were calculated. The fundamental mode of vibrations is shown in fig. 3. For the lowest natural frequency ($f_{1,y} = 0.75$ Hz) a standard deviation and an expected maximum acceleration value were calculated. The equivalent static deflections and accelerations at the top of the building are given in table II.
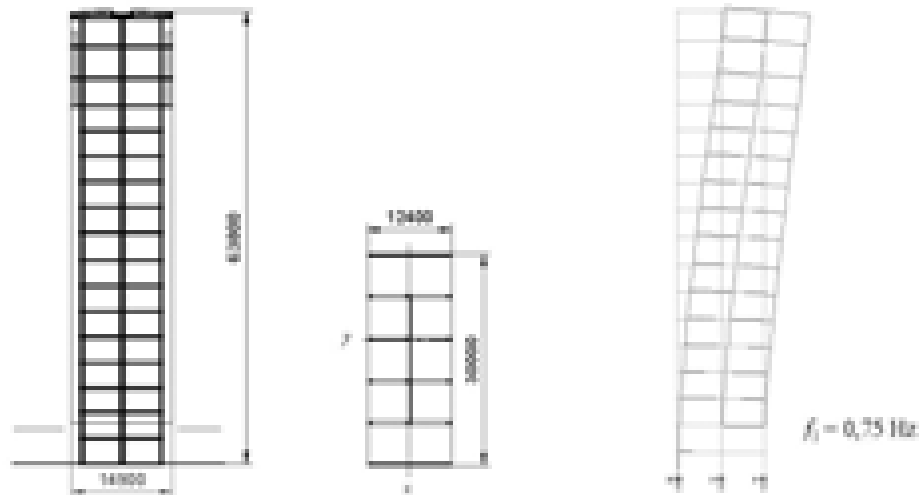

Fig. 3. The diagram of the building supporting system (a). The fundamental mode of vibration (b).

331

Table II: Calculated responses at the top of the building according standards loads.

National standard	Deflection [mm]				Acceleration [mm/s^2]	
	Standard load	Calculated load	Character. load	Design load	$\sigma_{a,x,char}$	$a_{x,peak}$
ČSN 73 0035	21.4	27.8	-	-	-	-
ČSN EN 1991-1-4 [*]	-	-	35.1	52.7	39.5	137
January 18, 2007	-	-	24.9	37.4	12.7	77.9

[*]Note: *Basic wind speed U = 27.5 m/s.*

4.2. Local meteorological information

In the north-western part of Prague, strong gusts of wind were recorded on the afternoon and night of 18/19 January, 2007. The overview of ten-minute mean wind speeds U_{mean} and wind gusts U_p in the nearest meteorological station Praha, Ruzyně is on the fig. 4.
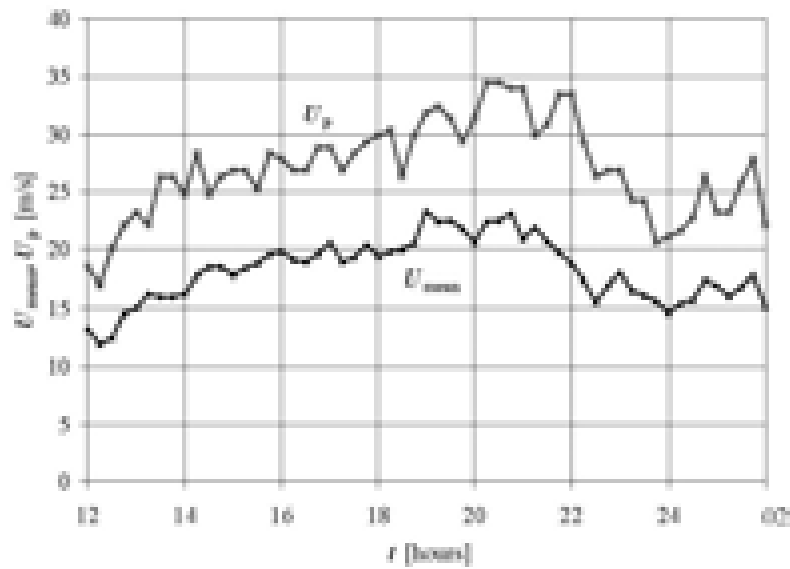

Fig. 4. Overview of wind speeds in the nearest meteorological station Praha, Ruzyně - January 18, 2007.

The maximum measured ten-minute mean speed at 10m was 23.3m/s (nearing a ten-year maximum) and the maximum wind gust speed was 34.5m/s (nearing a five-year maximum).

332

4.3. Dynamic response of the building

The Czech Institute of Hydrometeorology gave a danger alert of extreme wind speeds in the Czech Republic on that Thursday morning. On the 15th floor in the north-western corner of the building we installed an automatic measuring system controlled by a computer and with an accelerometer Type 4379 and a charge amplifier Nexus Type 2692A/0S4 (Brüel & Kjaer). The activity of the measuring system was controlled by means of a programme developed in the TestPoint environment. Monitoring took 12 hours and was terminated by a power failure in the building. The recordings were 300s long, followed by a lag of 300s (e.g. six recordings per hour). The total number of recordings was 72.

In fig. 5 there are standard deviations and maximum values of acceleration in direction y (direction of the shorter dimension of the cross-section) from separate records in dependence on the time of measuring. The measured values can be attached to the wind speeds in fig. 3.
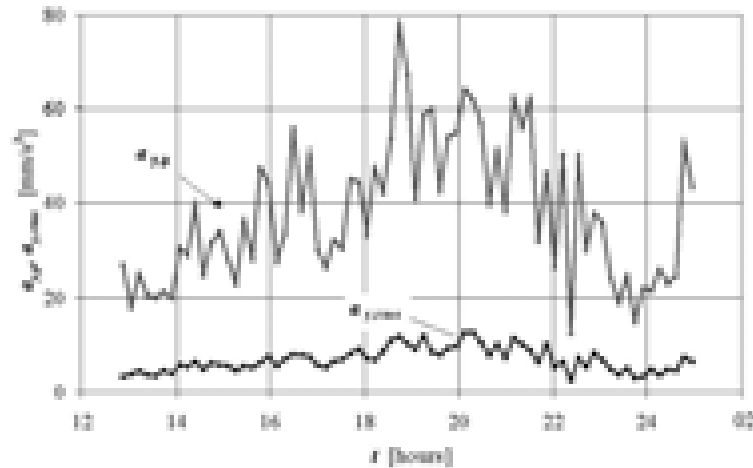
Fig. 5. Peak and rms values of the acceleration on the 15th floor.

In fig. 6 there is a part of the record containing the maximum measured acceleration value. Using the double integration of the record in zero initial conditions we obtained the course of the dynamic deviation of the top of the building. A part of the calculated course is in fig. 7. Acceleration spectra were calculated from all the records. They are shown in fig. 8. The spectra peaks correspond with the natural frequencies of the building during flexural and torsional modes of vibration. The lowest flexural frequency is 0.75 Hz. For big amplitudes of vibration the frequency moved towards lower frequencies (0.69 Hz). Based on the shapes of the peaks of spectra for the biggest amplitudes of vibration the effective value of the logarithmic decrement of damping $\delta = 0.08 - 0.1$ was estimated. These values are comparable to the value of the logarithmic decrement of damping from measuring building response after the impulse of the rocket engines $\delta = 0.074$ [4].

333
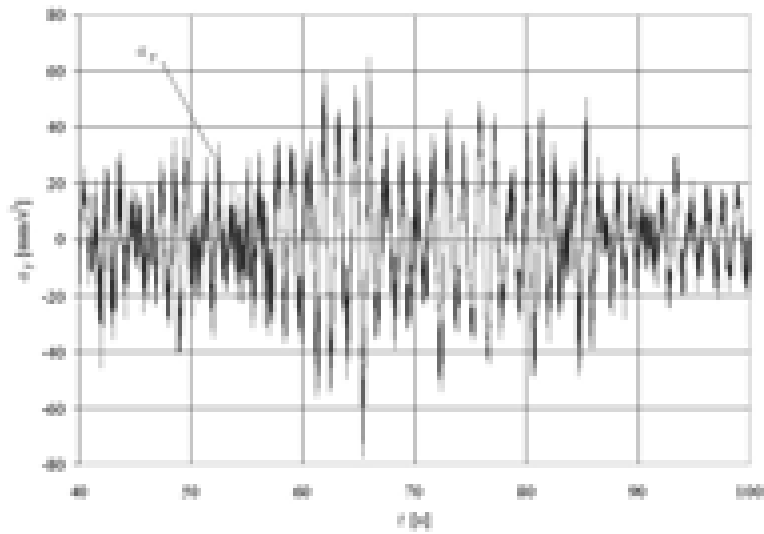
Fig. 6. Part of the acceleration recording at the 15th floor in the *y* direction.

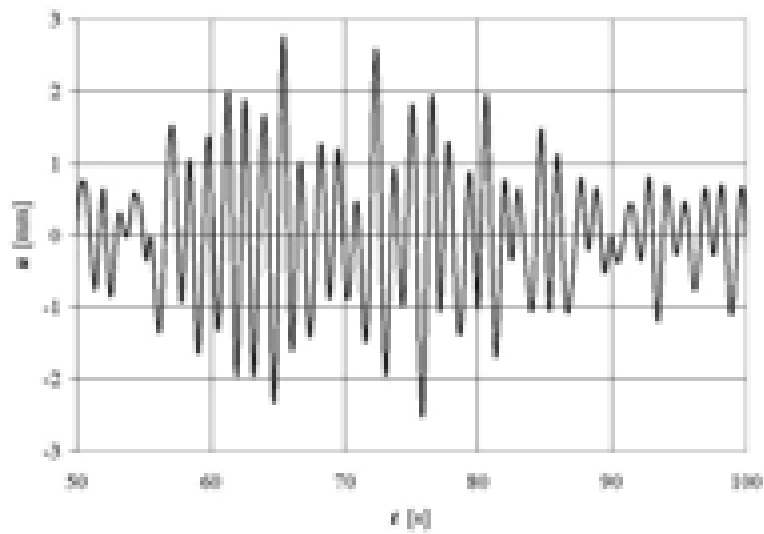Fig. 7. Part of the horizontal dynamic deflection at the 15th floor in the *y* direction.

The 10-years mean wind speed and 5-years wind gust were measured at the nearest windward meteorological station Praha Ruzyně (6 km). The characteristic response at the top of the building is approximately 35.1mm (Eurocode, 27.5 m/s, terrain category II, $\delta = 0.074$).

334

The characteristic response in given strong wind condition is 24.9 mm ($u_{max}(63.8) = 21.7 \pm 3.2$ mm). Dynamic part of the response corresponds to the ±12.5% of the total response ($n_1 = 0.75$ Hz). The building is not typical wind sensitive structure, but the dynamic response could not be neglected. For example: the acceleration limit according [5] for "office" as well as for "residence" was exceeded in this case. The building is suitable for the long term response monitoring.
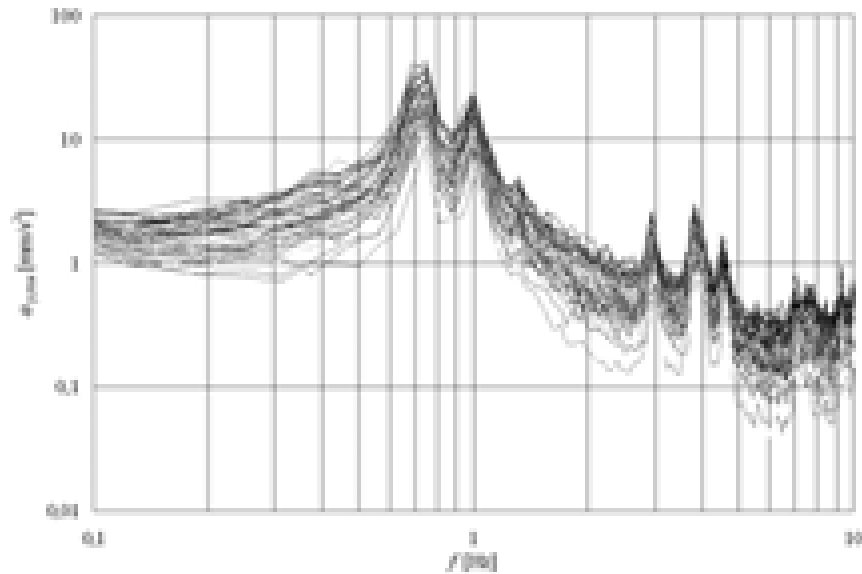
Fig. 8. Overview of acceleration spectra in the y direction.

5. Conclusion

10-year medium ten-minute wind speed and 5-year gust were measured in the nearest windward meteorological station. The dynamic item of the building response with the frequency of $n = 0.75$ Hz represents ±12.5% from the total response. It is not possible to consider the building a typical construction sensitive to wind effects, but a dynamic reaction cannot be omitted. The building is suitable for a long-term observation of wind effects. There will be a permanent measuring system installed on the building, the number of sensors will be increased and the installation will also include equipment for measuring the speed and direction of wind.

References
[1] Král, J., *Ten-minute Wind Velocities and Gusts of Wind in the Czech Republic*, In: Conference Proceedings [CD-ROM]. Prague: ITAM AV ČR, 2005, s. 1-10.

[2]   Hostýnek, J., Král, J., *Influence orography on design wind speeds in the Czech Republic*, (in Czech), Inženýrská Mechanika 2006, Svratka, 12 p.

[3]   *ČSN EN 1991-1-4 Zatížení konstrukcí - Část 1-4: Obecná zatížení – Zatížení větrem*, (in Czech), ČNI, 2007, Praha.

[4]   Pirner, M.,: *Dynamické charakteristiky vysokých budov při velmi malých buzeních*, (in Czech), Stavebnícky časopis SAV, XXI 2, 1973, Bratislava.

[5]   *ISO 10137:2007(E) Bases for design of structures — Serviceability of buildings and walkways against vibration*.

Acknowledgments

HIGH PERFORMANCE STEELS IN BRIDGE STRUCTURES – MINIMIZATION OF NEGATIVE INFLUENCE ONTO ENVIRONMENT

Grażyna Łagoda[*], Marek Łagoda[**], Anna Leniak-Tomczyk[***], Marcin Górecki[****]

[*] Institute of Roads and Bridges, Faculty of Civil Engineering,
Warsaw University of Technology, Armii Ludowej 16, 00-637 Warsaw, Poland.
[**] Department of Roads and Bridges, Faculty of Civil and Sanitary Engineering,
Lublin University of Technology, Nadbystrzycka 40, 20-618 Lublin, Poland and
Road and Bridge Research Institute, Jagiellońska 80, 03-301 Warsaw, Poland.
[***] DrogMost Lubelski Sp. z o.o., Zaciszna 16, 20-415 Lublin, Poland.
[****] Department of Building Structures, Faculty of Civil and Sanitary Engineering,
Lublin University of Technology, Nadbystrzycka 40, 20-618 Lublin, Poland.

1. Introduction

New steel production processes have lead to a remarkable improvement of steel products in the last couple of years and allows producing steels according to desired mechanical and chemical properties. Developments in the USA, Japan and Europe showed a remarkable increase in the use of these steel grades for structural purposes, especially in the field of bridge construction. Within these countries, a variety of steel grades were developed according to the specified requirements and priorities. As this paper is a focus on different aspects on High-Performance Steels (HPS), the following sections give a short summary concerning research, developments and applications, and include an overview and comparison of the properties of the commonly used international HPS.

2. Application of weathering steels for bridges structures

Corrosion resistance is often referred to as the weathering characteristic of HPS and other steels. In contrast to the original weathering steels, developed in the 1960s, steel manufactures especially in Japan and the USA have recently developed a new advanced weathering steel material by adding various alloy elements such as high contents of nicel (Ni) and copper (Cu). These new steels have a much higher corrosion resistance than the original ones and thus allow structures to be built without painting or other corrosion resistance techniques. Additionally, for the corrosion design, an advanced weathering index allows a better prediction of the weathering resistance depending on the amount of alloy element and the environmental conditions.

Weathering steel can dispense with painting because of its characteristics that the

337

development of rust is controlled steadily with a lapse of time. As a result, maintenance costs can be significantly reduced. Based on the results of survey of many bridges in the world, it was concluded that weathering steel can be used in atmospheres with chloride levels up to 0.05 mdd (mg/dm^2/day). Application of weathering steel is classified into unpainted and painted use, and rust stabilization treatment is categorized as unpainted use. It aims at not only preventing environmental contamination by initial rust – laden water but also at expanding the application range of unpainted weathering steel. A variety of rust stabilization treatments is now in practical use, and their effects are roughly categorized into four types in the table I. Each treatment available in the current market has the combined effects of these.

Table I. Effects of rust stabilization treatment.

No.	Effect	Explanation
1	Prevention of rust laden water outflow	To preclude the problems (rust outflow, etc.) in untreated weathering steel
2	Promotion of stable rust layer formation	To form protective stable rust layer in a short period of six months to a few years
3	Aesthetic improvement	To allow longer service life by means of surface color treatment than conventional painting
4	High resistance to chloride in the atmosphere	To form stable rust layer resistant to chloride in the atmosphere

The effect of rust stabilization testament in suppressing the outflow of initial rust is schematically shown in the fig. 1.

Although painted ordinary steel bridges need repainting every ten years on average, the use of weathering steel can eliminate it. Therefore, the cumulative cost of 40 years of service can be reduced as shown in the fig. 2.

Fig. 1. Schematic illustration comparing the rust outflow of untreated and rust stabilization treated weathering steels.

Fig. 2. Comparison of cumulative costs (example) [1].

338

3. Vibration-damping steel plates

During the mind 1980's there was a significant amount of using steel-resin-steel sandwich plates. The first Japanese solution (fig. 3) it's the VDS sandwich steel plate (2,3~10 mm) with visco- elastic resin (0,15~0,3 mm).
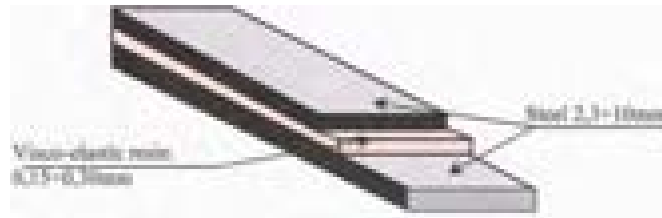
Fig. 3. Vibration-damping steel plate (VDS) [2].

In order to study the noise-damping effects of steel bridges constructed using VDS plates, noise–measurement tests were conducted using a pilot test railway track. As shown in the fig. 4, it was confirmed that vibration-damping effects of about 3 dB are obtained using vibration-damping steel plates in web plates. In particular, vibration-damping is considerable for through-type bridge girder and noise-damping effect of 8 dB was obtained. The fig. 5. shown comparison of any materials damping factors.
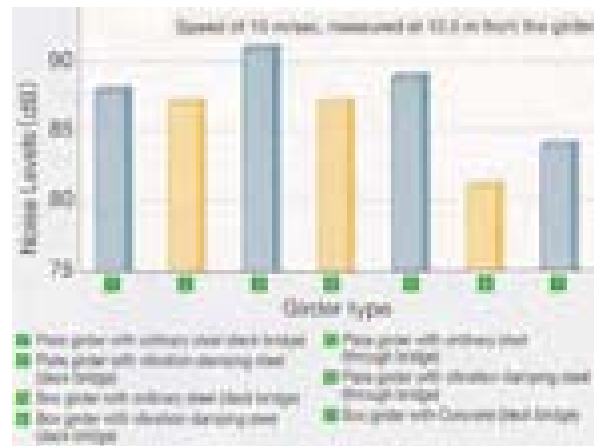
Fig. 4. Comparison of noise levels.
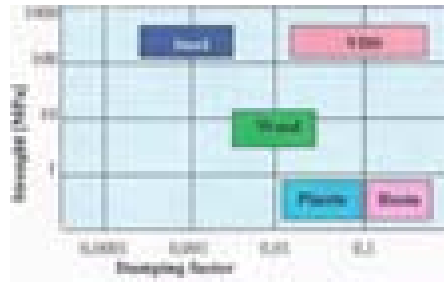
Fig. 5. Comparison of damping factors [2].

4. Sandwich Plate system

In the (second solution of Intelligent Engineering Ltd. in conjunction with industry partner, Elastogran GmbH, a member of the BASF Group) Sandwich Plate System, two steel (or other metal) plates are bonded to a compact polyurethane elastomer core, as shown in fig. 6. Sandwich-action is generated through the bond between the polymer core and the steel plates. it generates high bending resistance and bending stiffness where it is loaded as a plate, so that stiffeners usually used to reinforce thin plates can be abandoned. Due to this stiffness it can also be used for shear walls as local plate buckling is prevented.

Fig. 6. Sandwich Plate System (Fragment).

The flexural stiffness and strength of a sandwich plate can be tailored to meet particular structural requirements by selecting appropriate thicknesses for the sandwich elements so as to be structurally equivalent to a stiffened steel plate. The bonded elastomer provides continuous support to the steel plates, thus precluding local buckling and eliminating the need for closely spaced discrete stiffeners, and transfers shear from one steel plate to the other (fig.7).

Structural problems associated with corrosion, fatigue or with extreme or accidental loads (collisions and groundings including low energy impacts) acting on conventional stiffened steel plate structures are well documented and lead to failures. Welded stiffened steel plates are prone to cracking or rupture at locations of concentrated strains such as sharp load points, hard spots, rigid joints and localized bending over stiffeners, and are also susceptible to crack propagation.

340

Fig. 7. Equivalent structural strength and stiffness [3].

To increase its energy absorption capacity, a structure must be simplified and designed to allow localized progressive plastic membrane action. Simplification is achieved by eliminating stiffeners and by introducing a plate structure with equivalent in-plane buckling capacity and stiffness to the stiffened plate, and flexural capacity to sustain transverse loads. This is uniquely achieved with the SPS plate section. Furthermore, the ductile core eliminates hard spots over primary supports and provides continuous support to the faceplates, dissipating localized bending strains. A further benefit is that the polyurethane elastomer provides an effective crack arrest layer.

Vibration damping and structural borne noise transmission of SPS is very good [4]. Typical displacement attenuation curves for SPS and steel plates subject to a single pulse illustrates fig. 8. The inset picture illustrates a standard vibration characterization test conducted at BASF laboratories in Ludwigshaven.
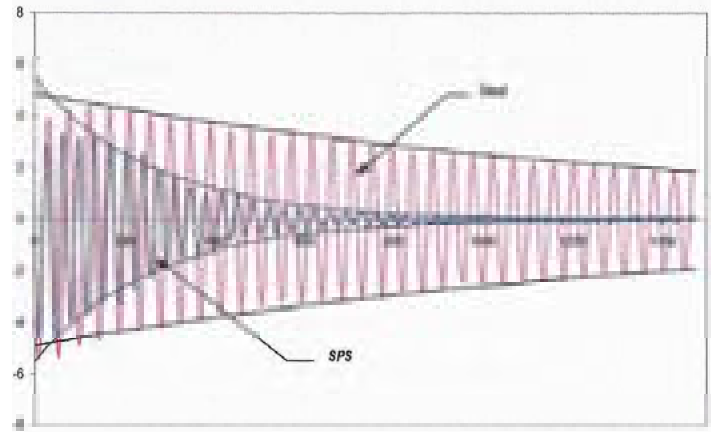

Fig. 8. Inherent vibration damping provided by visco-elastic core.

SPS has been used to construct 3 bridge decks in Canada, to provide life extension by enhancing the fatigue resistance of three orthotropic bridges, two in Germany and one in the UK.

5. Conclusion

The proposed site for a bridge should be evaluated with respect to the environment effects. Steel bridge constructions affect negatively onto environment. They can here to help suitable materials.

In case of weathering steel structures, the environmental problems associated with paint VOC emissions, and the disposal of blast cleaning debris from future maintenance work are avoided.

The decrease of noise from traffic is also very important. Here they can help vibration-damping steel plates and sandwich plate system. SPS-plates have an advantage in view of light weight aspects because of the low density of the core material ($\gamma = 1.1$ g/cm^3). They may be prefabricated in shop or fabricated on site by filling the resin into prepared cavities, where it polymerises to serviceability strength in about 2 hrs and full strength in about

24 hrs. [5]. They provide minimum steel surfaces exposed to corrosion, have excellent fatigue properties (due to the lack of welded stiffeners or attachments) and also exhibit good damping properties (for noise emission), and insulation properties (for temperature or fire resistance). SPS-plates are most suitable for both refurbishing existing steel decks by overlay – or underlay – techniques to make them durable and fit for increasing traffic loads and for building new steel decks.

References
[1] The Konzai Club, Research Group on Steel Bridges,: *High performance steels for bridge construction*, Japan Association of Steel Bridge Constrution. Tokyo 1998.
[2] Łagoda G., *Wiadukty nad autostradami – wybrane zagadnienia kształtowania konstrukcyjnego i estetycznego*, Oficyna Wydawnicza Politechniki Warszawskiej, Warszawa 2001.
[3] Kennedy S., *An innovative construction technology for engineered structures*, Intelligent Engineering Ltd. London 2007.
[4] Sedlacek G., Paschen M., Geβler A., Schäfer E., *Gutachten zum Nachweis der Verbesserung der Dauerhaftigkeit durch SPS-Verstärkungen der Stahlfarbahnplatten des Brückengerätes*. RWTH Aachen 2005.
[5] Sedlacek G., Feldmann M., Paschen M., Geβler A., *SPS-applications in bridge design-safety and economy aspects*, PU Magazine VOL 2. NO. 4/10, Ratingen 2005.

ANALYTICAL METHOD FOR RELIABILITY ESTIMATION OF STEEL STRUCTURES UNDER WIND AND SNOW LOADS

S.F. Pichugin[*], A.V. Makhinko[*], N.A. Makhinko[*]

[*] Chair of Metal and Wooden Structures, Structural Faculty, Poltava National Technical University in honour of Yuri Kondratyuk, Pervomaysky pr. 24, 36011, Poltava, Ukraine.

1. Introduction

On actual practice, the quantitative estimation of reliability is a necessary criterion in erecting any building facility. However, despite fifty years of applying probabilistic approach in estimation and their repeatedly description and systematization in technical literature, the application of probabilistic methods in engineering remains still insufficient nowadays. First, the mentioned above is due to the complicated mathematical process of reliability theory. Second, it may be explained by the absence of a common standpoint on probabilistic methods and models which must be preferable for estimating reliability of building structures. The aim of this paper is to describe the simple procedure of reliability estimation of steel structures without using complicated formulas and numerous computer aid operations. As a result the proposed method is suitable for rapid evaluation of the structure reliability under wind and snow stochastic actions.

2. The method of reliability estimation

The behaviour of any structural element to its utilization and interaction with the environment or other elements is determined, on the one hand, by the external loads acting on it; on the other hand, by the performances which determine the state of the element (internal force, stain or deformation).

This paper considers the steel elements of structures like stretched, bended, stretched-bent elements, etc. with the estimated model limited by the bumping properties of material. The parameters of structures are stationary (ignoring the alternation of mechanical properties of structural material during its life time T_{ef}) and stochastic (taking into consideration the alternative statistical data of mechanical properties of material). Serviceability of structural element is characterized by one feature it is the yield point of the steel R_y, ultimate stress R_u and by the value which is lineary depend on values R_y and R_u (for instance, estimated shearing the resistance of steel, estimated collapse resistance etc.).

The loads are characterized by the parameter $\tilde{q}(t)$ described in the technique of stationary

343

stochastic processes. The yield point and ultimate stress are considered to be the random values with the normal law of distribution. If that's the case, the values which lineary depend on yield point and ultimate stress, correspondingly are subjected to the normal law of distribution. To determine the carrying capacity of an element the common determination $\tilde{R}$. Will be used the value $\tilde{R}$ and the random process $\tilde{q}(t)$ are considered to be stochastically independent.

Estimating the reliability of structural elements the exhausting of its carrying capacity (failure) is explained as crossing of generalized load (effort, strain) by a random process $\tilde{S}(t)$) on random level $\tilde{R}$ of generalized carrying capacity of an element.

The stochastic properties of material inside steel structure are entirely and unambiguously determined through mathematical expectation $\overline{R}$ and standard deviation $\hat{R}$ of respective strength characteristics of material.

The dead load $\tilde{q}_d$ is considered to be a random value with a normal law of distribution. Statistical features are mathematical expectation, standard deviation $\hat{q}_d$ and coefficient of variation $V_d = \hat{q}_d / \overline{q}_d$. Estimating the reliability of steel structural elements, the dead load is introduced as allowance to the carrying capacity of an element. As a result, a random value of reduced carrying capacity $\tilde{R}_{ef}$ is to be considered. The statistical performances of this value are determined by the formulas [2, 3]:

$$\overline{R}_{ef} = \overline{R} - \alpha_{d,R}\overline{q}_d ; \tag{1}$$

$$\hat{R}_{ef} = \sqrt{\hat{R}^2 + \alpha_{d,R}^2 \hat{q}_d^2} . \tag{2}$$

where $\alpha_{d,R}$ − coefficient of dead load influence (effort or strain inside structure due to single load).

Snow and wind loads are considered to be stochastic processes. Their probabilistic characteristics are substantiated according to chapters 3 and 4 of the present paper. The separate or combined effect of snow and wind load on the elements of structures is the origin of stochastic processes of generalized strain $\tilde{S}(t)$:

$$\tilde{S}(t) = \alpha_{S,R}\tilde{q}_S(t) + \alpha_{W,R}\tilde{q}_W(t) \tag{3}$$

where $\alpha_{S,R}$ and $\alpha_{W,R}$ − coefficients of influence of snow and wind loads.

The statistical characteristics (mathematical expectation $\overline{S}$, standard deviation $\hat{S}$ and coefficient of variation $V_{\Sigma S}$) of a stochastic process of generalized strain $\tilde{S}(t)$ are determined by the following formulas [4-6, 10]:

$$\overline{S} = \eta_R R_y [C_{S,R} / \chi_S + C_{W,R} / \chi_W], \tag{4}$$

344

$$\hat{S} = \eta_R R_y \sqrt{(C_{S,R} V_S / \chi_S)^2 + (C_{W,R} V_W / \chi_W)^2} \,, \tag{5}$$

$$V_{\Sigma S} = \frac{\hat{S}}{\overline{S}} = \frac{\sqrt{(C_{S,R} V_S / \chi_S)^2 + (C_{W,R} V_W / \chi_W)^2}}{C_{S,R} / \chi_S + C_{W,R} / \chi_W} \,, \tag{6}$$

where R_y − yield point of the steel, η_R – coefficient of understrained or overstrained structural element; χ_S and χ_W – remoteness of estimated values of snow and wind loads correspondingly; V_S and V_W – coefficients of variation of random process of snow and wind load correspondingly; $C_{S,R}$ and $C_{W,R}$ − portion of influence of snow and wind loads.

The remoteness of estimated load magnitude χ_j is determined as a relation of calculated load magnitude q_j^p to its average magnitude:

$$\chi_j = q_j^p / \overline{q}_j, \qquad (j = S \vee W). \tag{7}$$

The estimated load in formula (7) is regarded as characteristic (or reference) value of the load in terms of Eurocode [1]: S_0 – for snow load and W_0 – for wind load. The estimation of S_0, W_0, $\overline{q}_S = \hat{q}_S / V_S$, $\overline{q}_W = \hat{q}_W / V_W$ in table I.

Table I. Parameters of wind and snow loads for determining maximum and intensity characteristic.

City of Ukraine	Parameters for snow load							
	$a_{\gamma,S}$	$b_{\gamma,S}$	$c_{\gamma,S}$	$a_{\lambda,S}$	$b_{\lambda,S}$	$c_{\lambda,S}$	V_S	$\hat{q}_S$, Pa
	0.15	-3.87	2.19	1.33	-2.87	1.14	1.30	390
	Parameters for wind load							
	$a_{\gamma,W}$	$b_{\gamma,W}$	$c_{\gamma,W}$	$a_{\lambda,W}$	$b_{\lambda,W}$	$c_{\lambda,W}$	V_W	$\hat{q}_W$, Pa
Kiev	2.11	0.40	6.04	-0.02	-1.25	0.54	1.45	11.6
	Parameters for joint action of wind and snow loads							
	$\mu_{S,1}$		$\mu_{W,1}$		$\mu_{S,2}$		$\mu_{W,2}$	
	1.35		1.67		2.31		1.01	
	Parameters for snow load							
	$a_{\gamma,S}$	$b_{\gamma,S}$	$c_{\gamma,S}$	$a_{\lambda,S}$	$b_{\lambda,S}$	$c_{\lambda,S}$	V_S	$\hat{q}_S$, Pa
	0.151	-3.74	2.222	1.316	-2.733	1.34	1.3	520
	Parameters for wind load							
	$a_{\gamma,W}$	$b_{\gamma,W}$	$c_{\gamma,W}$	$a_{\lambda,W}$	$b_{\lambda,W}$	$c_{\lambda,W}$	V_W	$\hat{q}_W$, Pa
Poltava	2.53	0.575	5.92	-0.021	-1.233	0.476	1.6	19.2
	Parameters for joint action of wind and snow loads							
	$\mu_{S,1}$		$\mu_{W,1}$		$\mu_{S,2}$		$\mu_{W,2}$	
	1.406		1.646		2.478		0.978	

The portion of load influence (dead load, snow and wind load) as a part of general strained state of structural element expressed as:

$$C_{j,R} = \alpha_{j,R} q_j^p / (\eta_R R_y), \qquad j \in d \vee S \vee W.$$ (8)

The reliability function $P(t)$ of any steel structural element is the function of two non-dimensional parameters. The reserve factor β_R and relation of standards p. Parameter p is a relationship of standards of stochastic process of generalized strain $\hat{S}$ and reduced carrying capacity $\hat{R}_{ef}$:

$$p = \hat{R}_{ef} / \hat{S}.$$ (9)

The reserve factor β_R is determined by the formula:

$$\beta_R = \frac{\lambda_0 (V_{\Sigma S} p - V_{R,ef}) - V_{R,ef} V_{\Sigma S} (\lambda_0 \gamma_0 + C)}{V_{R,ef} V_{\Sigma S} \sqrt{1.645 + \lambda_0^2 p^2}},$$ (10)

where $C \approx 0.577$ − Euler-Mascheroni's constant; $V_{R,ef} = \hat{R}_{ef} / \overline{R}_{ef}$ − coefficient of variation of reduced carrying capacity; γ_0 and λ_0 − normalized characteristic maximum and characteristic intensity of generalized stochastic process of internal force factor (strain, effort) $\tilde{S}(t)$ correspondingly. These parameters functionally depend on design of working life of structures and also account the frequency nature of load process. Besides the load characteristic maximum is always a function of characteristic intensity.

When the steel structural element is under snow and dead load consider $\gamma_0 \equiv \gamma_{0,S}$ and $\lambda_0 \equiv \lambda_{0,S}$. The numerical magnitudes of performances $\gamma_{0,S}$ and $\lambda_{0,S}$ are determined as in chapter 3 of this paper. We have to consider $\gamma_0 \equiv \gamma_{0,W}$ and $\lambda_0 \equiv \lambda_{0,W}$ under the effect of wind and dead load ($\gamma_{0,W}$ and $\lambda_{0,W}$ are determined as in chapter 4). In case of simultaneous wind and snow load, taking into consideration the dead load, we consider $\gamma_0 \equiv \gamma_{0,SW}$ and $\lambda_0 \equiv \lambda_{0,SW}$ ($\gamma_{0,SW}$ and $\lambda_{0,SW}$ are calculated according to chapter 5 of the present paper).

The no-failure exploitation of steel element structures during determined the life time T_{ef} is derived from the following formula:

$$P(T_{ef}) = 1 - \sqrt{\frac{1+p^{-2}}{2\pi}} \int_{-\infty}^{-\beta_R} \int_0^1 \exp[-0.5E^2(\gamma, Z)]dZd\gamma,$$ (11)

$$E(\gamma, Z) = \gamma\sqrt{1+p^{-2}} - 0.45/p - (0.78/p)\ln(-\ln Z).$$

It should be noted that the building structure reliability has to be close enough to the unit. Therefore the probability values of non-failure exploitation of steel structure element derived from (11) are more informative in the form of reliability logarithmic parameters (Bells) after the formula:

$$P_L = -\lg[1 - P(T_{ef})].$$ (12)

3. The probabilistic model of snow load

Estimating reliability of steel structural elements, the snow load is represented in the form of a quasi-stationary differentiated random process which is unambiguously determined by the following parameters: 1) the normalized probability density distribution $f_{nS}(\bullet)$ of random process; 2) mathematical expectation $\overline{q}_S$; 3) efficient frequency $\omega_{e,S}$; 4) band factor $\beta_{\omega,S}$; 5) coefficient of variation V_S; 6) coefficient of skewness A_S.

The normalized density of snow load distribution is described by the polynomial-exponential law [6, 8]:

$$f_{nS}(\gamma) = \exp[C_0 + C_1\gamma + C_2\gamma^2 + C_3\gamma^3],$$ (13)

where $\gamma = (q - \overline{q}_S)/\hat{q}_S$ the normalized declivity from the center of ordinate distribution of random process; $\overline{q}_S$ and $\hat{q}_S$ − mathematical expectation and standard deviation of snow load stochastic process; C_0, C_1, C_2, C_3 − coefficients of polynomial-exponential law, which are the functions of skewness A_S and coefficient of variation V_S of a random process for snow load. The parameters C_0, C_1, C_2, C_3 are determined after the method of moments as solution of transcendental equations:

$$\begin{cases} \int_{-V_S}^{\infty} f_{nS}(\gamma)d\gamma = 1; & \int_{-V_S}^{\infty}(1+\gamma V_S)f_{nS}(\gamma)d\gamma = 1; \\ \int_{-V_S}^{\infty} \gamma^2 f_{nS}(\gamma)d\gamma = 1; & \int_{-V_S}^{\infty} \gamma^3 f_{nS}(\gamma)d\gamma = A_S. \end{cases}$$ (14)

The efficient frequency $\omega_{e,S}$ and band factor $\beta_{\omega,S}$ act as the basic frequency characteristic of a random process of snow load. For example, the value of band factor for

347

Ukraine equals $\beta_{\omega,S} = 3$ and the value of efficient frequency $\omega_{e,S}$ for different areas of Ukraine lies within the limits of 0.09-0.18 1/day [8, 11].

The normalized characteristic maximum $\gamma_{0,S}$ is determined as a root of an equation:

$$\omega_{e,S} T_{ef} K_3 f_{nS}(\gamma_{0,S}) = \beta_\omega \sqrt{2\pi} . \tag{15}$$

The characteristic intensity $\lambda_{0,S}$ of a stochastic process of snow load is to be found from the formula:

$$\lambda_{0,S} = -(C_1 + 2C_2\gamma_{0,S} + 3C_3\gamma_{0,S}^2) \tag{16}$$

where T_{ef} − determined time of structure work life; K_3 − factor of winter duration (for example, for Ukraine it is to be $K_3 \approx 0.411$).

The normalized characteristic maximum $\gamma_{0,S}$ and characteristic intensity $\lambda_{0,S}$ of a stochastic process of snow load is also to be determined by the following asymptotic formulae:

$$\gamma_{0,S} = a_{\gamma,S} \ln(b_{\gamma,S} + T_{ef}) + c_{\gamma,S} \tag{17}$$
$$\lambda_{0,S} = a_{\lambda,S} \ln(b_{\lambda,S} + T_{ef}) + c_{\lambda,S} \tag{18}$$

where $a_{\gamma,S}, b_{\gamma,S}, c_{\gamma,S}$ and $a_{\lambda,S}, b_{\lambda,S}, c_{\lambda,S}$ are non-dimensional coefficients which are regulated in the table I.

After determining the meaning of $\gamma_{0,S}$ and $\lambda_{0,S}$ one is to proceed the direct estimation of steel elements reliability, which are loaded with the dead and snow loads (see chapter 2).

4. The probabilistic model of wind load

The wind load is usually represented in the form of quasi-stationary differentiated process, which is unambiguously defined by normalized probability density distribution $f_{nW}(\bullet)$ of stochastic process, mathematical expectation $\overline{q_W}$, efficient frequency $\omega_{e,W}$, band factor $\beta_{\omega,W}$ and coefficient of variation V_W.

The normalized probability density distribution of wind stochastic process was described by Weibull law [4, 8]:

$$f_{nW}(\gamma) = \beta V_W \Gamma(1+\beta^{-1})^\beta (\gamma V_W + 1)^{\beta-1} \exp\left\{-\left[(\gamma V_W + 1)\Gamma(1+\beta^{-1})\right]^\beta\right\}, \tag{19}$$

348

where $\gamma = (q - \overline{q}_W)/\hat{q}_W$ – normalized declivity from the center of ordinate distribution of a stochastic process; $\overline{q}_W$, $\hat{q}_W$ – mathematical expectation and standard deviation of the stochastic process of wind load; V_W – coefficient of variation of the stochastic process of wind load; β – parameter of Weibull distribution; $\Gamma(\bullet)$ – gamma-function.

The parameter of Weibull distribution is functionally connected with the coefficient of variation by relationship:

$$V_W = \sqrt{[\Gamma(1 + 2\beta^{-1})/\Gamma(1 + \beta^{-1})^2] - 1} . \tag{20}$$

The main frequency characteristics of the stochastic process of wind load are the efficient frequencies $\omega_{e,W}$ and the band factor $\beta_{\omega,W}$. For example, the value of the efficient frequency and band factor for all Ukrainian areas is equal to $\omega_{e,W} = 5.5 \, \text{day}^{-1}$ and $\beta_{\omega,W} = 3$.

The normalized characteristic maximum $\gamma_{0,W}$ and characteristic intensity $\lambda_{0,W}$ of the stochastic process of wind load are determined by the formulas:

$$\Gamma(1 + \beta^{-1})^\beta (\gamma_{0,W} V_W + 1)^\beta - \ln(\gamma_{0,W} V_W + 1)^{\beta - 1} - \ln(\gamma_{0,W} V_W^2 + 1)^{1/2} = \ln\left(\frac{\omega_{e,W} T_{ef}}{\beta_{\omega,W}\sqrt{2\pi}} \beta\Gamma(1 + \beta^{-1})^\beta \right), \tag{21}$$

$$\lambda_{0,W} = \frac{V_W}{\gamma_{0,W} V_W + 1} \left[\beta\Gamma(1 + \beta^{-1})^\beta (\gamma_{0,W} V_W + 1)^\beta + \frac{2(1 - \beta)(\gamma_{0,W} V_W + V_W^{-1}) - (\gamma_{0,W} V_W + 1)}{2(\gamma_{0,W} V_W + V_W^{-1})} \right], \tag{22}$$

where T_{ef} – determined life time of a structure.

The characteristic maximum $\gamma_{0,W}$ and the characteristic intensity $\lambda_{0,W}$ of the stochastic process of wind load may be also defined by the asymptotic formulas:

$$\gamma_{0,W} = a_{\gamma,W} \ln(b_{\gamma,W} + T_{ef}) + c_{\gamma,W}, \tag{23}$$

$$\lambda_{0,W} = a_{\lambda,W} \ln(b_{\lambda,W} + T_{ef}) + c_{\lambda,W}, \tag{24}$$

where $a_{\gamma,W}, b_{\gamma,W}, c_{\gamma,W}$ and $a_{\lambda,W}, b_{\lambda,W}, c_{\lambda,W}$ – non-dimensional coefficients regu-lated by the table I.

The direct reliability estimation of steel element structures loaded by dead and wind loads (after determining numerical meaning of $\gamma_{0,W}$ and $\lambda_{0,W}$) has to be performed as mentioned above. The technique of reliability estimation for structural metal elements is to be performed as in chapter 2 after finding $\gamma_{0,W}$ and $\lambda_{0,W}$ values.

5. Reliability estimation of steel elements of structures under joint effect of snow and wind loads

Under the simultaneous effect of wind and snow loads on the steel structural elements which are represented by the models of quasi-stationary random processes according to chapters 3 and 4, the summary strain (effort) inside structural elements may be also represented by the quasi-stationary random process $\tilde{S}(t)$. The normalized characteristic maximum $\gamma_{0,SW}$ and the characteristic intensity $\lambda_{0,SW}$ of the random process $\tilde{S}(t)$ are proposed to be identified by the following asymptomatic relationships:

$$\gamma_{0,SW} = \frac{(\gamma_{0,W} p_{WS} + \gamma_{0,S})\eta_\gamma - (V_S^{-1} + V_W^{-1} p_{WS})(1 - \eta_\gamma)}{\sqrt{1 + p_{WS}^2}}, \tag{25}$$

$$\lambda_{0,SW} = \frac{5\sqrt{1 + p_{WS}^2}}{(\eta_\lambda - \eta_\gamma)(\gamma_{0,W} p_{WS} + \gamma_{0,S} + V_W^{-1} p_{WS} + V_S^{-1}) + 5\eta_\lambda (p_{WS} \lambda_{0,W}^{-1} + \lambda_{0,S}^{-1})}, \tag{26}$$

where the auxiliary non-dimensional values are defined by the formulas:

$$\xi_S = 1 + \gamma_{0,S} V_S \qquad \xi_W = 1 + \gamma_{0,W} V_W, \tag{27}$$

$$p_{WS} = \alpha_{W,R} \hat{q}_W / (\alpha_{S,R} \hat{q}_S), \tag{28}$$

$$\Delta_{WS} = \frac{\xi_W V_S p_{WS}}{\xi_W V_S p_{WS} + \xi_S V_W}, \tag{29}$$

$$\eta_\gamma = \frac{1 - \Delta_{WS}}{(1 - \Delta_{WS})(1 - \mu_{S,1}) + \mu_{S,1}} + \frac{\Delta_{WS}}{\Delta_{WS}(1 - \mu_{W,1}) + \mu_{W,1}}, \tag{30}$$

$$\eta_\lambda = \frac{1 - \Delta_{WS}}{(1 - \Delta_{WS})(1 - \mu_{S,2}) + \mu_{S,2}} + \frac{\Delta_{WS}}{\Delta_{WS}(1 - \mu_{W,2}) + \mu_{W,2}}. \tag{31}$$

350

Table II. Sequential steps of definition of characteristic maximum and characteristic intensity.

Step	Assignment (or operations)
1	To depend on location structures assign parameters $a_{\gamma,S}$, $b_{\gamma,S}$, $c_{\gamma,S}$, $a_{\lambda,S}$, $b_{\lambda,S}$, $c_{\lambda,S}$, $a_{\gamma,W}$, $b_{\gamma,W}$, $c_{\gamma,W}$, $a_{\lambda,W}$, $b_{\lambda,W}$, $c_{\lambda,W}$, assign coefficients of variation of snow and wind loads V_S, V_W, assign standards deviation of snow and wind loads $\hat{q}_S$, $\hat{q}_W$ and assign parameters $\mu_{S,1}$, $\mu_{W,1}$, $\mu_{S,2}$, $\mu_{W,2}$ (see Table I)
2	To assign working life of structures T_{ef}
3	To calculate characteristic maximum and characteristic intensity of wind and snow loads for case when these loads influence separately $$\gamma_{0,S} = a_{\gamma,S}\ln(b_{\gamma,S}+T_{ef})+c_{\gamma,S}, \qquad \lambda_{0,S} = a_{\lambda,S}\ln(b_{\lambda,S}+T_{ef})+c_{\lambda,S};$$ $$\gamma_{0,W} = a_{\gamma,W}\ln(b_{\gamma,W}+T_{ef})+c_{\gamma,W}, \qquad \lambda_{0,W} = a_{\lambda,W}\ln(b_{\lambda,W}+T_{ef})+c_{\lambda,W}$$
4	To calculate parameters ξ_S and ξ_W: $\xi_S = 1+\gamma_{0,S}V_S$, $\quad \xi_W = 1+\gamma_{0,W}V_W$
5	To calculate of influence factors for wind $\alpha_{W,R}$ and snow $\alpha_{S,R}$ loads (influence factor is equal to stress in structures from unit load).
6	To calculate $p_{WS} = \alpha_{W,R}\hat{q}_W/(\alpha_{S,R}\hat{q}_S)$
7	To calculate $\Delta_{WS} = \dfrac{\xi_W V_S p_{WS}}{\xi_W V_S p_{WS}+\xi_S V_W}$
8	To calculate $\eta_\gamma = \dfrac{1-\Delta_{WS}}{(1-\Delta_{WS})(1-\mu_{S,1})+\mu_{S,1}}+\dfrac{\Delta_{WS}}{\Delta_{WS}(1-\mu_{W,1})+\mu_{W,1}}$
9	To calculate $\eta_\lambda = \dfrac{1-\Delta_{WS}}{(1-\Delta_{WS})(1-\mu_{S,2})+\mu_{S,2}}+\dfrac{\Delta_{WS}}{\Delta_{WS}(1-\mu_{W,2})+\mu_{W,2}}$
10	To calculate characteristic maximum and characteristic intensity for case of wind and snow loads simultaneously influence, by using eqs. (25)-(26)

where $\mu_{W,1}$, $\mu_{S,1}$ and $\mu_{S,2}$, $\mu_{W,2}$ – non-dimensional coefficients which must define the location of the building (see table I); $\alpha_{W,R}$, $\alpha_{S,R}$ – coefficients of wind and snow load influence.

Table II gives the sequential steps for determining all parameters used in these formulas (25), (26).

For example, the results of the reliability calculations of steel elements under snow and wind loads are presented on figs 1 and 2 where numerals show elements reliability in Bell P_L (for example, $P_L = 1$ Bell corresponds to the failure probability of an element 0.1, $P_L = 2$ Bell corresponds to 0.01, etc.). The data characterizes the elements reliability designed in accordance with Building Codes of Ukraine. Thus data in numerators corresponds to minimal reliability of elements for given region and numeral in the denominator corresponds to maximal region reliability (or on the contrary). The obtained reliability evaluation allows to detect the regions of Ukraine potentially dangerous for structure elements under wind and snow loads.
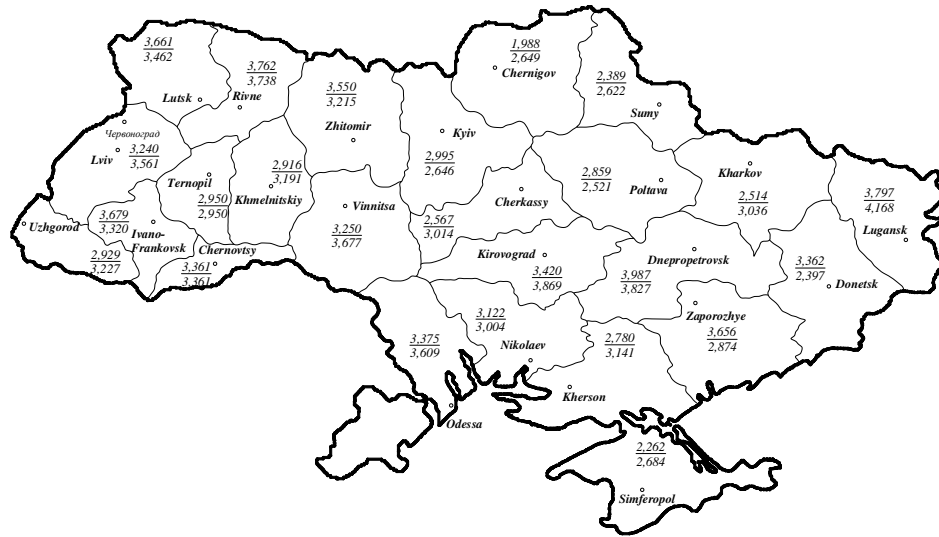
Fig. 1. Reliability of steel elements under snow load for territory of Ukraine: portion of snow load $C_{S.R} = 0.5$.

Fig. 2. Reliability of steel elements under wind load for territory of Ukraine: portion of snow load $C_{W.R} = 0.5$.

352

On fig. 3 planimetric surfaces of elements reliability for two cities of Ukraine are resulted. On these schedules on axes of coordinates are postponed portions influences of snow and wind loads, applicants points correspond to a logarithmic parameter of reliability P_L. These surfaces of reliability can be considered as the express train-estimation of reliability of steel elements of designs at simultaneous action of snow and wind loads.
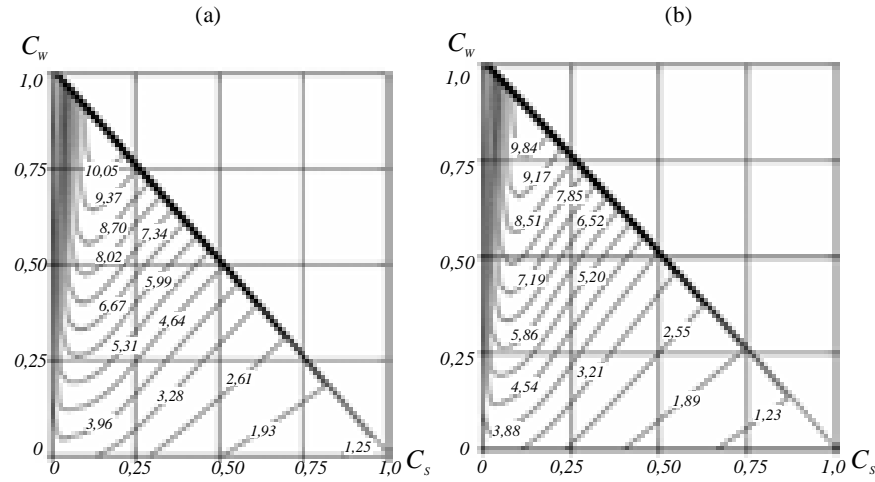

Fig. 3. Reliability of steel elements under snow and wind load for territory of Ukraine:
(a) for Kyiv; (b) for Poltava ($T_{ef} = 50$ years).

6. The example of reliability calculation of steel element on dead and snow loads

Initial data. It's necessary to calculate reliability of steel hammer beam, span $L = 12$ m, step of beams $B = 6$ m. The carrying capacity of the beam $R_y = 240$ MPa, mathematical expectation and standard – $\overline{R} = 350$ MPa, $\hat{R} = 35$ MPa. Working life of the beam $T_{ef} = 40$ years. The beam is a part of a building which is located in Poltava. The statistical characteristic of dead load: mathematical expectation $\overline{q}_d = 0.65$ kPa, standard $\hat{q}_d = 0.027$ kPa, coefficient of variation $V_d = \hat{q}_d / \overline{q}_d = 0.027 / 0.65 = 0.042$. Snow load on the roof $S_m = 1.4$ kPa. The cross-section of the beam is designed with a stock 14% ($\eta_R = 0.86$), secant modulus $W_x = 1125$ cm^3.

Calculation of reliability of steel hammer beam. Determine coefficient of influence of dead load:

$$\alpha_{d,R} = L^2 B / 8 W_x = 12^2 \cdot 10 \cdot 600 / (8 \cdot 1125) = 96 \text{ MPa/kPa}.$$

353

Calculate statistical characteristic (mathematical expectation, standard, coefficient of variation) of reduced carrying capacity $\tilde{R}_{ef}$ using eqs (1), (2):

$$\overline{R}_{ef} = \overline{R} - \alpha_{d,R}\overline{q}_d = 350 - 96 \cdot 0.65 = 287.6 \, \text{MPa};$$

$$\hat{R}_{ef} = \sqrt{\hat{R}^2 + \alpha_{d,R}^2 \hat{q}_d^2} = \sqrt{35^2 + (96 \cdot 0.027)^2} = 35.1 \, \text{MPa};$$

$$V_{R,ef} = \hat{R}_{ef} / \overline{R}_{ef} = 35.1 / 287.6 = 0.122 \,.$$

From the table I for Poltava it is written out statistical characteristics of snow load (mathematical expectation, coefficient of variation, standard):

$$\overline{q}_S = 0.4 \, \text{kPa}, \qquad V_S = 1.3 \,, \qquad \hat{q}_S = \overline{q}_S V_S = 0.4 \cdot 1.3 = 0.52 \, \text{kPa}.$$

Determine normalized characteristic maximum $\gamma_{0,S}$ and characteristic intensity $\lambda_{0,S}$ of a stochastic process of snow load. For this purpose from table I we write out values of parameters $a_{\gamma,S}, b_{\gamma,S}, c_{\gamma,S}$ та $a_{\lambda,S}, b_{\lambda,S}, c_{\lambda,S}$:

$$a_{\gamma,S} = 0.151, \; b_{\gamma,S} = -3.74, \; c_{\gamma,S} = 2.222 \,,$$

$$a_{\lambda,S} = 1.316, \; b_{\lambda,S} = -2.733, \; c_{\lambda,S} = 1.34 \,.$$

Using eqs (17), (18) and working life of the hammer beam $T_{ef} = 40 \, \text{years}$ determine variable $\gamma_{0,S}$ та $\lambda_{0,S}$:

$$\gamma_{0,S} = a_{\gamma,S} \ln(b_{\gamma,S} + T_{ef}) + c_{\gamma,S} = 0.151 \cdot \ln(-3.74 + 40) + 2.222 = 2.764 \,,$$

$$\lambda_{0,S} = a_{\lambda,S} \ln(b_{\lambda,S} + T_{ef}) + c_{\lambda,S} = 1.316 \cdot \ln(-2.733 + 40) + 1.34 = 6.1 \,.$$

Calculate the remoteness of estimated snow load magnitude by the formula (7):

$$\chi_S = S_m / \overline{q}_S = 1.4 / 0.4 = 3.5 \,.$$

Determine a portion of influence of snow load by eq. (8), considering that in this case the coefficient of influence of snow load is equal to coefficient of influence of dead load:

$$C_{S,R} = \alpha_{S,R} S_m / (\eta_R R_y) = 96 \cdot 1.4 / (0.859 \cdot 240) = 0.652 \,.$$

354

Calculate the standard of stochastic process of strain in an element from snow load:

$$\hat{S} = \eta_R R_y C_{S,R} V_S / \chi_S = 0.859 \cdot 240 \cdot 0.652 \cdot 1.3 / 3.5 = 50.0\,\text{MPa}.$$

Calculate parameter p (see formula (9)):

$$p = 35.1 / 50.0 = 0.70\,.$$

Calculate the reserve factor β_R:

$$\beta_R = \frac{6.1 \cdot (1.3 \cdot 0.7 - 0.122) - 0.122 \cdot 1.3(6.1 \cdot 2.764 + 0.577)}{0.122 \cdot 1.3\sqrt{1.645 + 6.1^2 0.7^2}} = 2.887\,.$$

The no-failure exploitation of steel hammer beam during determined life time $T_{ef} = 40$ years is derived from the formulae (11), (12):

$$P_L(T_{ef} = 40\,\text{years}) = 2.05\,\text{Bell or } P(T_{ef} = 40\,\text{years}) = 0.991\,.$$

7. Conclusions

The effective method of reliability estimation of steel structures under wind and snow loads has been proposed. Relative simplicity, wide range of application and precision of this method make it rather helpful for rapid engineering calculations. The worked out approach gives possibility to estimate to reliability of different structures under wind, snow and other loads. This technique allows specify some coefficients of design standards (for example combined factor).

References
[1] *Eurocode-Basis of Structural Design*. – Brussels: Final draft, 2001.
[2] Makhinko A., *Reliability of steel elements of building structures under stochastic variable loads*, Thesis for the Candidate Degree in Technical Science on speciality 05.23.01 – building structures, buildings and constructions. –Poltava, 2006. – 24p.
[3] Pichugin S., Makhinko A., *To Probabilistic Methods of Steel Structures Design*, Modern Building Structures from Metal and Wooden: Proceedings of the Tenth International Symposium. – Odessa, 2005. – P. 161-171 (in Ukrainian).
[4] Pichugin S., *Probabilistic Analysis of Wind Load and Reliability of Structures*, Proc. 2-nd European and African Conf. Wind Eng. – Genova (Italy), 1997. – P. 1883-1890.
[5] Pichugin S., Makhinko A., *Some Questions of Calculation of Steel Structures Reliability*, „Metal Constructions" Journal, Ukrainian Association of Metal Constructions, V. 11, number 3, 2006. – P. 187-196 (in Russian).

[6] Pichugin S., Makhinko A., *Reliability Estimation of Steel Structures under Stochastic Loads*, Proceedings of the Eighth Ukrainian Scientific and Technical Conference. – Kyiv, 2004. – P. 175-185 (in Ukrainian).

[7] Pichugin S., Makhinko A., *Wind Load on Building Structures*, Poltava, 2005. − 342p (in Russian).

[8] Pichugin S., Demchenko N., *Reliability of Building Structures*, Poltava, 2005. − 91p.

[9] Pichugin S., Makhinko A., *Probabilistic Model of Wind Load Maxima*, Proc. 3-rd Inter-national Conf. "Problems of the Technical Meteorology". – Lviv. – 2006. – P. 92-97.

[10] Pichugin S., Makhinko A., Makhinko N., *Recommendations are from the Calculation of Steel Elements Reliabilityof Structures on Snow and Wind Loads (for National Building Code of Ukraine "Loads and Loadings")*, Poltava, 2007. − 115p (in Ukrainian).

356

AN ASSESSMENT OF INTELLIGIBILITY OF SPEECH ON EXAMPLE OF A LECTURE HALL

Andrzej Czerwiński[*], Zygmunt Dziechciowski[*], Stanisław Michałowski[*], Bogdan Stolarski[*]

[*] Institute of Machine Design, Faculty of Mechanical Engineering, Cracow .University of Technology, Jana Pawła II 37, 31-864 Cracow, Poland.

1. Introduction

An assessment of acoustics properties of a room is always subjective that taking into account not only acoustic properties but also individual features of recipient. It might happened that the same room assessed by two recipients with very good hearing get different qualitative marks. There are attempts of preparing standards for subjective assessment of room acoustic properties. One of such attempt is Ando method, which determines in a complex way four main features of room acoustic properties. RASTI method is focused on one acoustic parameter which is intelligibility of speech.

2. The RASTI method for assessment of intelligibility of speech

RASTI method (Rapid Speech Transmission Index) is an objective method for determining parameter of intelligibility of speech. The intelligibility of speech is particularly important in theatres, lecture rooms, churches, cabin of vehicles. In many cases this parameter is not satisfactory. It is due to the quality of voice transmission system which is considered room. The principle of the RASTI method is based on nine measurements conducted in two octave bands with middle frequencies 500 and 2000 Hz. Signal of sound source (white noise filtrated by band filter) has the envelope modulated by sinusoidal signal with some frequency. Transmission system which is a room, decreasing the degree of signal modulation depending on after-sound effect and level of acoustic background.
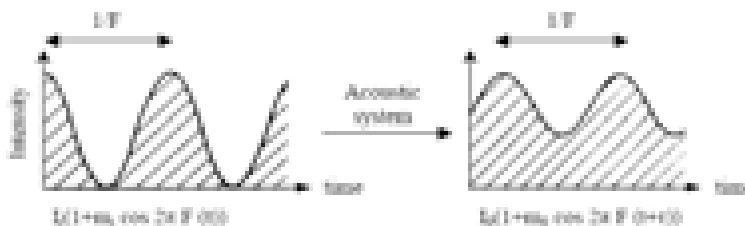

Fig. 1. The way of determining modulative transition function.

357

To assess the level of decreasing modulation of the input function the coefficient of modulation reduction was introduced – m. It depends on modulation frequency and frequency of main signal.

$$m(F) = \frac{m_o}{m_i} \tag{1}$$

Coefficient of modulation reduction $m(F)$ might be determined on the basis of the impulse response in given measurement point:

$$m(F) = \frac{\int\limits_0^\infty h_f^2(\tau) \cdot e^{(-j2\pi F\tau)} d\tau}{\int\limits_0^\infty h_f^2(\tau) d\tau} \tag{2}$$

where: h_f - impulse response, F - frequency [Hz].

After evaluating nine coefficients $m(F)$ are calculated nine values of parameter $(S/N)_{app}$ (apparent relation of signal to noise).

$$(S/N)_{app} = 10 \log \frac{m}{1-m} \tag{3}$$

In case of: when $(S/N)_{app} > 15dB$, $(S/N)_{app} = 15dB$, when $(S/N)_{app} < -15dB$, $(S/N)_{app} = -15dB$. The next step is calculation of mean value of parameter $(S/N)_{app}$.

$$\overline{(S/N)} = \frac{1}{9} \sum_{j=1}^{9} \left((S/N)_{app}\right)_j \tag{4}$$

Value of RASTI is calculated according to formula:

$$RASTI = \frac{[\overline{(S/N)} + 15]}{30} \tag{5}$$

Depending on what RASTI value was received, it might be presented in subjective scale of intelligibility of speech.

Table I. The assessment of room on the basis of RASTI coefficient.

RASTI	0.00 – 0.30	0.30 – 0.45	0.45 – 0.60	0.60 – 0.75	0.75 – 1.00
Intelligibility of speech	Bad	Poor	Fair	Good	Excellent

3. The assessment of a lecture hall on the basis of RASTI method

3.1. An object of investigation

An object of investigation was the lecture hall A3 of Cracow University of Technology campus located at Czyżyny. Section of the lecture hall is rectangular with dimensions 16m x 12.1m. Hall height is ca. 4.5m.

3.2. Methodology of testing

Measurement of intelligibility of speech by RASTI method was conducted in the lecture hall. To assess the hall intelligibility of speech was necessary to measure the impulse response in determined points. Recorded impulse responses were used to calculate RASTI parameters C_{50}, D_{50}, C_{80}. Measurements of impulse response were made by the system which is presented in fig. 2.
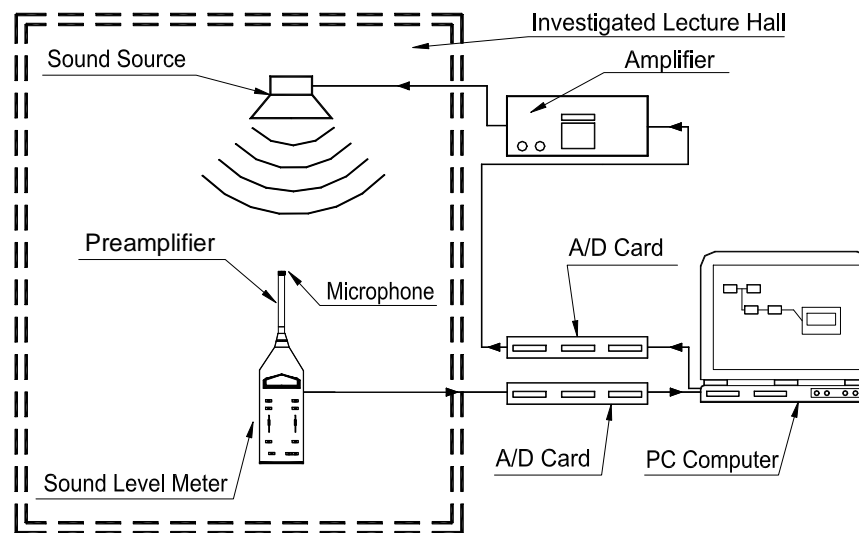
Fig. 2. Measurement system.

Input signal (modulated while noise) through the amplifier was transmitted to the loudspeaker. The output signals were recorded in 36 points uniformly distributed on the lecture hall. The level of sound intensity generated by loudspeaker was equal to level of human voice.

359

4. The map of RASTI

The results of measurement were impulse responses which were used to calculate the RASTI coefficients, definition of D_{50} as well as C_{50} coefficients. Distribution of RASTI in the lecture hall is presented in fig. 3.
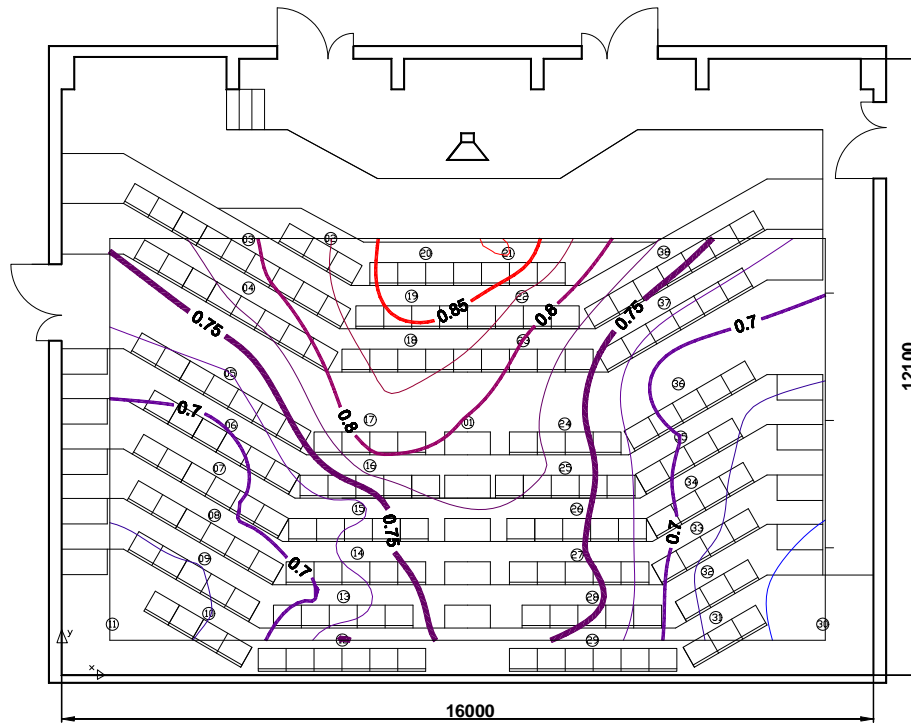

Fig. 3. The RASTI distribution in the lecture hall.

Assessment the lecture hall for the intelligibility of speech on the basis of RASTI leads to the following:

- very good intelligibility of speech determined by RASTI method (for RASTI≥0.75) is of the first three rows and also partially for middle rows,
- for the first three rows RASTI≥0.75 is not fulfilled for nine seats located in upper left corner,
- for rows from fourth further very good intelligibility of speech is only on 20 seats,
- for the rest of the lecture hall RESTI is from 0.6 to 0.75

360

5. Impulse response analysis of the A3 lecture hall

In acoustical measurements, for monitoring room reflections and reverberation, it is useful to analyze the impulse response envelope (Energy-Time-Curve (ETC)).

ETC is defined as magnitude of signal $h(t) + j\tilde{h}(t)$:

$$e(t) = \sqrt{h^2(t) + \tilde{h}^2(t)} \tag{6}$$

where $\tilde{h}(t)$ is the Hilbert transform of a function $h(t)$.

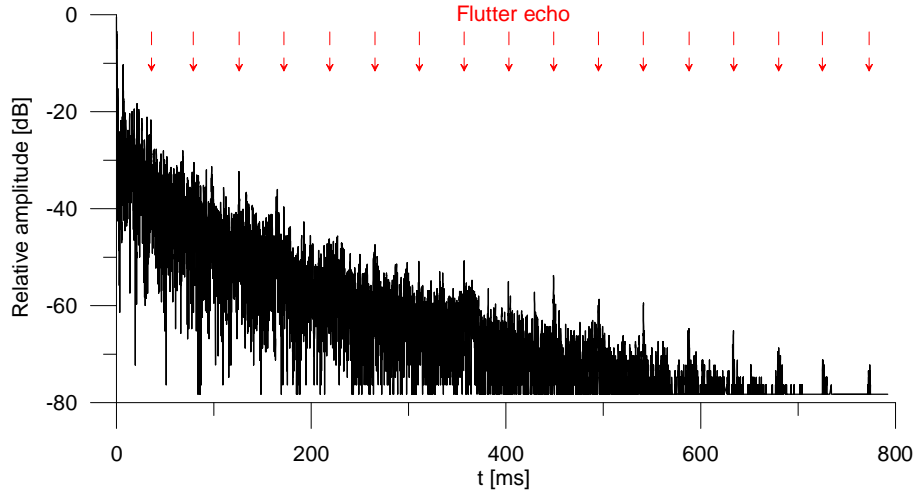In fig. 4 the ETC of the impulse response measured in point 01 is presented.

Fig. 4. Energy-Time Curve of IR in point 01.

The first part of impulse response in 01 point is shown in fig. 5.
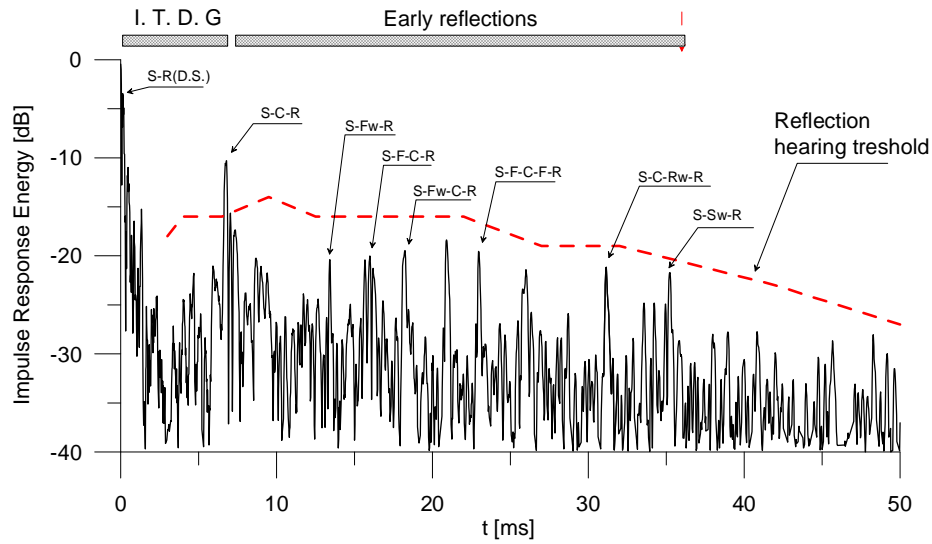
361

Fig. 5. The first part of ETC in point 01 with identification early reflection
(S – source, R – reciver, C – celing, F – floor, Fw – front wall, Rw – rear wall, Sw – side walls,
I.T.D.G. – initial time delay gap).

The early reflections time includes range for about 36 ms. The initial time delay gap is time between direct sound and first acoustic important reflections. On account of good intelligibility of speech time delay gap of first reflection should be less than 20 ms. In consider case initial time delay gap it was 7 ms. The first important reflection is ceiling reflection (S-C-R). In fig. 6 is presented sound rays for a few early reflections.
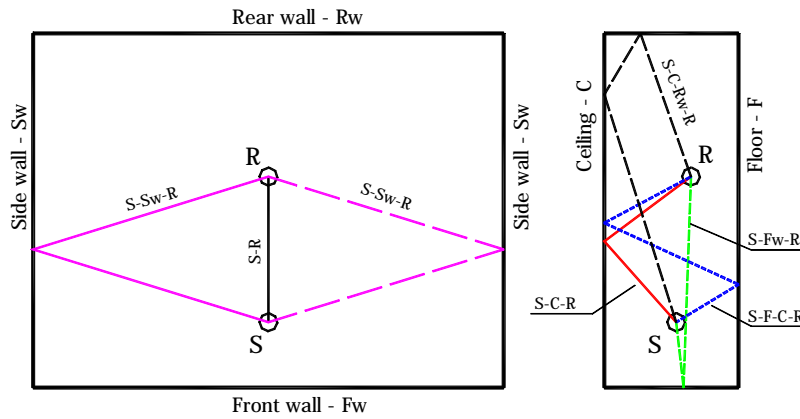

Fig. 6. The early reflection in the A3 lecture hall.

362

In the fig. 5 the reflection threshold hearing curve is given (dashed line). The most of previous reflections is appeared below threshold hearing, that's why they have not influence on sound quality form which is received.

Inside the investigated lecture hall occurs the flutter echo phenomenon which is undesirable. In fig. 7 following echoes occurring in impulse response (marked by arrows) are presented. Mechanism of formation flutter echo is shown in fig. 7.
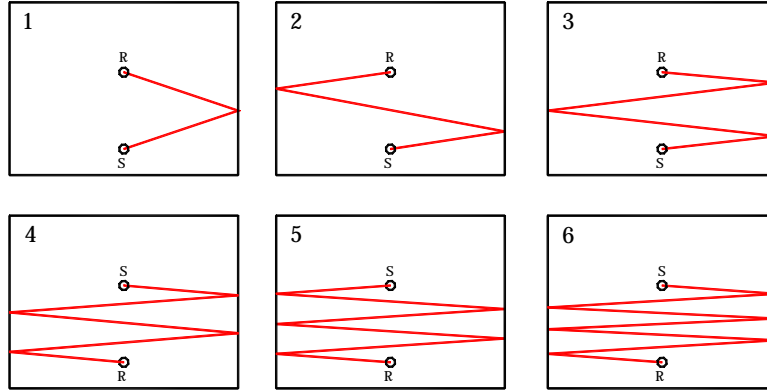

Fig. 7. Mechanism of formation flutter echo in the A3 hall (first six echoes).

The flatter echo phenomenon corresponds to reflection from the side wall of lecture hall, what is presented in fig. 7.

These walls have large area with any acoustic adaptation.

Harmful of investigated room acoustic defect is not large on account of speaker intelligibility of speech, where as for higher loudness level could be more important.

6. The intelligibility of speech assessment on the basis of C_{50} coefficient

For the objective assessment of room acoustic quality from the point of view of intelligibility of speech except STI (RASTI) coefficient could be use parameter which is based on energetic properties of impulse response. One of these parameters is C_{50} coefficient, which is defined as:

$$C_{50} = 10 \log \left\{ \frac{\int_0^{50ms} [h(t)]^2 \, dt}{\int_{50ms}^{\infty} [h(t)]^2 \, dt} \right\} \, dB \qquad (7)$$

where $h(t)$. is the impulse response.

363

The clarity (coefficient of clarity C_{50}) is defined as relation between energy of impulse response in first 50 ms to energy in time period from 50 ms to infinity.

Measurement of impulse response most often is made without filtration on output set, in this connection for some cases which determinate C_{50} coefficient value could be energy included in low band frequency. This band of frequency is not significant from the point of view of human hearing or for example quality of speech.

Inside the investigated lecture hall principal acoustic disturbance was working air condition. Spectrum of background noise for one measurement point is presented in fig. 8.
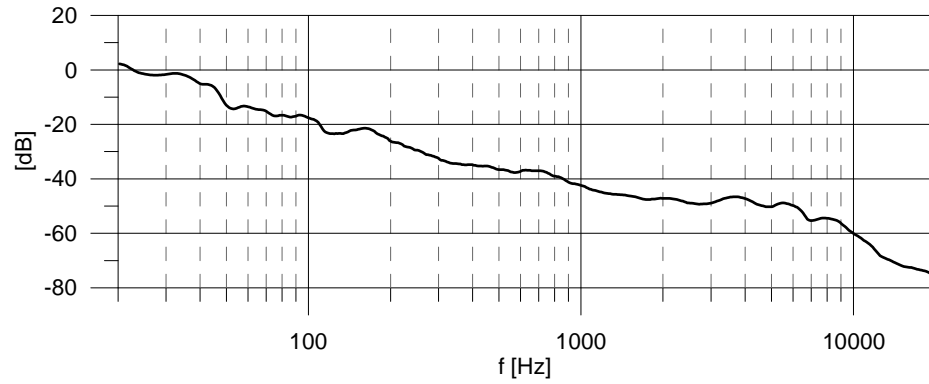

Fig. 8. Spectrum of background noise.

In fig. 8 could be seen, that for the most part of acoustic energy of background noise is included in band of frequency, where the sensitivity of human hearing is very low.

The energy-based acoustic parameter C_{50} is spectrally weighted and averaged according to Marshall Proposal [4] for clarity for speech. The weighting factors at the different octave bands are shown in table 2.

Table II. Weighting factors at the different octave bands, for C_{50} for speech.

f_{oct} [Hz]	500	1000	2000	4000
Weight factor	0.15	0.25	0.35	0.25

The parameter $C_{50\,(spav)}$ is obtained as:

$$C_{50(spav)} = 0.15 \cdot C_{50\,(500Hz)} + 0.25 \cdot C_{50\,(1000Hz)} + 0.35 \cdot C_{50\,(2000Hz)} + +0.25 \cdot C_{50\,(4000Hz)} \qquad (8)$$

where $C_{50\,(i\,-\,octeve)}$ is parameter C_{50} calculated for i – octave.

Table III. Qualitative interpretation $C_{50\,(spav)}$.

$C_{50(spav)}$ [dB]	-15 ÷ -7	-7 ÷ -2	-2 ÷ 2	2 ÷ 7	7 ÷ 15
intelligibility of speech	Bad	Poor	Fair	Good	Excellent

Comparing of C_{50} coefficient calculated for not filtrated impulse response and speech average $C_{50\,(spav)}$ is shown in fig. 9.

It could be seen large difference between both parameters, which disqualifies using for assessment of intelligibility of speech not filtrated C_{50} coefficient.
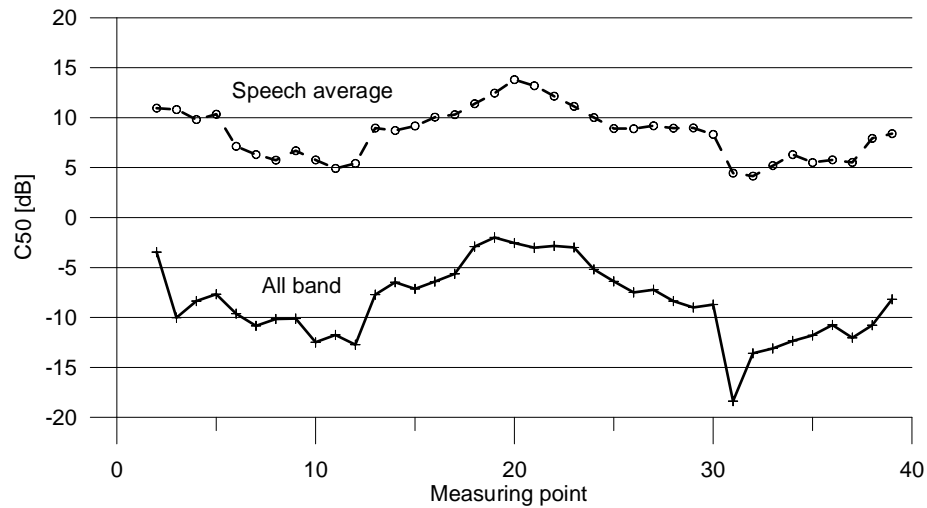

Fig. 9. Comparing of C_{50} coefficient calculated for not filtrated impulse response and speech average $C_{50\,(spav)}$.

The $C_{50\,(spav)}$ coefficient distribution in the A3 hall is presented in fig. 10.
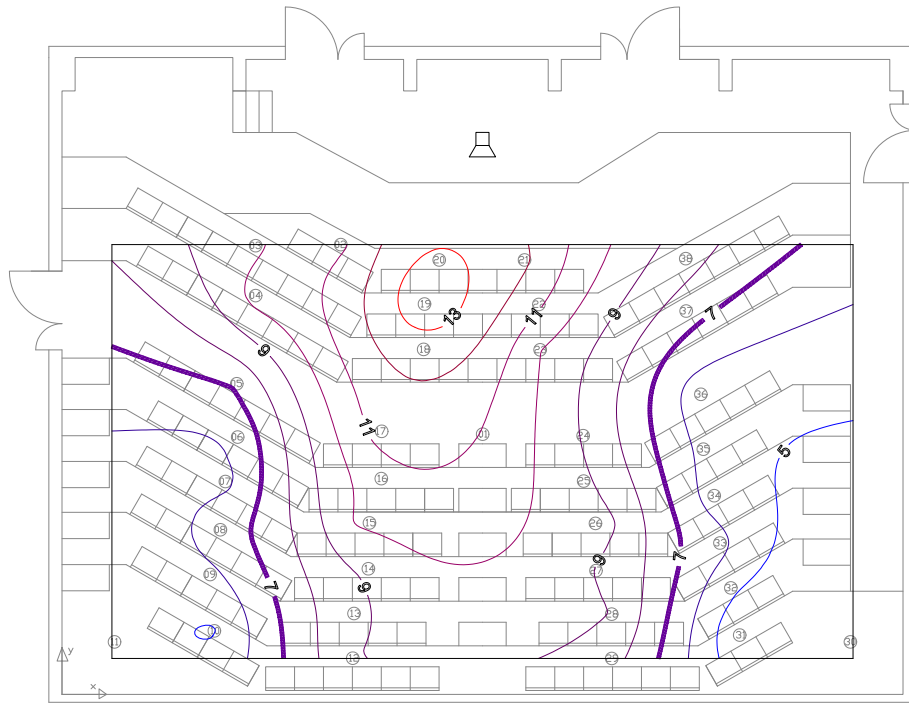
Fig. 10. The $C_{50\,(spav)}$ coefficient distribution in the A3 hall.

The assessment of the lecture hall for the speech quality on the basis of $C_{50\,(spav)}$ leads to the following:

- very good the intelligibility of speech determined by $C_{50\,(spav)}$ coefficient (for $C_{50(spav)} \geq 7dB$) is on the first three rows and also for middle rows,
- for the rest of the lecture hall $C_{50\,(spav)}$ is from 4 dB to 7 dB.

In fig. 11 is presented relationship between two quantities: RASTI coefficient and $C_{50\,(spav)}$, which were got during measurement process. This dependence was approximated by a linear function. In the graph is marked subjective intelligibility of speech for both coefficients. There is the approximated line lying nearly above a line which determines a range boundary.
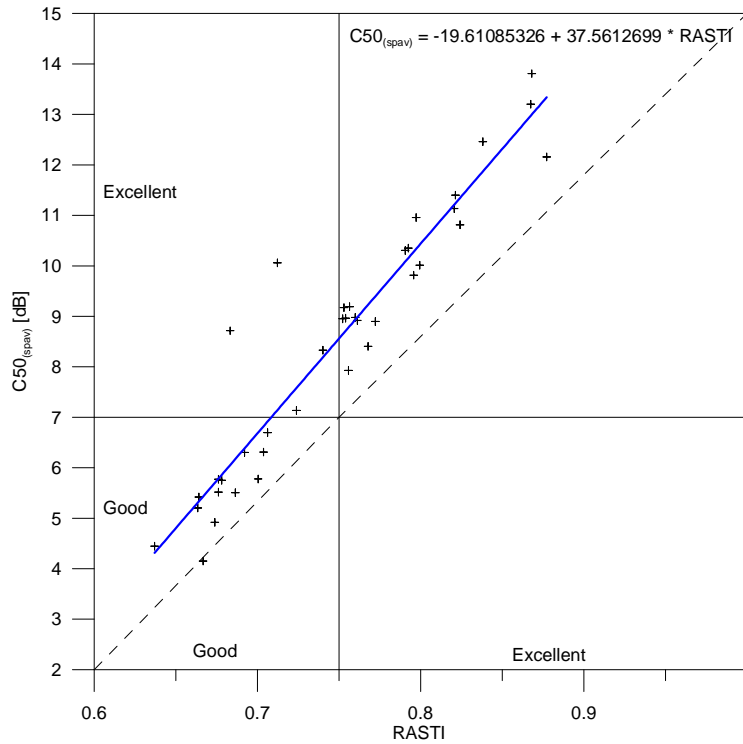
366

Fig. 11. The RASTI measured values versus $C_{50(spav)}$ which was measured in A3 lecture hall, with their subjective qualification range.

7. Conclusions

In this paper is shown the intelligibility of speech assessment based on two methods: RASTI coefficient and C_{50} coefficient which based on energetic relation.

For readjust C_{50} coefficient to the intelligibility of speech assessment was applied signal filtration which was proposed in [4].

The assessment the lecture hall for the intelligibility of speech on the basis of RASTI leads to the following:

- very good intelligibility of speech determined by RASTI method (for RASTI≥0.75) is for the first three rows and also partially for middle rows,
- for the first three rows RASTI≥0.75 is not fulfilled for nine seats located in upper left corner,
- for rows from fourth further very good speech quality is only on 20 seats,
- for the rest of the lecture hall RASTI is from 0.6 to 0.75.

367

Assessment the lecture hall for the intelligibility of speech on the basis of $C_{50\ (spav)}$ leads to the following:

- very good speech quality determined by $C_{50\ (spav)}$ parameter (for $C_{50(spav)} \geq 7$dB) is on the first three rows and also for middle rows,
- for the rest of the lecture hall $C_{50\ (spav)}$ is from 4 dB to 7 dB.

The comparing of RASTI coefficient and $C_{50\ (spav)}$ coefficient displayed similarity of obtained results.

In this article was analyzed also impulse response properties of investigated lecture hall.

It was found, that the lecture hall has good from the point of view of intelligibility of speech initial time delay gap value.

Inside the investigated lecture hall occurs of flutter echo phenomenon which is acoustic defect. This phenomenon has not appreciable influence on the intelligibility of speech inside the investigated hall.

References

[1] Gołaś A., *Metody komputerowe w akustyce wnętrz i środowiska*, Wydawnictwo AGH, Kraków 1995.

[2] Gołaś A., *Podstawy sterowania dźwiękiem w pomieszczeniach*, Wydawnictwo AGH, Kraków 2000.

[3] Sadowski J., *Akustyka w urbanistyce, architekturze i budownictwie*, Arkady, Warszawa 1971.

[4] Marshall LG., *An acoustic measurement program for evaluating auditoriums based on the early/late sound energy ratio*, J Acoust Soc Am 1994;96:2251–61.

[5] T. Zamarreno, S. Giron, M. Galindo, *Assessing the intelligibility of speech and singing in Mudejar-Gothic churches*.

[6] *ISO 3382. Measurement of the reverberation time of rooms with reference to other acoustical parameters*, 1997.

CALCULATING THE UNEQUAL BUILDING SETTLEMENTS LOCALISED ON THE EXPANSIVE GROUNDS IN REGARD TO CHANGES OF SOIL MOISTURE

Maria Mrówczyńska[*], Sławomir Gibowski[*]

[*] Institute of Structural Engineering, Faculty od f Civil and Environmental Engineering, University of Zielona Góra, Podgórna 50, 65-516 Zielona Góra, Poland.

1. Abstract

The displacement measurements are carried out to get some information on the object deformation. They are also done to determine essential changes in the object exploitation and in the improvements of designing the similar objects in the future. On account of both variables in time and their different action density of changeable random conditions, the displacement measurements are vital for the building safety in the period of object exploitation.

The calculating of unequal building displacements located on the glacitectonic disturbances grounds (called the expansive grounds) in regard to the changes of soil moisture was presented in this paper. Displacements of controlled points located on the building were calculated by the levelling measurements carried out during the five measurement periods. The model of controlled points' displacements was determined on a definite reference system as a set of given points within a fixed reciprocal constancy. The value changes of points' displacements were described in this paper as well. These value changes were observed before, during and after the building repair work.

2. Introduction

A lot of factors connected with the building construction have an impact on the building deformation. The building construction should be adequate for the conditions, in which a given building is to be built. The grounds are vital in the building engineering because the ground heterogeneity may cause a non-uniform building displacement. The ground deformation may happen (among other things) as a result of the changes of ground volume. These changes are caused by periodic soil moisture changes. The measurements results of periodic and non-uniform building displacements are presented in the paper. The building was located on expansive grounds. The measurements were carried out by a precise levelling method with the application of a levelling instrument Ni 007.

3. The geologic structure

The geotechnical and laboratory research was done to determine ground-water conditions of the area where a monitored object was located. As a result of this research the following groups and complex deposits were found under the footing [3]:

- Pliocene silt of basin accumulation formed as dusty silt in a geological way,
- Neogene silt and sand formed as dusty silt, dusty firm clay and thick sand,
- Pleistocene glacial deposit of the middle-Polish glaciation formed as fine and mean sand,
- Pleistocene deposits of direct continental glacier accumulation of the middle-Polish glaciation formed as clay sand, sandy clay, and dust sand.

There were four kinds of grounds under the footing in the geotechnical way. These ground kinds were marked as A, B, C and D [3]:

A zone – water glacier sand;
B zone – water glacier sand having a changeable soil depth. There was clay in the range from 1m to 6 m below this sand;
C zone – tertiary silty firm loam and silty clay;
D zone – glacier silty loam below the tertiary clay;

The ground water was only present near the northern-eastern corner of the building at the depth of 2,40 m below the ground level. The ground water was also noticed at the depth of 3,20 m in the sand ground.
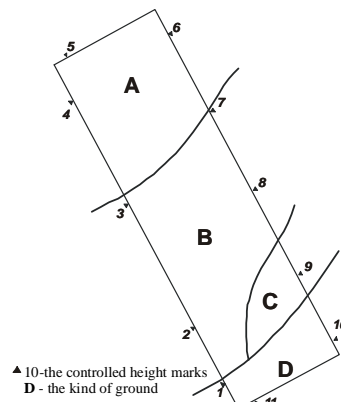

Fig. 1. The ground area below the footing.

4. The characteristic of measurements research

The examined object was represented by eleven controlled points located on the building walls at the height of about 0,50 m above the ground level. The layout of measuring points was dependent on the geologic and engineering conditions.

The displacement values were carried out on the basis of the following five measuring periods:

- January – June, 2000 – before the building reconditioning
- October – December, 2001 – during the building reconditioning
- February - June, 2002 – after the building reconditioning
- November, 2002 – the controlled measurement carried out 9 months after the end of the building reconditioning
- October – November, 2006 – the controlled measurement carried out 4 years after the end of the building reconditioning.

The measurements were done once a month in each period. The twenty-two observations of height differences were carried out in each period within an equal structure of the measuring-controlling set.
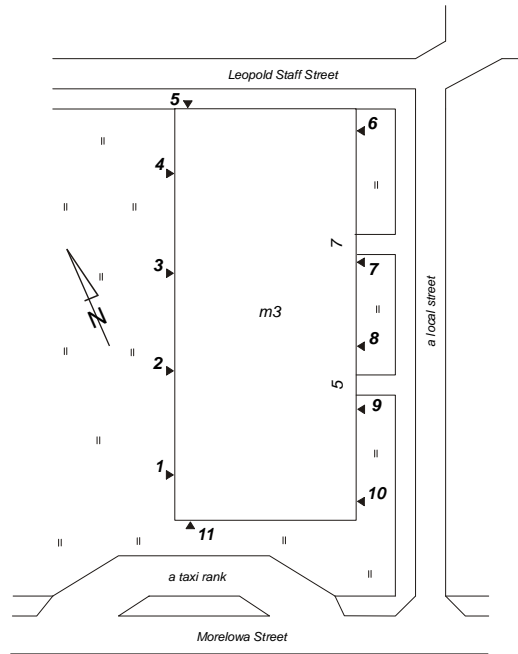

Fig. 2. The location of the controlled height marks on the monitored building.

5. A definition of a reference system

Determining of displacements values is dependent on a defined reference system. The defined reference system stands for a set of points having a fixed reciprocal constancy. Identification of the reference system points consists in carrying out the analysis of

changes of geometrical features values of the interior sets of space points $R^1 : \{S^1\}$ and $\{S^2\}$ and the elimination of all these elements of both sets which discriminate the objects (O^1) and (O^2) against the compatibility of these features. The identification process consisted of the two stages:

- the preliminary identification,
- the final identification.

The preliminary identification stage aims at determining the most possible numerous set of points which can remain the reciprocal constancy within the defined approximation. Firstly, the set was adjusted within the minimal limitation of the freedom degrees by the means of a least square method. The restriction was put on a random point in the following form:

$$\Delta h = 0 . \tag{1}$$

This preliminary way of working out of measurements results does not include conditions of the done observations; hence the relations between the observations results and the determined parameters are not deformed. The potential presence of wrong observations on the basis of a number ratio verification of correction values to their means errors can be observed in the course of the preliminary identification. If the following condition (2)

$$\frac{|v|}{m_v} \leq 2 \tag{2}$$

is met, hence it can be assumed that the done observations do not contain any large errors [4]. The observations adjustment carried out by the least square method is applied on the assumption that the observations errors come under a normal distribution $N(0,1)$. This assumption may be proved by applying a test of compatibility of corrections vector distribution $V = (v_1, v_2, ..., v_m)$ with a normal distribution by the means of the statistics χ^2.

The differences of geometrical features values of the interior points sets $\{S^1\}$ and $\{S^2\}$ were determined by the minimization of the modules sum of the components vector of apparent displacements [1]. The n-element set $\{P\}$ was created to meet the condition (3).

$$[|p|] = \min . \tag{3}$$

The elements of this set are sorted out on the following condition:

$$|p_{i-1}| \leq |p_i| \leq |p_{i+1}| . \tag{4}$$

372

The correct approximate values of controlled points' displacements can be obtained as a result of minimization of the modules sum of the component vector of apparent displacements. The final identification consisted in testing a reaction of an observation system. The above-mentioned reaction was caused by the increase of number of points meeting the condition of the absolute constancy $(\Delta h = 0)$ in the adjustment process. The minimal value of the square norm of a correction vector E_0 was obtained in the process of adjustment within the minimal limitation of freedom degrees. The critical value of the increase of the square norm of a correction vector ΔE_k (fig. 3) can be obtained, for any given points concentration within the size k classified as constant, from the following formula [1]:

$$\Delta E_k = -2(m^2 + \frac{m^2}{2r})\ln(1 - 0.95^{1/k}) ,$$ (5)

where:
ΔE_k – increase of square norm of a correction vector,

r – number of freedom degrees,

m – mean error of an observation obtained in the adjustment within the minimal limitation of freedom degrees,

k – number of points meeting the condition of the absolute constancy,

0,95 – confidence level of the points identification of a reference system.

The course of increase of the square norm of a correction vector, as a result of increasing number of points meeting the condition of the absolute constancy in the adjustment process, and the critical value of the increase of the square correction sum was presented in the fig. 3.
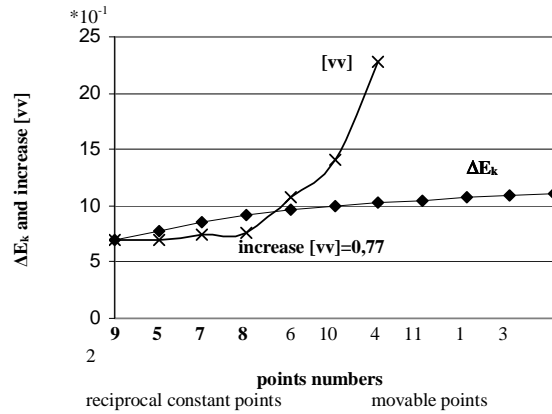

Fig. 3. Definition of a reference system based on the increase of the square norm of a correction vector ΔE_k.

A defined reference system based on a set of points having a reciprocal constancy is a flexible set because there is each point of this set in the range of $[-2m, +2m]$ (the confidence level $P = 0,95$ – the formula (5)). The vector of the base increase of interior features of the reference system points is a random vector, therefore the fixed displacements values may be attributed as being the most likely to be true.

6. Remarks on a discrete solving of displacements problem

The engineering-construction objects located on the glacitectonic disturbances grounds are exposed to the influence of vertical strengths. Therefore, in this given case the issue of geodetic measurements concentrates on the research of foundation settlements.

The deformation model of each object located on the expansive grounds has its own individual characteristic. This characteristic can be described by the relationship between the causes and the deformation parameters. Determining of a deformation state, which is in accordance with reality, requires determining a correct model of the controlled points' displacements. Furthermore, the correct model depends on a defined reference system.
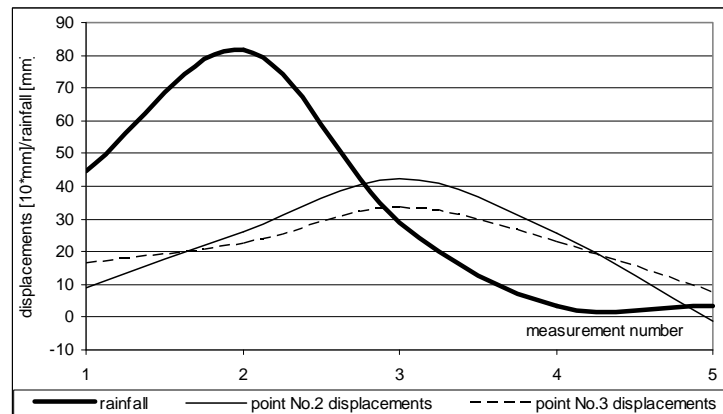

Fig. 4. The vertical displacements of points No. 2 and 3, depending on the rainfall intensity in the period from January to June, 2000.

The direction of displacements of the controlled points changed under the influence of the changes of ground-water conditions (rainfall) which had occurred in the course of the research (fig. 4).

7. The observation results

The values of determined displacements in the separate measuring periods were presented in the tables I-IV. The graphical displacements of a chosen measuring period

374

were presented in the figs 5-8. The changes of displacement of values for two pointes No. 2 and 3 were shown in the fig. 9. These two points' displacements were the highest in the measuring period from January to June, 2000 in the way of their value. Hence, the highest displacements occurred before the building reconditioning period.

**Table I. Displacement values of controlled points in the period
from January, 2000 to June, 2000.**

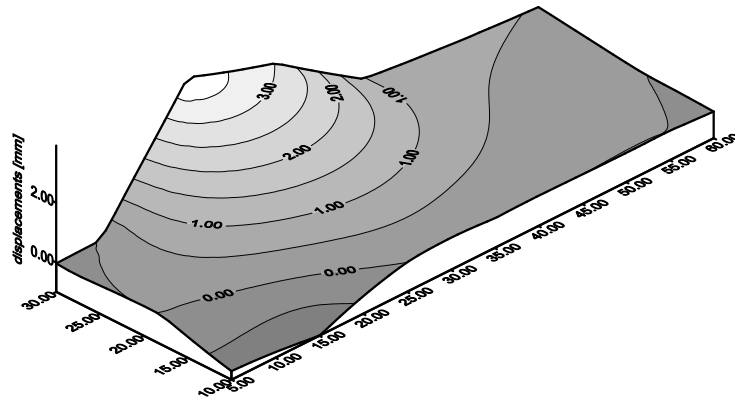| Date of measurement	Point number										
	1	2	3	4	5	6	7	8	9	10	11
02.2000	0.25	0.88	1.62	1.21	0.96	0.86	0.33	0.28	-0.21	0.00	0.04
03.2000	0.41	2.61	2.23	0.94	0.59	0.33	-0.07	0.00	-0.46	-0.47	0.10
04.2000	0.76	4.22	3.34	1.00	0.20	0.05	-0.23	0.00	-0.64	-1.11	-0.13
05.2000	0.65	2.57	2.31	1.30	0.58	0.28	0.00	-0.04	-0.63	-0.70	0.03
06.2000	0.34	-0.12	0.78	2.04	1.51	0.74	0.58	0.10	0.00	0.02	-0.02

Fig. 5. The displacements of controlled points observed in April 2000, before the building reconditioning.

**Table II. Displacement values of controlled points in the period
from October, 2000 to December, 2001.**

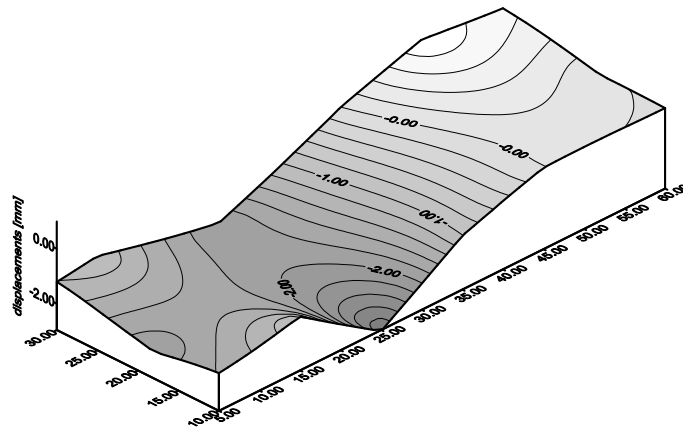| Date of measurement	Point number										
	1	2	3	4	5	6	7	8	9	10	11
10.2001	-0.11	-1.49	-0.19	0.02	-0.19	0.07	0.08	-0.82	-2.46	-0.30	0.29
11.2001	-1.97	-2.36	-0.16	1.09	0.06	0.33	-0.17	-1.44	-3.50	-1.64	-2.18
12.2001	-1.86	-2.84	-1.51	8.02	-0.31	0.08	-0.30	-23.21	-4.13	-1.26	-1.70
12.2001	-2.11	-1.82	-0.19	8.80	0.00	0.98	0.08	-22.93	-4.57	-1.24	-2.27

375

Fig. 6. The Displacements of controlled points obtained in November, 2001
(during the building reconditioning period).

**Table III. Displacement values of controlled points in the period
from February, 2002 to June, 2002 and November, 2002.**

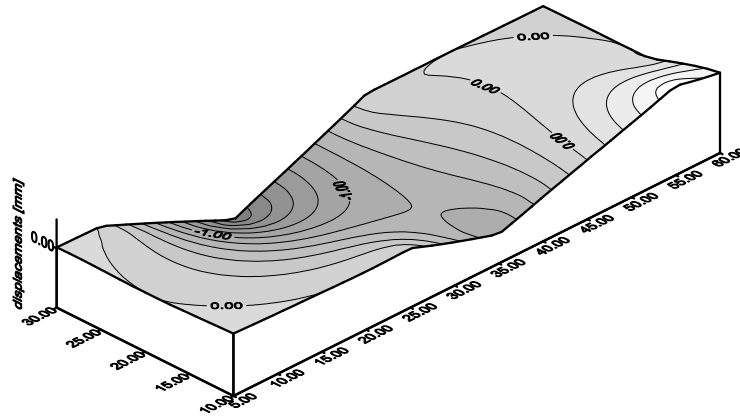| Date of measurement	Point number										
	1	2	3	4	5	6	7	8	9	10	11
03.2002	0.11	0.08	0.03	-0.16	-0.43	0.23	-0.05	0.11	-0.10	-0.03	0.04
04.2002	0.15	0.38	0.52	-0.02	-0.71	0.00	-0.25	0.04	-0.11	-0.08	-0.05
05.2002	0.15	0.78	0.71	0.01	-0.72	-0.08	-0.20	0.03	-0.06	-0.31	-0.17
06.2002	0.11	0.51	0.65	0.02	-0.50	0.00	-0.32	-0.25	-0.41	-0.75	-0.35
06.2002	0.15	0.00	0.31	-0.01	-0.11	0.46	0.04	0.00	-0.18	-0.09	-0.13
11.2002	-0.67	-2.23	-0.50	0.00	0.51	1.02	0.18	-1.06	-0.80	-0.02	-0.48

Fig. 7. The displacements of controlled points observed in November, 2002
(9 months after the end of the building reconditioning).

376

Table IV. Displacement values of controlled points in the period from October, 2006 to November, 2006.

Date of measurement	Point number										
	1	2	3	4	5	6	7	8	9	10	11
11.2006	-3.00	-5.34	-5.44	0.40	0.04	-0.24	-0.20	-4.54	-4.26	-2.42	-2.76
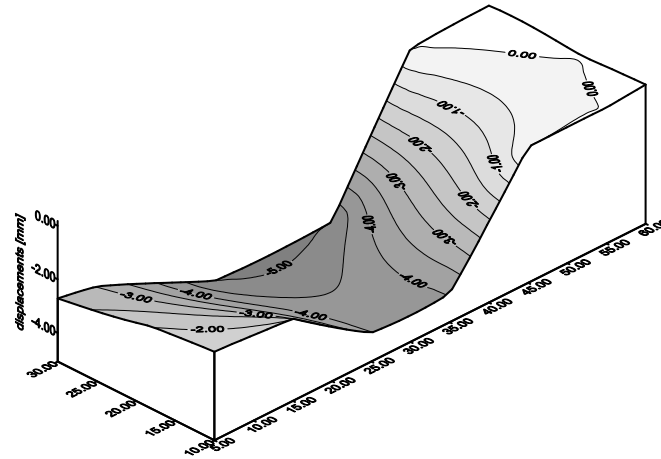
Fig. 8. The displacements of controlled points observed in November, 2006
(4 years after the end of the building reconditioning).
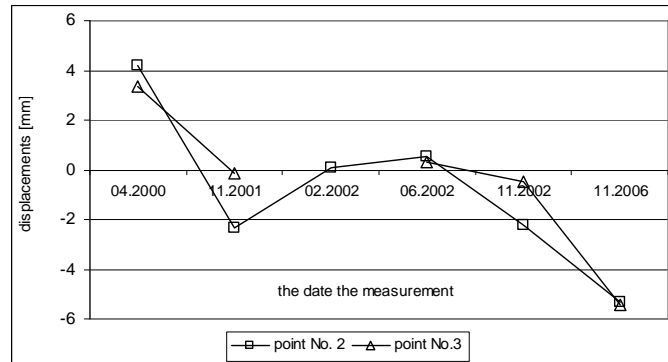
Fig. 9. The displacements of points No. 2 and 3 in the following measurements periods.

8. Summary and conclusions

The geodetic measurements are one of vital and helpful elements of the geologic and engineering research while determining the causes, the range and dynamics of the deformation of buildings located on the expansive grounds.

The obtained results prove the usefulness of the described geodetic method and they also enable to determine more precisely the cause, the value and the range of the object deformation. The obtained results of the geodetic observations were the basis for beginning the necessary building protection repairs in order to protect the building from disadvantageous influence of soil moisture changes. The geodetic measurements have been continued up till now and they have mainly aimed at carrying out the research on usefulness of the protection applied during the building reconditioning.

References

[1] Gil J., *Badanie nieliniowego geodezyjnego modelu kinematycznego przemieszczeń*, monografie nr 76, Wydawnictwo Wyższej Szkoły Inżynierskiej w Zielonej Górze, Zielona Góra 1995,

[2] Gil J., Mrówczyńska M., *Przemieszczenia budynku posadowionego na gruntach ekspansywnych*, Przegląd Geodezyjny nr 2/2002,

[3] Kotowski J., Kraiński A., *Geotechniczne uwarunkowania przyczyn zróżnicowanych osiadań budynku przy ul. Staffa w Zielonej Górze*, 2001

[4] Nowak E., *Badania przemieszczeń drogą statystycznej weryfikacji poprawności modelu i obserwacji*, Instytut Geodezji Wyższej i Astronomi Geodezyjnej Politechniki Warszawskiej – materiały sympozjum naukowo – technicznego.

CHOSEN ENVIRONMENTAL (METEOROLOGICAL) FACTORS INFLUENCING A CONSTRUCTION HAZARD

Marek Pałys[*], Dorota Latos[*], Andrzej Klewski[**], Konrad Maj[**],
Marek Antosz[***], Bogusław Bartosik[****]

* Institute of Roads and Bridges, Faculty of Civil Engineering,
Warsaw University of Technology, Armii Ludowej 16, 00-637 Warsaw, Poland.
**Department of Geodesy, Faculty of Civil Engineering and Geodesy,
Military University of Technology, Kaliskiego 2, 00-908 Warsaw, Poland.
***Centrum Operacji Powietrznych, Pyry, Poland.
****Civil Aviation Office, Żelazna 59, 00-848, Warsaw, Poland.

Hazards for construction objects in form of loads caused by natural atmospheric phenomena, as well as anthropogenic influences in the area of Poland require a complex approach. Loads in civil and communication engineering come from such phenomena as: insolation, winds, precipitation and lightning, as well as temperature differences.

A common denominator for the above phenomena is their identification in time and space in the area of Poland, as well as elaboration of methods of their measurement in real time. So, an idea has been coming to life in the last twenty years to realise a series of doctoral and MS theses, aiming at preparing theme extreme maps including values of the previously presented phenomena, as well as the measurement of the latter in real time. It gave rise to a number of doctoral theses related to connecting burdensome phenomena harmful for construction sector with geographic and spatial information systems, as well as standardization and maintenance works in communication construction sector. Below are presented some of above-mentioned theses in a lapidary way:

Dr Eng. Antoni Czajkowski – *"Model research of the dynamics of front areas in the lower troposphere* and creation of forecast maps"*. The aim of that work was automatic diagnosis of the activity of front areas and discontinuity areas.

Dr Eng. Leszek Korpus — *"Selected elements of atmosphere teledetection"*. That work includes measurements of wind laps on runways and lidar visibility measurement.

Dr Eng. Szymon Supernak – *"Use of teledetection results in the expert system structures"*. The work treats about the improvement of weather phenomena forecasting taking into account a huge amount of information from different sources such as satellites, radars, lidars, sodars and conventional sources (station observations, road sensors). The work presents effective integration of the stored data and effective processing of large streams of information about the environment from an extended computer network and from teledetection sources.

Dr Eng. Ewa Krzywańska – *"Mapping of insolation of an urbanised area"*. The work presents changes of insolation caused by the modification of environment and town

379

planning processes. The above changes are presented in form of a model. Subsequent theme maps of insolation were created for different stages of the investment process (Sadyba Housing Settlement, Szwoleżerów Housing Settlement) for study and project purposes.

Dr Eng. Marek Antosz – *"Teledetection identification of the condition of airports in different meteorological situations".* The work discusses environmental conditioning of a thermal status of the pavement of roads and airports, measurement methods used in the road thermal monitoring system, methods of forecasting glazed frost based on diagnostic methods, pavement energy balance model, operational capabilities of forecasting of icy runways.

MS Eng. Bogusław Bartosik – *"Teledetection and mapping of the electric condition of atmosphere over the area of Poland".* This work shows analysis of the electric condition of atmosphere, analysis of methods of detection and location of lightning and analysis of measurement data.

MS Eng. Dorota Latos – *"Management of the construction and exploitation of a highway in a spatial information system".* The work contains the analysis of the possibility to use numerous data in SIP/GIS in relation to a highway, among others, information about meteorological hazards on the basis of data obtained in real time – processed so that appropriate services can react rapidly.

Eng. Grzegorz Małetka – "*Organisation and support of the seasonal maintenance of roads and highways based on the Spatial Information System in changeable environmental conditions*".

There have also been a few postgraduate and MS works related to: lidar measurements of the wind speed; maintenance of runways of Okęcie airport with the load of snow and icing; environmental conditions of construction and communication objects in relation to the city island of heat; migration of transborder contamination.

At present the focus of attention of the above group returned thanks to the development of laser scanners and cameras to measurements of the geometric imperfection of construction objects (MS Eng. Krzysztof Wojciechowski), air pollution caused by industrial plants (senior doctor lecturer Marek Pałys), as well as port waters in the process of reloading crude oil (senior doctor lecturer Eng. Andrzej Klewski, D Eng. Konrad Maj). Those measurements are taken by teledetection (contactless, from a distance) and are related to local measurements.

Going back to the purpose of this paper. It is not to discuss a influence of specific factor but to show the importance of the whole atmospheric system on the strength basis of few examples.

The atmospheric environment ceaselessly affects built features. At spring and summer the most crucial elements are solar radiation, rain, wind, lighting; at autumn and winter they change to icing and very dangerous frozen water in cracks, the latter could cause even a scatter of a construction.

A weather caused building disaster – it is when it comes to people how much constructions are exposed to the action of environmental elements. Exactly in the very centre of natural disaster one fully understand how strongly a manmade structures are open to the environment phenomena.

During last few years, in Poland, there were a number of situations where an intensified impact of weather conditions brought a tragedy.

In 1997, enormous rains at the south of Poland, resulted in catastrophic flood in Wroclaw. Only in a few days, exposed to the water deeds buildings, roads and bridges have been destroyed. In the pictures below, it can be seen an affected construction of bridge, destroyed houses and routes.
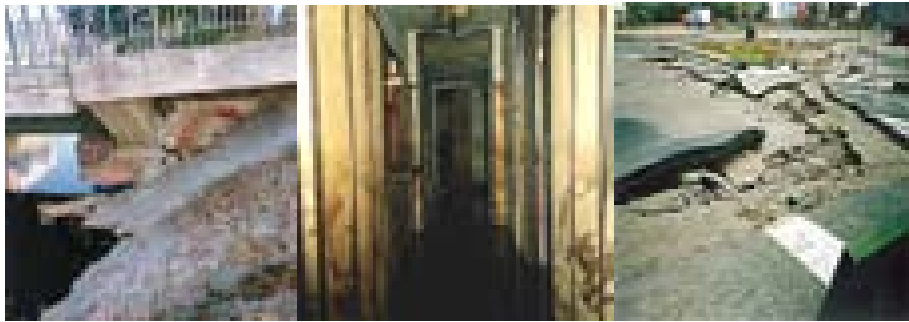
BRIDGE   HOUSE   ROUTE

Other element – wind – it's occurrence can be seen mainly regarding to the tall structures but not only. Strong winds could for example: part electric lines causing prolonged and major power failures, damage roofs, destroy bridges (see picture below).

BRIDGE

On account of the readers interest in the loads of constructions caused by the wind. The wind field is not numerical, but volumetric. The measurement of temperature gradients or a medium density – hence the idea of the wind as a phenomenon of potential compensation – is not limited to classic descriptions of a horizontal Kirchoffov's flow round of objects and vertical measurement of temperature gradient (translated into speed).

Lidar methods of measurement of vertical and horizontal components of the wind in real time have been for 20 years the most important telematic measurements locating density by-passes (wind laps) of constructions.

A heavy solar radiation affects and finally destroys a surface of roads. Lightings makes fires. An ice-covered roof was a trigger of deadly collapse of market hall in Katowice. There are many more examples of grievous impact of the nature on buildings and such way on people.

Each year, thousands of properties are damaged or destroyed by lightning. Lightning is responsible for more deaths and property loss than another meteorological phenomenon like tornadoes, hurricanes and floods. Lightning can strike anywhere on the earth. So its very important to know where and when it can appear.

The petroleum industry's history provides many evidence of the destructive nature of lightning activity and the resulting fires. Millions of euros of petrochemical products and facilities are destroyed each year by lightning related phenomena in many parts of the world. Each years lives are lost as the direct result of being in personal proximity to these facilities when they are ignited or explode due to lightning strike. The risk of losing a tank of product due to lightning is very small, but it can happen.

Examples of the foregoing may be found from Poland fire of 1971 in Czechowice Dziedzice where a tank was set on fire by lightning. The second example is Trzebinia fires of 2002 where tank was ignited by lightning related fires too. These are only two examples of very specific dangerous situations.

The direct lightning strike risk

The risk of a direct lightning strike to any facility can be estimated from the related isokeuranic number, the size, high and other factors related to the facility location. The isokeuranic number is a number of lightning per year for a given location. The best way for estimate a isokeuranic number is a preparation a lightning density map. For preparation we need a lot of historical lightning data (no less than 5 years period) which are transformed by GIS software into special thematic map.

The cause of lightning strike related fires

There are two major causes of lightning related flammables fires: a direct strike and secondary effects. A direct strike to the facility, where the flammables are stored can cause fires by heating effects of the stroke, or stroke channel. Secondary effects include four separate phenomenon: bound charge, electromagnetic pulse, electrostatic pulse and the earth currents.

382

Hazard identification

Cloud to ground related lightning strikes are identified as a major environmental factors that could cause flammable storage tank explosion. The main task for hazard identification is a calculate how many lightning strike is expected during a period of time, for example one year. To calculate of that number is necessary to use properly data from lightning density map.

Lightning density maps for Poland area

To obtain maps of the lightning density over Poland for any period we use data from the lightning detection system. The one year is the minimum period which is necessary to made that kind of the thematic maps, but recommended is five year period. Using secondary type of lightning data and any GIS software we can create our own different kind of maps according special requirements. For example we can made:

- maps of lightning density for year, month or season.
- maps of distribution of lightning current for year, month or season (see below).

383
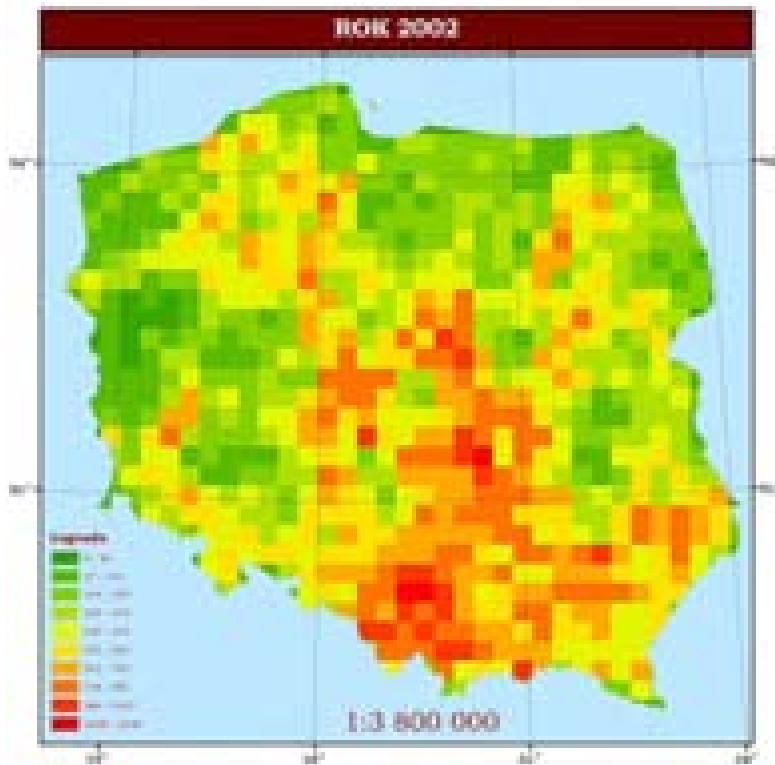
References

[1] ITS Polska, wrzesień 2001r.

[2] Fagerlund G., *Trwałość konstrukcji betonowych*, Arkady.

[3] Tracz, M. et al., *Oceny oddziaływania dróg na środowisko*, 1, 2.Ekodroga, 1997, Cracow.

[4] Kareem, A., *Wind Effects on Structures: A Probabilistic Viewpoint*, Probabilistic Mech., 2(4), 1987, 166-200.

[5] King R. W., *Construction Hazard and Safety Handbook*.

PRESENTATION
OF THE ORGANISERS

DEPARTMENT OF STRUCTURAL MECHANICS AT FACULTY OF CIVIL AND SANITARY ENGINEERING OF LUBLIN UNIVERSITY OF TECHNOLOGY (POLAND)

❖ **Employees of the Department of Structural Mechanics**

- **Head of the department:**
  1. Prof. Andrzej Flaga, Eng. Ph.D. D.Sc.
- **Secretary:**
  2. Marta Gregorczyk, Eng.
- **Assistant professors:**
  3. Ewa Błazik-Borowa, Eng. Ph.D.
  4. Jarosław Bęc, Eng. Ph.D.
  5. Jan Golec, Eng. Ph.D.
  6. Tomasz Lipecki, Eng. Ph.D.
  7. Jerzy Podgórski, Eng. Ph.D.
  8. Elżbieta Polonis-Gowin, Eng. Ph.D.
- **Assistants.**
  9. Tomasz Nowicki, Eng. M.Sc.
  10. Jacek Szulej, Eng. M.Sc.
  11. Piotr Wielgos, Eng. M.Sc.

- **The address of our website:**
  http://akropolis.pol.lublin.pl/users/kmb/

❖ **Lines of scientific activity**

Special fields of scientific workers are:
- building aerodynamic, wind engineering, environmental effects on buildings and people
- structural mechanics, computer methods in structural and fluid mechanics (Finite Element Analysis System, Finite Volume Method)
- fracture mechanics

❖ **Lines of didactic activity**

- Theoretical Mechanics, Structural Mechanics, Classical Mechanics, Theory of Plates and Shells
- Introduction to Computer Science, Computer Methods in Structural Engineering, Finite Element Analysis
- Facultative subjects: Environmental Effects on Buildings, Computer Graphics

❖ **The most important scientific work**

Our recent scientific researches were supported by Polish State Committee for Scientific Research:
- *Dynamic analysis of wind action on cable stayed structures in conditions of aerodynamic coupling* , 1997-2000
- *Simulation of wind load on two round cylinders in conditions of aerodynamic interference*, 1998
- *Static and strength analysis of crystal roofs*, 1999
- *Aerodynamics of beam cable structures*, 2000-2003
- *Aerodynamics of guyed masts*, 2001
- *Numerical researches into rock cutting zone*, 2001-2004, 2006-2008

❖ **Publications and monographs**

Our publications include both handbooks and scientific monographs.
- **Handbooks and manuals**
  1. A. Flaga, *Mechanika budowli (Structural mechanics)* (t2)
  2. J. Podgórski, E. Błazik-Borowa, *The Finite Element Method in Static Problems for Engineering Structures*
  3. E. Błazik-Borowa, J. Podgórski, P. Sulik, *Solutions of Structure Problems Using the Algor System*

388

- **Scientific monographs:**
  1. E. Błazik-Borowa, A. Flaga, M. Kazakiewicz, *Problemy interferencji aerodynamicznej dwóch walców kołowych* (*Problems Aerodynamic Interference of Two Circular Cylinders*)
  2. A. Flaga, J. Miełaszwili, *Konstrukcje sterowane w inżynierii lądowej* (*Controlled Structures in Civil Engineering*)
  3. A. Flaga, E. Błazik-Borowa, J. Podgórski, *Aerodynamika smukłych budowli i konstrukcji prętowo-cięgnowych* (*Aerodynamics of Slender Buildings and Bar Cable Structures*)

❖ **Computer programs**

Scientific workers are the authors of computer programs used in scientific researches, engineering planning and the didactic process of such subjects as: *Computer Methods in Structural Engineering, Structural Mechanics, Finite Element Analysis System*

- **Wind_Sym** –computer program for simulating random three-dimensional wind field
- **Aerodynbud** – program aids aerodynamical calculations of slender beam cable structures
- **Stelm** – program enables **SSAP1** (a module of **Algor** version 11 and lower) to carry out a modal analysis of beam cable structures
- **Pret_r2** – program for structural analysis of two-dimensional frame constructions
- **Sklerometria** – computer program which processes data obtained from a sclerometer test
- **KAM_Shell** – design environment facilitates for a KAM (© Z. Kacprzyk) system which is used for teaching FEA algorithms
- **RMA** – program for managing **Algor's** modules version 11 and lower (it replaces **Roadmap**)
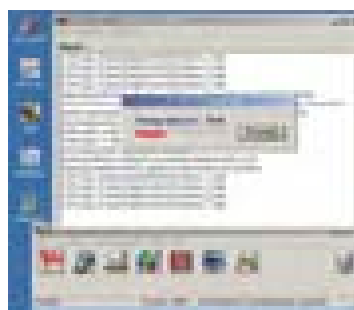
❖ **Scientific symposia**

The Department of Structural Mechanics organizes periodically scientific symposia on environmental effects on buildings and people. The first three symposia gathered members of Polish research groups engaged in these problems. The present one (the fourth symposium) became international in character. The symposia *"Environmental Effects on Building and People – actions, influences, interactions, discomfort"* take place in picturesque sites: Lublin (1994), Kazimierz Dolny (1997), Zwierzyniec (2001), Susiec (2004), Kazimierz Dolny (2007).

## ❖ Scientific work, analysis and expertise

Workers of the Structural Mechanics Department have realized many advanced jobs for industry. The most important problems are:

- Analysis of state caused by excessive ground settlement under spot footings of a boiler at Nitric Plant in Puławy (1994)
- A design for a Roman Catholic church in Tylmanowa (1994-1995)
- Assessment of technical state of a cooling tower's shell at a power plant "Adamów" near Konin (1995)
- An expert opinion of technical state of boiler's foundations at heat and power generating plant in Nitric Plant in Puławy (1996)

- Assessment of harmfulness of vibrations caused by traffic to two high blocks of flats (1997)
- An expert opinion of static stability of a reinforced concrete chimney 200 meters in height in Łódź (1998)
- A technical design for an aerial mast 120 meters in height in Giedlarowa near Leżajsk (1999)
- Complex aerodynamic calculations of the John Paul II cable-stayed bridge in Gdańsk (2000)
- Complex aerodynamic calculations of cable-stayed bridge on a Siekierki route in Warsaw (2001)
- Static and strength analysis of MID formwork produced by DELTA-ZREMB S.A. in Międzyrzec Podlaski (2002)

Most III Tysiąclecia
im. Jana Pawła II w Gdańsku

- Aerodynamic calculations of the arch bridge over Vistula river in Puławy (2007)
- Aerodynamic calculations of the roof over Lech Poznań stadium
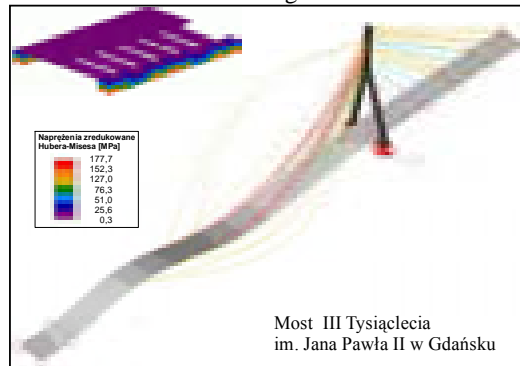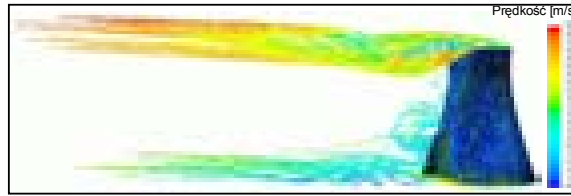
We offer realization of analyses, expert opinions and trainings.

- **Expert opinions:** on buildings and structures within the scope of stability and fulfilling standards
- **Calculations, modeling and simulations:** realization of all kinds of engineering calculations applying to civil engineering structures such as masts, bridges, towers, industrial structures and so on.
- **Planning and design:** realization of designs for all kinds of buildings
- **Trainings** and courses on computer technique in civil engineering planning especially courses in using computer systems such as **ALGOR**, **ABAQUS**, **FLUENT**.
- **Measurements:** providing measurements of building and ground vibrations
- **Aerodynamic measurements:** measurements in a wind tunnel (in cooperation with Cracow University of Technology)

Most Siekierkowski w Warszawie
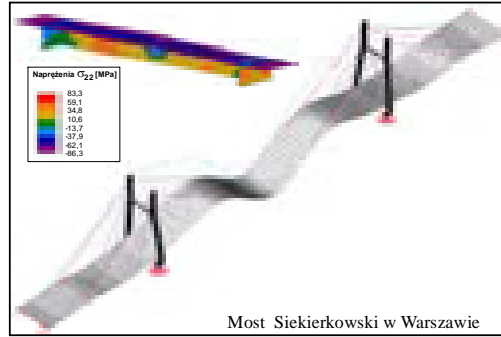
We have in our disposal measurement equipment and professional computer programs for performing advanced analysis:

- **SPIDER8:** an 8-channel universal measurement device (produced by Hottinger Baldwin Messtechnik HBM) for measurements of vibrations, displacement, temperature, sound and tensor quantities
- **Measurement sounders:** three HBM accelerometers of B12/200 type that enable measurements in the range of 0 to 200 Hz; two Brüel & Kjaer 4508 accelerometers that enables measurements in the range of 0.3 to 8 kHz; two HBM inductive displacement sensors of WA/200 and WA/20 type that enable measurement in the range of 0 to 20/200 mm.
- **CATMAN:** a computer program used as a controller and an analyzer for the SPIDER8 measurement device.
- **SVAN 910A:** portable vibration and sound analyzer with built-in vibration transducer.

- **ABAQUS:** computer finite element analysis system that enables static and dynamic calculations of all kinds of structures in the range of elastic, elastic and plastic geometrical non-linear work of construction, computer simulation of events and temperature or electric fields.
- **ALGOR**: computer finite element analysis system that is used for static and dynamic calculations with allowance of geometrical and material non-linearity, simulation of coupled mechanic and temperature fields.
- **FLUENT:** computer system that enables calculation and simulations of laminar or turbulent fluid flows and chemical changes.

Wind Engineering Laboratory
Institute of Structural Mechanics
Civil Engineering Departament
Cracow University of Technology
Ave. Jana Pawla II 37/3a, 31-864 Cracow
Tel. (012) 628 35 70
Fax.(012) 628 35 66
E-mail: aflaga@usk.pk.edu.pl
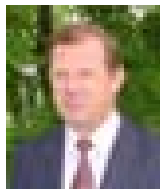
Andrzej FLAGA[*]

[*] Prof. dr hab. inż. - Lublin University of Technology and Cracow University of Technology

WIND ENGINEERING LABORATORY
WITH A BOUNDARY LAYER WIND TUNNEL
OF THE CRACOW UNIVERSITY OF TECHNOLOGY

1. Introductory

Wind Engineering Laboratory with a boundary layer wind tunnel which permits wind simulation in the ground boundary layer is a new organizational unit of the Cracow University of Technology (CUT). It functions within the Institute of Structural Mechanics of the Civil Engineering Faculty. The Laboratory is housed on the territory of the CUT in the building No. 3a, al. Jana Pawła II 37, Cracow-Czyżyny.

In the laboratory, experimental and computational works in the following fields of wind engineering are realized:

- Wind physics in the ground boundary layer (1);
- Aerodynamics of buildings and structures (2);
- Aerodynamics of mobile engineering objects (3);
- Wind and wind-environmental climate (4);
- Wind power engineering (5);
- Normalization, codification and regulation of various wind engineering problems (6).

393

The following faculties of CUT are interested in these fields of wind engineering: Civil Engineering Faculty (CEF) – fields: 1, 2, 4, 6; Environmental Engineering Faculty (EEF) – fields: 1, 4, 5; Architecture Faculty (AF) – field 4 and partly fields 1 and 2; Mechanical Engineering Faculty (MEF) – fields: 3, 5 and partly field 1.

Moreover, the mentioned fields of wind engineering are the subject of interest of structure engineers, architects, town development engineers, specialists in air conditioning and environmental engineering, mechanical engineers and others.

The basic data characterizing the wind tunnel are presented in figures 1 and 2.
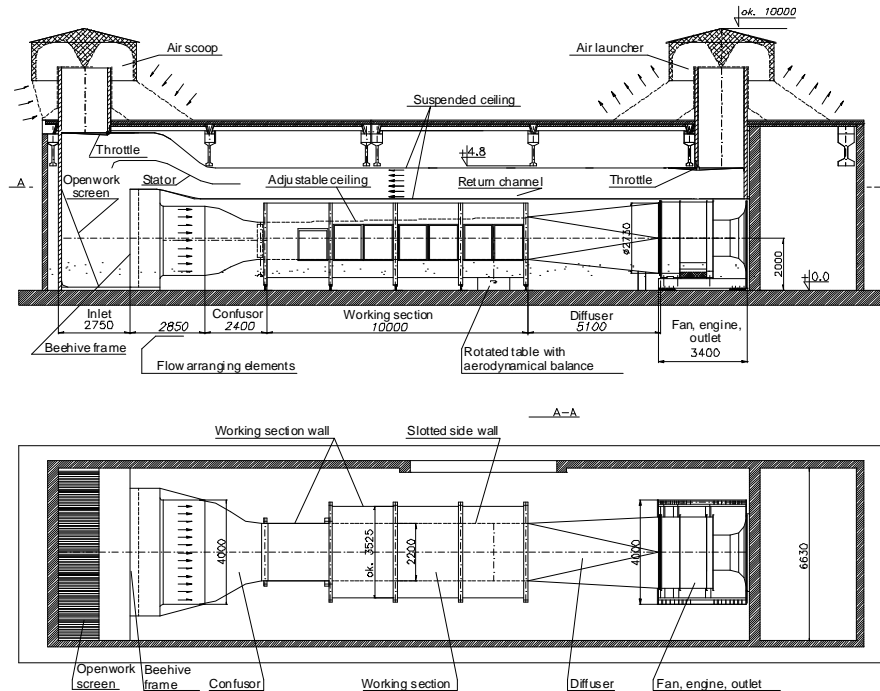
Fig.1. View from the side (a) and from the top (b) of the wind tunnel.

Kinds of experimental and computational works carried out in the wind tunnel are as below:

- Didactic works (lectures, laboratories, post graduate studies, training courses, diploma works) (CEF, EEF, AF, MEF);
- Studies and scientific researches, doctoral thesis (CEF – mainly, EEF, AF, MEF);
- Research investigation works (including grants) for the needs of national economy and individual and institutional customers;
- Services, consultations, expert opinions, standardization and codification works to individual and institutional orders.
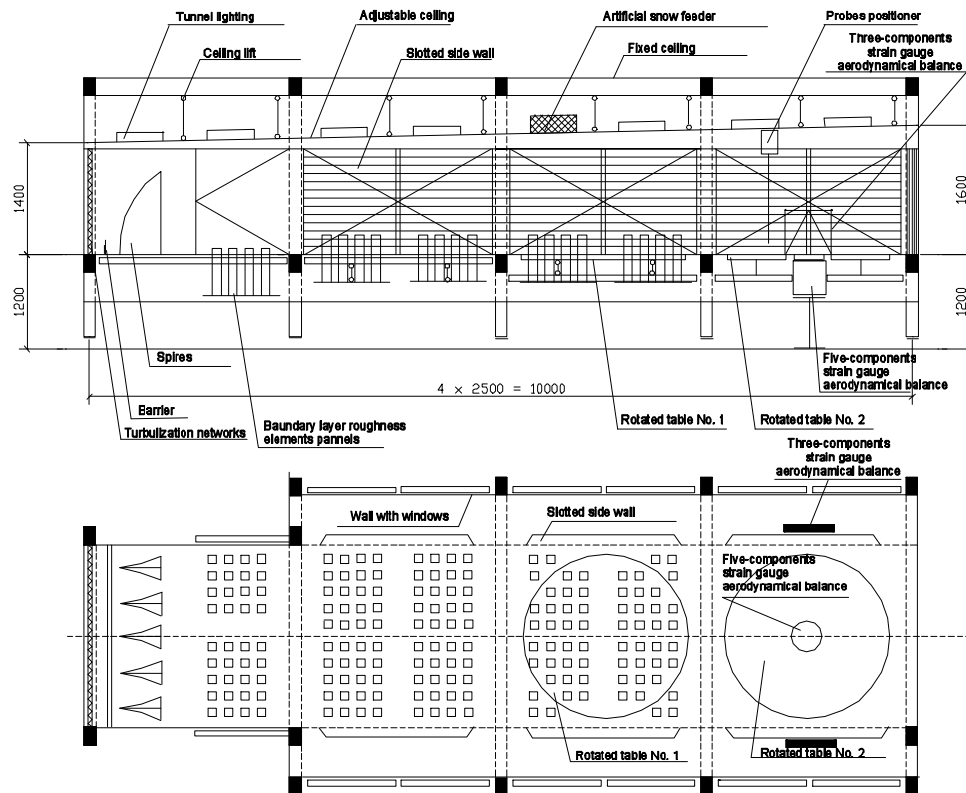
394

Fig. 2 Working section of the wind tunnel: vertical section (a), horizontal section (b).

2. Basic technical data of the boundary layer wind tunnel

- Type of the wind tunnel

Wind tunnel of a mixed circuit: 1. Closed (at closed throttles) when the air flowing out from the tunnel tube through the outlet returns to the tunnel tube through the return channel above the tunnel tube; 2. Open (at opened throttles) when the air inflowing into the inflow comes from outside the building by an air scoop located above the inflow on the building roof and is exhausted also outside the building by an air launcher located over the outlet on the building roof. The open air circuit in the wind tunnel is applied mainly in the case of visualization investigations.

395

- Stator, openwork screen, inflow, beehive frame, stabilization chamber, confusor.

These elements are to take over the stream returning either through the return channel above the wind tunnel or also taken above the building roof by external air scoop and direct it respectively, making the stream homogeneous and of a very low turbulence before the inflow to the working section.

- Working section

The basic geometric dimensions of the working section are: width – 2.20 m; height – from 1.40 m at the beginning and 1.60 m at the end of the working section; length – 10 m. Formation of the mean wind velocity profile and atmospheric turbulence takes place in the first part of the working section at the length of 6 m by use of respective turbulization networks, barriers, spires and blocks of respective geometry and a mechanically controlled height. Four characteristic segments each of 2.5 m long can be distinguished in the working section. The side walls of the front segment are full (with windows) 2.20 m apart. The other segments have slotted side walls (with horizontal controlled slots aiming at diminution of the so called blockage effect) 2.20 m apart and full side walls with windows 3.40 m apart. In the third and fourth segment of the working section there are two round tables 2 m in diameter, rotational of the rotation angle to 180°. The first one is designed mainly for examination of flow around phenomena and their visualization and for examination of wind environment climate. The other rotated table is designed mainly for aerodynamical and aeroelastic investigations of buildings and structures. In the upper part of the working section there is an equipment for fixing all kinds of measurement probes and their controlled displacement at the whole working section in directions x, y, z.

The roof of the working section may change its position in the direction up and down; this permits to control the gradient of static pressure in the working section. In the back part of the working section there are localized two tensometer aerodynamical balances for measurements of aerodynamic forces and moments: one of five-components for vertical models, the other of three-components for horizontal models.

- The diffuser with the net protecting the fan

The diffuser which is behind the working section is of a rectangular shape at the beginning part and of a circular shape at the end part (cross-section of the fan) and it's length is equal to 5 m.

- The fan

The axial fan, single-stage of efficiency 0.8-0.9, of the outer diameter 2.72 m and of the velocity of the end of the fan blade 100m/s, is located on the suction side of the wind tunnel.

- System of supply and rotation control

The engine of the alternate current, shorted, driving the fan axially of 200kW, nominal revolutions 750 r.p.m., supply voltage 220V, controlled by inverter.

- Maximum mean flow velocity in the working section

$V_{max} = 40$ m/s.

396

3. Characteristics of works carried out in the Wind Engineering Laboratory

3.1 Experimental works with the use of the wind tunnel

The following basic investigations are carried out in the wind tunnel:
- Measurements of velocity and turbulence of flow;
- Measurements of wind pressures in the flow;
- Measurements of wind pressures on the models walls;
- Measurements of aerodynamical forces and moments acting on the whole model or its sections in plane flow;
- Measurements of vibrations of aeroelastic models;
- Investigations of pollution spreading.

3.2. Computational works using computer technics

The Wind Engineering Laboratory is equipped with computers and its own and commercial programmes permitting the use of computational works concerning mainly the following items:
- Simulation of the wind velocity field for the typical categories of the territory roughness (e.g. category of terrain A, B, C accordingly to the standard) (own programmes);
- Simulation of statical and dynamical wind action on buildings and structures according to the quasi-steady theory considering vortex excitation and determination of static and dynamic response of tower structures (chimneys, towers, tall buildings, masts, cooling towers etc.), suspended bridges, light footbridges and other slender structures in rather typical situations but not comprised by standards (own programmes);
- Numerical analysis of aeroelastic instability of divergence, galloping, torsional flatter and bending-torsional type, vortex excitation in critical condition of vortex shedding, galloping in the wake etc. of slender buildings and structures (own programmes and computational approaches);
- Numerical simulation of wind pressure distribution (possibly aerodynamical forces and moments) and velocity fields of the air flow and flow around buildings and structures not susceptible to dynamic wind effects of simple geometry using various computer programmes of the vigorously developing numerical fluid dynamics or numerical wind engineering (commercial programmes).

3.3. Didactic works

The wind tunnel with its equipment offers a new practical approach for didactics which up till now was absent at CUT and other technical universities in Poland. It enables students to understand many problems which sometimes cannot be shown in another way which is especially valuable taking into account the fact that impact (both positive and negative) of the wind is often underestimated.

397

3.4. Consultations, expert opinions in the field of wind engineering

The Wind Engineering Laboratory realizes ordered works in the field of consultation, expert opinions etc. concerning wind engineering. These may be connected with: 1.Designing of bearing structures, housing walls and roofs of various structures; 2. Architectural and town development designing; 3. Various problems of environmental engineering; 4. Aerodynamics of various engineering objects etc.
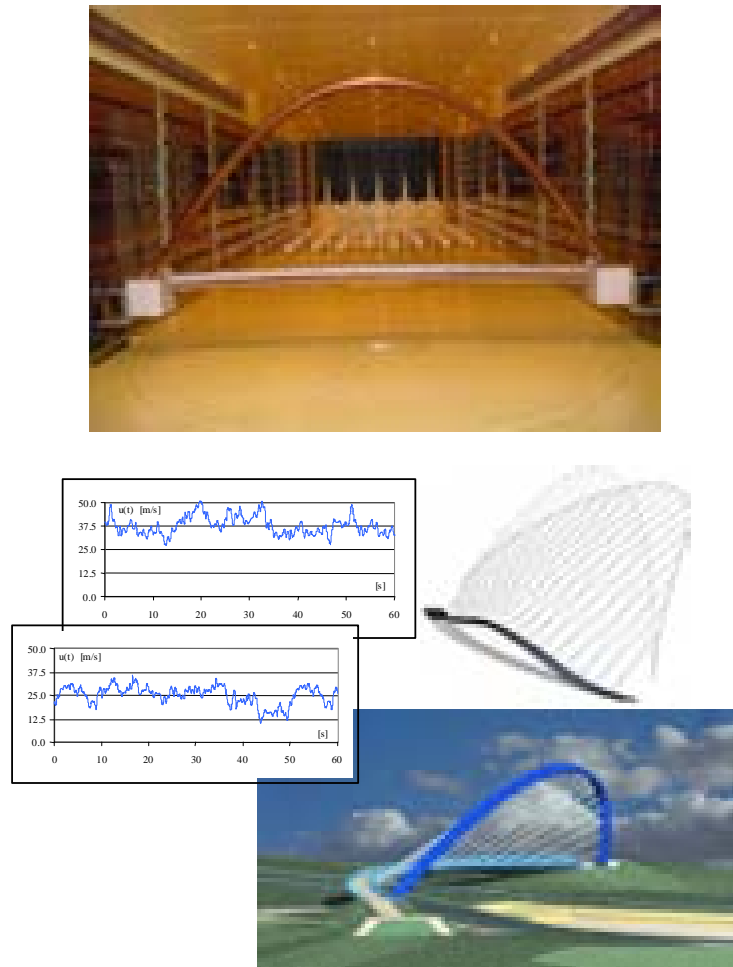

Fig. 3. Aeroelastic model of a footbridge over Drogowa Trasa Srednicowa in Katowice.
Aerodynamical calculations of the footbridge designed in Katowice.

398

Fig. 4. Sectional model of a steel chimney in a frame-truss housing.

Fig. 5. Model of the Christ the King World Saviour Monument and the Polonia Unity Center in Tarnow.
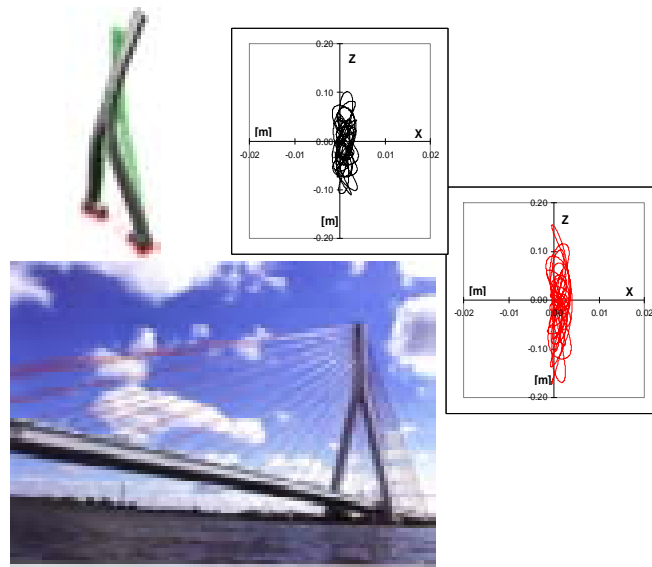
Fig. 6. Aerodynamic calculations of the Third Millenium John Paul II Bridge in Gdańsk.
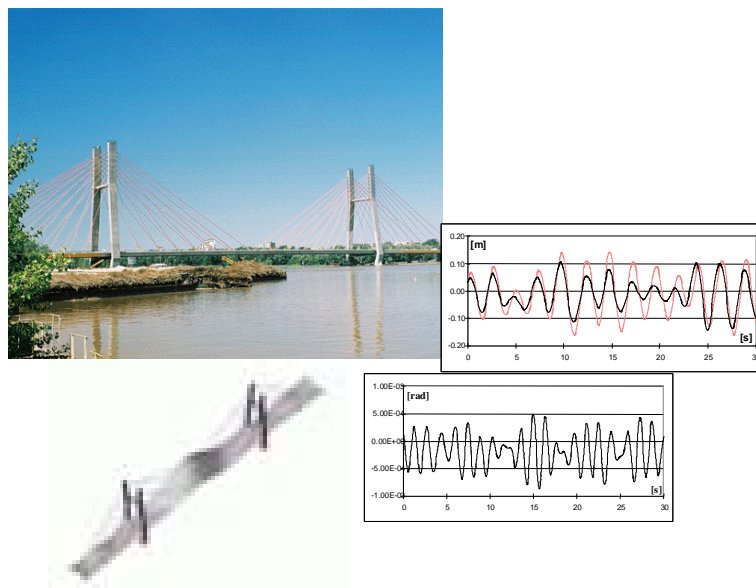
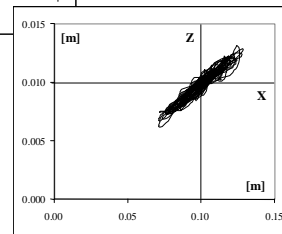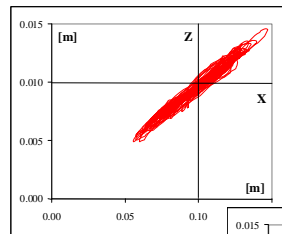Fig. 7. Aerodynamic calculations of the Siekierkowski Bridge in Warsaw.
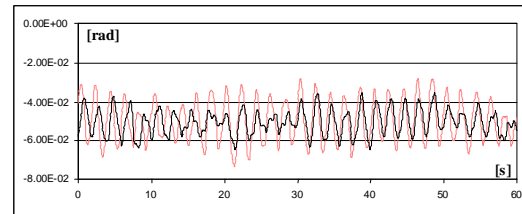
400

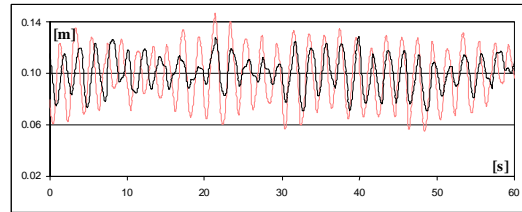Fig. 8. Aerodynamic calculations of the footbridges in:
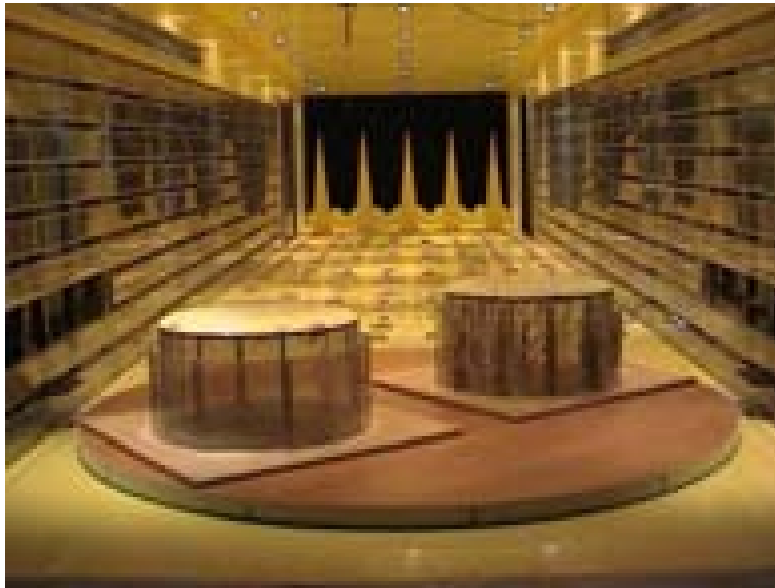Myślenice, Piwniczna, Tropie, Tylmanowa.

401

Fig. 9. Wind tunnel tests of aerodynamic interference between two steel double-wall fuel tanks.

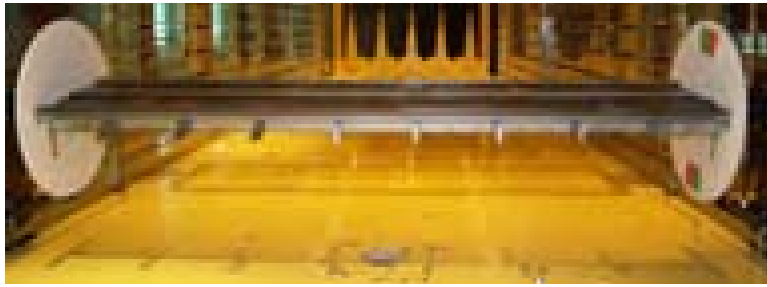Fig. 10. Wind tunnel tests of municipal stadium roof in Tarnów.

402

Fig .11. Model investigation of arch bridge over Vistula river in Puławy
Sectional models of: a) bridge deck (1:60), b) arch (1:10), c) hangers (1:1.1)
in working section of wind tunnel.

Fig. 12. Wind tunnel tests of stadium roof in Poznań.